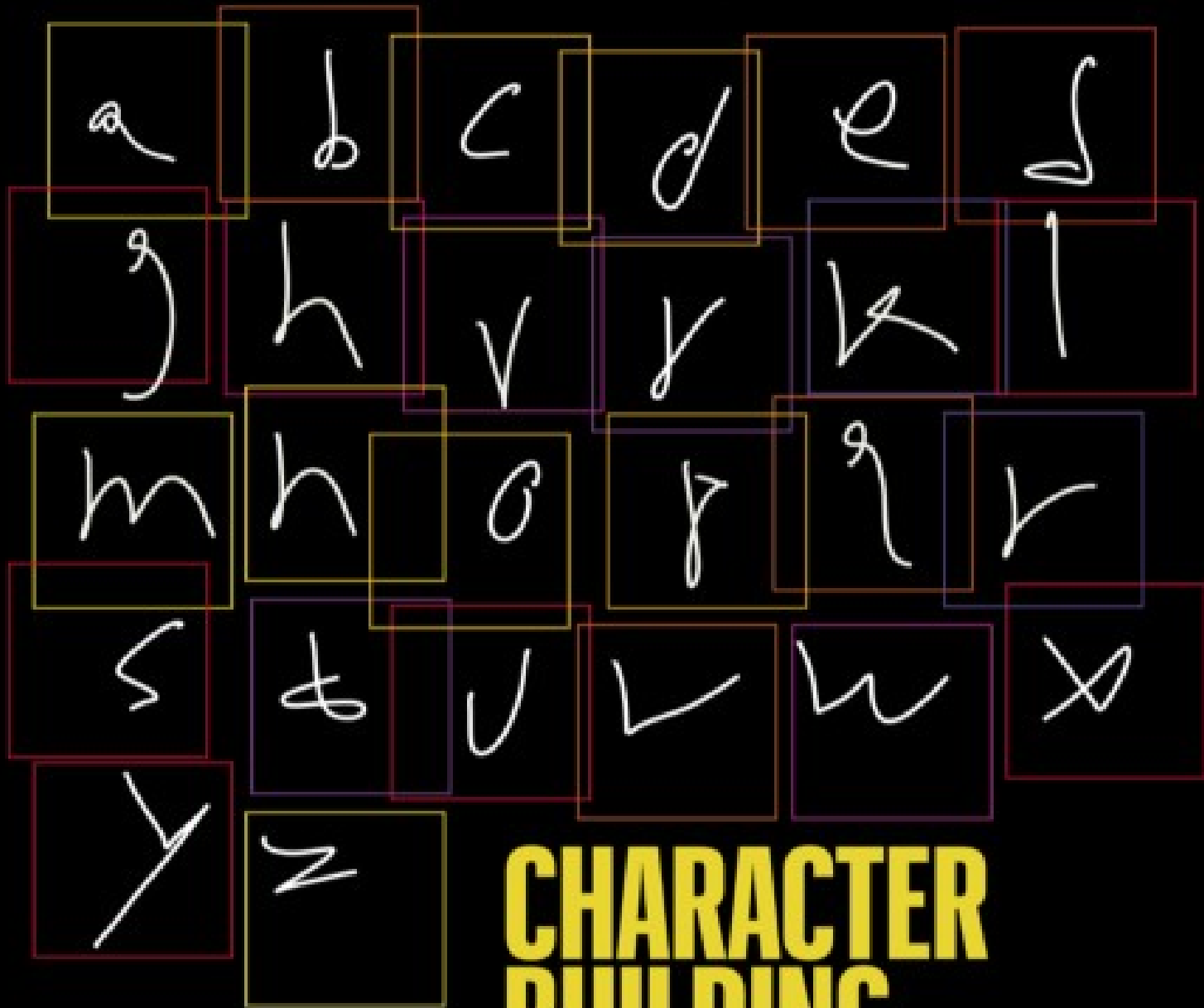


# nature



## CHARACTER BUILDING

Brain-computer interface translates thoughts of handwriting into typed text

### Coronavirus

How COVID-19 put evidence-based medicine to the test

### Natural resources

Protect, manage and restore ecosystems to cool the planet

### Up in the air

A mechanism for the formation of formic acid in the atmosphere

# Nature.2021.05.15

[Sat, 15 May 2021]

- [This Week](#)
- [News in Focus](#)
- [Books & Arts](#)
- [Opinion](#)
- [Work](#)
- [Research](#)
- [Amendments & Corrections](#)

---

| [Next section](#) | [Main menu](#) |

---

# Donation

---

| [Next section](#) | [Main menu](#) |

# This Week

- **[Give research into solar geoengineering a chance](#)** [ 12 May 2021]  
Editorial • There is no substitute for aggressive cuts in greenhouse-gas emissions. But the risks and benefits of technologies that could mitigate global warming need to be evaluated.
- **[Evidence-based medicine: how COVID can drive positive change](#)** [ 12 May 2021]  
Editorial • The pandemic has spawned too many uninformative clinical trials and reviews. Reform is needed to ensure the world gets the high-quality evidence it needs.
- **[Stop the emerging AI cold war](#)** [ 11 May 2021]  
World View • Proliferating military artificial intelligence will leave the world less safe — so we must focus on ethics and global cooperation.
- **[How does a cylinder levitate? Scientists explain the maths behind the magic](#)** [ 06 May 2021]  
Research Highlight • A model shows how a spinning cylinder can stay suspended in the air next to an oil-slicked moving belt.
- **[Antarctic rocks on the rebound could raise sea level much more than expected](#)** [ 06 May 2021]  
Research Highlight • When the ice covering the west of the continent disappears, the bedrock could rise up and shove extra water into the ocean.
- **[The error-prone step at the heart of making an embryo](#)** [ 07 May 2021]  
Research Highlight • High-resolution imaging shows why the union between two sets of chromosomes goes awry as least as often as not.
- **[Forests that float in the clouds are drifting away](#)** [ 04 May 2021]  
Research Highlight • Tropical cloud forests are safe havens for a vast range of creatures and plants, but they are under siege around the globe.
- **[Forget Stonehenge: the first known massive monuments are much older](#)** [ 04 May 2021]  
Research Highlight • The Arabian Peninsula is dotted with hundreds of mysterious structures dating to the sixth millennium BC.

- **How headless worms see the light to steer** [ 03 May 2021]  
Research Highlight • Light-sensitive cells, distributed throughout its body, help a simple creature to do the extraordinary.
- **How itchy are you? A new device knows precisely** [ 30 April 2021]  
Research Highlight • A skin patch that monitors scratching is far less invasive than the infrared camera recordings used now.

---

| [Next section](#) | [Main menu](#) | [Previous section](#) |

EDITORIAL

12 May 2021

# Give research into solar geoengineering a chance

There is no substitute for aggressive cuts in greenhouse-gas emissions. But the risks and benefits of technologies that could mitigate global warming need to be evaluated.



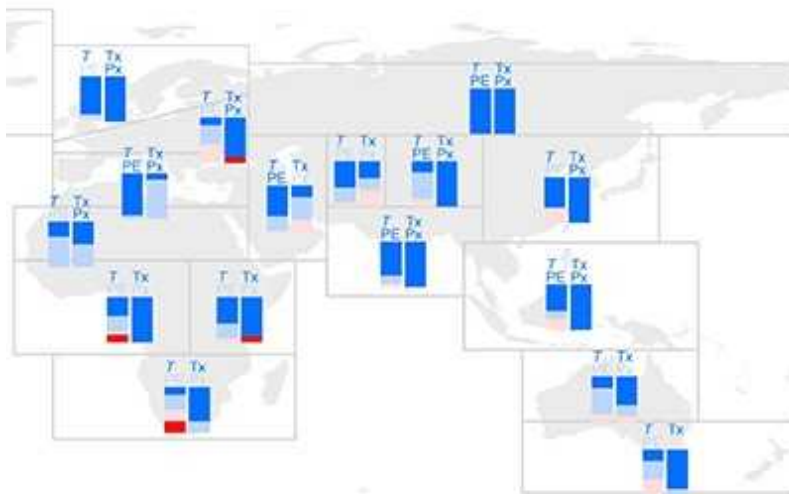
Solar geoengineering can involve adding reflective particles to Earth's atmosphere to cool the planet. Credit: NASA/ZUMA Wire/Shutterstock

By at least one measure, US President Joe Biden's online climate summit last month was a success: several governments, including that of the United States, made [fresh pledges to reduce greenhouse-gas emissions](#). Combined with earlier announcements from other countries and the European Union, these pledges would reduce emissions in 2030 by the equivalent of more than 3 billion tonnes of carbon dioxide, more than the current annual carbon

emissions of India. But even this reduction — if achieved — would not be enough for the world to remain on a plausible path to limit warming to 1.5 °C relative to pre-industrial times.

World leaders must look for ways to close that gap at the United Nations climate convention in Glasgow, UK, in November, and then implement their commitments. Clearly there is a long and difficult road ahead. So governments and scientists must continue evaluating carbon capture and other climate strategies that can be used to remove carbon dioxide from the atmosphere. They should also explore solar geoengineering, which involves altering clouds or adding reflective particles to the stratosphere to reflect sunlight back into space and cool the planet. The effect of such stratospheric injections would be similar to the cooling that happens after volcanic eruptions.

Some studies suggest that solar geoengineering could provide much-needed short-term relief if global warming becomes unbearable ([P. Irvine et al. \*Nature Clim. Change\* 9, 295–299; 2019](#)). But technical, environmental and ethical questions remain, including how to ensure that the cooling works as desired — and who decides the setting for the thermostat. And then there are the potential knock-on effects, which could vary across regions and sectors of society ([J. Proctor et al. \*Nature\* 560, 480–483; 2018](#)). More research is needed to understand these issues.



## Halving warming with solar geoengineering

Some scientists are vociferously opposed to solar geoengineering, which could go awry in unpredictable ways and, once started, could be difficult to safely shut down. There are also concerns that even a move to research solar geoengineering creates ‘moral hazard’, leading to misplaced confidence and detracting from efforts to rein in greenhouse-gas emissions. Some who oppose it fear that once research begins, the roll-out of the technology will be unstoppable, no matter what the findings.

Researchers who study geoengineering counter that the science needs to be understood, and that the world must consider the thorny questions of international governance that would arise if a country moves forward with an ill-conceived programme. But researchers have struggled to raise funding, conduct experiments and address legitimate concerns about their work.

In March, scientists working on the Stratospheric Controlled Perturbation Experiment (SCoPEx) had to cancel a balloon flight scheduled for June in Sweden. The flight, designed to test equipment that would be used in future experiments involving the release of particles, faced opposition from environmentalists and representatives of northern Scandinavia’s Sami communities, who argued that geoengineering research is a distraction from other work on climate change. An advisory committee recommended delaying the flight to allow for further public engagement.

Until now, public bodies have not prioritized reaching such a consensus. But two welcome developments suggest there is potential for this to happen.



## US pledges to slash greenhouse emissions

The US National Academies of Sciences, Engineering, and Medicine [recommended in March](#) that the US government establish a coordinated federal research programme to investigate solar geoengineering. It is the most explicit call yet from a major scientific body for a government research programme, and comes at the right time.

Costing US\$100 million to \$200 million over 5 years, the multi-agency programme would explore the core environmental science of altering clouds or releasing particles on a large scale, as well as the ethics and public perception of this technology. The proposal includes a code of conduct, and a public registry for research proposals and results. The academies also called for broad international engagement, information sharing and discussions about global governance. This is crucial: solar geoengineering would affect the entire planet, and the United States must not go it alone.

There is also progress on the international front. The Carnegie Climate Governance Initiative (C2G), an advocacy group based in New York City, has been working to engage the UN on solar-geoengineering research and governance issues. In March 2019, environment ministers debated a resolution calling on the UN Environment Programme to assess geoengineering science and technology. That measure failed, in part because of opposition from the administration of former US president Donald

Trump. Switzerland and other countries are preparing to bring forward a fresh resolution next year. And C2G is working to have solar geoengineering discussed at the UN General Assembly in 2023.

There are models for how to promote the collaboration sought by the US national academies. One is the Solar Radiation Management Governance Initiative, which promotes and funds solar geoengineering research in the global south. The organization has sponsored workshops in 14 countries and, since 2018, has paid out more than \$430,000 to fund research in eight countries, including Bangladesh, Iran, Benin and Jamaica.

Solar-geoengineering research brings risks, and there are other, more-promising ways to address global warming. But the world remains on a path to dangerous climate change, and future generations will bear an increasing burden. Governments need to step up climate efforts, and evaluate all possible options for action. If solar geoengineering is harmful, leaders will need evidence so that they can rule out the technology.

Nature **593**, 167 (2021)

doi: <https://doi.org/10.1038/d41586-021-01243-0>

## **Jobs from Nature Careers**

- - - [All jobs](#)
    - 
    - [Postdoctoral Research Fellow in Urban Climate Action](#)

[The University of British Columbia \(UBC\)](#)

[Vancouver, Canada](#)

[JOB POST](#)

- **Postdoctoral Fellow in Supercapacitor Technology**

The University of British Columbia (UBC)

Kelowna, Canada

JOB POST

- **Postdoctoral Researchers x 2 – Advancement of audit procedure for domestic and non-domestic energy compliance tools, SFI MaREI Centre, NUI Galway (NUIG-RES-095-21)**

National University of Ireland Galway (NUI Galway)

Galway, Ireland

JOB POST

- **Semantic Web Developer**

European Molecular Biology Laboratory (EMBL)

Hinxton, Cambridge, United Kingdom

JOB POST

---

This article was downloaded by **calibre** from <https://www.nature.com/articles/d41586-021-01243-0>

## EDITORIAL

12 May 2021

# Evidence-based medicine: how COVID can drive positive change

The pandemic has spawned too many uninformative clinical trials and reviews. Reform is needed to ensure the world gets the high-quality evidence it needs.



Evidence from randomized controlled trials has been essential to showing that COVID-19 vaccines work. Credit: Aloisio Mauricio/Fotoarena/ZUMA Press

The past year was a turbulent one for Archie Cochrane, despite his having been dead for more than 30 years. A Scottish doctor and seminal figure in the history of medicine, Cochrane questioned the standard way doctors

decide how to treat disease — which was based largely on their opinion. Fifty years ago, Cochrane proposed that decisions should instead be based on rigorous evidence<sup>1</sup> — particularly randomized controlled trials — and he later challenged medics to build useful summaries of such studies.

Billions of people alive today have probably benefited from these ideas. Cochrane and other pioneers inspired a movement called evidence-based medicine, in which research-based evidence informs doctors and patients in decisions about care. In 1993, an international network known as the Cochrane Collaboration (now called just Cochrane) was founded; this group and others have assembled a vast library of systematic reviews in medicine and other disciplines, providing a foundation of evidence that has helped to save many lives.



### How COVID broke the evidence pipeline

But the COVID-19 pandemic has been one of the biggest tests yet of evidence-based medicine — and has shown that the current system falls short in a fast-moving global emergency. There have, of course, been huge wins. Randomized controlled trials have been crucial to testing the safety and efficacy of drugs, as well as the vaccines that will bring the pandemic to an end. But as a [Feature in \*Nature\* reports](#), the pandemic also resulted in many wasteful clinical trials that were too small to produce useful results —

and an accompanying wave of systematic reviews, many of them of low quality, repetitive and quickly out of date.

## Time for change

It's important that researchers, doctors and global leaders assess what worked, what didn't and why, and make recommendations for change. They must fix the evidence pipeline so that it is stronger and better able to supply timely, high-quality evidence — not just for the next pandemic, but for everyday health emergencies, from malaria to heart disease.

A prime opportunity will arrive in October, at a meeting of global-health leaders organized by Cochrane and the World Health Organization (WHO), as well as other members of a group called COVID-END (COVID-19 Evidence Network to support Decision-making). The heads of COVID-END are also planning to convene a global commission of thought leaders to assess how best to supply evidence to address social challenges, such as climate change and inequality, that go well beyond health. This group has a unique opportunity to refine, re-imagine and re-engineer processes for the generation, supply and use of research-based evidence and so ensure that our future world is one better informed by rationality and fact.



## RECOVERY 1 year on: a rare success in the COVID-19 clinical trial landscape

In a systematic review, researchers typically define a question. Does keyhole surgery help knee pain in middle-aged people? Does hydroxychloroquine prevent COVID-19 deaths? They then search for and collate all the relevant, high-quality studies that can help to answer the question, and analyse the pooled results. A systematic review should make sense of the balance of evidence when individual studies conflict.

But during the pandemic, the challenges of producing such reviews were exposed. A rigorous systematic review often takes a year or two to complete, which is too long to wait when urgent answers are required. The pace of research and volume of results produced during the pandemic made it impossible to keep some reviews up to date; yet systematic reviews and other evidence syntheses have poured out. In 2010, researchers estimated that about 11 systematic reviews were published per day, in a paper<sup>2</sup> that asked despairingly, ‘how will we ever keep up?’ By 2019, that figure had exceeded 65; today, one database contains some 9,000 evidence syntheses related to COVID-19 alone, about 21 for every day since the WHO characterized the outbreak as a pandemic. Taken together, this means that doctors, policymakers and others who are desperate for authoritative reviews of evidence can struggle to find what they need.

## **Keeping up**

The fundamental principles of evidence-based medicine stand firm; it’s the processes that need to evolve. When the Cochrane Collaboration was formed, its founders knew that reviews must be regularly updated with the latest research. But, in practice, this is often difficult because of the laborious nature of the literature searches and data synthesis required.

New methods can help. Last year, a group at the Institute for Evidence-Based Healthcare at Bond University in Gold Coast, Australia, published a full systematic review completed in two weeks, using a skilled team and automated tools to search for and extract data<sup>3</sup>. And during the pandemic, scientists collaborated to quickly produce ‘living’ systematic reviews on

potential COVID-19 therapies, which are updated as new studies come out. Researchers must now evaluate the best methods for generating fast reviews and living ones, as well as deciding on which topics it's worth investing in them.



### [It's time to invite more people to join clinical trials](#)

The pandemic has shown that large, coordinated clinical trials that span hospitals and test multiple treatments against one condition offer an excellent way to include sufficient numbers of patients to provide firm conclusions about what works. The United Kingdom's RECOVERY trial and the WHO's SOLIDARITY trial are exemplars of this approach. It would be a powerful legacy of the pandemic if this model were widely adopted on an ongoing basis to provide the numbers necessary for trials in many health conditions. This would have the added bonus of involving many doctors and researchers, helping to educate them in what a well-designed trial looks like — and so ensuring that fewer poorly designed ones are done.

Cochrane and the other organizers of the October meeting say they hope to take any recommendations that emerge to the World Health Assembly in May 2022, to discuss with member states. It's important for countries to demand — and fund — changes. All these efforts must include diverse perspectives from patients, citizens and policymakers. This will help to ensure that evidence is equitably available, and that research and reviews

address the needs of communities worldwide, rather than just earning scientists more career-boosting papers. Getting there will require organizations such as Cochrane to take a hard look at their processes and be willing to change what they do.

As Hilda Bastian, an independent scientist who studies evidence-based medicine in Victoria, Australia, rightly argues, we need to ensure that when the next pandemic strikes and everyone is googling for evidence, that the high-quality reviews rise to the top, leaving the tide of questionable ones behind.

There is a danger that everyone will be so keen to move on and forget the trauma of the pandemic that we won't take time to reflect and improve. But Archie Cochrane's 50-year-old plea that decisions be based on rigorous evidence is more important than ever, and, tired though everyone is, we need to put in the work now so that we can deliver better, quicker evidence next time around.

Nature **593**, 168 (2021)

doi: <https://doi.org/10.1038/d41586-021-01255-w>

## References

1. 1.

Cochrane, A. L. *Effectiveness and Efficiency: Random Reflections on Health Services* (Nuffield Provincial Hospitals Trust, 1972).

2. 2.

Bastian, H., Glasziou, P. & Chalmers, I. *PLoS Med.* **7**, e1000326 (2010).

3. 3.

Clark, J. *et al. J. Clin. Epidemiol.* **121**, 81–90 (2020).

## Jobs from Nature Careers

- - - [All jobs](#)
    - - [Postdoctoral Research Fellow in Urban Climate Action](#)  
  
[The University of British Columbia \(UBC\)](#)  
[Vancouver, Canada](#)  
[JOB POST](#)
      - [Postdoctoral Fellow in Supercapacitor Technology](#)  
  
[The University of British Columbia \(UBC\)](#)  
[Kelowna, Canada](#)  
[JOB POST](#)
      - [Postdoctoral Researchers x 2 – Advancement of audit procedure for domestic and non-domestic energy compliance tools, SFI MaREI Centre, NUI Galway \(NUIG-RES-095-21\)](#)  
  
[National University of Ireland Galway \(NUI Galway\)](#)  
[Galway, Ireland](#)  
[JOB POST](#)
      - [Semantic Web Developer](#)

European Molecular Biology Laboratory (EMBL)

Hinxton, Cambridge, United Kingdom

**JOB POST**

---

This article was downloaded by **calibre** from <https://www.nature.com/articles/d41586-021-01255-w>

| [Section menu](#) | [Main menu](#) |

WORLD VIEW

11 May 2021

# Stop the emerging AI cold war



Proliferating military artificial intelligence will leave the world less safe — so we must focus on ethics and global cooperation.

- [Denise Garcia](#) 9

## 1. [Denise Garcia](#)

1. Denise Garcia is a professor at Northeastern University in Boston, Massachusetts, and the vice-chair of the International Committee for Robot Arms Control.

[View author publications](#)

You can also search for this author in [PubMed](#) [Google Scholar](#)

A race to militarize artificial intelligence is gearing up. Two years ago, the US Congress created the National Security Commission on Artificial

Intelligence (NSCAI). This March, it recommended that the United States must accelerate artificial-intelligence (AI) technologies to preserve national security and remain competitive with China and Russia.

This will undermine the United States' ability to lead emerging global norms on AI. In April, the European Commission published the first international legal framework for making AI secure and ethical; in January, the European Parliament issued guidelines stating that military AI should not replace human decisions and oversight. By contrast, the NSCAI recommendations advocate "the integration of AI-enabled technologies into every facet of war-fighting".

Enhancing AI war-fighting capacity will decrease security in a world where the biggest threats are instability — political, social, economic and planetary. The NSCAI should heed the research community. Some 4,500 AI and robotics researchers have declared that AI should not make the decision to take a human life — aligning with the European Parliament guidelines and the European Union regulation.



### The cold war online

The NSCAI resurrected disastrous ideas from the cold war and framed its report in terms of winning a competition for AI-enabled warfare. During the cold war, the drive to stay ahead in the technological race led to the

accumulation of 70,000 nuclear weapons and today's global arsenal of 13,100 warheads. This brought extortionate costs: US\$70 billion is spent annually to maintain nuclear weapons globally. Other threats demand similar investments: in 2019, climate-induced natural disasters displaced 25 million people, and decentralized conflicts forced 8.6 million to move. Still more threats affect infrastructure, such as the ransomware attack on 8 May that shut down a 8,850-kilometre US fuel pipeline.

The NSCAI does not prioritize international cooperation to create new regulations. Indeed, it speaks against a global ban on autonomous weapons, saying that other countries cannot be trusted to comply. But an AI-militarization race would be profoundly destabilizing. Unlike nuclear arms, AI is already ubiquitous in civilian spheres, so the dual-use risks of, say, flying drones or computer night vision are much higher.



## Regulate artificial intelligence to avert cyber arms race

Since 2014, I have been an observer and adviser at United Nations meetings, and I testified in 2017 as part of the International Panel on the Regulation of Autonomous Weapons. In my view, rather than focusing on counting weapons or on particular weapons systems, policies should specify human intention and human-machine interaction, obligating countries to maintain human control over military force. Other agreements could mitigate malicious uses of AI, such as using facial recognition to oppress

citizens or biased data to guide decisions about employment or incarceration. The world's people need protection from cyberattacks to infrastructure — such as those on US hospitals in 2020 or [those that hit national electrical grids.](#)

The NSCAI report calls for international standards for AI-enabled and autonomous weapons systems, arguing that if these systems are properly tested and designed, humans can use them to make the decision to kill, consistent with international humanitarian law. This is misleading: it's difficult to make machine learning's 'black box' nature fully interpretable, or to ensure that AI systems perform as expected after deployment. These systems learn from their environment, and the real world is never as simple as the laboratory.

The NSCAI argues that the United States should seek commitments from Russia and China against autonomous nuclear weapons, even as it argues against treaties regulating other autonomous and AI weapons. Instead, the United States should negotiate decreases in nuclear arsenals and establish standards to keep humans in meaningful control.



### [Redirect military budgets to tackle climate change and pandemics](#)

The NSCAI is too dismissive by discounting cooperation. The Chemical Weapons Convention, the Biological Weapons Convention, the UN

Sustainable Development Goals and the 1987 Montreal Protocol are examples of accountability on which all the major powers worked together. The United States and Russia established the International Space Station by cooperating closely.

Most nations want governance that controls the use of AI in war. In June 2020, the Global Partnership on Artificial Intelligence was created by the Group of Seven industrialized countries (G7) and called for human-centric development and use of AI. The partnership brings scientific and research communities together with industry and government to facilitate international cooperation. This is the path that the United States should take — with scientists, researchers and industry alike.

The relentless pursuit of militarization does not protect us. It diverts resources and attention from nearer existential threats, such as extreme weather events. With the world reeling from COVID-19 — the shock of the century — now is not the moment to hasten towards worldwide confrontation. In 2019 alone, climate disasters displaced almost one million people in the United States. China, too, is extremely vulnerable to global warming. This common ground could pave the way to cooperation, including stopping the emerging AI cold war. This is no time to embark on an exorbitant and ineffective race.

Nature **593**, 169 (2021)

doi: <https://doi.org/10.1038/d41586-021-01244-z>

## Jobs from Nature Careers

- - - [All jobs](#)
    - - [\*\*Postdoctoral Research Fellow in Urban Climate Action\*\*](#)

The University of British Columbia (UBC)

Vancouver, Canada

JOB POST

- **Postdoctoral Fellow in Supercapacitor Technology**

The University of British Columbia (UBC)

Kelowna, Canada

JOB POST

- **Postdoctoral Researchers x 2 – Advancement of audit procedure for domestic and non-domestic energy compliance tools, SFI MaREI Centre, NUI Galway (NUIG-RES-095-21)**

National University of Ireland Galway (NUI Galway)

Galway, Ireland

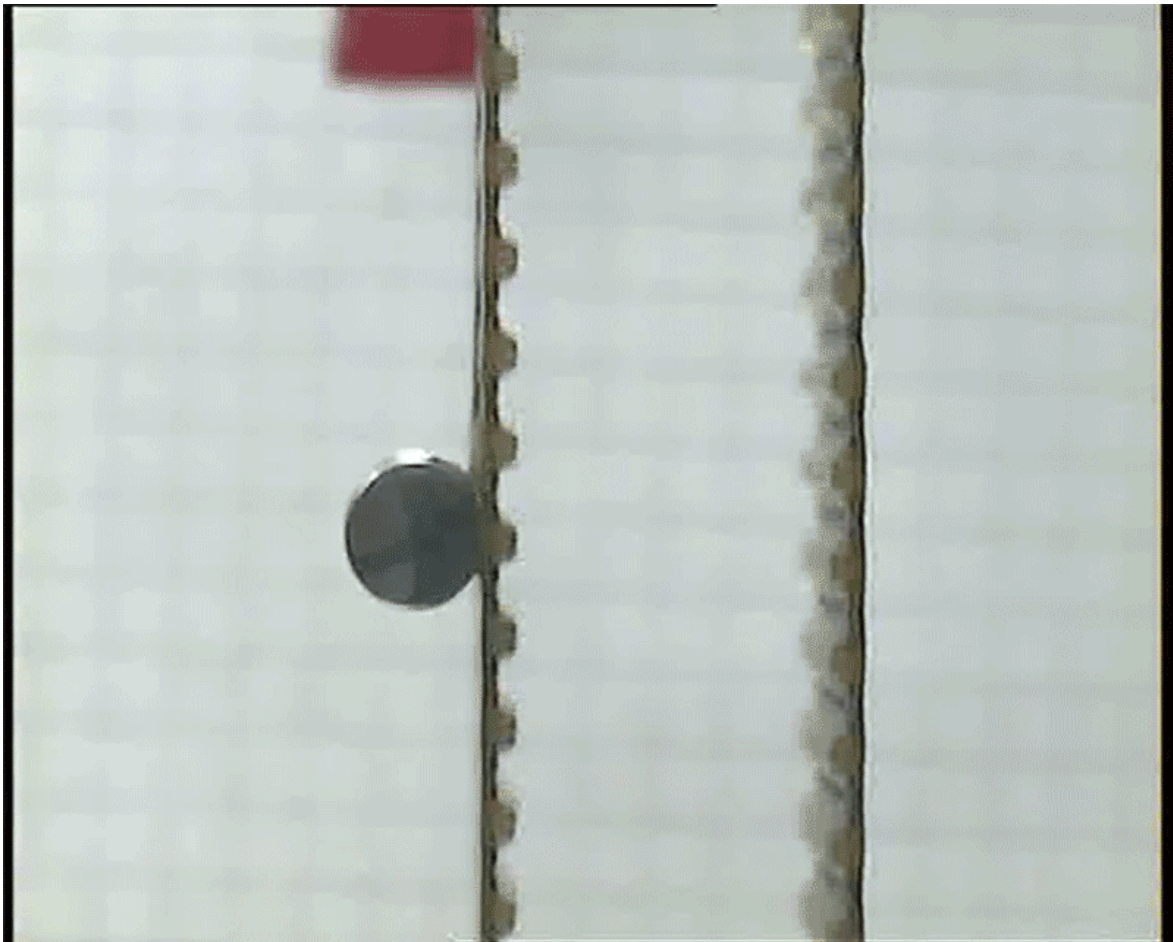
JOB POST

- **Semantic Web Developer**

European Molecular Biology Laboratory (EMBL)

Hinxton, Cambridge, United Kingdom

JOB POST



You spin me 'round: a cylinder hovers next to a greased belt moving at just the right speed. Credit: M. P. Dalwadi *et al./J. Fluid Mech.*

Fluid dynamics

06 May 2021

**How does a cylinder levitate?  
Scientists explain the maths behind  
the magic**

A model shows how a spinning cylinder can stay suspended in the air next to an oil-slicked moving belt.

An oil-coated belt run like a vertical treadmill can levitate a cylinder held next to it. Now researchers have developed a mathematical model to explain this goopy form of anti-gravity.

Previous research showed that a cylinder placed against the side of a moving belt covered in oil and then released will start to rotate, get coated in the fluid and, at the right belt speed, stay suspended against the belt. But the model devised to explain the phenomenon had some gaps.

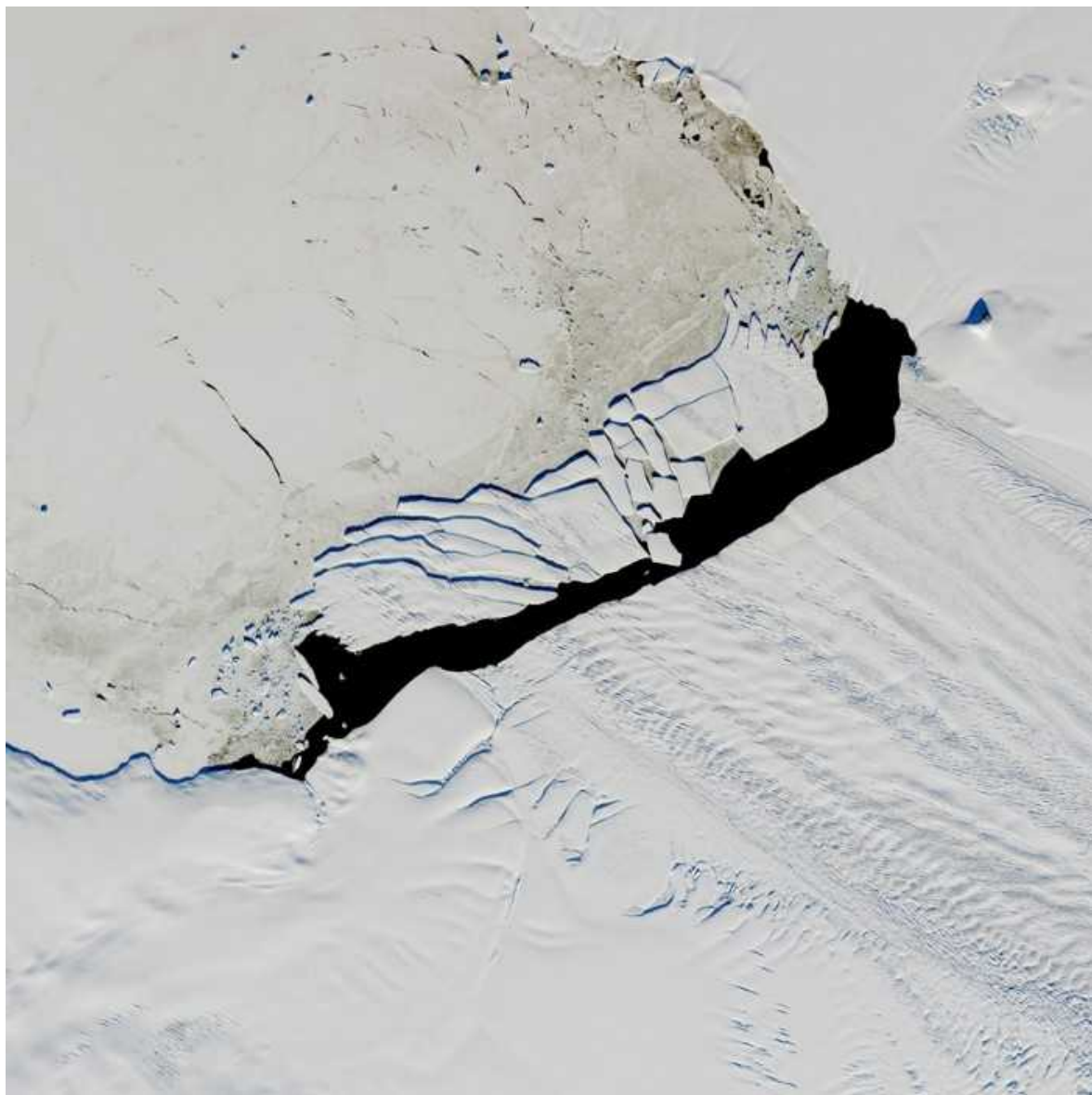
Mohit Dalwadi at the University of Oxford, UK, and his colleagues have fleshed out the details. The group experimented with cylinders of various masses and sizes to find the belt speed needed to levitate each object. The model that the team developed takes into account how the oil from the cylinder comes together with oil from the belt — and shows that pressures near that joining point support the cylinder against gravity.

[J. Fluid Mech. \(2021\)](#)

- [Fluid dynamics](#)

---

This article was downloaded by **calibre** from <https://www.nature.com/articles/d41586-021-01216-3>



Dark water borders chunks of iceberg broken off a West Antarctica glacier. The melting of the region's ice sheet could allow the bedrock to rise, sloughing water into the ocean. Credit: NASA

Climate change

06 May 2021

# Antarctic rocks on the rebound could raise sea level much more than expected

When the ice covering the west of the continent disappears, the bedrock could rise up and shove extra water into the ocean.

As West Antarctica's ice melts, the underlying rock will lift upwards and push meltwater into the ocean — further accelerating global sea-level rise.

If it were to thaw entirely, the thick ice sheet covering the western portion of Antarctica would generate enough meltwater to raise global sea levels by about 3 metres. The melting would also liberate the continent's bedrock from the weight of the ice, allowing it to spring up. Because the bedrock is below sea level, if it rises, it could push further water into the ocean.

Previous studies suggested that this rock 'rebound' wouldn't make a big contribution to sea-level rise. But Linda Pan at Harvard University in Cambridge, Massachusetts, and her colleagues modelled the aftermath of the ice sheet's disappearance and found that the newly exposed rock would rise quickly, allowing plenty of additional meltwater to run off into the ocean.

This effect could add an extra metre of sea-level rise within 1,000 years of the melting of the West Antarctic Ice Sheet. That's around 30% more than is estimated by models of the ice sheet's collapse that do not include this effect.

*[Sci. Adv. \(2021\)](#)*

- [Climate change](#)



As a human egg cell is fertilized, two chromosome-containing cellular structures (dotted circles, centre) merge into one — a process that often goes wrong. Credit: Pascal Goetgheluck/Science Photo Library

Developmental biology

07 May 2021

## The error-prone step at the heart of making an embryo

High-resolution imaging shows why the union between two sets of chromosomes goes awry as least as often as not.

After a sperm fertilizes an egg, the chromosomes of both unite into a single genome, if all goes according to plan. Now, observations of developing

embryos show that this all-important process often goes awry — a finding that helps to explain why at least half of newly formed human embryos have the wrong number of chromosomes.

Some 50–70% of embryos have aneuploidy, an abnormal number of chromosomes. Such embryos are often miscarried.

To find out why aneuploidy is so common, Melina Schuh at the Max Planck Institute for Biophysical Chemistry in Göttingen, Germany, and her collaborators used high-resolution microscopes to observe the early stages of human and cow development. They discovered a crucial step: maternal and paternal genomes, which start off enclosed in their own structures, cluster around the location where they will fuse.

This clustering enables rapid and error-free unification of the two genomes. But this complex process has many steps that can go wrong. Failures lead to aneuploidy and fragments of nuclei containing subsets of chromosomes — both of which impair the development of healthy embryos.

[Cell \(2021\)](#)

- [Developmental biology](#)

---

This article was downloaded by **calibre** from <https://www.nature.com/articles/d41586-021-01207-4>



Mist wafts through the trees at the Monteverde Cloud Forest Biological Preserve in Costa Rica. Cloud forests around the world are threatened by development, wood collection and climate change. Credit: Stefano Paterna/Alamy

Conservation biology

04 May 2021

## Forests that float in the clouds are drifting away

Tropical cloud forests are safe havens for a vast range of creatures and plants, but they are under siege around the globe.

Remote habitats called tropical cloud forests, which cling to misty mountains and tap humid air for water, are in decline. So says a global analysis also reporting that cloud forests, despite occupying just 0.4% of Earth's land, harbour around 15% of the global biodiversity of birds, mammals, amphibians and tree ferns.

Dirk Karger at the Swiss Federal Institute for Forest, Snow and Landscape Research in Birmensdorf, Walter Jetz at Yale University in New Haven, Connecticut, and their colleagues created habitat-prediction models that incorporate remote-sensing data on cloud cover and other conditions to predict the coverage of tropical cloud forests worldwide. They then studied satellite imagery of land cover from 2001 to 2018 to determine the rate of cloud-forest loss and analysed how this loss would affect 3,700 species living in this ecosystem.

The team estimates that more than 15,000 square kilometres of tropical cloud forest — 2.4% of the global total — were lost during the 18-year period. Africa and the Americas had the greatest losses. The authors note that the establishment of protected areas did little to halt the loss of habitat and its biodiversity, highlighting the urgent need for other safeguards.

*Nature Ecol. Evol. (2021)*

- [Conservation biology](#)

---

This article was downloaded by **calibre** from <https://www.nature.com/articles/d41586-021-01195-5>



Remnants of three monumental structures called mustatils crown a rocky outcrop on the border of the Khaybar and Al-Ula counties in Saudi Arabia.  
Credit: AAKSA and Royal Commission for AlUla

Archaeology

04 May 2021

## Forget Stonehenge: the first known massive monuments are much older

The Arabian Peninsula is dotted with hundreds of mysterious structures dating to the sixth millennium BC.

Cattle herders on the Arabian Peninsula built the world's first large-scale monuments some 7,000 years ago, more than 4 millennia before the ancient Egyptians built the pyramids or Stonehenge rose on Britain's plains.

The structures are called mustatils, the Arabic word for rectangle, in reference to the characteristic shape of the open courtyard at their centre. Melissa Kennedy and her colleagues at the University of Western Australia in Perth documented more than 1,000 mustatils that are scattered over a 200,000-square-kilometre area of the desert in modern-day Saudi Arabia. Built with local stone and often hundreds of metres long, they appear singly at some sites and in groups at others. Most have a narrow entrance way at one end.

The team excavated one site and found horns and bone fragments from cattle, gazelle and sheep. An analysis of the remains, which seem to be ritual offerings, dates the site to the sixth millennium BC.

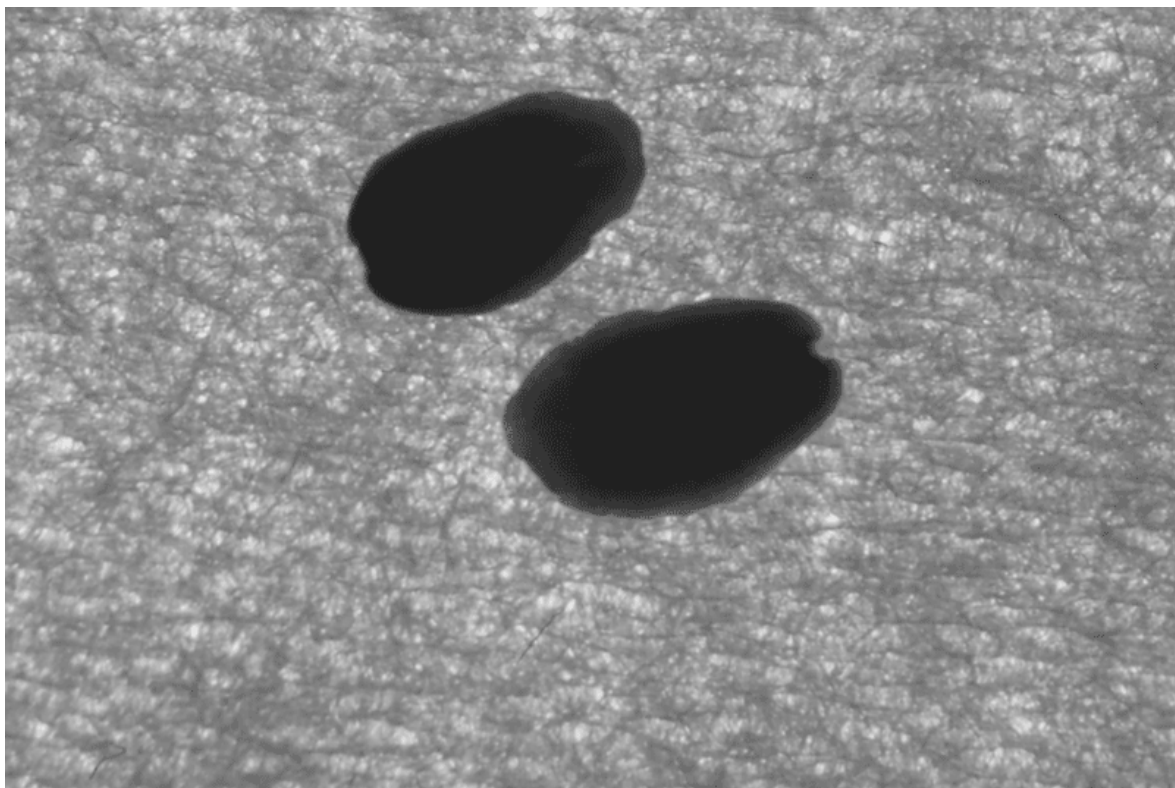
The bigger mustatils would have taken thousands of hours to construct, suggesting that people of the day were organizing and building collectively.

*[Antiquity \(2021\)](#)*

- [Archaeology](#)

---

This article was downloaded by **calibre** from <https://www.nature.com/articles/d41586-021-01158-w>



Decapitated flatworms glide away from a source of ultraviolet light. Credit: Nishan Shettigar

Neuroscience

03 May 2021

## How headless worms see the light to steer

Light-sensitive cells, distributed throughout its body, help a simple creature to do the extraordinary.

Decapitated flatworms can ‘see’ where they’re going, thanks to light-sensitive cells throughout their bodies.

Like most animals, flatworms have eyes that respond to light. But previous research had suggested that the worms could detect and react to light without using their eyes.

Akash Gulyani, now at the University of Hyderabad in India, and his colleagues cut the heads off *Schmidtea mediterranea* worms and then exposed the bodies to a type of ultraviolet light called UV-A. The headless worms moved away from the light, just like intact worms do.

By looking at gene expression throughout the animal's tissues, the researchers found that the flatworms' bodies were lined with networks of light-sensitive cells that coordinate this kind of movement. These cells contained a new type of light-sensitive protein, which was also found in pigment cells in the worms.

Newly hatched worms do not have this light-sensing ability, suggesting that it develops in adulthood. Because flatworms are nocturnal, the authors think the system evolved to help them to quickly hide from the Sun, even if they are resting and not using their eyes or brains.

[Proc. Natl Acad. Sci. USA \(2021\)](#)

- [Neuroscience](#)

---

This article was downloaded by **calibre** from <https://www.nature.com/articles/d41586-021-01192-8>



A child scratches an arm affected by atopic dermatitis. A new skin patch accurately detects such scratching. Credit: Lisa Kingdon/Getty

Engineering

30 April 2021

## How itchy are you? A new device knows precisely

A skin patch that monitors scratching is far less invasive than the infrared camera recordings used now.

A wearable sensor that measures how often a child scratches themselves could offer doctors a straightforward way to quantify itching.

Atopic dermatitis, a skin condition commonly known as eczema, causes chronic itching. It can be so severe that children scratch their itchy skin at night instead of sleeping, leading to stunted growth. Until now, the only reliable method to measure the effectiveness of treatments to stop itching at night was time-consuming analysis of infrared-camera recordings.

John Rogers and Shuai Xu at Northwestern University in Evanston, Illinois, and their colleagues developed a sensor that sits on the back of a child's hand and uses acoustic and mechanical signals to measure scratches initiated from the arm, wrist, fingers and fingertips. By wiring up healthy volunteers, the researchers trained an algorithm to detect which movements constitute scratching and which do not. They then tested the device in 11 children with moderate to severe atopic dermatitis over 46 nights.

When they compared these results with those obtained by infrared-camera data, they found that the device correctly identified 84% of scratching movements and 99% of non-scratching movements.

[Sci. Adv. \(2021\)](#)

- [Engineering](#)

---

This article was downloaded by **calibre** from <https://www.nature.com/articles/d41586-021-01159-9>

# News in Focus

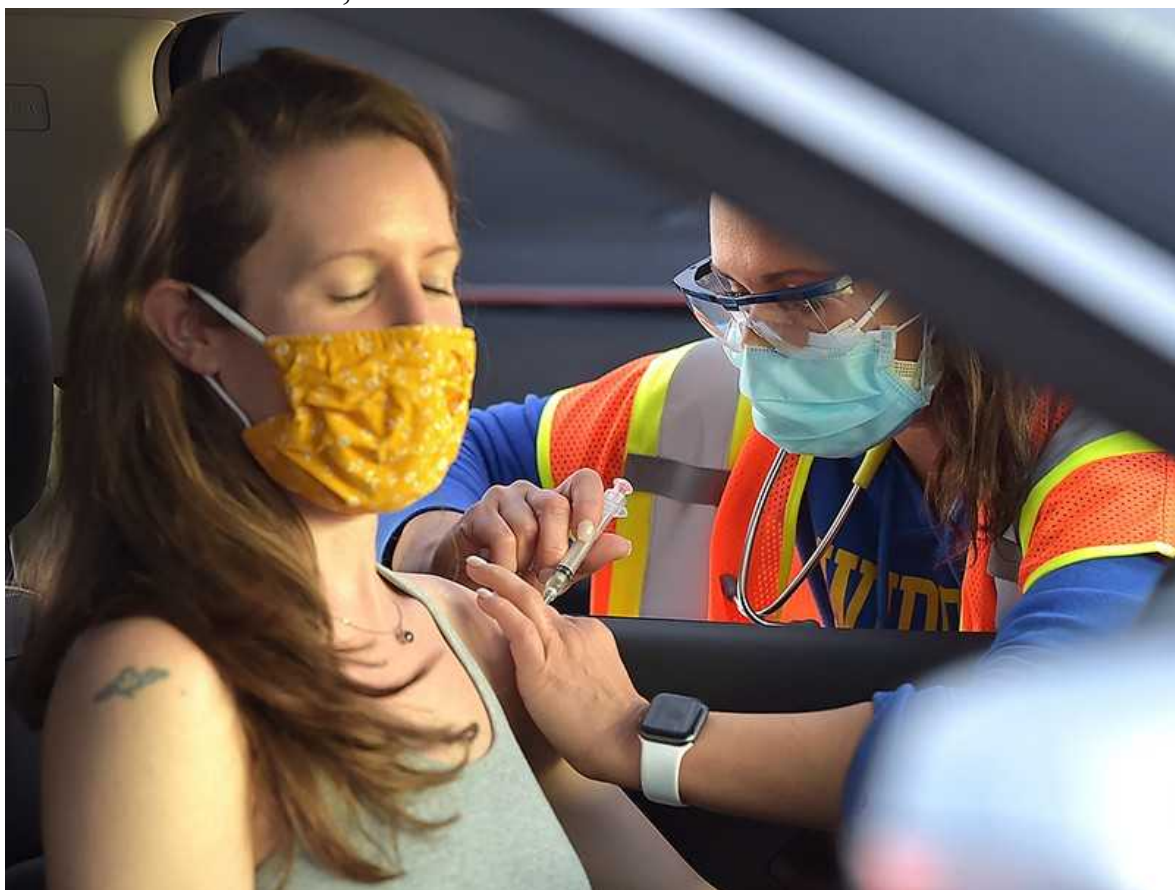
- **[Quantum drums, COVID patents and head injuries](#)** [ 12 May 2021]  
News Round-Up • The latest science news, in brief.
- **[First genetically modified mosquitoes released in the United States](#)** [ 03 May 2021]  
News • Biotech firm Oxitec launches controversial field test of its insects in Florida after years of push-back from residents and regulatory complications.
- **[Why some researchers oppose unrestricted sharing of coronavirus genome data](#)** [ 05 May 2021]  
News • Global-south scientists say that an open-access movement led by wealthy nations deprives them of credit and undermines their efforts.
- **[China's COVID vaccines are going global — but questions remain](#)** [ 04 May 2021]  
News • The WHO has approved one of China's COVID-19 vaccines for use worldwide and another is under review. But published trial data remain scarce.
- **[Failure of genetic therapies for Huntington's devastates community](#)** [ 05 May 2021]  
News • Hopes were high for drugs designed to lower levels of a mutant protein, but development has stalled.
- **[Weird viral DNA spills secrets to biologists](#)** [ 29 April 2021]  
News • Bacteria-infecting viruses have specialized enzymes to make genes with alternative nucleobase.
- **[How COVID broke the evidence pipeline](#)** [ 12 May 2021]  
News Feature • The pandemic stress-tested the way the world produces evidence — and revealed all the flaws.

## NEWS ROUND-UP

12 May 2021

# Quantum drums, COVID patents and head injuries

The latest science news, in brief.



The Johnson & Johnson COVID-19 vaccine is administered at a drive-through clinic in Marple, Pennsylvania. Credit: Pete Bannan/MediaNews Group/Daily Times via Getty

# In shock move, US backs waiving patents on COVID vaccines

In a historic move, the US government has announced that it supports [waiving patent protections for COVID-19 vaccines](#), a measure aimed at boosting supplies so that people around the world can get the shots. “The extraordinary circumstances of the COVID-19 pandemic call for extraordinary measures,” said US trade representative Katherine Tai in a statement.

The move came on 5 May, day one of a two-day meeting of the general council of the World Trade Organization, based in Geneva, Switzerland. Until now, the United States, the European Union, the United Kingdom and Japan have blocked efforts brought by India and South Africa to make it legal to manufacture generic versions of COVID-19 vaccines.

Former US presidents from both the Republican and the Democratic parties have staunchly defended intellectual-property rights, so the move by the administration of President Joe Biden has shocked people on both sides of the debate.

“This marks a major shift in US policy in a pro-public-health way,” says Matthew Kavanagh, a global-health researcher at Georgetown University in Washington DC.

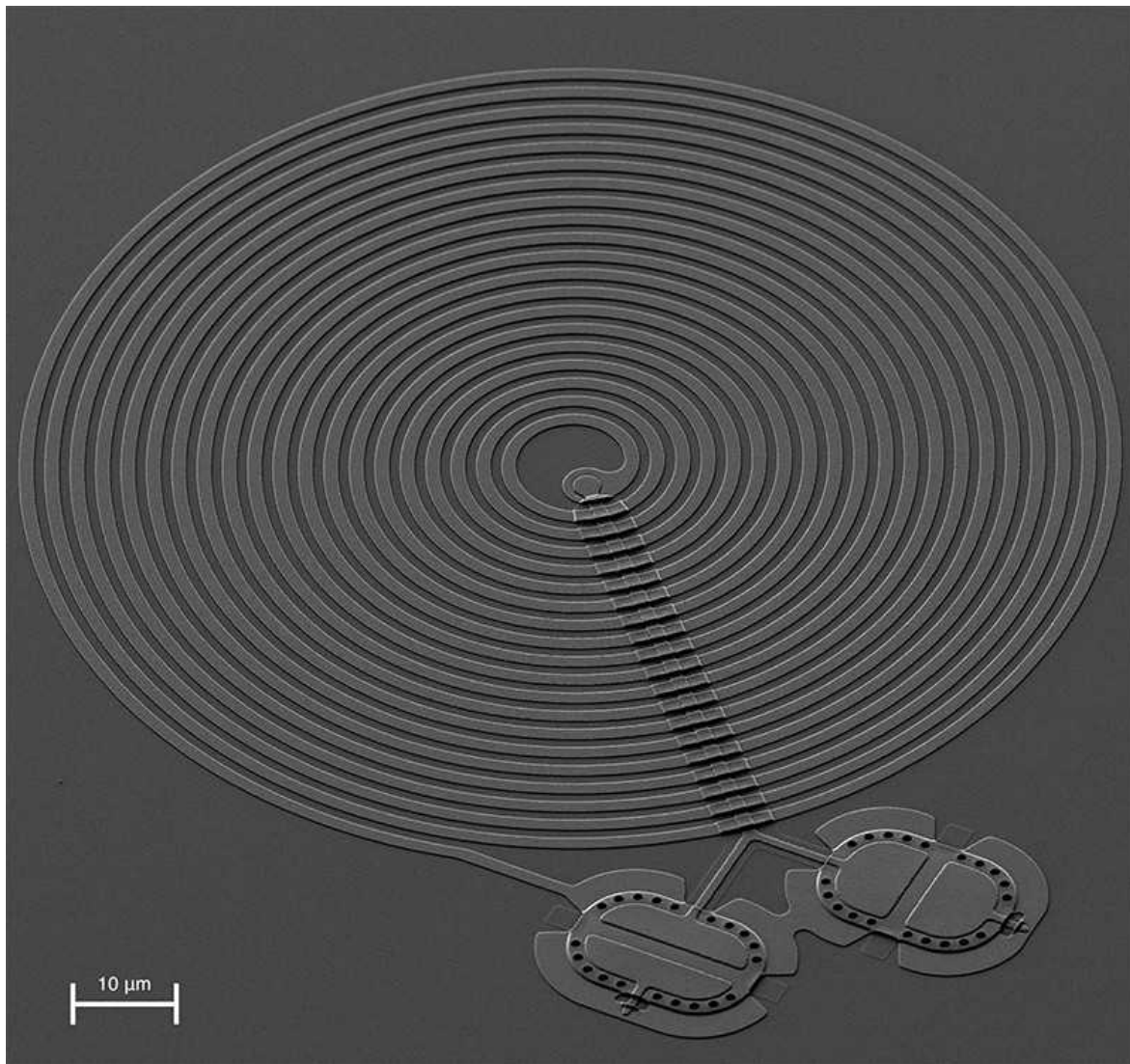
Kavanagh is part of the growing chorus of health-policy and global-health researchers advocating patent waivers, as the gap between vaccination rates in rich and poor nations grows larger every day.

Fewer than 1% of people in low-income countries have received COVID-19 vaccines. The researchers are quick to note, however, that a waiver on patents covering all aspects of COVID-19 vaccines would be just the first step in ramping up vaccine supply.

“It’s a one-two-three,” explains Rachel Cohen, US director of the non-profit Drugs and Neglected Diseases initiative in New York City. “First we need to remove patent obstacles, second we need to transfer the knowledge on how

to make them, and step three is a massive investment in manufacturing capacity.”

Drugmakers and others who oppose the measure say that waivers sabotage companies’ enormous investments in drug and vaccine development, which are compensated by their ability to set the price on products that they exclusively own.



The tiny aluminium membranes used by Kotler’s team to demonstrate quantum entanglement. Credit: Florent Lecoq and Shlomi Kotler/NIST

## Tiny drums push limits of quantum weirdness

By playing two tiny drums, physicists have provided the [most direct demonstration yet](#) that quantum entanglement — a bizarre effect normally associated with subatomic particles — works for larger objects as well.

In an experiment at the US National Institute of Standards and Technology in Boulder, Colorado, physicist Shlomi Kotler and his collaborators built a pair of vibrating aluminium membranes akin to two tiny drums, each around 10 micrometres long.

The team tickled the membranes with microwave photons to make them vibrate in sync, and in such a way that their motions were in a quantum-entangled state. At any given time, as the drums wobbled up and down, measuring their displacement from flat showed they were in exactly the same position, and probing their velocities returned exactly opposite values.

Although these structures are barely visible to the naked eye, they are enormous by quantum standards, consisting of around one trillion atoms each.

The findings, published on 6 May ([S. Kotler et al., Science 372, 622–625; 2021](#)), could help researchers to build quantum computers that can perform calculations beyond the reach of any ordinary computer.

## Head-injury risk higher for female soccer players

Female soccer players are almost [twice as likely to suffer concussion](#) as their male counterparts, a study of more than 80,000 teenage players across US high schools has found.

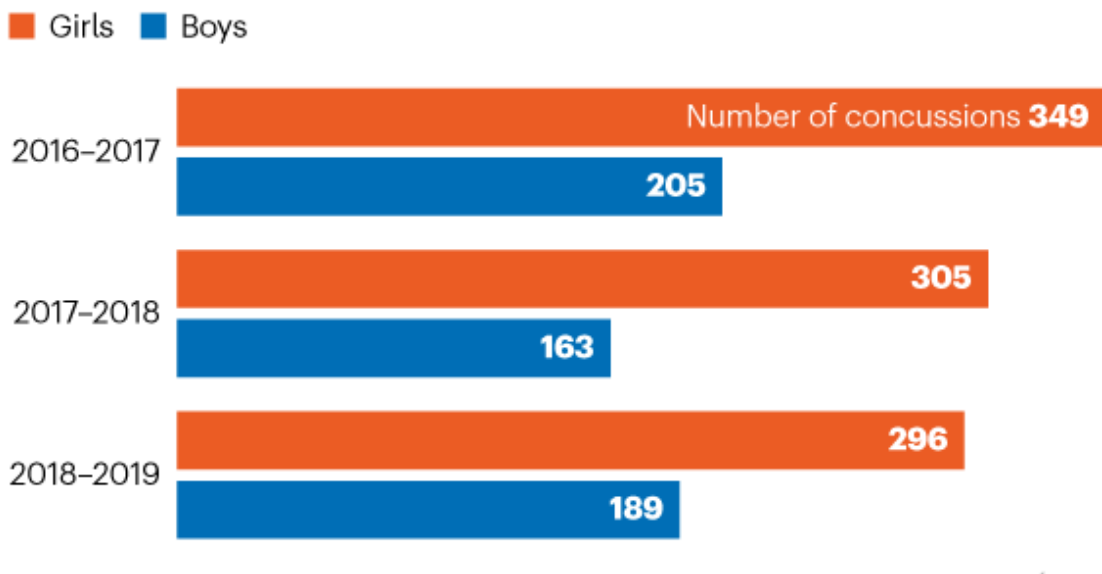
Researchers analysed survey data from around 43,000 male and 39,000 female players from schools in Michigan over 3 academic years (see ‘Concussion risk’). They found that the girls’ chance of having a sports-related head injury was 1.88 times higher than the boys’, according to the findings published on 27 April ([A. C. Bretzin et al. JAMA Netw. Open 4, e218191; 2021](#)).

How the players sustained their injuries also differed between male and female adolescents: the boys’ most common way of becoming concussed

was through bashing into another player. Girls were most likely to be concussed after colliding with another object, such as the ball or a goalpost. Boys were also more likely to be removed from play immediately after a suspected head injury than were girls.

## CONCUSSION RISK

A survey of more than 80,000 high-school soccer players found girls are twice as likely to suffer a concussion than boys.



©nature

Source: A. C. Bretzin *et al. JAMA Netw. Open* **4**, e218191; 2021.

Nature **593**, 173 (2021)

doi: <https://doi.org/10.1038/d41586-021-01245-y>

## Jobs from Nature Careers

- - - [All jobs](#)
  - 
  -

## **Postdoctoral Research Fellow in Urban Climate Action**

The University of British Columbia (UBC)

Vancouver, Canada

JOB POST

### **▪ Postdoctoral Fellow in Supercapacitor Technology**

The University of British Columbia (UBC)

Kelowna, Canada

JOB POST

### **▪ Postdoctoral Researchers x 2 – Advancement of audit procedure for domestic and non-domestic energy compliance tools, SFI MaREI Centre, NUI Galway (NUIG-RES-095-21)**

National University of Ireland Galway (NUI Galway)

Galway, Ireland

JOB POST

### **▪ Semantic Web Developer**

European Molecular Biology Laboratory (EMBL)

Hinxton, Cambridge, United Kingdom

JOB POST

---

This article was downloaded by **calibre** from <https://www.nature.com/articles/d41586-021-01245-y>.

| [Section menu](#) | [Main menu](#) |

NEWS

03 May 2021

# First genetically modified mosquitoes released in the United States

Biotech firm Oxitec launches controversial field test of its insects in Florida after years of push-back from residents and regulatory complications.

- [Emily Waltz](#)

1. Emily Waltz

[View author publications](#)

You can also search for this author in [PubMed](#) [Google Scholar](#)



Biotech firm Oxitec is working closely with the Florida Keys Mosquito Control District to monitor the field trial of its genetically modified mosquitoes. Credit: Oxitec 2021

After a decade of fighting for regulatory approval and public acceptance, a biotechnology firm has released genetically engineered mosquitoes into the open air in the United States for the first time. The experiment, launched this week in the Florida Keys — over the objections of some local critics — tests a method for suppressing populations of wild *Aedes aegypti* mosquitoes, which can carry diseases such as Zika, dengue, chikungunya and yellow fever.



### [US government approves 'killer' mosquitoes to fight disease](#)

Oxitec, the firm based in Abingdon, UK, that developed the mosquitoes, has previously field-tested the insects in [Brazil](#), Panama, the Cayman Islands and [Malaysia](#).

But until now, owing to a circuitous series of regulatory decisions and [pushback from Florida residents](#) (see ‘A long road’), no genetically engineered mosquito had been trialled in the United States — even though the country previously allowed tests of a genetically engineered [diamondback moth \(\*Plutella xylostella\*\) in New York](#) and an engineered pink bollworm (*Pectinophora gossypiella*) in Arizona, both developed by Oxitec. “When something new and revolutionary comes along, the immediate reaction of a lot of people is to say: ‘Wait.’,” says Anthony James, a

molecular biologist focused on bioengineered mosquitoes at the University of California, Irvine. “So the fact that [Oxitec] was able to get the trial on the ground in the United States is a big deal.”

## Experiment launched

*Aedes aegypti* makes up about 4% of the mosquito population in the Keys, a chain of tropical islands off the southern tip of Florida. But it is responsible for practically all mosquito-borne disease transmitted to humans in the region, according to the Florida Keys Mosquito Control District (FKMCD), which is working closely with Oxitec on the project. Researchers and technicians working on the project will release bioengineered male *Aedes aegypti* mosquitoes, which don't bite, to mate with the wild female population, responsible for biting prey and transmitting disease. The genetically engineered males carry a gene that passes to their offspring and kills female progeny in early larval stages. Male offspring won't die but instead will become carriers of the gene and pass it to future generations. As more females die, the *Aedes aegypti* population should dwindle.



### [Florida abuzz over mosquito plan](#)

FKMCD in 2010 approached Oxitec about testing its approach in the Keys, because Florida was — and still is — experiencing an increase in mosquito-borne disease. In 2009, the state began seeing cases of locally transmitted dengue, and, a few years later, locally transmitted Zika.

In late April of this year, project researchers placed boxes containing Oxitec's mosquito eggs at six locations in three areas of the Keys. The first males are expected to emerge within the first two weeks of May. About 12,000 males will exit the boxes each week over the next 12 weeks. In a second phase later this year, intended to collect even more data, nearly 20 million mosquitoes will emerge over a period of about 16 weeks, according to Oxitec.

Genetically engineered mosquitoes are an alternative to insecticides, which are used heavily in the United States to control insect populations. This has resulted in the evolution of mosquitoes that are resistant to insecticides.



Oxitec has placed boxes of its mosquito eggs in undisclosed locations in the Florida Keys to protect against vandalism. Credit: Oxitec 2021

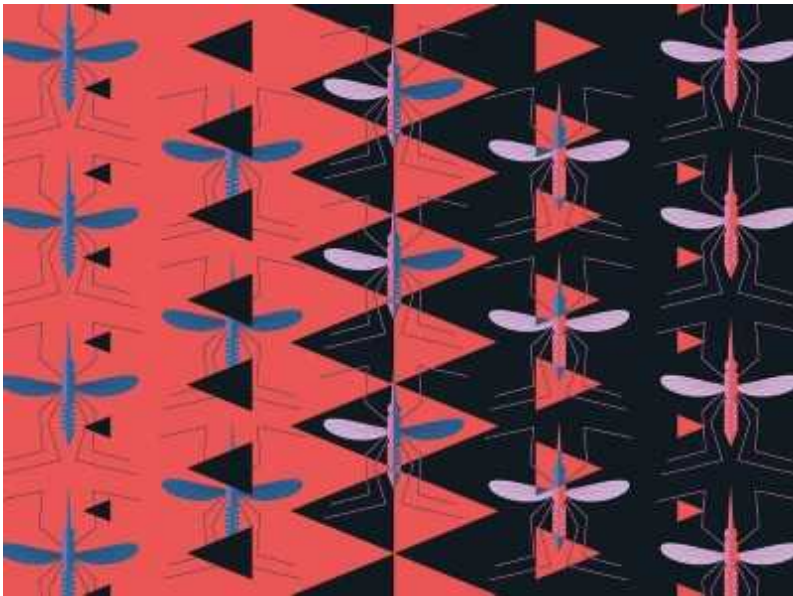
"Unfortunately, we're seeing our toolbox shrinking due to resistance," said Andrea Leal, executive director of FKMCD, at a press conference last week. "That's one of the reasons why we're really looking at these new innovative tools and new ways to control this mosquito."

To monitor the trial's progress, researchers will use capture devices to trap mosquitoes for study. They will measure how far the male mosquitoes travel from the boxes, how long they live, how effectively they squelch the wild female mosquito population and whether all of the females with the gene are indeed dying. Oxitec mosquitoes carry a fluorescent marker gene that makes them glow when exposed to a specific colour of light, which makes identification easier.

The biotech firm plans to present the results to the US Environmental Protection Agency (EPA), which gave the green light for the trial. The data will help the EPA to determine whether Oxitec can release the mosquitoes more broadly in the United States. The company is still testing them in Brazil and other countries.

## **Residential pushback**

Opposition to the Florida field trial has been fierce from some residents in the Keys. Worried about being bitten by the mosquitoes or that the insects will disrupt the Florida ecosystem — and generally unhappy about being chosen as a test site — some have threatened to derail the experiments by spraying insecticides near the release points. “As you can imagine, emotions run high, and there are people who feel really strongly either for or against it,” says molecular biologist Natalie Kofler, who lectures at Harvard Medical School in Cambridge, Massachusetts, and is the founder of Editing Nature, an organization that advocates for responsible development and oversight of gene-editing technologies. “And I can see how, if you didn’t agree to this, it could be really concerning to have mosquitoes released in your neighborhood.”



## [Self-destructing mosquitoes and sterilized rodents: the promise of gene drives](#)

Many of the concerns stem from the uncertainty of a new technology, says Kofler, who has been following this project for years. Oxitec has been engaging with the Florida Keys community to provide answers to queries. They explained, for instance, the very low likelihood that female mosquitoes with the lethal gene could reproduce. But many people don't have confidence in what they're hearing, because it's coming from a company, says Kofler.

Kofler is hoping that enough data are gathered to assess the mosquitoes' impact, including on other species in the Keys and local ecosystems, and that it's done "in a way that's transparent, and in a way that can make some community members feel better about the whole situation".

Oxitec employees have taken precautions against vandalism by placing their mosquito boxes on private, fenced-in properties, and not disclosing their precise locations to the public.

## **A Long Road**

Oxitec has faced regulatory assessments from three different US federal agencies and opposition from Florida residents over the past decade as it

sought approval to release its experimental mosquitoes in the United States for the first time.

**March 2010:** Oxitec submits a request to the US Department of Agriculture (USDA) to run a field trial with its genetically modified mosquitoes.

**October 2011:** The USDA says it doesn't have regulatory jurisdiction over Oxitec's mosquitoes.

**November 2011:** The US Food and Drug Administration (FDA) claims jurisdiction over regulating the mosquitoes, so Oxitec submits an application to the agency for a trial in Key Haven, Florida.

**August 2016:** The FDA approves the trial. The start date depends on the Florida Keys Mosquito Control District (FKMCD) board's approval of mosquito-release locations.

**November 2016:** Key Haven residents vote against the trial in a referendum, but elsewhere in Monroe County, Florida, enough residents vote in favour of it to keep the project afloat.

**October 2017:** The FDA transfers jurisdiction of Oxitec's mosquitoes to the US Environmental Protection Agency (EPA).

**March 2019:** Oxitec transitions to a second-generation mosquito because of advances in technology and requests from the EPA an experimental permit to conduct field trials in Monroe County.

**April 2020:** The EPA green-lights the project.

**August 2020:** The FKMCD board votes to proceed with the trial.

**April 2021:** The trial begins as boxes of genetically engineered mosquitoes are placed in Monroe County's Cudjoe Key, Ramrod Key and Vaca Key.

Nature **593**, 175-176 (2021)

doi: <https://doi.org/10.1038/d41586-021-01186-6>

## Jobs from Nature Careers

- - - [All jobs](#)
    - - [Postdoctoral Research Fellow in Urban Climate Action](#)  
  
[The University of British Columbia \(UBC\)](#)  
[Vancouver, Canada](#)  
[JOB POST](#)
      - [Postdoctoral Fellow in Supercapacitor Technology](#)  
  
[The University of British Columbia \(UBC\)](#)  
[Kelowna, Canada](#)  
[JOB POST](#)
      - [Postdoctoral Researchers x 2 – Advancement of audit procedure for domestic and non-domestic energy compliance tools, SFI MaREI Centre, NUI Galway \(NUIG-RES-095-21\)](#)  
  
[National University of Ireland Galway \(NUI Galway\)](#)  
[Galway, Ireland](#)  
[JOB POST](#)
      - [Semantic Web Developer](#)

European Molecular Biology Laboratory (EMBL)

Hinxton, Cambridge, United Kingdom

**JOB POST**

---

This article was downloaded by **calibre** from <https://www.nature.com/articles/d41586-021-01186-6>

| [Section menu](#) | [Main menu](#) |

NEWS

05 May 2021

# Why some researchers oppose unrestricted sharing of coronavirus genome data

Global-south scientists say that an open-access movement led by wealthy nations deprives them of credit and undermines their efforts.

- [Amy Maxmen](#)

1. Amy Maxmen

[View author publications](#)

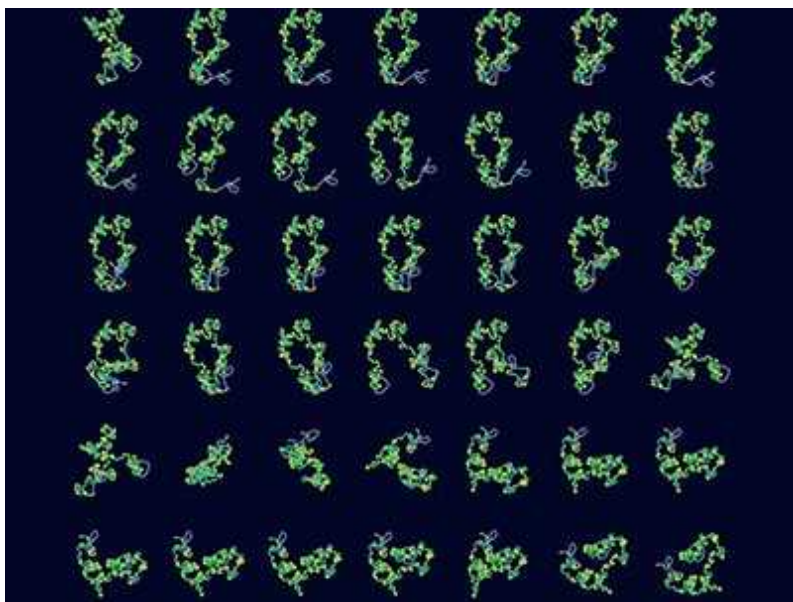
You can also search for this author in [PubMed](#) [Google Scholar](#)



Microbiologist Christian Happi works in the lab at the African Centre of Excellence for Genomics of Infectious Diseases in Ede, Nigeria. Credit: ACEGID

“I was up all last night,” says Nnaemeka Ndodo, a molecular bioengineer at the Nigeria Centre for Disease Control (CDC) in Abuja. He sequences coronavirus genomes during the day, and then analyses and uploads the results to an online database at night, working tirelessly alongside his colleagues. “We don’t know Saturday, we don’t know Sunday,” he says.

Researchers around the world are racing to spot variants of the coronavirus SARS-CoV-2 so that they can determine whether the mutated viruses will evade vaccines or make COVID-19 deadlier. Like many scientists, Ndodo shares SARS-CoV-2 genome sequences in a popular data repository, GISAID, that requires users to sign in and to credit those whose data they analyse.



### Scientists call for fully open sharing of coronavirus genome data

But a growing fraction of scientists, mostly from wealthy nations, [argues that sequences should be shared](#) on databases with no gatekeeping at all. They say this would allow huge analyses combining hundreds of thousands of genomes from different databases to flow seamlessly, and therefore deliver results more rapidly.

The debate has caught the attention of the US National Institutes of Health (NIH) — which runs its own genome repository, called GenBank — and the Bill & Melinda Gates Foundation, which has considered encouraging grantees to share on sites without such strong protections, *Nature* has learnt.

But many researchers — particularly those in resource-limited countries — are pushing back. They tell *Nature* that they see potential for exploitation in this no-strings-attached approach — and that GISAID's gatekeeping is one of its biggest attractions because it ensures that users who analyse sequences from GISAID acknowledge those who deposited them. The database also requests that users seek to collaborate with the depositors.

Fears of inequitable data use are amplified by the fact that only 0.3% of COVID-19 vaccines have gone to low-income countries. “Imagine Africans working so hard to contribute to a database that’s used to make or update vaccines, and then we don’t get access to the vaccines,” says Christian

Happi, a microbiologist at the African Centre of Excellence for Genomics of Infectious Diseases in Ede, Nigeria. “It’s very demoralizing.”

## Getting credit

GISAID is the [most popular repository](#) for SARS-CoV-2 genome sequences, holding 1.4 million sequences as of 4 May. Researchers from under-resourced laboratories say it gives them a chance to participate in big-data analyses or do their own, because of the platform’s terms on acknowledgement and collaboration. Without those, researchers like Ndodo worry that the fruits of their fieldwork and lab work will be scooped up by computer scientists who aren’t burdened with such tasks. Big-data analyses can result in top-tier journal publications — and that, in turn, might lead to lucrative grants and patents for technologies, such as diagnostic tests and vaccines.



Researcher Lavanya Singh handles samples in a genomics lab at the University of KwaZulu-Natal in Durban, South Africa. Credit: Tulio de Oliveira and Paul Harris/KRISP at UKZN

Continental Africa and South America more than doubled the number of SARS-CoV-2 sequences they contributed to GISAID between January and April this year. For researchers at the National Institute for Biomedical Research (INRB) in Kinshasa, Democratic Republic of the Congo, the decision to share those sequences was initially fraught. While working in Guinea during the Ebola virus outbreak of 2014–16, one senior scientist [was alarmed to learn](#) that all of the specimens collected by African researchers were being shipped out of the country. Most of the scientific papers and patents on those samples were [authored by scientists](#) from wealthy countries. Labs in Guinea didn't sustainably benefit from that work and today remain unable to sequence samples.

So researchers at INRB were wary to share SARS-CoV-2 genome data, says Eddy Kinganda-Lusamaki, a microbiologist at the institute. But after reviewing GISAID's crediting and collaboration requirements, Kinganda says they decided to share their data prior to publication.



### [One million coronavirus sequences: popular genome site hits mega milestone](#)

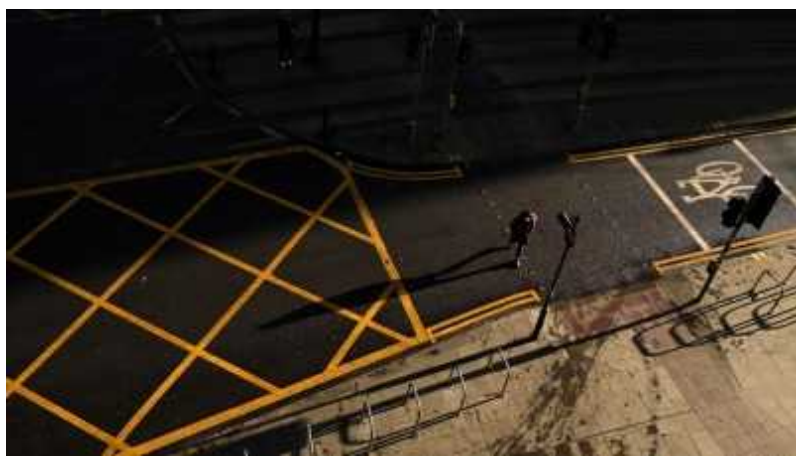
But such caution runs contrary to the growing open-source movement. As of 4 May, [an online letter](#) calling for researchers to put genome sequences in the public domain was signed by 778 scientists at universities and pharmaceutical companies — 99% of them based in Europe, the United States and Canada. Rolf Apweiler, the co-director of the group that posted the letter in late January, the European Bioinformatics Institute near

Cambridge, UK, tells *Nature*, “Sequencing is not for enriching the career of individual researchers, but for fighting a pandemic.”

Tulio de Oliveira, director of the KwaZulu-Natal Research and Innovation and Sequencing Platform in Durban, South Africa, agrees. But he counters that the most immediate goal for those sequencing SARS-CoV-2 is guiding their own country’s outbreak response, and that governments listen most often to their own scientists.

## Open-access requirements

Apweiler’s letter caught the attention of NIH director Francis Collins recently. In a 21 April e-mail to dozens of international scientists — shared anonymously with *Nature* — Collins links to the letter, along with news articles in [Nature](#) and [Science](#) about complaints over GISAID’s data-sharing policies. He says global health funders, such as the NIH, are best positioned to set standards on sharing, and requests a meeting to discuss how to improve data access while protecting the interests of the scientists depositing data. Glenda Gray, president of the South African Medical Research Council in Cape Town, replied in the e-mail chain that if an open-access requirement comes to fruition, many scientists will stop sharing rapidly. “If one is not careful,” she writes, “one will go back to the model of depositing data only after publication, which can take months or even years.”



### [Alarming COVID variants show vital role of genomic surveillance](#)

Collins did not respond to a request for comment from *Nature*.

The Gates Foundation is also talking about data sharing. It has told the Africa Centres for Disease Control and Prevention that, in the future, it might encourage grant recipients to share their results on open-access databases, says Yenew Kebede Tebeje, a microbiologist at the agency in Addis Ababa. A representative of the Gates Foundation says that GISAID or any accessible database suffices for sharing genome sequences, but did not answer *Nature*'s question about future requirements.

An [anonymous editorial posted 4 May](#) on the South African online news outlet *IOL* argues that a push from wealthy countries for open data is suspect, given how often scientists in the global south go unacknowledged. “A neocolonial mentality has long permeated the scientific community,” the editorial says.



### Why US coronavirus tracking can't keep up with concerning variants

Fears of exploitation haven't changed Apweiler's mind, however. "The focus on low- and middle-income countries is bizarre because their amount of data is relatively little," he says. Africa has uploaded around 13,000 sequences to GISAID, and South America has uploaded 14,000 sequences, for instance, compared with about 380,000 from the United Kingdom alone.

But others note that, as COVID-19 rates drop in Europe and the United States, dangerous variants are more likely to pop up in low- and middle-income countries with few vaccines. Sequences from these places will

therefore be in demand, says Nuno Faria, a computational virologist at the Institute for Tropical Medicine at the University of São Paulo in Brazil and Imperial College London. Because Brazilian researchers have shared data on GISAID, Faria points out, the P.1 variant, which appears to make vaccines slightly less effective<sup>1</sup>, is known to now account for 82% of all coronavirus genomes sequenced in the country. And, in Peru, where P.1 is also spreading, researchers say that if GISAID didn't offer data depositors protection, there would probably be less sharing.

Nature **593**, 176-177 (2021)

doi: <https://doi.org/10.1038/d41586-021-01194-6>

## References

1. 1.

Wang, P. *et al.* Preprint at bioRxiv  
<https://doi.org/10.1101/2021.03.01.433466> (2021).

## Jobs from Nature Careers

- - - [All jobs](#)
    - - [Postdoctoral Research Fellow in Urban Climate Action](#)  
  
[The University of British Columbia \(UBC\)](#)  
  
[Vancouver, Canada](#)  
  
[JOB POST](#)
  - [Postdoctoral Fellow in Supercapacitor Technology](#)

The University of British Columbia (UBC)

Kelowna, Canada

JOB POST

- **Postdoctoral Researchers x 2 – Advancement of audit procedure for domestic and non-domestic energy compliance tools, SFI MaREI Centre, NUI Galway (NUIG-RES-095-21)**

National University of Ireland Galway (NUI Galway).

Galway, Ireland

JOB POST

- **Semantic Web Developer**

European Molecular Biology Laboratory (EMBL).

Hinxton, Cambridge, United Kingdom

JOB POST

---

This article was downloaded by **calibre** from <https://www.nature.com/articles/d41586-021-01194-6>

## NEWS

04 May 2021

- Update [12 May 2021](#)

# China's COVID vaccines are going global — but questions remain

The WHO has approved one of China's COVID-19 vaccines for use worldwide and another is under review. But published trial data remain scarce.

- [Smriti Mallapaty](#)

1. Smriti Mallapaty

[View author publications](#)

You can also search for this author in [PubMed](#) [Google Scholar](#)



Students are inoculated at a mass vaccination hub at Peking University in Beijing. Credit: VCG via Getty

The World Health Organization (WHO) has authorized the first of China's COVID-19 vaccines for emergency use, and another could be listed in the coming days, opening the door to wide distribution in lower-income nations through the COVID-19 Vaccines Global Access (COVAX) initiative.

The listing will boost global confidence in these vaccines, say scientists. China's five different vaccines have not been used widely in wealthy nations, but are already sustaining immunization campaigns in the global south.

"There is big demand for the Chinese vaccines," says Firdausi Qadri, an immunologist at the International Centre for Diarrhoeal Disease Research, Bangladesh, in Dhaka.



### [What China's speedy COVID vaccine deployment means for the pandemic](#)

The first vaccine to be listed is made in Beijing by Chinese state-owned firm Sinopharm. The other under review — named CoronaVac — is produced by private company Sinovac, also based in Beijing. Five COVID-19 vaccines are already authorized by the WHO, but unlike these, the Chinese ones use inactivated virus and are not widely used in Western nations.

Sinopharm and Sinovac's vaccines account for the bulk of shots given in China, which has so far inoculated 243 million people. More than 45 countries have

already approved their use, but the WHO is among the first stringent regulatory authorities to review the data.

“It is very important to have the support of the WHO,” said Rafael Araos, a physician and epidemiologist at University for Development in Santiago, before the Sinopharm vaccine was listed. A positive response will be “very good news for the vaccine developers and for the countries that are interested in getting these vaccines”.

## Addressing the shortfall

The WHO approval process assesses safety, efficacy and manufacturing quality, says Qadri. Approved products can be purchased by United Nations agencies.

“Until that happens, it will be up to the individual countries to procure the vaccines, and most countries will be not be able to,” she adds.

The vaccines could also help to address the current shortfall in vaccines available through COVAX, an initiative led by international partnerships and agencies, including the WHO, to ensure that COVID-19 vaccines are distributed equitably.



### India's COVID-vaccine woes — by the numbers

By the end of April, COVAX had shipped only about 50 million of the 2 billion doses it aims to deliver globally in 2021. India is meant to contribute one billion doses of its Covishield vaccine, but exports have halted, owing to [the country's ongoing COVID-19 crisis](#). Deliveries to COVAX of another WHO-listed vaccine

produced by the pharmaceutical firm Pfizer have been limited, and none of Johnson & Johnson's have been shipped yet. Moderna's vaccine was listed by the WHO on 30 April.

As a result, Chinese vaccines are badly needed, says Gagandeep Kang, a virologist at the Christian Medical College in Vellore, India, and a member of a technical group on immunization that advises the WHO. The group met on 29 April to review data on the two Chinese vaccines, and will soon provide recommendations on their use.

Inactivated-virus vaccines have generally proven less effective than others in use. However, they still exceed the WHO's 50% efficacy threshold for emergency-use approval, making them important to reduce the global shortfall, argues Murat Akova, a clinical infectious-diseases researcher at Hacettepe University in Ankara. "If nothing else is available, I think these vaccines are a good choice."

## Scattered data

Chinese researchers were [among the first](#) to begin developing vaccines against COVID-19 in early 2020, but they have yet to publish full trial results. Some researchers have raised concerns that a lack of transparency could fuel vaccine hesitancy, but others say collating the data takes time and resources, and should be available for both front-runner vaccines within weeks.

China's vaccines (see 'How China's vaccines compare') have had to be trialled elsewhere because the country didn't have enough transmission itself to conduct them, says George Gao, who heads the Chinese Center for Disease Control and Prevention in Beijing.



## What scientists do and don't know about the Oxford–AstraZeneca COVID vaccine

So far, only scattered information from various nations has been released on Sinopharm's Beijing vaccine, says Hilda Bastian, an independent scientist who studies evidence-based medicine in Victoria, Australia (Sinopharm is producing a second inactivated-virus vaccine in Wuhan). She hopes the WHO will now release detailed data.

In early December, both the United Arab Emirates (UAE) and Bahrain approved it — making it among the [first COVID-19 vaccines to be granted full clearance](#) in any country. Approval was based on late-stage trial data, including a UAE study involving 31,000 participants. These showed the vaccine was 86% effective at preventing COVID-19 after 2 shots, with no deaths among immunized individuals. The WHO listed the vaccine on 7 May and reported an efficacy of 79%.

Data on CoronaVac from clinical trials and national vaccination campaigns have also emerged, [with mixed results](#). Trials from Brazil and Turkey have revealed efficacy figures of 50.7% and 83.5%, respectively. Researchers say the lower figure might be because Brazil includes mild cases of COVID-19 in its counting and because there is circulation of the P.1 variant, which is more transmissible and might be better at evading immunity. Results from an analysis following mass vaccinations in Chile have landed between these numbers, at 67%.

## **HOW CHINA'S VACCINES COMPARE**

Five vaccines have been approved for use in China. Unlike RNA vaccines being rolled out elsewhere, all can be stored in a fridge at 2–8 °C. Although full efficacy results have not been published, interim data come from clinical trials in more than a dozen nations, which have used these vaccines to protect tens of millions of people.

Vaccines:	Sinopharm (Beijing)	CoronaVac	Sinopharm (Wuhan)	Convidecia	Anhui Zhifei
Produced by	Sinopharm's Beijing Institute of Biological Products	Sinovac Biotech	Sinopharm's Wuhan Institute of Biological Products	CanSino Biologics; Academy of Military Medical Sciences	Anhui Zhifei Longcom; Chinese Academy of Sciences
Efficacy preventing COVID-19	79–86% (2 doses)	50–84% (2 doses)	73% (2 doses)	65–69% (1 dose)	Unavailable (2–3 doses)
Technology	Inactivated virus	Inactivated virus	Inactivated virus	Adenovirus vector	Protein-based
Total doses distributed	>100 million*	260 million	>100 million*	Unavailable	Unavailable
Countries/regions reached	>55 (~50 million doses)*	>40 (~156 million doses)	>55 (~50 million doses)*	Unavailable	Unavailable
Production goal in 2021	1 billion doses*	2 billion doses	1 billion doses*	100 million doses	Unavailable

Vaccines:	Sinopharm (Beijing)	CoronaVac	Sinopharm (Wuhan)	Convidecia	Anhui Zhifei
Phase III clinical trials	UAE, Peru, Argentina, Bahrain, Jordan, Egypt	Chile, Indonesia, Brazil, Turkey, Philippines, China	UAE, Peru, Bahrain, Jordan, Egypt, Morocco	Pakistan, Russia, Chile, Argentina, Mexico	China, Uzbekistan

\*Data for both Sinopharm vaccines are aggregated.

## China's vaccine drive

CoronaVac and both Sinopharm vaccines are the mainstay of China's own immunization drive, which aims to vaccinate 70% of its population of 1.4 billion by the end of 2021. China approved its first COVID-19 vaccines for emergency use in June 2020 and began rolling out doses more widely in January.

So far, only Chinese vaccines have been listed by the country's drug agency, which since December has approved both Sinopharm's vaccines; CoronaVac; and a fourth vaccine produced by CanSino Biologics in Tianjin, which uses an adenovirus to introduce DNA encoding the SARS-CoV-2 spike protein into human cells.

In March, China's drug agency also gave emergency-use authorization to a vaccine produced by Anhui Zhifei Longcom, a firm based in Hefei. It works by introducing part of the virus's receptor-binding domain protein to human cells, and is now undergoing phase III trials in Uzbekistan.

Gao says the Chinese vaccines generally provide good protection, but might need subsequent boosters to induce stronger protection. Mixing vaccines that use different technologies or different modes of entry, such as nasal sprays, might be useful, he adds.

## Global reach

China's vaccines have already catalysed immunization campaigns in more than 40 countries. The country aims to produce between three and five billion doses this year, and more may come from manufacturing deals with other countries, such as the UAE, which is making a version of Sinopharm's Beijing vaccine, called Hayat-Vax.

For many countries, Chinese vaccines were the only accessible ones. In others — such as Brazil, Turkey and Chile, where many tens of millions of people have been vaccinated — they make up some 80–90% of doses administered. And researchers in these countries are beginning to see evidence of their effect in controlling the pandemic<sup>1</sup>.



### J&J's single-dose COVID vaccine raises hopes for faster rollout

Anecdotal reports hint at a low incidence of breakthrough infections, severe illness and death among fully vaccinated individuals in Brazil, says Esper Kallas, an infectious-diseases researcher at the University of São Paulo, Brazil. “Because we have access to CoronaVac, we've got to use it,” he says. “I'm not saying this will be the preferred vaccine in the future.”

WHO's emergency-use listing of CoronaVac would further validate its use in countries that led with it. The decision to approve it would “provide confidence”, says Akova.

But many questions remain about the vaccines. Researchers want more data on how well they protect older people, children, pregnant women and immunocompromised groups. They also want to know what types of immune

response the jabs trigger, how long protection lasts and how well they work against emerging variants. “The more data we have, the better,” says Kallas.

Nature **593**, 178-179 (2021)

doi: <https://doi.org/10.1038/d41586-021-01146-0>

## Updates & Corrections

- **Update 12 May 2021:** This story was updated to include the news that on 7 May, the World Health Organization listed Sinopharm’s Beijing vaccine and reported an efficacy of 79%.

## References

1. 1.

Victora, C. G. *et al.* Preprint at medRxiv  
<https://doi.org/10.1101/2021.04.27.21256187> (2021).

## Jobs from Nature Careers

- - - [All jobs](#)
    - 
    - [\*\*Postdoctoral Research Fellow in Urban Climate Action\*\*](#)  
[The University of British Columbia \(UBC\)](#)  
[Vancouver, Canada](#)  
[JOB POST](#)
- [\*\*Postdoctoral Fellow in Supercapacitor Technology\*\*](#)  
[The University of British Columbia \(UBC\)](#)  
[Kelowna, Canada](#)

JOB POST

- **Postdoctoral Researchers x 2 – Advancement of audit procedure for domestic and non-domestic energy compliance tools, SFI MaREI Centre, NUI Galway (NUIG-RES-095-21)**

National University of Ireland Galway (NUI Galway).

Galway, Ireland

JOB POST

- **Semantic Web Developer**

European Molecular Biology Laboratory (EMBL)

Hinxton, Cambridge, United Kingdom

JOB POST

---

This article was downloaded by **calibre** from <https://www.nature.com/articles/d41586-021-01146-0>

NEWS

05 May 2021

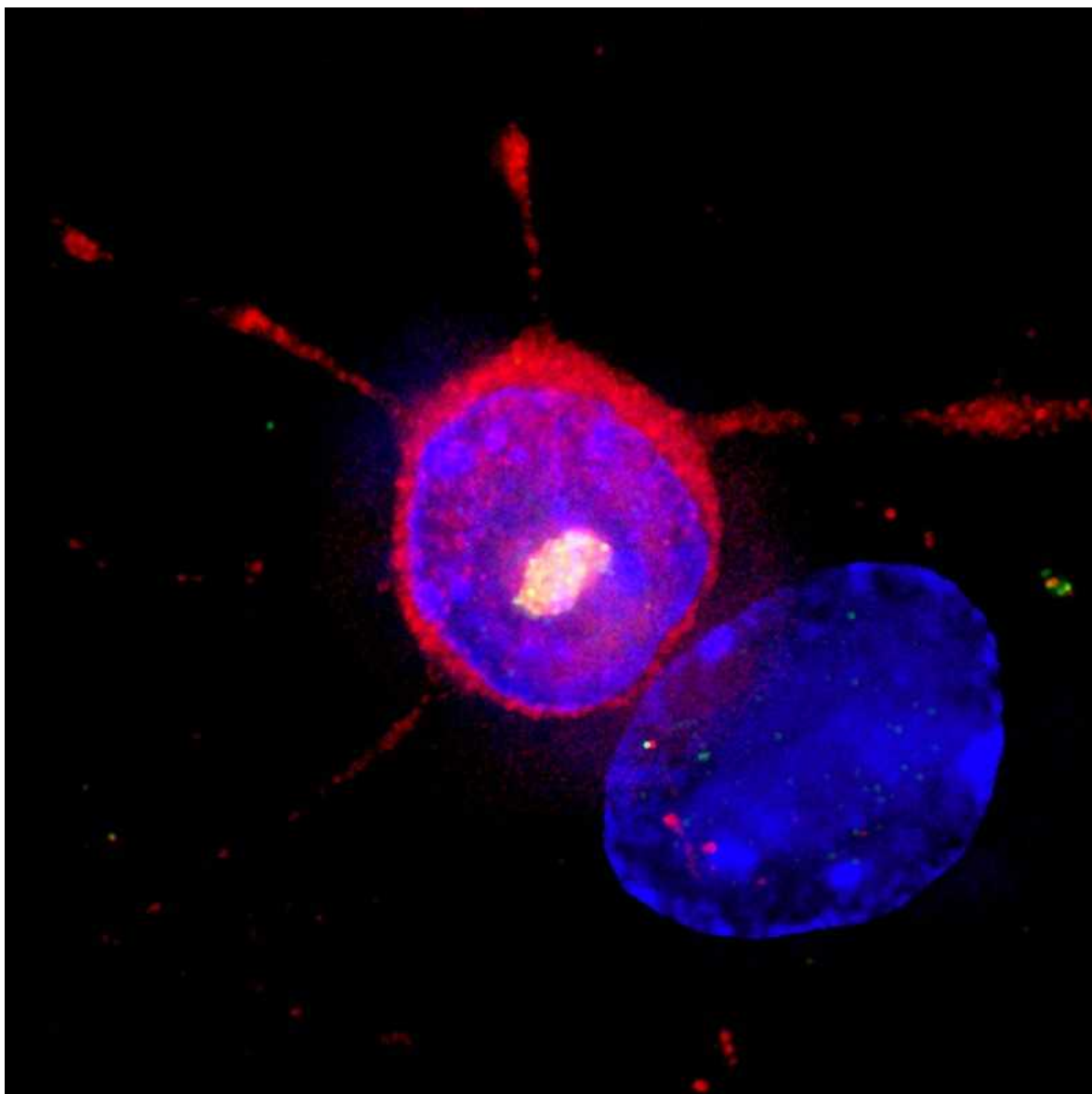
- Clarification [06 May 2021](#)

# Failure of genetic therapies for Huntington's devastates community

Hopes were high for drugs designed to lower levels of a mutant protein, but development has stalled.

- [Diana Kwon](#)
  1. Diana Kwon  
[View author publications](#)

You can also search for this author in [PubMed](#) [Google Scholar](#)



A mutant form of huntingtin protein, which causes Huntington's disease, accumulates in nerve cells. Credit: Frederic Sadou, ISM/Science Photo Library

Two pharmaceutical companies have halted clinical trials of gene-targeting therapies for Huntington's disease (HD), following the drugs' disappointing performance.

Researchers had hoped that the treatments — known as antisense oligonucleotides (ASOs) — would be a game changer for HD, an incurable genetic condition that affects cognition, behaviour and movement. But back-

to-back announcements from Roche, headquartered in Basel, Switzerland, and Wave Life Sciences, in Cambridge, Massachusetts, have dealt a crushing blow to those affected by the disease.

“I was really shocked, really tearful,” says Marion, a woman in London with HD, who was part of one of the trials. “We didn’t see it coming at all. I felt really frightened and worried about my future.” Marion requested that her last name be withheld to protect her privacy.



### [Genetic therapies offer new hope against incurable brain diseases](#)

In mid-March, Roche announced that it was halting a phase III study of its ASO drug, tominersen. A week later, Wave Life Sciences said that it would discontinue the development of two of its HD ASOs that were in phase I/II clinical trials.

“The Roche trial in particular left the community quite devastated,” says Cath Stanley, chief executive of the Huntington’s Disease Association, a UK advocacy group supporting people with the disease. “There has been so much positive noise around it, both from researchers and clinicians and from the drug company themselves. I think the community was really swept up by that hope.”

## **Problem proteins**

ASOs are short strands of DNA or RNA that modify the production of specific proteins by binding to sequences of RNA made by faulty genes. The

gene involved in Huntington's codes for a protein called huntingtin that is active in the brain. In people with HD, this gene repeats a short piece of its sequence — the nucleotide combination CAG — too many times. Both Roche and Wave Life Sciences were developing compounds aimed at lowering levels of the resulting mutant form of huntingtin.

Optimism around the Roche drug soared after the phase I/II trial showed that tominersen significantly lowered levels of mutant huntingtin in the cerebrospinal fluid, without serious side effects. But following a planned review of the data earlier this year, an independent committee of experts recommended the early termination of the trial, concluding that the drug's potential benefits did not outweigh its risks.

On 27 April, during a conference held by the CHDI Foundation — a US HD-research organization — Roche revealed that the trial had been halted because tominersen failed to show higher efficacy than placebo — and when given more frequently, led to worsened outcomes.

## **'The saddest possible result'**

The phase III tominersen trial tested 2 dosing regimens: 120 mg of the drug — the highest safe dose based on earlier trials — given either every 8 weeks or every 16 weeks.

Roche reported that after 69 weeks, patients on the 8-week regimen experienced more marked decline than those in the placebo group, with worsened outcomes in areas such as motor function and cognition. Participants in the 16-week treatment group had better outcomes than those in the 8-week arm, but experienced no overall benefit compared with those given a placebo. Those in the treatment group also showed larger increases in the size of fluid-filled cavities in the brain known as ventricles — a process that typically occurs in those with untreated HD — than did those who received a placebo.



## Huntington's antisense drug marches into clinic

“It’s the saddest possible result,” says Claudia Testa, a neurologist at Virginia Commonwealth University in Richmond, who has received consulting fees from Wave Life Sciences. “It’s clearly the right decision to halt dosing, even though I’m sure that was not the outcome anyone hoped for.”

Several factors could have contributed to tominersen’s failure, according to Sarah Tabrizi, a neurologist at University College London and one of the investigators in the Roche trial. The drug suppresses production of the healthy, as well as the mutant, form of huntingtin, and a decrease in levels of the normal protein could have caused problems. Other possibilities are that the ASO did not reach the right parts of the brain, or that the disease had simply progressed too far in the trial participants for the drug to be beneficial.

Tabrizi adds that it will take several months of further analysis to pinpoint what went wrong. Roche’s results were preliminary, and important data are still being assessed.

## **Guarded optimism**

Wave Life Sciences' trials were testing ASOs that leave the healthy version of huntingtin intact by targeting small mutations that only occur in the faulty gene, known as single-nucleotide polymorphisms (SNPs). These occur in a subset of people with HD.

But two such compounds failed to significantly lower levels of mutant huntingtin in early phase I/II trials, leading the company to abandon their development. The findings from those trials suggests that “we didn’t get enough drug where it needed to be to have an effect”, says Mike Panzara, the company’s chief medical officer. This is a different problem from that seen with tominersen, which did lower levels of the mutant protein but did not seem to slow progression of the disease.

### Leukaemia success heralds wave of gene-editing therapies

Wave does have a third Huntington’s ASO in development, which goes after a different SNP and has chemical modifications that improve the drug’s potency and ability to reach its targets.

And although hopes for a genetic therapy for Huntington’s have been dashed — at least temporarily — researchers are eagerly awaiting the results of a large phase III trial of an ASO for motor neuron disease (amyotrophic lateral sclerosis, or ALS). What happened with tominersen is not a cause for concern for this trial, says Don Cleveland, a neuroscientist at the University of California, San Diego, and consultant for Ionis Pharmaceuticals in Carlsbad, California, which developed both this drug and tominersen. This is because, unlike in the early trials for tominersen, the phase I/II trial of the ALS drug did show signs of slowing the disease’s progression in those with a rapidly advancing form of ALS.

“I think we have reason for guarded optimism,” Cleveland says.

Nature **593**, 180 (2021)

doi: <https://doi.org/10.1038/d41586-021-01177-7>

## Updates & Corrections

- **Clarification 06 May 2021:** This article has been updated to include more detail about the ASOs developed by Wave Life Sciences.

## Jobs from Nature Careers

- - - [All jobs](#)
    - - **[Postdoctoral Research Fellow in Urban Climate Action](#)**

[The University of British Columbia \(UBC\)](#)

[Vancouver, Canada](#)

[JOB POST](#)

▪ **[Postdoctoral Fellow in Supercapacitor Technology](#)**

[The University of British Columbia \(UBC\)](#)

[Kelowna, Canada](#)

[JOB POST](#)

▪ **[Postdoctoral Researchers x 2 – Advancement of audit procedure for domestic and non-domestic energy compliance tools, SFI MaREI Centre, NUI Galway \(NUIG-RES-095-21\)](#)**

[National University of Ireland Galway \(NUI Galway\)](#)

[Galway, Ireland](#)

[JOB POST](#)

▪ **Semantic Web Developer**

European Molecular Biology Laboratory (EMBL)

Hinxton, Cambridge, United Kingdom

**JOB POST**

---

This article was downloaded by **calibre** from <https://www.nature.com/articles/d41586-021-01177-7>

| [Section menu](#) | [Main menu](#) |

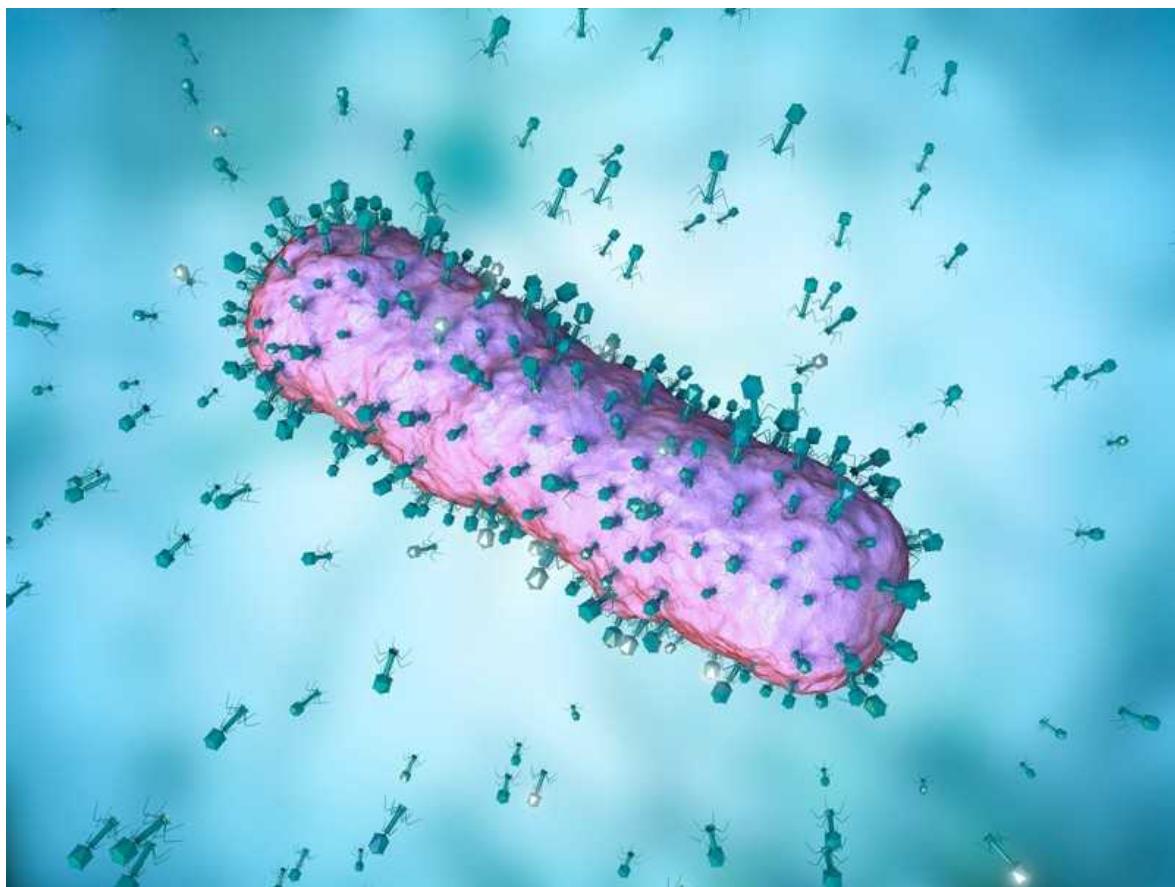
NEWS  
29 April 2021

# Weird viral DNA spills secrets to biologists

Bacteria-infecting viruses have specialized enzymes to make genes with alternative nucleobase.

- [Ewen Callaway](#)  
1. Ewen Callaway  
[View author publications](#)

You can also search for this author in [PubMed](#) [Google Scholar](#)



Bacteriophage viruses — seen attacking an *E. coli* cell in this computer illustration — can have exotic chemistries in their DNA. Credit: Maurizio De Angelis/Science Photo Library

‘Alien’ genomes can be found on Earth. Some viruses that infect bacteria use an alternative genetic alphabet that’s distinct from the code used by nearly all other organisms — and, now, two teams have spelt out how the system works.

More than four decades in the making, the studies show how dozens of these bacteriophages (or just ‘phages’), as they are known, write their genomes using a chemical base called 2-aminoadenine, Z for short, instead of adenine — the A in the As, Ts, Cs and Gs of genetics textbooks.

“Scientists have long dreamed of increasing the diversity of bases. Our work shows that nature has already come up with a way to do that,” write Suwen Zhao, a computational biologist at ShanghaiTech University in China, and her team in a 29 April *Science* paper, showing how ‘Z-DNA’ is made<sup>1</sup>.

Researchers in France described similar insights in a pair of papers in the same journal<sup>[2,3](#)</sup>.

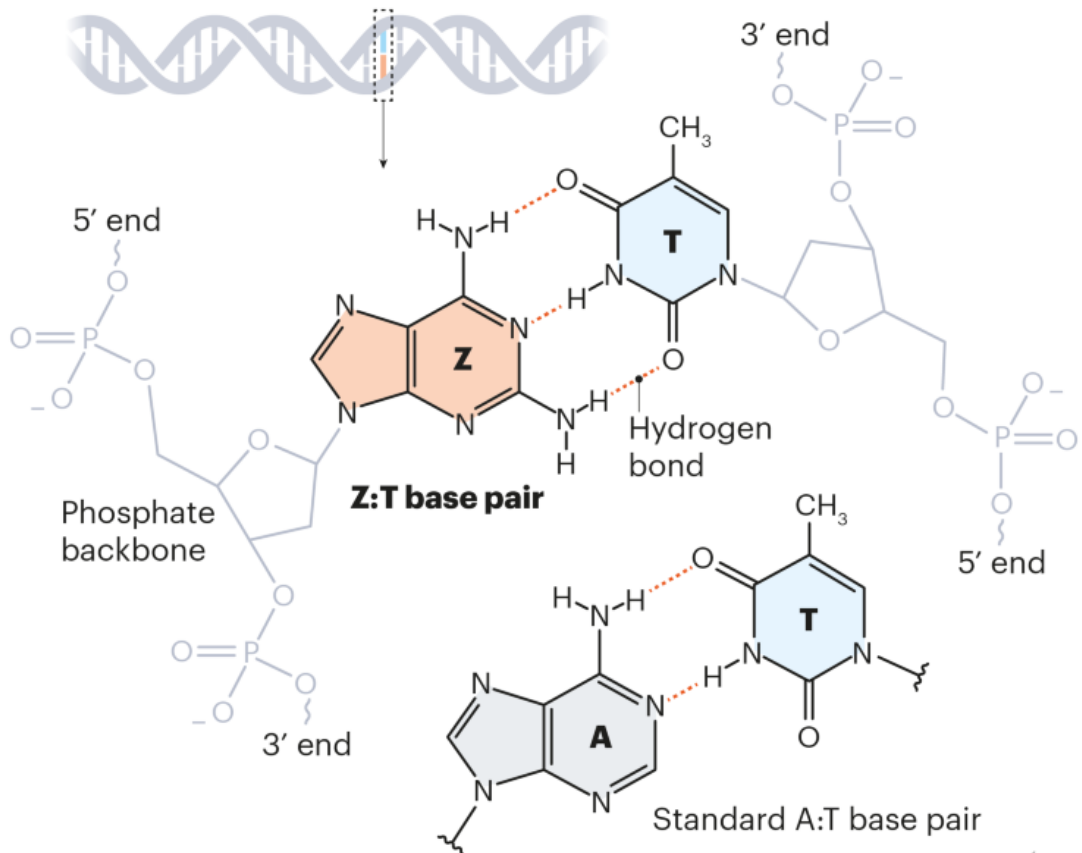
The work is seminal, says Steven Benner, a synthetic biologist and founder of the Foundation for Applied Molecular Evolution in Alachua, Florida, who compares it to US microbiologist Carl Woese's discovery of a new branch of single-celled life. "It represents the first discovery of a 'shadow biosphere' since Woese identified the Archaea a half century ago."

## Bond booster

Scientists in the Soviet Union were the first to discover Z-DNA, in the late 1970s, in a phage called S-2L, which infects photosynthetic bacteria<sup>[4](#)</sup>. They found that the phage DNA behaved oddly when its two helical strands were melted apart. The bond that forms between G and C bases breaks at a higher temperature, compared with that joining A and T, and the phage's DNA behaved as if it was made primarily from G and C. But further analysis by the Soviet team showed that the phage had replaced A with Z, which formed a stronger bond with T.

## HARDY GENOME

The 'Z' base that replaces the 'A' in the genetic alphabet of certain viruses forms three hydrogen bonds instead of two, making the two DNA strands tougher to pull apart.



“It looked like something transgressive,” says Philippe Marlière, an inventor and geneticist at the University of Evry, France, who led one of the *Science* studies. “Why did this phage have a special base like this?”



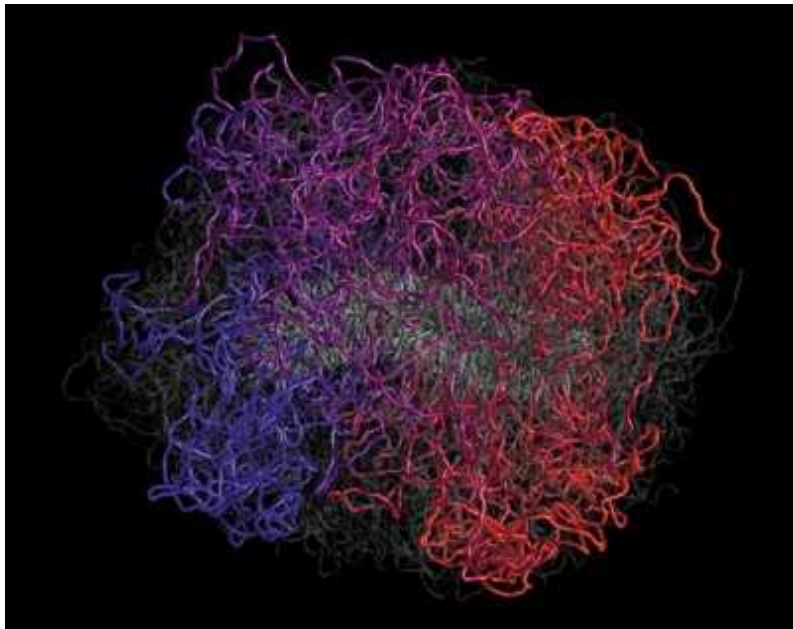
## [Scientists glimpse oddball microbe that could help explain rise of complex life](#)

Follow-up studies showed that S-2L's heartier genome was resistant to DNA-chomping enzymes and other anti-phage defences that bacteria wield. But researchers didn't know how the Z-DNA system worked or whether it was common. Z-DNA is only one of a host of modifications known to exist in phage DNA.

To answer those questions, a team led by Marlière and Pierre-Alexandre Kaminski, a biochemist at the Pasteur Institute in Paris, sequenced the phage's genome in the early 2000s. They found a gene that's potentially involved in one step of making Z-DNA, but not in others. But the sequence had no matches in genomic databases at the time, and the team's quest to understand the basis for Z-DNA hit a dead end.

Marlière and his colleagues patented the S-2L genome, but also made it public, and he continued to scour genomic databases. Finally, in 2015, the team got a hit: a phage that infects aquatic bacteria of the genus *Vibrio* harboured a gene that matched a stretch of S-2L's genome. The gene encoded an enzyme that resembled one that bacteria use to make adenine. "It was an exhilarating moment," says Marlière.

In 2019, Zhao's team found similar database matches. Both teams showed that the phages all had a gene named PurZ. This codes for an enzyme that plays an early but crucial part in making the Z nucleotide from a precursor molecule that is present in bacterial cells. They then identified additional enzymes — encoded in the genomes of bacteria that the phages infect — that complete the pathway.



### DNA's secret weapon against knots and tangles

But a key question lingered. The enzymes that the teams identified produced the raw ingredient for Z-DNA — a molecule called dZTP — but that didn't explain how phages insert the molecule into DNA strands, while excluding A bases (in the form of a chemical called dATP).

Here, the teams' conclusions differed slightly. Alongside PurZ in the *Vibrio* phage's genome sits a gene that makes an enzyme called a polymerase, which copies DNA strands. Marlière and Kaminski found that the phage polymerase incorporates dZTP into DNA, while cutting out any A bases that were introduced. "This explained to us why A was excluded," says Kaminski. "This was really spectacular."

Zhao thinks this isn't the whole story. Her work suggests that another phage enzyme is needed, one that breaks up dATP but preserves dZTP inside cells.

Her team found that increasing dZTP levels relative to those of dATP was enough to trick a cell's own polymerase into making Z-DNA.

## Missing links

“There’s a lot we don’t know,” Zhao says. It’s not clear how hosts keep Z out of their DNA. Nor it is apparent how cellular machinery that reads DNA to make proteins copes with Z-DNA, which forms a double helix that’s shaped slightly differently from ordinary DNA molecules. It’s also not fully understood how Z-DNA is copied (a process that might require specialized enzymes in addition to polymerase), Kaminski adds. “We still don’t know how the whole system works.”

The functionality of host enzymes could be improved or impaired when working on Z-DNA, says David Dunlap, a biophysicist at Emory University in Atlanta, Georgia, who has found that an *E. coli* enzyme struggles to coil and bend the exotic double helix<sup>5</sup>. The discovery of more phages with Z-DNA, and of genes involved in making the molecule, should help researchers to understand how phages benefit from using it.

Having these genes in hand could speed potential applications of Z-DNA, by making it easier and cheaper to make, says Zhao. Z-DNA’s hardness could make the nascent technique of DNA data storage more stable and long-lasting. Nanomachines made of precisely arranged Z-DNA — known as DNA origami — might fold into shape faster. The French team is working on incorporating the molecule into bacterial genomes. “We have *E. coli* cells that are getting invaded with ‘Zed’. It’s not as toxic as I feared,” says Marlière.

Benner — whose research has expanded the genetic alphabet [to include several artificial DNA bases<sup>6</sup>](#) — hopes that the new studies will rattle researchers into realizing the power of altering the genetic alphabet. “The fact that nature has taken a small step in the same direction may be the intellectual caffeine needed to get the molecular-biology community to understand that DNA can be improved, and beneficially so,” he says.

doi: <https://doi.org/10.1038/d41586-021-01157-x>

## References

1. 1.  
Zhou, Y. *et al.* *Science* **372**, 512–516 (2021).
2. 2.  
Sleiman, D. *et al.* *Science* **372**, 516–520 (2021).
3. 3.  
Pezo, V. *et al.* *Science* **372**, 520–524 (2021).
4. 4.  
Kirmos, M. D., Khudyakov, I. Y., Alexandrushkina, N. I. & Vanyushin, B. F. *Nature* **270**, 369–370 (1977).
5. 5.  
Fernández-Sierra, M., Shao, Q., Fountain, C., Finzi, L. & Dunlap, D. *J. Mol. Biol.* **427**, 2305–2318 (2015).
6. 6.  
Hoshika, S. *et al.* *Science* **363**, 884–887 (2019).

## [\*\*Jobs from Nature Careers\*\*](#)

- - - [All jobs](#)
    - 
    -

## **Postdoctoral Research Fellow in Urban Climate Action**

The University of British Columbia (UBC)

Vancouver, Canada

JOB POST

### **▪ Postdoctoral Fellow in Supercapacitor Technology**

The University of British Columbia (UBC)

Kelowna, Canada

JOB POST

### **▪ Postdoctoral Researchers x 2 – Advancement of audit procedure for domestic and non-domestic energy compliance tools, SFI MaREI Centre, NUI Galway (NUIG-RES-095-21)**

National University of Ireland Galway (NUI Galway)

Galway, Ireland

JOB POST

### **▪ Semantic Web Developer**

European Molecular Biology Laboratory (EMBL)

Hinxton, Cambridge, United Kingdom

JOB POST

---

This article was downloaded by **calibre** from <https://www.nature.com/articles/d41586-021-01157-x>

| [Section menu](#) | [Main menu](#) |

## NEWS FEATURE

12 May 2021

# How COVID broke the evidence pipeline

The pandemic stress-tested the way the world produces evidence — and revealed all the flaws.

- [Helen Pearson](#)

1. Helen Pearson

[View author publications](#)

You can also search for this author in [PubMed](#) [Google Scholar](#)



Illustration by Jasiek Krzysztofiak/*Nature*

It wasn't long into the pandemic before Simon Carley realized we had an evidence problem. It was early 2020, and COVID-19 infections were starting to lap at the shores of the United Kingdom, where Carley is an emergency-medicine doctor at hospitals in Manchester. Carley is also a specialist in evidence-based medicine — the transformative idea that physicians should decide how to treat people by referring to rigorous evidence, such as clinical trials.

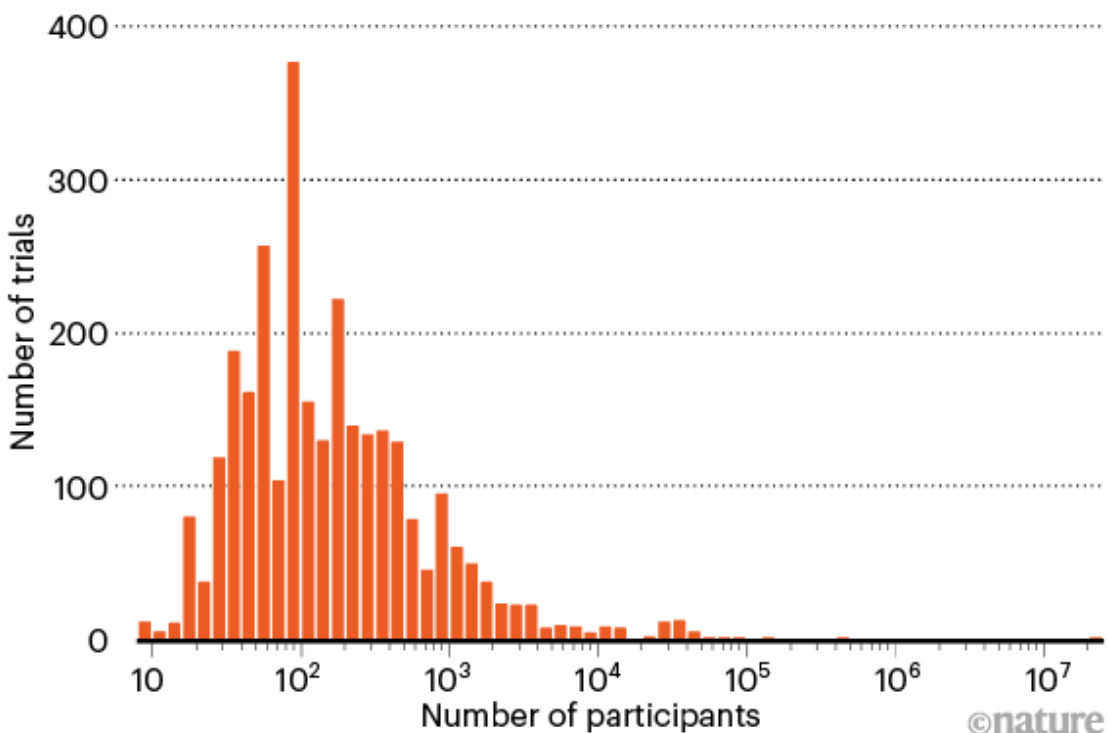
As cases of COVID-19 climbed in February, Carley thought that clinicians were suddenly abandoning evidence and reaching for drugs just because they sounded biologically plausible. Early studies Carley saw being published often lacked control groups or enrolled too few people to draw firm conclusions. "We were starting to treat patients with these drugs initially just on what seemed like a good idea," he says. He understood the

desire to do whatever is possible for someone gravely ill, but he also knew how dangerous it is to assume a drug works when so many promising treatments prove to be ineffective — or even harmful — in trials. “The COVID-19 pandemic has arguably been one of the greatest challenges to evidence-based medicine since the term was coined in the last century,” Carley and his colleagues wrote of the problems they were seeing<sup>1</sup>.

Other medical experts echo these concerns. With the pandemic now deep into its second year, it’s clear the crisis has exposed major weaknesses in the production and use of research-based evidence — failures that have inevitably cost lives. Researchers have registered more than 2,900 clinical trials related to COVID-19, but the majority are too small or poorly designed to be of much use (see ‘Small samples’). Organizations worldwide have scrambled to synthesize the available evidence on drugs, masks and other key issues, but can’t keep up with the outpouring of new research, and often repeat others’ work. There’s been “research waste at an unprecedented scale”, says Huseyin Naci, who studies health policy at the London School of Economics.

## SMALL SAMPLES

In one database of COVID-19 trials, 40% stated that they were enrolling fewer than 100 patients — a sample size that is generally too small to be useful.



Source: COVID-NMA

At the same time, shining examples of good practice have emerged: medical advances based on rigorous evidence have helped to chart a route out of the pandemic. The rapid trials of vaccines were spectacular successes, and well-run trials of possible treatments have shown, for instance, that some steroids help to fight COVID-19, but the drug hydroxychloroquine doesn't. Many physicians point to the United Kingdom's RECOVERY trial as exemplary in showing how quick action and simple protocols make it possible to conduct a large clinical trial in a crisis. And researchers have launched 'living' systematic reviews that are constantly updated as research emerges — essential in a fast-moving disease outbreak.

As the COVID-19 response turns from a sprint to a marathon, researchers are taking stock and looking ahead. In October, global-health leaders will meet for three days to discuss what's been learnt from COVID-19 about

supplying evidence in health emergencies. COVID-19 is a stress test that revealed the flaws in systems that produce evidence, says Elie Akl, an internal-medicine specialist and clinical epidemiologist at the American University of Beirut. “It would be shameful if we come out of this experience and not make the necessary change for the next crisis.”



A man with coronavirus is treated in Cambridge, UK, as part of a trial to test immune-system drugs.Credit: Kirsty Wigglesworth/Getty

## The evidence revolution

The idea that medicine should be based on research and evidence is a surprisingly recent development. Many doctors practising today weren't taught too much about clinical trials in medical school. It was standard to offer advice largely on the basis of opinion and experience, which, in practice, often meant following the advice of the most senior physician in the room. (Today, this is sometimes called eminence-based medicine.)

In 1969, a young physician called Iain Chalmers realized the lethal flaw in this approach when he worked in a Palestinian refugee camp in the Gaza

Strip. Chalmers had been taught in medical school that young children with measles should not be treated with antibiotics unless it was certain that they had a secondary bacterial infection. He obediently withheld the drugs. But he found out later that what he'd been taught was wrong: six controlled clinical trials had shown that antibiotics given early to children with measles were effective at preventing serious bacterial infections. He knows that some children in his care died as a result, a tragedy that helped set him on a mission to put things right.



### Evidence-based medicine: how COVID can drive positive change

In the 1970s, Chalmers and a team set about systematically scouring the medical literature for controlled clinical trials relating to care in pregnancy and childbirth, a field in which the use of evidence was shockingly poor. A decade or so later, they published what they'd found in a database and two thick books with hundreds of systematic reviews showing that many routine procedures — such as shaving the pubic hair of women in labour or restricting access to their newborn babies — were either useless or harmful. Other procedures, such as giving antenatal steroids for premature births, convincingly saved lives. It was a landmark study<sup>2</sup>, and in 1993, Chalmers was central in founding the Cochrane collaboration, which aimed to follow this model and synthesize evidence across other medical specialties.

On the other side of the world, meanwhile, a group of doctors led by David Sackett working at McMaster University in Hamilton, Canada, had been developing a new way of teaching medicine, in which students were trained to critically appraise the medical literature to inform their decisions. In 1991, the term evidence-based medicine was coined, and it was later defined<sup>3</sup> as the “conscientious, explicit, and judicious use of current best evidence in making decisions about the care of individual patients”.

Today, it's common for doctors to use evidence, alongside their clinical expertise and a patient's preferences, to work out what to do. A bedrock of evidence is built from systematic reviews, in which researchers follow standard methods to analyse all relevant, rigorous evidence to answer a question. These reviews often include meta-analyses — the statistical combining of data from multiple studies, such as clinical trials. Cochrane and other groups published more than 24,000 systematic reviews in 2019 alone.



Some US protesters against COVID-19 restrictions promoted drugs not backed by evidence. Credit: Brian Snyder/Reuters/Alamy

Organizations in areas ranging from education to conservation also create evidence syntheses, and policymakers find them an invaluable tool. When faced with a slew of conflicting studies, an evidence synthesis “has the power to identify important conclusions about what works that would never be possible from assessing the underlying trials in isolation”, says Karla Soares-Weiser, editor-in-chief of the Cochrane Library and acting chief executive of Cochrane, based in Tel Aviv, Israel.

The rise of evidence syntheses has been “an invisible and gentle revolution”, says Jeremy Grimshaw, a senior scientist and implementation researcher at the Ottawa Hospital Research Institute. Once you see the compelling logic of assessing an entire landscape of science in this way, “it’s very hard to do anything else”, he says.

At least, that is, until COVID-19 hit.

## Tumult of trials

Carley compares the time before and after COVID-19 to a choice of meals. Before the pandemic, physicians wanted their evidence like a gourmet plate from a Michelin-starred restaurant: of exceptional quality, beautifully presented and with the provenance of all the ingredients — the clinical trials — perfectly clear. But after COVID-19 hit, standards slipped. It was, he says, as if doctors were staggering home from a club after ten pints of lager and would swallow any old evidence from the dodgy burger van on the street. “They didn’t know where it came from or what the ingredients were, they weren’t entirely sure whether it was meat or vegetarian, they would just eat anything,” he says. “And it just felt like you’ve gone from one to the other overnight.”



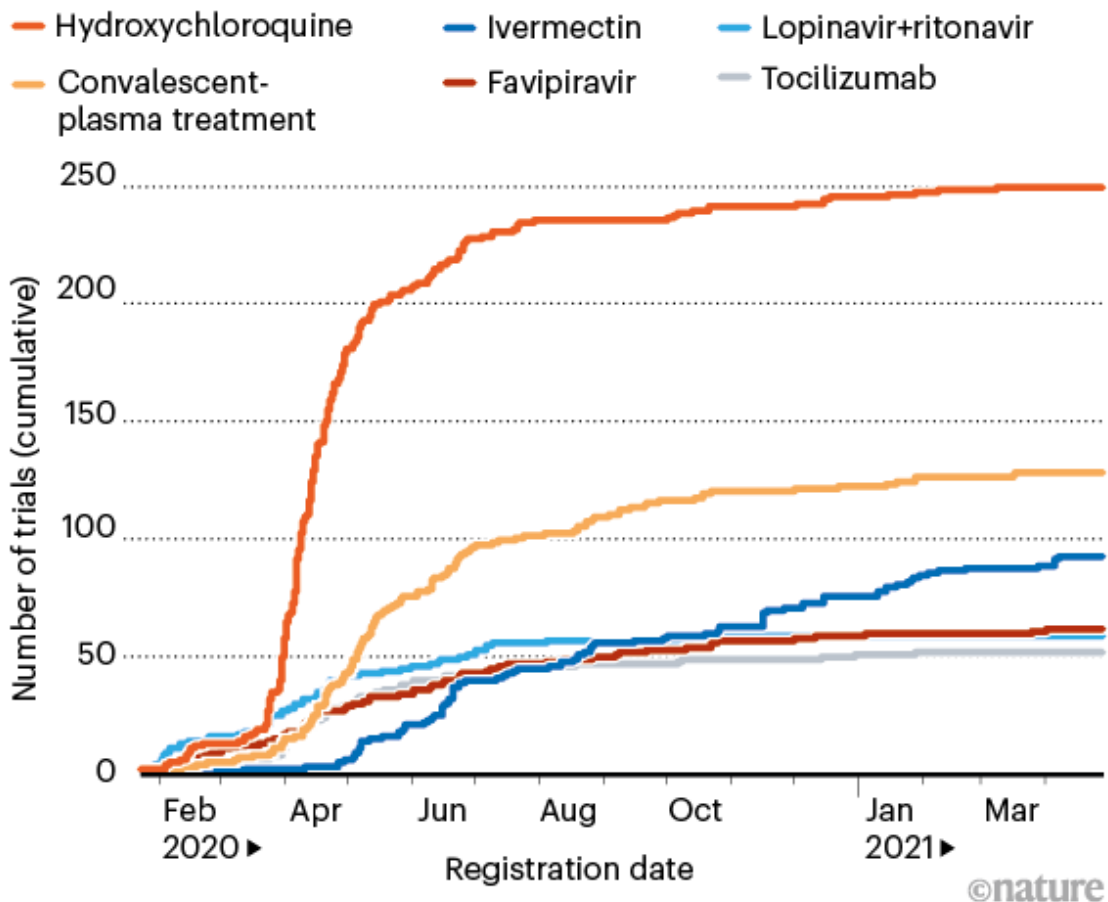
### International COVID-19 trial to restart with focus on immune responses

Kari Tikkinen, a urologist at the University of Helsinki who had run clinical trials in the past, was equally shocked early last year to talk to physicians who were so confident that untested therapies such as hydroxychloroquine were effective that they questioned the need to test them in clinical trials. It was “hype-based medicine”, he says — fuelled by former US president Donald Trump, who announced last May that he had started taking the drug himself. “It very quickly got ahead of us, where people were prescribing any variety of crazy choices for COVID,” says Reed Siemieniuk, a doctor and methodologist at McMaster University.

Many doctors and researchers did race to launch clinical trials — but most were too small to produce statistically meaningful results, says Tikkinen, who leads the Finnish arm of SOLIDARITY, an international clinical trial of COVID-19 treatments coordinated by the World Health Organization (WHO). Hydroxychloroquine was the most-tested drug according to a database of 2,900 COVID-19 clinical trials called [COVID-NMA](#): it was tested in 250 studies involving nearly 89,000 people (see ‘Too many trials?’). Many are still under way, despite convincing evidence that the drug doesn’t help: the RECOVERY trial concluded that hydroxychloroquine should not be recommended to treat COVID-19 in June last year.

## TOO MANY TRIALS?

Studies assessing drugs against COVID-19 included 250 trials of hydroxychloroquine — a duplication that researchers say represents wasted effort.



Source: COVID-NMA

Researchers have known for well over a decade that colossal amounts of medical research are wasted because of poorly designed trials and a failure to assess what research has been done before<sup>4</sup>. A basic calculation at the start of a COVID-19 trial, Tikkinen says, would have shown the large number of participants necessary to produce a meaningful result. “There was no coordination,” he says.

Instead, hospitals should have joined up, as was done in a handful of mega-trials. SOLIDARITY has enrolled nearly 12,000 people with COVID-19 in more than 30 countries. And many researchers look with awe at the

RECOVERY trial, which the United Kingdom launched rapidly in March 2020, in part because it was kept simple — a short consent procedure and one outcome measure: death within 28 days of being randomly assigned to a treatment or control group. The trial has now enrolled nearly 40,000 people at 180 sites and its results [showing that the steroid dexamethasone reduced death rates](#) changed standard practice almost overnight.

One clear take-home lesson, researchers say, is that countries need more large-scale national and international clinical-trial protocols sitting on the shelf, ready to fire up quickly when a pandemic strikes. “We will learn a lot of lessons from this, and I think RECOVERY has set the standard,” Tikkinen says.

Carley says that in February, he treated a man with COVID-19 who desperately wanted to receive monoclonal antibodies, but the only route to do so at Carley’s hospital was by enrolling him in RECOVERY. The randomization protocol assigned him to receive standard care, rather than the therapy. “Which was tough — I still think it’s the right thing to do,” says Carley, who adds that the man did OK. The RECOVERY trial announced<sup>5</sup> in February that the monoclonal antibody tocilizumab cut the risk of death in people hospitalized with severe COVID-19; testing of another antibody cocktail is still under way.

## The rise of reviews

The pandemic is “evidence on steroids”, says Gabriel Rada, who directs the evidence-based health-care programme at the Pontifical Catholic University of Chile in Santiago. Research on the disease has been produced at a phenomenal rate. And that created a knock-on problem for researchers who try to make sense of it.



### The epic battle against coronavirus misinformation and conspiracy theories

The number of evidence syntheses concerning COVID-19 went through the roof, as governments, local authorities and professional bodies flocked to commission them. “We’ve never seen this level of demand from decision makers saying ‘help, tell us what’s going on’,” Grimshaw says. Rada runs a giant database of systematic reviews in health called [Epistemonikos](#) (a Greek term meaning ‘what is worth knowing’). It now contains nearly 9,000 systematic reviews and other evidence syntheses related to COVID-19. But ironically, just like the primary research they are synthesizing, many of the syntheses themselves are of poor quality or repetitive. Earlier this year, Rada found 30 systematic reviews for convalescent plasma, based on only 11 clinical trials, and none of the reviews had included all the trials. He counted more than 100 on hydroxychloroquine, all out of date. “You have this huge amount of inappropriate and probably wasteful duplication of effort,” Grimshaw says. “There’s a fundamental noise-to-signal problem.”

One possible solution lies in [PROSPERO](#), a database started in 2011 in which researchers can register their planned systematic reviews. Lesley Stewart, who oversees it at the Centre for Reviews and Dissemination at the University of York, UK, says that more than 4,000 reviews on COVID-19 topics have been registered so far, and the PROSPERO team appeals to researchers to check the database before embarking on a review, to see whether similar work already exists. She’d like to see better ways to identify

the most important questions in health policy and treatment and make sure that researchers generating and synthesizing evidence are tackling those.

Researchers already knew that evidence syntheses took too long to produce and fell quickly out of date, and the pandemic threw those problems into sharp relief. Cochrane's median time to produce a review is more than two years and, although it commits to updating them, that isn't nimble enough when new research is flooding out. So, during the pandemic, Cochrane cut the time of some reviews to three to six months.

Systematic reviews are slow to produce in part because academics have to work hard even to identify relevant clinical trials in publication databases: the studies are not clearly tagged and researchers who do trials rarely talk to those collecting them into reviews. Julian Elliott, who directs Australia's COVID-19 Clinical Evidence Taskforce, based at Cochrane Australia, Monash University in Melbourne, says it's as if one group creates a precious artefact — its clinical-trial paper — and then tosses it into the desert, leaving the reviewers to come along like archaeologists with picks and brushes to try to unearth it in the dust. "It sounds completely insane, doesn't it?" he says.

Rada is trying to help. During the pandemic, he has compiled one of the largest repositories of COVID-19 research in the world, containing more than 410,000 articles by early May. The team uses automated and manual methods to trawl literature databases for research and then classify and tag it, for example as a randomized controlled trial. The goal is for the database, called [COVID-19 Living Overview of Evidence \(L·OVE\)](#), to be the raw material for evidence syntheses, saving everyone a monumental amount of work.



### The race for antiviral drugs to beat COVID — and the next pandemic

Drawing on this and other sources, a handful of groups including Cochrane have been developing living systematic reviews. Siemieniuk had produced such reviews before and helped to convene a group to build one on COVID-19 therapies. The international team, now about 50–60 people, combs the literature daily for clinical trials that could change practice and distils findings into a living guideline that doctors can quickly refer to at a patient's bedside and which is used by the WHO. "It's a very good concept," says Janita Chau, a specialist in evidence-based nursing at the Chinese University of Hong Kong and co-chair of a network of Cochrane centres in China. Chau says it's important to compile the evidence now rather than see interest in it fade away with the disease itself, as she saw during the SARS outbreak in 2003.

Isabelle Boutron, an epidemiologist at the University of Paris and director of Cochrane France, is co-leading another extensive living evidence synthesis, the COVID-NMA initiative, which is mapping where registered trials are taking place, evaluating their quality, synthesizing results and making the data openly available in real time. Ideally, she says, researchers planning trials would talk to evidence-synthesis specialists in advance to ensure that they are measuring the types of outcome that can be usefully combined with others in reviews. "We're really trying to link the different communities," she says.

Grimshaw, Elliott and others would like to see living reviews expanded. That's one focus of [COVID-END](#) (COVID-19 Evidence Network to support Decision-making), a network of organizations including Cochrane and the WHO that came together in days in April 2020 to better coordinate COVID-19 evidence syntheses and direct people to the best available evidence. The group is now working out its longer-term strategy, which includes a priority list for living evidence syntheses.

As the world moves into a recovery phase, Grimshaw, who co-leads COVID-END, argues that it will be served best by a global library of a few hundred living systematic reviews that address issues ranging from vaccine roll-out to recovery from school closures. “I think there’s a strong argument that you’ll get more bang for the buck if, in selected areas, you invest in living reviews,” he says.

## Mosaic of evidence

Even when rigorous clinical trials are too slow or difficult to run, the pandemic served as a reminder that it’s still possible to recommend what to do. In the United Kingdom, Trish Greenhalgh, a health researcher and doctor at the University of Oxford, expressed frustration at those who wanted bullet-proof evidence from randomized controlled trials [before recommending the widespread use of face masks](#), even though there was a wealth of other evidence that masks could be effective and, unlike an experimental drug, that they posed little potential harm. (The United Kingdom mandated face masks on public transport in June 2020, long after some other countries.) “I think that was just a blast of common sense,” says David Tovey, co-editor in chief of the *Journal of Clinical Epidemiology* and an adviser to COVID-END, based in London. “People have focused too much on randomized trials as being the one source of truth.”



## Face masks: what the data say

The issue is familiar in public health, says David Ogilvie, who works in the field at the MRC Epidemiology Unit at the University of Cambridge, UK. In the standard paradigm of evidence-based medicine, researchers collect evidence on a therapy from randomized controlled trials until it gets a green or red light. But in many situations, such trials are unethical, impractical or unfeasible: it's impossible to do a randomized controlled trial to test whether a new urban motorway improves people's health by siphoning traffic out of town, for example. Often, researchers have to pragmatically assess a range of different evidence — surveys, natural experiments, observational studies and trials — and mosaic them together to give a picture of whether something is worthwhile. "You have to get on and do what we can with the best available evidence, then continue to evaluate what we're doing," says Ogilvie.

However well scientists synthesize and package evidence, there's of course no guarantee that it will be listened to or used. The pandemic has shown how hard it can be to change the minds of ideologically driven politicians and hardened vaccine sceptics or to [beat back disinformation on Twitter](#). "We're definitely fighting against big forces," says Per Olav Vandvik, who heads the MAGIC Evidence Ecosystem Foundation in Oslo, which supports the use of trustworthy evidence.

Leaders in the field will pick up these debates in October during the virtual meeting organized by Cochrane, COVID-END and the WHO, to discuss what has been learnt about evidence supply and demand during the pandemic — and where to go next. One key issue, Soares-Weiser says, is ensuring that evidence addresses issues faced by low- and middle-income countries, as well as richer ones, and that access to evidence is equitable, too. “I really believe that we will come out of this crisis stronger,” she says.

Carley, meanwhile, is still treating people with COVID-19 in Manchester, and sometimes still seeing new treatments recommended before they’ve been tested in trials. The last year has been exhausting and awful, he says, “seeing young, fit, healthy people coming in with quite horrific chest X-rays and not do terribly well”.

At the same time, there’s a thrill in seeing the enormous difference that evidence — that science — can make. “When results come out and you see that dexamethasone is going to save literally hundreds of thousands of lives worldwide,” he says, “you think — ‘that’s amazing’.”

Nature **593**, 182-185 (2021)

doi: <https://doi.org/10.1038/d41586-021-01246-x>

## References

1. 1.

Carley, S. et al. *Emerg. Med. J.* **37**, 572–575 (2020).

2. 2.

Chalmers, I., Enkin, M. & Keirse, M. J. N. C. *Effective Care in Pregnancy and Childbirth* (Oxford Univ. Press, 1989).

3. 3.

Sackett, D. L., Rosenberg, W. M. C., Gray, J. A. M., Haynes, R. B. & Richardson, W. S. *Br. Med. J.* **312**, 71 (1996).

4. 4.

Chalmers, I. & Glasziou, P. *Lancet* **374**, 86–89 (2009).

5. 5.

RECOVERY Collaborative Group. *Lancet* **397**, 1637–1645 (2021).

## Jobs from Nature Careers

- - - [All jobs](#)
    - - **[Postdoctoral Research Fellow in Urban Climate Action](#)**  
[The University of British Columbia \(UBC\)](#)  
[Vancouver, Canada](#)  
[JOB POST](#)
      - **[Postdoctoral Fellow in Supercapacitor Technology](#)**  
[The University of British Columbia \(UBC\)](#)  
[Kelowna, Canada](#)  
[JOB POST](#)
      - **[Postdoctoral Researchers x 2 – Advancement of audit procedure for domestic and non-domestic energy compliance tools, SFI MaREI Centre, NUI Galway \(NUIG-RES-095-21\)](#)**

National University of Ireland Galway (NUI Galway).

Galway, Ireland

JOB POST

▪ **Semantic Web Developer**

European Molecular Biology Laboratory (EMBL).

Hinxton, Cambridge, United Kingdom

JOB POST

---

This article was downloaded by **calibre** from <https://www.nature.com/articles/d41586-021-01246-x>

| [Section menu](#) | [Main menu](#) |

## Books & Arts

- **From spoons to semiconductors — we are what we make**

[ 11 May 2021]

Book Review • Through a tour of ten materials, a scientist explores knowing through doing.

- **An incomparable intellectual who fell through the cracks of history** [ 10 May 2021]

Book Review • Katherine Jones, Lady Ranelagh, worked at the heart of seventeenth-century scientific debates — in the shadow of her brother, Robert Boyle.

- **Elegant chemistry, a humane view of robots, and refugee economics: Books in brief** [ 12 May 2021]

Book Review • Andrew Robinson reviews five of the week's best science picks.

## BOOK REVIEW

11 May 2021

# From spoons to semiconductors — we are what we make

Through a tour of ten materials, a scientist explores knowing through doing.

- [Anna Novitzky](#)<sup>0</sup>

1. Anna Novitzky

1. Anna Novitzky is a subeditor team leader at *Nature* in London.

[View author publications](#)

You can also search for this author in [PubMed](#) [Google Scholar](#)



Fired up: Anna Ploszajski gets to grips with the art of glass-making in her quest to fuse scientific theory and creative practice. Credit: Charlie Murphy

### **Handmade: A Scientist's Search for Meaning through Making** *Anna Ploszajski* Bloomsbury (2021)

When materials scientist Anna Ploszajski took up science communication, she found that the more she discussed her research with others, the less she could answer their questions. She knew all about the molecular interactions that give materials their strength, flexibility or hardness, but she couldn't tell her friends and family about the best alternative to plastic, or why phone screens are made from glass even though it's prone to smashing. To address these gaps in her knowledge, she got hands-on, exploring how artisans interact with substances that she knew only in theory.

In *Handmade*, Ploszajski investigates ten materials. She starts with the classic categories of her field: glass, plastic, metals such as steel and brass, and ceramics. She then moves on to materials common in making and crafts,

and less often considered in the laboratory: sugar, wool, wood, paper and stone. She tries glass-blowing, pottery, steel casting, knitting and spoon carving; learns about plastic art, trumpet-making and stonemasonry; and gains a holistic perspective on objects to which she had never given a second thought. The efforts bring an understanding of the properties and cultural impact of materials that helps her to communicate more clearly. As a chemist-turned-wordsmith, and a keen dabbler in crafts from knitting to origami, I related deeply to her search.



### Medicine: Discovery through doing

Płoszajski intersperses her experiences with the materials-science view of these media, from the amorphous molecular structure of glass to the chemical reactions between calcium minerals, moisture and carbon dioxide that give lime mortar its remarkable self-healing properties. She describes the history of each material's use, with snippets of tradition and archaeology from around the globe — ranging from 3,000-year-old ancient Egyptian knitted socks to wind-operated furnaces in Iron Age Sri Lanka. And she offers anecdotes about what the materials have meant to her: her immigrant grandfather's plastics-manufacturing business; the sugary snacks that got her through a swim across the English Channel; how paper, relaying thoughts and stories written by lesbians of centuries past, helped her to grasp her own sexuality. The result is fascinating and affecting.

## **Real-world impact**

Under ‘Steel’, Ploszajski describes how, as an undergraduate, she won a place on a team building a vehicle to tackle a land-speed record. She worked out that cogs in the car’s engine were breaking under stress owing to carbon atoms clumping inside the metal. But, lacking the confidence to share her ideas with the older, male mechanics, she was unable to apply the understanding in a practical way that could help the team to reach its goal.

This disconnect between doing good science and presenting it in the way that people need has become all too obvious during the COVID-19 pandemic. Researchers can understand the mechanisms of infection, produce effective vaccines and report compelling epidemiological data. Yet without an appreciation of why people cannot or will not take vaccines, the findings might not help people.



Spoons that Ploszajski carved as she explored the medium of wood.Credit:  
Anna Ploszajski

Płoszajski's experiences also shine light on how people shape research. Scientists aim for objectivity, but often forget that their experiences and culture affect every aspect of their work. Just as the grain of a piece of wood dictates the shape of the spoon that Płoszajski carves, the structure of a society dictates the research questions that scholars pursue. This isn't necessarily a bad thing; trouble arrives when researchers forget that their approaches are shaped by their circumstances. Similarly, Płoszajski, a trumpet player since childhood, learns with surprise that the instruments are not always made of brass; some players prefer the sound produced by silver or copper. This put me in mind of how astronomy is usually considered a visual science — but some blind astronomers have [pioneered investigating the cosmos through sound](#).

I did wish for more from Płoszajski's accounts. Directed mainly at lay readers, the book's scientific explanations stopped just as I began to be intrigued. And she only scratches the surface of the history, cultural connotations and potential uses of each material. I almost wished for a volume based on each chapter, an encyclopedia of science and craft.

It's enlightening to reflect on how our physical experience affects our thoughts. And, as Płoszajski points out, it's unhealthy to compartmentalize: each can improve the other. As a crafter, I well understand the comfort Płoszajski finds in creation. There's something magical about spinning disparate, fragile fibres into warm, strong yarn, or coaxing solid cheese curds out of liquid milk. After a day of thought and theory, it's delightful to hold something real in my hand and say: I made this.

Nature **593**, 186-187 (2021)

doi: <https://doi.org/10.1038/d41586-021-01247-w>

## [Jobs from Nature Careers](#)

- - - [All jobs](#)
    -

- **Postdoctoral Research Fellow in Urban Climate Action**

The University of British Columbia (UBC)

Vancouver, Canada

JOB POST

- **Postdoctoral Fellow in Supercapacitor Technology**

The University of British Columbia (UBC)

Kelowna, Canada

JOB POST

- **Postdoctoral Researchers x 2 – Advancement of audit procedure for domestic and non-domestic energy compliance tools, SFI MaREI Centre, NUI Galway (NUIG-RES-095-21)**

National University of Ireland Galway (NUI Galway)

Galway, Ireland

JOB POST

- **Semantic Web Developer**

European Molecular Biology Laboratory (EMBL)

Hinxton, Cambridge, United Kingdom

JOB POST

---

This article was downloaded by **calibre** from <https://www.nature.com/articles/d41586-021-01247-w>

| [Section menu](#) | [Main menu](#) |

## BOOK REVIEW

10 May 2021

# An incomparable intellectual who fell through the cracks of history

Katherine Jones, Lady Ranelagh, worked at the heart of seventeenth-century scientific debates — in the shadow of her brother, Robert Boyle.

- [Georgina Ferry](#) 0

### 1. [Georgina Ferry](#)

1. Georgina Ferry is a science writer and the biographer of researchers Dorothy Crowfoot Hodgkin and Max Perutz.

[View author publications](#)

You can also search for this author in [PubMed](#) [Google Scholar](#)



Lady Ranelagh was a noted member of the Hartlib circle, a precursor to the Royal Society.Credit: Michael Chevis/15th Earl of Cork and Orrery

**Lady Ranelagh: The Incomparable Life of Robert Boyle's Sister**  
*Michelle DiMeo Univ. Chicago Press (2021)*

The foundation of the Royal Society of London in 1660 established an institutional focus for experimental science. The society did not admit female fellows until 1945. A glance at its history gives the impression that seventeenth-century natural philosophy was an entirely male enterprise. Fortunately, feminist scholarship over the past few decades has unearthed women such as philosopher Anne Conway and writers Dorothy Moore and Mary Evelyn, who were active in the intellectual ferment of the time.

Now, Michelle DiMeo has produced a portrait of another influential female thinker who has been hiding in plain sight — as a footnote in the story of her more famous brother, chemist and Royal Society co-founder Robert Boyle. DiMeo reveals Katherine Jones, Lady Ranelagh, as central to political, religious, philosophical and medical discussions, yet destined to be forgotten, because she obeyed the convention that women should not put their thoughts into print. DiMeo, a librarian at the Science History Institute in Philadelphia, Pennsylvania, has used her archival skills to trawl the papers of Ranelagh's mostly male contemporaries to uncover her role as a public intellectual.



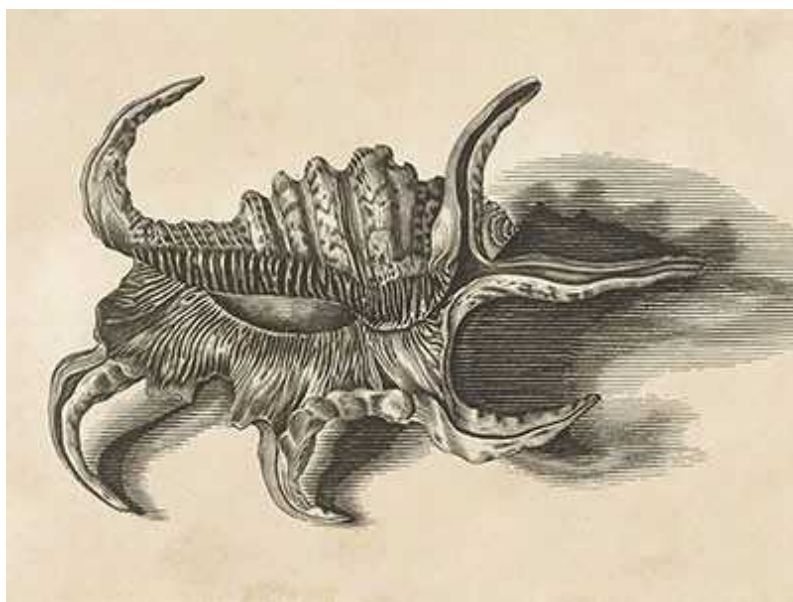
### Women at the edge of science

Katherine Boyle was born in Ireland in 1615, one of 15 children of the Earl of Cork, who raised them to be opinionated and ambitious. Katherine's piety and social standing later opened doors without risking her reputation. Unlike

her brothers, she had no formal schooling, yet she grew up literate, articulate and curious. After her mother died in 1630, she took care of Robert, then only three years old. It was the beginning of a lifelong bond, although they were separated for much of his childhood. Robert grew up to be the “father of chemistry”, for his discoveries on the nature of air and his approach to experimental natural philosophy.

Married off to Arthur Jones (later Viscount Ranelagh), Katherine had four children by the time she was 25. In 1642, she fled an uprising of Catholic rebels and settled in London with her children. She lived apart from her husband — a boor and gambler — but kept her title.

In London, she became one of the most active members of the circle of correspondents cultivated by the polymath Samuel Hartlib. The group shared, copied and discussed letters and manuscripts; Ranelagh hosted meetings in her home. Members admired her contributions on politics, religion and natural philosophy, dubbing her “the Incomparable” and citing her frequently. The interests of the circle evolved, converging on new, ‘useful’ knowledge revealed through experimental science, especially chemistry. One letter mentions Ranelagh as an early user of optical instruments such as a telescope.



[How seventeenth-century sisters broke the mould on scientific illustration](#)

Ranelagh introduced her teenage brother Robert to the circle after he returned from a tour of Europe in 1644; she became his spiritual and intellectual mentor. As he focused on chemistry, she equipped a laboratory at his Dorset home. He thanked her: “the delights I taste in it, make me fancy my laboratory a kind of Elysium” (spelling modernized). In 1668, he moved permanently into Ranelagh’s home in London’s fashionable Pall Mall.

Ranelagh collected and exchanged recipes to treat common ailments, not unusual for women of the time. However, she and Boyle used empirical methods, testing products in the laboratory and recording the results. Boyle claimed that Ranelagh had cured dozens of children of rickets using a copper-based compound. She also took down another’s first-hand account of an experiment that would now be classified as alchemy: the transmutation of metals. She influenced Boyle’s writing on moral matters, and encouraged his advocacy of empiricism and dismissal of Aristotelian ideas.

## Edged out

During the 1660s, the Royal Society moved into the intellectual space of the Hartlib circle, but it was more exclusive and politically conservative. It communicated through print publication and public demonstration, from which women were almost entirely excluded. A visit in 1667 by the outspoken writer Margaret Cavendish, Duchess of Newcastle, was an experiment not repeated. Cavendish arrived late, dressed ‘immodestly’ and treated the demonstrations with condescension. Her “boldness and profaneness is allowed to pass for wit”, Ranelagh wrote to another brother. This criticism of Cavendish burnished her own reputation for propriety, which enabled her to establish links with many of the society’s members even though she could not be admitted.

DiMeo is scrupulous in tethering her observations to their archival sources. As a result, she sometimes underplays the historical context of this impressive woman’s story. Ranelagh lived through violent rebellion, civil war, a king’s execution, religious intolerance, a grim protectorate followed by a riotous restoration, plague, fire and another king deposed. DiMeo notes these events, but I longed for the sound and colour of such turbulent times.

Ranelagh died in 1691. Boyle, brokenhearted, followed a week later, and they were buried together. At the funeral, the bishop of Salisbury declared that Ranelagh “made the greatest figure … of any woman of our age”. Yet, DiMeo tells us, her life “quickly became a shadow”. Whereas Boyle made sure that his papers and published works survived for posterity, Ranelagh left no archive and published nothing. That her story is gathered from the papers of her male relatives and associates highlights how easy it is for women to fall through the cracks of history.

Nature **593**, 188-189 (2021)

doi: <https://doi.org/10.1038/d41586-021-01248-9>

## Jobs from Nature Careers

- - - [All jobs](#)
    - 
    - [Postdoctoral Research Fellow in Urban Climate Action](#)
      - [The University of British Columbia \(UBC\)](#)
      - [Vancouver, Canada](#)
      - [JOB POST](#)
    - [Postdoctoral Fellow in Supercapacitor Technology](#)
      - [The University of British Columbia \(UBC\)](#)
      - [Kelowna, Canada](#)
      - [JOB POST](#)

- **Postdoctoral Researchers x 2 – Advancement of audit procedure for domestic and non-domestic energy compliance tools, SFI MaREI Centre, NUI Galway (NUIG-RES-095-21).**

National University of Ireland Galway (NUI Galway).

Galway, Ireland

JOB POST

- **Semantic Web Developer**

European Molecular Biology Laboratory (EMBL).

Hinxton, Cambridge, United Kingdom

JOB POST

---

This article was downloaded by **calibre** from <https://www.nature.com/articles/d41586-021-01248-9>

| [Section menu](#) | [Main menu](#) |

## BOOK REVIEW

12 May 2021

# Elegant chemistry, a humane view of robots, and refugee economics: Books in brief

Andrew Robinson reviews five of the week's best science picks.

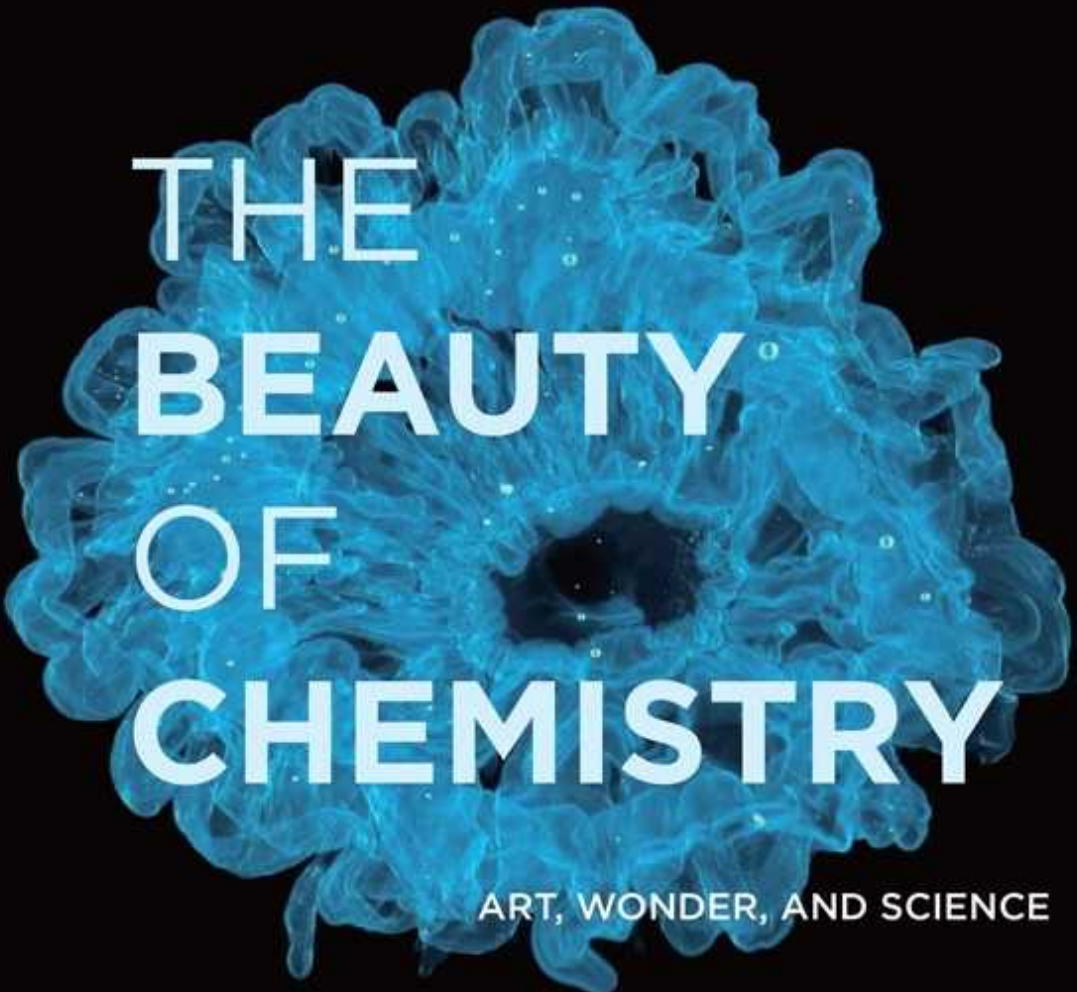
- [Andrew Robinson](#) 0

### 1. [Andrew Robinson](#)

1. Andrew Robinson's many books include *Lost Languages: The Enigma of the World's Undeciphered Scripts* and *Einstein on the Run: How Britain Saved the World's Greatest Scientist*. He is based in London.

[View author publications](#)

You can also search for this author in [PubMed](#) [Google Scholar](#)



# THE BEAUTY OF CHEMISTRY

ART, WONDER, AND SCIENCE

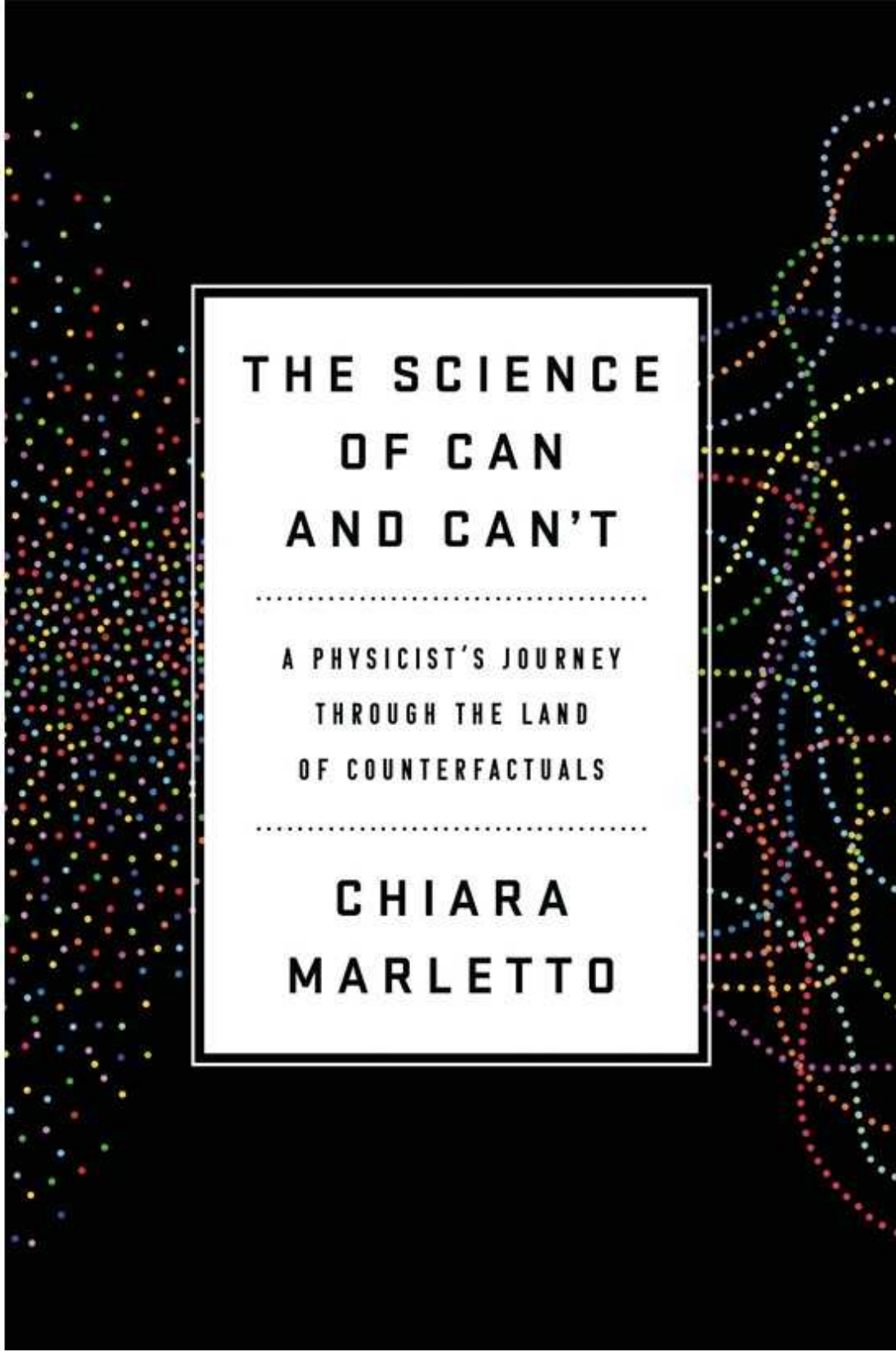
**PHILIP BALL**

photographs by Wenting Zhu and Yan Liang

The Beauty of Chemistry

Philip Ball *MIT Press* (2021)

When Francis Crick and James Watson discovered DNA's double helix, they privately called it "beautiful", says science writer Philip Ball. But in 1953, "such expressions of exuberance were not welcomed in the austere annals of science". Ball's scintillating book is a paean to chemical beauty in nature and laboratories, with lavish images created by Wenting Zhu, Yan Liang and the Chinese Chemical Society, using microphotography, time lapse, thermal imaging and more. Would that it had existed when I was an undergraduate chemist.



# THE SCIENCE OF CAN AND CAN'T

A PHYSICIST'S JOURNEY  
THROUGH THE LAND  
OF COUNTERFACTUALS

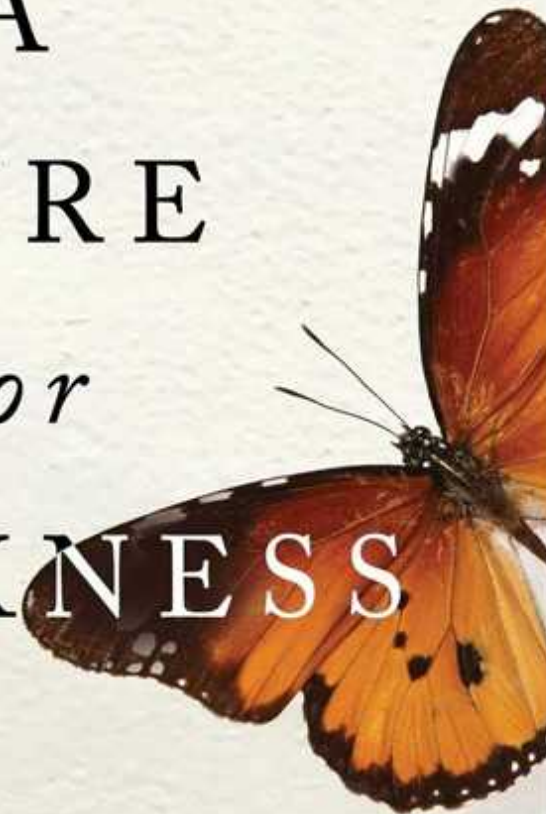
CHIARA  
MARLETTA

The Science of Can and Can't

Chiara Marletto *Viking* (2021)

GPS depends on phenomena described in the general theory of relativity, but nothing in the theory predicted it. The possibility of GPS was thus a “counterfactual”, notes theoretical physicist Chiara Marletto, whose engaging book centres on these “facts about what could be”. By restricting itself to statements about initial conditions and laws of motion, she says, physics “is missing something essential”. Similarly, electron–proton attraction underlies our bodies’ chemistry — but there is no trace of biological complexity in the laws of physics.

A  
CURE  
*for*  
DARKNESS



THE STORY OF DEPRESSION  
AND HOW WE TREAT IT

Alex Riley

"Boldly ambitious, deeply affecting, and magisterial in scope."

—STEVE SILBERMAN, author of  
*NeuroTribes: The Legacy of Autism and the Future of Neurodiversity*

A Cure for Darkness

*Alex Riley Scribner (2021)*

Working at London's Natural History Museum, Alex Riley published his first academic paper. It didn't satisfy him. Later, he began to cry in a supervisory meeting, and left academia. Now a science journalist, he has received diverse professional advice and treatment for depression. His first book, a substantial and revealing history of the condition, is thus both subjective and objective, grappling with the opposing psychological and biological therapies of pioneering psychiatrists Sigmund Freud and Emil Kraepelin, and their divided successors.

WHAT OUR HISTORY  
WITH ANIMALS REVEALS  
ABOUT OUR FUTURE  
WITH ROBOTS

---

## THE NEW BREED



KATE DARLING

The New Breed

## Kate Darling *Henry Holt* (2021)

The word ‘robot’, from the Czech for ‘forced labour’, was coined in a 1920 play by Karel Čapek about artificial people, exploited in factories, who rebel against their makers: a conflict-based, influential vision of artificial intelligence. Technology ethicist Kate Darling pursues a different view in her original, humane book. She compares robots with animals, long used for work, weaponry and companionship. “Like robots, animals can sense, make their own decisions, act on the world, and learn.” But they cannot replace human beings.

ALEXANDER BETTS

# THE WEALTH OF REFUGEES

HOW DISPLACED PEOPLE CAN BUILD ECONOMIES



**The Wealth of Refugees**

Alexander Betts *Oxford Univ. Press* (2021)

More than 80 million people are currently displaced; at least 25 million are refugees, driven to leave their country. Alexander Betts has studied them for many years, focusing on camps and cities in Africa. The challenging title of his avowedly practical study — considering ethics, economics, politics and policy — was inspired by Adam Smith's 1776 book *The Wealth of Nations*, which argued that countries flourish when citizens can pursue their own interests. Such autonomy is also desirable, argues Betts, for today's refugees.

Nature **593**, 189 (2021)

doi: <https://doi.org/10.1038/d41586-021-01249-8>

## **Jobs from Nature Careers**

- - - [All jobs](#)
    - 
    - [Postdoctoral Research Fellow in Urban Climate Action](#)  
[The University of British Columbia \(UBC\)](#)  
[Vancouver, Canada](#)  
[JOB POST](#)
    - [Postdoctoral Fellow in Supercapacitor Technology](#)  
[The University of British Columbia \(UBC\)](#)  
[Kelowna, Canada](#)  
[JOB POST](#)

- **Postdoctoral Researchers x 2 – Advancement of audit procedure for domestic and non-domestic energy compliance tools, SFI MaREI Centre, NUI Galway (NUIG-RES-095-21).**

National University of Ireland Galway (NUI Galway).

Galway, Ireland

JOB POST

- **Semantic Web Developer**

European Molecular Biology Laboratory (EMBL).

Hinxton, Cambridge, United Kingdom

JOB POST

---

This article was downloaded by **calibre** from <https://www.nature.com/articles/d41586-021-01249-8>

| [Section menu](#) | [Main menu](#) |

# Opinion

- **[Thomas Cavalier-Smith \(1942–2021\)](#)** [ 10 May 2021]  
Obituary • Polymath of cellular evolution who shaped understanding of the tree of life.
- **[Nature-based solutions can help cool the planet — if we act now](#)** [ 12 May 2021]  
Comment • Analysis suggests that to limit global temperature rise, we must slash emissions and invest now to protect, manage and restore ecosystems and land for the future.
- **[Afghanistan: vaccinate drug users against COVID-19](#)** [ 11 May 2021]  
Correspondence •
- **[Stop using ‘master–slave’ terminology in biology](#)** [ 11 May 2021]  
Correspondence •
- **[Value of Mexican nature reserve is more than monetary](#)** [ 11 May 2021]  
Correspondence •
- **[COVID-19: build on Belgium’s psychosocial findings](#)** [ 11 May 2021]  
Correspondence •

## OBITUARY

10 May 2021

# Thomas Cavalier-Smith (1942–2021)

Polymath of cellular evolution who shaped understanding of the tree of life.

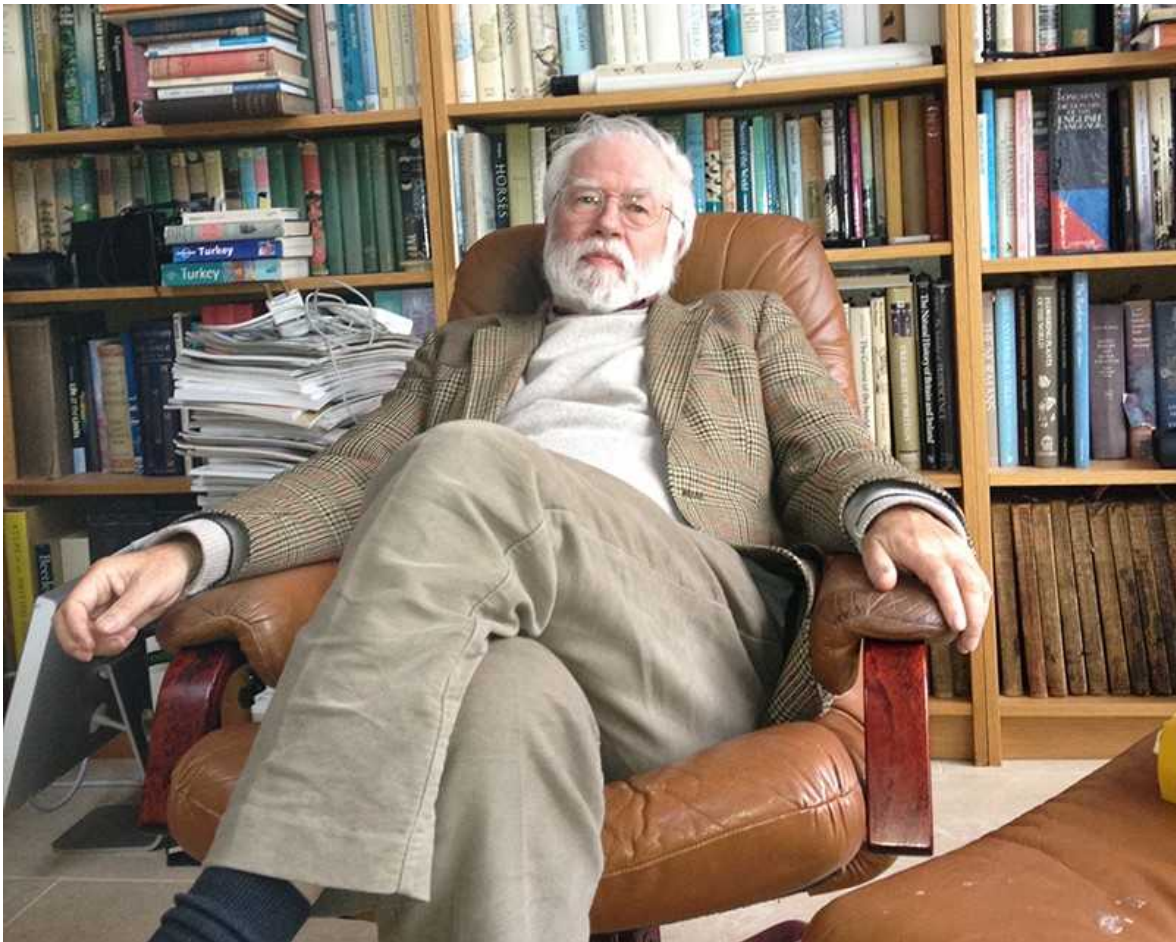
- [Thomas Richards](#) 0

### 1. [Thomas Richards](#)

1. Thomas Richards is professor of evolutionary genomics in the Department of Zoology at the University of Oxford, UK. He was a graduate student in Thomas Cavalier-Smith's group from 2001 to 2006.

[View author publications](#)

You can also search for this author in [PubMed](#) [Google Scholar](#)



Credit: John M. Archibald

Since Charles Darwin first proposed his theory of evolution, biologists have struggled to fit all life forms — from the tiniest bacterium to the blue whale — onto a tree of life that explains their ancestry. The tree, it turned out, was more of a web. Branches were fused by the demonstration that endosymbiosis can lead to the integration of a microbial cell into another cell to form a discrete compartment passed from generation to generation over hundreds of millions of years. Thomas (Tom) Cavalier-Smith played a crucial part in understanding major transitions in evolution, including the role of endosymbiosis. He has died, aged 78.

Cavalier-Smith's aim was to understand the rise of the eukaryotes — organisms with complex, compartmentalized cells, including plants, animals and fungi. His passion was the huge diversity of single-celled eukaryotes — the protists. His ideas were based on the thesis that we cannot grasp

evolutionary history without understanding how all dimensions of a cellular system — function, structure, biochemistry, economy and spatial organization — arose. How this network varies across the tree, he argued, defines the tree.

Historically, the study of microbial forms focused on interpretations gleaned from light microscopy. With his second wife and colleague Ema Chao, Cavalier-Smith rationalized the comparative study of protists. He and Chao combined light and electron microscopy with genetic analysis to construct a new systematics for the eukaryotes and to pursue a unified taxonomy for all life.



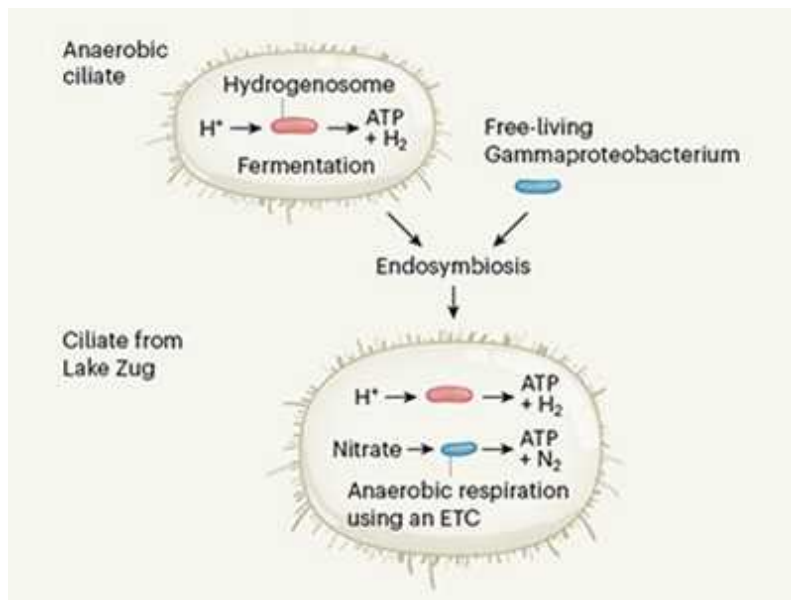
### Lynn Margulis (1938–2011)

Cavalier-Smith was born in London in 1942. He studied at Gonville & Caius College at the University of Cambridge, UK, and completed a PhD at King's College London in 1967, with the biophysicist John Randall. When Cavalier-Smith turned to electron microscopy, he began to reveal the diversity of protists and algae and the complexity of organelles such as mitochondria and chloroplasts, the products of endosymbiosis.

After postdoctoral studies at the Rockefeller University, New York City, Cavalier-Smith returned to King's in 1969 as lecturer, and then reader, in biophysics. He moved to the University of British Columbia in Vancouver,

Canada, in 1989. Observing that some living protists seemed to lack mitochondria, he suggested that the eukaryotes originated before the endosymbiotic event that led to mitochondrial evolution. He placed these intermediate forms in a new kingdom, the Archezoa, developing a scheme for the stepwise evolution of cellular complexity in eukaryotes.

Another of his hypotheses proposed that a huge branch of eukaryotic life, including large multicellular forms such as the seaweed kelp, were the product of endosymbiosis between one eukaryote and another, much earlier than had been suggested. In the group he designated the chromalveolates, this event left behind a chloroplast — the cellular compartment for photosynthesis. The group contains lineages as divergent as marine phytoplankton (such as diatoms) and the malaria parasite, whose chloroplasts are colourless and non-photosynthetic.



### A microbial marriage reminiscent of mitochondrial evolution

These hypotheses represented confident strides towards an evolutionary synthesis that was new in two ways. They were detailed, but spoke of billion-year timescales; and they offered testable predictions. He gave the infant field of evolutionary cell biology a common language and a set of ideas to either work with or to disprove.

Cavalier-Smith's ideas were indeed challenged and subject to extensive revision. Nobody championed these revisions more than he, with, for example, the ultimate demise of the Archezoa. The idea that a scientist (indeed any intellectual adventurer) could not completely restructure their understanding, or even destroy their own previous synthesis in response to new data, was anathema to him.

In 2000, he returned to the United Kingdom as professor of evolutionary biology in the Department of Zoology at the University of Oxford. He made fundamental contributions to understanding the origins of sexual reproduction, the origins and diversification of prokaryotes (bacteria and archaea), genome structure, and the evolutionary history of almost every eukaryotic organelle.

Influential examples I often re-read include his works on the relationship between the size of an organism's genome and the volume of its cells, and how an early organism could arise from the interaction of a self-replicating nucleic acid and a proto-membrane. These contributions again brought the multiple dimensions of a cellular system to an evolutionary problem.

A highlight of his many honours was the International Prize for Biology, received from the Emperor of Japan in 2004. I remember the day he told me of this award, announcing that he was learning parts of his speech in Japanese — further evidence of his many intellectual gifts.

Time with Tom was precious yet given generously. Debates at conferences were robust, but his attention and interaction with all were unbounded. He grilled graduate students and eminent professors alike, offered advice and radiated enthusiasm. Supervisions would often last for six hours: discussion would roam over the whole of biology. We might not all have agreed with Tom all the time — many of us argued with him again and again — yet at every turn he was there, providing ideas, hypotheses accurately framed to test, syntheses to absorb and data to digest. His mark on the field is indelible. Evolutionary biology will miss him greatly.

Nature **593**, 190 (2021)

doi: <https://doi.org/10.1038/d41586-021-01250-1>

## Jobs from Nature Careers

- - - [All jobs](#)
    - - [Postdoctoral Research Fellow in Urban Climate Action](#)  
  
[The University of British Columbia \(UBC\)](#)  
[Vancouver, Canada](#)  
[JOB POST](#)
      - [Postdoctoral Fellow in Supercapacitor Technology](#)  
  
[The University of British Columbia \(UBC\)](#)  
[Kelowna, Canada](#)  
[JOB POST](#)
      - [Postdoctoral Researchers x 2 – Advancement of audit procedure for domestic and non-domestic energy compliance tools, SFI MaREI Centre, NUI Galway \(NUIG-RES-095-21\)](#)  
  
[National University of Ireland Galway \(NUI Galway\)](#)  
[Galway, Ireland](#)  
[JOB POST](#)
      - [Semantic Web Developer](#)

European Molecular Biology Laboratory (EMBL)

Hinxton, Cambridge, United Kingdom

**JOB POST**

---

This article was downloaded by **calibre** from <https://www.nature.com/articles/d41586-021-01250-1>

| [Section menu](#) | [Main menu](#) |

## COMMENT

12 May 2021

# Nature-based solutions can help cool the planet — if we act now

Analysis suggests that to limit global temperature rise, we must slash emissions and invest now to protect, manage and restore ecosystems and land for the future.

- [Cécile A. J. Girardin](#)<sup>0</sup>,
- [Stuart Jenkins](#)<sup>1</sup>,
- [Nathalie Seddon](#)<sup>2</sup>,
- [Myles Allen](#)<sup>3</sup>,
- [Simon L. Lewis](#)<sup>4</sup>,
- [Charlotte E. Wheeler](#)<sup>5</sup>,
- [Bronson W. Griscom](#)<sup>6</sup> &
- [Yadvinder Malhi](#)<sup>7</sup>

## 1. [Cécile A. J. Girardin](#)

1. Cécile A. J. Girardin is science lead for the Oxford Biodiversity Network, University of Oxford, UK; and technical director of the Nature-based Solutions Initiative, Oxford, UK.

[View author publications](#)

You can also search for this author in [PubMed](#) [Google Scholar](#)

## 2. Stuart Jenkins

1. Stuart Jenkins is a graduate student in the Department of Physics, University of Oxford, UK.

[View author publications](#)

You can also search for this author in [PubMed](#) [Google Scholar](#)

3. Nathalie Seddon

1. Nathalie Seddon is professor of biodiversity and director of the Nature-based Solutions Initiative, University of Oxford, UK.

[View author publications](#)

You can also search for this author in [PubMed](#) [Google Scholar](#)

4. Myles Allen

1. Myles Allen is professor of geosystem science, School of Geography and the Environment and Department of Physics, University of Oxford, UK; and director of Oxford Net Zero.

[View author publications](#)

You can also search for this author in [PubMed](#) [Google Scholar](#)

5. Simon L. Lewis

1. Simon L. Lewis is professor of global-change science in the Department of Geography, University College London, and the School of Geography, University of Leeds, UK.

[View author publications](#)

You can also search for this author in [PubMed](#) [Google Scholar](#)

6. Charlotte E. Wheeler

1. Charlotte E. Wheeler is a forest researcher at the School of GeoSciences, University of Edinburgh, UK.

[View author publications](#)

You can also search for this author in [PubMed](#) [Google Scholar](#)

## 7. Bronson W. Griscom

1. Bronson W. Griscom is senior director of natural climate solutions at Conservation International, Arlington, Virginia, USA.

[View author publications](#)

You can also search for this author in [PubMed](#) [Google Scholar](#)

## 8. Yadvinder Malhi

1. Yadvinder Malhi is professor of ecosystem science in the School of Geography and the Environment, University of Oxford, UK.

[View author publications](#)

You can also search for this author in [PubMed](#) [Google Scholar](#)



Women in northern Mumbai, India, have planted mangrove saplings to protect the area against rising sea levels. Credit: Mahendra Parikh/Hindustan

Times via Getty

Projects that manage, protect and restore ecosystems are widely viewed as win-win strategies for addressing two of this century's biggest global challenges: climate change and biodiversity loss. Yet the potential contribution of such nature-based solutions to mitigating climate change remains controversial.

Decision-makers urgently need to know: what role do nature-based solutions have in the race to net-zero emissions and stop further global temperature increases?

Analyses of nature-based solutions often focus on how much carbon they can remove from the atmosphere. Here, we provide a new perspective by modelling how these solutions will affect global temperatures — a crucial metric as humanity attempts to limit global warming.

Our analysis shows that nature-based solutions can have a powerful role in reducing temperatures in the long term. Land-use changes will continue to act long past the point at which net-zero emissions are achieved and global temperatures peak (known as peak warming), and will have an important role in planetary cooling in the second half of this century. Before then, nature-based solutions can provide real but limited mitigation benefits. Crucially, the more ambitious the climate target, the shorter the time frame for such solutions to have an effect on peak warming.

In other words, nature-based solutions must be designed for longevity. This means paying closer attention to their long-term carbon-sink potential, as well as their impacts on biodiversity, equity and sustainable development goals. It also means continuing to limit global warming through other methods, from decarbonization to geological storage of carbon dioxide.

Our model reinforces the conclusion that an ambitious scaling-up of nature-based solutions needs to be implemented fast and thoughtfully — and not at the expense of other measures.

## Win-wins

The world is currently likely to hit 3 °C of warming above pre-industrial levels by 2100 (although recent policy announcements from the United States and China could reduce this). The 2015 Paris climate agreement aims to limit the global temperature rise this century to well below 2 °C, and, ideally, to 1.5 °C. There is no date for either goal, beyond the “end of this century”. The metric that matters most is the peak temperature, with more-aggressive efforts required to stay below 1.5 °C of warming than for the 2 °C target.



### Emissions: world has four times the work or one-third of the time

It is impossible to achieve the needed reduction in peak warming solely through cuts to greenhouse gases, because emissions from certain sectors, such as agriculture and some heavy industry, cannot be driven to zero any time soon. For this reason, we also need to remove greenhouse gases from the atmosphere on an unprecedented scale<sup>1</sup>.

There are various options for doing this. For example, when biomass vegetation is burnt for energy, the emitted CO<sub>2</sub> can be retained and stored underground. This process, known as bioenergy with carbon capture and storage (BECCS), requires vast areas of land — compromising food security and biodiversity — as well as time to develop on a large scale. Other options

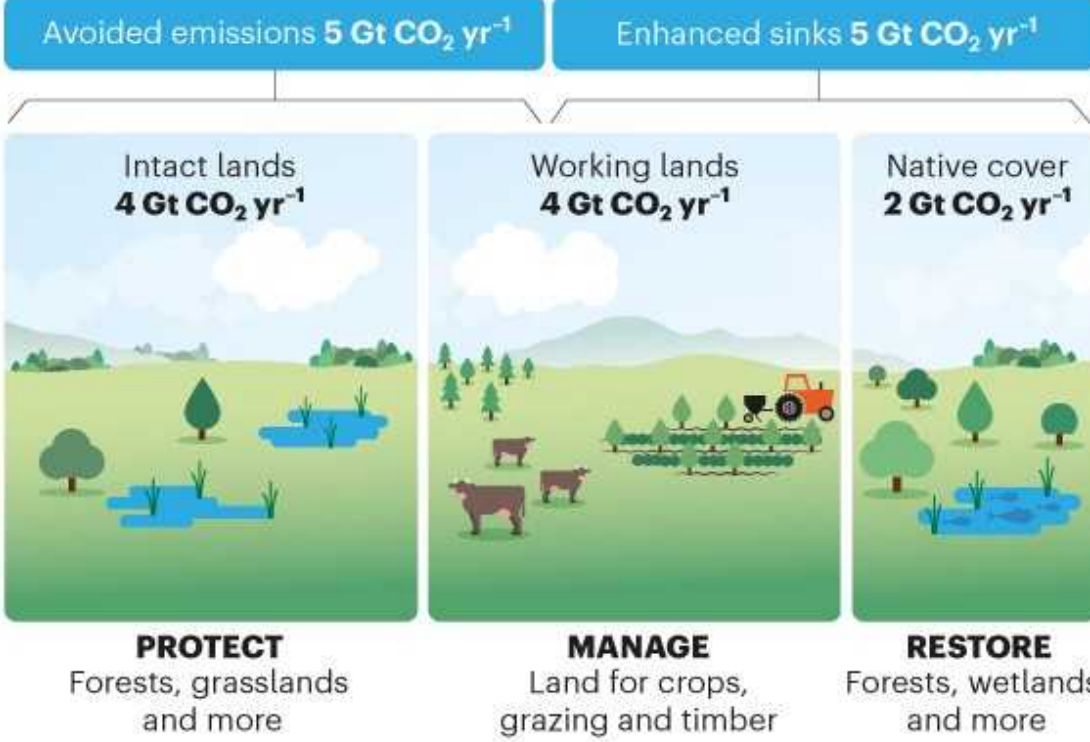
involve industrial machines that capture CO<sub>2</sub> from the air; these are currently nascent, expensive technologies.

A subset of nature-based solutions can be used specifically to limit warming. These ‘natural climate solutions’ aim to reduce atmospheric greenhouse-gas concentrations in three ways. One is to avoid emissions by protecting ecosystems and thus reducing carbon release; this includes efforts to limit deforestation. Another is to restore ecosystems, such as wetlands, so that they sequester carbon. The third is to improve land management — for timber, crops and grazing — to reduce emissions of carbon, methane and nitrous oxide, as well as to sequester carbon (see ‘Three steps to natural cooling’).

## THREE STEPS TO NATURAL COOLING

Protect intact ecosystems, manage working lands and restore native cover to avoid emissions and enhance carbon sinks.

Nature-based solutions could save **10 gigatonnes** of carbon dioxide equivalent per year



Source: S. Jenkins *et al.* *Geophys. Res. Lett.* **45**, 2795–2804 (2018).

Decades of work provide strong evidence that nature-based solutions can deliver many local ecological and socio-economic benefits<sup>2</sup>. Restoring a forest next to a stream, for example, might reduce flooding, improve carbon storage and support fisheries. Growing recognition of such benefits means that interest in nature-based solutions is soaring: they can help people adapt to climate change, achieve sustainable development goals, protect biodiversity and mitigate climate change<sup>3</sup>.

## Quantifying nature's role

There is still debate around how much nature-based solutions can contribute to achieving net-zero targets by mid-century. This is because results have been estimated across a range of objectives, time frames and model assumptions<sup>4,5</sup> (see Supplementary information; SI). Some researchers say that tree restoration is the most effective climate-change solution we have available<sup>6</sup> (this in itself has been robustly contested); others argue that nature-based solutions won't be nearly as fast or as effective as is often stated<sup>7</sup>.

Part of the reason for the impasse is this: many well-known papers discuss the annual carbon uptake possibilities of nature-based solutions; they do not discuss their cooling impact year on year. Because the Paris agreement is framed in terms of temperature, we argue that this gap is critical: researchers need to know how nature-based solutions will affect global temperature.

To model this, we consider an ambitious but realistic scenario — an update to previous estimates by one of our co-authors (B.W.G)<sup>4,8,9</sup>. This scenario considers only those projects for nature-based solutions that are constrained by many factors: they are cost-effective (costing less than US\$100 per tonne of CO<sub>2</sub> equivalent); ensure adequate global production of food and wood-based products; and involve sufficient biodiversity conservation. They also respect land tenure rights and don't change the amount of sunlight reflected from Earth, or albedo (see SI). In our scenario, nature-based solutions that avoid emissions ramp up quickly — by 2025 — and absorb carbon while

avoiding emissions at a rate of 10 gigatonnes of CO<sub>2</sub> per year (Gt CO<sub>2</sub> yr<sup>-1</sup>). This rises to 20 Gt CO<sub>2</sub> yr<sup>-1</sup> in the most ambitious scenario (peak warming of 1.5 °C by 2055), in which we assume a higher price of carbon. The 10-Gt value is cost-contained. But we also account for 30 years of higher-priced nature-based solutions in the 1.5 °C scenario (up to \$200 per tonne of CO<sub>2</sub> equivalent; see SI). For comparison, 10 Gt CO<sub>2</sub> yr<sup>-1</sup> is more than the emissions from the entire global transportation sector.



Instituto Terra, an initiative in Aimorés, Brazil, is restoring a devastated ecosystem. Credit: Christian Ender/Getty

Achieving 10 Gt CO<sub>2</sub> yr<sup>-1</sup> of mitigation in this way would involve stopping the destruction of ecosystems worldwide (including 270 million hectares of deforestation); restoring 678 million hectares of ecosystems (more than twice the size of India); and improving the management of around 2.5 billion hectares of land by mid-century<sup>4</sup>. This is ambitious, but it is important to note that the bulk of land required (85%) comes from improving management of existing lands for agriculture, grazing and

production forest without displacing yields of food, wood-based products or fuel (see ‘Three steps to natural cooling’).

These estimates come with caveats (see SI). The role of nature-based solutions could be larger if one considers, for example, their impacts on other greenhouse gases besides CO<sub>2</sub>. This could represent an additional amount of roughly 1–3 Gt CO<sub>2</sub> equivalent yr<sup>-1</sup> of climate mitigation.

Alternatively, the contribution of such solutions might be smaller in the long term, if the carbon drawdown from land-based interventions decreased over time. This could happen if these natural sinks became saturated or were affected by climate impacts such as forest fires. These caveats are not included in our estimates.

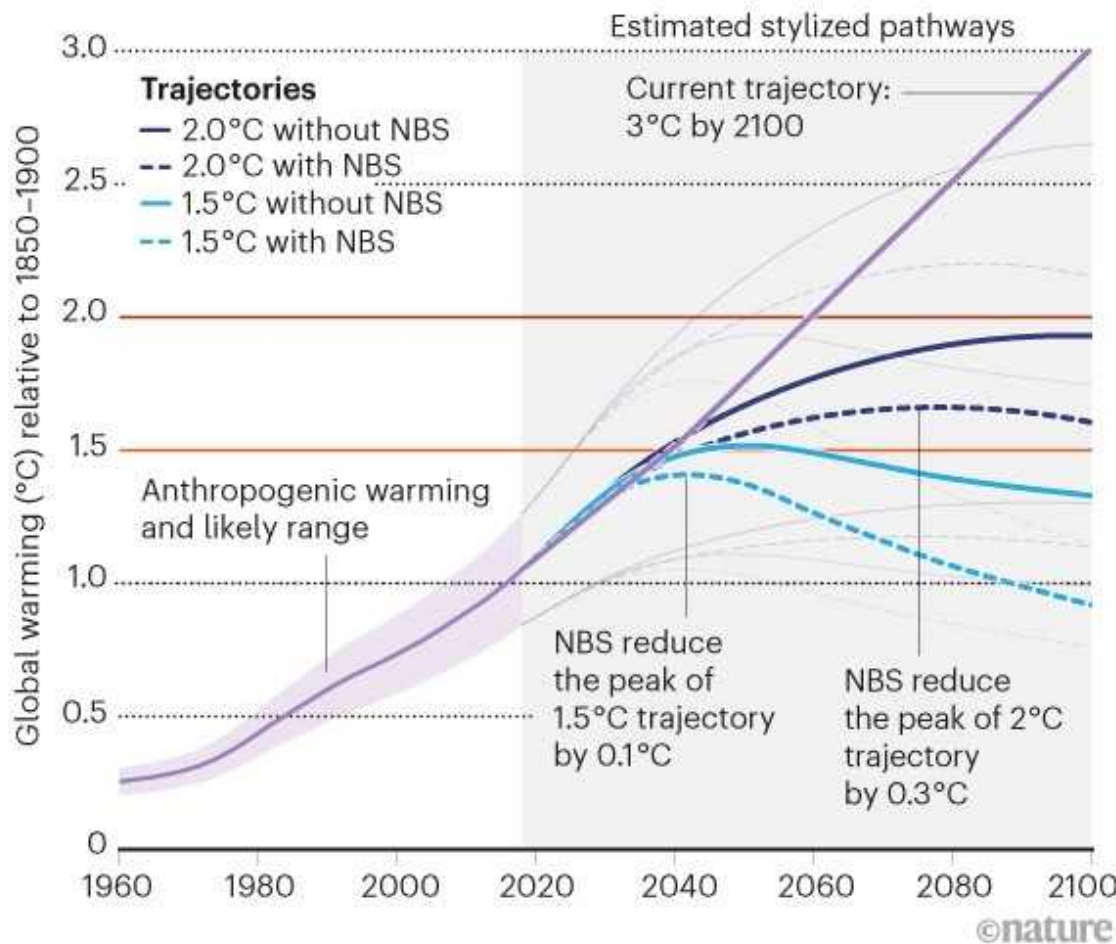
We then modelled how this level of nature-based solutions would affect global temperature up to 2100 (see ‘The long game’ and SI). We looked at illustrative pathways from the Intergovernmental Panel on Climate Change, in which peak warming is constrained to 1.5 °C or 2 °C, and ran these scenarios with the added contribution of nature-based solutions as described. These pathways include BECCS, but no nature-based solutions beyond some avoided deforestation.

## Taking the temperature

Our analysis shows that implementing this level of nature-based solutions could reduce the peak warming by an additional 0.1 °C under a scenario consistent with a 1.5 °C rise by 2055; 0.3 °C under a scenario consistent with a 2 °C rise by 2085; and 0.3 °C under a 3 °C-by-2100 scenario (see ‘The long game’).

## THE LONG GAME

Nature-based solutions (NBS) could reduce the global peak temperature and suppress warming beyond 2100 — if they are ambitious and designed for longevity.



Adapted from Fig. SPM.1 of Ref. 1

The most significant contribution nature-based solutions can make to mitigating the peak temperature is in the 2 °C scenario. In a more ambitious 1.5 °C scenario, there isn't enough time for nature-based solutions to have as great an impact on peak warming. In the 3 °C scenario, several issues constrain the impact of nature-based solutions, including the limited ability of ecosystems to absorb carbon in a warmer world.

Overall, the mitigation potential of nature-based solutions remains small compared to what can be achieved by decarbonizing the economy. Yet,

assuming that decarbonization takes place, nature-based solutions can still suppress a chunk of the warming (see SI).

Crucially, nature-based solutions cool the planet long after the peak temperature is reached. In the 1.5 °C scenario, they take a total of 0.4 °C off warming by 2100 — four times their suppression to the 2055 peak temperature (see SI, Table S2).



### Restoring natural forests is the best way to remove atmospheric carbon

Achieving these significant long-term benefits requires several things. Nature-based solutions of good quality must be scaled up rapidly — and not at the expense of other robust strategies. Long-term geological storage of CO<sub>2</sub>, for example, will need to be ramped up significantly in the next decade as technologies mature and prices fall. The long-term benefits of nature-based solutions also depend on warming being held in check. The increased frequency and intensity of impacts such as wildfires can undermine ecosystems and their capacity to store carbon or provide other benefits to society.

Ecosystems that are protected and carefully managed — such as intact peatlands and old-growth tropical rainforests — are very likely to continue to store carbon for thousands of years. These are also more resilient to climate extremes and pathogens.

## The right metrics

Restoration of forest cover is widely considered the most viable near-term opportunity for carbon removal. Unfortunately, some of this enthusiasm has been used to promote plantation forestry — growing trees of a limited variety of ages and species (for example, in monoculture plantations) does not have the same carbon benefits as maintaining an intact forest ecosystem<sup>[10](#)</sup>.

One serious problem is that some nature-based solutions, as currently implemented, can have unintended and unwanted consequences. For example, an area of 34,007 hectares of intact forest ecosystem in Cambodia became a logging concession, with much of it replaced with an acacia monoculture. This was the first large-scale reforestation project to be funded in Cambodia in the context of climate-change mitigation. The project resulted in unethical ecological devastation, affecting 1,900 families in the area<sup>[11](#)</sup>.

Similarly, Chilean government subsidies for new plantations of pine and eucalyptus have resulted in plantations expanding by 1.3 million hectares since 1986, with an associated sequestration of about 5.6 million tonnes of carbon. However, regulations stating that expansion cannot happen at the expense of native biodiverse forests were not enforced, resulting in large-scale reductions in native forest cover. Clearing of the original forest has resulted in a net decrease of approximately 0.05 million tonnes of stored carbon since 1986<sup>[12](#)</sup>.

These examples show how a singular focus on rapid carbon sequestration as the metric of success for land-based climate mitigation can result in perverse outcomes. Activities should be evaluated and monitored with the right metrics, to account for the multitude of benefits they provide in the long term.



### Adopt a carbon tax to protect tropical forests

To ensure long-term resilience, projects involving nature-based solutions should adhere to four high-level principles (see [nbsguidelines.info](http://nbsguidelines.info)). First, nature-based solutions are not an alternative to decarbonization; second, they need to involve a wide range of ecosystems; third, they should be designed in partnership with local communities while respecting Indigenous and other rights; and, finally, they must support biodiversity, from the level of the gene to the ecosystem. In addition, the Oxford principles<sup>13</sup> for high-quality offsets call for safe and durable CO<sub>2</sub> removal and storage for every tonne of CO<sub>2</sub> emitted. Metrics of success should include those for carbon dynamics, biodiversity across multiple trophic levels, and socio-economic factors such as women's empowerment and youth employment.

There are many examples of good-practice projects (see also case studies by the University of Oxford's [Nature-based Solutions Initiative](#), where N.S. and C.A.J.G. work). For example, mangrove forests in eastern India that have been protected from deforestation since 1985 have been shown to protect coastal regions from the negative impacts of cyclones much better than artificial defences do, while also soaking up carbon<sup>14</sup>. In Sierra Leone's tropical rainforest, cocoa agroforestry — where cocoa is planted with trees for shade, alongside pineapples, chillies and maize (corn) as an additional source of food and income — has been shown to produce cocoa sustainably

while diminishing forest clearance. One agroforestry project in the [Gola Rainforest National Park](#), initiated 30 years ago, has increased biodiversity and the profitability of crops while saving an estimated 500,000 tonnes of carbon each year through sequestration and avoiding deforestation.

## Invest wisely

This much is clear: we urgently need to increase investment in high-quality nature-based solutions. They currently receive a small proportion of existing climate-mitigation financing<sup>4,15</sup>, which does not reflect their potential.

Carbon markets are increasingly relied on to finance nature-based solutions. But carbon offsets on the voluntary market are of variable quality. It can be unclear whether projects really represent a carbon sink, whether they are permanent or if they safeguard social and ecological factors. Offsets that adhere to standards can allow organizations to deliver lower-cost and hence larger climate-mitigation outcomes through nature-based solutions; however, budgets to emit fossil fuels should be ratcheted down rapidly to avoid delaying decarbonization from continued greenhouse-gas emissions.



## [Account for depreciation of natural capital](#)

Nature-based solutions need both public and private finance; in particular, governments need to reward ecosystem stewardship while taxing polluters and ramping up regulation to ensure that companies meet strict social and environmental safeguards.

The United Nations Framework Convention on Climate Change (UNFCCC) needs to provide clear guidelines on national-level accounting for nature-based solutions. This will guide the targets set in the Paris agreement's Nationally Determined Contributions, and the monitoring, reporting and verification methodologies required to comply with these targets.

The next UNFCCC meeting, COP26, is due to be held in Glasgow, UK, this November and provides an opportunity for national reporting systems to tighten national carbon accounting related to nature-based solutions. This would ensure that such solutions make a real, long-term contribution to carbon mitigation and could set metrics to ensure high biodiversity levels and maximize human well-being. One pressing issue for COP26 is Article 6 of the Paris agreement, which established a “mechanism to contribute to the mitigation of greenhouse gas emissions and support sustainable development”. A tightly regulated compliance market defined in Article 6 will provide the grounding for a tightly regulated voluntary offsetting market.

COP26 also presents the chance to harmonize the goals of the UNFCCC and those of the Convention on Biological Diversity. For example, nature-based solutions projects are likely to be required to adhere to the principle of free prior informed consent of local people: local communities need to be involved at all stages of project planning and management. Similarly, nature-based solutions should be required to protect and enhance biodiversity. This work can build on existing social and biodiversity standards<sup>3</sup>.

Our economy must be decarbonized at unprecedented rates to achieve net-zero targets by mid-century. Carbon must also be removed from the atmosphere to counter emissions that are hard to eliminate, using nature-based solutions and other means. To transform social and economic systems to deliver resilience in the face of ongoing climate impacts, the world must invest now in nature-based solutions that are ecologically sound, socially

equitable and designed to pay dividends over a century or more. Properly managed, these could benefit many generations to come.

Nature **593**, 191–194 (2021)

doi: <https://doi.org/10.1038/d41586-021-01241-2>

## References

1. 1.

Intergovernmental Panel on Climate Change. Summary for Policymakers. In *Global Warming of 1.5°C* (eds Masson-Delmotte, V. *et al.*) (World Meteorological Organization, 2018).

2. 2.

Chausson, A. *et al.* *Glob. Change Biol.* **26**, 6134–6155 (2020).

3. 3.

Seddon, N. *et al.* *Glob. Change Biol.* **27**, 1518–1546 (2021).

4. 4.

Griscom, B. W. *et al.* *Proc. Natl Acad. Sci. USA* **114**, 11645–11650 (2017).

5. 5.

Roe, S. *et al.* *Nature Clim. Change* **9**, 817–828 (2019).

6. 6.

Bastin, J.-F. *et al.* *Science* **365**, 76–79 (2019).

7. 7.

Baldocchi, D. & Penuelas, J. *Glob. Change Biol.* **25**, 1191–1197 (2019).

8. 8.

Griscom, B. W. *et al. Phil. Trans. R. Soc. B* **375**, 20190126 (2020).

9. 9.

Busch, J. *et al. Nature Clim. Change* **9**, 463–466 (2019).

10. 10.

Lewis, S. L., Wheeler, C. E., Mitchard, E. T. A. & Koch, A. *Nature* **568**, 25–28 (2019).

11. 11.

Scheidel, A. & Work, C. *Land Use Policy* **77**, 9–18 (2018).

12. 12.

Heilmayr, R., Echeverría, C. & Lambin, E. F. *Nature Sustain.* **3**, 701–709 (2020).

13. 13.

Allen, M. *et al. The Oxford Principles for Net Zero Aligned Carbon Offsetting* (Univ. Oxford, 2020).

14. 14.

Badola, R. & Hussain, S. A. *Environ. Conserv.* **32**, 85–92 (2005).

15. 15.

Buchner, B. *et al. Global Landscape of Climate Finance 2019* (Climate Policy Initiative, 2019).

## **Supplementary Information**

1. Estimating annual carbon uptake and avoided emissions

## **Jobs from Nature Careers**

- - - [All jobs](#)
    - 
    - [Postdoctoral Research Fellow in Urban Climate Action](#)  
The University of British Columbia (UBC)  
Vancouver, Canada  
[JOB POST](#)
    - [Postdoctoral Fellow in Supercapacitor Technology](#)  
The University of British Columbia (UBC)  
Kelowna, Canada  
[JOB POST](#)
    - [Postdoctoral Researchers x 2 – Advancement of audit procedure for domestic and non-domestic energy compliance tools, SFI MaREI Centre, NUI Galway \(NUIG-RES-095-21\)](#)  
National University of Ireland Galway (NUI Galway)  
Galway, Ireland

## JOB POST

### ▪ Semantic Web Developer

European Molecular Biology Laboratory (EMBL)

Hinxton, Cambridge, United Kingdom

## JOB POST

---

This article was downloaded by **calibre** from <https://www.nature.com/articles/d41586-021-01241-2>

| [Section menu](#) | [Main menu](#) |

## CORRESPONDENCE

11 May 2021

# Afghanistan: vaccinate drug users against COVID-19

- [Attaullah Ahmadi](#)<sup>0</sup>,
- [Blaise Ntacyabukura](#)<sup>1</sup> &
- [Don Eliseo Lucero-Prisno III](#)<sup>2</sup>

1. [Attaullah Ahmadi](#)

1. Kateb University, Kabul, Afghanistan.

[View author publications](#)

You can also search for this author in [PubMed](#) [Google Scholar](#)

2. Blaise Ntacyabukura

1. Karolinska Institute, Stockholm, Sweden.

[View author publications](#)

You can also search for this author in [PubMed](#) [Google Scholar](#)

3. Don Eliseo Lucero-Prisno III

1. London School of Hygiene & Tropical Medicine, London, UK.

[View author publications](#)

You can also search for this author in [PubMed](#) [Google Scholar](#)

Afghanistan has the highest proportion of opiate users in the world ([B. Rasekh et al. Nagoya J. Med. Sci. 80, 329–340; 2018](#)). We call on the Afghan government and its health allies to ensure that people who use drugs are given priority for COVID-19 vaccination. This is justified by the size and spread of the group and its extreme vulnerability to infection.

People in this group are typically criminalized, stigmatized and marginalized ([S. E. Wakeman et al. Nature Med. 26, 819–820; 2020](#)). Weakened immune systems and chronic conditions such as hepatitis and infection with HIV mean that people who use drugs are at high risk of contracting COVID-19, especially if they are homeless and living in densely populated and insanitary urban areas.

Access to vaccines during a pandemic is a human right, so no groups should be left out ([J. N. Nkengasong et al. Nature 586, 197–199; 2020](#)). The United Nations' 2030 Agenda for Sustainable Development recommends that the most disadvantaged and marginalized people should be the first to receive the help they need. No one is safe until everyone is safe.

Nature **593**, 195 (2021)

doi: <https://doi.org/10.1038/d41586-021-01275-6>

## Jobs from Nature Careers

- - - [All jobs](#)
    - 
    - [Postdoctoral Research Fellow in Urban Climate Action](#)

[The University of British Columbia \(UBC\)](#)

[Vancouver, Canada](#)

JOB POST

- **Postdoctoral Fellow in Supercapacitor Technology**

The University of British Columbia (UBC)

Kelowna, Canada

JOB POST

- **Postdoctoral Researchers x 2 – Advancement of audit procedure for domestic and non-domestic energy compliance tools, SFI MaREI Centre, NUI Galway (NUIG-RES-095-21)**

National University of Ireland Galway (NUI Galway)

Galway, Ireland

JOB POST

- **Semantic Web Developer**

European Molecular Biology Laboratory (EMBL)

Hinxton, Cambridge, United Kingdom

JOB POST

---

This article was downloaded by **calibre** from <https://www.nature.com/articles/d41586-021-01275-6>

## CORRESPONDENCE

11 May 2021

# Stop using ‘master–slave’ terminology in biology

- [Dan Graur](#) <sup>✉</sup>

1. [Dan Graur](#)

1. University of Houston, Texas, USA.

[View author publications](#)

You can also search for this author in [PubMed](#) [Google Scholar](#)

In my view, biologists should stop using ‘master–slave’ terminology. This is an all-too-common descriptor for entities that control many others and processes that occur exclusively at the expense of alternatives. A precedent for ending use of such terminology has been set by the IEEE, the world’s largest association of technical professionals (see [go.nature.com/3e4yp4k](https://go.nature.com/3e4yp4k)). Language freighted with racism, degradation, brutality and human suffering has no place in the scientific lexicon.

A literature search reveals that use of ‘master–slave’ is still widespread in publications on topics from immunology to gene conversion and DNA methylation (see also [A. Khan \*eLife\* 10, e65604; 2021](#)). For example, the gene that triggers sex determination in *Drosophila* fruit flies is currently referred to as the ‘master’ gene; those with roles later in the sequence are called ‘slave’ genes (see [C. Dechaud \*et al. Mob. DNA\* 10, 42; 2019](#)). Papers on the subject often contain offensive extended metaphors.

Case-specific alternatives are readily found. For instance, ‘donor’ and ‘acceptor’ could be used in discussing gene conversion, and ‘controller’

and ‘responder’ would work in the case of sex determination.

Nature **593**, 195 (2021)

doi: <https://doi.org/10.1038/d41586-021-01276-5>

## Jobs from Nature Careers

- - - [All jobs](#)
    - 
    - [Postdoctoral Research Fellow in Urban Climate Action](#)  
[The University of British Columbia \(UBC\)](#)  
[Vancouver, Canada](#)  
[JOB POST](#)
    - [Postdoctoral Fellow in Supercapacitor Technology](#)  
[The University of British Columbia \(UBC\)](#)  
[Kelowna, Canada](#)  
[JOB POST](#)
    - [Postdoctoral Researchers x 2 – Advancement of audit procedure for domestic and non-domestic energy compliance tools, SFI MaREI Centre, NUI Galway \(NUIG-RES-095-21\)](#)  
[National University of Ireland Galway \(NUI Galway\)](#)

[Galway, Ireland](#)

[JOB POST](#)

▪ [Semantic Web Developer](#)

[European Molecular Biology Laboratory \(EMBL\)](#)

[Hinxton, Cambridge, United Kingdom](#)

[JOB POST](#)

---

This article was downloaded by **calibre** from <https://www.nature.com/articles/d41586-021-01276-5>

| [Section menu](#) | [Main menu](#) |

## CORRESPONDENCE

11 May 2021

# Value of Mexican nature reserve is more than monetary

- [Enrique J. Jardel-Peláez](#)<sup>0</sup>,
- [Sergio Graf-Montero](#)<sup>1</sup>,
- [Eduardo Santana-C.](#)<sup>2</sup> &
- [Angélica Jiménez-Hernández](#)<sup>3</sup>

1. Enrique J. Jardel-Peláez

1. Universidad de Guadalajara-CUCSUR, Jalisco, Mexico.

[View author publications](#)

You can also search for this author in [PubMed](#) [Google Scholar](#)

2. Sergio Graf-Montero

1. Gobierno del Estado de Jalisco, Guadalajara, Jalisco, Mexico.

[View author publications](#)

You can also search for this author in [PubMed](#) [Google Scholar](#)

3. [Eduardo Santana-C.](#)

1. Universidad de Guadalajara-CUCSUR, Jalisco, Mexico.  
(University of Wisconsin-Madison, Wisconsin, USA.)

[View author publications](#)

You can also search for this author in [PubMed](#) [Google Scholar](#)

#### 4. Angélica Jiménez-Hernández

1. Fundación Manantlán para la Biodiversidad de Occidente AC, Colima, Mexico.

[View author publications](#)

You can also search for this author in [PubMed](#) [Google Scholar](#)

Our monetary compensation programme for poor rural communities in Mexico's Sierra de Manantlán Biosphere Reserve encouraged them to forgo exploitation of their natural resources to provide ecosystem services for the city of Colima (see [Nature 591, 178; 2021](#)). But focusing solely on the monetary value of ecosystems isn't enough.

The National Forestry Commission of Mexico and the Fund for Natural Protected Areas have made compensatory payments of almost US\$1 million to communities in the Cerro Grande region of the reserve since 2003, backed since 2013 by a local fiduciary fund of voluntary contributions from Colima's citizens. However, the voluntary payments are minimal because most people don't acknowledge the importance of the mountain forest that provides 90% of their water.

As well as monetary schemes, the cultural traditions and the land-tenure rights of communal organizations must be recognized. They should be empowered to draw up contracts between owners of natural resources and urban beneficiaries that will promote their common social, economic and livelihood interests. To increase productivity and family income for impoverished small landowners, payment for ecosystem services could be implemented by using diverse marketing approaches that include sustainable agroforestry and livestock production.

Nature **593**, 195 (2021)

doi: <https://doi.org/10.1038/d41586-021-01218-1>

## Jobs from Nature Careers

- - - [All jobs](#)
    - - [Postdoctoral Research Fellow in Urban Climate Action](#)  
  
[The University of British Columbia \(UBC\)](#)  
  
[Vancouver, Canada](#)  
  
[JOB POST](#)
      - [Postdoctoral Fellow in Supercapacitor Technology](#)  
  
[The University of British Columbia \(UBC\)](#)  
  
[Kelowna, Canada](#)  
  
[JOB POST](#)
      - [Postdoctoral Researchers x 2 – Advancement of audit procedure for domestic and non-domestic energy compliance tools, SFI MaREI Centre, NUI Galway \(NUIG-RES-095-21\)](#)  
  
[National University of Ireland Galway \(NUI Galway\)](#)  
  
[Galway, Ireland](#)  
  
[JOB POST](#)
  - [Semantic Web Developer](#)

European Molecular Biology Laboratory (EMBL)

Hinxton, Cambridge, United Kingdom

JOB POST

---

This article was downloaded by **calibre** from <https://www.nature.com/articles/d41586-021-01218-1>

| [Section menu](#) | [Main menu](#) |

## CORRESPONDENCE

11 May 2021

# COVID-19: build on Belgium's psychosocial findings

- [Elke Van Hoof](#) <sup>0</sup> &
- [Nele Van den Cruyce](#) <sup>1</sup>

1. [Elke Van Hoof](#)

1. Free University Brussels, Belgium.

[View author publications](#)

You can also search for this author in [PubMed](#) [Google Scholar](#)

2. Nele Van den Cruyce

1. Free University Brussels, Belgium.

[View author publications](#)

You can also search for this author in [PubMed](#) [Google Scholar](#)

As president and a member of Belgium's Superior Health Council, respectively, we suggest that an international consortium of researchers could help to accelerate society's recovery from COVID-19. The researchers would be drawn from the social sciences, the humanities and the arts to help mitigate the psychosocial effects of the pandemic for people and the economy.

The council issued recommendations a year ago for offsetting the impact of the pandemic on Belgians' mental health (updated in February; see

[go.nature.com/3359qkf](https://go.nature.com/3359qkf)). These are in broad agreement with those discussed by Hetan Shah ([Nature 591, 503; 2021](https://doi.org/10.1038/nature23021)). It has since set up the Belgian Mental Health Data Repository (see <https://doi.org/10.1101/2021.01.27.479125>) as a tool for analysis of Belgian research on the topic.

Similar projects are running in other countries. Governments need such local data and information for policymaking. An international knowledge-sharing network could coordinate these efforts, consolidate the outcome and underscore the importance of the consortium's input for responding to global challenges.

Nature **593**, 195 (2021)

doi: <https://doi.org/10.1038/d41586-021-01277-4>

## Jobs from Nature Careers

- - - [All jobs](#)
    - 
    - [\*\*Postdoctoral Research Fellow in Urban Climate Action\*\*](#)
      - [The University of British Columbia \(UBC\)](#)
      - [Vancouver, Canada](#)
      - [JOB POST](#)
    - [\*\*Postdoctoral Fellow in Supercapacitor Technology\*\*](#)
      - [The University of British Columbia \(UBC\)](#)
      - [Kelowna, Canada](#)

JOB POST

- **Postdoctoral Researchers x 2 – Advancement of audit procedure for domestic and non-domestic energy compliance tools, SFI MaREI Centre, NUI Galway (NUIG-RES-095-21)**

National University of Ireland Galway (NUI Galway)

Galway, Ireland

JOB POST

- **Semantic Web Developer**

European Molecular Biology Laboratory (EMBL)

Hinxton, Cambridge, United Kingdom

JOB POST

---

This article was downloaded by **calibre** from <https://www.nature.com/articles/d41586-021-01277-4>

# Work

- **[How to blow the whistle on an academic bully](#)** [ 11 May 2021]  
Career Feature • Standing up to a persecutor is tough, particularly if they are your supervisor. But you can take steps to report abuse and protect yourself.
- **[Smartphone science: apps test and track infectious diseases](#)**  
[ 10 May 2021]  
Technology Feature • The prevalence, power and portability of smartphones make them valuable tools for pathogen monitoring and citizen science.
- **[A deep-rooted appreciation for the health benefits of plants](#)**  
[ 10 May 2021]  
Where I Work • Kehinde Apara draws on artificial intelligence and her own family background to source flora for her work at a California bioprospecting company.

## CAREER FEATURE

11 May 2021

# How to blow the whistle on an academic bully

Standing up to a persecutor is tough, particularly if they are your supervisor. But you can take steps to report abuse and protect yourself.

- [Virginia Gewin](#) 0

1. Virginia Gewin

1. Virginia Gewin is a freelance writer in Portland, Oregon.

[View author publications](#)

You can also search for this author in [PubMed](#) [Google Scholar](#)

[Find a new job](#)



It's time to call time on bullies' attempts to humiliate, ridicule and undermine.Credit: Getty

Bullying is endemic in academia, an environment riddled with hierarchies and hyper-competition, exacerbated by an over-reliance on temporary contracts and the pressure to land highly coveted tenured positions.

To give a sense of the size of the problem, in any 12-month period, on average, 25% of faculty members self-identify as being bullied, while 40–50% say they have witnessed others being bullied, according to a synthesis of studies published in 2019 ([L. Keashly in \*Special Topics and Particular Occupations, Professions and Sectors\* \(eds P. D'Cruz \*et al.\*\)](#)  
<https://doi.org/gbgn>; [Springer, 2019](#)).

A survey of 9,000 staff at the Max Planck Society, the German research organization, found that 10% had experienced bullying behaviour in the past 12 months, and 17.5% reported bullying events over a longer time frame (see [Nature 571, 14–15; 2019](#)). One in five of the graduate

students who responded to *Nature*'s 2019 global PhD survey reported experiencing bullying, and 57% of those reported feeling unable to discuss their situation without fear of personal repercussions (see [\*Nature\* 575, 403–406; 2019](#)).

As universities around the world grapple with pandemic-related stressors, including cutbacks, layoffs and furloughs, an environment could emerge in which bullying behaviours increase, says Loraleigh Keashly, a researcher at Wayne State University in Detroit, Michigan, who studies academic bullying.

A 2020 paper that she co-authored with Morteza Mahmoudi, a nanotechnologist at Michigan State University in East Lansing, suggests that the pandemic could fuel abusive academic-workplace behaviours owing to worsening psychological health and economic and social inequities ([M. Mahmoudi and L. Keashly \*Bioimpacts\* 10, 139–140; 2020](#)).



### [Does science have a bullying problem?](#)

Mahmoudi is co-founder and director of the [Academic Parity Movement](#), a global initiative that aims to document bullying and increase legal protections for bullied researchers. It defines bullying by an academic superior as “sustained hostile behaviour … including, but not limited to, ridiculing, threatening, blaming, invasion of privacy, [and] put-downs”. The

definition also includes “interference with matriculation and career progress”, such as “removing funding, writing falsely negative recommendation letters, taking credit for others’ work and threatening to cancel visas or fellowships”.

In what follows, Keashly and Mahmoudi, along with six other higher-education professionals who research bullying in academia, tell *Nature* about some of the options available to those who are faced with a bullying supervisor, and how researchers can protect their careers and mental well-being in the process. They also outline how universities are putting in place policies and reporting procedures — often despite the absence of national laws to offer protection from workplace bullying.

Finally, a researcher who complained about a PhD supervisor’s bullying behaviour towards him and others at a university in Australia describes his experience and the toll it took. Because of the sensitivity surrounding his situation, *Nature* is not revealing his identity.

Here is a step-by-step approach to confronting an academic bully.

## **Step 1: Confirm that it is bullying**

In 2016, the PhD student mentioned above witnessed his adviser’s extreme response to a fellow graduate student. Two years later, he himself was the focus of his supervisor’s ire. The abuse “was always for little mistakes — for example, submitting a paper to a journal with a typo”, he says. It was always disproportionate, including yelling, ostracization and threats, such as removing his name from the authorship of a paper or discontinuing supervision, he adds.

He says that the experience of being bullied caused a mental breakdown, and led to the collapse of his personal relationship because of the stress it caused.

But bullying is not always clear-cut, and Keashly stresses that it does not include negative comments delivered appropriately in a performance evaluation.



### Research is set up for bullies to thrive

“You need to make sure at the first stage that what you are experiencing is academic bullying, and that it’s not a misunderstanding or something that will fall into the academic-freedom realm,” says Mahmoudi. The key difference is that academics should be free to criticize ideas, he says, but without fear or threat of retaliation or consequences.

To make sense of any untoward behaviour, the two researchers recommend documenting any and all instances of it. “Bullying often starts off quite subtly and, if unaddressed, can escalate over time,” says Keashly.

The target of a bully should write down what happened, how they felt about it, how they responded, and anything else going on at the time, she says. “Having records helps the recipient get a sense as to whether this is an aberration or if it is becoming established as a pattern,” she says. Furthermore, says Mahmoudi, “academic bullies are clever; they can leave no trace”.

## **Step 2: Seek support**

Keashly encourages those who have been bullied to check their institution’s formal policies and procedures for raising concerns about hostile, unfair

treatment. This can be done either by asking human-resources colleagues or by checking the university website to see whether there are workplace discrimination, harassment or anti-bullying policies in place.

Leah Hollis, a workplace-bullying researcher based at Rutgers University in New Brunswick, New Jersey, recommends checking whether the institution has a grievance policy or faculty senate (or similar faculty governing body) that can offer support to those who have been bullied. Unions can also offer advice, she adds.



Look up grievance policies, says Leah Hollis. Credit: Ken Barboza Associates

Another important step is to consult with the university's ombudsman or an equivalent office, says Mahmoudi. These offices exist at most large research institutions, in the United States and around the world, to offer an informal, impartial and confidential conflict-management service that operates independently of the university. "Nothing will be leaked to your PI [principal investigator] or department; you are ensured confidentiality," he says of these offices.

Most UK institutions have established complaint procedures or mediation services. If university-based options don't satisfy, students in England and Wales can take their concerns to the [Office of the Independent Adjudicator](#). It addresses unresolved complaints, including those to do with bullying, harassment and discrimination.

Beyond university anti-bullying and grievance policies, some countries have introduced legislation aimed at tackling the issue. In France, for example, a labour code put in place by the 2002 Social Modernization Act protects employees from bullying or harassment that intentionally or unintentionally degrades their working conditions, violates their rights and dignity, impairs their physical or mental health, or jeopardizes their professional future.

Still, when asked whether academics in France are better protected from workplace bullying, Loïc Lerouge, a labour-law researcher at the University of Bordeaux, France, says: "On paper, yes; in practice, no."

"People don't always trust the procedures," says Christina Björklund, a researcher at the Karolinska Institute in Stockholm who studies workplace bullying. It is still quite rare for bullies to be held accountable for their behaviour, she says. The Swedish government has asked Björklund and colleagues to develop evidence-based guidelines for all workplaces.

"Bullying is about power," she adds. "If you choose to report it, it will be tough and will take a lot of your energy."

To that end, says Hollis, victims need to build a support community, which could include peers and family members, with whom to share what happened and how it made the bullying target feel. “Find your allies first,” she advises. There’s no shame in talking to a mental-health counsellor, she adds. “Always remember: it’s not your fault.”

## Step 3: Consider informal and formal complaint routes

Following a spate of high-profile investigations at prominent institutions (see [\*Nature\* 563, 616–618; 2018](#)), a growing number of universities, mindful of the financial and reputational cost of bullying, are introducing reporting mechanisms alongside anti-bullying policies.

Alexandra Olaya-Castro, vice-dean for equality, diversity and inclusion in the faculty of mathematical and physical sciences at University College London (UCL), says her institution established a ‘[Report + Support](#)’ tool in 2019. It walks users through both informal and formal resolution processes for addressing bullying claims, and allows problems to be reported anonymously.



[Germany’s prestigious Max Planck Society conducts huge bullying survey](#)

Olaya-Castro encourages people to go on the record through university channels, because anonymous reports can only help to address prevention and intervention university-wide; taking action to address an individual's behaviour requires the target to report it through a formal or informal process, which requires details. Complainants need to report their grievances to the right people, she adds.

UCL has three informal resolution processes. The first involves mediation, in the form of a facilitated discussion between the target and the bully, says Olaya-Castro. The second option calls on a senior member of staff to explain to the bully why their behaviour is unacceptable.

Finally, if the target of a bullying supervisor doesn't want to involve anyone in the department, they can speak to a designated dignity adviser, she adds. These are volunteers among campus employees who are trained to offer confidential support on matters of bullying, harassment and sexual misconduct. An informal resolution can work well if bullying is confronted early, she says.

If mediation doesn't resolve the concern, a formal procedure might follow at UCL, or at other institutions where similar processes are in place. A preliminary investigation, typically conducted by human-resources staff, would aim to establish whether there are grounds for the complaint, as a way to weed out baseless accusations.

If there are grounds, a formal hearing is then scheduled. At UCL, this would involve a grievance panel; Human Resources and the head of department appoint one manager, one trade-union representative and a senior member of staff who will chair the proceedings. If the target of the bullying accepts the outcome, that's the end of it; if not, they have the option to appeal. "It is not an easy process — either the formal or informal paths," says Olaya-Castro of reporting at UCL or elsewhere. But reaching an informal resolution can be preferable because it consumes less time and energy for all involved, she adds, while acknowledging that unfortunately, "some situations require a formal procedure".

Keashly says the processes at UCL are similar to those at many institutions, but she also encourages faculty members to keep one another's unacceptable

behaviours in check. Most importantly, she says, they should challenge narratives that enable bullying — such as ‘that’s just the way he is’ or ‘smart people are just abrasive’.



### [Leading cancer-research charity takes tough stance on bullying](#)

The anonymous PhD student says the investigation of his case dragged on for 12 months as the university repeatedly delayed its responses. It took the university a week to respond to his e-mails, a month to schedule his first interview, and there were two extensions to the deadline for publishing the investigation’s final report. In the middle of the process, he was told that any outcome or punishment would be kept between the university and his supervisor.

“I want to encourage targets to report bullying, but the system is so fraught, reporting can perpetuate the harm if the university is not equipped to protect people,” says Erika Marín-Spiotta, a biogeographer at the University of Wisconsin–Madison and recipient of a US National Science Foundation grant to conduct bystander training. The training offers safe intervention strategies to protect and support targets of bullying or harassment. Keashly highlights the [\*\*‘four D’s’ of bystanding\*\*](#): distract the bully or target to defuse the situation; directly engage the bully; delegate to someone, for example, in a position of authority, who can offer help; and delay an offer of support if you can’t intervene there and then.

## **Step 4: Know what to expect after filing a complaint**

As soon as someone lodges a formal complaint, everything changes, says Mahmoudi. It's a decision that requires a good deal of consideration, and people should think about how strong their support network is and their personal fortitude before deciding whether to go through what will probably be a gruelling experience.

Hollis recommends that the targets of bullying ask their informal network or a trusted faculty member how their institution has responded to others' complaints, to know what might await them if they file a formal complaint themselves. Some universities, she says, want the problem to go away more than they want to listen to the people who have been bullied, adding: "It really depends on how the organization has responded before." She also cautions that a supervisor accused of bullying might go after the complainant after a report has been filed. Mahmoudi says it's not uncommon for some institutions to use delaying tactics in the hope that a complainant will drop their accusation.

Saman Hosseinpour, a materials scientist at the Friedrich Alexander University in Erlangen, Germany, and an Academic Parity Movement advisory-board member, notes that universities' support for the targets of bullying can often be lacklustre, because the institution wants the least disruptive resolution possible. And, often, the bully has more power and clout, and brings desirable resources to the university. For example, Hosseinpour adds, if a target opts for mediation, mediators might try to persuade them that academia is simply a tough environment, and that everyone faces issues similar to what they went through.

Mahmoudi has amassed 2,000 responses to a survey about satisfaction with investigations of bullying. Only 7% reported that they experienced a fair and unbiased process, he says of his as-yet unpublished work. "International students will have a much rougher time than national ones," he says, given that their PI might have the power to cancel their appointment, which could impact their visa status, and they might find it hard to access support resources because of cultural or language barriers.

Still, if a university has policies and procedures around bullying, Keashly says, it is legally obligated to follow them, including taking appropriate action in the event that charges of bullying are confirmed. And the more policies and procedures there are, the greater the recognition that this is a significant problem, she adds.

The anonymous PhD student feels that his university had a greater incentive to support a high-profile faculty member — who brought in multimillion-dollar grants — than a PhD student. Ultimately, he left the institution and, after setting into a new role, filed a formal complaint. If he had it to do again, he says would have come forward two years before he did. Targets “are afraid because they perceive that bullies have more power over them than they [actually] do”, he says. “Life’s too short. The best thing,” he says, is to “move on as fast as you can”.

Despite the emergence of reporting mechanisms, policies and intervention training, the targets of bullying often remain reluctant to report abuse for fear of retaliation that could jeopardize their careers.

Mahmoudi advises the targets of bullying to formulate a back-up plan. This can include leaving a toxic working environment and seeking employment elsewhere.

Keashly advises that it’s not an either/or choice. “You can leave an organization and still continue to address the issue,” she says, through an exit interview — which many institutions offer before an employee leaves — a formal complaint process or lawsuit, depending on what is appropriate.

Nature **593**, 299-301 (2021)

doi: <https://doi.org/10.1038/d41586-021-01252-z>

## Jobs from Nature Careers

- - - [All jobs](#)
    -

- **Postdoctoral Research Fellow in Urban Climate Action**

The University of British Columbia (UBC)

Vancouver, Canada

JOB POST

- **Postdoctoral Fellow in Supercapacitor Technology**

The University of British Columbia (UBC)

Kelowna, Canada

JOB POST

- **Postdoctoral Researchers x 2 – Advancement of audit procedure for domestic and non-domestic energy compliance tools, SFI MaREI Centre, NUI Galway (NUIG-RES-095-21)**

National University of Ireland Galway (NUI Galway)

Galway, Ireland

JOB POST

- **Semantic Web Developer**

European Molecular Biology Laboratory (EMBL)

Hinxton, Cambridge, United Kingdom

JOB POST

---

This article was downloaded by **calibre** from <https://www.nature.com/articles/d41586-021-01252-z>

| [Section menu](#) | [Main menu](#) |

## TECHNOLOGY FEATURE

10 May 2021

# Smartphone science: apps test and track infectious diseases

The prevalence, power and portability of smartphones make them valuable tools for pathogen monitoring and citizen science.

- [Sandeep Ravindran](#) 0

1. Sandeep Ravindran

1. Sandeep Ravindran is a science writer in Washington DC.

[View author publications](#)

You can also search for this author in [PubMed](#) [Google Scholar](#)



A composite image of a smartphone showing a picture of a mosquito on the screen

Credit: Adapted from Getty

Debojyoti Chakraborty took just a few months to develop a COVID-19 diagnostic test that worked in his lab; the challenge was to optimize it for the field.

Based on the gene-editing technology CRISPR, the test produces a band on a paper strip if viral RNA is present. But Chakraborty, who heads an RNA biology group at the Institute of Genomics and Integrative Biology in New Delhi, says he and his colleagues couldn't always agree on whether a faint band counted as a positive signal. What they needed was an objective —

and, ideally, portable — quantification tool. Then Chakraborty realized he already had one: his smartphone.

The researchers developed an app to photograph the paper strip, identify and quantify bands using machine learning, and export the results to the cloud. Called TOPSE<sup>1</sup>, their app laid the foundation for a test that has now been approved by the Drugs Controller General of India. “You can actually do this test in local pathology labs in places that are resource-limited,” Chakraborty says. “Perhaps one day it can be done even at home.”

The billions of smartphones in use worldwide offer unprecedented opportunities for disease tracking, diagnostics and citizen science, as Chakraborty learnt. Examples include apps that enable phone users to monitor COVID-19 symptoms, count disease-carrying mosquitoes and detect microscopic pathogens. They could even help the world to prepare for the next pandemic.

“These tools can be incredibly cheap to deploy, and they get real-time insights directly from people on the ground,” says John Brownstein, a computational epidemiologist at Boston Children’s Hospital in Massachusetts. “That kind of data can outpace what traditional surveillance provides.”

## Portable epidemiology

Smartphone science didn’t start with COVID-19. But the pandemic has spurred researchers to fast-track citizen-science efforts that use smartphones to gather information about the disease. Volunteers can regularly log details about their symptoms, testing status and location through apps or websites. For instance, data from 5 million users of Brownstein’s crowdsourced tracker for influenza and COVID-19 — called [Outbreaks Near Me](#) — provided early evidence of the benefits of masking<sup>2</sup>. “You get these impressive insights that would be harder to collect from traditional health care quickly,” he says.



## [Coronavirus contact-tracing apps: can they slow the spread of COVID-19?](#)

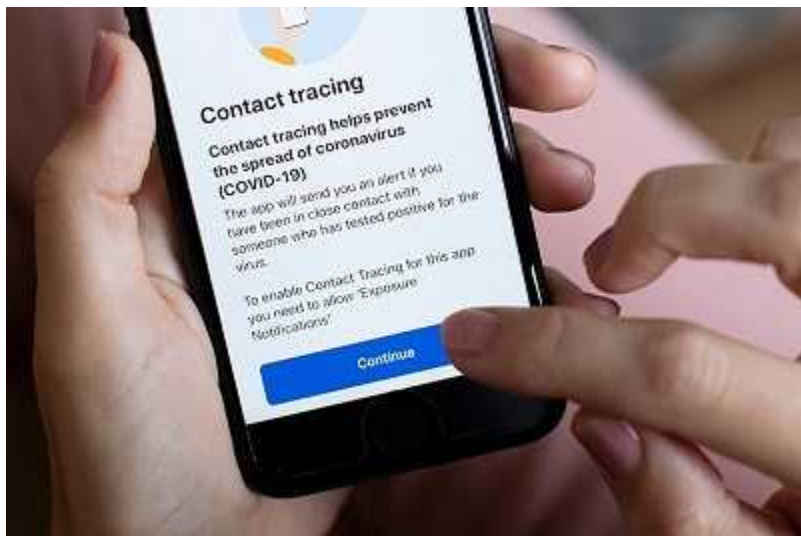
Such projects can be rapidly deployed, an advantage in a fast-moving public-health crisis. Cardiologist Gregory Marcus at the University of California, San Francisco, was able to take his team's [COVID-19 Citizen Science app](#) from concept to 50,000 participants in under a year. "That would be impossible in a conventional research study," he says. And because users enrol by downloading an app, such studies are easy to scale up and tweak: researchers can add questions about new vaccines or virus variants, for instance.

Claire Steves, who studies ageing at King's College London, analysed data from the United Kingdom's [COVID Symptom Study app](#), which has been downloaded by some 4.5 million people. She and her team used data from the app to develop a predictive model that found that a loss of the sense of smell (known as anosmia) was a predictor of testing positive for COVID-19<sup>3</sup>. The team also used data from the app to identify COVID-19 hotspots in the United Kingdom<sup>4</sup> and to establish that long COVID, in which people experience persistent symptoms, was more likely in app users who had reported experiencing more than five COVID-19 symptoms in the first week of illness<sup>5</sup>.

Young children and older adults, who often don't have smartphones, are under-represented in the COVID Symptom Study, Steves and her colleagues found. But thoughtful outreach, statistical analyses and cross-

validation against other research can blunt those biases, she says. By comparing their results to the findings of UK COVID-19 tracking studies that used conventional designs, the team was able to validate its models<sup>4</sup>. “We’ve been able to show that our data very much reflect the data from [those] big population studies.”

Smartphones can track other diseases, too, such as malaria, Zika and dengue, which are spread through mosquitoes. Instead of sending technicians to trap and collect mosquitoes, Craig Williams, a public- and environmental-health scientist at the University of South Australia in Adelaide, posted traps to 126 volunteers in southern Australia and asked them to e-mail him smartphone photos of the trapped insects.



### Contact-tracing apps help reduce COVID infections, data suggest

The project, called [Mozzie Monitors](#), provided large-scale mosquito surveillance at 20% of the cost of a comparable professional surveillance programme<sup>6</sup>. “It has been surprising that citizen scientists were able to collect a higher abundance of mosquitoes than professional programmes in the same period, through a low-cost project from their backyards,” says Larissa Braz Sousa, a graduate student on Williams’s team who works on the project.

Williams has since added the option for volunteers in Australia to eschew traps and instead use a third-party app, iNaturalist, to photograph and

identify the insects. This led to a nationwide trial in February, dubbed Mozzie Month. “We’re hoping to have the first national citizen-science mosquito-surveillance programme,” he says. “The smartphone is at the centre of that.”

## Diagnosis by smartphone

Smartphone science comes down to three features: computing power, connectivity and cameras.

“Cameras on phones have become more and more sensitive over the past ten years, and what I needed a microscope for before I can do with my phone now,” says Rashid Bashir, a bioengineer at the University of Illinois in Urbana-Champaign. In 2017, Bashir and his team harnessed smartphone cameras in a point-of-care test that uses blood samples to check for viral infections. The cameras can spot fluorescent signals generated from amplified viral RNA, enabling detection of Zika, dengue and another mosquito-borne virus called chikungunya<sup>7</sup>. He has now updated the test to detect COVID-19<sup>8</sup>.



## Pocket laboratories

In some cases, smartphone-based diagnostics can match expensive and bulky lab equipment for speed and accuracy, while remaining portable enough for field settings. Jeong-Yeol Yoon, a biomedical engineer at the University of Arizona in Tucson, coupled a smartphone with some off-the-shelf microscope components and the MATLAB Mobile app to detect norovirus, which causes about 20 million cases of gastrointestinal illness each year in the United States<sup>9</sup>. “We duplicated the bench-top fluorescence microscope, which can easily be US\$50,000, for less than \$40,” says Yoon, who is currently setting up clinical trials for both norovirus and COVID-19 versions of the test.

Melanie Ott, a virologist at the Gladstone Institute of Virology and Immunology in San Francisco, California, co-developed a smartphone-based COVID-19 diagnostic test<sup>10</sup> with Daniel Fletcher, a bioengineer at the University of California, Berkeley. According to Fletcher, the test is more sensitive than standard laboratory plate readers, and faster than the gold-standard reverse-transcription PCR test for SARS-CoV-2. The smartphone-based test can also quantify how much virus a person is carrying, which could help to predict the risk of disease transmission and severity. Says Ott: “The phone is doing everything: it’s the camera that actually acquires the results, the computer that analyses the results, and it can send the result to the cloud for storage.”

## Ensuring trust

Smartphones are a powerful way to do science, but gaining users’ trust is crucial if an app is going to be widely used and provide good data. Developers and other experts can help with this, as well as with the technological hurdles. App development is often tricky, but apps that collect health data require extra levels of privacy, security, support and regulatory compliance. Likewise, citizen-science projects must take care to anonymize and encrypt users’ data. “If we don’t get those things right, then it’s going to be impossible to build trust and get people to use these tools, so it’s a priority for us,” says Brownstein.



## NatureTech hub

Such tools also generate a lot of data. The COVID Symptom Study app, for instance, was developed with the London-based data-science firm Zoe, which helped with both app design and data analysis. “You’re having responses from four-and-a-half million people potentially on a daily basis, so it’s very big data and it can be quite complicated,” says Steves.

Marcus helped to create a research platform called [Eureka](#), funded by the US National Institutes of Health, which includes infrastructure that enables scientists to build and deploy mobile apps for health research. Eureka hosts the COVID Citizen Science Study, as well as more than 30 others. “The point is to help researchers utilize mobile technologies without having to have technology expertise, so they can focus on their clinical research and medical expertise,” he says.

That could help users and public-health efforts, too. Yoon envisions a future in which consumers pair over-the-counter kits with apps on their phones for convenient and regular testing, which could help to control future pandemics. “We need to identify the people who get infected, and if you can actually do it at home, I believe that can greatly decrease the spread of the disease,” he says. “We need to be ready for the next pandemic.”

doi: <https://doi.org/10.1038/d41586-021-01253-y>

## References

1. 1.  
Azhar, M. *et al.* Preprint at medRxiv  
<https://doi.org/10.1101/2020.09.13.20193581> (2020).
2. 2.  
Rader, B. *et al.* *Lancet Digital Health* **3**, 148–157 (2021).
3. 3.  
Menni, C. *et al.* *Nature Med.* **26**, 1037–1040 (2020).
4. 4.  
Varsavsky, T. *et al.* *Lancet Public Health* **6**, 21–29 (2021).
5. 5.  
Sudre, C. H. *et al.* *Nature Med.* **27**, 626–631 (2021).
6. 6.  
Sousa, L. B. *et al.* *Sci. Total Environ.* **704**, 135349 (2020).
7. 7.  
Ganguli, A. *et al.* *Biomed. Microdevices* **19**, 73 (2017).
8. 8.  
Ganguli, A. *et al.* *Proc. Natl Acad. Sci. USA* **117**, 22727–22735 (2020).
9. 9.

Chung, S. *et al.* *Nature Protoc.* **16**, 1452–1475 (2021).

10. 10.

Fozouni, P. *et al.* *Cell* **184**, 323–333 (2021).

## Jobs from Nature Careers

- - - [All jobs](#)
    - 
    - [Postdoctoral Research Fellow in Urban Climate Action](#)  
[The University of British Columbia \(UBC\)](#)  
[Vancouver, Canada](#)  
[JOB POST](#)
    - [Postdoctoral Fellow in Supercapacitor Technology](#)  
[The University of British Columbia \(UBC\)](#)  
[Kelowna, Canada](#)  
[JOB POST](#)
    - [Postdoctoral Researchers x 2 – Advancement of audit procedure for domestic and non-domestic energy compliance tools, SFI MaREI Centre, NUI Galway \(NUIG-RES-095-21\)](#)  
[National University of Ireland Galway \(NUI Galway\)](#)

Galway, Ireland

JOB POST

▪ **Semantic Web Developer**

European Molecular Biology Laboratory (EMBL)

Hinxton, Cambridge, United Kingdom

JOB POST

---

This article was downloaded by **calibre** from <https://www.nature.com/articles/d41586-021-01253-y>.

| [Section menu](#) | [Main menu](#) |

## WHERE I WORK

10 May 2021

# A deep-rooted appreciation for the health benefits of plants

Kehinde Apara draws on artificial intelligence and her own family background to source flora for her work at a California bioprospecting company.

- [James Mitchell Crow](#) <sup>0</sup>

1. James Mitchell Crow

1. James Mitchell Crow is a freelance science writer in Melbourne, Australia.

[View author publications](#)

You can also search for this author in [PubMed](#) [Google Scholar](#)



Kehinde Apara is a raw-materials research and sourcing associate at Brightseed in San Francisco, California. Credit: Ian Tuttle for *Nature*

I love being surrounded by plants every day. Here, it's February, and I'm in my laboratory in San Francisco, California, where I work for a company called Brightseed. I break plants down into fine powders so our scientists can uncover each plant's metabolome — the complete set of small molecules that it makes. Brightseed aims to find the molecules that matter in terms of human health and nutrition.

My bachelor's degree is in environmental science, but plants are in my bloodline. My family is from New Orleans, Louisiana, and my grandmother was considered a hoodoo woman, a medicine woman, and was very knowledgeable about plants. My father would help her to gather them. I love marrying that cultural side with my formal science background.

I 'equalize' fresh and dried plants for analysis by lyophilizing, or freeze-drying, them, and cryo-milling them into a uniform powder. I often need to treat each part of the plant — from fruits to roots — differently. Berries, for example, can be hard to mill because of their sugar content. The powders are then washed with solvents to dissolve their metabolomic content for analysis.

Our current focus is traditional medicinal plants and major edible ones. I'm processing and archiving specimens for our botanical library. We use Forager, our proprietary artificial-intelligence platform, to predict plants' human-health benefits. The more information Forager has, the better it can predict which plants are likely to have metabolomic 'personalities' supportive of human health.

I seek plants with a healthy metabolome that are grown by people with strong links to the land, so I visit farmers' markets and source Indigenous food and medicinal plants globally, from Australia to the Caribbean. I'm really interested in medicine traditions from the Americas — of grandmothers in the Appalachians, for instance — that have not been highly regarded by scientists.

Nature **593**, 306 (2021)

doi: <https://doi.org/10.1038/d41586-021-01254-x>

## Jobs from Nature Careers

- - - [All jobs](#)
    -

- **Postdoctoral Research Fellow in Urban Climate Action**

The University of British Columbia (UBC)

Vancouver, Canada

JOB POST

- **Postdoctoral Fellow in Supercapacitor Technology**

The University of British Columbia (UBC)

Kelowna, Canada

JOB POST

- **Postdoctoral Researchers x 2 – Advancement of audit procedure for domestic and non-domestic energy compliance tools, SFI MaREI Centre, NUI Galway (NUIG-RES-095-21)**

National University of Ireland Galway (NUI Galway)

Galway, Ireland

JOB POST

- **Semantic Web Developer**

European Molecular Biology Laboratory (EMBL)

Hinxton, Cambridge, United Kingdom

JOB POST

---

This article was downloaded by **calibre** from <https://www.nature.com/articles/d41586-021-01254-x>

| [Section menu](#) | [Main menu](#) |

# Research

- **[Neural interface translates thoughts into type](#)** [ 12 May 2021]  
News & Views • A neural interface has been developed that could enable people with paralysis to type faster than they could using other technologies, by directly translating attempts at handwriting into text.
- **[Cloud droplets aid the production of formic acid in the atmosphere](#)** [ 12 May 2021]  
News & Views • Known sources of formic acid could not explain the observed atmospheric concentrations of this compound. The discovery of a previously unknown pathway that generates formic acid in the atmosphere resolves this discrepancy.
- **[A continuous model of early mammalian development](#)** [ 30 April 2021]  
News & Views • Characterization of the early developmental process called gastrulation has mostly been limited to snapshots at different time points. A model of mouse gastrulation now maps the transitions between cell types continuously in time.
- **[A molecular connection hints at how a genetic risk factor drives Crohn's disease](#)** [ 19 April 2021]  
News & Views • Mutations of the NOD2 gene are risk factors for Crohn's disease. Many aspects of how they contribute to the condition are unknown. The discovery of cell populations that are involved suggests new therapeutic options.
- **[Nitrogen deletion offers fresh strategy for organic synthesis](#)**  
[ 12 May 2021]  
News & Views • Many scientific fields and industries rely on the synthesis of small organic molecules. A chemical reagent has been developed that allows such molecules to be made by 'deleting' nitrogen atoms from readily accessible precursors.
- **[CMOS-based cryogenic control of silicon quantum circuits](#)**  
[ 12 May 2021]  
Article • A cryogenic CMOS control chip operating at 3 K is used to demonstrate coherent control and simple algorithms on silicon qubits operating at 20 mK.
- **[Ultralow contact resistance between semimetal and monolayer semiconductors](#)** [ 12 May 2021]  
Article • Electric contacts of semimetallic bismuth on monolayer semiconductors are shown to suppress metal-induced gap states and thus have very low contact resistance and a zero Schottky barrier height.

- **A dynamic stability design strategy for lithium metal solid state batteries** [ 12 May 2021]

Article • A multi-layered electrolyte, in which a less stable electrolyte is sandwiched between two electrolyte layers that are more stable, can inhibit the growth of lithium dendrites in highly pressurized solid-state lithium metal batteries.

- **Skeletal editing through direct nitrogen deletion of secondary amines** [ 12 May 2021]

Article • Nitrogen is ‘deleted’ from secondary amines using anomeric amide reagents, which react with the amine to form an isodiazene, after which nitrogen gas is released and the resulting carbon radicals combine to form a carbon–carbon bond.

- **Widespread six degrees Celsius cooling on land during the Last Glacial Maximum** [ 12 May 2021]

Article • Analyses and modelling of noble gases in groundwater show that the mean annual surface temperatures of low-altitude, low-to-mid-latitude land masses were about 6 °C cooler during the Last Glacial Maximum than during the Late Holocene.

- **Ubiquitous atmospheric production of organic acids mediated by cloud droplets** [ 12 May 2021]

Article • The oxidation of hydrated formaldehyde from cloud droplets is the dominant source of atmospheric formic acid, increasing atmospheric acidity by reducing cloud and rainwater pH.

- **Genome-wide enhancer maps link risk variants to disease genes** [ 07 April 2021]

Article • Mapping enhancer regulation across human cell types and tissues illuminates genome function and provides a resource to connect risk variants for common diseases to their molecular and cellular functions.

- **Coupling of activity, metabolism and behaviour across the Drosophila brain** [ 28 April 2021]

Article • Two-photon microscopy across the fly brain using sensors that permit simultaneous measurement of neural activity and metabolic flux reveals global and local coordination of neural activity and energy metabolism.

- **High-performance brain-to-text communication via handwriting** [ 12 May 2021]

Article • A brain–computer interface enables rapid communication through neural decoding of attempted handwriting movements in a person with paralysis.

- **Meningeal lymphatics affect microglia responses and anti- $\text{A}\beta$  immunotherapy** [ 28 April 2021]

Article • Meningeal lymphatic drainage can affect the microglial inflammatory response and anti-amyloid- $\beta$  immunotherapy in mouse models of Alzheimer's disease.

- **C. difficile exploits a host metabolite produced during toxin-mediated disease** [ 28 April 2021]

Article • RNA-sequencing experiments determine that sorbitol, a metabolite produced by the host enzyme aldose reductase, is exploited by Clostridium difficile in its adaptation to inflammatory conditions in the gut.

- **Assessing transmissibility of SARS-CoV-2 lineage B.1.1.7 in England** [ 25 March 2021]

Article • Genetic and testing data from England show that the SARS-CoV-2 variant of concern B.1.1.7 has a transmission advantage over other lineages.

- **Increased mortality in community-tested cases of SARS-CoV-2 lineage B.1.1.7** [ 15 March 2021]

Article • Analysis of community-tested cases of SARS-CoV-2 indicates that the B.1.1.7 variant is not only more transmissible than pre-existing variants, but may also cause more severe illness, and is associated with a higher risk of death.

- **A myeloid–stromal niche and gp130 rescue in NOD2-driven Crohn's disease** [ 31 March 2021]

Article • NOD2 deficiency drives fibrosis and stricturing complications in Crohn's disease through dysregulated homeostasis of activated fibroblasts and macrophages, which is ameliorated by gp130 blockade in human cell and zebrafish models.

- **Cell-programmed nutrient partitioning in the tumour microenvironment** [ 07 April 2021]

Article • Positron emission tomography measurements of nutrient uptake in cells of the tumour microenvironment reveal cell-intrinsic partitioning in which glucose uptake is higher in myeloid cells, whereas glutamine is preferentially acquired by cancer cells.

- **HP1 drives de novo 3D genome reorganization in early Drosophila embryos** [ 14 April 2021]

Article • The heterochromatin protein HP1 has an essential role in establishing several features of the 3D nuclear organization of the genome during early embryonic development in Drosophila.

- **Structural basis of long-range to short-range synaptic transition in NHEJ** [ 14 April 2021]

Article • Double-strand DNA break repair by the non-homologous end joining pathway involves the transition from a complex that bridges the DNA ends to a complex that aligns the DNA for ligation through the dissociation of the kinase subunits of the DNA-PK complexes.

| [Next section](#) | [Main menu](#) | [Previous section](#) |

## NEWS AND VIEWS

12 May 2021

# Neural interface translates thoughts into type

A neural interface has been developed that could enable people with paralysis to type faster than they could using other technologies, by directly translating attempts at handwriting into text.

- [Pavithra Rajeswaran](#)<sup>0</sup> &
- [Amy L. Orsborn](#)<sup>1</sup>

1. Pavithra Rajeswaran

1. Pavithra Rajeswaran is in the Department of Bioengineering, University of Washington, Seattle, Washington 98195, USA.

[View author publications](#)

You can also search for this author in [PubMed](#) [Google Scholar](#)

2. [Amy L. Orsborn](#)

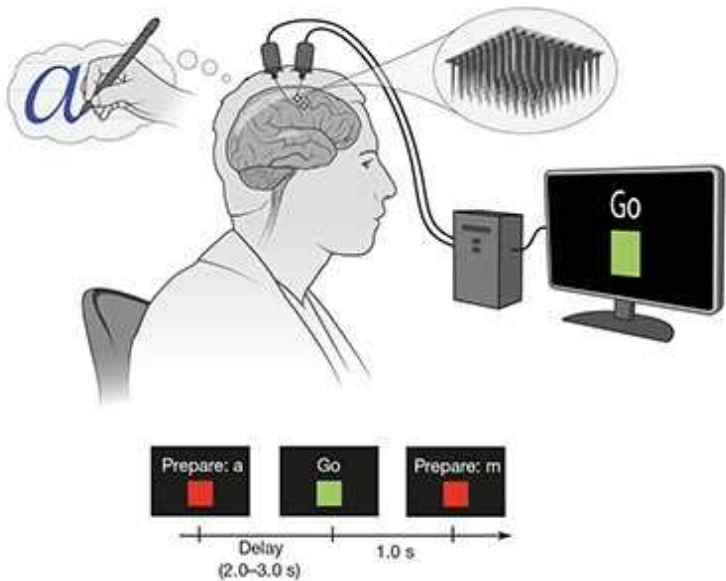
1. Amy L. Orsborn is in the Department of Bioengineering, University of Washington, Seattle, Washington 98195, USA; and in the Department of Electrical and Computer Engineering, and at the Washington National Primate Research Center, University of Washington.

[View author publications](#)

You can also search for this author in [PubMed](#) [Google Scholar](#)

We can think much faster than we can communicate — a fact that many of us feel aware of as we struggle with our smartphone keyboards. For people with severe paralysis, this information bottleneck is much more extreme.

Willett *et al.*<sup>1</sup> report in [a paper in \*Nature\*](#) the development of a brain–computer interface (BCI) for typing that could eventually let people with paralysis communicate at the speed of their thoughts.



[Read the paper: High-performance brain-to-text communication via handwriting](#)

Commercially available assistive typing devices predominantly rely on the person using the device being able to make eye movements or deliver voice commands. Eye-tracking keyboards can let people with paralysis type at around 47.5 characters per minute<sup>2</sup>, slower than the 115-per-minute speeds achieved by people without a comparable injury. However, these technologies do not work for people whose paralysis impairs eye movements or vocalization. And the technology has limitations. For instance, it is hard to reread an e-mail, so that you can compose your reply, while you are typing with your eyes.

By contrast, BCIs restore function by deciphering patterns of brain activity. Such interfaces have successfully restored simple movements — such as reaching for and manipulating large objects — to people with paralysis<sup>3–7</sup>.

By directly tapping into neural processing, BCIs hold the tantalizing promise of seamlessly restoring function to a wide range of people.

But, so far, BCIs for typing have been unable to compete with simpler assistive technologies such as eye-trackers. One reason is that typing is a complex task. In English, we select from 26 letters of the Latin alphabet. Building a classification algorithm to predict which letter a user wants to choose, on the basis of their neural activity, is challenging, so BCIs have solved typing tasks indirectly. For instance, non-invasive BCI spellers present several sequential visual cues to the user and analyse the neural responses to all cues to determine the desired letter<sup>8</sup>. The most successful invasive BCI (iBCI; one that involves implanting an electrode into the brain) for typing allowed users to control a cursor to select keys, and achieved speeds of 40 characters per minute<sup>6</sup>. But these iBCIs, like non-invasive eye-trackers, occupy the user's visual attention and do not provide notably faster typing speeds.

Willett and colleagues developed a different approach, which directly solves the typing task in an iBCI and thereby leapfrogs far beyond past devices, in terms of both performance and functionality. The approach involves decoding letters as users imagine writing at their own pace (Fig. 1).

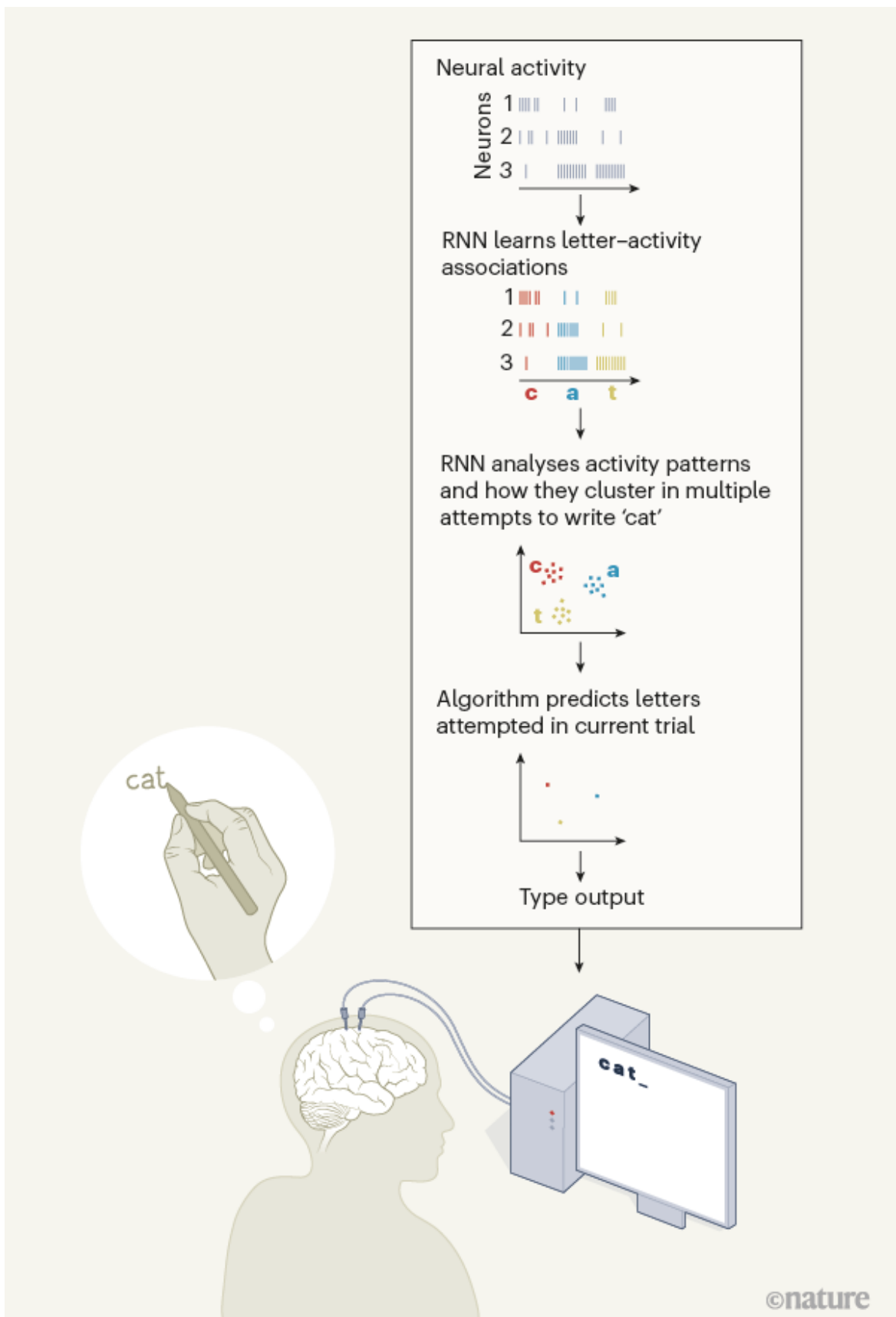
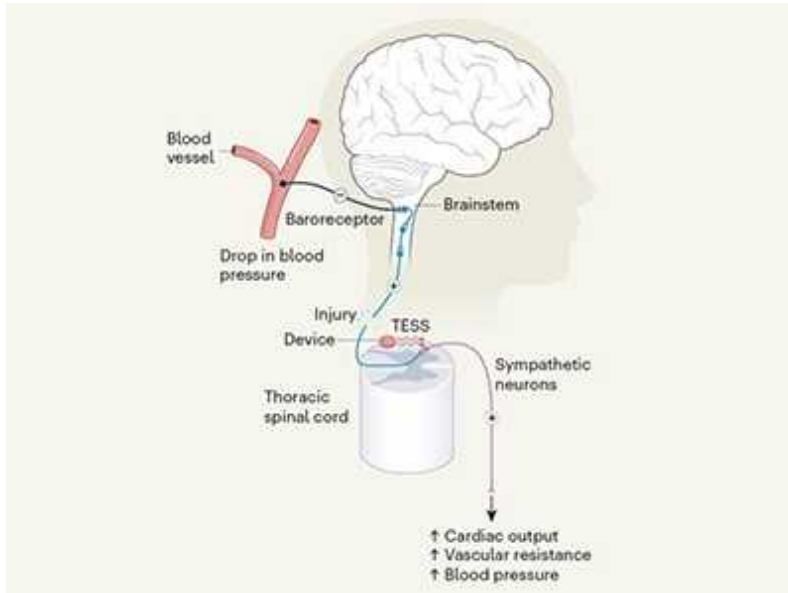


**Figure 1 | A brain–computer interface (BCI) for typing.** Willett *et al.*<sup>1</sup> have developed a BCI that enables a person with paralysis to type, by translating the neural activity produced from imagined attempts at handwriting into text on the computer screen. As a simplified description, electrodes implanted into the brain measure the activity of many neurons as the user imagines writing each letter (lines indicate time points at which each neuron fires). A deep-learning model called a recurrent neural network (RNN) learns the neural activity patterns produced from each character, and analyses how these activity patterns relate across multiple trials, generating cluster plots. This information is used by an algorithm to predict the letters being imagined by the participant in the current trial, and the prediction is translated into a typographic output. (Figure adapted from Fig. 2a of ref. 1.)

Such an approach required a classification algorithm that predicts which of 26 letters or 5 punctuation marks a user with paralysis is trying to write — a challenging feat when the attempts cannot be observed and occur whenever the user chooses. To overcome this challenge, Willett *et al.* first repurposed another type of algorithm — a machine-learning algorithm originally developed for speech recognition. This allowed them to estimate, on the basis of neural activity alone, when a user started attempting to write a character. The pattern of neural activity generated each time their study participant imagined a given character was remarkably consistent. From this information, the group produced a labelled data set that contained the neural-activity patterns corresponding to each character. They used this data set to train the classification algorithm.

To achieve accurate classification in such a high-dimensional space, Willett and colleagues' classification algorithm used current machine-learning methods, along with a type of artificial neural network called a recurrent neural network (RNN), which is especially good at predicting sequential data. Harnessing the power of RNNs requires ample training data, but such data are limited in neural interfaces, because few users want to imagine writing for hours on end. The authors solved this problem using an approach known as data augmentation, in which neural activity patterns previously generated by the participant are used to produce artificial sentences on which to train the RNN. They also expanded their training data by introducing artificial variability into the patterns of neural activity, to mimic

changes that occur naturally in the human brain. Such variability can make RNN BCIs more robust<sup>9</sup>.



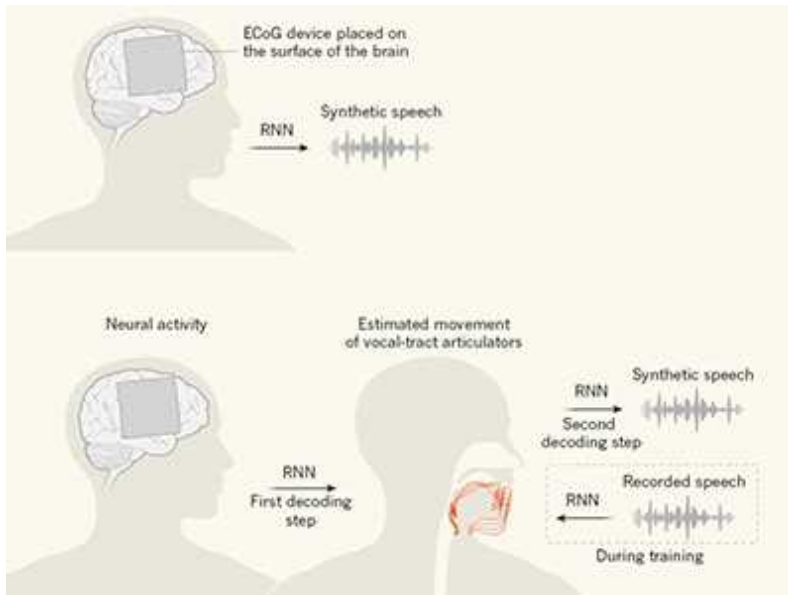
### Neuroprosthetic device maintains blood pressure after spinal-cord injury

Thanks to these methods, Willett and colleagues' algorithm provided impressively accurate classification, picking the correct character 94.1% of the time. By including predictive-language models (similar to those that drive auto-correct functions on a smartphone), they further improved accuracy to 99.1%. The participant was able to type accurately at a speed of 90 characters per minute — a twofold improvement on his performance with past iBCIs.

This study's achievements, however, stem from more than machine learning. A decoder's performance is ultimately only as good as the data that are fed into it. The researchers found that neural data associated with attempted handwriting are particularly well-suited for typing tasks and classification. In fact, handwriting could be classified quite well even with simpler, linear algorithms, suggesting that the neural data themselves played a large part in the success of the authors' approach.

By simulating how the classification algorithm performed when tested with different types of neural activity, Willett *et al.* made a key insight — neural activity during handwriting has more temporal variability between

characters than does neural activity when users attempt to draw straight lines, and this variability actually makes classification easier. This knowledge should inform future BCIs. Perhaps counter-intuitively, it might be advantageous to decode complex behaviours rather than simple ones, particularly for classification tasks.



### Brain implants that let you speak your mind

Willett and co-workers' study begins to deliver on the promise of BCI technologies. iBCIs will need to provide tremendous performance and usability benefits to justify the expense and risks associated with implanting electrodes into the brain. Importantly, typing speed is not the only factor that will determine whether the technology is adopted — the longevity and robustness of the approach also require analysis. The authors present promising evidence that their algorithms will perform well with limited training data, but further research will probably be required to enable the device to maintain performance over its lifetime as neural activity patterns change. It will also be crucial to conduct studies to test whether the approach can be generalized for other users, and for settings outside the laboratory.

Another question is how the approach will scale and translate to other languages. Willett and colleagues' simulations highlight that several characters of the Latin alphabet are written similarly (r, v and u, for instance), and so are harder to classify than are others. One of us (P.R.)

speaks Tamil, which has 247, often very closely related, characters, and so might be much harder to classify. And the question of translation is particularly pertinent for languages that are not yet well represented in machine-learning predictive-language models.

Although much work remains to be done, Willett and co-workers' study is a milestone that broadens the horizon of iBCI applications. Because it uses machine-learning methods that are rapidly improving, plugging in the latest models offers a promising path for future improvements. The team is also making its data set publicly available, which will accelerate advances. The authors' approach has brought neural interfaces that allow rapid communication much closer to a practical reality.

Nature **593**, 197–198 (2021)

doi: <https://doi.org/10.1038/d41586-021-00776-8>

## References

1. 1.

Willett, F. R., Avansino, D. T., Hochberg, L. R., Henderson, J. M. & Shenoy, K. V. *Nature* **593**, 249–254 (2021).

2. 2.

Mott, M. E., Williams, S., Wobbrock, J. O. & Morris, M. R. in *Proc. 2017 CHI Conf. Human Factors in Computing Systems* 2558–2570 (ACM, 2017).

3. 3.

Hochberg, L. R. *et al.* *Nature* **442**, 164–171 (2006).

4. 4.

Hochberg, L. R. *et al.* *Nature* **485**, 372–375 (2012).

5. 5.

Collinger, J. L. *et al. Lancet* **381**, 557–564 (2013).

6. 6.

Pandarinath, C. *et al. eLife* **6**, e18554 (2017).

7. 7.

Ajiboye, A. B. *et al. Lancet* **389**, 1821–1830 (2017).

8. 8.

Rezeika, A. *et al. Brain Sci.* **8**, 57 (2018).

9. 9.

Sussillo, D., Stavisky, S. D., Kao, J. C., Ryu, S. I. & Shenoy, K. V. *Nature Commun.* **7**, 13749 (2016).

## Jobs from Nature Careers

- - - [All jobs](#)
    - - [Postdoctoral Research Fellow in Urban Climate Action](#)  
  
[The University of British Columbia \(UBC\)](#)  
[Vancouver, Canada](#)  
[JOB POST](#)
  - [Postdoctoral Fellow in Supercapacitor Technology](#)

The University of British Columbia (UBC)

Kelowna, Canada

JOB POST

- **Postdoctoral Researchers x 2 – Advancement of audit procedure for domestic and non-domestic energy compliance tools, SFI MaREI Centre, NUI Galway (NUIG-RES-095-21)**

National University of Ireland Galway (NUI Galway).

Galway, Ireland

JOB POST

- **Semantic Web Developer**

European Molecular Biology Laboratory (EMBL).

Hinxton, Cambridge, United Kingdom

JOB POST

---

This article was downloaded by **calibre** from <https://www.nature.com/articles/d41586-021-00776-8>

## NEWS AND VIEWS

12 May 2021

# Cloud droplets aid the production of formic acid in the atmosphere

Known sources of formic acid could not explain the observed atmospheric concentrations of this compound. The discovery of a previously unknown pathway that generates formic acid in the atmosphere resolves this discrepancy.

- [Joost de Gouw](#) <sup>0</sup> &
- [Delphine Farmer](#) <sup>1</sup>

### 1. [Joost de Gouw](#)

1. Joost de Gouw is at the Cooperative Institute for Research in Environmental Sciences and in the Department of Chemistry, University of Colorado, Boulder, Colorado 80309, USA.

[View author publications](#)

You can also search for this author in [PubMed](#) [Google Scholar](#)

### 2. Delphine Farmer

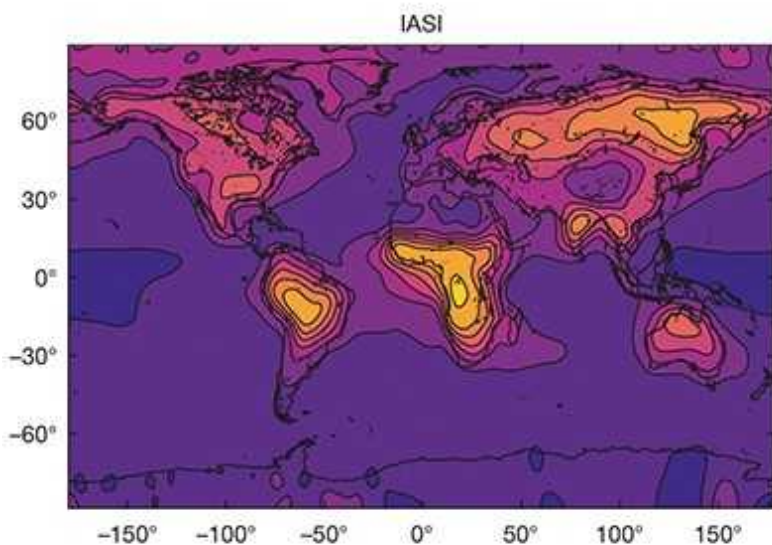
1. Delphine Farmer is in the Department of Chemistry, Colorado State University, Fort Collins, Colorado 80523, USA.

[View author publications](#)

You can also search for this author in [PubMed](#) [Google Scholar](#)

Formic acid is one of the simplest and most abundant organic molecules in Earth's atmosphere, but its sources have been poorly understood for many

years. Laboratory and field studies<sup>1–3</sup> have shown that most formic acid is not emitted directly from sources, but is produced by chemical reactions in the atmosphere. However, the chemistry responsible has been a mystery. [Writing in Nature](#), Franco *et al.*<sup>4</sup> report that formic acid could be formed by a mechanism that starts with formaldehyde reacting with water in cloud droplets.



[Read the paper: Ubiquitous atmospheric production of organic acids mediated by cloud droplets](#)

The word ‘formic’ derives from *formica*, the Latin word for ant, and the compound is indeed released from ant hills<sup>5</sup>. Other, and larger, emission sources include vegetation, biomass burning<sup>6</sup> and fossil-fuel combustion<sup>7</sup>. However, the combined emissions from known sources are too small to explain the concentrations of formic acid in the atmosphere, and several studies have concluded that formation in the atmosphere is a much bigger contributor (see ref. 1, for example).

Levels of formic acid can be measured by mass spectrometry and optical spectroscopy, and from satellite instruments, so there is excellent information about the distribution of this compound in the atmosphere. Observations have shown that atmospheric concentrations of formic acid increase rapidly in urban<sup>8</sup> and forest<sup>9</sup> air during the day. However,

researchers have been unable to identify the chemical reactions responsible for this increase. Detailed studies that considered all of the possible known chemical pathways could explain only a fraction of formic acid produced, both in polluted and remote regions<sup>3,9</sup>, and so the search for alternative chemical pathways has continued<sup>10</sup>.

Formic acid constitutes a substantial fraction of the organic carbon in the atmosphere<sup>11</sup>. Organic compounds in the gas phase have a key role in atmospheric oxidation reactions. They therefore influence the lifetime of greenhouse gases and the formation of ozone and aerosols — microscopic particles suspended in the air — in the troposphere, the lowest approximately 10 kilometres of the atmosphere. Organic compounds in the aerosol phase are air pollutants and have a cooling effect on climate. The simple fact that formic acid formation is so poorly understood calls into question our understanding of atmospheric organic carbon as a whole. Formic acid also contributes to acidity in the atmosphere and to the deposition of acids in ecosystems, particularly in remote regions.

Franco *et al.* now show that hydrolysis of formaldehyde in cloud droplets can lead to the formation of formic acid (Fig. 1). Inside cloud droplets, formaldehyde ( $\text{HCHO}$ ) converts to its hydrated form, methanediol ( $\text{HOCH}_2\text{OH}$ ). The authors demonstrate that methanediol can outgas from the cloud droplets and react with hydroxyl radicals ( $\text{OH}^\bullet$ ) in the atmosphere to form formic acid ( $\text{HCOOH}$ ) in the gas phase.

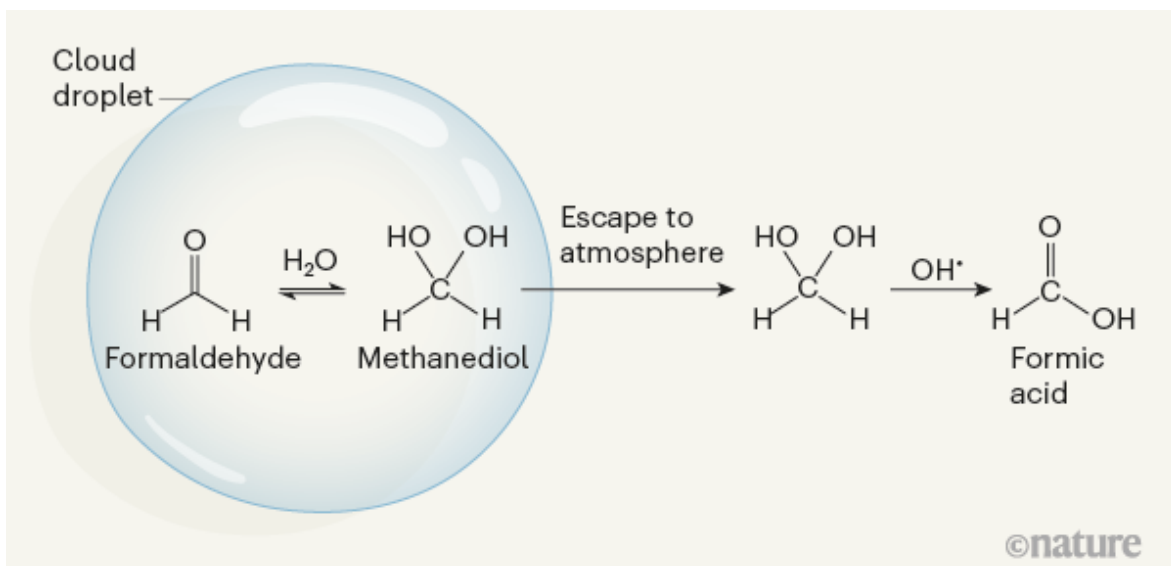


**Figure 1 | A pathway for the formation of formic acid.** Franco *et al.*<sup>4</sup> report evidence of a previously unknown mechanism for the production of atmospheric formic acid. The authors propose that formaldehyde reacts with water in cloud droplets to form methanediol. This compound escapes to the atmosphere, where it reacts with oxidants such as hydroxyl radicals ( $\text{OH}^\bullet$ ) to form formic acid. The mechanism potentially explains why atmospheric levels of formic acid are higher than would be expected on the basis of previously known sources.

Why did it take so long to uncover this pathway? It had previously been assumed that two other processes short-circuit this chemistry: dehydration of methanediol, which re-forms formaldehyde; and rapid oxidation of methanediol inside cloud droplets. Simply put, methanediol was thought to be so short-lived that it never leaves the cloud droplet. However, by carefully considering the timescale for dehydration, and combining this analysis with results from experiments in an atmospheric-simulation chamber, Franco and colleagues show that methanediol can volatilize into the gas phase from cloud droplets and then oxidize to formic acid.

Franco *et al.* go on to incorporate methanediol oxidation into a global climate–chemistry model (a computational climate model that incorporates atmospheric-chemistry pathways) and evaluate the predicted levels of formic acid by comparing them with measurements obtained from a space-based instrument. The authors adopted an innovative approach to do this in more detail than was previously possible: they identified columns of formic acid in the atmosphere by analysing satellite data using a computer algorithm known as an artificial neural network. Such approaches are increasingly being used to quantify, at relatively low computational cost, atmospheric chemical species that have weak spectroscopic signatures. Crucially, the authors show that levels of atmospheric formic acid simulated by models that include methanediol oxidation agree with observations much more closely than with levels predicted by models that do not include this chemistry.



### Ozone mystery laid to rest

Methanediol oxidation potentially explains some of the previously reported field observations. Formaldehyde is predominantly formed by photochemistry (light-induced reactions in the atmosphere), and a key precursor of formaldehyde on a global scale is isoprene — a compound emitted by trees and shrubs. Methanediol oxidation involves formaldehyde, and so it makes sense that concentrations of formic acid over forested regions are large. Moreover, formaldehyde formation in air is enhanced when atmospheric levels of the pollutant nitrogen oxide are high<sup>12</sup>. This could explain why formic acid formation is observed in urban air at nitrogen oxide concentrations that would prohibit formation of this acid by other gas-phase reactions (such as reactions between alkene compounds and ozone<sup>13</sup>).

Nevertheless, many questions remain. Formic acid can form in cloud-free atmospheres<sup>8</sup> and in the canopies of forests<sup>14</sup>. Could methanediol oxidation occur not only in cloud droplets, but also in aqueous aerosol particles or on wet surfaces? And are atmospheric concentrations of methanediol as high as the levels implied by Franco and colleagues' study? This will need to be evaluated by measurements.

Several other organic acids behave similarly to formic acid in the atmosphere<sup>8</sup>. Could their formation be explained by analogous pathways involving other aldehydes? The devil is in the detail — the rates of the

various processes involved will determine whether these putative pathways contribute much to the atmospheric levels of other acids. And what are the sinks of formic acid? Franco and colleagues suggest that formic acid is removed from the atmosphere by scavenging (absorption by precipitation and cloud droplets) and photochemical reactions more quickly than was reported in previous studies, which implies that formic acid sinks should be further investigated. The authors' findings will motivate many follow-up studies, both in the laboratory and in the field, and methanediol oxidation adds to the array of pathways that atmospheric chemists can use to explain observations of formic acid.

Nature **593**, 198–199 (2021)

doi: <https://doi.org/10.1038/d41586-021-01206-5>

## References

1. 1.

Paulot, F. *et al.* *Atmos. Chem. Phys.* **11**, 1989–2013 (2011).

2. 2.

Yuan, B. *et al.* *Atmos. Chem. Phys.* **15**, 1975–1993 (2015).

3. 3.

Millet, D. B. *et al.* *Atmos. Chem. Phys.* **15**, 6283–6304 (2015).

4. 4.

Franco, B. *et al.* *Nature* **593**, 233–237 (2021).

5. 5.

Graedel, T. E. & Eisner, T. *Tellus B* **40B**, 335–339 (1988).

6. 6.

Akagi, S. K. *et al.* *Atmos. Chem. Phys.* **11**, 4039–4072 (2011).

7. 7.

Crisp, T. A. *et al.* *Atmos. Environ.* **98**, 426–433 (2014).

8. 8.

Veres, P. R. *et al.* *Geophys. Res. Lett.* **38**, L17807 (2011).

9. 9.

Link, M. F., Nguyen, T. B., Bates, K., Müller, J.-F. & Farmer, D. K. *ACS Earth Space Chem.* **4**, 730–740 (2020).

10. 10.

Shaw, M. F. *et al.* *Nature Commun.* **9**, 2584 (2018).

11. 11.

Heald, C. L. *et al.* *Atmos. Chem. Phys.* **8**, 2007–2025 (2008).

12. 12.

Wolfe, G. M. *et al.* *Atmos. Chem. Phys.* **16**, 2597–2610 (2016).

13. 13.

Jenkin, M. E., Saunders, S. M. & Pilling, M. J. *Atmos. Environ.* **31**, 81–104 (1997).

14. 14.

Fulgham, S. R. *et al.* *Geophys. Res. Lett.* **47**, e2020GL088745 (2020).

## **Jobs from Nature Careers**

•

- - [All jobs](#)
- - **[Postdoctoral Research Fellow in Urban Climate Action](#)**  
[The University of British Columbia \(UBC\)](#)  
[Vancouver, Canada](#)  
[JOB POST](#)
  - **[Postdoctoral Fellow in Supercapacitor Technology](#)**  
[The University of British Columbia \(UBC\)](#)  
[Kelowna, Canada](#)  
[JOB POST](#)
  - **[Postdoctoral Researchers x 2 – Advancement of audit procedure for domestic and non-domestic energy compliance tools, SFI MaREI Centre, NUI Galway \(NUIG-RES-095-21\)](#)**  
[National University of Ireland Galway \(NUI Galway\)](#)  
[Galway, Ireland](#)  
[JOB POST](#)
  - **[Semantic Web Developer](#)**  
[European Molecular Biology Laboratory \(EMBL\)](#)  
[Hinxton, Cambridge, United Kingdom](#)

## JOB POST

---

This article was downloaded by **calibre** from <https://www.nature.com/articles/d41586-021-01206-5>

| [Section menu](#) | [Main menu](#) |

## NEWS AND VIEWS

30 April 2021

# A continuous model of early mammalian development

Characterization of the early developmental process called gastrulation has mostly been limited to snapshots at different time points. A model of mouse gastrulation now maps the transitions between cell types continuously in time.

- [Chengxiang Qiu](#)<sup>0</sup> &
- [Jay Shendure](#)<sup>1</sup>

1. Chengxiang Qiu

1. Chengxiang Qiu is in the Department of Genome Sciences, University of Washington, Seattle, Washington 98195, USA.

[View author publications](#)

You can also search for this author in [PubMed](#) [Google Scholar](#)

2. [Jay Shendure](#)

1. Jay Shendure is in the Department of Genome Sciences, University of Washington, Seattle, Washington 98195, USA, and at the Brotman Baty Institute for Precision Medicine, the Allen Discovery Center for Cell Lineage Tracing, and the Howard Hughes Medical Institute, Seattle.

[View author publications](#)

You can also search for this author in [PubMed](#) [Google Scholar](#)

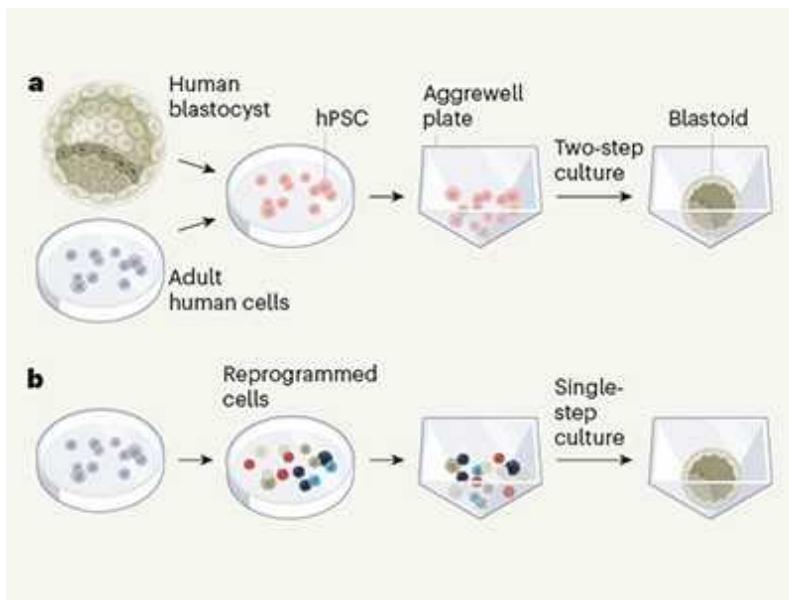
During embryonic development, new cell types emerge with stunning speed and robustness. The process of gastrulation — in which a single layer of cells gives rise to multiple ‘germ layers’ — is fundamental to the early development of most animals. Although studied for more than 150 years, many aspects of gastrulation remain elusive, not least a comprehensive understanding of the molecular factors governing the specification of the many cell lineages that emerge from this process. [Writing in Cell](#), Mittnenzweig *et al.*<sup>1</sup> densely sample gene expression in gastrulating mouse embryos over a 36-hour window and construct a continuous model of cell-lineage specification.

If we think of cells during gastrulation as characters in a silent film (and, indeed, there are beautiful films of gastrulation<sup>2</sup>), how can we understand the internal monologues and ever-changing motivations of the personas on the screen? Only in the past five years or so, with the emergence of technologies that characterize the molecular profiles of individual cells, have we been in a position to fully monitor cells’ ‘inner lives’ throughout gastrulation, as cell lineages develop. One such technology is single-cell RNA sequencing (scRNA-seq), which profiles the messenger RNA contents of individual cells.

Several key questions remain that could be addressed through single-cell techniques. For example, what is the precise timing of cell-type specifications in the developing embryo? Can we find a model that accurately describes these specifications? What are the principal molecular factors involved? And which of these factors ‘drive’ cell-type specifications, and which ‘respond’ to them?

In most animals, including mammals, three germ layers result from gastrulation: the ectoderm, the mesoderm and the endoderm. In the mouse, the pre-eminent model system for mammalian development, gastrulation begins about 6.5 days after fertilization (that is, embryonic day 6.5, or E6.5). Although we and others have performed scRNA-seq across early mouse development at what might seem like reasonable temporal resolution (for example, sampling every 6 hours from E6.5 to E8.5<sup>3</sup>, or every 24 hours from E9.5 to E13.5<sup>4</sup>), the pace of change during mouse development is so fast that

this might be woefully inadequate. In our film analogy, this would be akin to watching a film but with only a handful of scenes narrated.



### First complete model of the human embryo

In this context, Mittnenzweig *et al.* set out to generate a continuous representation of cell-state dynamics during mouse gastrulation<sup>1</sup>. They applied scRNA-seq to 153 mouse embryos from E6.5 to E8.1, altogether profiling gene expression in about 33,000 individual cells. Because the accuracy of estimating embryo age on the basis of morphological landmarks is limited, the embryos' ages were instead inferred from the molecular data, resulting in each embryo being assigned to one of 13 time points.

To increase the temporal resolution of their representation of development beyond a series of snapshots, Mittnenzweig *et al.* posited that cells within any given embryo are, to some extent at least, at different stages of developmental maturity relative to one another. The authors grouped cells according to their molecular similarity into 461 subsets termed 'metacells', each consisting of cells that were very similar, but that, notably, might have come from different embryos and/or from different time points. The authors then applied an algorithm to estimate the fraction of cells from each metacell at time  $t$  that 'flow' to other metacells at time  $t + 1$ . Crucially, the inferred flows between these metacells are continuous with respect to time, despite the temporally discrete nature of the embryos from which they were derived.

With this continuous model of mouse gastrulation in hand (Fig. 1), Mittnenzweig and colleagues are able to investigate several interesting questions. First, how and when do new cell types emerge during gastrulation, and what are the associated changes in the patterns of gene expression? For example, their model not only predicts that primitive erythroid cells (which give rise to early red blood cells) originate from a region called the primitive streak, but also constrains the timing of that contribution to before E6.7, and places in order the successive waves of expression of different transcription factors associated with this lineage.

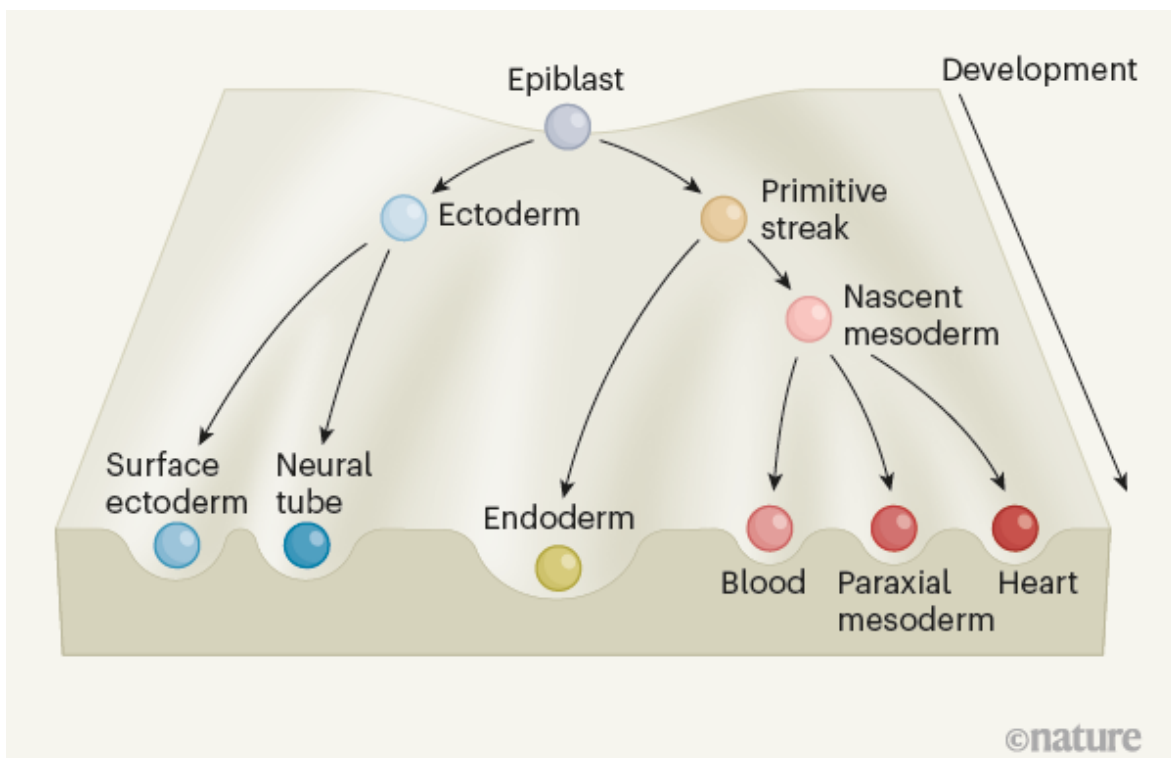
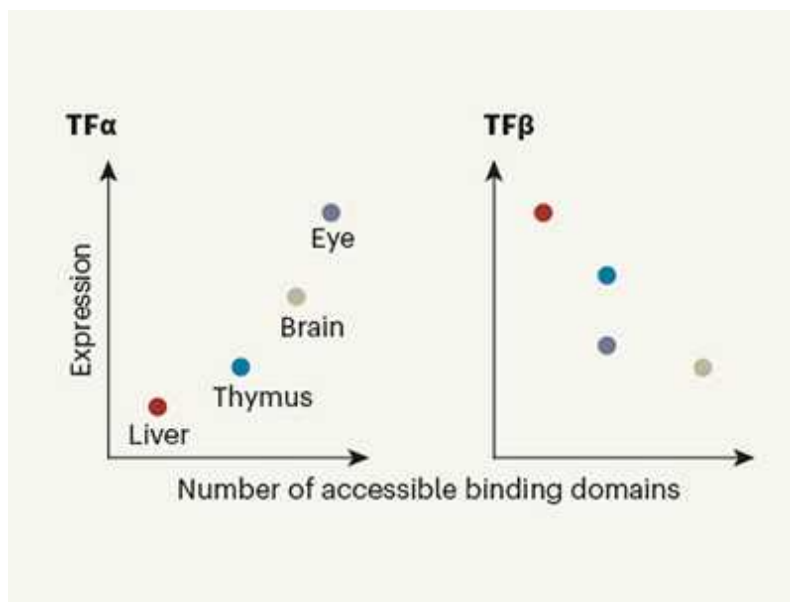


**Figure 1 | A continuous-flow model of mouse gastrulation.** Mittnenzweig *et al.*<sup>1</sup> profiled the RNA contents of cells from mouse embryos during gastrulation, a process during which a single cell layer called the epiblast transforms into three layers: ectoderm, endoderm and mesoderm. In doing so, the authors generated a model of gastrulation that is continuous over time, showing the transitions between different cell types; a simplified version is shown here. Shallower, basin-like regions are intended to depict gradual, continuous transitions, whereas deeper, canyon-like regions depict more-definitive separations. Both bifurcations and multifurcations of cell lineages are observed.

Second, what are the characteristics of *in vivo* cell-type specification? Do new cell types emerge through a series of rapidly made ‘decisions’ between two different cell fates, resulting in the sharp, branch-like bifurcations that often appear in textbook flow charts of cell development, or are more-complex patterns observed, such as multifurcations and continuous transitions? Mitnenzweig *et al.* suggest the answer to be ‘all of the above’.

For example, the developmental trajectory of cells in the primitive streak bifurcates sharply, such that these cells become either mesodermal or endodermal cells (Fig. 1). By contrast, the differentiation of cells in the nascent mesoderm is inferred to be gradual and continuous, and with more than two destinations. The model also enables the inference of flows that change with time; for instance, before E7.1, epiblast cells overwhelmingly transition to acquiring primitive-streak fates, but shortly after that point, they mostly transition to acquiring ectodermal fates.



### A molecular handbook for human development

Finally, what are the molecular factors that underlie differentiation, and do individual factors act alone or in combination? The authors claim that, with the exception of some lineages (notably, the node, cardiomyocyte and haemato-endothelial lineages), the landscape of gastrulation is predominantly characterized by a dependence on overlapping combinations of factors, as well as on a gradual unfolding of commitment. For example,

although cells of the nascent mesoderm progress into a spectrum of fates, these fates are not sharply separated from one another, and there is no clear delineation between the sets of transcription factors that seem to specify each fate. The authors propose that, rather than a series of specific factors governing a stepwise, hierarchical progression of specification, combinations of molecular factors regulate diverse mesodermal fates in a ‘fuzzy’ and almost probabilistic manner. To highlight the delicacy of this program, the authors carried out experiments in which inferred key regulators were genetically disrupted, which led to delayed differentiation of affected lineages.

Of course, all models have limitations, and this model has its own. First, its resolution is limited by the underlying data, although simply processing more embryos would address this. Second, its metacells and flows are inferred solely from the similarity of the transcriptional profiles of the cells, and so there is a risk of missing or misinterpreting certain bona fide relationships<sup>5</sup>. Particularly rapid changes in the nematode worm *Caenorhabditis elegans*, for instance, elude efforts to reconstruct lineages in ‘pseudotime’ — that is, ordering cells by their developmental stage rather than their age in real time<sup>6</sup>. Third, the model ignores cells’ spatial coordinates within embryos as well as their actual lineage relationships, two crucial aspects of development that are increasingly amenable to measuring and recording, respectively<sup>7,8</sup>.

Notwithstanding these limitations, the model of mouse gastrulation developed by Mittenzweig *et al.* is impressive, and shows how continuous maps of complex differentiation landscapes might be recovered despite discrete sampling. Together with other work published in the past few years<sup>3,6,9</sup>, it represents a substantial step forward on the path to a complete understanding of cells’ inner lives during this most important of times in an animal’s life<sup>10</sup>.

Nature **593**, 200-201 (2021)

doi: <https://doi.org/10.1038/d41586-021-01153-1>

## References

1. 1.

Mitnnenzweig, M. *et al.* *Cell* <https://doi.org/10.1016/j.cell.2021.04.004> (2021).

2. 2.

McDole, K. M. *et al.* *Cell* **175**, 859–876 (2018).

3. 3.

Pijuan-Sala, B. *et al.* *Nature* **566**, 490–495 (2019).

4. 4.

Cao, J. *et al.* *Nature* **566**, 496–502 (2019).

5. 5.

Wagner, D. E. & Klein, A. M. *Nature Rev. Genet.* **21**, 410–427 (2020).

6. 6.

Packer, J. S. *et al.* *Science* **365**, eaax1971 (2019).

7. 7.

McKenna, A. *et al.* *Science* **353**, aaf7907 (2016).

8. 8.

Lohhoff, T. *et al.* Preprint at bioRxiv  
<https://doi.org/10.1101/2020.11.20.391896> (2020).

9. 9.

Argelaguet, R. *et al.* *Nature* **576**, 487–491 (2019).

10. 10.

Vicente, C. *Development* **142**, 2547–2548 (2015).

## Jobs from Nature Careers

- - - [All jobs](#)
    - 
    - [Postdoctoral Research Fellow in Urban Climate Action](#)  
[The University of British Columbia \(UBC\)](#)  
[Vancouver, Canada](#)  
[JOB POST](#)
    - [Postdoctoral Fellow in Supercapacitor Technology](#)  
[The University of British Columbia \(UBC\)](#)  
[Kelowna, Canada](#)  
[JOB POST](#)
    - [Postdoctoral Researchers x 2 – Advancement of audit procedure for domestic and non-domestic energy compliance tools, SFI MaREI Centre, NUI Galway \(NUIG-RES-095-21\)](#)  
[National University of Ireland Galway \(NUI Galway\)](#)  
[Galway, Ireland](#)  
[JOB POST](#)

▪ **Semantic Web Developer**

European Molecular Biology Laboratory (EMBL)

Hinxton, Cambridge, United Kingdom

**JOB POST**

---

This article was downloaded by **calibre** from <https://www.nature.com/articles/d41586-021-01153-1>

| [Section menu](#) | [Main menu](#) |

## NEWS AND VIEWS

19 April 2021

# A molecular connection hints at how a genetic risk factor drives Crohn's disease

Mutations of the *NOD2* gene are risk factors for Crohn's disease. Many aspects of how they contribute to the condition are unknown. The discovery of cell populations that are involved suggests new therapeutic options.

- [Scott Plevy](#) 0

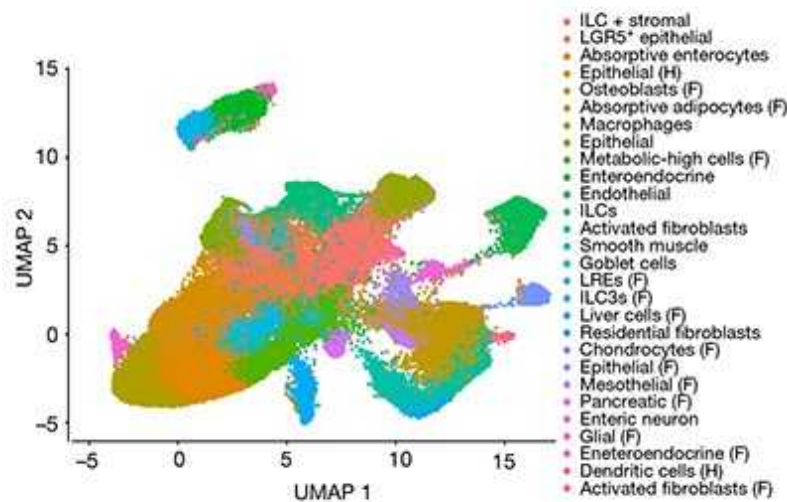
1. [Scott Plevy](#)

1. Scott Plevy is at Senda Biosciences, Cambridge, Massachusetts 02140, USA.

[View author publications](#)

You can also search for this author in [PubMed](#) [Google Scholar](#)

Crohn's disease, a chronic inflammatory bowel disease, affects many people. For example, more than 0.3% of the populations of Canada and Germany have the condition, and its incidence is increasing worldwide<sup>1</sup>. Better therapies are needed, but progress in treating Crohn's disease has been hampered by the lack of understanding of how it arises. [Writing in Nature](#), Nayar *et al.*<sup>2</sup> shed light on a long-standing mystery about one risk factor for Crohn's disease, and their findings have important clinical implications.



## [Read the paper: A myeloid–stromal niche and gp130 rescue in NOD2-driven Crohn’s disease](#)

Crohn's disease can affect any part of the gut. Most commonly, it affects the ileum region, causing inflammation that frequently results in fibrosis (the deposition of fibrous connective tissue as an injury response). This leads to the narrowing (or stricture) of the lumen of the ileum, which often requires surgical intervention<sup>3</sup>. Crohn's disease provides a useful model of illnesses that are mediated by genes and environmental interactions. In this case, genetic susceptibility underpins the disease-causing inflammatory responses to gut microorganisms.

Genetic variations, called polymorphisms, of the *NOD2* gene are the strongest genetic risk association for Crohn's disease; approximately 20% of all such risk of developing the disease is related to three single nucleotide polymorphisms of this gene<sup>4</sup>. Furthermore, *NOD2* mutations are strong predictive factors for the development of ileum strictures and for the need for surgery in Crohn's disease, which is a widely validated association between the genetic underpinnings of this condition and manifestations of the disease<sup>3</sup>.

However, connecting the *NOD2* gene to disease susceptibility presented a paradox. *NOD2* is an intracellular receptor (Fig. 1) that recognizes the molecule muramyl dipeptide (MDP) — a ubiquitous component of bacterial

cell walls. Before *NOD2* was described as a risk gene for Crohn's disease, *NOD2* function was best understood in immune cells that aid the innate branch of immune defences. *NOD2* activation in these cells leads to the expression of inflammatory molecules called cytokines, and an abnormally intense inflammatory response can mediate intestinal damage in Crohn's disease<sup>5,6</sup>. One might therefore have expected that *NOD2* mutations known as loss-of-function mutations, which do not generate a fully functional version of the encoded protein, would protect against Crohn's disease. Yet such loss-of-function mutations of *NOD2* were identified as risk factors for the disease. Subsequent research therefore pivoted to focus on a different aspect of *NOD2* biology in the intestine, investigating how functional *NOD2* maintains homeostasis in the intestine, where the body's largest biomass of immunologically active cells is constantly exposed to MDP from gut microbes, and how *NOD2* mutations perturb this balance and lead to disease<sup>5</sup>.

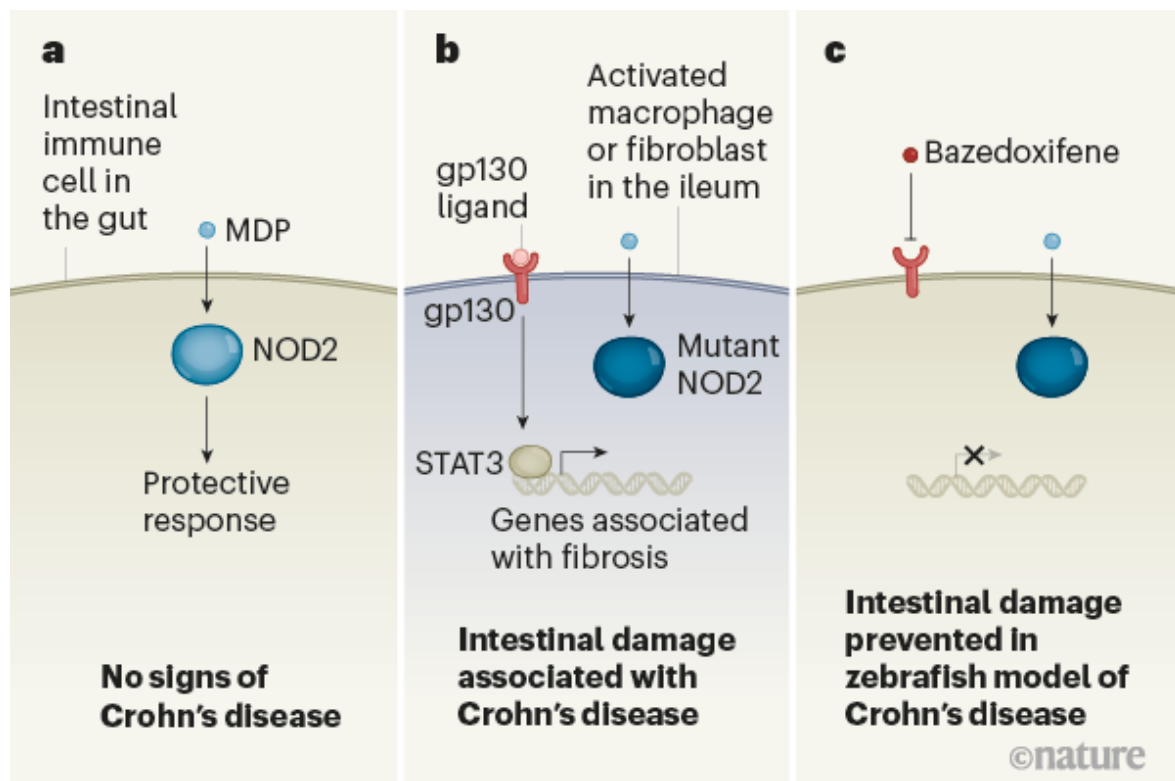


**Figure 1 | Molecular underpinnings of an inflammatory bowel disease.** The causes of Crohn's disease are not fully understood. **a**, *NOD2* is an intracellular protein that can recognize the bacterial molecule muramyl dipeptide (MDP), which is commonly found in the gut. This is part of a

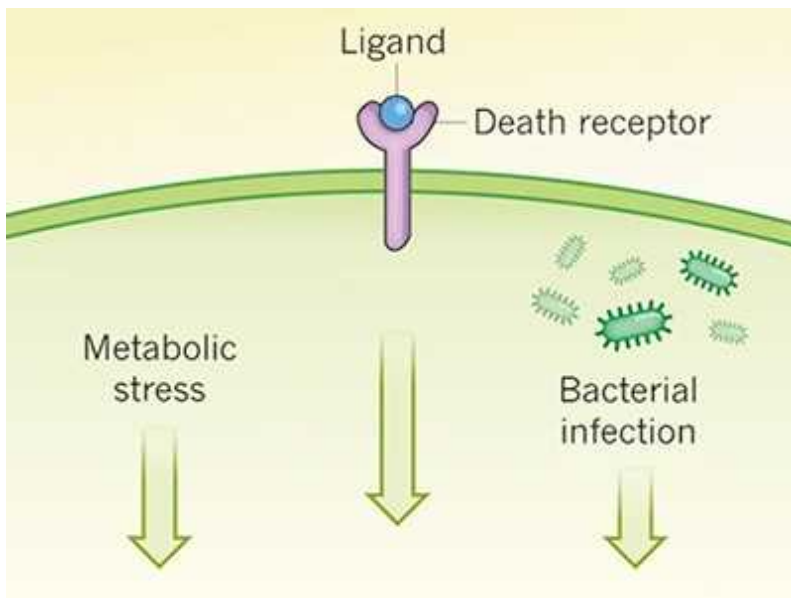
normal protective response by immune cells to maintain gut homeostasis. **b**, Mutations that generate a non-functional version of NOD2 are a risk factor for Crohn's disease<sup>4</sup>. Studying zebrafish and clinical samples, Nayar *et al.*<sup>2</sup> reveal details of processes underlying the disease that are associated with mutant NOD2. The authors identify populations of activated immune cells called macrophages and fibroblasts as being responsible for fibrosis, a tissue abnormality in the ileum region of the bowel that occurs in Crohn's disease. Ligand binding to the gp130 receptor of these immune cells triggers a gene-expression pathway mediated by the STAT3 transcription factor. **c**, The authors report that a gp130 inhibitor molecule called bazedoxifene prevented gene expression that leads to damage in a zebrafish model of Crohn's disease.

The role of *NOD2* mutations in the emergence of fibrosis of the ileum was unknown before the present study. The authors sought to understand what drives inflammation and fibrosis in Crohn's disease, and linked these biological insights to *NOD2* through research using human cells, human intestinal tissue and a zebrafish model.

First, the authors used single-cell sequencing of RNA from the inflamed tissue of ileum samples removed during surgery from people with Crohn's disease. These cells revealed a gene-expression signature associated with activated macrophage and fibroblast cells. The authors also identified a key cell type that expresses markers of both myeloid and fibroblast cellular lineages. These discoveries suggest that a population of inflammatory macrophages in the ileum differentiates to become activated fibroblasts during the course of disease.

Strikingly, the authors demonstrate the evolutionary conservation of these cellular populations in an experimental model of intestinal inflammation — zebrafish treated with the molecule dextran sodium sulfate (DSS). This molecule has long been used to induce intestinal damage and inflammation in a standard rodent model. The *in vivo* modelling of human inflammatory bowel diseases has been dominated by mouse models. However, as Nayar and colleagues demonstrate, zebrafish offer a useful alternative for relatively high-throughput investigations and rapid assessment of correlations with human disease. Indeed, zebrafish and mammalian intestines have a similar form (morphology). Moreover, like humans, zebrafish have innate and

adaptive branches of their immune-defence responses, and intestinal inflammation of zebrafish is also dependent on the community of gut microorganisms<sup>7</sup>. Gene-editing tools, such as CRISPR, aid the rapid modification of genes of interest in zebrafish.



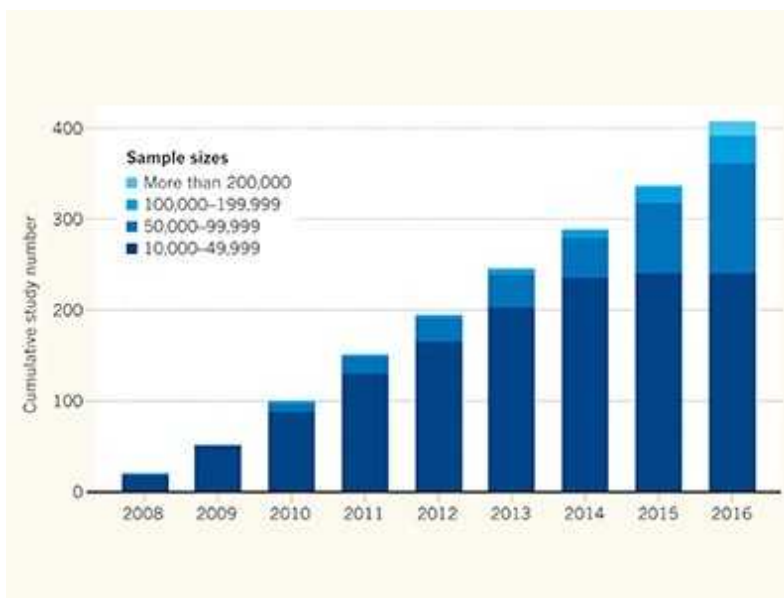
### Stressful genetics in Crohn's disease

The authors studied intestinal inflammation in zebrafish engineered to have *nod2* deficiency. These fish, treated with DSS, had increased numbers of leukocyte immune cells in their intestines, a hallmark of inflammation, compared with zebrafish with normal *nod2*. But the zebrafish model is relevant only if a human correlation can be established. Accordingly, using data from children newly diagnosed with Crohn's disease, the authors show that an increase in the number of copies of a *NOD2* mutation (associated with the risk of Crohn's disease) indeed correlated with an activated macrophage and fibroblast gene-expression signature in ileum tissue.

To understand *NOD2* function in human cells that can differentiate *in vitro*, the authors used peripheral blood monocytes from healthy volunteers, and determined whether the cells had one, two or no copies of *NOD2* mutations linked to susceptibility to Crohn's disease. The cells were then differentiated *in vitro* with and without MDP. The authors observed a higher number of activated fibroblasts for cells with two copies of *NOD2* mutations compared with cells with wild-type *NOD2*. Furthermore, an increase in the number of

*NOD2* mutations was associated with a corresponding enrichment in the number of fibroblasts with a gene-expression signature characteristic of activated cells. Interestingly, zebrafish with *nod2* deficiencies, which were given MDP, had a gene-expression signature characteristic of activated fibroblasts that persisted even during recovery from injury mediated by DSS, compared with zebrafish that have wild-type *nod2*. These data suggest that *nod2* deficits inhibit efficient recovery (resolution) from fibrosis and inflammation.

To further elucidate the molecular basis of the fibrosis-linked gene-expression signature associated with *NOD2* risk mutations, the authors searched for upstream transcriptional regulators of this pathway. They identified the gene encoding STAT3 as being markedly upregulated in activated fibroblasts and macrophages. STAT3 is a transcriptional regulator of key components of inflammatory and fibrotic responses in inflammatory bowel diseases, and acts through the cytokine receptor gp130. Analyses of clinical data revealed upregulated expression of gp130-regulated genes encoding the proteins IL-6, oncostatin M and IL-11 in people with Crohn's disease who did not respond to therapy targeting the tumour-necrosis factor (TNF) protein (anti-TNF antibodies are a common treatment for Crohn's disease). The discovery supports a role for gp130 signalling in this group of therapy-resistant individuals.



## A decade of shared genomic associations

The authors hypothesized that gp130 blockade might lessen the abnormalities that occur with *NOD2* mutation. They tested this idea by using bazedoxifene, a gp130 inhibitor, on MDP-treated human cells with *NOD2* mutations. Bazedoxifene indeed lessened the fibrotic-associated gene-expression signature and reversed the cellular shape changes that are characteristic of activated fibroblasts. This drug also reduced the intestinal damage found in *nod2* mutant zebrafish treated with DSS.

Starting with the clinical characteristics of fibrosis in Crohn's disease, this work describes a molecular pathway linked to *NOD2* mutations associated with the disease, and concludes with a potential therapeutic insight to address the pressing clinical problems of fibrosis and anti-TNF drug resistance. By underpinning the genetics and the clinical outcomes to this cellular and molecular pathway, the study provides a road map to understanding present and future therapeutic approaches.

Many interesting avenues of investigation remain. *NOD2* is the only described recognition pathway for MDP, yet this paper demonstrates MDP-induced cellular and molecular changes in the absence of *nod2* in zebrafish. This implies that there are MDP signalling pathways that have not yet been described. Bazedoxifene was initially characterized as a selective inhibitor of the oestrogen receptor<sup>8</sup>, raising the concern that the drug might have adverse effects on other signalling pathways if used as a therapeutic for Crohn's disease. The gp130 receptor has multiple ligand binding partners that influence a broad range of immune responses. Hence, understanding the specific gp130 ligands that orchestrate *NOD2*-mediated molecular events could lead to more selective, effective and safer therapeutic interventions than would globally inhibiting gp130 signalling, or targeting other clinically relevant signalling pathways, such as the Janus kinase enzymes (inhibitors for which are in late-stage clinical development for Crohn's disease).

Not everyone with Crohn's disease has *NOD2* mutations associated with disease risk. Indeed, in individuals of certain ethnic groups, such as people of Chinese, Malay or Indian heritage, disease of the ileum is a prominent clinical feature of Crohn's disease, yet *NOD2* is not associated with disease risk in this population<sup>5,9</sup>. Perhaps the molecular signature of activated macrophages and fibroblasts is the relevant unifying signature for individuals with Crohn's disease of the ileum. It is probable that different

genetic landscapes might result in the same clinical and molecular outcomes. Hence, Nayar and colleagues' results move the field a step closer to a molecular classification of Crohn's disease that might clarify a complex condition that has approximately 200 genetic regions associated with disease risk<sup>10</sup>, and diverse clinical manifestations.

Nature **593**, 201-203 (2021)

doi: <https://doi.org/10.1038/d41586-021-00979-z>

## References

1. 1.

Ng, S. C. *et al.* *Lancet* **390**, 2769–2778 (2017).

2. 2.

Nayar, S. *et al.* *Nature* **593**, 275–281 (2021).

3. 3.

Rieder, F., Zimmermann, E. M., Remzi, F. H. & Sandborn, W. J. *Gut* **62**, 1072–1084 (2013).

4. 4.

Cuthbert, A. P. *et al.* *Gastroenterology* **122**, 867–874 (2002).

5. 5.

Sidiq, T., Yoshihama, S., Downs, I. & Kobayashi, K. S. *Front. Immunol.* **7**, 367 (2016).

6. 6.

Franchi, L., Warner, N., Viani, K. & Nuñez, G. *Immunol. Rev.* **227**, 106–128 (2009).

7. 7.

Brugman, S. *Dev. Comp. Immunol.* **64**, 82–92 (2016).

8. 8.

Duggan, S. T. & McKeage, K. *Drugs* **71**, 2193–2212 (2011).

9. 9.

Hilmi, I., Tan, Y. M. & Goh, K. L. *World J. Gastroenterol.* **12**, 1435–1438 (2006).

10. 10.

Mondal, K. & Kugathasan, S. *Nature Rev. Gastroenterol. Hepatol.* **14**, 266–268 (2017).

## Jobs from Nature Careers

- - - [All jobs](#)
    - - [Postdoctoral Research Fellow in Urban Climate Action](#)  
  
[The University of British Columbia \(UBC\)](#)  
  
[Vancouver, Canada](#)  
  
[JOB POST](#)
      - [Postdoctoral Fellow in Supercapacitor Technology](#)  
  
[The University of British Columbia \(UBC\)](#)

Kelowna, Canada

JOB POST

- **Postdoctoral Researchers x 2 – Advancement of audit procedure for domestic and non-domestic energy compliance tools, SFI MaREI Centre, NUI Galway (NUIG-RES-095-21)**

National University of Ireland Galway (NUI Galway).

Galway, Ireland

JOB POST

- **Semantic Web Developer**

European Molecular Biology Laboratory (EMBL)

Hinxton, Cambridge, United Kingdom

JOB POST

---

This article was downloaded by **calibre** from <https://www.nature.com/articles/d41586-021-00979-z>

## NEWS AND VIEWS

12 May 2021

# Nitrogen deletion offers fresh strategy for organic synthesis

Many scientific fields and industries rely on the synthesis of small organic molecules. A chemical reagent has been developed that allows such molecules to be made by ‘deleting’ nitrogen atoms from readily accessible precursors.

- [William P. Unsworth](#) <sup>0</sup> &
- [Alyssa-Jennifer Avestro](#) <sup>1</sup>

### 1. [William P. Unsworth](#)

1. William P. Unsworth is in the Department of Chemistry,  
University of York, York YO10 5DD, UK.

[View author publications](#)

You can also search for this author in [PubMed](#) [Google Scholar](#)

### 2. [Alyssa-Jennifer Avestro](#)

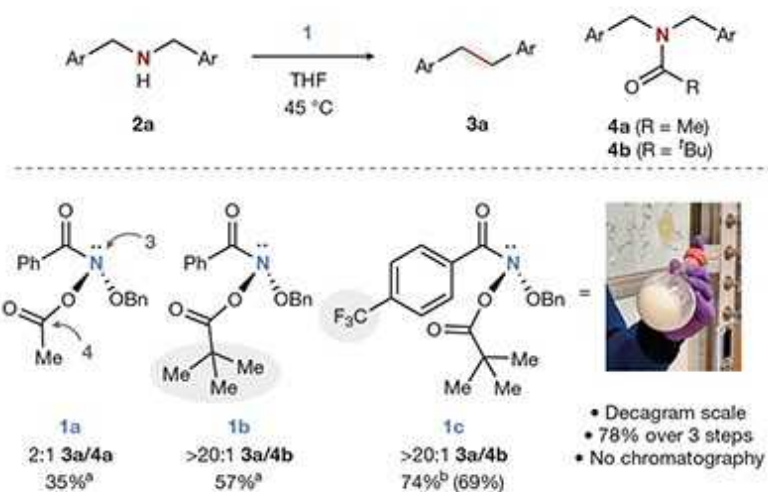
1. Alyssa-Jennifer Avestro is in the Department of Chemistry,  
University of York, York YO10 5DD, UK.

[View author publications](#)

You can also search for this author in [PubMed](#) [Google Scholar](#)

In [a paper in \*Nature\*](#), Kennedy *et al.*<sup>1</sup> report a strategy for molecular editing in which nitrogen atoms are ‘deleted’ from organic molecules. The idea of deleting, rather than adding, atoms to molecules runs counter to the way

chemists usually think about making organic molecules (with a few notable exceptions; see ref. 2, for example). But the authors' reactions could dramatically change the way in which such synthesis is planned.

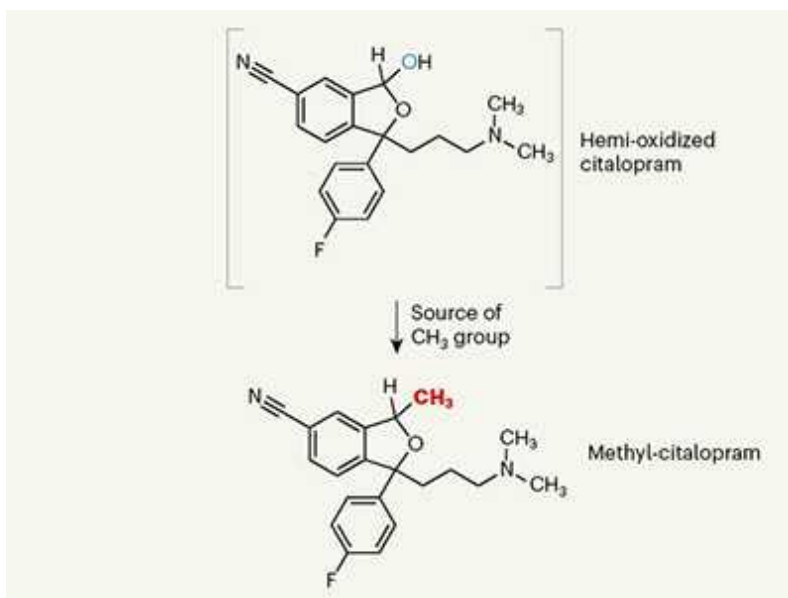


### [Read the paper: Skeletal editing through direct nitrogen deletion of secondary amines](#)

Chemists attach great pride to the idea that, given sufficient time and resources, they can synthesize almost any small organic molecule. Such efforts are the basis of many technologies that have enormous societal value, such as medicines, polymers and agrochemicals. To make the range of molecules that is needed for these applications, chemists are armed with an array of methods that promote specific chemical changes, often with exquisite selectivity.

Moreover, countless chemical-synthesis methods are discovered and published daily. Most involve relatively small, practical changes to existing methods, or modest advances in the scope of known reaction types. These advances are important — incremental improvements are crucial to scientific progress. Nonetheless, methods occasionally emerge that have more far-reaching implications. Kennedy and colleagues' chemistry is one such example. To explain why, let's consider the way in which chemical syntheses are usually conceived, using a process known as retrosynthetic analysis<sup>3,4</sup>.

In retrosynthetic analysis, the chemist starts by considering the chemical structure of the target molecule, and then works backwards by mentally ‘disconnecting’ individual bonds in the target molecule — the idea being to break it down into smaller and simpler chemical fragments. A synthetic route is then devised by working out a series of reactions that leads from the fragments back to the target, in the reverse sequence. Typically, there are multiple possible ways to disconnect any given target molecule, but a key consideration is that each step in the forward chemical synthesis must be a known type of chemistry, or a reaction that can be developed. Chemists therefore typically rely on tried-and-tested disconnections for common molecular motifs, because this usually ensures that the forward synthesis is productive.



### Manganese catalyst enables exploration of the magic methyl effect

Knowledge of which bonds can (or cannot) be disconnected using established chemistry, and the ability to apply this knowledge systematically, is crucial. But there is also a large creative aspect to synthesis; indeed, many of the best syntheses are said to be on the borderline between science and art<sup>5</sup>. Proposing a disconnection for which no synthetic methods exist for the equivalent forward reaction requires inspiration and creativity, and subsequent development of the requisite methods is hard. But chemists will always be drawn to such challenges<sup>6–9</sup>, because they open up strategies for synthesis that would previously have been considered impossible.

This is precisely what Kennedy *et al.* have achieved. They report a reaction that enables challenging molecular targets to be made by excising single nitrogen atoms from easily accessible starting materials (Fig. 1). The authors developed a new, easily prepared chemical reagent to promote the reaction, the mechanism of which involves an unprecedented molecular rearrangement: a molecule of nitrogen is lost from a reaction intermediate, producing two highly reactive free radicals that combine to form a new carbon–carbon (C–C) bond (see Fig. 1b of the paper<sup>1</sup>).

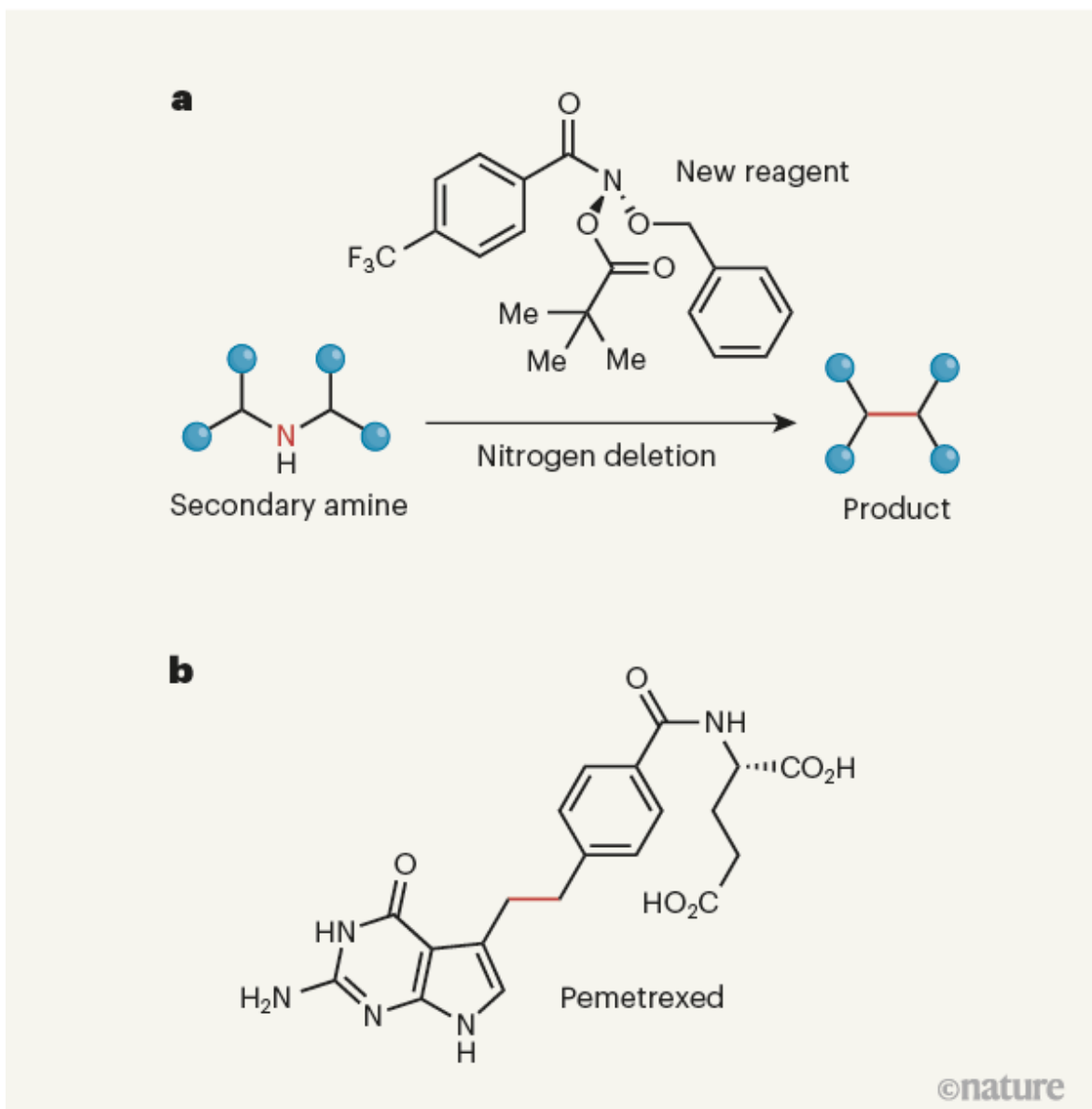
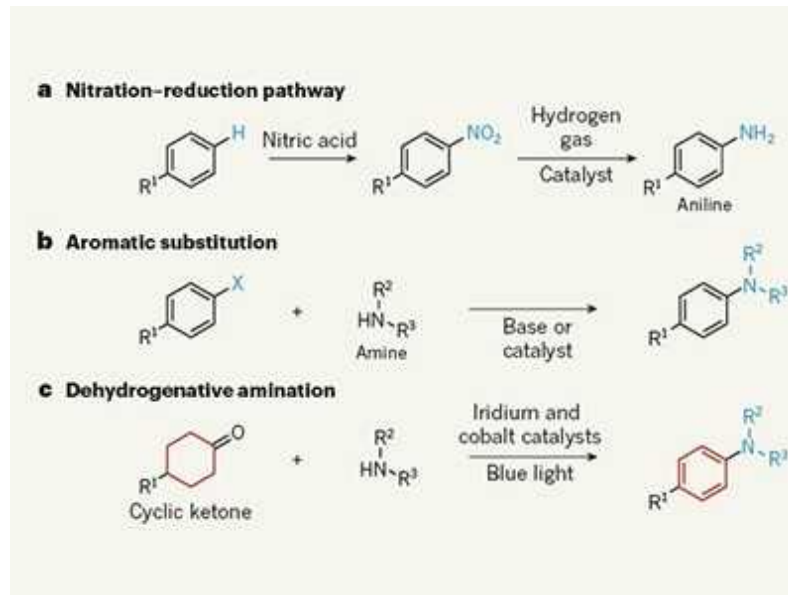


**Figure 1 | Nitrogen-deletion reactions.** **a**, Kennedy *et al.*<sup>1</sup> report an easily prepared reagent that removes nitrogen atoms from compounds known as

secondary amines, thus providing a new way to synthesize organic molecules. The reaction produces the carbon–carbon bond shown in red in the product. Blue circles represent a variety of chemical groups. **b**, The authors demonstrate that the reactions can be used to make a range of compounds, including pemetrexed, an anticancer drug.

The Oxford English Dictionary defines ‘synthesis’ as the “combination of components or elements to form a connected whole” — so isn’t deleting atoms, rather than adding them, counterproductive to this goal? The value of Kennedy and colleagues’ strategy lies in the fact that the nitrogen-containing starting materials are typically much easier to make, or to source commercially, than are the analogous molecules that don’t contain nitrogen. Chemists can therefore simplify their syntheses by making intermediates that contain a nitrogen atom, and then removing it later. This is similar to the way in which scaffolding aids in the construction of a skyscraper, but is removed once the main structure has been built. Notably, the removal of nitrogen fundamentally alters the molecular skeleton of the molecule, because an internal atom is lost<sup>10–13</sup>; this contrasts with most other molecular-editing strategies, which focus on making less drastic changes on the molecule’s periphery.



Reactions for making widely used aniline compounds break the norms of synthesis

A practical advantage to Kennedy and colleagues' synthetic strategy is that it mitigates the costs and safety problems associated with many established C–C bond-forming methods, which usually require expensive or toxic metal reagents. The authors also demonstrate that their chemistry can delete nitrogen from commercially available drugs and natural products, and could therefore be used to generate new biologically active compounds.

As would be expected, the reactions do not work equally well in every instance studied: the authors acknowledge that reaction yields are typically higher when the starting molecule has features that stabilize the reactive species formed when nitrogen is extruded. Nonetheless, the present scope of the reaction is easily sufficient to suggest that it will be widely adopted. Improvements that address its present limitations are likely to emerge.

Molecules made using Kennedy and colleagues' chemistry could help to stimulate advances and technologies in applied fields, beyond drug discovery, that rely heavily on the availability of efficient methods for chemical synthesis. The nitrogen-deletion strategy could also enable a long-standing dream to be fulfilled: the development of truly ‘traceless’ reactions, in which no evidence of the molecular features that assisted the synthesis remain in the products. Nitrogen deletion might be especially helpful for the traceless synthesis of advanced materials in which the presence of nitrogen atoms can be detrimental to function — such as molecular machines, or elastic or self-healable polymers for heat-resilient electronic devices. Although the part played by the deleted nitrogen atoms would not always be apparent in the molecules ultimately used in these applications, the atoms' impact in enabling the synthesis of the materials could be transformative.

Nature **593**, 203-204 (2021)

doi: <https://doi.org/10.1038/d41586-021-01205-6>

## References

1. 1.

Kennedy, S. H., Dherange, B. D., Berger, K. J. & Levin, M. D. *Nature* **593**, 223–227 (2021).

2. 2.

Ramberg, L. & Bäcklund, B. *Arkiv Kemi Mineral. Geol.* **13A**, 50 (1940).

3. 3.

Corey, E. J. & Cheng, X.-M. *The Logic of Chemical Synthesis* (Wiley, 1995).

4. 4.

McCowan, S. V., Doering, N. A. & Sarpong, R. *Chem. Sci.* **11**, 7538–7552 (2020).

5. 5.

Nicolaou, K. C. *Chem* **1**, 331–334 (2016).

6. 6.

Szpileman, A. M. & Carreira, E. M. *Angew. Chem. Int. Edn* **49**, 9592–9628 (2010).

7. 7.

Cernak, T., Dykstra, K. D., Tyagarajan, S., Vachal, P. & Krska, S. W. *Chem. Soc. Rev.* **45**, 546–576 (2016).

8. 8.

Hu, Y., Stumpfe, D. & Bajorath, J. *J. Med. Chem.* **60**, 1238–1246 (2017).

9. 9.

Mahjour, B., Shen, Y., Liu, W. & Cernak, T. *Nature* **580**, 71–75 (2020).

10. 10.

Cao, Z.-C. & Shi, Z.-J. *J. Am. Chem. Soc.* **139**, 6546–6549 (2017).

11. 11.

Roque, J. B., Kuroda, Y., Göttemann, L. T. & Sarpong, R. *Nature* **564**, 244–248 (2018).

12. 12.

Smaligo, A. J. *et al. Science* **364**, 681–685 (2019).

13. 13.

Fier, P. S., Kim, S. & Maloney, K. M. *J. Am. Chem. Soc.* **141**, 18416–18420 (2019).

## **Jobs from Nature Careers**

- - - [All jobs](#)
    - - [Postdoctoral Research Fellow in Urban Climate Action](#)  
[The University of British Columbia \(UBC\)](#)  
[Vancouver, Canada](#)  
[JOB POST](#)
      - [Postdoctoral Fellow in Supercapacitor Technology](#)  
[The University of British Columbia \(UBC\)](#)  
[Kelowna, Canada](#)

JOB POST

- **Postdoctoral Researchers x 2 – Advancement of audit procedure for domestic and non-domestic energy compliance tools, SFI MaREI Centre, NUI Galway (NUIG-RES-095-21)**

National University of Ireland Galway (NUI Galway),  
Galway, Ireland

JOB POST

- **Semantic Web Developer**

European Molecular Biology Laboratory (EMBL),  
Hinxton, Cambridge, United Kingdom

JOB POST

---

This article was downloaded by **calibre** from <https://www.nature.com/articles/d41586-021-01205-6>

- Article
- [Published: 12 May 2021](#)

# CMOS-based cryogenic control of silicon quantum circuits

- [Xiao Xue](#)<sup>1,2 na1</sup>,
- [Bishnu Patra](#) [ORCID: orcid.org/0000-0003-1913-1337](#)<sup>1,2,3 na1</sup>,
- [Jeroen P. G. van Dijk](#) [ORCID: orcid.org/0000-0002-2751-316X](#)<sup>1,2,3 na1</sup>,
- [Nodar Samkharadze](#)<sup>1,4</sup>,
- [Sushil Subramanian](#) [ORCID: orcid.org/0000-0002-4733-1398](#)<sup>5</sup>,
- [Andrea Corna](#) [ORCID: orcid.org/0000-0003-2028-3995](#)<sup>1,2</sup>,
- [Brian Paquelet Wuetz](#) [ORCID: orcid.org/0000-0003-2139-1306](#)<sup>1,2</sup>,
- [Charles Jeon](#) [ORCID: orcid.org/0000-0001-8753-5080](#)<sup>5</sup>,
- [Farhana Sheikh](#) [ORCID: orcid.org/0000-0001-5078-0816](#)<sup>5</sup>,
- [Esdras Juarez-Hernandez](#)<sup>6</sup>,
- [Brando Perez Esparza](#)<sup>6</sup>,
- [Huzaifa Rampurawala](#)<sup>5</sup>,
- [Brent Carlton](#) [ORCID: orcid.org/0000-0003-4542-4715](#)<sup>5</sup>,
- [Surej Ravikumar](#)<sup>5</sup>,
- [Carlos Nieva](#) [ORCID: orcid.org/0000-0002-9471-5386](#)<sup>5</sup>,
- [Sungwon Kim](#) [ORCID: orcid.org/0000-0002-3475-1713](#)<sup>5</sup>,
- [Hyung-Jin Lee](#)<sup>5</sup>,
- [Amir Sammak](#) [ORCID: orcid.org/0000-0002-9776-9099](#)<sup>1,4</sup>,
- [Giordano Scappucci](#) [ORCID: orcid.org/0000-0003-2512-0079](#)<sup>1,2</sup>,
- [Menno Veldhorst](#) [ORCID: orcid.org/0000-0001-9730-3523](#)<sup>1,2</sup>,
- [Fabio Sebastiano](#) [ORCID: orcid.org/0000-0002-8489-9409](#)<sup>1,3 na2</sup>,
- [Masoud Babaie](#) [ORCID: orcid.org/0000-0001-7635-5324](#)<sup>1,3 na2</sup>,
- [Stefano Pellerano](#)<sup>5 na2</sup>,

- [Edoardo Charbon](#) ORCID: [orcid.org/0000-0002-0620-3365<sup>1,2,5,7 na2</sup>](https://orcid.org/0000-0002-0620-3365)  
&
- [Lieven M. K. Vandersypen](#) ORCID: [orcid.org/0000-0003-4346-7877<sup>1,2,5 na2</sup>](https://orcid.org/0000-0003-4346-7877)

[Nature](#) volume 593, pages 205–210 (2021) [Cite this article](#)

- 1643 Accesses
- 12 Altmetric
- [Metrics details](#)

## Subjects

- [Electrical and electronic engineering](#)
- [Qubits](#)

## Abstract

The most promising quantum algorithms require quantum processors that host millions of quantum bits when targeting practical applications<sup>1</sup>. A key challenge towards large-scale quantum computation is the interconnect complexity. In current solid-state qubit implementations, an important interconnect bottleneck appears between the quantum chip in a dilution refrigerator and the room-temperature electronics. Advanced lithography supports the fabrication of both control electronics and qubits in silicon using technology compatible with complementary metal oxide semiconductors (CMOS)<sup>2</sup>. When the electronics are designed to operate at cryogenic temperatures, they can ultimately be integrated with the qubits on the same die or package, overcoming the ‘wiring bottleneck’<sup>3,4,5,6</sup>. Here we report a cryogenic CMOS control chip operating at 3 kelvin, which outputs tailored microwave bursts to drive silicon quantum bits cooled to 20 millikelvin. We first benchmark the control chip and find an electrical performance consistent with qubit operations of 99.99 per cent fidelity, assuming ideal qubits. Next, we use it to coherently control actual qubits

encoded in the spin of single electrons confined in silicon quantum dots<sup>7,8,9</sup> and find that the cryogenic control chip achieves the same fidelity as commercial instruments at room temperature. Furthermore, we demonstrate the capabilities of the control chip by programming a number of benchmarking protocols, as well as the Deutsch–Josza algorithm<sup>10</sup>, on a two-qubit quantum processor. These results open up the way towards a fully integrated, scalable silicon-based quantum computer.

[Access through your institution](#)

[Change institution](#)

[Buy or subscribe](#)

## Access options

Subscribe to Journal

Get full journal access for 1 year

\$199.00

only \$3.90 per issue

[Subscribe](#)

All prices are NET prices.

VAT will be added later in the checkout.

Tax calculation will be finalised during checkout.

Rent or Buy article

Get time limited or full article access on ReadCube.

from \$8.99

[Rent or Buy](#)

All prices are NET prices.

## **Additional access options:**

- [Log in](#)
- [Access through your institution](#)
- [Learn about institutional subscriptions](#)

**Fig. 1: The cryogenic quantum control system.**



**Fig. 2: The Horse Ridge cryogenic controller characterized at 3 K.**



**Fig. 3: Frequency-multiplexed qubit control and fidelity benchmarks with the cryo-controller.**



**Fig. 4: Programming a quantum processor with the cryo-controller.**



## Data availability

Data supporting this work are available at  
<https://doi.org/10.5281/zenodo.4061970>.

## Code availability

The codes used for data acquisition and processing are from the open-source Python packages QCoDeS (available at <https://github.com/QCoDeS/Qcodes>), QTT (available at <https://github.com/QuTech-Delft/qtt>) and PycQED (available at [https://github.com/DiCarloLab-Delft/PycQED\\_py3](https://github.com/DiCarloLab-Delft/PycQED_py3)).

## References

1. 1.

Van Meter, R. & Horsman, C. A blueprint for building a quantum computer. *Commun. ACM* **56**, 84–93 (2013).

[Article](#) [Google Scholar](#)

2. 2.

Pillarisetty, R. et al. Qubit device integration using advanced semiconductor manufacturing process technology. In *2018 IEEE International Electron Devices Meeting* 6.3.1–6.3.4 (IEEE, 2018).

3. 3.

Vandersypen, L. M. K. et al. Interfacing spin qubits in quantum dots and donors—hot, dense, and coherent. *npj Quantum Inf.* **3**, 34 (2017).

[ADS](#) [Article](#) [Google Scholar](#)

4. 4.

Patra, B. et al. Cryo-CMOS circuits and systems for quantum computing applications. *IEEE J. Solid-State Circuits* **53**, 309–321 (2018).

[ADS](#) [Article](#) [Google Scholar](#)

5. 5.

Pauka, S. J. et al. A cryogenic CMOS chip for generating control signals for multiple qubits. *Nat. Electronics* **4**, 64–70 (2021).

[CAS](#) [Article](#) [Google Scholar](#)

6. 6.

Geck, L., Kruth, A., Bluhm, H., van Waasen, S. & Heinen, S. Control electronics for semiconductor spin qubits. *Quantum Sci. Technol.* **5**, 015004 (2019).

[ADS](#) [Article](#) [Google Scholar](#)

7. 7.

Watson, T. F. et al. A programmable two-qubit quantum processor in silicon. *Nature* **555**, 633–637 (2018).

[ADS](#) [CAS](#) [Article](#) [Google Scholar](#)

8. 8.

Zajac, D. M. et al. Resonantly driven CNOT gate for electron spins. *Science* **359**, 439–442 (2018).

[ADS](#) [MathSciNet](#) [CAS](#) [Article](#) [Google Scholar](#)

9. 9.

Huang, W. et al. Fidelity benchmarks for two-qubit gates in silicon. *Nature* **569**, 532–536 (2019).

[ADS](#) [CAS](#) [Article](#) [Google Scholar](#)

10. 10.

Deutsch, D. & Jozsa, R. Rapid solution of problems by quantum computation. *Proc. R. Soc. Lond. A* **439**, 553–558 (1992).

[ADS](#) [MathSciNet](#) [Article](#) [Google Scholar](#)

11. 11.

Arute, F. et al. Quantum supremacy using a programmable superconducting processor. *Nature* **574**, 505–510 (2019).

[ADS](#) [CAS](#) [Article](#) [Google Scholar](#)

12. 12.

Bardin, J. C. et al. Design and characterization of a 28-nm bulk-CMOS cryogenic quantum controller dissipating less than 2 mW at 3 K. *IEEE J. Solid-State Circuits* **54**, 3043–3060 (2019).

[ADS](#) [Article](#) [Google Scholar](#)

13. 13.

Patra, B. et al. A scalable cryo-CMOS 2-to-20GHz digitally intensive controller for  $4 \times 32$  frequency multiplexed spin qubits/transmons in 22nm FinFET technology for quantum computers. In *2020 IEEE International Solid-State Circuits Conference* 304–306 (IEEE, 2020).

14. 14.

Le Guevel, L. et al. A 110mK 295 $\mu$ W 28nm FDSOI CMOS quantum integrated circuit with a 2.8 GHz excitation and nA current sensing of an on-chip double quantum dot. In *2020 IEEE International Solid-State Circuits Conference* 306–308 (IEEE, 2020).

15. 15.

Bonen, S. et al. Cryogenic characterization of 22-nm FDSOI CMOS technology for quantum computing ICs. *IEEE Electron. Device Lett.* **40**, 127–130 (2018).

[Google Scholar](#)

16. 16.

Esmailiyan, A. et al. A fully integrated DAC for CMOS position-based charge qubits with single-electron detector loopback testing. *IEEE Solid-State Circuits Lett.* **3**, 354–357 (2020).

[Article](#) [Google Scholar](#)

17. 17.

Ekanayake, S. R. et al. Characterization of SOS-CMOS FETs at low temperatures for the design of integrated circuits for quantum bit control and readout. *IEEE Trans. Electron Dev.* **57**, 539–547 (2010).

[ADS](#) [CAS](#) [Article](#) [Google Scholar](#)

18. 18.

Mukhanov, O. et al. Scalable quantum computing infrastructure based on superconducting electronics. In *2019 IEEE International Electron Devices Meeting* 31.2.1–31.2.4 (IEEE, 2019).

19. 19.

Xu, Y. et al. On-chip integration of Si/SiGe-based quantum dots and switched-capacitor circuits. *Appl. Phys. Lett.* **117**, 144002 (2020).

[ADS](#) [CAS](#) [Article](#) [Google Scholar](#)

20. 20.

Batey, G., Matthews, A. J. & Patton, M. A new ultralow- temperature cryogen-free experimental platform. *J. Phys. Conf. Ser.* **568**, 032014

(2014).

[Article](#) [Google Scholar](#)

21. 21.

Green, M. A. The cost of coolers for cooling superconducting devices at temperatures at 4.2 K, 20 K, 40 K and 77 K. In *IOP Conference Series: Materials Science and Engineering* Vol. 101, 012001 (IOP, 2015).

22. 22.

Petit, L. et al. Universal quantum logic in hot silicon qubits. *Nature* **580**, 355–359 (2020).

[ADS](#) [CAS](#) [Article](#) [Google Scholar](#)

23. 23.

Yang, C. H. et al. Operation of a silicon quantum processor unit cell above one kelvin. *Nature* **580**, 350–354 (2020).

[ADS](#) [CAS](#) [Article](#) [Google Scholar](#)

24. 24.

Urdampilleta, M. et al. Gate-based high fidelity spin readout in a CMOS device. *Nat. Nanotechnol.* **14**, 737–741 (2019).

[CAS](#) [Article](#) [Google Scholar](#)

25. 25.

van Dijk, J. P. G. et al. Designing a DDS-based SoC for high-fidelity multi-qubit control. *IEEE Trans. Circuits Syst. I* **67**, 5380–5393 (2020).

[Article](#) [Google Scholar](#)

26. 26.

Beckers, A., Jazaeri, F. & Enz, C. Characterization and modeling of 28-nm bulk CMOS technology down to 4.2 K. *IEEE J. Electr. Dev. Soc.* **6**, 1007–1018 (2018).

[CAS](#) [Article](#) [Google Scholar](#)

27. 27.

Hart, P. A. T., Babaie, M., Charbon, E., Vladimirescu, A. & Sebastiano, F. Subthreshold mismatch in nanometer CMOS at cryogenic temperatures. *IEEE J. Electr. Dev. Soc.* **8**, 797–806 (2020).

[CAS](#) [Article](#) [Google Scholar](#)

28. 28.

Patra, B. et al. Characterization and analysis of on-chip microwave passive components at cryogenic temperatures. *IEEE J. Electr. Dev. Soc.* **8**, 448–456 (2020).

[CAS](#) [Article](#) [Google Scholar](#)

29. 29.

Pioro-Ladrière, M. et al. Electrically driven single-electron spin resonance in a slanting Zeeman field. *Nat. Phys.* **4**, 776–779 (2008).

[Article](#) [Google Scholar](#)

30. 30.

Vandersypen, L. M. K. & Chuang, I. L. NMR techniques for quantum control and computation. *Rev. Mod. Phys.* **76**, 1037–1069 (2005).

[ADS](#) [Article](#) [Google Scholar](#)

31. 31.

Petta, J. R. et al. Coherent manipulation of coupled electron spins in semiconductor quantum dots. *Science* **309**, 2180–2184 (2005).

[ADS](#) [CAS](#) [Article](#) [Google Scholar](#)

32. 32.

Meunier, T., Calado, V. E. & Vandersypen, L. M. K. Efficient controlled-phase gate for single-spin qubits in quantum dots. *Phys. Rev. B* **83**, 121403 (2011).

[ADS](#) [Article](#) [Google Scholar](#)

33. 33.

Xue, X. et al. Repetitive quantum nondemolition measurement and soft decoding of a silicon spin qubit. *Phys. Rev. X* **10**, 021006 (2020).

[CAS](#) [Google Scholar](#)

34. 34.

Saul, P. H. & Mudd, M. S. J. A direct digital synthesizer with 100-MHz output capability. *IEEE J. Solid-State Circuits* **23**, 819–821 (1988).

[ADS](#) [Article](#) [Google Scholar](#)

35. 35.

Reed, M. Entanglement and Quantum Error Correction with Superconducting Qubits. PhD Thesis, Yale Univ. (2013).

36. 36.

Altepeter, J. B., Jeffrey, E. R. & Kwiat, P. G. Photonic state tomography. *Adv. At. Mol. Opt. Phys.* **52**, 105–159 (2005).

[ADS](#) [CAS](#) [Article](#) [Google Scholar](#)

37. 37.

Knill, E. et al. Randomized benchmarking of quantum gates. *Phys. Rev. A* **77**, 012307 (2008).

[ADS](#) [Article](#) [Google Scholar](#)

38. 38.

Magesan, E., Gambetta, J. M. & Emerson, J. Characterizing quantum gates via randomized benchmarking. *Phys. Rev. A* **85**, 042311 (2012).

[ADS](#) [Article](#) [Google Scholar](#)

39. 39.

Fowler, A. G., Mariantoni, M., Martinis, J. M. & Cleland, A. N. Surface codes: towards practical large-scale quantum computation. *Phys. Rev. A* **86**, 032324 (2012).

[ADS](#) [Article](#) [Google Scholar](#)

40. 40.

Svore, K. M., Aho, A. V., Cross, A. W., Chuang, I. & Markov, I. L. A layered software architecture for quantum computing design tools. *Computer* **39**, 74–83 (2006).

[Article](#) [Google Scholar](#)

41. 41.

Preskill, J. Quantum computing in the NISQ era and beyond. *Quantum* **2**, 79 (2018).

[Article](#) [Google Scholar](#)

42. 42.

Boter, J. M. et al. A sparse spin qubit array with integrated control electronics. In *2019 IEEE International Electron Devices Meeting* 31.4.1–31.4.4 (IEEE, 2019).

43. 43.

Sabbagh, D. et al. Quantum transport properties of industrial  $^{28}\text{Si}/^{28}\text{SiO}_2$ . *Phys. Rev. Appl.* **12**, 014013 (2019).

[ADS](#) [CAS](#) [Article](#) [Google Scholar](#)

44. 44.

Lawrie, W. I. L. et al. Quantum dot arrays in silicon and germanium. *Appl. Phys. Lett.* **116**, 080501 (2020).

[ADS](#) [CAS](#) [Article](#) [Google Scholar](#)

45. 45.

Zinner, E. Depth profiling by secondary ion mass spectrometry. *Scanning* **3**, 57–78 (1980).

[CAS](#) [Article](#) [Google Scholar](#)

46. 46.

Srinivasa, V. et al. Simultaneous spin-charge relaxation in double quantum dots. *Phys. Rev. Lett.* **110**, 196803 (2013).

[ADS](#) [CAS](#) [Article](#) [Google Scholar](#)

[Download references](#)

## Acknowledgements

This research was funded by Intel Corporation. We acknowledge discussions with the members in the Spin Qubit team, the Cryo-CMOS

team and Intel Corporation, and technical assistance by O. Benningshof, M. Sarsby, R. Schouten and R. Vermeulen.

## Author information

### Author notes

1. These authors contributed equally: Xiao Xue, Bishnu Patra, Jeroen P. G. van Dijk
2. These authors jointly supervised this work: Fabio Sebastian, Masoud Babaie, Stefano Pellerano, Edoardo Charbon, Lieven M. K. Vandersypen

## Affiliations

1. QuTech, Delft University of Technology, Delft, The Netherlands  
Xiao Xue, Bishnu Patra, Jeroen P. G. van Dijk, Nodar Samkharadze, Andrea Corna, Brian Paquelet Wuetz, Amir Sammak, Giordano Scappucci, Menno Veldhorst, Fabio Sebastian, Masoud Babaie, Edoardo Charbon & Lieven M. K. Vandersypen
2. Kavli Institute of Nanoscience, Delft University of Technology, Delft, The Netherlands  
Xiao Xue, Bishnu Patra, Jeroen P. G. van Dijk, Andrea Corna, Brian Paquelet Wuetz, Giordano Scappucci, Menno Veldhorst, Edoardo Charbon & Lieven M. K. Vandersypen
3. Department of Quantum and Computer Engineering, Delft University of Technology, Delft, The Netherlands  
Bishnu Patra, Jeroen P. G. van Dijk, Fabio Sebastian & Masoud Babaie

4. Netherlands Organization for Applied Scientific Research (TNO),  
Delft, The Netherlands

Nodar Samkharadze & Amir Sammak

5. Intel Corporation, Hillsboro, OR, USA

Sushil Subramanian, Charles Jeon, Farhana Sheikh, Huzaifa  
Rampurawala, Brent Carlton, Surej Ravikumar, Carlos  
Nieva, Sungwon Kim, Hyung-Jin Lee, Stefano Pellerano, Edoardo  
Charbon & Lieven M. K. Vandersypen

6. Intel Guadalajara, Zapopan, Mexico

Esdras Juarez-Hernandez & Brando Perez Esparza

7. École Polytechnique Fédérale de Lausanne (EPFL), Lausanne,  
Switzerland

Edoardo Charbon

## Authors

1. Xiao Xue

[View author publications](#)

You can also search for this author in [PubMed](#) [Google Scholar](#)

2. Bishnu Patra

[View author publications](#)

You can also search for this author in [PubMed](#) [Google Scholar](#)

3. Jeroen P. G. van Dijk

[View author publications](#)

You can also search for this author in [PubMed](#) [Google Scholar](#)

4. Nodar Samkharadze

[View author publications](#)

You can also search for this author in [PubMed](#) [Google Scholar](#)

5. Sushil Subramanian

[View author publications](#)

You can also search for this author in [PubMed](#) [Google Scholar](#)

6. Andrea Corna

[View author publications](#)

You can also search for this author in [PubMed](#) [Google Scholar](#)

7. Brian Paquelet Wuetz

[View author publications](#)

You can also search for this author in [PubMed](#) [Google Scholar](#)

8. Charles Jeon

[View author publications](#)

You can also search for this author in [PubMed](#) [Google Scholar](#)

9. Farhana Sheikh

[View author publications](#)

You can also search for this author in [PubMed](#) [Google Scholar](#)

10. Esdras Juarez-Hernandez

[View author publications](#)

You can also search for this author in [PubMed](#) [Google Scholar](#)

11. Brando Perez Esparza

[View author publications](#)

You can also search for this author in [PubMed](#) [Google Scholar](#)

12. Huzaifa Rampurawala

[View author publications](#)

You can also search for this author in [PubMed](#) [Google Scholar](#)

13. Brent Carlton

[View author publications](#)

You can also search for this author in [PubMed](#) [Google Scholar](#)

14. Surej Ravikumar

[View author publications](#)

You can also search for this author in [PubMed](#) [Google Scholar](#)

15. Carlos Nieva

[View author publications](#)

You can also search for this author in [PubMed](#) [Google Scholar](#)

16. Sungwon Kim

[View author publications](#)

You can also search for this author in [PubMed](#) [Google Scholar](#)

17. Hyung-Jin Lee

[View author publications](#)

You can also search for this author in [PubMed](#) [Google Scholar](#)

18. Amir Sammak

[View author publications](#)

You can also search for this author in [PubMed](#) [Google Scholar](#)

19. Giordano Scappucci

[View author publications](#)

You can also search for this author in [PubMed](#) [Google Scholar](#)

20. Menno Veldhorst

[View author publications](#)

You can also search for this author in [PubMed](#) [Google Scholar](#)

21. Fabio Sebastiano

[View author publications](#)

You can also search for this author in [PubMed](#) [Google Scholar](#)

22. Masoud Babaie

[View author publications](#)

You can also search for this author in [PubMed](#) [Google Scholar](#)

23. Stefano Pellerano

[View author publications](#)

You can also search for this author in [PubMed](#) [Google Scholar](#)

24. Edoardo Charbon

[View author publications](#)

You can also search for this author in [PubMed](#) [Google Scholar](#)

25. Lieven M. K. Vandersypen

[View author publications](#)

You can also search for this author in [PubMed](#) [Google Scholar](#)

## Contributions

X.X., B.P. and J.P.G.v.D. performed the experiment. N.S. fabricated the quantum device. A.S., B.P.W. and G.S. designed, grew and characterized the Si/SiGe heterostructure. A.C. contributed to the preparation of the experiment. X.X. and B.P. analysed the data presented in the main manuscript. F. Sebastiano, M.B., S.P., E.C. and L.M.K.V. conceived and

supervised the project. X.X., B.P. and L.M.K.V. wrote the manuscript with input from all authors.

## Corresponding authors

Correspondence to [Edoardo Charbon](#) or [Lieven M. K. Vandersypen](#).

## Ethics declarations

### Competing interests

The authors declare no competing interests.

## Additional information

**Peer review information** *Nature* thanks Fernando Gonzalez-Zalba, Stefan van Waasen and the other, anonymous, reviewer(s) for their contribution to the peer review of this work. Peer reviewer reports are available.

**Publisher's note** Springer Nature remains neutral with regard to jurisdictional claims in published maps and institutional affiliations.

## Extended data figures and tables

### [Extended Data Fig. 1 Experiment setup.](#)

The quantum dot device is wire-bonded onto a PCB placed on a cold finger attached to the mixing chamber plate ( $\sim 20$  mK) of a dilution refrigerator (Bluefors XLD). Voltage pulses onto gates RP and LP are generated by the AWG at RT, and go through a low-pass filter (Minicircuits) and attenuators before reaching the device. These pulses are used to control the electrochemical potentials of the quantum dots and load/unload electrons from/to the electron reservoir (see Extended Data Fig. 6). A programmable mechanical switch at 3 K is used to connect gate MW either to a vector signal generator (VSG) at RT or to the cryo-controller at 3 K (represented

as two boxes next to the switch) through a 12–14 GHz band-pass filter to filter out wide-band noise. The mechanical switch can also be configured to send the output signals from the cryo-controller to the oscilloscope and the spectrum analyser at RT for electrical characterization in the time and frequency domains. The cryo-controller is programmed via an FPGA to generate the microwave bursts using an external LO signal and a clock (CLK) signal from a microwave signal generator (MSG) at RT. The SET next to the quantum dots is voltage-biased, and the current signal ( $I_{\text{SET}}$ ) through it is converted to a voltage signal through a transimpedance amplifier and digitized by a digitizer card after an analogue low-pass filter employed to remove out-of-band ( $>10$  kHz) noise.  $I_{\text{SET}}$  is sensitive to the charge occupation of the quantum dots, allowing binary single-shot readout of the qubit states via spin-to-charge conversion (Extended Data Fig. 6).

### **Extended Data Fig. 2 Dilution refrigerator setup.**

**a**, Location of the cryo-controller and the quantum device inside the dilution refrigerator (left). Top and bottom views of the 3-K plate, showing the mounted chip enclosure and the fixed holder for the enclosure, respectively (right). **b**, Top view of the gold-plated annealed copper enclosure (without the lid), which is used to mount and thermalize the cryo-controller. **c**, Ball-grid array (BGA 324) package hosting the cryo-controller chip with on-package decoupling capacitors (shown as a white box in **b**). **d**, The Wilkinson power divider (WPD) splits the input LO power into two equal paths with half power in each, implemented on a PCB. Discrete I/Q hybrids that create the in-phase and quadrature-phase components of the input LO are wire-bonded on the PCB for LO distribution between the different transmitters inside the cryo-controller (shown as a red box in **b**).

### **Extended Data Fig. 3 Detailed cryo-controller schematic.**

**a**, Detailed representation of the digital circuitry. **b**, Detailed system-level schematic of the analogue circuitry inside the controller.

### **Extended Data Fig. 4 Power consumption and self-heating of the cryo-controller.**

**a**, Power-consumption pie chart showing the contribution of the digital and analogue circuits in the cryo-controller. A breakdown of the power consumption of individual circuit blocks is shown for the analogue circuits. The digital circuits use a 0.7-V supply and the analogue circuits use a 1-V supply. **b**, Chip micrograph showing the on-chip bumps used as inputs/outputs. The locations of on-chip temperature-sensing diodes and the analogue and digital circuitry (in TX0) are highlighted. **c**, On-chip and 3-K plate temperature, measured using different sensors, versus the power consumption of TX0, as reported in ref. [13](#). The power consumption is varied by changing the clock frequency of the chip. The nominal operating point for the work presented here and the corresponding temperatures are highlighted with a dashed vertical line. All the other transmitters (TX1, TX2, TX3) are switched off in this measurement.

### Extended Data Fig. 5 Detailed electrical characterization of the cryo-controller.

**a**, Schematic of the output driver (complete version in Extended Data Fig. [3](#)) showing the two different RF outputs, which use the same external LO to generate two different frequencies—that is, a 1-GHz band around the LO frequency ( $f_{\text{LO}}$ ) or a 1-GHz band around  $3 \times f_{\text{LO}}$ —by selecting the ‘RF-Low’ or ‘RF-High’ path, respectively. RF-High uses the third harmonic output of the mixer to generate the tone around  $3 \times f_{\text{LO}}$ . **b**, Peak output power versus frequency generated using the RF-Low and RF-High path, respectively, as reported in ref. [13](#). The output power can be lowered by up to 40 dB below the peak power in the entire frequency range; for example, at 6 GHz the amplitude range is from −56 dBm to −16 dBm. **c**, Two-tone output spectrum of the cryo-controller used in the simultaneous Rabi oscillation experiment. **d**, SNR and SFDR of the cryo-controller at various NCO frequencies around 13.54 GHz.

### Extended Data Fig. 6 Pulsing scheme used in qubit experiments.

**a**, Charge-stability diagram of the DQD system, showing the differential current signal ( $dI_{\text{SET}}/dV_{\text{RP}}$ ) and charge occupation ( $M, N$ ) (where  $M$  denotes

the number of electrons in the dot below LP and  $N$  represents the number of electrons in the dot below RP) as a function of the voltages applied to gates LP ( $V_{LP}$ ) and RP ( $V_{RP}$ ). The three main stages of a typical pulse sequence are marked by the numbered circles. The gate voltages of stage 3 vary between different experiments: in the experiments with exchange coupling turned on, owing to the cross-capacitance between the barrier (gate T) and the plungers (gates RP and LP), the LP and RP voltages differ from those in the experiments without exchange coupling by  $\sim 15$  mV. **b**, Schematic representations of the DQD system during the experiment cycle.  $Q_1$  is first initialized to its ground state (spin down) via fast relaxation by pulsing to the charge transition line between (1, 0) and (0, 1) (stage 1), which is a spin-relaxation hotspot<sup>46</sup>. Then,  $Q_2$  is initialized by pulsing it to the transition line between (1, 0) and (1, 1) (stage 2), where the Fermi energy of the electron reservoir is placed in between the two spin states of  $Q_2$ . This allows a spin-down electron to tunnel into the dot but forbids spin-up electrons from tunnelling in—a mechanism called spin-selective tunnelling. During the qubit operations, the system is pulsed to the middle of the (1, 1) region (stage 3), so both electrons are well confined inside the DQD. The barrier (gate T) voltage is used to turn off the exchange coupling between the two spins in the operation of uncoupled qubits (all measurements in Fig. 3) and to turn on the coupling for two-qubit logic operations (all measurements in Fig. 4). After the operations, the  $Q_2$  state is read out via spin-selective tunnelling and reinitialized into the spin-down state (stage 2). The state of  $Q_1$  is read out by mapping its state onto  $Q_2$  via a two-qubit CROT gate (stage 3), followed by readout of  $Q_2$  again (stage 2).

### Extended Data Fig. 7 Magnetic field gradient.

**a**, Wafer stack schematic with corresponding layer thicknesses. **b**, Depth concentration SIMS profile of  $^{28}\text{Si}$  (red),  $^{29}\text{Si}$  (blue),  $^{30}\text{Si}$  (purple), Ge (black), oxygen (green) and carbon (blue). The residual  $^{29}\text{Si}$  concentration in the quantum well is 0.08%, considerably reducing qubit decoherence due to hyperfine interaction. Both carbon and oxygen concentrations are below their respective detection limits of  $3 \times 10^{16} \text{ cm}^{-3}$  and  $1 \times 10^{17} \text{ cm}^{-3}$ . **c**, Schematic showing the first and second Al gate layers in green and purple,

respectively. A cobalt micro-magnet is located on top of the metallic gates (pink-shaded area). **d**, The micromagnet is magnetized by sweeping the external magnetic field (in the  $\hat{z}$  direction) from 0 to 3 T and back to 380 mT. The magnetized micro-magnet provides an additional magnetic field (brown dashed lines) that has a longitudinal ( $\hat{z}$ ) component with a field gradient along the double quantum dots. This longitudinal magnetic field gradient (light blue arrows) makes the Zeeman splittings (resonance frequencies) of the two qubits different by  $\sim$ 110 MHz. Additionally, the micro-magnet also induces a transverse ( $\hat{x}$ ) magnetic field gradient (green arrows). When a microwave pulse is sent to the device through gate MW, the wave functions of the electrons are oscillating in the  $\hat{z}$  direction. If the microwave frequency is in resonance with the qubit frequency, the electron is subject to an oscillating magnetic field along the  $\hat{x}$  direction, which induces electric-dipole spin resonance<sup>29</sup>.

### Extended Data Fig. 8 Electron temperature measured at different configurations.

**a, b**, SET current signal ( $I_{\text{SET}}$ ) as a function of RP voltage ( $V_{\text{RP}}$ ) measured at the charge transition between (1, 0) and (1, 1) when the quantum device is connected to the VSG (**a**) and to the cryo-controller (**b**) (at zero magnetic field). The electron temperatures are extracted by fitting the curves with the Fermi–Dirac distribution, with a lever arm of 0.172 eV V<sup>-1</sup>. The measurements indicate that the output noise of the cryo-controller does not affect the electron temperature more than the noise from the RT setup reduced by 6 dB at the 3-K plate.

### Extended Data Fig. 9 Rabi oscillations of qubits individually driven by the cryo-controller.

The output frequency of two NCOs are set to the frequencies of  $Q_1$  and  $Q_2$ , respectively, but only one NCO is active each time. Using the same method as described in the main text, the Rabi oscillations of  $Q_1$  (**a**) and  $Q_2$  (**b**) are measured individually. Compared to the simultaneous Rabi oscillations

shown in Fig. 3b, the decay is much slower in the individual driving experiments.

## Supplementary information

### [Peer Review File](#)

## Rights and permissions

### [Reprints and Permissions](#)

## About this article



Check for  
updates

## Cite this article

Xue, X., Patra, B., van Dijk, J.P.G. *et al.* CMOS-based cryogenic control of silicon quantum circuits. *Nature* **593**, 205–210 (2021).  
<https://doi.org/10.1038/s41586-021-03469-4>

### [Download citation](#)

- Received: 01 October 2020
- Accepted: 18 March 2021
- Published: 12 May 2021
- Issue Date: 13 May 2021
- DOI: <https://doi.org/10.1038/s41586-021-03469-4>

# Comments

By submitting a comment you agree to abide by our [Terms](#) and [Community Guidelines](#). If you find something abusive or that does not comply with our terms or guidelines please flag it as inappropriate.

[Access through your institution](#)

[Change institution](#)

[Buy or subscribe](#)

---

This article was downloaded by **calibre** from <https://www.nature.com/articles/s41586-021-03469-4>

| [Section menu](#) | [Main menu](#) |

- Article
- [Published: 12 May 2021](#)

# Ultralow contact resistance between semimetal and monolayer semiconductors

- [Pin-Chun Shen](#) ORCID: [orcid.org/0000-0001-6908-6488<sup>1 na1</sup>](https://orcid.org/0000-0001-6908-6488),
- [Cong Su<sup>2,3,4,5 na1</sup>](#),
- [Yuxuan Lin](#) ORCID: [orcid.org/0000-0003-0638-2620<sup>1,6 na1</sup>](https://orcid.org/0000-0003-0638-2620),
- [Ang-Sheng Chou<sup>7,8 na1</sup>](#),
- [Chao-Ching Cheng<sup>7</sup>](#),
- [Ji-Hoon Park](#) ORCID: [orcid.org/0000-0003-4776-5206<sup>1</sup>](https://orcid.org/0000-0003-4776-5206),
- [Ming-Hui Chiu](#) ORCID: [orcid.org/0000-0003-3753-8149<sup>1,9</sup>](https://orcid.org/0000-0003-3753-8149),
- [Ang-Yu Lu<sup>1</sup>](#),
- [Hao-Ling Tang<sup>1,9</sup>](#),
- [Mohammad Mahdi Tavakoli<sup>1</sup>](#),
- [Gregory Pitner<sup>10</sup>](#),
- [Xiang Ji<sup>1</sup>](#),
- [Zhengyang Cai](#) ORCID: [orcid.org/0000-0001-5048-5673<sup>1</sup>](https://orcid.org/0000-0001-5048-5673),
- [Nannan Mao<sup>1</sup>](#),
- [Jiangtao Wang<sup>1</sup>](#),
- [Vincent Tung<sup>9</sup>](#),
- [Ju Li](#) ORCID: [orcid.org/0000-0002-7841-8058<sup>5</sup>](https://orcid.org/0000-0002-7841-8058),
- [Jeffrey Bokor](#) ORCID: [orcid.org/0000-0002-4541-0156<sup>4,6</sup>](https://orcid.org/0000-0002-4541-0156),
- [Alex Zettl<sup>2,3,4</sup>](#),
- [Chih-I Wu<sup>8</sup>](#),
- [Tomás Palacios<sup>1</sup>](#),
- [Lain-Jong Li](#) ORCID: [orcid.org/0000-0002-4059-7783<sup>7</sup>](https://orcid.org/0000-0002-4059-7783) &
- [Jing Kong](#) ORCID: [orcid.org/0000-0003-0551-1208<sup>1</sup>](https://orcid.org/0000-0003-0551-1208)

- 3129 Accesses
- 52 Altmetric
- [Metrics details](#)

## Subjects

- [Electronic devices](#)
- [Two-dimensional materials](#)

## Abstract

Advanced beyond-silicon electronic technology requires both channel materials and also ultralow-resistance contacts to be discovered<sup>1,2</sup>. Atomically thin two-dimensional semiconductors have great potential for realizing high-performance electronic devices<sup>1,3</sup>. However, owing to metal-induced gap states (MIGS)<sup>4,5,6,7</sup>, energy barriers at the metal–semiconductor interface—which fundamentally lead to high contact resistance and poor current-delivery capability—have constrained the improvement of two-dimensional semiconductor transistors so far<sup>2,8,9</sup>. Here we report ohmic contact between semimetallic bismuth and semiconducting monolayer transition metal dichalcogenides (TMDs) where the MIGS are sufficiently suppressed and degenerate states in the TMD are spontaneously formed in contact with bismuth. Through this approach, we achieve zero Schottky barrier height, a contact resistance of 123 ohm micrometres and an on-state current density of 1,135 microamps per micrometre on monolayer MoS<sub>2</sub>; these two values are, to the best of our knowledge, the lowest and highest yet recorded, respectively. We also demonstrate that excellent ohmic contacts can be formed on various monolayer semiconductors, including MoS<sub>2</sub>, WS<sub>2</sub> and WSe<sub>2</sub>. Our reported contact resistances are a substantial improvement for two-dimensional semiconductors, and approach the quantum limit. This technology unveils the potential of high-performance monolayer transistors that are on par with state-of-the-art

three-dimensional semiconductors, enabling further device downscaling and extending Moore's law.

[Access through your institution](#)

[Change institution](#)

[Buy or subscribe](#)

## Access options

Subscribe to Journal

Get full journal access for 1 year

\$199.00

only \$3.90 per issue

[Subscribe](#)

All prices are NET prices.

VAT will be added later in the checkout.

Tax calculation will be finalised during checkout.

Rent or Buy article

Get time limited or full article access on ReadCube.

from \$8.99

[Rent or Buy](#)

All prices are NET prices.

### Additional access options:

- [Log in](#)
- [Access through your institution](#)
- [Learn about institutional subscriptions](#)

**Fig. 1: The concept of gap-state saturation at semimetal–semiconductor contact.**

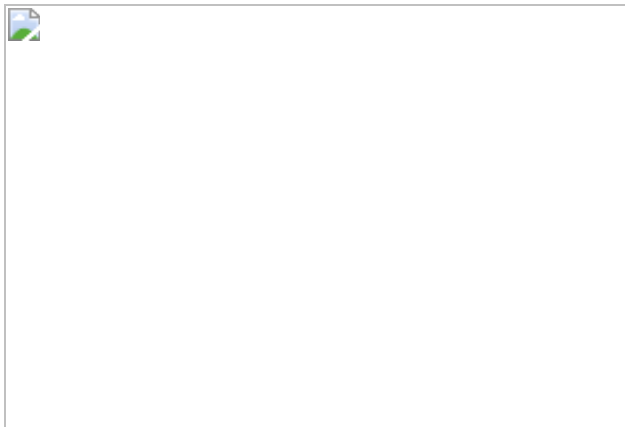


**Fig. 2: Comparison of ohmic and Schottky contacts in monolayer MoS<sub>2</sub> FETs.**

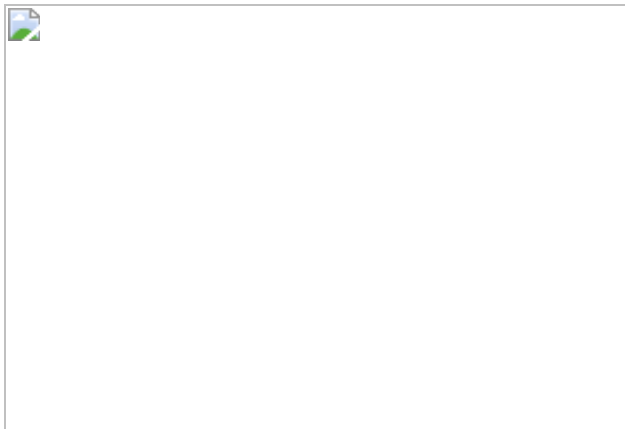
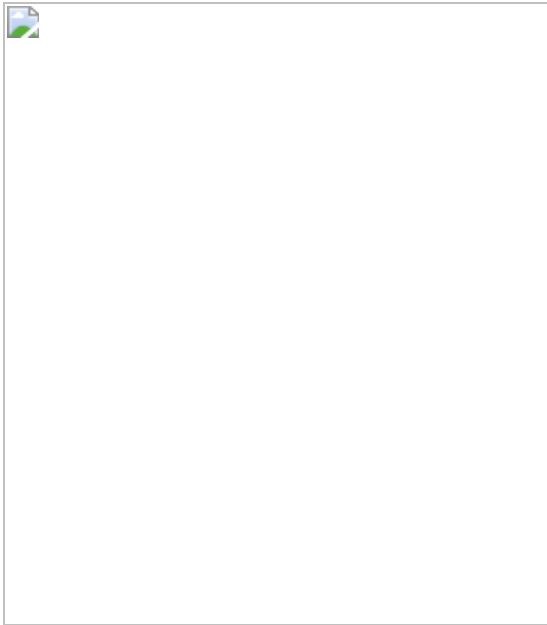


**Fig. 3: Crystal structure and mechanism of ohmic contact.**



**Fig. 4: Benchmark of Bi-contacted 2D semiconductor technology.**



## Data availability

All data needed to evaluate the conclusions herein are present in the Article.

## References

1. 1.

Chhowalla, M., Jena, D. & Zhang, H. Two-dimensional semiconductors for transistors. *Nat. Rev. Mater.* **1**, 16052 (2016).

[ADS](#) [CAS](#) [Google Scholar](#)

2. 2.

Allain, A., Kang, J., Banerjee, K. & Kis, A. Electrical contacts to two-dimensional semiconductors. *Nat. Mater.* **14**, 1195–1205 (2015).

[ADS](#) [CAS](#) [PubMed](#) [PubMed Central](#) [Google Scholar](#)

3. 3.

Akinwande, D. et al. Graphene and two-dimensional materials for silicon technology. *Nature* **573**, 507–518 (2019).

[ADS](#) [CAS](#) [PubMed](#) [PubMed Central](#) [Google Scholar](#)

4. 4.

Louie, S. G. & Cohen, M. L. Electronic structure of a metal-semiconductor interface. *Phys. Rev. B* **13**, 2461–2469 (1976).

[ADS](#) [CAS](#) [Google Scholar](#)

5. 5.

Nishimura, T., Kita, K. & Toriumi, A. Evidence for strong Fermi-level pinning due to metal-induced gap states at metal/germanium interface. *Appl. Phys. Lett.* **91**, 123123 (2007).

[ADS](#) [Google Scholar](#)

6. 6.

Kobayashi, M., Kinoshita, A., Saraswat, K., Wong, H.-S. P. & Nishi, Y. Fermi level depinning in metal/Ge Schottky junction for metal source/drain Ge metal-oxide-semiconductor field-effect-transistor application. *J. Appl. Phys.* **105**, 023702 (2009).

[ADS](#) [Google Scholar](#)

7. 7.

Sotthewes, K. et al. Universal Fermi-level pinning in transition-metal dichalcogenides. *J. Phys. Chem. C* **123**, 5411–5420 (2019).

[CAS](#) [Google Scholar](#)

8. 8.

Tung, R. T. The physics and chemistry of the Schottky barrier height. *Appl. Phys. Rev.* **1**, 011304 (2014).

[ADS](#) [Google Scholar](#)

9. 9.

Razavieh, A., Zeitzoff, P. & Nowak, E. J. Challenges and limitations of CMOS scaling for FinFET and beyond architectures. *IEEE Trans. NanoTechnol.* **18**, 999–1004 (2019).

[ADS](#) [CAS](#) [Google Scholar](#)

10. 10.

Tersoff, J. Schottky barrier heights and the continuum of gap states. *Phys. Rev. Lett.* **52**, 465 (1984).

[ADS](#) [CAS](#) [Google Scholar](#)

11. 11.

Sze, S. M. & Ng, K. K. *Physics of Semiconductor Devices* (Wiley, 2006).

12. 12.

Vilan, A., Shanzer, A. & Cahen, D. Molecular control over Au/GaAs diodes. *Nature* **404**, 166–168 (2000).

[ADS](#) [CAS](#) [PubMed](#) [PubMed Central](#) [Google Scholar](#)

13. 13.

Wang, Y. et al. Van der Waals contacts between three-dimensional metals and two-dimensional semiconductors. *Nature* **568**, 70–74 (2019).

[ADS](#) [CAS](#) [PubMed](#) [PubMed Central](#) [Google Scholar](#)

14. 14.

Cui, X. et al. Low-temperature ohmic contact to monolayer MoS<sub>2</sub> by van der Waals bonded Co/h-BN electrodes. *Nano Lett.* **17**, 4781–4786 (2017).

[ADS](#) [CAS](#) [PubMed](#) [PubMed Central](#) [Google Scholar](#)

15. 15.

Liu, Y., Stradins, P. & Wei, S.-H. Van der Waals metal–semiconductor junction: weak Fermi level pinning enables effective tuning of Schottky barrier. *Sci. Adv.* **2**, e1600069 (2016).

[ADS](#) [PubMed](#) [PubMed Central](#) [Google Scholar](#)

16. 16.

Liu, Y. et al. Approaching the Schottky–Mott limit in van der Waals metal–semiconductor junctions. *Nature* **557**, 696–700 (2018).

[ADS](#) [CAS](#) [PubMed](#) [PubMed Central](#) [Google Scholar](#)

17. 17.

Kim, C. et al. Fermi level pinning at electrical metal contacts of monolayer molybdenum dichalcogenides. *ACS Nano* **11**, 1588–1596 (2017).

[CAS](#) [PubMed](#) [PubMed Central](#) [Google Scholar](#)

18. 18.

English, C. D., Shine, G., Dorgan, V. E., Saraswat, K. C. & Pop, E. Improved contacts to MoS<sub>2</sub> transistors by ultra-high vacuum metal deposition. *Nano Lett.* **16**, 3824–3830 (2016).

[ADS](#) [CAS](#) [PubMed](#) [PubMed Central](#) [Google Scholar](#)

19. 19.

Chee, S. S. et al. Lowering the Schottky barrier height by graphene/Ag electrodes for high-mobility MoS<sub>2</sub> field-effect transistors. *Adv. Mater.* **31**, 1804422 (2019).

[Google Scholar](#)

20. 20.

Cao, Z., Lin, F., Gong, G., Chen, H. & Martin, J. Low Schottky barrier contacts to 2H-MoS<sub>2</sub> by Sn electrodes. *Appl. Phys. Lett.* **116**, 022101 (2020).

[ADS](#) [Google Scholar](#)

21. 21.

Das, S., Chen, H.-Y., Penumatcha, A. V. & Appenzeller, J. High performance multilayer MoS<sub>2</sub> transistors with scandium contacts. *Nano Lett.* **13**, 100–105 (2013).

[ADS](#) [CAS](#) [PubMed](#) [PubMed Central](#) [Google Scholar](#)

22. 22.

Smithe, K. K., English, C. D., Suryavanshi, S. V. & Pop, E. Intrinsic electrical transport and performance projections of synthetic monolayer MoS<sub>2</sub> devices. *2D Mater.* **4**, 011009 (2016).

[Google Scholar](#)

23. 23.

Qian, X., Liu, J., Fu, L. & Li, J. Quantum spin Hall effect in two-dimensional transition metal dichalcogenides. *Science* **346**, 1344–1347 (2014).

[ADS](#) [CAS](#) [PubMed](#) [PubMed Central](#) [Google Scholar](#)

24. 24.

Nagao, T. et al. Nanofilm allotrope and phase transformation of ultrathin Bi film on Si(111)- $7 \times 7$ . *Phys. Rev. Lett.* **93**, 105501 (2004).

[ADS](#) [CAS](#) [PubMed](#) [PubMed Central](#) [Google Scholar](#)

25. 25.

Zhong, H. et al. Interfacial properties of monolayer and bilayer MoS<sub>2</sub> contacts with metals: beyond the energy band calculations. *Sci. Rep.* **6**, 21786 (2016).

[ADS](#) [CAS](#) [PubMed](#) [PubMed Central](#) [Google Scholar](#)

26. 26.

Kang, J., Liu, W., Sarkar, D., Jena, D. & Banerjee, K. Computational study of metal contacts to monolayer transition-metal dichalcogenide semiconductors. *Phys. Rev. X* **4**, 031005 (2014).

[CAS](#) [Google Scholar](#)

27. 27.

Chakraborty, B. et al. Symmetry-dependent phonon renormalization in monolayer MoS<sub>2</sub> transistor. *Phys. Rev. B* **85**, 161403 (2012).

[ADS](#) [Google Scholar](#)

28. 28.

Michail, A., Delikoukos, N., Parthenios, J., Galiotis, C. & Papagelis, K. Optical detection of strain and doping inhomogeneities in single layer MoS<sub>2</sub>. *Appl. Phys. Lett.* **108**, 173102 (2016).

[ADS](#) [Google Scholar](#)

29. 29.

Moe, Y. A., Sun, Y., Ye, H., Liu, K. & Wang, R. Probing evolution of local strain at MoS<sub>2</sub>–metal boundaries by surface-enhanced Raman scattering. *ACS Appl. Mater. Interfaces* **10**, 40246–40254 (2018).

[CAS](#) [PubMed](#) [PubMed Central](#) [Google Scholar](#)

30. 30.

Yang, L. et al. Chloride molecular doping technique on 2D materials: WS<sub>2</sub> and MoS<sub>2</sub>. *Nano Lett.* **14**, 6275–6280 (2014).

[ADS](#) [CAS](#) [PubMed](#) [PubMed Central](#) [Google Scholar](#)

31. 31.

Liu, W. et al. Role of metal contacts in designing high-performance monolayer n-type WSe<sub>2</sub> field effect transistors. *Nano Lett.* **13**, 1983–1990 (2013).

[ADS](#) [CAS](#) [PubMed](#) [PubMed Central](#) [Google Scholar](#)

32. 32.

Yeh, C.-H., Cao, W., Pal, A., Parto, K. & Banerjee, K. in 2019 *IEEE International Electron Devices Meeting (IEDM)* 23.24.21–23.24.24 (IEEE, 2019); <https://ieeexplore.ieee.org/abstract/document/8993600>.

33. 33.

English, C. D., Smithe, K. K., Xu, R. L. & Pop, E. in 2016 *IEEE International Electron Devices Meeting (IEDM)* 5.6.1–5.6.4 (IEEE, 2016); <https://ieeexplore.ieee.org/abstract/document/7838355>.

34. 34.

McClellan, C. J., Yalon, E., Smithe, K. K., Suryavanshi, S. V. & Pop, E. High current density in monolayer MoS<sub>2</sub> doped by AlO<sub>x</sub>. *ACS Nano* **15**, 1587–1596 (2021).

[CAS](#) [PubMed](#) [PubMed Central](#) [Google Scholar](#)

35. 35.

Kwon, J. et al. Thickness-dependent Schottky barrier height of MoS<sub>2</sub> field-effect transistors. *Nanoscale* **9**, 6151–6157 (2017).

[CAS](#) [PubMed](#) [PubMed Central](#) [Google Scholar](#)

36. 36.

Li, S.-L. et al. Thickness scaling effect on interfacial barrier and electrical contact to two-dimensional MoS<sub>2</sub> layers. *ACS Nano* **8**, 12836–12842 (2014).

[CAS](#) [PubMed](#) [PubMed Central](#) [Google Scholar](#)

37. 37.

Wang, Q., Shao, Y., Gong, P. & Shi, X. Metal–2D multilayered semiconductor junctions: layer-number-dependent Fermi-level pinning. *J. Mater. Chem. C* **8**, 3113–3119 (2020).

[CAS](#) [Google Scholar](#)

38. 38.

Badaroglu, M. et al. More Moore. In *International Roadmap for Devices and Systems 2017* [https://irds.ieee.org/images/files/pdf/2017/2017IRDS\\_MM.pdf](https://irds.ieee.org/images/files/pdf/2017/2017IRDS_MM.pdf) (IEEE, 2017).

39. 39.

Ghani, T. et al. A 90-nm high volume manufacturing logic technology featuring novel 45-nm gate length strained silicon CMOS transistors. In *IEEE International Electron Devices Meeting 2003* 11.16.11–11.16.13 (IEEE, 2003);  
<https://ieeexplore.ieee.org/abstract/document/1269442>.

40. 40.

Thompson, S. et al. A 90-nm logic technology featuring 50-nm strained silicon channel transistors, 7 layers of Cu interconnects, low- $k$  ILD, and 1  $\mu\text{m}^2$  SRAM cell. In *International Electron Devices Meeting 2002* 61–64 (IEEE, 2002);  
<https://ieeexplore.ieee.org/abstract/document/1175779>.

41. 41.

Kim, S. et al. High-mobility and low-power thin-film transistors based on multilayer MoS<sub>2</sub> crystals. *Nat. Commun.* **3**, 1011 (2012).

[ADS](#) [PubMed](#) [PubMed Central](#) [Google Scholar](#)

42. 42.

Liu, Y. et al. Pushing the performance limit of sub-100-nm molybdenum disulfide transistors. *Nano Lett.* **16**, 6337–6342 (2016).

[ADS](#) [CAS](#) [PubMed](#) [PubMed Central](#) [Google Scholar](#)

43. 43.

Nourbakhsh, A. et al. MoS<sub>2</sub> field-effect transistor with sub-10-nm channel length. *Nano Lett.* **16**, 7798–7806 (2016).

[ADS](#) [CAS](#) [PubMed](#) [PubMed Central](#) [Google Scholar](#)

44. 44.

Yang, L., Lee, R., Rao, S. P., Tsai, W. & Ye, P. in *2015 73rd Annual Device Research Conference (DRC)* 237–238 (IEEE, 2015).

45. 45.

Jung, Y. et al. Transferred via contacts as a platform for ideal two-dimensional transistors. *Nature Electron.* **2**, 187–194 (2019).

[Google Scholar](#)

46. 46.

Nguyen, L. D., Tasker, P. J., Radulescu, D. C. & Eastman, L. F. Characterization of ultra-high-speed pseudomorphic AlGaAs/InGaAs (on GaAs) MODFETs. *IEEE Trans. Electron Dev.* **36**, 2243–2248 (1989).

[ADS](#) [Google Scholar](#)

47. 47.

Smithe, K. K., Suryavanshi, S. V., Muñoz Rojo, M., Tedjarati, A. D. & Pop, E. Low variability in synthetic monolayer MoS<sub>2</sub> devices. *ACS Nano* **11**, 8456–8463 (2017).

[CAS](#) [PubMed](#) [PubMed Central](#) [Google Scholar](#)

48. 48.

Yue, D., Kim, C., Lee, K. Y. & Yoo, W. J. Ohmic contact in 2D semiconductors via the formation of a benzyl viologen interlayer. *Adv. Funct. Mater.* **29**, 1807338 (2019).

[Google Scholar](#)

49. 49.

Guimarães, M. H. et al. Atomically thin ohmic edge contacts between two-dimensional materials. *ACS Nano* **10**, 6392–6399 (2016).

[PubMed](#) [PubMed Central](#) [Google Scholar](#)

50. 50.

Smets, Q. et al. Ultra-scaled MOCVD MoS<sub>2</sub> MOSFETs with 42 nm contact pitch and 250 μA/μm drain current. In *2019 IEEE International Electron Devices Meeting (IEDM)* 23.2.21–23.2.24 (IEEE, 2019).

51. 51.

Gao, J. et al. Transition-metal substitution doping in synthetic atomically thin semiconductors. *Adv. Mater.* **28**, 9735–9743 (2016).

[CAS](#) [PubMed](#) [PubMed Central](#) [Google Scholar](#)

52. 52.

Kresse, G. & Joubert, D. From ultrasoft pseudopotentials to the projector augmented-wave method. *Phys. Rev. B* **59**, 1758 (1999).

[ADS](#) [CAS](#) [Article](#) [Google Scholar](#)

53. 53.

Simmons, J. G. Generalized formula for the electric tunnel effect between similar electrodes separated by a thin insulating film. *J. Appl. Phys.* **34**, 1793–1803 (1963).

[ADS](#) [Google Scholar](#)

54. 54.

Simmons, J. G. Electric tunnel effect between dissimilar electrodes separated by a thin insulating film. *J. Appl. Phys.* **34**, 2581–2590 (1963).

[ADS](#) [MATH](#) [Google Scholar](#)

55. 55.

Fiori, G., Szafranek, B. N., Iannaccone, G. & Neumaier, D. Velocity saturation in few-layer MoS<sub>2</sub> transistor. *Appl. Phys. Lett.* **103**, 233509 (2013).

[ADS](#) [Google Scholar](#)

56. 56.

Kim, J. J. et al. Intrinsic time zero dielectric breakdown characteristics of HfAlO alloys. *IEEE Trans. Electron Dev.* **60**, 3683–3689 (2013).

[ADS](#) [CAS](#) [Google Scholar](#)

[Download references](#)

## Acknowledgements

P.-C.S., J.B. and J.K. acknowledge financial support from the Center for Energy Efficient Electronics Science (NSF award no. 0939514), which provided funding for development of high-performance monolayer TMD transistors. P.-C.S., Y.L., J.-H.P., A.-Y.L., T.P. and J.K. acknowledge the US Army Research Office through the Institute for Soldier Nanotechnologies at MIT, under cooperative agreement no. W911NF-18-2-0048. C.S., J.-H.P., J.W. and J.K. acknowledge the support from the US Army Research Office (ARO) under grant no. W911NF-18-1-0431. C.S. is currently supported by the Kavli Energy NanoScience Institute/Heising–Simons Fellowship, Berkeley, California, USA. C.S. and A.Z. are supported by the Director, Office of Science, Office of Basic Energy Sciences, Materials Sciences and Engineering Division, of the US Department of Energy under contract no. DE-AC02-05-CH11231, within the sp<sub>2</sub>-Bonded Materials Program (KC2207), which provided for TEM characterizations. C.S. and A.Z. are further supported by the National Science Foundation under grant no. DMR-1807233, which provided funding for development of TEM image-processing methods. J.L. acknowledges support by the Office of Naval Research MURI through grant no. N00014-17-1-2661. Y.L. and J.B.

acknowledge support by the Office of Naval Research MURI programme N00014-16-1-2921, and the NSF award RAISE TAQS under grant no. DMR-1839098. Y.L. and N.M. acknowledge support by the US Department of Energy (DOE), Office of Science, Basic Energy Sciences (BES) under award DE-SC0020042. A.-S.C. and C.-I.W. acknowledge support from the Ministry of Science and Technology of Taiwan (MOST 108-2622-8-002-016). J.W. and J.K. acknowledge support from the joint development project (JDP) from TSMC. V.T. and M.-H.C. are indebted to the support from the King Abdullah University of Science and Technology (KAUST) Office of Sponsored Research (OSR) under award no: OSR-2018-CARF/CCF-3079. H.-L.T. acknowledges partial support from the Ministry of Science and Technology of Taiwan (MOST-108-2917-I-564-036). We acknowledge H.-S.P. Wong for guidance. We thank Y. Guo, E. Shi and H. Wang for technical assistance with materials characterizations, and Y.-T. Shao for discussions on SAED pattern simulation.

## Author information

### Author notes

1. These authors contributed equally: Pin-Chun Shen, Cong Su, Yuxuan Lin, Ang-Sheng Chou

## Affiliations

1. Department of Electrical Engineering and Computer Science, Massachusetts Institute of Technology (MIT), Cambridge, MA, USA

Pin-Chun Shen, Yuxuan Lin, Ji-Hoon Park, Ming-Hui Chiu, Ang-Yu Lu, Hao-Ling Tang, Mohammad Mahdi Tavakoli, Xiang Ji, Zhengyang Cai, Nannan Mao, Jiangtao Wang, Tomás Palacios & Jing Kong

2. Kavli Energy NanoSciences Institute, University of California, Berkeley, CA, USA

Cong Su & Alex Zettl

3. Department of Physics, University of California, Berkeley, CA, USA

Cong Su & Alex Zettl

4. Materials Sciences Division, Lawrence Berkeley National Laboratory, Berkeley, CA, USA

Cong Su, Jeffrey Bokor & Alex Zettl

5. Department of Nuclear Science and Engineering, Massachusetts Institute of Technology (MIT), Cambridge, MA, USA

Cong Su & Ju Li

6. Department of Electrical Engineering and Computer Sciences, University of California, Berkeley, CA, USA

Yuxuan Lin & Jeffrey Bokor

7. Corporate Research, Taiwan Semiconductor Manufacturing Company (TSMC), Hsinchu, Taiwan

Ang-Sheng Chou, Chao-Ching Cheng & Lain-Jong Li

8. Graduate Institute of Photonics and Optoelectronics, National Taiwan University, Taipei, Taiwan

Ang-Sheng Chou & Chih-I Wu

9. Physical Science and Engineering Division, King Abdullah University of Science & Technology (KAUST), Thuwal, Saudi Arabia

Ming-Hui Chiu, Hao-Ling Tang & Vincent Tung

10. Corporate Research, Taiwan Semiconductor Manufacturing Company (TSMC), San Jose, CA, USA

Gregory Pitner

## Authors

1. Pin-Chun Shen

[View author publications](#)

You can also search for this author in [PubMed](#) [Google Scholar](#)

2. Cong Su

[View author publications](#)

You can also search for this author in [PubMed](#) [Google Scholar](#)

3. Yuxuan Lin

[View author publications](#)

You can also search for this author in [PubMed](#) [Google Scholar](#)

4. Ang-Sheng Chou

[View author publications](#)

You can also search for this author in [PubMed](#) [Google Scholar](#)

5. Chao-Ching Cheng

[View author publications](#)

You can also search for this author in [PubMed](#) [Google Scholar](#)

6. Ji-Hoon Park

[View author publications](#)

You can also search for this author in [PubMed](#) [Google Scholar](#)

7. Ming-Hui Chiu

[View author publications](#)

You can also search for this author in [PubMed](#) [Google Scholar](#)

8. Ang-Yu Lu

[View author publications](#)

You can also search for this author in [PubMed](#) [Google Scholar](#)

9. Hao-Ling Tang

[View author publications](#)

You can also search for this author in [PubMed](#) [Google Scholar](#)

10. Mohammad Mahdi Tavakoli

[View author publications](#)

You can also search for this author in [PubMed](#) [Google Scholar](#)

11. Gregory Pitner

[View author publications](#)

You can also search for this author in [PubMed](#) [Google Scholar](#)

12. Xiang Ji

[View author publications](#)

You can also search for this author in [PubMed](#) [Google Scholar](#)

13. Zhengyang Cai

[View author publications](#)

You can also search for this author in [PubMed](#) [Google Scholar](#)

14. Nannan Mao

[View author publications](#)

You can also search for this author in [PubMed](#) [Google Scholar](#)

15. Jiangtao Wang

[View author publications](#)

You can also search for this author in [PubMed](#) [Google Scholar](#)

16. Vincent Tung

[View author publications](#)

You can also search for this author in [PubMed](#) [Google Scholar](#)

17. Ju Li

[View author publications](#)

You can also search for this author in [PubMed](#) [Google Scholar](#)

18. Jeffrey Bokor

[View author publications](#)

You can also search for this author in [PubMed](#) [Google Scholar](#)

19. Alex Zettl

[View author publications](#)

You can also search for this author in [PubMed](#) [Google Scholar](#)

20. Chih-I Wu

[View author publications](#)

You can also search for this author in [PubMed](#) [Google Scholar](#)

21. Tomás Palacios

[View author publications](#)

You can also search for this author in [PubMed](#) [Google Scholar](#)

22. Lain-Jong Li

[View author publications](#)

You can also search for this author in [PubMed](#) [Google Scholar](#)

23. Jing Kong

[View author publications](#)

You can also search for this author in [PubMed](#) [Google Scholar](#)

## Contributions

J.K. and L.-J.L. supervised the project. P.-C.S. and J.K. proposed the project. P.-C.S., C.S., Y.L. and J.K. designed the experiments. P.-C.S. carried out the device fabrication. P.-C.S., H.-L.T. and Y.L. performed the electrical characterization supervised by T.P. C.S. carried out the TEM measurements and analysis and first-principles calculations supervised by A.Z. and J.L. P.-C.S., Y.L. and C.S. conducted the device modelling and data analysis. A.-S.C., C.-C.C. and G.P. carried out additional fabrication and characterization of the short-channel devices supervised by L.-J.L. The work of A.-S.C. is also co-supervised by C.-I.W. Y.L. and J.W. performed the SEM measurements. J.-H.P., P.-C.S., Z.C. and N.M. contributed to the growth, exfoliation and transfer of materials supervised by J.K. M.-H.C., A.-Y.L., M.M.T., and P.-C.S. carried out the materials characterizations. P.-C.S., C.S., Y.L. and J.K. wrote the manuscript. All authors discussed the results and provided constructive comments on the manuscript.

## Corresponding authors

Correspondence to [Pin-Chun Shen](#) or [Lain-Jong Li](#) or [Jing Kong](#).

## Ethics declarations

## Competing interests

P.-C.S. and J.K. are co-inventors on a patent application (provisional filling number US 63/024,141) related to the research presented in this paper.

## Additional information

**Peer review information** *Nature* thanks Hyeon-Jin Shin and the other, anonymous, reviewer(s) for their contribution to the peer review of this work. Peer reviewer reports are available.

**Publisher's note** Springer Nature remains neutral with regard to jurisdictional claims in published maps and institutional affiliations.

# Extended data figures and tables

## Extended Data Fig. 1 Temperature-dependent electrical characteristics.

**a, b,** Typical  $I_{DS}$ – $V_{DS}$  curves at 150 K (**a**) and 77 K (**b**) for the Bi–MoS<sub>2</sub> FET. The device exhibits linear output characteristics at all the temperatures measured. **c**, Schottky barrier height ( $\Phi_{SB}$ ) extraction for the Bi–MoS<sub>2</sub> FET, showing a negligible contact barrier. Inset, logarithmic plot of the  $I_{DS}$ – $V_{DS}$  curve at 77 K and  $n_{2D} \approx 4 \times 10^{12} \text{ cm}^{-2}$ , demonstrating ohmic contact in the Bi–MoS<sub>2</sub> FETs. **d, e**, Typical  $I_{DS}$ – $V_{DS}$  curves at room temperature (**d**) and 77 K (**e**) for the Ni–MoS<sub>2</sub> FET. The nonlinear output characteristics at low temperatures suggest the existence of a Schottky barrier at the Ni–MoS<sub>2</sub> junction. **f**, Schottky barrier ( $\Phi_{SB}$ ) extracted by equation (3) as a function of the gate voltage for the Ni–MoS<sub>2</sub> FET.  $\Phi_{SB}$  is around 100 meV at the flatband voltage (the elbow of the curve)<sup>2</sup>. **g**, Typical  $I_{DS}$ – $V_{GS}$  curves of the Ti–MoS<sub>2</sub> FET. **h**, Typical  $I_{DS}$ – $V_{DS}$  curves at 77 K for the Ti–MoS<sub>2</sub> FET. Similar to the Ni–MoS<sub>2</sub> device, the Ti–MoS<sub>2</sub> FET exhibits both drain-current suppression and obviously nonlinear output characteristics at low temperatures, owing to the presence of a Schottky barrier at the Ti–MoS<sub>2</sub> interface. **i**, Extracted  $\Phi_{SB}$  for the Ti–MoS<sub>2</sub> FET as a function of the gate voltage, which is around 150 meV at the flatband voltage.

## Extended Data Fig. 2 Arrhenius plots and extraction of contact resistance.

**a, b,** Arrhenius plots of Ni-contacted (**a**) and Bi-contacted (**b**) monolayer (1L) MoS<sub>2</sub> FETs. The two transistors yield opposite slopes derived from equation (3), reflecting different metal–semiconductor junction configurations. The good agreement between the data extracted from the Ni–MoS<sub>2</sub> FET and the thermionic emission model suggests that there is thermally activated electronic transport at an energy barrier, that is, a Schottky barrier at the Ni–MoS<sub>2</sub> interface. By contrast, the deviation from

the thermionic emission model and nearly saturated slopes at low temperatures observed in the Bi–MoS<sub>2</sub> FET indicate the disappearance of an energy barrier for electron injection. The light blue curve represents the off state of the Bi–MoS<sub>2</sub> FET biased at a negative gate voltage of –60 V. The device at this condition shows a negative slope in the Arrhenius plot and the effective barrier height is extracted to be ~130 meV. This barrier originates from the energy difference between the Fermi level of the degenerate MoS<sub>2</sub> underneath Bi and the conduction band minimum of the depleted MoS<sub>2</sub> channel. **c**, Transfer characteristics,  $I_{DS}$ – $V_{GS}$ , of Bi-contacted monolayer MoS<sub>2</sub> FETs on 100-nm-thick SiN<sub>x</sub> with various channel lengths ( $L_{CH}$ ) at a  $V_{DS}$  of 0.5 V for the TLM study. **d**, Plots of total device resistance  $R_{TOT}$  (normalized by width) versus  $L_{CH}$  for the Bi–MoS<sub>2</sub> FETs at various carrier densities, from which the total contact resistance ( $2R_C$ ) can be extracted from the  $y$ -axis intercepts. Symbols are experimental data and lines are linear fits in **a** and **d**.

### Extended Data Fig. 3 SAED patterns of the freestanding Au/Bi/monolayer–MoS<sub>2</sub> and Au/Bi/amorphous carbon.

**a, e**, Schematics of the Au/Bi layer deposited directly on the monolayer (1L) MoS<sub>2</sub> (**a**) and amorphous carbon (a-carbon; **e**) in the TEM grid. **b–d**, SAED patterns of Au/Bi/1L–MoS<sub>2</sub> at three different locations. The [0001] zone axis of Bi is always observed in parallel to the electron beam throughout the whole sample. The diffraction spots of MoS<sub>2</sub> at 3.6 nm<sup>–1</sup> can be clearly identified. The in-plane rotations of MoS<sub>2</sub> with respect to the Bi (0001) plane are 30° (**b**), 4° (to the nearest Bi diffraction spots; **c**), and 8° (**d**). For most of the areas, Bi demonstrates homogeneous orientation, as shown in **b** and **d**, but polycrystalline areas can also be found, as shown in **c**. The selected-area aperture is 1 μm. **f–h**, The diffraction ring located at 3.0 nm<sup>–1</sup> is identified to be from Bi<sub>2</sub>O<sub>3</sub> polycrystal, as confirmed from the atomic structure of Bi<sub>2</sub>O<sub>3</sub> viewing at zone axes [110] (**g**), and its simulated diffraction pattern (**h**), demonstrating the diffraction pattern at 3.0 nm<sup>–1</sup>.

## Extended Data Fig. 4 DFT results for Sb–MoS<sub>2</sub>, Bi–MoS<sub>2</sub> with sulfur vacancy and Bi–WS<sub>2</sub>.

**a**, PLDOS of MoS<sub>2</sub> before (upper) and after (lower) contact with Sb. The valence band (VB) is shaded in light blue and conduction band (CB) in light red. The Fermi level ( $E_F$ ) is shifted from the valence band maximum inside the gap (before Bi contact) into the conduction band (after Bi contact). **b, c**, LDOS of MoS<sub>2</sub> with a sulfur vacancy (**b**) and WS<sub>2</sub> (**c**) when in contact with Bi. The Fermi level is pinned at the sulfur vacancy defect state inside the bandgap. This implies that a high-quality TMD crystal with a low defect density is critical to form ohmic contact to Bi. The result of LDOS of WS<sub>2</sub> in contact with Bi, predicting that ohmic contact can also be formed at the Bi–WS<sub>2</sub> interface owing to gap-state saturation.

## Extended Data Fig. 5 Characterization of transition metal dichalcogenide monolayers.

**a**, Raman characterization of MOCVD-grown monolayer MoS<sub>2</sub> (blue) and mechanically exfoliated WS<sub>2</sub> (green) and WSe<sub>2</sub> (red) monolayers for device fabrication. **b**, Raman characterization of Ni–MoS<sub>2</sub> and Au–MoS<sub>2</sub> interfaces. Samples are prepared using the mechanically tape-assisted exfoliation. No substantial shifts in A<sub>1g</sub> are observed for Ni and Au contacts. The shift in E<sup>1</sup><sub>2g</sub> is prevalently observed in the metal–MoS<sub>2</sub> system, probably originating from the strain induced at the metal–MoS<sub>2</sub> boundary. **c**, Deconvolution of the XPS spectra of S 2p and Bi 4f for pristine monolayer MoS<sub>2</sub> and Bi-contacted MoS<sub>2</sub>. The blueshifted core-level binding energies for the Bi-contacted MoS<sub>2</sub> indicate the upward shift of its Fermi level induced by the Bi contact, which is in good agreement with the DFT calculation and the Raman spectroscopy analysis. Moreover, the absence of characteristic peaks for Bi<sub>2</sub>O<sub>3</sub> suggest that the Bi contact is free of oxidation when in contact with MoS<sub>2</sub>, which is consistent with the TEM results (Fig. 3b and Extended Data Fig. 3).

## Extended Data Fig. 6 Transfer characteristics of monolayer WS<sub>2</sub> and WSe<sub>2</sub> FETs with Bi contacts.

**a, b**, Typical transfer characteristics of Bi–WS<sub>2</sub> (**a**) and Bi–WSe<sub>2</sub> (**b**) FETs on 100-nm SiN<sub>x</sub> at room temperature. Both transistors exhibit n-type conduction with a high  $I_{\text{ON}}/I_{\text{OFF}}$  ratio of  $>10^7$ .

## Extended Data Fig. 7 Monolayer MoS<sub>2</sub> transistors with very high $I_{\text{ON}}$ .

**a**, Transfer characteristics of a 35-nm  $L_{\text{CH}}$  Bi–MoS<sub>2</sub> FET. **b, c**, Transfer and output characteristics of a 50-nm  $L_{\text{CH}}$  Bi–MoS<sub>2</sub> FET. **d**, Output characteristics of a 120-nm  $L_{\text{CH}}$  Bi–MoS<sub>2</sub> FET. The excellent current-delivery capacities represent, to our knowledge, new records for monolayer MoS<sub>2</sub> at these device dimensions, outperform thicker TMD devices, and are comparable to three-dimensional semiconductor devices such as 90-nm node-strained Si and AlGaAs/InGaAs HEMT transistors with similar channel lengths<sup>39,40,46</sup>. Note that the required drain voltage for the ohmic Bi–monolayer MoS<sub>2</sub> FET to achieve a high  $I_{\text{ON}}$  is relatively small compared to previously reported high-performance TMD transistors (that is, typically  $V_{\text{DS}} > 2$  V with a thicker channel thickness)<sup>18,22,30,31,32,33,34,42,43,44,45</sup>. Inset, optical microscopic image of the device. **e**, Semi-logarithmic plot of the transfer characteristic of a different Bi–MoS<sub>2</sub> FET showing an excellent  $I_{\text{ON}}/I_{\text{OFF}}$  ratio of  $10^8$ . Insets, SEM image of a representative 150-nm  $L_{\text{CH}}$  Bi-contacted monolayer MoS<sub>2</sub> FET on 100-nm-thick SiN<sub>x</sub> and its channel region. **f**, Output characteristics of the same Bi–MoS<sub>2</sub> transistor as in **e**. The drain current saturates at a  $V_{\text{DS}}$  of  $\sim 1.5$  V and scales linearly with the gate voltage, which suggests that the electrons travelling in the monolayer MoS<sub>2</sub> channel reach its saturation velocity. The gate dielectrics of devices presented in this figure are 100-nm SiN<sub>x</sub>.

## Extended Data Fig. 8 Effects of TMD quality on the output characteristics.

**a, b**, Sample-quality-dependent contact performance for the case of monolayer MoS<sub>2</sub>. The room-temperature output characteristics of the Bi–MoS<sub>2</sub> transistors fabricated with a CVD-grown defective MoS<sub>2</sub> monolayer (**a**) and MOCVD-grown MoS<sub>2</sub> monolayer (**b**). Inset to **a**, optical image of a typical low-quality MoS<sub>2</sub> crystal with a non-clean surface and curved edges; scale bar, 5 μm. Inset to **b**, optical image of a typical high-quality MoS<sub>2</sub> crystal with a clean surface; scale bar, 10 μm. **c, d**, Output characteristics of Bi-contact transistors fabricated with fresh CVD-grown monolayer WS<sub>2</sub> (**c**) and monolayer WSe<sub>2</sub> (**d**) FETs, showing that the proposed gap-state-saturation-induced ohmic contact can also be formed on high-quality WS<sub>2</sub> and WSe<sub>2</sub> CVD samples. **e, f**, Room-temperature output characteristics (**e**) and transfer curves (**f**) of the Bi–WSe<sub>2</sub> transistors fabricated with an aged CVD-grown WSe<sub>2</sub> monolayer (low quality). Scale bar, 10 μm. **g, h**, Room-temperature output characteristics (**g**) and transfer curves (**h**) of the Bi–WSe<sub>2</sub> transistors fabricated with a fresh CVD-grown WSe<sub>2</sub> monolayer (medium quality). Scale bar, 10 μm. **i, j**, Room-temperature output characteristics (**i**) and transfer curves (**j**) of the Bi–WSe<sub>2</sub> transistors fabricated with a mechanically exfoliated WSe<sub>2</sub> monolayer (high quality). Scale bar, 5 μm. The results show a clear evolution from p-type conduction to enhanced n-type conduction with the sample quality improvement. These variations could be attributed to the gap-state pinning effect induced by the chalcogen vacancies (Extended Data Fig. 4b). Insets to **f, h** and **j** are the optical images of a typical low-quality CVD WSe<sub>2</sub> crystal with an obviously defective surface (**f**), a medium-quality CVD WSe<sub>2</sub> with an irregular crystal shape (**h**), and a high-quality, freshly exfoliated WSe<sub>2</sub> with a clean surface (**j**).

## Extended Data Fig. 9 Performance projection of Bi–monolayer TMD technology.

**a**, Fraction of channel resistance ( $R_{\text{CH}}$ , green line) and total contact resistance ( $2R_C$ , blue line) with respect to the total device resistance ( $R_{\text{TOT}} = R_{\text{CH}} + 2R_C$ ) in Bi–MoS<sub>2</sub> FETs as a function of the channel length ( $L_{\text{CH}}$ ) at room temperature based on the device and material parameters extracted from Fig. 2c. The dashed lines show the quantum limit, representing the minimum  $R_C$  that can be achieved in a transistor. The quantum limit  $R_C$  is  $\pi h/(4q^2k_F) \approx 0.036(n_{2D})^{-0.5} \text{ k}\Omega \mu\text{m}$ , which is determined by the quantum resistance ( $h/2q^2 \approx 12.9 \text{ k}\Omega$ ) and the number of conducting modes per channel width ( $k_F/\pi$ ), which is related to the 2D sheet carrier density ( $n_{2D}$ , in units of  $10^{13} \text{ cm}^{-2}$ )<sup>2</sup>. **b**, Projection of  $2R_C$  as a function of the contact length ( $L_C$ ) in monolayer TMD transistors based on the transmission line model with various metal contacts at room temperature. The vertical dashed line represents the current transfer length ( $L_T$ ) for each metal contact. The results are calculated based on the data extracted from previously reported TLM results<sup>13,47</sup>. As can be seen,  $R_C$  increases as  $L_C$  becomes comparable to  $L_T$ , owing to the current-crowding effect (equation (4))<sup>18</sup>. Note that In, hexagonal boron nitride (hBN)/Co, Ni and high-vacuum Au contacts to monolayer MoS<sub>2</sub> exhibit similar values of  $R_C$  ( $\sim 3\text{--}6 \text{ k}\Omega \mu\text{m}$ ) and  $\rho_C$  ( $\sim 10^{-6}\text{--}10^{-5} \Omega \text{ cm}^2$ )<sup>13,14,18,50</sup>. **c**, Required minimum  $V_{\text{DS}}$  for Bi-contacted monolayer TMD transistors to work in the velocity saturation regime using our best  $R_C$  of  $123 \Omega \mu\text{m}$  and a theoretical  $F_C$  of  $1.15 \times 10^5 \text{ V cm}^{-1}$ . The  $V_{\text{DD}}$  required by IRDS is also plotted. **d**, The required  $V_{\text{DS}}$  to bias monolayer MoS<sub>2</sub> transistors in the velocity-saturation regime for different contact technologies.

### Extended Data Table 1 Key performance metrics of representative devices

[Full size table](#)

## Supplementary information

[Peer Review File](#)

# Rights and permissions

[Reprints and Permissions](#)

## About this article



## Cite this article

Shen, PC., Su, C., Lin, Y. *et al.* Ultralow contact resistance between semimetal and monolayer semiconductors. *Nature* **593**, 211–217 (2021). <https://doi.org/10.1038/s41586-021-03472-9>

[Download citation](#)

- Received: 01 July 2020
- Accepted: 18 March 2021
- Published: 12 May 2021
- Issue Date: 13 May 2021
- DOI: <https://doi.org/10.1038/s41586-021-03472-9>

## Comments

By submitting a comment you agree to abide by our [Terms](#) and [Community Guidelines](#). If you find something abusive or that does not comply with our terms or guidelines please flag it as inappropriate.

[Access through your institution](#)

[Change institution](#)

## Buy or subscribe

---

This article was downloaded by **calibre** from <https://www.nature.com/articles/s41586-021-03472-9>

| [Section menu](#) | [Main menu](#) |

- Article
- [Published: 12 May 2021](#)

# A dynamic stability design strategy for lithium metal solid state batteries

- [Luhan Ye](#) [ORCID: orcid.org/0000-0002-2684-424X<sup>1</sup>](#) &
- [Xin Li](#) [ORCID: orcid.org/0000-0001-9390-0830<sup>1</sup>](#)

[Nature](#) volume 593, pages 218–222 (2021) [Cite this article](#)

- 4688 Accesses
- 204 Altmetric
- [Metrics details](#)

## Subjects

- [Batteries](#)

## Abstract

A solid-state electrolyte is expected to suppress lithium (Li) dendrite penetration with high mechanical strength<sup>1,2,3,4</sup>. However, in practice it still remains challenging to realise a lithium metal anode for batteries, because micrometre- or submicrometre-sized cracks in ceramic pellets can frequently be generated during battery assembly or long-time cycling<sup>3,5</sup>. Once cracks form, lithium dendrite penetration is inevitable<sup>6,7</sup>. Here we describe a solid-state battery design with a hierarchy of interface stabilities

(to lithium metal responses), to achieve an ultrahigh current density with no lithium dendrite penetration. Our multilayer design has the structure of a less-stable electrolyte sandwiched between more-stable solid electrolytes, which prevents any lithium dendrite growth through well localized decompositions in the less stable electrolyte layer. A mechanism analogous to the expansion screw effect is proposed, whereby any cracks are filled by dynamically generated decompositions that are also well constrained, probably by the ‘anchoring’ effect the decompositions induce. The cycling performance of the lithium metal anode paired with a  $\text{LiNi}_{0.8}\text{Mn}_{0.1}\text{Co}_{0.1}\text{O}_2$  cathode is very stable, with an 82 per cent capacity retention after 10,000 cycles at a 20C rate (8.6 milliamps per centimetre squared) and 81.3 per cent capacity retention after 2,000 cycles at a 1.5C rate (0.64 milliamps per centimetre squared). Our design also enables a specific power of 110.6 kilowatts per kilogram and specific energy up to 631.1 watt hours per kilogram at the micrometre-sized cathode material level.

[Access through your institution](#)

[Change institution](#)

[Buy or subscribe](#)

## Access options

Subscribe to Journal

Get full journal access for 1 year

\$199.00

only \$3.90 per issue

[Subscribe](#)

All prices are NET prices.

VAT will be added later in the checkout.

Tax calculation will be finalised during checkout.

Rent or Buy article

Get time limited or full article access on ReadCube.

from \$8.99

[Rent or Buy](#)

All prices are NET prices.

### **Additional access options:**

- [Log in](#)
- [Access through your institution](#)
- [Learn about institutional subscriptions](#)

**Fig. 1: Superior symmetric battery cycling performance from the multilayer design.**

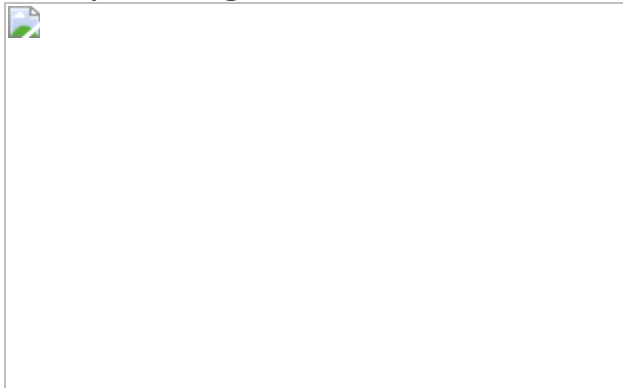


**Fig. 2: Structure, chemistry and morphology of solid electrolyte after cycling.**

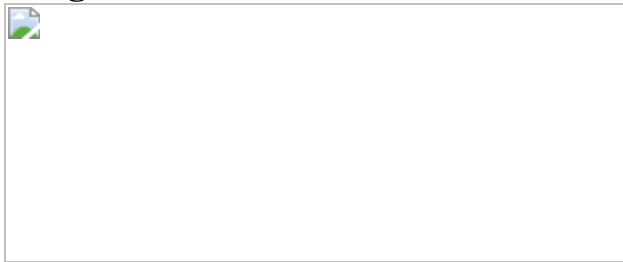


**Fig. 3: Cycling performance of solid-state batteries with the multilayer design.**

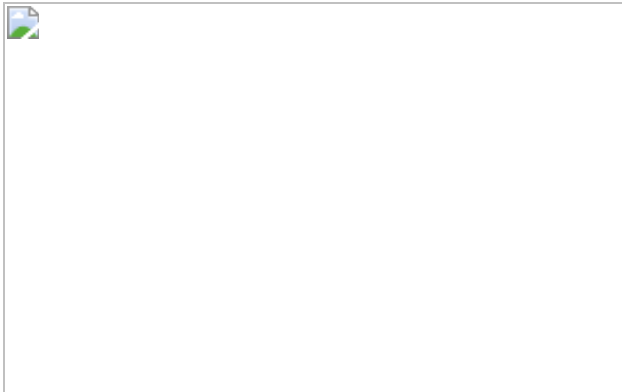
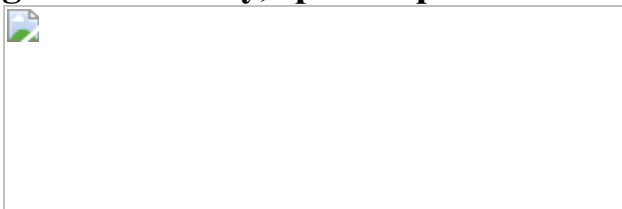


**Fig. 4: Versatility, specific power and energy of the multilayer design.**



## Data availability

The data that support the findings of this study are available from the corresponding author upon reasonable request.

## References

1. 1.

Goodenough, J. B. & Park, K. S. The Li-ion rechargeable battery: a perspective. *J. Am. Chem. Soc.* **135**, 1167–1176 (2013).

[CAS Article](#) [Google Scholar](#)

2. 2.

Liu, J. et al. Pathways for practical high-energy long-cycling lithium metal batteries. *Nat. Energy* **4**, 180–186 (2019).

[ADS](#) [CAS Article](#) [Google Scholar](#)

3. 3.

Su, Y. et al. A more stable lithium anode by mechanical constriction for solid state batteries. *Energy Environ. Sci.* **13**, 908–916 (2020).

[CAS](#) [Article](#) [Google Scholar](#)

4. 4.

Chen, Y. et al. Li metal deposition and stripping in a solid-state battery via Coble creep. *Nature* **578**, 251–255 (2020).

[ADS](#) [CAS](#) [Article](#) [Google Scholar](#)

5. 5.

Kasemchainan, J. et al. Critical stripping current leads to dendrite formation on plating in lithium anode solid electrolyte cells. *Nat. Mater.* **18**, 1105–1111 (2019).

[ADS](#) [CAS](#) [Article](#) [Google Scholar](#)

6. 6.

Tu, Q., Barroso-Luque, L., Shi, T. & Ceder, G. Electrodeposition and mechanical stability at lithium-solid electrolyte interface during plating in solid-state batteries. *Cell Rep. Phys. Sci.* **1**, 100106 (2020).

[Article](#) [Google Scholar](#)

7. 7.

Qi, Y., Ban, C. & Harris, S. J. A new general paradigm for understanding and preventing Li metal penetration through solid electrolytes. *Joule* **4**, 2599–2608 (2020).

[CAS](#) [Article](#) [Google Scholar](#)

8. 8.

Xu, C. et al. Bulk fatigue induced by surface reconstruction in layered Ni-rich cathodes for Li-ion batteries. *Nat. Mater.* **20**, 84–92 (2021).

[ADS](#) [CAS](#) [Article](#) [Google Scholar](#)

9. 9.

Xin, F. et al. Li-Nb-O coating/substitution enhances the electrochemical performance of the  $\text{LiNi}_{0.8}\text{Mn}_{0.1}\text{Co}_{0.1}\text{O}_2$  (NMC 811) cathode. *ACS Appl. Mater. Interfaces* **11**, 34889–34894 (2019).

[CAS](#) [Article](#) [Google Scholar](#)

10. 10.

Sallard, S., Billaud, J., Sheptyakov, D., Novák, P. & Villevieille, C. Cr-doped Li-rich nickel cobalt manganese oxide as a positive electrode material in Li-ion batteries to enhance cycling stability. *ACS Appl. Energy Mater.* **3**, 8646–8657 (2020).

[Article](#) [Google Scholar](#)

11. 11.

Wenzel, S. et al. Direct observation of the interfacial instability of the fast ionic conductor  $\text{Li}_{10}\text{GeP}_2\text{S}_{12}$  at the lithium metal anode. *Chem. Mater.* **28**, 2400–2407 (2016).

[CAS](#) [Article](#) [Google Scholar](#)

12. 12.

Kamaya, N. et al. A lithium superionic conductor. *Nat. Mater.* **10**, 682–686 (2011).

[ADS](#) [CAS](#) [Article](#) [Google Scholar](#)

13. 13.

Adeli, P. et al. Boosting solid-state diffusivity and conductivity in lithium superionic argyrodites by halide substitution. *Angew. Chem. Int. Ed.* **58**, 8681–8686 (2019).

[CAS](#) [Article](#) [Google Scholar](#)

14. 14.

Lee, Y. G. et al. High-energy long-cycling all-solid-state lithium metal batteries enabled by silver–carbon composite anodes. *Nat. Energy* **5**, 299–308 (2020).

[ADS](#) [CAS](#) [Article](#) [Google Scholar](#)

15. 15.

Wenzel, S., Sedlmaier, S. J., Dietrich, C., Zeier, W. G. & Janek, J. Interfacial reactivity and interphase growth of argyrodite solid electrolytes at lithium metal electrodes. *Solid State Ion.* **318**, 102–112 (2018).

[CAS](#) [Article](#) [Google Scholar](#)

16. 16.

Auvergniot, J. et al. Interface stability of argyrodite  $\text{Li}_6\text{PS}_5\text{Cl}$  toward  $\text{LiCoO}_2$ ,  $\text{LiNi}_{1/3}\text{Co}_{1/3}\text{Mn}_{1/3}\text{O}_2$ , and  $\text{LiMn}_2\text{O}_4$  in bulk all-solid-state batteries. *Chem. Mater.* **29**, 3883–3890 (2017).

[CAS](#) [Article](#) [Google Scholar](#)

17. 17.

Krauskopf, T., Richter, F. H., Zeier, W. G. & Janek, J. Physicochemical concepts of the lithium metal anode in solid-state batteries. *Chem. Rev.* **120**, 7745–7794 (2020).

[CAS](#) [Article](#) [Google Scholar](#)

18. 18.

Wu, F., Fitzhugh, W., Ye, L., Ning, J. & Li, X. Advanced sulfide solid electrolyte by core-shell structural design. *Nat. Commun.* **9**, 4037 (2018).

[ADS](#) [Article](#) [Google Scholar](#)

19. 19.

Kato, Y. et al. High-power all-solid-state batteries using sulfide superionic conductors. *Nat. Energy* **1**, 16030 (2016).

[ADS](#) [CAS](#) [Article](#) [Google Scholar](#)

20. 20.

Ye, L. et al. Toward higher voltage solid-state batteries by metastability and kinetic stability design. *Adv. Energy Mater.* **10**, 2001569 (2020).

[CAS](#) [Article](#) [Google Scholar](#)

21. 21.

Fitzhugh, W., Wu, F., Ye, L., Su, H. & Li, X. Strain-stabilized ceramic-sulfide electrolytes. *Small* **15**, 1901470 (2019).

[Article](#) [Google Scholar](#)

22. 22.

Saroha, R., Panwar, A. K., Sharma, Y., Tyagi, P. K. & Ghosh, S. Development of surface functionalized ZnO-doped LiFePO<sub>4</sub>/C composites as alternative cathode material for lithium ion batteries. *Appl. Surf. Sci.* **394**, 25–36 (2017).

[ADS](#) [CAS](#) [Article](#) [Google Scholar](#)

23. 23.

Jin, S. et al. Covalently connected carbon nanostructures for current collectors in both the cathode and anode of Li–S Batteries. *Adv. Mater.* **28**, 9094–9102 (2016).

[CAS](#) [Article](#) [Google Scholar](#)

24. 24.

Kang, B. & Ceder, G. Battery materials for ultrafast charging and discharging. *Nature* **458**, 190–193 (2009).

[ADS](#) [CAS](#) [Article](#) [Google Scholar](#)

25. 25.

Wang, S. et al. Lithium chlorides and bromides as promising solid-state chemistries for fast ion conductors with good electrochemical stability. *Angew. Chem. Int. Ed.* **58**, 8039–8043 (2019).

[CAS](#) [Article](#) [Google Scholar](#)

26. 26.

Fitzhugh, W., Ye, L. & Li, X. The effects of mechanical constriction on the operation of sulfide based solid-state batteries. *J. Mater. Chem. A* **7**, 23604–23627 (2019).

27. 27.

Schwiertet, T. K. et al. Clarifying the relationship between redox activity and electrochemical stability in solid electrolytes. *Nat. Mater.* **19**, 428–435 (2020).

[ADS](#) [CAS](#) [Article](#) [Google Scholar](#)

[Download references](#)

# Acknowledgements

The work was supported by the Dean's Competitive Fund for Promising Scholarship at Harvard University and the Harvard Data Science Initiative Competitive Research Fund. The SEM and XPS experiments were conducted at the Center for Nanoscale Systems (CNS) at Harvard University, supported by the National Science Foundation.

# Author information

## Affiliations

1. John A. Paulson School of Engineering and Applied Sciences, Harvard University, Cambridge, MA, USA

Luhan Ye & Xin Li

## Authors

1. Luhan Ye

[View author publications](#)

You can also search for this author in [PubMed](#) [Google Scholar](#)

2. Xin Li

[View author publications](#)

You can also search for this author in [PubMed](#) [Google Scholar](#)

## Contributions

X.L. and L.Y. conceived the multilayer design. X.L. supervised all aspects of the research. L.Y. performed the experiments. L.Y. and X.L. analysed the results and wrote the manuscript.

## Corresponding author

Correspondence to [Xin Li](#).

## Ethics declarations

### Competing interests

X.L. and L.Y. report a US provisional patent application of Batteries with Solid State Electrolyte Multilayers filed on 30 October 2020. Application serial no. 63/108,075.

## Additional information

**Peer review information** *Nature* thanks the anonymous reviewer(s) for their contribution to the peer review of this work. Peer reviewer reports are available.

**Publisher's note** Springer Nature remains neutral with regard to jurisdictional claims in published maps and institutional affiliations.

## Extended data figures and tables

### [Extended Data Fig. 1 SEM images of LPSCl, LGPS and LS<sub>2</sub>PS particles.](#)

**a–c**, SEM images of LPSCl (**a**), LGPS (**b**) and LS<sub>2</sub>PS (**c**) particles.

### [Extended Data Fig. 2 Electrochemical voltage profiles, optical and SEM images of lithium discharged asymmetric batteries with different electrolytes.](#)

Asymmetric batteries with Li/G as anode (lithium capacity loading = 3 mAh cm<sup>-2</sup>), stainless steel (SS) current collector as cathode, and solid electrolytes as separator were assembled. Lithium was enforced to deposit on the surface of solid electrolytes at 0.25 mA cm<sup>-2</sup>. Different electrochemical behaviours and surface information were observed. **a**,

Short-circuiting happened immediately after lithium was deposited on the surface of pure LPSCl pellet. A metallic colour (silver or grey) was observed from the optical image and a small level of cracking was observed from the SEM image. **b**, Voltage ramping up quickly after lithium was deposited on the surface of pure LGPS pellet in a few hours. Decomposition (dark black) was observed from the optical image and no crack was observed from the SEM image. **c**, Voltage ramping up gradually, reaching cut-off voltage after lithium was fully deposited on the surface of the LGPS separated LPSCl pellet. Metallic colour (silver or grey) on large area was observed from the optical image and cracks were observed from the SEM image.

**Extended Data Fig. 3 XPS characterization on the dark region of LGPS and LPSCl after lithium discharge.**

**a–c**, XPS data of the black region on the LGPS surface after lithium discharging at  $0.25 \text{ mA cm}^{-2}$  (shown in Supplementary Fig. 2b) with the chemical information of S (**a**), P (**b**) and Ge (**c**). **d–f**, XPS data of the silver region on the LPSCl surface after lithium discharging (shown in Supplementary Fig. 2c) with the chemical information of S (**d**), P (**e**) and Cl (**f**). The beam size of XPS is  $400 \mu\text{m}$ .

**Extended Data Fig. 4 Performance difference of LSPS as the single layer and the central layer of multilayer in symmetric battery configurations.**

**a**, Symmetric battery with  $\text{Li}_{9.54}\text{Si}_{1.74}(\text{P}_{0.9}\text{Sb}_{0.1})_{1.44}\text{S}_{11.7}\text{Cl}_{0.3}$  (LSPS) as electrolyte and graphite covered lithium (Li/G) as electrodes. **b**, Symmetric battery with the combination of  $\text{Li}_{9.54}\text{Si}_{1.74}(\text{P}_{0.9}\text{Sb}_{0.1})_{1.44}\text{S}_{11.7}\text{Cl}_{0.3}$  (LSPS) and  $\text{Li}_{5.5}\text{PS}_{4.5}\text{Cl}_{1.5}$  (LPSCl) in the configuration of LPSCl–LSPS–LPSCl as electrolyte and graphite covered lithium as electrodes.

**Extended Data Fig. 5 Cycling performance of symmetric batteries with LGPS or LPSCl as the single solid electrolyte layer.**

**a**, High rate ( $10 \text{ mA cm}^{-2}$ ) cycling for  $\text{Li}_{10}\text{Ge}_1\text{P}_2\text{S}_{12}$  (LGPS) symmetric battery with Li/G as electrodes. The over potential starts from 0.6 V and quickly ramp up to over 1.5 V in the first few cycles. **b**, High rate ( $15 \text{ mA cm}^{-2}$ ) cycling for LGPS symmetric battery with Li/G as electrodes. The over potential ramping up to over 5 V in the first cycle. **c**, Symmetric battery with LPSCl as electrolyte and Li/G as electrodes, cycling at  $0.25 \text{ mA cm}^{-2}$ . Short-circuiting shows up in the first two cycles.

**Extended Data Fig. 6 Optical image, XRD and XPS of cross-sections of symmetric batteries before and after cycling.**

**a**, Optical image of cross-section of Li/G-LPSCl-LGPS-LPSCl-G/Li after 300 h cycling at  $0.25 \text{ mA cm}^{-2}$  at room temperature, showing another region without decomposition. **b**, Post-treated image of **a** in only black and white. **c**, Optical image of cross-section of Li/G–LPSCl–LGPS–LPSCl–G/Li after 30 cycles at  $20 \text{ mA cm}^{-2}$  at  $55^\circ\text{C}$ . XPS spot size is marked in the black region for a comparison with the size of the black region. **d**, Optical image of the cross-section of the LPSCl–LGPS–LPSCl pellet before cycling. **e**, Optical image of the cross-section of the LPSCl–LGPS–LPSCl pellet after 300 h cycling at  $0.25 \text{ mA cm}^{-2}$  (**e1**) and 30 cycles at  $20 \text{ mA cm}^{-2}$  (**e2**). The images in **d** and **e** are from the same pellet in **a** and **c** in a larger view, which were taken by an optical microscope in the glovebox. **f**, XRD of LGPS before and after cycling at  $0.25 \text{ mA cm}^{-2}$  for 300 h, with features of XRD peaks shown in **g1–g5**. **h–j**, XPS measurement of S 2p (**h**), P 2p (**i**) and Ge 3d (**j**) on the black region in the cross-section of the sandwich pellet after battery cycling at  $0.25 \text{ mA cm}^{-2}$  for 300 h. The beam size of the XPS is  $70 \mu\text{m}$ .

**Extended Data Fig. 7 Morphology difference of LGPS and LPSCl before and after cycling.**

SEM images of the solid electrolytes before cycling (first row), and after cycling for 100 h (second row) and 300 h (third row) in the region of LPSCl, LGPS, and their transition areas. The fourth column: LPSCl side with a  $10\text{-}\mu\text{m}$  scale bar. The SEM images were from the symmetric battery in the configuration of Li/G–LPSCl–LGPS–LPSCl–G/Li.

## Extended Data Fig. 8 Half-battery cycling performance using pure LGPS and/or LPSCl as electrolytes.

**a**, The discharging profiles of graphite covered Li paired with  $\text{LiNi}_{0.8}\text{Mn}_{0.1}\text{Co}_{0.1}\text{O}_2$  (Li/G-NMC811) batteries, using  $\text{Li}_{5.5}\text{PS}_{4.5}\text{Cl}_{1.5}$  (LPSCl, green 10C),  $\text{Li}_{9.54}\text{Si}_{1.74}(\text{P}_{0.9}\text{Sb}_{0.1})_{1.44}\text{S}_{11.7}\text{Cl}_{0.3}$  (LSPS, blue 10C), and multilayer LPSCl-LSPS-LPSCl configuration (purple 10C, black 1C, red 0.1C) as the electrolyte. The batteries were first charged at 0.1C and then discharged at various rates at room temperature. **b, c**, The cycling performance of the same multilayer battery at 5C (**b**) and 10C (**c**) in the range of 2.5–4.3 V in the environment without humidity control (55 °C). **d, e**, The first charge and discharge profiles of Li-LiCoO<sub>2</sub> (Li-LCO) batteries with (**d**)  $\text{Li}_{5.5}\text{PS}_{4.5}\text{Cl}_{1.5}$  (LPSCl) and (**e**)  $\text{Li}_{10}\text{Ge}_1\text{P}_2\text{S}_{12}$  (LGPS) as the electrolyte. Uncoated LCO and  $\text{LiNbO}_3$ -coated LCO is applied for LPSCl and LGPS, respectively. **f, g**, The first charge and discharge profiles of graphite covered Li paired with  $\text{LiNi}_{0.8}\text{Mn}_{0.1}\text{Co}_{0.1}\text{O}_2$  (Li/G-NMC811) batteries with LPSCl as the electrolyte at (**f**) 0.3C and (**g**) 0.5C; along with the cycling performance at (**h**) 0.3C (LCO at 0.1C is also shown) and (**i**) 0.5C. All batteries in **d–i** were tested at room temperature. The battery configuration and materials used are summarized in Supplementary Table 2. **j**, Cycling performance of solid-state battery with multilayer electrolytes at different Li/graphite capacity ratios of 10:1, 5:1 and 2.5:1. **k**, Cycling performance of solid-state battery with multilayer electrolytes under different operating pressures of 50–75 MPa, 150 MPa and 250 MPa. **l**, Cycling performance of solid-state battery with thin multilayer: Li/G–LPSCl (100 μm)–LSPS (50 μm)–LPSCl (50 μm)–NMC811. **m**, High-power voltage profile of the Li/G–LPSCl–LSPS–LPSCl–NMC811 battery at 100C–500C at 55 °C with a cut-off voltage of 2–4.3 V. Red, blue and pink curves are from batteries first charged at 0.5C and then discharged at high C rates, and black curves are at 100C charge and discharge. 1C = 0.43 mA cm<sup>-2</sup>.

## **Extended Data Table 1 Mechanical and (electro)chemical properties of different electrolytes**

[Full size table](#)

**Extended Data Table 2 Battery configurations and materials ratios applied in this work**

[Full size table](#)

## Supplementary information

[Peer Review File](#)

## Rights and permissions

[Reprints and Permissions](#)

## About this article



Check for  
updates

## Cite this article

Ye, L., Li, X. A dynamic stability design strategy for lithium metal solid state batteries. *Nature* **593**, 218–222 (2021). <https://doi.org/10.1038/s41586-021-03486-3>

[Download citation](#)

- Received: 06 November 2020
- Accepted: 23 March 2021
- Published: 12 May 2021
- Issue Date: 13 May 2021
- DOI: <https://doi.org/10.1038/s41586-021-03486-3>

# Comments

By submitting a comment you agree to abide by our [Terms](#) and [Community Guidelines](#). If you find something abusive or that does not comply with our terms or guidelines please flag it as inappropriate.

[Access through your institution](#)

[Change institution](#)

[Buy or subscribe](#)

---

This article was downloaded by **calibre** from <https://www.nature.com/articles/s41586-021-03486-3>

| [Section menu](#) | [Main menu](#) |

- Article
- [Published: 12 May 2021](#)

# Skeletal editing through direct nitrogen deletion of secondary amines

- [Sean H. Kennedy](#) ORCID: [orcid.org/0000-0002-7422-3114<sup>1</sup>](https://orcid.org/0000-0002-7422-3114),
- [Balu D. Dherange](#) ORCID: [orcid.org/0000-0002-4123-5012<sup>1</sup>](https://orcid.org/0000-0002-4123-5012)
- [Kathleen J. Berger](#) ORCID: [orcid.org/0000-0002-7959-6331<sup>1</sup>](https://orcid.org/0000-0002-7959-6331)
- [Mark D. Levin](#) ORCID: [orcid.org/0000-0002-4461-363X<sup>1</sup>](https://orcid.org/0000-0002-4461-363X)

*Nature* volume **593**, pages 223–227 (2021) [Cite this article](#)

- 9859 Accesses
- 232 Altmetric
- [Metrics details](#)

## Subjects

- [Synthetic chemistry methodology](#)
- [Reaction mechanisms](#)

## Abstract

Synthetic chemistry aims to build up molecular complexity from simple feedstocks<sup>1</sup>. However, the ability to exert precise changes that manipulate the connectivity of the molecular skeleton itself remains limited, despite possessing substantial potential to expand the accessible chemical space<sup>2,3</sup>.

Here we report a reaction that ‘deletes’ nitrogen from organic molecules. We show that *N*-pivaloyloxy-*N*-alkoxyamides, a subclass of anomeric amides, promote the intermolecular activation of secondary aliphatic amines to yield intramolecular carbon–carbon coupling products. Mechanistic experiments indicate that the reactions proceed via isodiazene intermediates that extrude the nitrogen atom as dinitrogen, producing short-lived diradicals that rapidly couple to form the new carbon–carbon bond. The reaction shows broad functional-group tolerance, which enables the translation of routine amine synthesis protocols into a strategy for carbon–carbon bond constructions and ring syntheses. This is highlighted by the use of this reaction in the syntheses and skeletal editing of bioactive compounds.

[Access through your institution](#)

[Change institution](#)

[Buy or subscribe](#)

## Access options

Subscribe to Journal

Get full journal access for 1 year

\$199.00

only \$3.90 per issue

[Subscribe](#)

All prices are NET prices.

VAT will be added later in the checkout.

Tax calculation will be finalised during checkout.

Rent or Buy article

Get time limited or full article access on ReadCube.

from \$8.99

[Rent or Buy](#)

All prices are NET prices.

**Additional access options:**

- [Log in](#)
- [Access through your institution](#)
- [Learn about institutional subscriptions](#)

**Fig. 1: Background.**

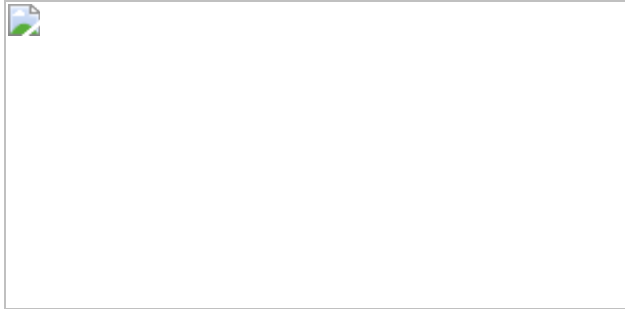


**Fig. 2: Development of an anomeric amide reagent.**

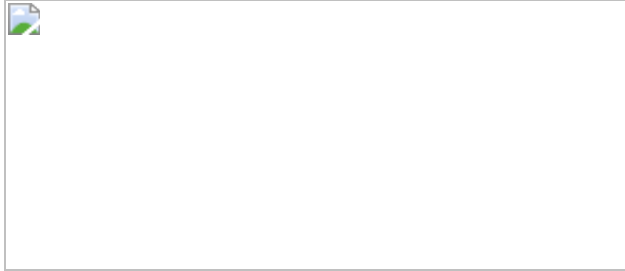


**Fig. 3: Scope of the nitrogen-deletion reaction promoted by reagent 1c.**



**Fig. 4: Mechanistic experiments.**



## Data availability

All data are available from the corresponding author upon reasonable request.

## References

1. 1.

Corey, E. J. & Cheng, X.-M. *The Logic of Chemical Synthesis* (Wiley, 1995).

2. 2.

Blakemore, D. C. et al. Organic synthesis provides opportunities to transform drug discovery. *Nat. Chem.* **10**, 383–394 (2018).

[CAS](#) [Article](#) [Google Scholar](#)

3. 3.

Huigens, R. W., III et al. A ring-distortion strategy to construct stereochemically complex and structurally diverse compounds from natural products. *Nat. Chem.* **5**, 195–202 (2013).

[CAS](#) [Article](#) [Google Scholar](#)

4. 4.

Szpileman, A. M. & Carreira, E. M. Probing the biology of natural products: molecular editing by diverted total synthesis. *Angew. Chem. Int. Ed.* **49**, 9592–9628 (2010).

[CAS](#) [Article](#) [Google Scholar](#)

5. 5.

Cernak, T., Dykstra, K. D., Tyagarajan, S., Vachal, P. & Krska, S. W. The medicinal chemist's toolbox for late stage functionalization of drug-like molecules. *Chem. Soc. Rev.* **45**, 546–576 (2016).

[CAS](#) [Article](#) [Google Scholar](#)

6. 6.

Hu, Y., Stumpfe, D. & Bajorath, J. Recent advances in scaffold hopping. *J. Med. Chem.* **60**, 1238–1246 (2017).

[CAS](#) [Article](#) [Google Scholar](#)

7. 7.

Mahjour, B., Shen, Y., Liu, W. & Cernak, T. A map of the amine–carboxylic acid coupling system. *Nature* **580**, 71–75 (2020).

[ADS](#) [CAS](#) [Article](#) [Google Scholar](#)

8. 8.

Cao, Z.-C. & Shi, Z.-J. Deoxygenation of ethers to form carbon–carbon bonds via nickel catalysis. *J. Am. Chem. Soc.* **139**, 6546–6549 (2017).

[CAS](#) [Article](#) [Google Scholar](#)

9. 9.

Roque, J. B., Kuroda, Y., Göttemann, L. T. & Sarpong, R. Deconstructive diversification of cyclic amines. *Nature* **564**, 244–248 (2018).

[ADS](#) [CAS](#) [Article](#) [Google Scholar](#)

10. 10.

Smaligo, A. J. et al. Hydrodealkenylative C( $sp^3$ )–C( $sp^2$ ) bond fragmentation. *Science* **364**, 681–685 (2019).

[ADS](#) [CAS](#) [Article](#) [Google Scholar](#)

11. 11.

Fier, P. S., Kim, S. & Maloney, K. M. Reductive cleavage of secondary sulfonamides: converting terminal functional groups into versatile synthetic handles. *J. Am. Chem. Soc.* **141**, 18416–18420 (2019).

[CAS](#) [Article](#) [Google Scholar](#)

12. 12.

Xu, Y. et al. Deacylative transformations of ketones via aromatization-promoted C–C bond activation. *Nature* **567**, 373–378 (2019).

[ADS](#) [CAS](#) [Article](#) [Google Scholar](#)

13. 13.

Silva Jr, L. F. in *Stereoselective Synthesis of Drugs and Natural Products* Vol. 1 (eds Andrushko, N. & Andrushko, V.) Ch. 18 (Wiley, 2013).

14. 14.

Donald, J. R. & Unsworth, W. P. Ring-expansion reactions in the synthesis of macrocycles and medium-sized rings. *Chem. Eur. J.* **23**, 8780–8799 (2017).

[CAS](#) [Article](#) [Google Scholar](#)

15. 15.

Glover, S. A. Anomeric amides — Structure, properties and reactivity. *Tetrahedron* **54**, 7229–7271 (1998).

[CAS](#) [Article](#) [Google Scholar](#)

16. 16.

Glover, S. A. & Mo, G. Hindered ester formation by S<sub>N</sub>2 azidation of *N*-acetoxy-*N*-alkoxyamides and *N*-alkoxy-*N*-chloroamides—novel application of HERON rearrangements. *J. Chem. Soc., Perkin Trans. 2* 1728–1739 (2002).

[Article](#) [Google Scholar](#)

17. 17.

Hinman, R. L. & Hamm, K. L. The oxidation of 1,1-dibenzylhydrazines. *J. Am. Chem. Soc.* **81**, 3294–3297 (1959).

[CAS Article](#) [Google Scholar](#)

18. 18.

Hinsberg, W. D. & Dervan, P. B. Synthesis and direct spectroscopic observation of a 1,1-dialkyldiazene. Infrared and electronic spectrum of *N*-(2,2,6,6-tetramethylpiperidyl)nitrene. *J. Am. Chem. Soc.* **100**, 1608–1610 (1978).

[CAS Article](#) [Google Scholar](#)

19. 19.

Kuznetsov, M. A. & Ioffe, B. V. The present state of the chemistry of aminonitrenes and oxynitrenes. *Russ. Chem. Rev.* **58**, 732 (1989).

[ADS Article](#) [Google Scholar](#)

20. 20.

Urry, W. H., Kruse, H. W. & McBride, W. R. Novel organic reactions of the intermediate from the two-electron oxidation of 1,1-dialkyl hydrazines in acid. *J. Am. Chem. Soc.* **79**, 6568–6569 (1957).

[CAS Article](#) [Google Scholar](#)

21. 21.

Lemal, D. M. & Rave, T. W. Diazenes from Angeli's Salt. *J. Am. Chem. Soc.* **87**, 393–394 (1965).

[CAS Article](#) [Google Scholar](#)

22. 22.

Zou, X., Zou, J., Yang, L., Li, G. & Lu, H. Thermal rearrangement of sulfamoyl azides: reactivity and mechanistic study. *J. Org. Chem.* **82**, 4677–4688 (2017).

[CAS](#) [Article](#) [Google Scholar](#)

23. 23.

Brown, D. G. & Boström, J. Analysis of past and present synthetic methodologies on medicinal chemistry: where have all the new reactions gone? *J. Med. Chem.* **59**, 4443–4458 (2016).

[CAS](#) [Article](#) [Google Scholar](#)

24. 24.

Berger, K. J. & Levin, M. D. Reframing primary alkyl amines as aliphatic building blocks. *Org. Biomol. Chem.* **19**, 11–36 (2021).

[CAS](#) [Article](#) [Google Scholar](#)

25. 25.

Plunkett, S., Basch, C. H., Santana, S. O. & Watson, M. P. Harnessing alkylpyridinium salts as electrophiles in deaminative alkyl–alkyl cross-couplings. *J. Am. Chem. Soc.* **141**, 2257–2262 (2019).

[CAS](#) [Article](#) [Google Scholar](#)

26. 26.

Brown, H. C. & Okamoto, Y. Electrophilic substituent constants. *J. Am. Chem. Soc.* **80**, 4979–4987 (1958).

[CAS](#) [Article](#) [Google Scholar](#)

27. 27.

Banert, K. et al. Steric hindrance underestimated: it is a long, long way to tri-*tert*-alkylamines. *J. Org. Chem.* **83**, 5138–5148 (2018).

[CAS Article](#) [Google Scholar](#)

28. 28.

Procopiou, G., Lewis, W., Harbottle, G. & Stockman, R. A. Cycloaddition of chiral *tert*-butanesulfinimines with trimethylenemethane. *Org. Lett.* **15**, 2030–2033 (2013).

[CAS Article](#) [Google Scholar](#)

29. 29.

Chandrasekaran, R. Y. & Wager, T. T. Histamine-3 receptor modulators. US patent US2005171181A1 (2005).

30. 30.

Wager, T. T. et al. Discovery of two clinical histamine H<sub>3</sub> receptor antagonists: *trans*-N-ethyl-3-fluoro-3-[3-fluoro-4-(pyrrolidinylmethyl)phenyl]cyclobutanecarboxamide (PF-03654746) and *trans*-3-fluoro-3-[3-fluoro-4-(pyrrolidin-1-ylmethyl)phenyl]-N-(2-methylpropyl)cyclobutanecarboxamide (PF-03654764). *J. Med. Chem.* **54**, 7602–7620 (2011).

[CAS Article](#) [Google Scholar](#)

31. 31.

Taylor, E. C. in *Successful Drug Discovery* (eds Fischer, J. & Rotella, D. P.) 157–180 (John Wiley & Sons, Ltd, 2015).

32. 32.

Barrett, T. N., Braddock, D. C., Monta, A., Webb, M. R. & White, A. J. P. Total synthesis of the marine metabolite ( $\pm$ )-polysiphenol via

highly regioselective intramolecular oxidative coupling. *J. Nat. Prod.* **74**, 1980–1984 (2011).

[CAS Article](#) [Google Scholar](#)

33. 33.

Moy, B., Kirkpatrick, P., Kar, S. & Goss, P. Lapatinib. *Nat. Rev. Drug Discov.* **6**, 431–432 (2007).

[CAS Article](#) [Google Scholar](#)

34. 34.

Ayer, W. A. & Habgood, T. E. in *The Alkaloids: Chemistry and Physiology* Vol. 11 (ed. Manske, R. H. F.) Ch. 12, 459–510 (Academic Press, 1968).

35. 35.

Münch, G. et al. The cognition-enhancing drug tenilsetam is an inhibitor of protein crosslinking by advanced glycosylation. *J Neural Transm. Park. Dis. Dement. Sect.* **8**, 193–208 (1994).

[Article](#) [Google Scholar](#)

36. 36.

De Almeida, M. V. et al. Preparation and thermal decomposition of *N,N'*-diacyl-*N,N'*-dialkoxyhydrazines: synthetic applications and mechanistic insights. *J. Am. Chem. Soc.* **117**, 4870–4874 (1995).

[Article](#) [Google Scholar](#)

37. 37.

Glover, S. A. et al. The HERON reaction — origin, theoretical background, and prevalence. *Can. J. Chem.* **83**, 1492–1509 (2005).

[CAS](#) [Article](#) [Google Scholar](#)

38. 38.

Strick, B. F., Mundal, D. A. & Thomson, R. J. An oxidative [2,3]-sigmatropic rearrangement of allylic hydrazides. *J. Am. Chem. Soc.* **133**, 14252–14255 (2011).

[CAS](#) [Article](#) [Google Scholar](#)

39. 39.

Nwachukwu, C. I., McFadden, T. P. & Roberts, A. G. Ni-catalyzed iterative alkyl transfer from nitrogen enabled by the in situ methylation of tertiary amines. *J. Org. Chem.* **85**, 9979–9992 (2020).

[CAS](#) [Article](#) [Google Scholar](#)

40. 40.

Newcomb, M. in *Encyclopedia of Radicals in Chemistry, Biology and Materials* (eds Chatgilialoglu, C. & Studer, A.) (Wiley, 2012).

41. 41.

Herk, L., Feld, M. & Szwarc, M. Studies of “Cage” Reactions. *J. Am. Chem. Soc.* **83**, 2998–3005 (1961).

[CAS](#) [Article](#) [Google Scholar](#)

42. 42.

Carpenter, B. K. Dynamic behavior of organic reactive intermediates. *Angew. Chem. Int. Ed.* **37**, 3340–3350 (1998).

[Article](#) [Google Scholar](#)

[Download references](#)

# Acknowledgements

We thank D. Nagib, F. D. Toste, M. Johnson and Z. Wickens for discussions. Financial support for this work was provided by start-up funding from the University of Chicago.

# Author information

## Author notes

1. These authors contributed equally: Balu D. Dherange, Kathleen J. Berger

## Affiliations

1. Department of Chemistry, University of Chicago, Chicago, IL, USA

Sean H. Kennedy, Balu D. Dherange, Kathleen J. Berger & Mark D. Levin

## Authors

1. Sean H. Kennedy

[View author publications](#)

You can also search for this author in [PubMed](#) [Google Scholar](#)

2. Balu D. Dherange

[View author publications](#)

You can also search for this author in [PubMed](#) [Google Scholar](#)

3. Kathleen J. Berger

[View author publications](#)

You can also search for this author in [PubMed](#) [Google Scholar](#)

4. Mark D. Levin

[View author publications](#)

You can also search for this author in [PubMed](#) [Google Scholar](#)

## Contributions

S.H.K., K.J.B. and B.D.D. designed and conducted experiments, and collected and analysed the data. M.D.L. supervised the research, conceived of the project and wrote the manuscript with input from all authors.

## Corresponding author

Correspondence to [Mark D. Levin](#).

## Ethics declarations

## Competing interests

Reagent **1c** is under development for commercialization with Sigma-Aldrich (product number 919799), but the authors have retained no financial interest and no patents have been filed.

## Additional information

**Peer review information** *Nature* thanks the anonymous reviewers for their contribution to the peer review of this work.

**Publisher's note** Springer Nature remains neutral with regard to jurisdictional claims in published maps and institutional affiliations.

## Supplementary information

[Supplementary Information](#)

This file contains Supplementary Sections 1-59, including Supplementary Materials and Methods, Procedures, Supplementary Figures 1-17, Supplementary References and NMR Spectra data – see contents page for details.

## Rights and permissions

### [Reprints and Permissions](#)

## About this article



## Cite this article

Kennedy, S.H., Dherange, B.D., Berger, K.J. *et al.* Skeletal editing through direct nitrogen deletion of secondary amines. *Nature* **593**, 223–227 (2021). <https://doi.org/10.1038/s41586-021-03448-9>

### [Download citation](#)

- Received: 02 November 2020
- Accepted: 11 March 2021
- Published: 12 May 2021
- Issue Date: 13 May 2021
- DOI: <https://doi.org/10.1038/s41586-021-03448-9>

## Comments

By submitting a comment you agree to abide by our [Terms](#) and [Community Guidelines](#). If you find something abusive or that does not comply with our terms or guidelines please flag it as inappropriate.

[Access through your institution](#)

[Change institution](#)

[Buy or subscribe](#)

## Associated Content

### [Nitrogen deletion offers fresh strategy for organic synthesis](#)

- William P. Unsworth
- Alyssa-Jennifer Avestro

Nature News & Views 12 May 2021

---

This article was downloaded by **calibre** from <https://www.nature.com/articles/s41586-021-03448-9>

| [Section menu](#) | [Main menu](#) |

- Article
- [Published: 12 May 2021](#)

# Widespread six degrees Celsius cooling on land during the Last Glacial Maximum

- [Alan M. Seltzer](#) ORCID: [orcid.org/0000-0003-2870-1215](https://orcid.org/0000-0003-2870-1215)<sup>1</sup>,
- [Jessica Ng](#)<sup>2</sup>,
- [Werner Aeschbach](#) ORCID: [orcid.org/0000-0003-0917-1239](https://orcid.org/0000-0003-0917-1239)<sup>3</sup>,
- [Rolf Kipfer](#)<sup>4,5,6</sup>,
- [Justin T. Kulongoski](#)<sup>2</sup>,
- [Jeffrey P. Severinghaus](#)<sup>2</sup> &
- [Martin Stute](#) ORCID: [orcid.org/0000-0002-8453-9067](https://orcid.org/0000-0002-8453-9067)<sup>7,8</sup>

[Nature](#) volume 593, pages 228–232 (2021) [Cite this article](#)

- 956 Accesses
- 121 Altmetric
- [Metrics details](#)

## Subjects

- [Geochemistry](#)
- [Palaeoclimate](#)

## Abstract

The magnitude of global cooling during the Last Glacial Maximum (LGM, the coldest multimillennial interval of the last glacial period) is an important constraint for evaluating estimates of Earth's climate sensitivity<sup>1,2</sup>. Reliable LGM temperatures come from high-latitude ice cores<sup>3,4</sup>, but substantial disagreement exists between proxy records in the low latitudes<sup>1,5,6,7,8</sup>, where quantitative low-elevation records on land are scarce. Filling this data gap, noble gases in ancient groundwater record past land surface temperatures through a direct physical relationship that is rooted in their temperature-dependent solubility in water<sup>9,10</sup>. Dissolved noble gases are suitable tracers of LGM temperature because of their complete insensitivity to biological and chemical processes and the ubiquity of LGM-aged groundwater around the globe<sup>11,12</sup>. However, although several individual noble gas studies have found substantial tropical LGM cooling<sup>13,14,15,16</sup>, they have used different methodologies and provide limited spatial coverage. Here we use noble gases in groundwater to show that the low-altitude, low-to-mid-latitude land surface (45 degrees south to 35 degrees north) cooled by  $5.8 \pm 0.6$  degrees Celsius (mean  $\pm$  95% confidence interval) during the LGM. Our analysis includes four decades of groundwater noble gas data from six continents, along with new records from the tropics, all of which were interpreted using the same physical framework. Our land-based result broadly supports a recent reconstruction based on marine proxy data assimilation<sup>1</sup> that suggested greater climate sensitivity than previous estimates<sup>5,6,7</sup>.

[Access through your institution](#)

[Change institution](#)

[Buy or subscribe](#)

## Access options

Subscribe to Journal

Get full journal access for 1 year

\$199.00

only \$3.90 per issue

[Subscribe](#)

All prices are NET prices.

VAT will be added later in the checkout.

Tax calculation will be finalised during checkout.

Rent or Buy article

Get time limited or full article access on ReadCube.

from \$8.99

[Rent or Buy](#)

All prices are NET prices.

**Additional access options:**

- [Log in](#)
- [Access through your institution](#)
- [Learn about institutional subscriptions](#)

**Fig. 1: Overview of the noble gas palaeothermometer and its key components.**

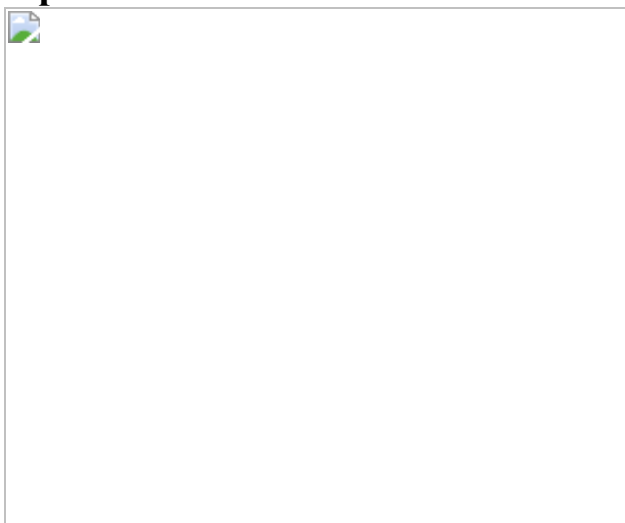
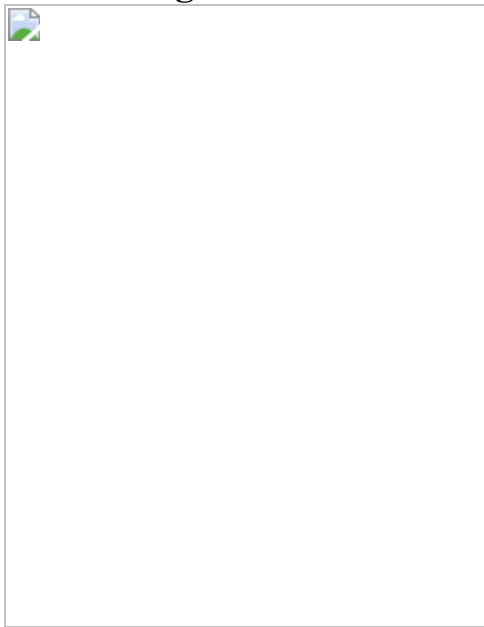


**Fig. 2: Noble gases in young groundwater accurately record modern temperatures.**



**Fig. 3: Noble gases suggest around 6 °C of low-elevation, low-latitude LGM cooling on land.**



## Data availability

All original groundwater data (noble gas concentrations, ages, water temperatures (if available)), recharge elevations, study locations, fitted parameters and statistical uncertainties are freely available for download through PANGAEA (<https://doi.org/10.1594/PANGAEA.929176>). NGT

time series plots of each study are available as supplementary files. [Source data](#) are provided with this paper.

## Code availability

All MATLAB scripts for NGT fitting (including documentation) are freely available from zenodo (<https://doi.org/10.5281/zenodo.4589442>).

## References

1. 1.

Tierney, J. E. et al. Glacial cooling and climate sensitivity revisited. *Nature* **584**, 569–573 (2020).

[ADS](#) [CAS](#) [PubMed](#) [PubMed Central](#) [Google Scholar](#)

2. 2.

Schmittner, A. et al. Climate sensitivity estimated from temperature reconstructions of the Last Glacial Maximum. *Science* **334**, 1385–1388 (2011).

[ADS](#) [CAS](#) [PubMed](#) [PubMed Central](#) [Google Scholar](#)

3. 3.

Jouzel, J. et al. Orbital and millennial Antarctic climate variability over the past 800,000 years. *Science* **317**, 793–796 (2007).

[ADS](#) [CAS](#) [PubMed](#) [PubMed Central](#) [Google Scholar](#)

4. 4.

Petit, J. R. et al. Climate and atmospheric history of the past 420,000 years from the Vostok ice core, Antarctica. *Nature* **399**, 429–436 (1999).

[ADS](#) [CAS](#) [Google Scholar](#)

5. 5.

CLIMAP Project Members. The surface of the Ice-Age Earth. *Science* **191**, 1131–1137 (1976).

[ADS](#) [Google Scholar](#)

6. 6.

MARGO Project Members. Constraints on the magnitude and patterns of ocean cooling at the Last Glacial Maximum. *Nat. Geosci.* **2**, 127–132 (2009).

[ADS](#) [Google Scholar](#)

7. 7.

Annan, J. D. & Hargreaves, J. C. A new global reconstruction of temperature changes at the Last Glacial Maximum. *Clim. Past* **9**, 367–376 (2013).

[Google Scholar](#)

8. 8.

Farrera, I. et al. Tropical climates at the Last Glacial Maximum: a new synthesis of terrestrial palaeoclimate data. I. Vegetation, lake-levels and geochemistry. *Clim. Dyn.* **15**, 823–856 (1999).

[Google Scholar](#)

9. 9.

Jenkins, W. J., Lott, D. E. & Cahill, K. L. A determination of atmospheric helium, neon, argon, krypton, and xenon solubility concentrations in water and seawater. *Mar. Chem.* **211**, 94–107 (2019).

[CAS](#) [Google Scholar](#)

10. 10.

Kipfer, R., Aeschbach-Hertig, W., Peeters, F. & Stute, M. Noble gases in lakes and ground waters. *Rev. Mineral. Geochem.* **47**, 615–700 (2002).

[CAS](#) [Google Scholar](#)

11. 11.

Befus, K. M., Jasechko, S., Luijendijk, E., Gleeson, T. & Bayani Cardenas, M. The rapid yet uneven turnover of Earth's groundwater. *Geophys. Res. Lett.* **44**, 5511–5520 (2017).

[ADS](#) [CAS](#) [Google Scholar](#)

12. 12.

Jasechko, S. et al. Global aquifers dominated by fossil groundwaters but wells vulnerable to modern contamination. *Nat. Geosci.* **10**, 425–429 (2017).

[ADS](#) [CAS](#) [Google Scholar](#)

13. 13.

Stute, M. et al. Cooling of tropical Brazil (5 °C) during the Last Glacial Maximum. *Science* **269**, 379–383 (1995).

[ADS](#) [CAS](#) [Google Scholar](#)

14. 14.

Weyhenmeyer, C. E. et al. Cool glacial temperatures and changes in moisture source recorded in Oman groundwaters. *Science* **287**, 842–845 (2000).

[ADS](#) [CAS](#) [PubMed](#) [PubMed Central](#) [Google Scholar](#)

15. 15.

Stute, M., Schlosser, P., Clark, J. F. & Broecker, W. S.  
Paleotemperatures in the southwestern United States derived from  
noble gases in ground water. *Science* **256**, 1000–1003 (1992).

[ADS](#) [CAS](#) [PubMed](#) [PubMed Central](#) [Google Scholar](#)

16. 16.

Kulogoski, J. T., Hilton, D. R. & Selaolo, E. T. Climate variability in  
the Botswana Kalahari from the late Pleistocene to the present day.  
*Geophys. Res. Lett.* **31**, L10204 (2004).

[ADS](#) [Google Scholar](#)

17. 17.

Porter, S. C. Snowline depression in the tropics during the last  
glaciation. *Quat. Sci. Rev.* **20**, 1067–1091 (2000).

[ADS](#) [Google Scholar](#)

18. 18.

Rind, D. & Peteet, D. Terrestrial conditions at the Last Glacial  
Maximum and CLIMAP sea-surface temperature estimates: are they  
consistent? *Quat. Res.* **24**, 1–22 (1985).

[Google Scholar](#)

19. 19.

Klein, A. G., Seltzer, G. O. & Isacks, B. L. Modern and last local  
glacial maximum snowlines in the Central Andes of Peru, Bolivia, and  
Northern Chile. *Quat. Sci. Rev.* **18**, 63–84 (1999).

[ADS](#) [Google Scholar](#)

20. 20.

Tierney, J. E. et al. Northern Hemisphere controls on tropical southeast African climate during the past 60,000 years. *Science* **322**, 252–255 (2008).

[ADS](#) [CAS](#) [Google Scholar](#)

21. 21.

Powers, L. A. et al. Large temperature variability in the southern African tropics since the Last Glacial Maximum. *Geophys. Res. Lett.* **32**, L08706 (2005).

[ADS](#) [Google Scholar](#)

22. 22.

Loomis, S. E. et al. The tropical lapse rate steepened during the Last Glacial Maximum. *Sci. Adv.* **3**, e1600815 (2017).

[ADS](#) [PubMed](#) [PubMed Central](#) [Google Scholar](#)

23. 23.

Bartlein, P. J. et al. Pollen-based continental climate reconstructions at 6 and 21 ka: a global synthesis. *Clim. Dyn.* **37**, 775–802 (2011).

[Google Scholar](#)

24. 24.

Mazor, E. Paleotemperatures and other hydrological parameters deduced from noble gases dissolved in groundwaters; Jordan Rift Valley, Israel. *Geochim. Cosmochim. Acta* **36**, 1321–1336 (1972).

[ADS](#) [CAS](#) [Google Scholar](#)

25. 25.

Stute, M. & Schlosser, P. in *Climate Change in Continental Isotopic Records* Vol. 78 (eds Swart, P. K. et al.) 89–100 (American Geophysical Union (AGU), 1993).

26. 26.

Aeschbach-Hertig, W. & Solomon, D. K. in *The Noble Gases as Geochemical Tracers* (ed. Burnard, P.) 81–122 (Springer, 2013).

27. 27.

Pepin, R. O. & Porcelli, D. Origin of noble gases in the terrestrial planets. *Rev. Mineral. Geochem.* **47**, 191–246 (2002).

[CAS](#) [Google Scholar](#)

28. 28.

Klump, S., Cirpka, O. A., Surbeck, H. & Kipfer, R. Experimental and numerical studies on excess-air formation in quasi-saturated porous media. *Wat. Resour. Res.* **44**, W05402 (2008).

[ADS](#) [CAS](#) [Google Scholar](#)

29. 29.

Klump, S. et al. Field experiments yield new insights into gas exchange and excess air formation in natural porous media. *Geochim. Cosmochim. Acta* **71**, 1385–1397 (2007).

[ADS](#) [CAS](#) [Google Scholar](#)

30. 30.

Aeschbach-Hertig, W., El-Gamal, H., Wieser, M. & Palcsu, L. Modeling excess air and degassing in groundwater by equilibrium partitioning with a gas phase. *Wat. Resour. Res.* **44**, W08449 (2008).

[ADS](#) [Google Scholar](#)

31. 31.

Aeschbach-Hertig, W., Peeters, F., Beyerle, U. & Kipfer, R. Palaeotemperature reconstruction from noble gases in ground water taking into account equilibration with entrapped air. *Nature* **405**, 1040–1044 (2000).

[ADS](#) [CAS](#) [PubMed](#) [PubMed Central](#) [Google Scholar](#)

32. 32.

Hersbach, H. et al. The ERA5 global reanalysis. *Q. J. R. Meteorol. Soc.* **146**, 1999–2049 (2020).

[ADS](#) [Google Scholar](#)

33. 33.

Hall, C. M., Castro, M. C., Lohmann, K. C. & Ma, L. Noble gases and stable isotopes in a shallow aquifer in southern Michigan: implications for noble gas paleotemperature reconstructions for cool climates. *Geophys. Res. Lett.* **32**, L18404 (2005).

[ADS](#) [Google Scholar](#)

34. 34.

Chang, J. *Ground Temperature* (Blue Hill Meteorological Observatory, Harvard University, 1958).

35. 35.

Hall, C. M., Castro, M. C., Lohmann, K. C. & Sun, T. Testing the noble gas paleothermometer with a yearlong study of groundwater noble gases in an instrumented monitoring well. *Wat. Resour. Res.* **48**, W04517 (2012).

[ADS](#) [Google Scholar](#)

36. 36.

Han, L. F. & Plummer, L. N. A review of single-sample-based models and other approaches for radiocarbon dating of dissolved inorganic carbon in groundwater. *Earth Sci. Rev.* **152**, 119–142 (2016).

[ADS](#) [CAS](#) [Google Scholar](#)

37. 37.

Aeschbach-Hertig, W., Stute, M., Clark, J. F., Reuter, R. F. & Schlosser, P. A paleotemperature record derived from dissolved noble gases in groundwater of the Aquia Aquifer (Maryland, USA). *Geochim. Cosmochim. Acta* **66**, 797–817 (2002).

[ADS](#) [CAS](#) [Google Scholar](#)

38. 38.

Jung, M., Wieser, M., von Oehsen, A. & Aeschbach-Hertig, W. Properties of the closed-system equilibration model for dissolved noble gases in groundwater. *Chem. Geol.* **339**, 291–300 (2013).

[ADS](#) [CAS](#) [Google Scholar](#)

39. 39.

Prentice, I. C., Harrison, S. P. & Bartlein, P. J. Global vegetation and terrestrial carbon cycle changes after the last ice age. *New Phytol.* **189**, 988–998 (2011).

[CAS](#) [Google Scholar](#)

40. 40.

Stute, M. & Sonntag, C. in *Isotopes of Noble Gases as Tracers in Environmental Studies* 111–122 (International Atomic Energy Agency,

1992).

41. 41.

Seltzer, A. M. et al. Deglacial water-table decline in Southern California recorded by noble gas isotopes. *Nat. Commun.* **10**, 5739 (2019).

[ADS](#) [CAS](#) [PubMed](#) [PubMed Central](#) [Google Scholar](#)

42. 42.

Seltzer, A. M., Severinghaus, J. P., Andraski, B. J. & Stonestrom, D. A. Steady state fractionation of heavy noble gas isotopes in a deep unsaturated zone. *Wat. Resour. Res.* **53**, 2716–2732 (2017).

[ADS](#) [CAS](#) [Google Scholar](#)

43. 43.

Mélières, M. A., Martinerie, P., Raynaud, D. & Lliboutry, L. Glacial–interglacial mean sea level pressure change due to sea level, ice sheet and atmospheric mass changes. *Global Planet. Change* **3**, 333–340 (1991).

[ADS](#) [Google Scholar](#)

44. 44.

Cey, B. D. On the accuracy of noble gas recharge temperatures as a paleoclimate proxy. *J. Geophys. Res.* **114**, D04107 (2009).

[ADS](#) [Google Scholar](#)

45. 45.

Broecker, W. S. & Denton, G. H. The role of ocean–atmosphere reorganizations in glacial cycles. *Geochim. Cosmochim. Acta* **53**, 2465–2501 (1989).

[ADS](#) [CAS](#) [Google Scholar](#)

46. 46.

Manabe, S., Stouffer, R. J., Spelman, M. J. & Bryan, K. Transient responses of a coupled ocean–atmosphere model to gradual changes of atmospheric CO<sub>2</sub>. Part I. annual mean response. *J. Clim.* **4**, 785–818 (1991).

[ADS](#) [Google Scholar](#)

47. 47.

Joshi, M. M., Gregory, J. M., Webb, M. J., Sexton, D. M. H. & Johns, T. C. Mechanisms for the land/sea warming contrast exhibited by simulations of climate change. *Clim. Dyn.* **30**, 455–465 (2008).

[Google Scholar](#)

48. 48.

Sutton, R. T., Dong, B. & Gregory, J. M. Land/sea warming ratio in response to climate change: IPCC AR4 model results and comparison with observations. *Geophys. Res. Lett.* **34**, L02701 (2007).

[ADS](#) [Google Scholar](#)

49. 49.

Knutti, R. & Hegerl, G. C. The equilibrium sensitivity of the Earth's temperature to radiation changes. *Nat. Geosci.* **1**, 735–743 (2008).

[ADS](#) [CAS](#) [Google Scholar](#)

50. 50.

Steiger, N. J., Hakim, G. J., Steig, E. J., Battisti, D. S. & Roe, G. H. Assimilation of time-averaged pseudoproxies for climate reconstruction. *J. Clim.* **27**, 426–441 (2014).

[ADS](#) [Google Scholar](#)

51. 51.

Ghadiri, E. et al. Noble gas based temperature reconstruction on a Swiss stalagmite from the last glacial–interglacial transition and its comparison with other climate records. *Earth Planet. Sci. Lett.* **495**, 192–201 (2018).

[ADS](#) [CAS](#) [Google Scholar](#)

52. 52.

Heaton, T. H. E., Talma, A. S. & Vogel, J. C. Dissolved gas paleotemperatures and  $^{18}\text{O}$  variations derived from groundwater near Uitenhage, South Africa. *Quat. Res.* **25**, 79–88 (1986).

[CAS](#) [Google Scholar](#)

53. 53.

Freundt, F., Schneider, T. & Aeschbach-Hertig, W. Response of noble gas partial pressures in soil air to oxygen depletion. *Chem. Geol.* **339**, 283–290 (2013).

[ADS](#) [CAS](#) [Google Scholar](#)

54. 54.

Castro, M. C., Hall, C. M., Patriarche, D., Goblet, P. & Ellis, B. R. A new noble gas paleoclimate record in Texas—basic assumptions revisited. *Earth Planet. Sci. Lett.* **257**, 170–187 (2007).

[ADS](#) [CAS](#) [Google Scholar](#)

55. 55.

Ma, L., Castro, M. C. & Hall, C. M. A late Pleistocene–Holocene noble gas paleotemperature record in southern Michigan. *Geophys.*

*Res. Lett.* **31**, L23204 (2004).

[ADS](#) [Google Scholar](#)

56. 56.

Masbruch, M. D., Chapman, D. S. & Solomon, D. K. Air, ground, and groundwater recharge temperatures in an alpine setting, Brighton Basin, Utah. *Wat. Resour. Res.* **48**, W10530 (2012).

[ADS](#) [Google Scholar](#)

57. 57.

Saraceno, J., Kulongoski, J. T. & Mathany, T. M. A novel high-frequency groundwater quality monitoring system. *Environ. Monit. Assess.* **190**, 477 (2018).

[Google Scholar](#)

58. 58.

Jung, M. & Aeschbach, W. A new software tool for the analysis of noble gas data sets from (ground)water. *Environ. Model. Softw.* **103**, 120–130 (2018).

[Google Scholar](#)

59. 59.

Clark, J. F., Stute, M., Schlosser, P., Drenkard, S. & Bonani, G. A tracer study of the Floridan Aquifer in southeastern Georgia: implications for groundwater flow and paleoclimate. *Wat. Resour. Res.* **33**, 281–289 (1997).

[ADS](#) [CAS](#) [Google Scholar](#)

60. 60.

Stuiver, M. & Polach, H. A. Reporting of  $^{14}\text{C}$  data. *Radiocarbon* **19**, 355–363 (1977).

[Google Scholar](#)

61. 61.

Bereiter, B., Shackleton, S., Baggenstos, D., Kawamura, K. & Severinghaus, J. Mean global ocean temperatures during the last glacial transition. *Nature* **553**, 39–44 (2018).

[ADS](#) [CAS](#) [Google Scholar](#)

62. 62.

Schwander, J. in *The Environmental Record in Glaciers and Ice Sheets* (eds Oeschger, H. & Langway, C. C.) 53–67 (Wiley, 1989).

63. 63.

Andrews, J. N. & Lee, D. J. Inert gases in groundwater from the Bunter Sandstone of England as indicators of age and palaeoclimatic trends. *J. Hydrol.* **41**, 233–252 (1979).

[ADS](#) [CAS](#) [Google Scholar](#)

64. 64.

Stute, M., Clark, J. F., Schlosser, P., Broecker, W. S. & Bonani, G. A. 30,000 yr Continental paleotemperature record derived from noble gases dissolved in groundwater from the San Juan Basin, New Mexico. *Quat. Res.* **43**, 209–220 (1995).

[CAS](#) [Google Scholar](#)

65. 65.

Beyerle, U. et al. Climate and groundwater recharge during the last glaciation in an ice-covered region. *Science* **282**, 731–734 (1998).

[ADS](#) [CAS](#) [Google Scholar](#)

66. 66.

Clark, J. F., Davisson, M. L., Hudson, G. B. & MacFarlane, P. A. Noble gases, stable isotopes, and radiocarbon as tracers of flow in the Dakota aquifer, Colorado and Kansas. *J. Hydrol.* **211**, 151–167 (1998).

[ADS](#) [CAS](#) [Google Scholar](#)

67. 67.

Kulogoski, J. T., Hilton, D. R., Izicki, J. A. & Belitz, K. Evidence for prolonged El Niño-like conditions in the Pacific during the Late Pleistocene: a 43 ka noble gas record from California groundwaters. *Quat. Sci. Rev.* **28**, 2465–2473 (2009).

[ADS](#) [Google Scholar](#)

68. 68.

Seltzer, A. M., Stute, M., Morgenstern, U., Stewart, M. K. & Schaefer, J. M. Mean annual temperature in New Zealand during the last glacial maximum derived from dissolved noble gases in groundwater. *Earth Planet. Sci. Lett.* **431**, 206–216 (2015).

[ADS](#) [CAS](#) [Google Scholar](#)

69. 69.

Zhu, C. & Kipfer, R. Noble gas signatures of high recharge pulses and migrating jet stream in the late Pleistocene over Black Mesa, Arizona, United States. *Geology* **38**, 83–86 (2010).

[ADS](#) [CAS](#) [Google Scholar](#)

70. 70.

Edmunds, W. M., Ma, J., Aeschbach-Hertig, W., Kipfer, R. & Darbyshire, D. P. F. Groundwater recharge history and hydrogeochemical evolution in the Minqin Basin, North West China. *Appl. Geochem.* **21**, 2148–2170 (2006).

[CAS](#) [Google Scholar](#)

71. 71.

Kreuzer, A. M. et al. A record of temperature and monsoon intensity over the past 40 kyr from groundwater in the North China Plain. *Chem. Geol.* **259**, 168–180 (2009).

[ADS](#) [CAS](#) [Google Scholar](#)

72. 72.

Stute, M. & Deak, J. Environmental isotope study ( $^{14}\text{C}$ ,  $^{13}\text{C}$ ,  $^{18}\text{O}$ , D, noble gases) on deep groundwater circulation systems in Hungary with reference to paleoclimate. *Radiocarbon* **31**, 902–918 (1989).

[Google Scholar](#)

73. 73.

Beyerle, U. et al. Evidence for periods of wetter and cooler climate in the Sahel between 6 and 40 kyr BP derived from groundwater. *Geophys. Res. Lett.* **30**, 1173 (2003).

[ADS](#) [Google Scholar](#)

74. 74.

Varsányi, I., Palcsu, L. & Kovács, L. Ó. Groundwater flow system as an archive of palaeotemperature: noble gas, radiocarbon, stable isotope and geochemical study in the Pannonian Basin, Hungary. *Appl. Geochem.* **26**, 91–104 (2011).

[Google Scholar](#)

75. 75.

Corcho Alvarado, J. A. et al. European climate variations over the past half-millennium reconstructed from groundwater. *Geophys. Res. Lett.* **36**, L15703 (2009).

[ADS](#) [Google Scholar](#)

76. 76.

Blaser, P. C. et al. A 40 ka record of temperature and permafrost conditions in northwestern Europe from noble gases in the Ledo-Paniselian Aquifer (Belgium). *J. Quat. Sci.* **25**, 1038–1044 (2010).

[Google Scholar](#)

77. 77.

Klump, S., Grundl, T., Purtschert, R. & Kipfer, R. Groundwater and climate dynamics derived from noble gas,  $^{14}\text{C}$ , and stable isotope data. *Geology* **36**, 395–398 (2008).

[ADS](#) [CAS](#) [Google Scholar](#)

78. 78.

Stute, M. & Talma, A. Glacial temperatures and moisture transport regimes reconstructed from noble gases and  $\delta^{18}\text{O}$ , Stampriet aquifer, Namibia. In *Isotope Techniques in the Study of Past and Current Environmental Changes in the Hydrosphere and the Atmosphere* 307–328 (1998).

79. 79.

Carreira, P. M. *Paleoágua de Aveiro* (Universidade de Aviero, 1998).

80. 80.

Sundal, A., Brennwald, M. S., Aagaard, P. & Kipfer, R. Noble gas composition and  $^3\text{H}/^3\text{He}$  groundwater ages in the Gardermoen Aquifer, Norway: improved understanding of flow dynamics as a tool for water management. *Sci. Total Environ.* **660**, 1219–1231 (2019).

[ADS](#) [CAS](#) [Google Scholar](#)

81. 81.

Trabelsi, R., Matsumoto, T., Zouari, K., Trabelsi, M. & Kumar, B. Investigation of paleoclimate signatures in Sfax deep groundwater (Southeastern Tunisia) using environmental isotopes and noble gases. *Quat. Int.* **547**, 208–219 (2020).

[Google Scholar](#)

82. 82.

Abouelmagd, A. et al. Paleoclimate record in the Nubian Sandstone Aquifer, Sinai Peninsula, Egypt. *Quat. Res.* **81**, 158–167 (2014).

[CAS](#) [Google Scholar](#)

83. 83.

Wieser, M. *Imprints of Climatic and Environmental Change in a Regional Aquifer System in an Arid Part of India using Noble Gases and Other Environmental Tracers* (University of Heidelberg, 2011).

84. 84.

Wieser, M., Aeschbach-Hertig, W., Schneider, T., Deshpande, R. D. & Gupta, S. K. A temperature and monsoon record derived from environmental tracers in the groundwater of northwest India. In *International Symposium on Isotopes in Hydrology, Marine Ecosystems and Climate Change Studies* 7–14 (International Atomic Energy Agency, 2013).

[Download references](#)

# Acknowledgements

We thank the entire community of groundwater noble gas geochemists, particularly the pioneers E. Mazor and J. N. Andrews, for decades of careful work in analysing groundwater from around the world and furthering our physical understanding of inert gases in groundwater; A. Moulla and T. Condesso de Melo for sharing data, and D. Bekaert for helpful discussions. The manuscript was improved by helpful suggestions from A. Manning, J. Clark and David McGee. This work was supported in part by NSF-EAR-1702704, NSF-EAR-1702571, and NSF-OCE-1923915.

# Author information

## Affiliations

1. Marine Chemistry and Geochemistry Department, Woods Hole Oceanographic Institution, Woods Hole, MA, USA  
Alan M. Seltzer
2. Geosciences Research Division, Scripps Institution of Oceanography, La Jolla, CA, USA  
Jessica Ng, Justin T. Kulongoski & Jeffrey P. Severinghaus
3. Institute of Environmental Physics, Heidelberg University, Heidelberg, Germany  
Werner Aeschbach
4. Department of Water Resources and Drinking Water, Swiss Federal Institute of Aquatic Science and Technology, Eawag, Dübendorf, Switzerland  
Rolf Kipfer

5. Institute of Biogeochemistry and Pollutant Dynamics, Department of Environmental Systems Science, Swiss Federal Institute Technology, ETHZ, Zurich, Switzerland

Rolf Kipfer

6. Institute of Geochemistry and Petrology, Department of Earth Sciences, Swiss Federal Institute Technology, ETHZ, Zurich, Switzerland

Rolf Kipfer

7. Geochemistry Division, Lamont–Doherty Earth Observatory, Palisades, NY, USA

Martin Stute

8. Environmental Science Department, Barnard College, New York, NY, USA

Martin Stute

## Authors

1. Alan M. Seltzer

[View author publications](#)

You can also search for this author in [PubMed](#) [Google Scholar](#)

2. Jessica Ng

[View author publications](#)

You can also search for this author in [PubMed](#) [Google Scholar](#)

3. Werner Aeschbach

[View author publications](#)

You can also search for this author in [PubMed](#) [Google Scholar](#)

4. Rolf Kipfer

[View author publications](#)

You can also search for this author in [PubMed](#) [Google Scholar](#)

5. Justin T. Kulongoski

[View author publications](#)

You can also search for this author in [PubMed](#) [Google Scholar](#)

6. Jeffrey P. Severinghaus

[View author publications](#)

You can also search for this author in [PubMed](#) [Google Scholar](#)

7. Martin Stute

[View author publications](#)

You can also search for this author in [PubMed](#) [Google Scholar](#)

## Contributions

A.M.S. wrote the manuscript and carried out modelling and data analysis. J.N. and A.M.S. created the database. J.P.S. developed the LGM atmospheric pressure model. A.M.S., J.N., W.A., M.S., J.T.K. and R.K. contributed groundwater datasets, all authors contributed to weekly discussions about data interpretation and modelling. All authors edited and revised the manuscript.

## Corresponding author

Correspondence to [Alan M. Seltzer](#).

## Ethics declarations

## Competing interests

The authors declare no competing interests.

## Additional information

**Peer review information** *Nature* thanks Jordan Clark, Andrew Manning, David McGee and the other, anonymous, reviewer(s) for their contribution to the peer review of this work. Peer reviewer reports are available.

**Publisher's note** Springer Nature remains neutral with regard to jurisdictional claims in published maps and institutional affiliations.

## Extended data figures and tables

### Extended Data Fig. 1 Evaluation of leading noble gas models.

Comparison of Late Holocene NGTs to ERA5-Land 1981–2019 MASTs across three NGT models and  $\chi^2$  goodness-of-fit histogram comparison of all groundwater samples ( $n = 753$ ) included in this work (normalized by degrees of freedom,  $n$ ) (inset). The closed-system equilibration (CE) model agrees closest with ERA5-Land temperatures (r.m.s.d. = 1.4 °C), followed by the partial re-equilibration (PR) (r.m.s.d. = 1.5 °C) and oxygen depletion (OD) (r.m.s.d. = 5.7 °C) models. The closed-system equilibration model also exhibits the best goodness-of-fit (lowest median  $\chi^2/n$ ). Data are mean  $\pm$  1 s.e.m.

### Extended Data Fig. 2 ERA5-Land temperatures are unbiased above 5 °C.

Comparison of 1981–2019 mean annual ERA5-Land ground (upper soil) temperatures to a global database of modern mean annual measured ground temperatures<sup>34</sup>, using the approach described in the Methods to project ERA5-Land temperatures to the observation elevations. Whereas below approximately 5 °C, ERA5-Land temperatures appear to be systematically biased to be warmer than the observed temperature, above 5 °C they consistently overlap the 1:1 line with an r.m.s.d. of 1.6 °C. Observed temperatures tend to be slightly warmer than ERA5-Land temperatures on

average, perhaps because of the typical locations of micrometeorological stations in barren fields, with little cooling from the shade provided by vegetation.

### **Extended Data Fig. 3 Leading sources of systematic error in LGM noble gas palaeothermometry.**

**a–d**, Modelled sensitivity of apparent NGTs to leading sources of systematic error. In each case, NGT bias ( $T$ ) is reported with respect to a starting recharge temperature of 10 °C at 1 km elevation (except for mixing tests (**d**) in which  $T$  is given relative to the temperature of an equal-parts mixture of 10 °C equilibrated water with a given equilibrium mixing end-member temperature). The NGT bias associated with a source of error is shown, including LGM–Late-Holocene changes in recharge elevation (**a**), water table depth ( $\Delta$ WTD, **b**) and pressure ( $\Delta P$ , **c**), and the direct NGT bias induced by mixing (**d**) relative to the admixture temperature. Green squares indicate the  $\pm 1\sigma$  confidence region for the range of likely glacial–interglacial variability (Supplementary Table 1; see [Methods](#) for a detailed description of each sensitivity test and Supplementary Table 2 for a compilation of the results).

### **Extended Data Fig. 4 Atmospheric pressure changes during the LGM.**

Box model result for changes in LGM atmospheric pressure with elevation at a fixed point. **a**, The absolute pressure ( $P$ ) is shown during the LGM and in the modern atmosphere. **b**, LGM anomalies in pressure ( $\Delta P$ ) relative to the modern atmosphere are shown. In brief, the model assumes a fixed lapse rate (6.5 °C km<sup>-1</sup>) and uses the barometric equation to estimate the vertical distribution of atmospheric pressure during the LGM, accounting for loss of atmospheric air by dissolution into a colder ocean and occlusion in high-latitude ice sheets, as well as displacement of air by the growth of large ice sheets (see [Methods](#) for further details).

### **Extended Data Fig. 5 Comparison of AP2 LGM cooling estimates to literature values.**

Comparison by latitude of noble-gas-derived  $\Delta T_{\text{LGM}}$  (this study, approach AP2) to zonal-mean land-surface (solid lines) and sea-surface (dashed lines) estimates of  $\Delta T_{\text{LGM}}$  from key previous studies<sup>1,5,7</sup>. Data are mean  $\pm$  1 s.e.m. Our AP2 low latitude ( $45^{\circ}$  S– $35^{\circ}$  N) mean estimate of LGM cooling ( $4.8 \pm 0.6$  °C; thick green dashed line, with 95% confidence error envelope) is around 1 °C smaller in magnitude (warmer) than AP1. Although the AP2 estimate seems to more closely overlap the previously published land cooling data<sup>1</sup>, we note that this data-assimilation study was entirely constrained by marine proxies and therefore the implications for cooling over land should be treated with caution. For the physical and statistical reasons described in the main text, we suggest that AP1 is more robust, and we emphasize that the relatively good agreement between AP1 and AP2, compared with the range of disagreement among literature values, adds confidence to the reliability of the NGT reconstruction.

### **Extended Data Table 1 Leading sources of systematic error**

[Full size table](#)

### **Extended Data Table 2 Overview of groundwater noble gas datasets**

[Full size table](#)

## **Supplementary information**

[\*\*Peer Review File\*\*](#)

## **Source data**

[\*\*Source Data Fig. 2\*\*](#)

[\*\*Source Data Fig. 3\*\*](#)

## **Rights and permissions**

[\*\*Reprints and Permissions\*\*](#)

## About this article



## Cite this article

Seltzer, A.M., Ng, J., Aeschbach, W. *et al.* Widespread six degrees Celsius cooling on land during the Last Glacial Maximum. *Nature* **593**, 228–232 (2021). <https://doi.org/10.1038/s41586-021-03467-6>

### Download citation

- Received: 06 November 2020
- Accepted: 17 March 2021
- Published: 12 May 2021
- Issue Date: 13 May 2021
- DOI: <https://doi.org/10.1038/s41586-021-03467-6>

## Comments

By submitting a comment you agree to abide by our [Terms](#) and [Community Guidelines](#). If you find something abusive or that does not comply with our terms or guidelines please flag it as inappropriate.

### Access through your institution

### Change institution

### Buy or subscribe

| [Section menu](#) | [Main menu](#) |

Ubiquitous atmospheric production of organic acids mediated by cloud droplets  
[Download PDF](#)

- Article
- Open Access
- [Published: 12 May 2021](#)

# Ubiquitous atmospheric production of organic acids mediated by cloud droplets

- [B. Franco](#) [ORCID: orcid.org/0000-0003-0736-458X<sup>1,2 na1</sup>](#),
- [T. Blumenstock](#) [ORCID: orcid.org/0000-0003-4005-900X<sup>3</sup>](#),
- [C. Cho<sup>1</sup>](#),
- [L. Clarisse](#) [ORCID: orcid.org/0000-0002-8805-2141<sup>2</sup>](#),
- [C. Clerbaux](#) [ORCID: orcid.org/0000-0003-0394-7200<sup>2,4</sup>](#),
- [P.-F. Coheur<sup>2</sup>](#),
- [M. De Mazière<sup>5</sup>](#),
- [I. De Smedt<sup>5</sup>](#),
- [H.-P. Dorn](#) [ORCID: orcid.org/0000-0001-5945-7708<sup>1</sup>](#),
- [T. Emmerichs](#) [ORCID: orcid.org/0000-0002-0165-9574<sup>1</sup>](#),
- [H. Fuchs](#) [ORCID: orcid.org/0000-0003-1263-0061<sup>1</sup>](#),
- [G. Gkatzelis<sup>1</sup>](#),
- [D. W. T. Griffith](#) [ORCID: orcid.org/0000-0002-7986-1924<sup>6</sup>](#),
- [S. Gromov](#) [ORCID: orcid.org/0000-0002-2542-3005<sup>7,8</sup>](#),
- [J. W. Hannigan](#) [ORCID: orcid.org/0000-0002-4269-1677<sup>2</sup>](#),
- [F. Hase<sup>3</sup>](#),
- [T. Hohaus](#) [ORCID: orcid.org/0000-0001-5722-6244<sup>1</sup>](#),
- [N. Jones<sup>6</sup>](#),
- [A. Kerkweg<sup>1</sup>](#),
- [A. Kiendler-Scharr](#) [ORCID: orcid.org/0000-0003-3166-2253<sup>1</sup>](#),
- [E. Lutsch](#) [ORCID: orcid.org/0000-0001-5072-0979<sup>10</sup>](#),
- [E. Mahieu](#) [ORCID: orcid.org/0000-0002-5251-0286<sup>11</sup>](#),
- [A. Novelli<sup>1</sup>](#),
- [I. Ortega](#) [ORCID: orcid.org/0000-0002-0067-617X<sup>9</sup>](#),

- [C. Paton-Walsh](#) ORCID: [orcid.org/0000-0003-1156-4138<sup>6</sup>](https://orcid.org/0000-0003-1156-4138),
- [M. Pommier<sup>4,12</sup>](#),
- [A. Pozzer](#) ORCID: [orcid.org/0000-0003-2440-6104<sup>7</sup>](https://orcid.org/0000-0003-2440-6104),
- [D. Reimer<sup>1</sup>](#),
- [S. Rosanka](#) ORCID: [orcid.org/0000-0001-5929-163X<sup>1</sup>](https://orcid.org/0000-0001-5929-163X),
- [R. Sander](#) ORCID: [orcid.org/0000-0001-6479-2092<sup>7</sup>](https://orcid.org/0000-0001-6479-2092),
- [M. Schneider<sup>3</sup>](#),
- [K. Strong](#) ORCID: [orcid.org/0000-0001-9947-1053<sup>10</sup>](https://orcid.org/0000-0001-9947-1053),
- [R. Tillmann<sup>1</sup>](#),
- [M. Van Roozendael<sup>5</sup>](#),
- [L. Vereecken](#) ORCID: [orcid.org/0000-0001-7845-684X<sup>1</sup>](https://orcid.org/0000-0001-7845-684X),
- [C. Vigouroux<sup>5</sup>](#),
- [A. Wahner](#) ORCID: [orcid.org/0000-0001-8948-1928<sup>1</sup>](https://orcid.org/0000-0001-8948-1928) &
- [D. Taraborrelli](#) ORCID: [orcid.org/0000-0003-2213-6307<sup>1 na1</sup>](https://orcid.org/0000-0003-2213-6307)

*Nature* volume **593**, pages233–237(2021)[Cite this article](#)

- 350 Accesses
- 75 Altmetric
- [Metrics details](#)

## Subjects

- [Atmospheric chemistry](#)

## Abstract

Atmospheric acidity is increasingly determined by carbon dioxide and organic acids<sup>1,2,3</sup>. Among the latter, formic acid facilitates the nucleation of cloud droplets<sup>4</sup> and contributes to the acidity of clouds and rainwater<sup>1,5</sup>. At present, chemistry–climate models greatly underestimate the atmospheric burden of formic acid, because key processes related to its sources and sinks remain poorly understood<sup>2,6,7,8,9</sup>. Here we present atmospheric chamber experiments that show that formaldehyde is efficiently converted to gaseous formic acid via a multiphase pathway that involves its hydrated form, methanediol. In warm cloud droplets, methanediol undergoes fast outgassing but slow dehydration. Using a chemistry–climate model, we estimate that the gas-phase oxidation of methanediol produces up to four times more formic acid than all other known chemical sources combined. Our findings reconcile model predictions and measurements of formic acid abundance. The additional formic acid burden increases

atmospheric acidity by reducing the pH of clouds and rainwater by up to 0.3. The diol mechanism presented here probably applies to other aldehydes and may help to explain the high atmospheric levels of other organic acids that affect aerosol growth and cloud evolution.

[Download PDF](#)

## Main

Chemical production is estimated to be the dominant atmospheric source of formic acid (HCOOH), with a substantial contribution ascribed to sunlight-induced degradation of volatile organic compounds (VOCs) emitted by plants<sup>6,8,9</sup>. Direct HCOOH emissions are thought to account for less than 15% of the total production<sup>6,8,9</sup>. The overall atmospheric lifetime of HCOOH is 2–4 days, owing to efficient wet and dry deposition in the atmospheric boundary layer<sup>6,7,10</sup>, but increases to about 25 days in cloud-free tropospheric conditions.

Here we use the global chemistry–climate model ECHAM5/MESSy<sup>11</sup> (EMAC) to simulate atmospheric HCOOH abundance. The reference simulation (EMAC<sub>(base)</sub>) implements the chemical formation pathways that are usually accounted for<sup>8,9,12</sup> (Methods). Using Infrared Atmospheric Sounding Interferometer (IASI)/Metop-A satellite column measurements<sup>13</sup> to determine the HCOOH burden (Methods), EMAC<sub>(base)</sub> illustrates the issue (Fig. 1a,b): the model globally underpredicts the satellite columns by a factor of 2–5. Similar biases relative to ground-based Fourier transform infrared (FTIR) columns are observed at several latitudes (Extended Data Fig. 1). These persistent discrepancies point to substantial unidentified sources of atmospheric HCOOH.

**Fig. 1: Formic acid abundance from satellite and model.**

---

 **figure1**

**a–d**, Total formic acid (HCOOH) column (colour scale) derived from IASI satellite observations (**a**), or simulated by the base version of the model (EMAC<sub>(base)</sub>; **b**) or by the model that implements the multiphase production of HCOOH (**c**, EMAC<sub>(diol)</sub>; **d**, EMAC<sub>(diol)</sub>). The HCOOH columns are means over 2010–2012. **e, f**, Probability histograms of the HCOOH column bias between EMAC simulations and satellite data. For EMAC<sub>(base)</sub> versus IASI (purple; **e, f**), the mean column bias over 2010–2012 is  $-1.97 \times 10^{15}$  molecules cm<sup>-2</sup>, the median is  $-1.59 \times 10^{15}$  molecules cm<sup>-2</sup> and the  $1\sigma$  standard deviation is  $1.64 \times 10^{15}$  molecules cm<sup>-2</sup>. For EMAC<sub>(diol)</sub> versus IASI (blue; **e**), the mean is  $-0.88 \times 10^{15}$  molecules cm<sup>-2</sup>, the median is  $-0.66 \times 10^{15}$  molecules cm<sup>-2</sup> and the  $1\sigma$  standard deviation is  $1.62 \times 10^{15}$  molecules cm<sup>-2</sup>. For EMAC<sub>(diol)</sub> versus IASI (green; **f**), the mean is  $0.99 \times 10^{15}$  molecules cm<sup>-2</sup>, the

median is  $0.97 \times 10^{15}$  molecules cm $^{-2}$  and the  $1\sigma$  standard deviation is  $2.16 \times 10^{15}$  molecules cm $^{-2}$ . A seasonal comparison is provided in Extended Data Figs. 3, 4.

[Source data](#)

[Full size image](#)

Recent studies have proposed several missing sources to explain the model underprediction. These include locally enhanced emissions of HCOOH and its precursors, and updated or tentative chemical pathways that involve a broad range of precursors, primarily of biogenic origin<sup>6,9,12,14</sup>. To match the observed concentrations, the required increase in emissions of the known HCOOH precursors and/or HCOOH yields from hydrocarbon oxidation is inconsistent with our understanding of the reactive carbon budget<sup>7,8,15</sup>. Furthermore, such attempts do not account for the elevated HCOOH concentrations observed in free-tropospheric, low-VOC air masses<sup>13,16,17</sup>. Owing to a lack of supporting laboratory measurements, the proposed chemical pathways are often affected by large uncertainties or are speculative. Currently, no atmospheric model offers a consistent picture of tropospheric organic acids.

Here we present a large, ubiquitous chemical source of HCOOH from a multiphase pathway (Fig. 2). In cloud water, formaldehyde (HCHO)—the most abundant aldehyde in the atmosphere—is a known source of HCOOH in remote regions<sup>5,10,18</sup>, via rapid oxidation of its monohydrated form, methanediol ( $\text{HOCH}_2\text{OH}$ ). Nevertheless, most of the HCOOH produced in this manner is efficiently oxidized by OH in the aqueous phase before outgassing. As a result, the net contribution of in-cloud HCOOH formation is small<sup>18</sup>. Because most methanediol is assumed to instantaneously dehydrate to formaldehyde before it volatilizes, global models do not explicitly represent methanediol and instead account for direct aqueous-phase formation of HCOOH from formaldehyde<sup>19,20</sup> (Fig. 2). Using experimental kinetic data<sup>21</sup>, we calculate that under typical warm cloud conditions (260–300 K) methanediol dehydration takes place on timescales of 100–900 s. This is longer than the timescales of cloud-droplet evaporation and aqueous-phase diffusion, which are shorter than 100 s and 0.1–0.01 s, respectively<sup>22,23</sup>. Moreover, methanediol transfer at the gas–liquid interface proceeds rapidly<sup>22</sup>. Therefore, the net flux is driven by the difference in chemical potential between the two phases. We provide evidence that methanediol reaction with OH in the gas phase quantitatively yields HCOOH under atmospheric conditions (Fig. 2). By conducting experiments with the atmospheric simulation chamber SAPHIR (Supplementary Information, section 1), we show that formaldehyde in aqueous solution is efficiently converted to gaseous methanediol immediately after injection, which quantitatively yields HCOOH on photo-oxidation

(Fig. 3). This is supported by theoretical calculations (Supplementary Information, section 2). Hence, the competition between the gas- and aqueous-phase oxidation of methanediol determines the phase in which HCOOH is predominantly produced.

**Fig. 2: Schematic of the multiphase production of formic acid.**



The common assumption in global atmospheric chemistry models is illustrated in black: aqueous-phase methanediol ( $\text{HOCH}_2\text{OH}$ ) is neglected and aqueous-phase formic acid (HCOOH) is assumed to form directly from formaldehyde (HCHO) on reaction with OH. The implementation of  $\text{HOCH}_2\text{OH}$  multiphase equilibria is illustrated in red: the explicit representation of the slow dehydration of aqueous-phase  $\text{HOCH}_2\text{OH}$ , of its fast outgassing from cloud droplets and of its OH-initiated oxidation in the gas phase leads to a pervasive production of gaseous HCOOH. Under typical daytime conditions with average  $[\text{OH}]_{(\text{g})} = 1 \times 10^6 \text{ molecules cm}^{-3}$  and  $[\text{OH}]_{(\text{aq})} = 1 \times 10^{-13} \text{ mol l}^{-1}$ , the lifetimes of  $\text{HOCH}_2\text{OH}$  against OH are about  $1 \times 10^5 \text{ s}$ .

and  $3 \times 10^4$  s, respectively. Under typical midday conditions with  $[\text{OH}]_{(\text{g})} = 5 \times 10^6$  molecules  $\text{cm}^{-3}$ , the gas-phase sink is five times stronger. Thus, gas-phase oxidation sustains the chemical gradient that drives  $\text{HOCH}_2\text{OH}$  from the aqueous to the gas phase.

[Full size image](#)

**Fig. 3: Multiphase production of formic acid in the SAPHIR chamber.**

 [figure3](#)



The formaldehyde (HCHO) mixing ratio was measured (in parts per billion by volume, ppbv) by differential optical absorption spectroscopy (black), whereas the sum of HCHO and methanediol ( $\text{HOCH}_2\text{OH}$ ) was measured using the Hantzsch method. The difference between the Hantzsch and differential optical absorption spectroscopy signals enables visualization of  $\text{HOCH}_2\text{OH}$  (blue). Formic acid (HCOOH) was monitored by using proton-transfer reaction time-of-flight mass spectrometry (red). The instrument uncertainties (shading) are 5% for HCHO, 12% for  $\text{HOCH}_2\text{OH}$  and 20% for HCOOH. On injection of the formalin (stabilized formaldehyde) solution into the Teflon chamber,  $\text{HOCH}_2\text{OH}$  immediately outgasses from the droplets. The chamber roof is initially closed (stage I). The gas-phase HCHO

mixing ratio is initially very low, but increases to be as abundant as HOCH<sub>2</sub>OH just before the start of the photo-oxidation when the roof is opened (stage II). The decay of the HCHO and HOCH<sub>2</sub>OH signals is concurrent with an additional production of HCOOH. Finally, addition of carbon monoxide (CO) as an OH scavenger enabled quantification of the wall effects (stage III). Experimental details are provided in Supplementary Information, sections 1 and 4.

[Source data](#)

[Full size image](#)

We implemented in EMAC the explicit kinetic model for the aqueous-phase transformations and bidirectional phase transfer of methanediol (Supplementary Information, section 3). The solubility of methanediol is not known at any temperature and estimates of it span two orders of magnitude at 298 K. We gauge the effect of this uncertainty on the results by performing the simulations EMAC<sub>(diol)</sub> and EMAC<sub>(dioh)</sub>, which implement the multiphase chemistry of methanediol with Henry's law constants (solubilities) for methanediol of around 10<sup>4</sup> M atm<sup>-1</sup> and 10<sup>6</sup> M atm<sup>-1</sup>, respectively (Methods). At the temperatures prevailing inside the clouds, the kinetic barrier strongly limits the dehydration of methanediol, allowing large amounts to be produced and then outgassed. Over regions with high levels of gas-phase formaldehyde and in the presence of clouds, large methanediol fluxes to the gas phase are predicted (Extended Data Fig. 2). Eventually, rapid gas-phase oxidation of methanediol by OH forms HCOOH, resulting in a substantial increase in the predicted HCOOH columns, by a factor of 2–4 compared to EMAC<sub>(base)</sub> (Fig. 1, Extended Data Figs. 3, 4). Because cloud droplets may potentially form everywhere and formaldehyde is ubiquitous in the troposphere (Extended Data Fig. 5), the HCOOH enhancement occurs both in high-VOC concentration regions and in remote environments. The additional HCOOH production allows the model predictions to reach the measured HCOOH levels derived from IASI and to reduce the mean ( $\pm 1\sigma$ ) model-to-satellite biases from  $-1.97(\pm 1.64) \times 10^{15}$  molecules cm<sup>-2</sup> for EMAC<sub>(base)</sub> to  $-0.88(\pm 1.62) \times 10^{15}$  molecules cm<sup>-2</sup> for EMAC<sub>(dioh)</sub> and  $0.99(\pm 2.16) \times 10^{15}$  molecules cm<sup>-2</sup> for EMAC<sub>(diol)</sub> (Fig. 1). Similar improvements are observed with respect to the FTIR data (Extended Data Fig. 1).

Although the multiphase mechanism fills the gap between model and measurements globally, the EMAC<sub>(dioh)</sub> and EMAC<sub>(diol)</sub> simulations overpredict the HCOOH columns over tropical forests and underpredict the columns over boreal forests. We ascribe these remaining discrepancies primarily to inaccuracies in the predicted formaldehyde distributions as compared to Ozone Monitoring Instrument (OMI)/Aura measurements (Extended Data Fig. 5). Regional underestimation (overestimation) of

modelled formaldehyde translates through the multiphase conversion to underprediction (overprediction) of HCOOH (Extended Data Fig. 6). For instance, underestimated biomass-burning emissions of VOCs lead to an underpredicted abundance of formaldehyde, and hence of HCOOH, such as during the 2010 Russian wildfires (Extended Data Fig. 6a–d). Conversely, the too-high model temperatures over Amazonia during the dry season induce an excess in isoprene emissions, which results in too-high formaldehyde and HCOOH levels (Extended Data Fig. 6i–l). More realistic VOC emissions, and enhanced modelling of formaldehyde and its dependence on  $\text{NO}_x$ , will eventually lead to further improvements in predicted HCOOH. Fast reaction of HCOOH with stabilized Criegee intermediates have recently been emphasized<sup>24,25</sup>. The overprediction of HCOOH over the tropical forests might be reduced if this additional sink were considered. Implementation of  $\alpha$ -hydroperoxycarbonyls photolysis<sup>9,26</sup> and photo-oxidation of aromatics<sup>27</sup>, and of a temperature-dependent solubility for methanediol, would further improve the representation of HCOOH.

We present in Table 1 a revised atmospheric budget for HCOOH, which we compare to estimates from recent studies<sup>6,7,8,9</sup> (the contribution of single chemical terms is provided in Extended Data Table 1). EMAC<sub>(dioh)</sub> and EMAC<sub>(diol)</sub> provide, respectively, lower and higher estimates of the extra HCOOH produced via the multiphase processing of formaldehyde. EMAC<sub>(diol)</sub> yields an increase by a factor of five of the total photochemical source predicted by EMAC<sub>(base)</sub> ( $190.9 \text{ Tg yr}^{-1}$  compared to  $37.7 \text{ Tg yr}^{-1}$ ), and gas-phase oxidation of methanediol becomes the dominant contributor to atmospheric HCOOH ( $150.6 \text{ Tg yr}^{-1}$ ). Although EMAC<sub>(dioh)</sub> assumes that methanediol is 100 times more soluble (compared to EMAC<sub>(diol)</sub>), it still yields an increase by a factor of two in photochemical production ( $83.5 \text{ Tg yr}^{-1}$ ). This is in line with previous estimates of the missing HCOOH sources, which include, from source inversions, direct HCOOH emissions from vegetation or the OH-initiated oxidation of a short-lived, unidentified biogenic precursor<sup>7</sup>. The second largest source is VOC ozonolysis (about  $31 \text{ Tg yr}^{-1}$ ); other sources are below  $4 \text{ Tg yr}^{-1}$ .

**Table 1 Atmospheric budget for formic acid**  
[Full size table](#)

The extra HCOOH production leads to a more realistic prediction of atmospheric organic acids and substantially increases atmospheric acidity globally (Extended Data Fig. 7). Compared to EMAC<sub>(base)</sub>, EMAC<sub>(dioh)</sub> and EMAC<sub>(diol)</sub> predict a decrease in the pH of clouds and rainwater in the tropics by as much as 0.2 and 0.3, respectively. The high moisture content, extended cloud cover and high temperatures that prevail in tropical and similar environments facilitate the production of HCOOH via formation and outgassing of the relevant gem-diol. Higher acidity is also predicted at North

Hemisphere mid-latitudes in summertime, notably over boreal forests, consistent with previous predictions<sup>7</sup>.

The multiphase production of HCOOH affects predictions for formaldehyde and carbon monoxide (CO). Both gases are important for tropospheric ozone and radical cycles, and are usually the target of satellite-driven inversion modelling. EMAC<sub>(diox)</sub> and EMAC<sub>(diol)</sub> predict decreases of up to 10% and 20%, respectively, in formaldehyde columns over tropical source regions during specific months (Extended Data Fig. 8). We anticipate that the estimates of regional hydrocarbon emissions based on formaldehyde source inversions will be improved once the multiphase mechanism is accounted for. The reduced formaldehyde concentrations result in lower modelled CO yield from methane oxidation, notably over remote areas, where methane oxidation is the main source of atmospheric CO (Extended Data Fig. 9). Globally, the average tropospheric CO yield from methane oxidation changes from 0.91 for EMAC<sub>(base)</sub> to 0.88 for EMAC<sub>(diol)</sub> and 0.90 for EMAC<sub>(diox)</sub>, in agreement with isotope-enabled inversion estimates<sup>28</sup>.

We have shown that a multiphase pathway involving aldehyde hydrates is decisive in predicting organic acid formation and atmospheric acidity. It could also be important in the presence of deliquescent aerosols and would explain the elevated HCOOH levels in cloud-free conditions<sup>29</sup>. Given the favourable hydration equilibrium constants for major C<sub>2</sub>–C<sub>3</sub> carbonyls<sup>30</sup>, this pathway opens up avenues for more realistic representation of other abundant organic acids, and hence of cloud-droplet nucleation and cloud evolution. We expect the multiphase processing for glyoxal and methylglyoxal to be important for explaining the observed concentrations of oxalic and pyruvic acids<sup>4</sup>. Understanding these multiphase processes advances our knowledge of atmospheric reactive carbon oxidation chains and of chemistry–climate interactions.

## Methods

### Model setup and simulations

Simulations were performed with the ECHAM5/MESSy v2.53.0 model<sup>11</sup> (EMAC) on the JURECA supercomputer<sup>31</sup>. A horizontal resolution of T63 (about 1.8° × 1.8°), with 31 vertical layers from the surface up to the lower stratosphere at 10 hPa, was applied. Chemical feedbacks are deactivated by using the quasi chemical transport mode<sup>32</sup>. Biomass-burning emissions are calculated with the Global Fire Assimilation System (GFAS) inventory<sup>33</sup>. The emission factors for organic compounds were taken from ref. <sup>34</sup>, except the ones for aromatics, which were taken from refs. <sup>35,36</sup>.

Anthropogenic emissions of  $\text{NO}_x$  and organic compounds were taken from ACCMIP<sup>37</sup>. The chosen gas-phase chemical mechanism includes a state-of-the-art representation of terpene and aromatics oxidation chemistry<sup>20</sup>. The EMAC cloud and precipitation parameterization follows ref. <sup>38</sup>.

In the reference model simulation (EMAC<sub>(base)</sub>), HCOOH production proceeds through the ozonolysis of alkenes with terminal double bonds (simple alkenes and degradation products of isoprene and monoterpenes), alkyne oxidation, reaction of formaldehyde with the peroxy radical, oxidation of enols, and formation from vinyl alcohol<sup>39</sup>. Nonetheless, we exclude the OH-initiated oxidation of isoprene and monoterpenes, the corresponding mechanisms of which are still speculative<sup>6,8,40,41</sup>, as well as the reaction of methyl peroxy radical with OH, which was shown not to yield HCOOH<sup>42</sup>. A detailed description of the relevant chemical kinetics, budget terms and deposition parameters for each model simulation is provided in Supplementary Information, section <sup>3a</sup>.

Two simulations with the explicit multiphase model for methanediol, EMAC<sub>(diox)</sub> and EMAC<sub>(diol)</sub>, are described in detail in Supplementary Information, section <sup>3b</sup>. The simulations differ only by the value of the Henry's law constant (solubility) of methanediol, for which no experimental measurements are available. Values of about  $10^4 \text{ M atm}^{-1}$  and  $10^6 \text{ M atm}^{-1}$  are used for EMAC<sub>(diol)</sub> and EMAC<sub>(diox)</sub>, respectively. These are possible values of the Henry's law constant for methanediol, given the spread of estimates at 298 K by semi-empirical methods and the expected temperature dependence. However, higher values (around  $10^7 \text{ M atm}^{-1}$ ) cannot be excluded at typical temperatures of warm clouds (Supplementary Information, section <sup>3b.iii</sup>).

For the comparison with IASI and OMI observations (Fig. 1, Extended Data Figs. 3–6), the HCOOH and formaldehyde volume mixing ratio profiles simulated by EMAC are sampled along the Sun-synchronous satellite Metop-A and Aura orbits, respectively, at the time and location of the IASI and OMI measurements, using the SORBIT submodel<sup>11</sup>. The sampled volume mixing ratios are then daily averaged and computed in HCOOH and formaldehyde columns.

Model sources of uncertainties, including the formation of a HCOOH·H<sub>2</sub>O complex with water vapour<sup>43</sup>, are discussed in Supplementary Information, section <sup>5</sup>.

## IASI column observations

IASI<sup>44</sup> is a nadir-viewing Fourier transform spectrometer launched on board the Metop-A, -B and -C platforms in October 2006, September 2012 and November 2018, respectively. IASI measures in the thermal infrared, between  $645 \text{ cm}^{-1}$  and

$2,760\text{ cm}^{-1}$ . It records radiance from the Earth's surface and the atmosphere, with an apodized spectral resolution of  $0.5\text{ cm}^{-1}$ , spectrally sampled at  $0.25\text{ cm}^{-1}$ . In the spectral range in which the HCOOH  $\nu_6$  Q branch absorbs (about  $1,105\text{ cm}^{-1}$ ), IASI has a radiometric noise of around  $0.15\text{ K}$  for a reference blackbody at  $280\text{ K}$ . IASI provides near global coverage twice per day, with observations at around 09:30 am and 09:30 pm, local time. Here, the HCOOH columns are derived from IASI/Metop-A (covering 2010–2012). Only the morning satellite overpasses are used, because such observations have a higher measurement sensitivity<sup>13</sup>. For comparison with EMAC simulations, the 2010–2012 IASI data are daily averaged on the model spatial grid. On average, 17 satellite measurements per day (more than 18,000 over 2010–2012) are used per  $1.8^\circ \times 1.8^\circ$  model grid box at the Equator. This number increases with latitude and with the higher spatial sampling of IASI, owing to the satellite polar orbits.

Version 3 of the artificial neural network for IASI (ANNI) was applied to retrieve HCOOH abundances from the IASI measurements (see refs. [13,45](#) for a comprehensive description of the retrieval algorithm and the HCOOH product). The ANNI framework was specifically designed to provide a robust and unbiased retrieval of weakly absorbing trace gases such as HCOOH. The retrieval relies on a neural network to convert weak spectral signatures to a total column, accounting for the state of the surface and atmosphere at the time and place of the overpass of IASI. The vertical sensitivity of IASI to HCOOH peaks between 1 km and 6 km, gradually decreasing outside that range<sup>46</sup>. However, by assuming that HCOOH is distributed vertically according to a certain profile, the neural network is able to provide an estimate of the total column of HCOOH. Because the ANNI retrievals do not rely on a priori information, no averaging kernels are produced and the retrieved columns are meant to be used at face value for carrying out unbiased comparisons with model data (see ref. [13](#) and references therein for the rationale). Data filtering prevents retrieval over cloudy scenes and post-filtering discards scenes for which the sensitivity to HCOOH is too low for a meaningful retrieval.

The HCOOH product comes with its own pixel-dependent estimate of random uncertainties, calculated by propagating the uncertainties of each input variable of the neural network<sup>13</sup>. For a typical non-background HCOOH abundance ( $(0.3\text{--}2.0) \times 10^{15}\text{ molecules cm}^{-2}$ ), the relative uncertainty on an individual retrieved column ranges from 10% to 50%, with the highest uncertainties found for the low columns. This uncertainty increases for lower-background columns as the weaker HCOOH concentrations approach the IASI detection threshold. However, these random uncertainties become negligible for the column averages presented here, because of the total number of measurements per grid cell. With respect to systematic uncertainties, the main term is related to the assumption of a fixed HCOOH vertical profile. It is not possible to quantify this uncertainty on an individual-pixel basis, but it

was estimated to not exceed 20% on average<sup>13</sup>. A comparison with independent HCOOH columns from ground-based FTIR measurements at various latitudes and environments confirmed the absence of any large systematic biases of the IASI data<sup>45</sup>. Although biases of around 20% cannot be excluded, in the context of this work, the accuracy of the IASI product is sufficient to demonstrate the initial model underprediction (EMAC<sub>(base)</sub>) of the HCOOH columns and the large improvements from the multiphase mechanism.

## Theoretical predictions

Quantum chemical calculations were performed at various levels of theory, up to CCSD(T)/CBS(DTQ)//IRCMax(CCSD(T)//M06-2X/aug-cc-pVQZ), and combined with E,J- $\mu$ VTST multi-conformer microvariational transition-state calculations to obtain rate coefficients for the gas-phase high-pressure-limit rate coefficients (Supplementary Information, section 2).

## Data availability

The EMAC model data are publicly accessible at <https://doi.org/10.5281/zenodo.4315292>, <https://doi.org/10.5281/zenodo.4315276> and <https://doi.org/10.5281/zenodo.4314730>. The IASI measurements may be found at <https://doi.org/10.5281/zenodo.4314367>. The OMI measurements are openly distributed via the Quality Assurance for Essential Climate Variables repository (<https://doi.org/10.18758/71021031>). The FTIR observations are publicly accessible at <https://doi.org/10.5281/zenodo.4321348> and <https://doi.org/10.5445/IR/1000127831>. Data from the experiments are available on the Eurochamp database (<https://doi.org/10.25326/Q00C-MY65>, <https://doi.org/10.25326/KHYY-FP10>, <https://doi.org/10.25326/BC4N-TY93> and <https://doi.org/10.25326/DAS4-7Q54>). The raw quantum chemical data are provided in Supplementary Information, section 10. [Source data](#) are provided with this paper.

## Code availability

The Modular Earth Submodel System (MESSy) is continuously being developed and applied by a consortium of institutions. The usage of MESSy and access to the source code is licensed to all affiliates of institutions that are members of the MESSy Consortium. Institutions can become a member of the MESSy Consortium by signing the MESSy Memorandum of Understanding (more information at <http://www.messy-interface.org>). The modifications presented here were implemented on MESSy v2.53.0. The source code used to produce the results is archived at the Jülich

Supercomputing Centre and can be made available to members of the MESSy community on request.

## References

1. 1.

Galloway, J. N., Likens, G. E., Keene, W. C. & Miller, J. M. The composition of precipitation in remote areas of the world. *J. Geophys. Res.* **87**, 8771–8786 (1982).

[ADS](#) [CAS](#) [Google Scholar](#)

2. 2.

Keene, W. C. et al. Atmospheric wet deposition in remote regions: benchmarks for environmental change. *J. Atmos. Sci.* **72**, 2947–2978 (2015).

[ADS](#) [Google Scholar](#)

3. 3.

Kjær, H. A. et al. An optical dye method for continuous determination of acidity in ice cores. *Environ. Sci. Technol.* **50**, 10485–10493 (2016).

[ADS](#) [PubMed](#) [Google Scholar](#)

4. 4.

Yu, S. Role of organic acids (formic, acetic, pyruvic and oxalic) in the formation of cloud condensation nuclei (CCN): a review. *Atmos. Res.* **53**, 185–217 (2000).

[CAS](#) [Google Scholar](#)

5. 5.

Chameides, W. L. & Davis, D. D. Aqueous-phase source of formic acid in clouds. *Nature* **304**, 427–429 (1983).

[ADS](#) [CAS](#) [Google Scholar](#)

6. 6.

Paulot, F. et al. Importance of secondary sources in the atmospheric budgets of formic and acetic acids. *Atmos. Chem. Phys.* **11**, 1989–2013 (2011).

[ADS](#) [CAS](#) [PubMed](#) [PubMed Central](#) [Google Scholar](#)

7. 7.

Stavrakou, T. et al. Satellite evidence for a large source of formic acid from boreal and tropical forests. *Nat. Geosci.* **5**, 26–30 (2012).

[ADS](#) [CAS](#) [Google Scholar](#)

8. 8.

Millet, D. B. et al. A large and ubiquitous source of atmospheric formic acid. *Atmos. Chem. Phys.* **15**, 6283–6304 (2015).

[ADS](#) [CAS](#) [Google Scholar](#)

9. 9.

Müller, J.-F., Stavrakou, T. & Peeters, J. Chemistry and deposition in the model of atmospheric composition at global and regional scales using inversion techniques for trace gas emissions (MAGRITTE v1.1). Part 1: chemical mechanism. *Geosci. Model Dev.* **12**, 2307–2356 (2019).

[ADS](#) [Google Scholar](#)

10. 10.

Chebbi, A. & Carlier, P. Carboxylic acids in the troposphere, occurrence, sources, and sinks: a review. *Atmos. Environ.* **30**, 4233–4249 (1996).

[ADS](#) [CAS](#) [Google Scholar](#)

11. 11.

Jöckel, P. et al. Development cycle 2 of the modular earth submodel system (MESSy2). *Geosci. Model Dev.* **3**, 717–752 (2010).

[ADS](#) [Google Scholar](#)

12. 12.

Shaw, M. F. et al. Photo-tautomerization of acetaldehyde as a photochemical source of formic acid in the troposphere. *Nat. Commun.* **9**, 2584 (2018).

[ADS](#) [PubMed](#) [PubMed Central](#) [Google Scholar](#)

13. 13.

Franco, B. et al. A general framework for global retrievals of trace gases from IASI: application to methanol, formic acid, and PAN. *J. Geophys. Res. Atmospheres* **123**, 13963–13984 (2018).

[ADS](#) [CAS](#) [Google Scholar](#)

14. 14.

Chaliyakunnel, S., Millet, D. B., Wells, K. C., Cady-Pereira, K. E. & Shephard, M. W. A large underestimate of formic acid from tropical fires: constraints from space-borne measurements. *Environ. Sci. Technol.* **50**, 5631–5640 (2016).

[ADS](#) [CAS](#) [PubMed](#) [Google Scholar](#)

15. 15.

Alwe, H. D. et al. Oxidation of volatile organic compounds as the major source of formic acid in a mixed forest canopy. *Geophys. Res. Lett.* **46**, 2940–2948 (2019).

[ADS](#) [CAS](#) [PubMed](#) [PubMed Central](#) [Google Scholar](#)

16. 16.

Chen, X. et al. On the sources and sinks of atmospheric VOCs: an integrated analysis of recent aircraft campaigns over North America. *Atmos. Chem. Phys.* **19**, 9097–9123 (2019).

[ADS](#) [CAS](#) [PubMed](#) [PubMed Central](#) [Google Scholar](#)

17. 17.

Mungall, E. L. et al. High gas-phase mixing ratios of formic and acetic acid in the High Arctic. *Atmos. Chem. Phys.* **18**, 10237–10254 (2018).

[ADS](#) [CAS](#) [Google Scholar](#)

18. 18.

Jacob, D. J. Chemistry of OH in remote clouds and its role in the production of formic acid and peroxymonosulfate. *J. Geophys. Res.* **91**, 9807–9826 (1986).

[ADS](#) [CAS](#) [Google Scholar](#)

19. 19.

Tost, H., Jöckel, P., Kerkweg, A., Sander, R. & Lelieveld, J. Technical note: a new comprehensive SCAVenging submodel for global atmospheric chemistry modelling. *Atmos. Chem. Phys.* **6**, 565–574 (2006).

[ADS](#) [CAS](#) [Google Scholar](#)

20. 20.

Sander, R. et al. The community atmospheric chemistry box model CAABA/MECCA-4.0. *Geosci. Model Dev.* **12**, 1365–1385 (2019).

[ADS](#) [CAS](#) [Google Scholar](#)

21. 21.

Winkelmann, J. G. M., Voorwinde, O. K., Ottens, M., Beenackers, A. A. C. M. & Janssen, L. P. B. M. Kinetics and chemical equilibrium of the hydration of formaldehyde. *Chem. Eng. Sci.* **57**, 4067–4076 (2002).

[CAS](#) [Google Scholar](#)

22. 22.

Sander, R. Modeling atmospheric chemistry: interactions between gas-phase species and liquid cloud/aerosol particles. *Surv. Geophys.* **20**, 1–31 (1999).

[ADS](#) [Google Scholar](#)

23. 23.

Jarecka, D., Grabowski, W. W., Morrison, H. & Pawlowska, H. Homogeneity of the subgrid-scale turbulent mixing in large-eddy simulation of shallow convection. *J. Atmos. Sci.* **70**, 2751–2767 (2013).

[ADS](#) [Google Scholar](#)

24. 24.

Vereecken, L., Novelli, A. & Taraborrelli, D. Unimolecular decay strongly limits the atmospheric impact of Criegee intermediates. *Phys. Chem. Chem. Phys.* **19**, 31599–31612 (2017).

[CAS](#) [PubMed](#) [Google Scholar](#)

25. 25.

Caravan, R. L. et al. Direct kinetic measurements and theoretical predictions of an isoprene-derived Criegee intermediate. *Proc. Natl Acad. Sci. USA* **117**, 9733–9740 (2020).

[CAS](#) [PubMed](#) [Google Scholar](#)

26. 26.

Liu, Z., Nguyen, V. S., Harvey, J., Müller, J.-F. & Peeters, J. The photolysis of  $\alpha$ -hydroperoxycarbonyls. *Phys. Chem. Chem. Phys.* **20**, 6970–6979 (2018).

[CAS](#) [PubMed](#) [Google Scholar](#)

27. 27.

Wang, S. et al. Aromatic photo-oxidation, a new source of atmospheric acidity. *Environ. Sci. Technol.* **54**, 7798–7806 (2020).

[ADS](#) [CAS](#) [PubMed](#) [Google Scholar](#)

28. 28.

Bergamaschi, P., Hein, R., Brenninkmeijer, C. A. M. & Crutzen, P. J. Inverse modeling of the global CO cycle: 2. Inversion of  $^{13}\text{C}/^{12}\text{C}$  and  $^{18}\text{O}/^{16}\text{O}$  isotope ratios. *J. Geophys. Res. Atmospheres* **105**, 1929–1945 (2000).

[ADS](#) [CAS](#) [Google Scholar](#)

29. 29.

Yuan, B. et al. Investigation of secondary formation of formic acid: urban environment vs. oil and gas producing region. *Atmos. Chem. Phys.* **15**, 1975–1993 (2015).

[ADS](#) [CAS](#) [Google Scholar](#)

30. 30.

Doussin, J.-F. & Monod, A. Structure–activity relationship for the estimation of OH-oxidation rate constants of carbonyl compounds in the aqueous phase. *Atmos. Chem. Phys.* **13**, 11625–11641 (2013).

[ADS](#) [Google Scholar](#)

31. 31.

Krause, D. & Thörnig, P. JURECA: modular supercomputer at Jülich Supercomputing Centre. *J. Large-scale Res. Facil.* **4**, A132 (2018).

[Google Scholar](#)

32. 32.

Deckert, R., Jöckel, P., Grewe, V., Gottschaldt, K.-D. & Hoor, P. A quasi chemistry-transport model mode for EMAC. *Geosci. Model Dev.* **4**, 195–206 (2011).

[ADS](#) [Google Scholar](#)

33. 33.

Kaiser, J. W. et al. Biomass burning emissions estimated with a global fire assimilation system based on observed fire radiative power. *Biogeosciences* **9**, 527–554 (2012).

[ADS](#) [CAS](#) [Google Scholar](#)

34. 34.

Akagi, S. K. et al. Emission factors for open and domestic biomass burning for use in atmospheric models. *Atmos. Chem. Phys.* **11**, 4039–4072 (2011).

[ADS](#) [CAS](#) [Google Scholar](#)

35. 35.

Andreae, M. O. & Merlet, P. Emission of trace gases and aerosols from biomass burning. *Glob. Biogeochem. Cycles* **15**, 955–966 (2001).

[ADS](#) [CAS](#) [Google Scholar](#)

36. 36.

Cabrera-Perez, D., Taraborrelli, D., Sander, R. & Pozzer, A. Global atmospheric budget of simple monocyclic aromatic compounds. *Atmos. Chem. Phys.* **16**, 6931–6947 (2016).

[ADS](#) [CAS](#) [Google Scholar](#)

37. 37.

Lamarque, J.-F. et al. Historical (1850–2000) gridded anthropogenic and biomass burning emissions of reactive gases and aerosols: methodology and application. *Atmos. Chem. Phys.* **10**, 7017–7039 (2010).

[ADS](#) [CAS](#) [Google Scholar](#)

38. 38.

Tost, H., Jöckel, P. & Lelieveld, J. Influence of different convection parameterisations in a GCM. *Atmos. Chem. Phys.* **6**, 5475–5493 (2006).

[ADS](#) [CAS](#) [Google Scholar](#)

39. 39.

So, S., Wille, U. & da Silva, G. Atmospheric chemistry of enols: a theoretical study of the vinyl alcohol + OH + O<sub>2</sub> reaction mechanism. *Environ. Sci. Technol.* **48**, 6694–6701 (2014).

[ADS](#) [CAS](#) [PubMed](#) [Google Scholar](#)

40. 40.

Butkovskaya, N. I., Pouvesle, N., Kukui, A., Mu, Y. & Bras, G. L. Mechanism of the OH-initiated oxidation of hydroxyacetone over the temperature range 236–298 K. *J. Phys. Chem. A* **110**, 6833–6843 (2006).

[CAS](#) [PubMed](#) [Google Scholar](#)

41. 41.

Butkovskaya, N. I., Pouvesle, N., Kukui, A. & Bras, G. L. Mechanism of the OH-initiated oxidation of glycolaldehyde over the temperature range 233–296 K. *J. Phys. Chem. A* **110**, 13492–13499 (2006).

[CAS](#) [PubMed](#) [Google Scholar](#)

42. 42.

Assaf, E. et al. The reaction between CH<sub>3</sub>O<sub>2</sub> and OH radicals: product yields and atmospheric implications. *Environ. Sci. Technol.* **51**, 2170–2177 (2017).

[ADS](#) [CAS](#) [PubMed](#) [Google Scholar](#)

43. 43.

Iuga, C., Alvarez-Idaboy, J. R. & Vivier-Bunge, A. Mechanism and kinetics of the water-assisted formic acid + OH reaction under tropospheric conditions. *J. Phys. Chem. A* **115**, 5138–5146 (2011).

[CAS](#) [PubMed](#) [Google Scholar](#)

44. 44.

Clerbaux, C. et al. Monitoring of atmospheric composition using the thermal infrared IASI/MetOp sounder. *Atmos. Chem. Phys.* **9**, 6041–6054 (2009).

[ADS](#) [CAS](#) [Google Scholar](#)

45. 45.

Franco, B. et al. Spaceborne measurements of formic and acetic acids: a global view of the regional sources. *Geophys. Res. Lett.* **47**, e2019GL086239 (2020).

[ADS](#) [CAS](#) [Google Scholar](#)

46. 46.

Pommier, M. et al. HCOOH distributions from IASI for 2008–2014: comparison with ground-based FTIR measurements and a global chemistry-transport model. *Atmos. Chem. Phys.* **16**, 8963–8981 (2016).

[ADS](#) [CAS](#) [Google Scholar](#)

[Download references](#)

## Acknowledgements

We acknowledge the computing time granted by the JARA-HPC Vergabegremium and VSR commission on the supercomputer JURECA at Forschungszentrum Jülich. B.F. was partly supported by a Marie Curie COFUND postdoctoral fellow grant co-funded by the University of Liège and the European Union (FP7-PEOPLE, project ID 600405). L.C. and E.M. are research associates with the F.R.S.–FNRS (Brussels). The IASI mission is a joint mission of EUMETSAT and the Centre National d’Etudes Spatiales (CNES, France). This work received funding from the Initiative and Networking Fund of the Helmholtz Association through the projects ‘Advanced Earth System Modelling Capacity (ESM)’ and ‘Pilot Lab Exascale Earth System Modelling (PL-ExaESM)’. The content of this paper is the sole responsibility of the author(s) and it does not represent the opinion of the Helmholtz Association, and the Helmholtz Association is not responsible for any use that might be made of the information contained. Most IASI activities were supported by the Belgian State Federal Office for Scientific, Technical and Cultural Affairs (Prodex arrangement IASI.FLOW). OMI HCHO developments at BIRA were supported by the EU FP7 QA4ECV project, in close cooperation with KNMI, University of Bremen, MPIC-Mainz and WUR (<http://www.qa4ecv.eu/ecv/hcho-p>). The FTIR monitoring program of ULiège at Jungfraujoch benefited from the involvement of C. Servais and O. Flock. It was primarily funded by the F.R.S.–FNRS (grant no. J.0147.18), the Fédération Wallonie-Bruxelles and the GAW-CH program of MeteoSwiss. We acknowledge the International Foundation High Altitude Research Stations Jungfraujoch and Gornergrat (HFSJG, Bern) for supporting the facilities needed to perform the FTIR observations at Jungfraujoch. Eureka FTIR measurements were made at the Polar Environment Atmospheric Research Laboratory (PEARL) by the Canadian Network for the Detection of Atmospheric Change (CANDAC), led by J. R. Drummond, and in part by the Canadian Arctic ACE/OSIRIS Validation Campaigns, led by K. A. Walker; support was provided by AIF/NSRIT, CFI, CFCAS, CSA, ECCC, GOC-IPY, NSERC, NSTP, OIT, PCSP and ORF. Toronto FTIR measurements were made at the University of Toronto Atmospheric Observatory, supported by CSA, NSERC, ECCC and UofT. The National Center for Atmospheric Research is sponsored by the National Science Foundation. The NCAR FTS observation programmes at Thule (GR) and Boulder (CO) are supported under contract by NASA. The Thule work is also supported by the NSF Office of Polar Programs (OPP). We thank the Danish Meteorological Institute for support at the Thule site. The Wollongong solar remote sensing program has been supported through a series of Australian Research Council grants, most recently DP160101598. Funding via Helmholtz ATMO programme has enabled sustained NDACC FTIR activities at Kiruna and Izana since the late 1990s. The Izana NDACC FTIR observations strongly rely on the support (facilities and operational activities) of the Izana Atmospheric Research Centre of the Spanish Weather Service (AEMET), with lead contributions of O. E. García. Researchers from KIT thank U. Raffalski and P. Voelger (Swedish Institute of Space Physics; IRF) for continuing support of the NDACC FTIR site Kiruna. We thank Université de La Réunion and CNRS (LACy-

UMR8105 and UMS3365) for financial support of the FTIR instrumentation at St-Denis, and C. Hermans, F. Scolas (BIRA-IASB) and J.-M. Metzger (Université de La Réunion) for FTIR maintenance. The IASI HCOOH data and FTIR HCOOH data at St-Denis are currently obtained through the BRAIN-be project OCTAVE, financed by the Belgian Science Policy Office (BELSPO).

## Funding

Open access funding provided by Forschungszentrum Jülich GmbH.

## Author information

### Author notes

1. These authors contributed equally: B. Franco, D. Taraborrelli

### Affiliations

1. Institute of Energy and Climate Research, IEK-8: Troposphere, Forschungszentrum Jülich, Jülich, Germany  
B. Franco, C. Cho, H.-P. Dorn, T. Emmerichs, H. Fuchs, G. Gkatzelis, T. Hohaus, A. Kerkweg, A. Kiendler-Scharr, A. Novelli, D. Reimer, S. Rosanka, R. Tillmann, L. Vereecken, A. Wahner & D. Taraborrelli
2. Université libre de Bruxelles (ULB), Spectroscopy, Quantum Chemistry and Atmospheric Remote Sensing, Brussels, Belgium  
B. Franco, L. Clarisse, C. Clerbaux & P.-F. Coheur
3. Institute of Meteorology and Climate Research, Karlsruhe Institute of Technology, Karlsruhe, Germany  
T. Blumenstock, F. Hase & M. Schneider
4. LATMOS/IPSL, Sorbonne Université, UVSQ, CNRS, Paris, France  
C. Clerbaux & M. Pommier
5. Royal Belgian Institute for Space Aeronomy, Brussels, Belgium  
M. De Mazière, I. De Smedt, M. Van Roozendael & C. Vigouroux

6. Centre for Atmospheric Chemistry, School of Earth Atmospheric and Life Sciences, University of Wollongong, Wollongong, New South Wales, Australia

D. W. T. Griffith, N. Jones & C. Paton-Walsh

7. Max Planck Institute for Chemistry, Mainz, Germany

S. Gromov, A. Pozzer & R. Sander

8. Institute of Global Climate and Ecology (Roshydromet and RAS), Moscow, Russia

S. Gromov

9. National Center for Atmospheric Research, Boulder, CO, USA

J. W. Hannigan & I. Ortega

10. Department of Physics, University of Toronto, Toronto, Ontario, Canada

E. Lutsch & K. Strong

11. Institute of Astrophysics and Geophysics, University of Liège, Liège, Belgium

E. Mahieu

12. Ricardo Energy and Environment, Harwell, UK

M. Pommier

## Authors

1. B. Franco

[View author publications](#)

You can also search for this author in [PubMed](#) [Google Scholar](#)

2. T. Blumenstock

[View author publications](#)

You can also search for this author in [PubMed](#) [Google Scholar](#)

3. C. Cho

[View author publications](#)

You can also search for this author in [PubMed](#) [Google Scholar](#)

4. L. Clarisse

[View author publications](#)

You can also search for this author in [PubMed](#) [Google Scholar](#)

5. C. Clerbaux

[View author publications](#)

You can also search for this author in [PubMed](#) [Google Scholar](#)

6. P.-F. Coheur

[View author publications](#)

You can also search for this author in [PubMed](#) [Google Scholar](#)

7. M. De Mazière

[View author publications](#)

You can also search for this author in [PubMed](#) [Google Scholar](#)

8. I. De Smedt

[View author publications](#)

You can also search for this author in [PubMed](#) [Google Scholar](#)

9. H.-P. Dorn

[View author publications](#)

You can also search for this author in [PubMed](#) [Google Scholar](#)

10. T. Emmerichs

[View author publications](#)

You can also search for this author in [PubMed](#) [Google Scholar](#)

11. H. Fuchs

[View author publications](#)

You can also search for this author in [PubMed](#) [Google Scholar](#)

12. G. Gkatzelis

[View author publications](#)

You can also search for this author in [PubMed](#) [Google Scholar](#)

13. D. W. T. Griffith

[View author publications](#)

You can also search for this author in [PubMed](#) [Google Scholar](#)

14. S. Gromov

[View author publications](#)

You can also search for this author in [PubMed](#) [Google Scholar](#)

15. J. W. Hannigan

[View author publications](#)

You can also search for this author in [PubMed](#) [Google Scholar](#)

16. F. Hase

[View author publications](#)

You can also search for this author in [PubMed](#) [Google Scholar](#)

17. T. Hohaus

[View author publications](#)

You can also search for this author in [PubMed](#) [Google Scholar](#)

18. N. Jones

[View author publications](#)

You can also search for this author in [PubMed](#) [Google Scholar](#)

19. A. Kerkweg

[View author publications](#)

You can also search for this author in [PubMed](#) [Google Scholar](#)

20. A. Kiendler-Scharr

[View author publications](#)

You can also search for this author in [PubMed](#) [Google Scholar](#)

21. E. Lutsch

[View author publications](#)

You can also search for this author in [PubMed](#) [Google Scholar](#)

22. E. Mahieu

[View author publications](#)

You can also search for this author in [PubMed](#) [Google Scholar](#)

23. A. Novelli

[View author publications](#)

You can also search for this author in [PubMed](#) [Google Scholar](#)

24. I. Ortega

[View author publications](#)

You can also search for this author in [PubMed](#) [Google Scholar](#)

25. C. Paton-Walsh

[View author publications](#)

You can also search for this author in [PubMed](#) [Google Scholar](#)

26. M. Pommier

[View author publications](#)

You can also search for this author in [PubMed](#) [Google Scholar](#)

27. A. Pozzer

[View author publications](#)

You can also search for this author in [PubMed](#) [Google Scholar](#)

28. D. Reimer

[View author publications](#)

You can also search for this author in [PubMed](#) [Google Scholar](#)

29. S. Rosanka

[View author publications](#)

You can also search for this author in [PubMed](#) [Google Scholar](#)

30. R. Sander

[View author publications](#)

You can also search for this author in [PubMed](#) [Google Scholar](#)

31. M. Schneider

[View author publications](#)

You can also search for this author in [PubMed](#) [Google Scholar](#)

32. K. Strong

[View author publications](#)

You can also search for this author in [PubMed](#) [Google Scholar](#)

33. R. Tillmann

[View author publications](#)

You can also search for this author in [PubMed](#) [Google Scholar](#)

34. M. Van Roozendaal

[View author publications](#)

You can also search for this author in [PubMed](#) [Google Scholar](#)

35. L. Vereecken

[View author publications](#)

You can also search for this author in [PubMed](#) [Google Scholar](#)

36. C. Vigouroux

[View author publications](#)

You can also search for this author in [PubMed](#) [Google Scholar](#)

37. A. Wahner

[View author publications](#)

You can also search for this author in [PubMed](#) [Google Scholar](#)

38. D. Taraborrelli

[View author publications](#)

You can also search for this author in [PubMed](#) [Google Scholar](#)

## Contributions

B.F. and D.T. initiated and coordinated the study, designed and performed the EMAC simulations, performed the data analyses, prepared the figures and wrote the manuscript. D.T., R.S. and S.R. developed and implemented the multiphase mechanism for formaldehyde. S.G. prepared the initial setup of the model, provided the tools to obtain the formic acid budget and CO yield from methane oxidation. T.E. and A.K. implemented the revised dry deposition scheme. C. Cho, H.-P.D., H.F., G.G., T.H., A.N., D.R., R.T., D.T. and L.V. conducted, analysed and described the SAPHIR experiments; L.V. performed and described the theoretical calculations for the gas-phase methanediol oxidation. B.F., L.C., M.P., C. Clerbaux and P.-F.C. performed the IASI retrievals and provided the IASI dataset. I.D.S. and M.V.R. provided the OMI dataset and expertise on OMI data usage. E.M., T.B., M.D.M., D.W.T.G., J.W.H., F.H., N.J., E.L., I.O., C.P.-W., M.S., K.S. and C.V. contributed to instrument operation, performed the retrievals and/or provided the FTIR datasets. A.K.-S., A.W., A.P., L.C., P.-F.C. and E.M. contributed to discussions of the results and preparation of the manuscript.

## Corresponding authors

Correspondence to [B. Franco](#) or [D. Taraborrelli](#).

## Ethics declarations

## Competing interests

The authors declare no competing interests.

## Additional information

**Peer review information** *Nature* thanks the anonymous reviewer(s) for their contribution to the peer review of this work. Peer reviewer reports are available.

**Publisher's note** Springer Nature remains neutral with regard to jurisdictional claims in published maps and institutional affiliations.

## Extended data figures and tables

## Extended Data Fig. 1 Seasonal cycle of formic acid from FTIR and model.

**a–i**, Formic acid (HCOOH) monthly average columns at nine different FTIR stations, displayed on a 1-year time base, from the 2010–2012 ground-based FTIR observations and EMAC simulations. The grey shaded areas correspond to the  $1\sigma$  standard deviation of the individual FTIR measurements around the monthly average. The mean column bias and root-mean-squared error (RMSE) were calculated between the daily mean FTIR and EMAC data, over the days with FTIR measurements available. The vertical sensitivity of the FTIR retrievals was accounted for by applying averaging kernels (except at Wollongong, where no averaging kernels were produced). Details on the ground-based FTIR retrievals are provided in Supplementary Information, section 6. m a.s.l., metres above sea level.

## Extended Data Fig. 2 Global methanediol distribution simulated by EMAC.

**a–d**, Zonal mean (**a, c**) and surface (**b, d**) methanediol ( $\text{HOCH}_2\text{OH}$ ) mole fraction simulated by EMAC<sub>(dioh)</sub> (**a, b**) and EMAC<sub>(diol)</sub> (**c, d**) over 2010–2012. The EMAC<sub>(dioh)</sub> and EMAC<sub>(diol)</sub> simulations implement the multiphase chemistry of methanediol. On reaction with OH in the gas phase, methanediol yields formic acid (HCOOH).

## Extended Data Fig. 3 Global formic acid abundance from satellite and model.

**a–l**, Formic acid (HCOOH) column derived from IASI satellite observations (**a, d, g, j**), and simulated by the EMAC model that implements the additional production of HCOOH via the multiphase chemistry of methanediol (**b, e, h, k**, EMAC<sub>(dioh)</sub>; **c, f, i, l**, EMAC<sub>(diol)</sub>). Model data were sampled at the time and location of the satellite measurements. The total columns are seasonal averages over December–

February (**a–c**), March–May (**d–f**), June–August (**g–i**) and September–November (**j–l**) 2010–2012. Statistics on the EMAC-to-IASI HCOOH column biases are presented in Extended Data Fig. 4.

#### Extended Data Fig. 4 Formic acid column biases between model and satellite.

**a–h**, Probability histograms of the seasonal formic acid (HCOOH) column bias between EMAC simulations and IASI satellite data over December–February (**a, b**), March–May (**c, d**), June–August (**e, f**) and September–November (**g, h**) 2010–2012. The statistics correspond to the mean, median and  $1\sigma$  standard deviation of the column biases calculated between the EMAC and IASI columns for each season. The associated global HCOOH column distributions are displayed in Extended Data Fig. 3.

#### Extended Data Fig. 5 Global formaldehyde abundance from satellite and model.

**a–d**, Formaldehyde (HCHO) column derived from OMI/Aura satellite observations (**a**), or simulated by EMAC<sub>(base)</sub> (**b**), EMAC<sub>(diox)</sub> (**c**) or EMAC<sub>(diol)</sub> (**d**). Model data were sampled at the time and location of the satellite measurements, and the OMI averaging kernels were applied to the model profiles to account for the vertical sensitivity and resolution of OMI. The HCHO columns are means over 2010–2012. **e, f**, Probability histograms of the HCHO column bias between EMAC simulations and satellite data. The statistics correspond to the mean, median and  $1\sigma$  standard deviation of the column biases calculated over 2010–2012. Details on the OMI HCHO retrievals and the comparison with model data are provided in Supplementary Information, section 7.

#### Extended Data Fig. 6 Effect of modelled formaldehyde biases on formic acid prediction.

**a–l**, Monthly average formaldehyde (HCHO; **a, b, e, f, i, j**) and formic acid (HCOOH; **c, d, g, h, k, l**) columns from IASI and OMI satellite measurements (**a, c, e, g, i, k**), respectively, and from the EMAC<sub>(diol)</sub>

simulation (**b**, **d**, **f**, **h**, **j**, **l**), over Russia in August 2010 (**a–d**), North America in August 2012 (**e–h**) and Amazonia in October 2010 (**i–l**). HCHO and HCOOH model data were sampled at the time and location of the OMI and IASI satellite measurements, respectively. The OMI averaging kernels were applied to the model profiles to account for the vertical sensitivity and resolution of OMI (IASI averaging kernels are not available). The same comparison, but for EMAC<sub>(diol)</sub>, is provided in Supplementary Fig. 7 (Supplementary Information, section 8).

### Extended Data Fig. 7 Effect of cloud processing on cloud and rainwater acidity.

**a–h**, pH difference of the large-scale clouds (**a**, **e**) and associated rain (**b**, **f**), and of the convective clouds (**c**, **g**) and associated rain (**d**, **h**), between the EMAC<sub>(diol)</sub> and EMAC<sub>(base)</sub> simulations. The pH differences are seasonal averages over June–August (**a–d**) and September–November (**e–h**) 2010–2012. The pH decrease is due to the additional production of formic acid (HCOOH) via the multiphase chemistry of methanediol implemented in EMAC<sub>(diol)</sub>. The effect on cloud and rain pH of the EMAC<sub>(diol)</sub> simulation is displayed in Supplementary Fig. 8 (Supplementary Information, section 8).

### Extended Data Fig. 8 Effect of cloud processing on formaldehyde modelling.

Monthly average formaldehyde (HCHO) total column simulated by EMAC<sub>(diol)</sub> (**a**, **c**, **e**), and relative difference in HCHO total column between EMAC<sub>(diol)</sub> and EMAC<sub>(base)</sub> (**b**, **d**, **f**), over Amazonia in November 2012 (**a**, **b**), central Africa in December 2010 (**c**, **d**) and southeast Asia in April 2010 (**e**, **f**). The effect on HCHO modelling of the EMAC<sub>(diol)</sub> simulation is presented in Supplementary Fig. 9 (Supplementary Information, section 8).

### Extended Data Fig. 9 Effect of cloud processing on modelled carbon monoxide.

**a–d**, Yield of CO originating from methane ( $\text{CH}_4$ ) oxidation modelled by EMAC<sub>(dioh)</sub> (**a**) and EMAC<sub>(diol)</sub> (**c**), and change in CO yield from  $\text{CH}_4$  oxidation between EMAC<sub>(dioh)</sub> (**b**) or EMAC<sub>(diol)</sub> (**d**) and EMAC<sub>(base)</sub>. The data presented are annual averages over 2010–2012.

### Extended Data Table 1 Atmospheric chemical budget of formic acid calculated by EMAC

[Full size table](#)

## Supplementary information

### [Supplementary Information](#)

The Supplementary Information describes the SAPHIR chamber experiments (Sect. 1), the theoretical calculations of the methanediol + OH reaction (Sect. 2), and the EMAC simulations (Sect. 3). Uncertainty sources in the model and methanediol measurements are discussed in Sect. 4 and 5, respectively. The retrievals of formic acid from ground-based FTIR observations and formaldehyde from OMI satellite measurements are presented in Sect. 6 and 7, respectively. Sect. 8 contains supplementary figures. The Supplementary References are listed in Sect. 9. Sect. 10 contains the raw quantum chemical data.

### [Peer Review File](#)

## Source data

### [Source Data Fig. 1](#)

### [Source Data Fig. 3](#)

## Rights and permissions

**Open Access** This article is licensed under a Creative Commons Attribution 4.0 International License, which permits use, sharing,

adaptation, distribution and reproduction in any medium or format, as long as you give appropriate credit to the original author(s) and the source, provide a link to the Creative Commons license, and indicate if changes were made. The images or other third party material in this article are included in the article's Creative Commons license, unless indicated otherwise in a credit line to the material. If material is not included in the article's Creative Commons license and your intended use is not permitted by statutory regulation or exceeds the permitted use, you will need to obtain permission directly from the copyright holder. To view a copy of this license, visit <http://creativecommons.org/licenses/by/4.0/>.

## Reprints and Permissions

## About this article



Check for  
updates

## Cite this article

Franco, B., Blumenstock, T., Cho, C. *et al.* Ubiquitous atmospheric production of organic acids mediated by cloud droplets. *Nature* **593**, 233–237 (2021). <https://doi.org/10.1038/s41586-021-03462-x>

## Download citation

- Received: 21 September 2020
- Accepted: 17 March 2021
- Published: 12 May 2021
- Issue Date: 13 May 2021
- DOI: <https://doi.org/10.1038/s41586-021-03462-x>

## Comments

By submitting a comment you agree to abide by our [Terms](#) and [Community Guidelines](#). If you find something abusive or that does not comply with our terms or guidelines please flag it as inappropriate.

[Download PDF](#)

## Associated Content

### [Cloud droplets aid the production of formic acid in the atmosphere](#)

- Joost de Gouw
- Delphine Farmer

Nature News & Views 12 May 2021

---

This article was downloaded by **calibre** from <https://www.nature.com/articles/s41586-021-03462-x>

| [Section menu](#) | [Main menu](#) |

- Article
- [Published: 07 April 2021](#)

# Genome-wide enhancer maps link risk variants to disease genes

- [Joseph Nasser](#)<sup>1</sup> na1,
- [Drew T. Bergman](#) [ORCID: orcid.org/0000-0002-8314-7088](#)<sup>1</sup> na1,
- [Charles P. Fulco](#)<sup>1</sup> na1 nAff24,
- [Philine Guckelberger](#) [ORCID: orcid.org/0000-0002-1057-2518](#)<sup>1,2</sup> na1,
- [Benjamin R. Doughty](#)<sup>1,3</sup> na1,
- [Tejal A. Patwardhan](#)<sup>1,4</sup>,
- [Thouis R. Jones](#)<sup>1</sup>,
- [Tung H. Nguyen](#)<sup>1</sup>,
- [Jacob C. Ulirsch](#) [ORCID: orcid.org/0000-0002-7947-0827](#)<sup>1,5</sup>,
- [Fritz Lekschas](#) [ORCID: orcid.org/0000-0001-8432-4835](#)<sup>6</sup>,
- [Kristy Mualim](#)<sup>3</sup>,
- [Heini M. Natri](#)<sup>3</sup>,
- [Elle M. Weeks](#) [ORCID: orcid.org/0000-0002-4317-4444](#)<sup>1</sup>,
- [Glen Munson](#)<sup>1</sup>,
- [Michael Kane](#)<sup>1</sup>,
- [Helen Y. Kang](#)<sup>3,7</sup>,
- [Ang Cui](#) [ORCID: orcid.org/0000-0002-1087-8568](#)<sup>1,8</sup>,
- [John P. Ray](#) [ORCID: orcid.org/0000-0001-7294-4260](#)<sup>1</sup> nAff25,
- [Thomas M. Eisenhaure](#)<sup>1</sup>,
- [Ryan L. Collins](#) [ORCID: orcid.org/0000-0003-1268-9995](#)<sup>1,9,10</sup>,
- [Kushal Dey](#)<sup>11</sup>,
- [Hanspeter Pfister](#)<sup>6</sup>,
- [Alkes L. Price](#) [ORCID: orcid.org/0000-0002-2971-7975](#)<sup>1,11,12</sup>,
- [Charles B. Epstein](#) [ORCID: orcid.org/0000-0001-8358-8345](#)<sup>1</sup>,

- [Anshul Kundaje](#) ORCID: orcid.org/0000-0003-3084-2287<sup>3,13</sup>,
- [Ramnik J. Xavier](#) ORCID: orcid.org/0000-0002-5630-5167<sup>1,14,15,16</sup>,
- [Mark J. Daly](#) ORCID: orcid.org/0000-0002-0949-8752<sup>1,17,18,19</sup>,
- [Hailiang Huang](#)<sup>1,17,18</sup>,
- [Hilary K. Finucane](#) ORCID: orcid.org/0000-0003-3864-9828<sup>1,17,18</sup>,
- [Nir Hacohen](#) ORCID: orcid.org/0000-0002-2349-2656<sup>1,18,20</sup>,
- [Eric S. Lander](#) ORCID: orcid.org/0000-0003-2662-4631<sup>1,21,22,23 na2</sup>  
&
- [Jesse M. Engreitz](#) ORCID: orcid.org/0000-0002-5754-1719<sup>1,3,7 na2</sup>

[Nature](#) volume 593, pages 238–243 (2021) [Cite this article](#)

- 17k Accesses
- 254 Altmetric
- [Metrics details](#)

## Subjects

- [Gene expression](#)
- [Gene regulation](#)
- [Genome-wide association studies](#)
- [Immunogenetics](#)
- [Inflammatory bowel disease](#)

## Abstract

Genome-wide association studies (GWAS) have identified thousands of noncoding loci that are associated with human diseases and complex traits, each of which could reveal insights into the mechanisms of disease<sup>1</sup>. Many of the underlying causal variants may affect enhancers<sup>2,3</sup>, but we lack accurate maps of enhancers and their target genes to interpret such variants. We recently developed the activity-by-contact (ABC) model to predict which enhancers regulate which genes and validated the model using CRISPR perturbations in several cell types<sup>4</sup>. Here we apply this ABC

model to create enhancer–gene maps in 131 human cell types and tissues, and use these maps to interpret the functions of GWAS variants. Across 72 diseases and complex traits, ABC links 5,036 GWAS signals to 2,249 unique genes, including a class of 577 genes that appear to influence multiple phenotypes through variants in enhancers that act in different cell types. In inflammatory bowel disease (IBD), causal variants are enriched in predicted enhancers by more than 20-fold in particular cell types such as dendritic cells, and ABC achieves higher precision than other regulatory methods at connecting noncoding variants to target genes. These variant-to-function maps reveal an enhancer that contains an IBD risk variant and that regulates the expression of *PPIF* to alter the membrane potential of mitochondria in macrophages. Our study reveals principles of genome regulation, identifies genes that affect IBD and provides a resource and generalizable strategy to connect risk variants of common diseases to their molecular and cellular functions.

[Access through your institution](#)

[Change institution](#)

[Buy or subscribe](#)

## Access options

Subscribe to Journal

Get full journal access for 1 year

\$199.00

only \$3.90 per issue

[Subscribe](#)

All prices are NET prices.

VAT will be added later in the checkout.

Tax calculation will be finalised during checkout.

Rent or Buy article

Get time limited or full article access on ReadCube.

from \$8.99

[Rent or Buy](#)

All prices are NET prices.

### **Additional access options:**

- [Log in](#)
- [Access through your institution](#)
- [Learn about institutional subscriptions](#)

**Fig. 1: ABC maps connect fine-mapped variants to enhancers, genes and cell types.**



**Fig. 2: Connecting variants to target genes.**

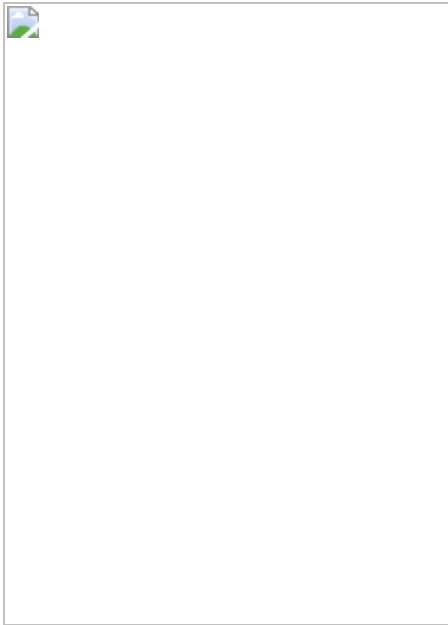


**Fig. 3: Cell-type specificity of ABC predictions.**

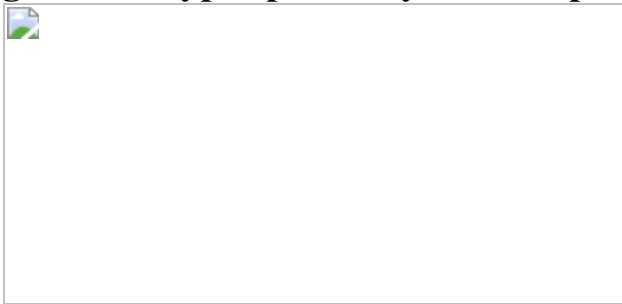
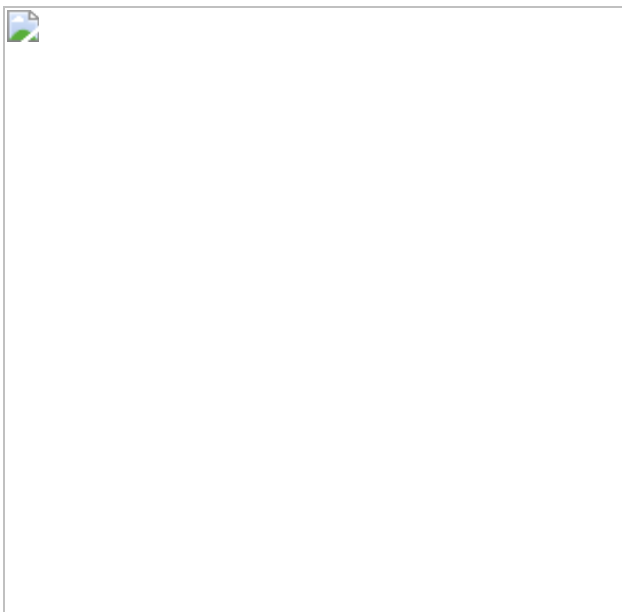


**Fig. 4: An enhancer regulates *PPIF* expression and mitochondrial function.**



## Data availability

Data for the immune cell line ATAC-seq and H3K27ac ChIP-seq analyses can be found in the NCBI GEO under accession number [GSE155555](#). gRNA counts from CRISPRi screens can be found in Supplementary Tables [3](#), [14](#). UK Biobank fine-mapping data for 71 traits are available from <https://www.finucanelab.org/data>. ABC predictions in 131 biosamples can be found at <https://www.engreitzlab.org/abc/>.

## Code availability

The ABC model is available on GitHub (<https://github.com/broadinstitute/ABC-Enhancer-Gene-Prediction>). This is the codebase used to generate the ABC predictions for this manuscript, and can be used to run the ABC model on new biosamples. ABC-Max and paper-specific analyses can be found on GitHub (<https://github.com/EngreitzLab/ABC-GWAS-Paper>). This repository implements the ABC-Max pipeline and can be used to reproduce specific analyses in this study.

## References

1. 1.

Claussnitzer, M. et al. A brief history of human disease genetics. *Nature* **577**, 179–189 (2020).

[ADS](#) [CAS](#) [PubMed](#) [PubMed Central](#) [Google Scholar](#)

2. 2.

Farh, K. K.-H. et al. Genetic and epigenetic fine mapping of causal autoimmune disease variants. *Nature* **518**, 337–343 (2015).

[ADS](#) [CAS](#) [PubMed](#) [Google Scholar](#)

3. 3.

Maurano, M. T. et al. Systematic localization of common disease-associated variation in regulatory DNA. *Science* **337**, 1190–1195 (2012).

[ADS](#) [CAS](#) [PubMed](#) [PubMed Central](#) [Google Scholar](#)

4. 4.

Fulco, C. P. et al. Activity-by-contact model of enhancer-promoter regulation from thousands of CRISPR perturbations. *Nat. Genet.* **51**, 1664–1669 (2019).

[CAS](#) [PubMed](#) [PubMed Central](#) [Google Scholar](#)

5. 5.

Westra, H.-J. & Franke, L. From genome to function by studying eQTLs. *Biochim. Biophys. Acta* **1842**, 1896–1902 (2014).

[CAS](#) [PubMed](#) [Google Scholar](#)

6. 6.

Gasperini, M., Tome, J. M. & Shendure, J. Towards a comprehensive catalogue of validated and target-linked human enhancers. *Nat. Rev. Genet.* **21**, 292–310 (2020).

[CAS](#) [PubMed](#) [PubMed Central](#) [Google Scholar](#)

7. 7.

van Arensbergen, J., van Steensel, B. & Bussemaker, H. J. In search of the determinants of enhancer–promoter interaction specificity. *Trends Cell Biol.* **24**, 695–702 (2014).

[PubMed](#) [PubMed Central](#) [Google Scholar](#)

8. 8.

The ENCODE Project Consortium. An integrated encyclopedia of DNA elements in the human genome. *Nature* **489**, 57–74 (2012).

[ADS](#) [PubMed Central](#) [Google Scholar](#)

9. 9.

Huang, H. et al. Fine-mapping inflammatory bowel disease loci to single-variant resolution. *Nature* **547**, 173–178 (2017).

[ADS](#) [CAS](#) [PubMed](#) [PubMed Central](#) [Google Scholar](#)

10. 10.

Maller, J. B. et al. Bayesian refinement of association signals for 14 loci in 3 common diseases. *Nat. Genet.* **44**, 1294–1301 (2012).

[CAS](#) [PubMed](#) [PubMed Central](#) [Google Scholar](#)

11. 11.

Ulirsch, J. C. et al. Interrogation of human hematopoiesis at single-cell and single-variant resolution. *Nat. Genet.* **51**, 683–693 (2019).

[CAS](#) [PubMed](#) [PubMed Central](#) [Google Scholar](#)

12. 12.

Fulco, C. P. et al. Systematic mapping of functional enhancer–promoter connections with CRISPR interference. *Science* **354**, 769–773 (2016).

[ADS](#) [CAS](#) [PubMed](#) [PubMed Central](#) [Google Scholar](#)

13. 13.

Rescigno, M. & Di Sabatino, A. Dendritic cells in intestinal homeostasis and disease. *J. Clin. Invest.* **119**, 2441–2450 (2009).

[CAS](#) [PubMed](#) [PubMed Central](#) [Google Scholar](#)

14. 14.

Graham, D. B. & Xavier, R. J. Pathway paradigms revealed from the genetics of inflammatory bowel disease. *Nature* **578**, 527–539 (2020).

[ADS](#) [CAS](#) [PubMed](#) [PubMed Central](#) [Google Scholar](#)

15. 15.

Mountjoy, E. et al. Open Targets Genetics: an open approach to systematically prioritize causal variants and genes at all published human GWAS trait-associated loci. Preprint at <https://doi.org/10.1101/2020.09.16.299271> (2020).

16. 16.

Buniello, A. et al. The NHGRI-EBI GWAS Catalog of published genome-wide association studies, targeted arrays and summary statistics 2019. *Nucleic Acids Res.* **47**, D1005–D1012 (2019).

[CAS](#) [PubMed](#) [Google Scholar](#)

17. 17.

Stacey, D. et al. ProGeM: a framework for the prioritization of candidate causal genes at molecular quantitative trait loci. *Nucleic Acids Res.* **47**, e3 (2019).

[CAS](#) [PubMed](#) [Google Scholar](#)

18. 18.

Chun, S. et al. Limited statistical evidence for shared genetic effects of eQTLs and autoimmune-disease-associated loci in three major

immune-cell types. *Nat. Genet.* **49**, 600–605 (2017).

[CAS](#) [PubMed](#) [PubMed Central](#) [Google Scholar](#)

19. 19.

Carvalho-Silva, D. et al. Open Targets Platform: new developments and updates two years on. *Nucleic Acids Res.* **47**, D1056–D1065 (2019).

[CAS](#) [PubMed](#) [Google Scholar](#)

20. 20.

Barbeira, A. N. et al. Integrating predicted transcriptome from multiple tissues improves association detection. *PLoS Genet.* **15**, e1007889 (2019).

[PubMed](#) [PubMed Central](#) [Google Scholar](#)

21. 21.

Hauberg, M. E. et al. Large-scale identification of common trait and disease variants affecting gene expression. *Am. J. Hum. Genet.* **100**, 885–894 (2017).

[CAS](#) [PubMed](#) [PubMed Central](#) [Google Scholar](#)

22. 22.

Javierre, B. M. et al. Lineage-specific genome architecture links enhancers and non-coding disease variants to target gene promoters. *Cell* **167**, 1369–1384 (2016).

[CAS](#) [PubMed](#) [PubMed Central](#) [Google Scholar](#)

23. 23.

Pers, T. H. et al. Biological interpretation of genome-wide association studies using predicted gene functions. *Nat. Commun.* **6**, 5890 (2015).

[CAS](#) [PubMed](#) [PubMed Central](#) [Google Scholar](#)

24. 24.

Cao, Q. et al. Reconstruction of enhancer–target networks in 935 samples of human primary cells, tissues and cell lines. *Nat. Genet.* **49**, 1428–1436 (2017).

[CAS](#) [PubMed](#) [Google Scholar](#)

25. 25.

Liu, Y., Sarkar, A., Kheradpour, P., Ernst, J. & Kellis, M. Evidence of reduced recombination rate in human regulatory domains. *Genome Biol.* **18**, 193 (2017).

[PubMed](#) [PubMed Central](#) [Google Scholar](#)

26. 26.

Granja, J. M. et al. Single-cell multiomic analysis identifies regulatory programs in mixed-phenotype acute leukemia. *Nat. Biotechnol.* **37**, 1458–1465 (2019).

[CAS](#) [PubMed](#) [PubMed Central](#) [Google Scholar](#)

27. 27.

Andersson, R. et al. An atlas of active enhancers across human cell types and tissues. *Nature* **507**, 455–461 (2014).

[ADS](#) [CAS](#) [PubMed](#) [PubMed Central](#) [Google Scholar](#)

28. 28.

Sheffield, N. C. et al. Patterns of regulatory activity across diverse human cell types predict tissue identity, transcription factor binding, and long-range interactions. *Genome Res.* **23**, 777–788 (2013).

[CAS](#) [PubMed](#) [PubMed Central](#) [Google Scholar](#)

29. 29.

Thurman, R. E. et al. The accessible chromatin landscape of the human genome. *Nature* **489**, 75–82 (2012).

[ADS](#) [CAS](#) [PubMed](#) [PubMed Central](#) [Google Scholar](#)

30. 30.

Gao, T. & Qian, J. EnhancerAtlas 2.0: an updated resource with enhancer annotation in 586 tissue/cell types across nine species. *Nucleic Acids Res.* **48**, D58–D64 (2020).

[CAS](#) [PubMed](#) [Google Scholar](#)

31. 31.

Whalen, S., Truty, R. M. & Pollard, K. S. Enhancer-promoter interactions are encoded by complex genomic signatures on looping chromatin. *Nat. Genet.* **48**, 488–496 (2016).

[CAS](#) [PubMed](#) [PubMed Central](#) [Google Scholar](#)

32. 32.

GTEx Consortium. Genetic effects on gene expression across human tissues. *Nature* **550**, 204–213 (2017).

[PubMed Central](#) [Google Scholar](#)

33. 33.

Engreitz, J. M. et al. Local regulation of gene expression by lncRNA promoters, transcription and splicing. *Nature* **539**, 452–455 (2016).

[ADS](#) [CAS](#) [PubMed](#) [PubMed Central](#) [Google Scholar](#)

34. 34.

Wainberg, M. et al. Opportunities and challenges for transcriptome-wide association studies. *Nat. Genet.* **51**, 592–599 (2019).

[CAS](#) [PubMed](#) [PubMed Central](#) [Google Scholar](#)

35. 35.

Franke, A. et al. Genome-wide meta-analysis increases to 71 the number of confirmed Crohn's disease susceptibility loci. *Nat. Genet.* **42**, 1118–1125 (2010).

[CAS](#) [PubMed](#) [PubMed Central](#) [Google Scholar](#)

36. 36.

Jostins, L. et al. Host–microbe interactions have shaped the genetic architecture of inflammatory bowel disease. *Nature* **491**, 119–124 (2012).

[CAS](#) [PubMed](#) [PubMed Central](#) [Google Scholar](#)

37. 37.

Linares, P. M. & Gisbert, J. P. Role of growth factors in the development of lymphangiogenesis driven by inflammatory bowel disease: a review. *Inflamm. Bowel Dis.* **17**, 1814–1821 (2011).

[PubMed](#) [Google Scholar](#)

38. 38.

Wang, X. & Goldstein, D. B. Enhancer domains predict gene pathogenicity and inform gene discovery in complex disease. *Am. J. Hum. Genet.* **106**, 215–233 (2020).

[CAS](#) [PubMed](#) [PubMed Central](#) [Google Scholar](#)

39. 39.

Imielinski, M. et al. Common variants at five new loci associated with early-onset inflammatory bowel disease. *Nat. Genet.* **41**, 1335–1340 (2009).

[CAS](#) [PubMed](#) [PubMed Central](#) [Google Scholar](#)

40. 40.

Elrod, J. W. & Molkentin, J. D. Physiologic functions of cyclophilin D and the mitochondrial permeability transition pore. *Circ. J.* **77**, 1111–1122 (2013).

[CAS](#) [PubMed](#) [PubMed Central](#) [Google Scholar](#)

41. 41.

Ip, W. K. E., Hoshi, N., Shouval, D. S., Snapper, S. & Medzhitov, R. Anti-inflammatory effect of IL-10 mediated by metabolic reprogramming of macrophages. *Science* **356**, 513–519 (2017).

[ADS](#) [CAS](#) [PubMed](#) [PubMed Central](#) [Google Scholar](#)

42. 42.

Bick, A. G. et al. Inherited causes of clonal haematopoiesis in 97,691 whole genomes. *Nature* **586**, 763–768 (2020).

[ADS](#) [CAS](#) [PubMed](#) [PubMed Central](#) [Google Scholar](#)

43. 43.

Buenrostro, J. D., Wu, B., Chang, H. Y. & Greenleaf, W. J. ATAC-seq: a method for assaying chromatin accessibility genome-wide. *Curr. Protoc. Mol. Biol.* **109**, 21.29.1–21.29.9 (2015).

[Google Scholar](#)

44. 44.

Zhu, J. et al. Genome-wide chromatin state transitions associated with developmental and environmental cues. *Cell* **152**, 642–654 (2013).

[CAS](#) [PubMed](#) [PubMed Central](#) [Google Scholar](#)

45. 45.

Kundaje, A. et al. Integrative analysis of 111 reference human epigenomes. *Nature* **518**, 317–330 (2015).

[CAS](#) [PubMed](#) [PubMed Central](#) [Google Scholar](#)

46. 46.

Li, H. & Durbin, R. Fast and accurate short read alignment with Burrows–Wheeler transform. *Bioinformatics* **25**, 1754–1760 (2009).

[CAS](#) [PubMed](#) [PubMed Central](#) [Google Scholar](#)

47. 47.

Li, H. et al. The Sequence Alignment/Map format and SAMtools. *Bioinformatics* **25**, 2078–2079 (2009).

[PubMed](#) [PubMed Central](#) [Google Scholar](#)

48. 48.

Amemiya, H. M., Kundaje, A. & Boyle, A. P. The ENCODE blacklist: identification of problematic regions of the genome. *Sci. Rep.* **9**, 9354 (2019).

[ADS](#) [PubMed](#) [PubMed Central](#) [Google Scholar](#)

49. 49.

Vierstra, J. et al. Global reference mapping of human transcription factor footprints. *Nature* **583**, 729–736 (2020).

[ADS](#) [CAS](#) [PubMed](#) [PubMed Central](#) [Google Scholar](#)

50. 50.

Langmead, B. & Salzberg, S. L. Fast gapped-read alignment with Bowtie 2. *Nat. Methods* **9**, 357–359 (2012).

[CAS](#) [PubMed](#) [PubMed Central](#) [Google Scholar](#)

51. 51.

Liu, J. Z. et al. Association analyses identify 38 susceptibility loci for inflammatory bowel disease and highlight shared genetic risk across populations. *Nat. Genet.* **47**, 979–986 (2015).

[CAS](#) [PubMed](#) [PubMed Central](#) [Google Scholar](#)

52. 52.

de Lange, K. M. et al. Genome-wide association study implicates immune activation of multiple integrin genes in inflammatory bowel disease. *Nat. Genet.* **49**, 256–261 (2017).

[PubMed](#) [PubMed Central](#) [Google Scholar](#)

53. 53.

Loh, P. R., Kichaev, G., Gazal, S., Schoech, A. P. & Price, A. L. Mixed-model association for biobank-scale datasets. *Nat. Genet.* **50**, 906–908 (2018).

[CAS](#) [PubMed](#) [PubMed Central](#) [Google Scholar](#)

54. 54.

Zhou, W. et al. Efficiently controlling for case–control imbalance and sample relatedness in large-scale genetic association studies. *Nat. Genet.* **50**, 1335–1341 (2018).

[CAS](#) [PubMed](#) [PubMed Central](#) [Google Scholar](#)

55. 55.

Benner, C. et al. Prospects of fine-mapping trait-associated genomic regions by using summary statistics from genome-wide association studies. *Am. J. Hum. Genet.* **101**, 539–551 (2017).

[CAS](#) [PubMed](#) [PubMed Central](#) [Google Scholar](#)

56. 56.

Wang, G., Sarkar, A., Carbonetto, P. & Stephens, M. A simple new approach to variable selection in regression, with application to genetic fine mapping. *J. R. Stat. Soc. B* **82**, 1273–1300 (2020).

[MathSciNet](#) [Google Scholar](#)

57. 57.

McLaren, W. et al. The Ensembl variant effect predictor. *Genome Biol.* **17**, 122 (2016).

[PubMed](#) [PubMed Central](#) [Google Scholar](#)

58. 58.

Fujita, P. A. et al. The UCSC genome browser database: update 2011. *Nucleic Acids Res.* **39**, D876–D882 (2011).

[CAS](#) [PubMed](#) [Google Scholar](#)

59. 59.

Carrillo-de-Santa-Pau, E. et al. Automatic identification of informative regions with epigenomic changes associated to hematopoiesis. *Nucleic Acids Res.* **45**, 9244–9259 (2017).

[CAS](#) [PubMed](#) [PubMed Central](#) [Google Scholar](#)

60. 60.

Astle, W. J. et al. The allelic landscape of human blood cell trait variation and links to common complex disease. *Cell* **167**, 1415–1429 (2016).

[CAS](#) [PubMed](#) [PubMed Central](#) [Google Scholar](#)

61. 61.

Finucane, H. K. et al. Partitioning heritability by functional annotation using genome-wide association summary statistics. *Nat. Genet.* **47**, 1228–1235 (2015).

[CAS](#) [PubMed](#) [PubMed Central](#) [Google Scholar](#)

62. 62.

Chen, L. et al. Genetic drivers of epigenetic and transcriptional variation in human immune cells. *Cell* **167**, 1398–1414 (2016).

[CAS](#) [PubMed](#) [PubMed Central](#) [Google Scholar](#)

63. 63.

Liberzon, A. et al. Molecular signatures database (MSigDB) 3.0. *Bioinformatics* **27**, 1739–1740 (2011).

[CAS](#) [PubMed](#) [PubMed Central](#) [Google Scholar](#)

64. 64.

Kerimov, N. et al. eQTL Catalogue: a compendium of uniformly processed human gene expression and splicing QTLs. Preprint at <https://doi.org/10.1101/2020.01.29.924266> (2021).

65. 65.

de Leeuw, C. A., Mooij, J. M., Heskes, T. & Posthuma, D. MAGMA: generalized gene-set analysis of GWAS data. *PLOS Comput. Biol.* **11**, e1004219 (2015).

[PubMed](#) [PubMed Central](#) [Google Scholar](#)

66. 66.

Kerpedjiev, P. et al. HiGlass: web-based visual exploration and analysis of genome interaction maps. *Genome Biol.* **19**, 125 (2018).

[PubMed](#) [PubMed Central](#) [Google Scholar](#)

67. 67.

Rao, S. S. et al. A 3D map of the human genome at kilobase resolution reveals principles of chromatin looping. *Cell* **159**, 1665–1680 (2014).

[CAS](#) [PubMed](#) [PubMed Central](#) [Google Scholar](#)

68. 68.

Novakovic, B. et al.  $\beta$ -Glucan reverses the epigenetic state of LPS-induced immunological tolerance. *Cell* **167**, 1354–1368 (2016).

[CAS](#) [PubMed](#) [PubMed Central](#) [Google Scholar](#)

69. 69.

Donnard, E. et al. Comparative analysis of immune cells reveals a conserved regulatory lexicon. *Cell Syst.* **6**, 381–394 (2018).

[CAS](#) [PubMed](#) [PubMed Central](#) [Google Scholar](#)

[Download references](#)

## Acknowledgements

This work was supported by the Broad Institute (E.S.L.); an NIH Pathway to Independence Award (K99HG009917 and R00HG009917 to J.M.E.); an NHGRI Genomic Innovator Award (R35HG011324 to J.M.E.); the Harvard Society of Fellows (J.M.E.); Gordon and Betty Moore and the BASE Research Initiative at the Lucile Packard Children's Hospital at Stanford University (J.M.E.); NHGRI P50HG006193 (N.H.); NIDDK P30DK043351 (R.J.X.); NIH U01CA200059 (H.P.); NHGRI U01HG009379, NIMH R01MH101244 and NIMH R37MH107649 (A.K.P.); NIDDK K01DK114379 (H.H.); the Zhengxu and Ying He Foundation, the Stanley Center for Psychiatric Research and NIAID K22AI153648 (J.P.R.); NHGRI U24HG009446 (A.K.); an NSF Graduate Research Fellowship (DGE-1656518 to B.R.D.); and a Siebel Scholarship (F.L.). We thank L. Schweitzer, M. Gentili, M. Biton, C. Smillie, A. Regev, M. Kanai, D. Graham, N. Shores, S. Gazal, B. Cleary, R. Cui, P. Rogers, V. Subramanian, G. Schnitzler, R. Gupta, M. Claussnitzer, N. Sinnott-Armstrong, T. Majarian, A. Manning and members of the Lander lab, Hacohen lab and Variant-to-Function Initiative for discussions or technical assistance. This research has been conducted using the UK Biobank Resource.

## Author information

### Author notes

1. Charles P. Fulco

Present address: Bristol Myers Squibb, Cambridge, MA, USA

2. John P. Ray

Present address: Systems Immunology, Benaroya Research Institute at Virginia Mason, Seattle, WA, USA

3. These authors contributed equally: Joseph Nasser, Drew T. Bergman, Charles P. Fulco, Philine Guckelberger, Benjamin R. Doughty
4. These authors jointly supervised this work: Eric S. Lander, Jesse M. Engreitz

## Affiliations

1. Broad Institute of MIT and Harvard, Cambridge, MA, USA

Joseph Nasser, Drew T. Bergman, Charles P. Fulco, Philine Guckelberger, Benjamin R. Doughty, Tejal A. Patwardhan, Thouis R. Jones, Tung H. Nguyen, Jacob C. Ulirsch, Elle M. Weeks, Glen Munson, Michael Kane, Ang Cui, John P. Ray, Thomas M. Eisenhaure, Ryan L. Collins, Alkes L. Price, Charles B. Epstein, Ramnik J. Xavier, Mark J. Daly, Hailiang Huang, Hilary K. Finucane, Nir Hacohen, Eric S. Lander & Jesse M. Engreitz

2. Department of Biology, Chemistry, and Pharmacy, Freie Universität Berlin, Berlin, Germany

Philine Guckelberger

3. Department of Genetics, Stanford University School of Medicine, Stanford, CA, USA

Benjamin R. Doughty, Kristy Mualim, Heini M. Natri, Helen Y. Kang, Anshul Kundaje & Jesse M. Engreitz

4. Department of Statistics, Harvard University, Cambridge, MA, USA

Tejal A. Patwardhan

5. Program in Biological and Biomedical Sciences, Harvard Medical School, Boston, MA, USA

Jacob C. Ulirsch

6. Harvard John A. Paulson School of Engineering and Applied Sciences,  
Harvard University, Cambridge, MA, USA

Fritz Lekschas & Hanspeter Pfister

7. BASE Initiative, Betty Irene Moore Children's Heart Center, Lucile  
Packard Children's Hospital, Stanford University School of Medicine,  
Stanford, CA, USA

Helen Y. Kang & Jesse M. Engreitz

8. Harvard-MIT Division of Health Sciences and Technology, MIT,  
Cambridge, MA, USA

Ang Cui

9. Program in Bioinformatics and Integrative Genomics, Harvard  
Medical School, Boston, MA, USA

Ryan L. Collins

10. Center for Genomic Medicine, Massachusetts General Hospital,  
Boston, MA, USA

Ryan L. Collins

11. Department of Epidemiology, Harvard T. H. Chan School of Public  
Health, Boston, MA, USA

Kushal Dey & Alkes L. Price

12. Department of Biostatistics, Harvard T. H. Chan School of Public  
Health, Boston, MA, USA

Alkes L. Price

13. Department of Computer Science, Stanford University, Stanford, CA,  
USA

Anshul Kundaje

14. Klarman Cell Observatory, Broad Institute of MIT and Harvard,  
Cambridge, MA, USA

Ramnik J. Xavier

15. Center for Computational and Integrative Biology, Massachusetts  
General Hospital, Boston, MA, USA

Ramnik J. Xavier

16. Department of Molecular Biology, Massachusetts General Hospital  
and Harvard Medical School, Boston, MA, USA

Ramnik J. Xavier

17. Analytic and Translational Genetics Unit, Massachusetts General  
Hospital, Boston, MA, USA

Mark J. Daly, Hailiang Huang & Hilary K. Finucane

18. Department of Medicine, Harvard Medical School, Boston, MA, USA

Mark J. Daly, Hailiang Huang, Hilary K. Finucane & Nir Hacohen

19. Institute for Molecular Medicine Finland, University of Helsinki,  
Helsinki, Finland

Mark J. Daly

20. Center for Cancer Research, Massachusetts General Hospital, Boston,  
MA, USA

Nir Hacohen

21. Department of Biology, MIT, Cambridge, MA, USA

Eric S. Lander

22. Department of Systems Biology, Harvard Medical School, Boston, MA, USA

Eric S. Lander

23. Office of Science and Technology Policy, Executive Office of the President, White House, Washington, DC, USA

Eric S. Lander

## Authors

1. Joseph Nasser

[View author publications](#)

You can also search for this author in [PubMed](#) [Google Scholar](#)

2. Drew T. Bergman

[View author publications](#)

You can also search for this author in [PubMed](#) [Google Scholar](#)

3. Charles P. Fulco

[View author publications](#)

You can also search for this author in [PubMed](#) [Google Scholar](#)

4. Philine Guckelberger

[View author publications](#)

You can also search for this author in [PubMed](#) [Google Scholar](#)

5. Benjamin R. Doughty

[View author publications](#)

You can also search for this author in [PubMed](#) [Google Scholar](#)

6. Tejal A. Patwardhan

[View author publications](#)

You can also search for this author in [PubMed](#) [Google Scholar](#)

7. Thouis R. Jones

[View author publications](#)

You can also search for this author in [PubMed](#) [Google Scholar](#)

8. Tung H. Nguyen

[View author publications](#)

You can also search for this author in [PubMed](#) [Google Scholar](#)

9. Jacob C. Ulirsch

[View author publications](#)

You can also search for this author in [PubMed](#) [Google Scholar](#)

10. Fritz Lekschas

[View author publications](#)

You can also search for this author in [PubMed](#) [Google Scholar](#)

11. Kristy Mualim

[View author publications](#)

You can also search for this author in [PubMed](#) [Google Scholar](#)

12. Heini M. Natri

[View author publications](#)

You can also search for this author in [PubMed](#) [Google Scholar](#)

13. Elle M. Weeks

[View author publications](#)

You can also search for this author in [PubMed](#) [Google Scholar](#)

14. Glen Munson

[View author publications](#)

You can also search for this author in [PubMed](#) [Google Scholar](#)

15. Michael Kane

[View author publications](#)

You can also search for this author in [PubMed](#) [Google Scholar](#)

16. Helen Y. Kang

[View author publications](#)

You can also search for this author in [PubMed](#) [Google Scholar](#)

17. Ang Cui

[View author publications](#)

You can also search for this author in [PubMed](#) [Google Scholar](#)

18. John P. Ray

[View author publications](#)

You can also search for this author in [PubMed](#) [Google Scholar](#)

19. Thomas M. Eisenhaure

[View author publications](#)

You can also search for this author in [PubMed](#) [Google Scholar](#)

20. Ryan L. Collins

[View author publications](#)

You can also search for this author in [PubMed](#) [Google Scholar](#)

21. Kushal Dey

[View author publications](#)

You can also search for this author in [PubMed](#) [Google Scholar](#)

22. Hanspeter Pfister

[View author publications](#)

You can also search for this author in [PubMed](#) [Google Scholar](#)

23. Alkes L. Price

[View author publications](#)

You can also search for this author in [PubMed](#) [Google Scholar](#)

24. Charles B. Epstein

[View author publications](#)

You can also search for this author in [PubMed](#) [Google Scholar](#)

25. Anshul Kundaje

[View author publications](#)

You can also search for this author in [PubMed](#) [Google Scholar](#)

26. Ramnik J. Xavier

[View author publications](#)

You can also search for this author in [PubMed](#) [Google Scholar](#)

27. Mark J. Daly

[View author publications](#)

You can also search for this author in [PubMed](#) [Google Scholar](#)

28. Hailiang Huang

[View author publications](#)

You can also search for this author in [PubMed](#) [Google Scholar](#)

29. Hilary K. Finucane

[View author publications](#)

You can also search for this author in [PubMed](#) [Google Scholar](#)

30. Nir Hacohen

[View author publications](#)

You can also search for this author in [PubMed](#) [Google Scholar](#)

31. Eric S. Lander

[View author publications](#)

You can also search for this author in [PubMed](#) [Google Scholar](#)

32. Jesse M. Engreitz

[View author publications](#)

You can also search for this author in [PubMed](#) [Google Scholar](#)

## Contributions

J.N. and J.M.E. developed computational methods. J.N., D.T.B., J.M.E., C.P.F., B.R.D., T.A.P., T.R.J., K.M., H.M.N., H.Y.K., A.C. and R.L.C. conducted data analysis. D.T.B., C.P.F., P.G., B.R.D., G.M. and T.H.N. conducted CRISPR experiments. T.H.N., J.P.R., T.M.E., C.B.E. and M.K. collected epigenomic datasets. J.C.U., E.M.W., M.J.D., H.H. and H.K.F. contributed fine-mapping analysis. F.L. and H.P. built visualization tools. K.D., A.L.P., A.K., R.J.X., M.J.D., H.H. and H.K.F. contributed to data interpretation and design of analyses. N.H., E.S.L. and J.M.E. supervised the study. J.N., D.T.B., C.P.F., P.G., B.R.D., E.S.L. and J.M.E. wrote the manuscript. All authors reviewed and approved the final manuscript.

## Corresponding authors

Correspondence to [Eric S. Lander](#) or [Jesse M. Engreitz](#).

## Ethics declarations

## Competing interests

J.M.E., C.P.F. and E.S.L. are inventors on a patent application on CRISPR methods filed by the Broad Institute related to this work (16/337,846). Until recently, E.S.L. served on the Board of Directors for Codiak BioSciences and Neon Therapeutics; served on the Scientific Advisory Board of F-Prime

Capital Partners and Third Rock Ventures; was affiliated with several non-profit organizations including serving on the Board of Directors of the Innocence Project, Count Me In and Biden Cancer Initiative, and the Board of Trustees for the Parker Institute for Cancer Immunotherapy; and served on various federal advisory committees. E.S.L. is currently on leave from MIT and Harvard. C.P.F. is now an employee of Bristol Myers Squibb. T.A.P. is now an employee of Boston Consulting Group. R.J.X. is a cofounder of Jnana Therapeutics and Celsius Therapeutics. M.J.D. is a founder of Maze Therapeutics. N.H. holds equity in BioNTech and consults for Related Therapeutics. All other authors declare no competing interests.

## Additional information

**Peer review information** *Nature* thanks Annique Claringbould, Judith Zaugg and the other, anonymous, reviewer(s) for their contribution to the peer review of this work.

**Publisher's note** Springer Nature remains neutral with regard to jurisdictional claims in published maps and institutional affiliations.

## Extended data figures and tables

### [Extended Data Fig. 1 ABC maps connect fine-mapped variants to enhancers, genes and cell types.](#)

**a**, Overview of approach. **b**, ABC predictions connect two IBD GWAS signals to *IL10*. Signal tracks show DNase-seq or ATAC-seq (based on availability of data). Red arrows represent ABC predictions connecting variants to *IL10*. Dashed line shows the TSS. Grey bars highlight fine-mapped variants that overlap with ABC enhancers in at least one cell type. Credible set 1 contains two variants, both of which overlap with enhancers predicted to regulate *IL10* in various cell types. Credible set 2 contains four variants, one of which overlaps with an enhancer predicted to regulate *IL10* in monocytes stimulated with LPS.

### [Extended Data Fig. 2 Properties of ABC predictions.](#)

**a**, Cumulative fraction of the number of ABC enhancers within each biosample (median = 17,605). **b**, Cumulative fraction of the number of enhancer–gene connections within each biosample (median = 48,441). **c**, Cumulative fractions of the number of enhancers predicted to regulate each gene across all biosamples (black line; median = 2, mean = 2.8) and the mean number of enhancers predicted to regulate each gene within each biosample (red line; median = 2.8). **d**, Cumulative fractions of the number of genes regulated by each ABC enhancer across all genes and all biosamples (black line; median = 1, mean = 2.7) and the mean number of genes regulated by each ABC enhancer within each biosample (red line; median = 2.7). **e**, Cumulative fractions of the genomic distances between the enhancer and the gene for each predicted enhancer–gene connection across all genes and all biosamples (black line; median = 62,929 bp) and the median genomic distance between each enhancer–gene connection within each biosample (red line; median = 62,782 bp). **f**, Number of ABC enhancers predicted in 131 biosamples stratified by whether the epigenomic data for the biosample is derived from one or multiple donors. We do not observe significant differences between these distributions (two-sided Wilcoxon rank-sum test,  $P = 0.10$ ). Box plot displays median, 25th and 75th percentiles. **g**, Summary of ABC predictions in K562. Plot includes 122,410 non-promoter Dnase hypersensitive sites (DHS elements) in K562. Each element is classified as an ‘ABC enhancer’ if the element is predicted to regulate at least one gene, or ‘other accessible region’ otherwise. The  $x$  axis represents the distance from the element to the closest TSS of an expressed gene. The  $y$  axis represents the percentile bin of the activity of the element (in terms of DHS and H3K27ac signals) among these 122,410 elements. The colouring of the heat map represents the fraction of elements in the corresponding distance and activity bins that are ABC enhancers.

### Extended Data Fig. 3 Distinctness and reproducibility of ABC predictions.

**a**, Distinctness of predictions across biosamples. Biosample versus biosample ( $131 \times 131$ ) heat map. The colour of the  $(i,j)$  pixel in the heat map represents the fraction of enhancer–gene connections (‘E-G connections’—which are defined to be an element–gene pair for which the ABC score is greater than 0.015) in biosample  $i$  that have a corresponding

overlapping prediction in biosample  $j$ . Two connections are considered overlapping if the predicted genes are the same and the enhancer elements overlap. Rows and columns are ordered by hierarchical clustering. A median of 19% (median of row medians) of enhancer–gene connections are shared across distinct biosamples. **b**, Distribution of shared connections by relatedness of samples. Distribution of the fraction of shared connections in **a** stratified by the relatedness of the samples. Each pair of biosamples is classified as: ‘same cell line’, which indicates the same cell line under different perturbation conditions or from different compendia; ‘same primary tissue type’, which indicates the same tissue type from different compendia; ‘same lineage’, which indicates samples from the same lineage classification as in **a**; ‘other’ refers to all other pairs of samples. **c**, Quantitative reproducibility of ABC predictions. ABC scores computed using independent biological replicates of epigenomic data (ATAC-seq and H3K27ac ChIP-seq) from the BJAB cell line. Each data point is an element–gene pair. **d**, Fraction of shared enhancer–gene connections between replicates increases as ABC score cut-off increases.  $x$  axis, cut-off on the ABC score;  $y$  axis, for a given cut-off of the ABC score, the fraction of element–gene pairs with an ABC score greater than the cut-off in sample 1 that have an ABC score  $> 0.015$  in sample 2. Each biosample is classified as: ‘multiple donors’, which indicates that the epigenetic data for this biosample is derived from different donors, or ‘single donor’, which indicates that the epigenetic data for this biosample is derived from the same donor or cell line. For ‘single donor’ biosamples, replicates represent independent epigenomic experiments from the same donor or cell line; for ‘multiple donor’ biosamples, replicates represent epigenomic experiments from different donors. Separate curves are computed for each biosample and then the average across biosamples is plotted. **e**, Fraction of shared enhancer–gene connections increases as reproducibility of underlying epigenetic data increases. Each data point represents a biosample.  $x$  axis, geometric mean of correlation of ATAC-seq (or DNase-seq) and H3K27ac ChIP-seq signal in candidate regions computed using replicate epigenetic experiments.  $y$  axis, fraction of enhancer–gene connections with ABC score  $> 0.015$  in replicate 1 that also have ABC score  $> 0.015$  in replicate 2. Colours as in **d**.

## Extended Data Fig. 4 ABC performs well at identifying regulatory enhancer–gene connections in CRISPR datasets.

**a**, Comparison of enhancer–gene predictors to experimental CRISPR data in K562 cells. Each of these predictors makes K562-specific predictions. Curves represent continuous predictors. Dots represent binary predictors as follows: E, each gene is predicted to be regulated only by the element closest to its TSS; G, each element is predicted to regulate only the nearest (to TSS) expressed gene; T, TargetFinder method<sup>31</sup>; L, elements and genes at opposite ends of HiCCUPS loops derived from Hi-C data are predicted as a connection<sup>67</sup>; D, an element–gene pair is a predicted positive if and only if the element and the gene are contained within the same contact domain<sup>67</sup>. The red dot on ABC score curve: precision and recall achieved using a threshold on the ABC score of 0.015. Dashed black line, rate of experimental positives. **b**, Comparison of ABC predictions using a binary distance threshold to experimental CRISPR data in K562 cells. ‘Activity ( $<X$  kb)’ represents a model in which the score for an element–gene pair is the activity of the element (in terms of DHS and H3K27ac signals) multiplied by a binary indicator (1 if the distance is  $<X$  kb, and 0 otherwise). The ABC model using quantitative Hi-C outperforms the models based on binary thresholds indicating that Hi-C data are a critical component of the ABC model. **c**, Comparison of ABC and other enhancer–gene predictors in full CRISPR dataset. Comparison of enhancer–gene predictors to experimental CRISPR data in K562, GM12878, NCCIT, BJAB (with or without stimulation), Jurkat (with or without stimulation), THP1 (with or without stimulation) cells and primary hepatocytes. For ABC, we used the predictions in the cell type corresponding to the CRISPR experiments. Because ABC is the only method that makes predictions in all of these cell types, we used this plot to compare ABC to other methods that make predictions without cell-type information. We consider each enhancer–gene pair predicted by these methods to be a prediction in all cell types. **d**, Comparison of ABC and Ernst-Roadmap predictions<sup>25</sup>. Comparison of enhancer–gene predictors to experimental CRISPR data in K562, GM12878 and unstimulated Jurkat, BJAB and THP1 cells. The red line represents a comparison of ABC scores computed using epigenetic data from the same cell type as the CRISPR experiment was performed. To

compare Roadmap predictions to CRISPR data, we made cell-type substitutions because the Roadmap predictions did not include BJAB, Jurkat and THP1 cells: for BJAB CRISPR data we compared to predictions in the Roadmap B cell sample (E032); for THP1 data we used the Roadmap monocyte sample (E124); and for Jurkat data we used the Roadmap T cell sample (E034). To directly compare the performance of ABC and Ernst-Roadmap methods in matched cell types, we also calculated ABC performance using the same cell type substitutions (green line)—for example, CRISPR data in BJAB cells were compared to ABC scores computed using epigenetic data from the Roadmap B cell sample (E032). **e**, Comparison of ABC to PC-Hi-C. Comparison of enhancer–gene predictors to experimental CRISPR data in K562 and unstimulated BJAB, THP1 and Jurkat cells. The red line represents a comparison of ABC scores computed using epigenetic data from the same cell type as the CRISPR experiment was performed. To compare PC-Hi-C CHiCAGO predictions (purple line) to CRISPR data, we made cell-type substitutions because PC-HiC data are not available for K562, BJAB, Jurkat and THP1 cells: for K562 CRISPR data we compared to CHiCAGO scores in erythroblasts; for BJAB CRISPR data we compared to total B cells; for THP1 data we compared to monocytes; and for Jurkat data we compared to activated CD4<sup>+</sup> T cells. To directly compare the performance of ABC and PC-HiC methods in matched cell types, we also calculated ABC performance using the same cell-type substitutions (green lines). The solid green line represents ABC scores for which the contact component is derived from the average Hi-C dataset used throughout this study. The dashed green line represents ABC scores for which the contact component is derived from the raw counts in PC-HiC experiments (see Methods). **f–h**, Comparison of ABC to PC-Hi-C stratified by distance. These panels represent the comparison of the same predictors as in **e** while stratifying the experimental dataset in **e** based on the distance between the tested element and gene TSS. Of the 4,078 element–gene connections in the experimental dataset, 398 are at a distance of <50 kb (of which 94 are experimental positives, 24% positive rate), 1,102 are between 50 kb and 200 kb (20 positives, 2% positive rate) and 2,578 are at a distance of >200 kb (10 positives, 0.4% positive rate). Given the differences in positive rates between the stratifications (indicated by dashed black lines), it is appropriate to compare precision–recall curves within each stratification,

but it is not appropriate to compare the precision–recall curve of the same predictor across stratifications.

## Extended Data Fig. 5 Fine-mapped GWAS variants are highly enriched in ABC enhancers.

**a**, Number of credible sets analysed for 72 diseases and complex traits. Light grey shows the total number of fine-mapped credible sets. Dark grey shows the number of such credible sets with no coding or splice site variants, and at least one variant with  $\text{PIP} \geq 10\%$ . Red shows the number of credible sets for which ABC-Max makes a prediction (that is, a variant with  $\text{PIP} \geq 10\%$  overlaps an ABC enhancer in a biosample that shows global enrichment for that trait). See Supplementary Table 7 for trait descriptions and additional statistics. **b**, Enrichment of fine-mapped variants ( $\text{PIP} \geq 10\%$ ) associated with four blood cell traits in ABC enhancers in the corresponding blood cell types or progenitors. Enrichment = (fraction of fine-mapped variants/fraction of all common variants) overlapping regions in each cell type. Numbers of biosamples in each category are shown in parentheses. **c**, Enrichment of fine-mapped IBD variants ( $\text{PIP} \geq 10\%$ ) in ABC enhancers and other sets of previously defined enhancers. Cumulative density function shows distribution across cell types. **d**, Enrichment of fine-mapped variants ( $\text{PIP} \geq 10\%$ ) in ABC enhancers resized in different ways. Regions of at least 500-bp (blue line) are used to count reads, as defined previously. Regions were then shrunk by 150-bp on each side (minimum size of element = 200 bp) for overlapping with variants. Grey lines show alternative sizes, which do not appear to notably affect enrichments of fine-mapped variants. **e**, Percentage of noncoding variants across all traits that overlap an ABC enhancer in an enriched biosample, as a function of the number of cell types analysed. Biosamples (131) were grouped into 74 cell types or tissues; and analysed in random order. Black line, mean across 20 random orderings. Dashed grey lines, 95% confidence intervals. **f**, Fraction of variants or heritability for all 72 traits contained in different categories of genomic regions: coding sequences (CDS), untranslated regions (UTR), splice sites (within 10 bp of an intron–exon junction of a protein-coding gene), promoters ( $\pm 250$  bp from the gene TSS), ABC enhancers in 131 biosamples, other accessible regions not called as ABC enhancers, and other intronic or intergenic regions. In cases in which a variant overlaps

more than one category, the variant was assigned to the first category that it overlapped (that is, variants in coding sequences were not also counted in the ABC category; Methods). Left, all common variants or heritability ( $h^2$ , as estimated by S-LDSC in inverse-variance-weighted meta-analysis across 72 traits). Right, fraction of variants above a threshold on the fine-mapping PIP.

## Extended Data Fig. 6 ABC enhancer maps connect GWAS variants to known genes.

**a**, ABC predictions for IBD credible sets linked to *IL10*. Heat map shows ABC scores for each gene within 1 Mb in selected primary immune cell types. Credible set 1 is linked by ABC to multiple genes, but *IL10* (red) has the strongest ABC score in any cell type. **b**, Cumulative density plot showing enrichment for gene sets in MSigDB among the genes prioritized by each method<sup>63</sup>. Methods are coloured and categories as in Fig. 1c. For each method, we first identified the top 5 most enriched significant gene sets in the predictions of that method (82 gene sets total). Then, we calculated the levels of enrichment of all 82 gene sets in the predictions of each method. **c**, Comparison of predictions for the 37 IBD credible sets near known genes. Fraction predictions shared = (credible sets for which both methods predict the same gene)/(credible sets for which both methods make a prediction). For example, 16 credible sets have predictions from both ABC-Max and ChromHMM-RNA correlation, and the two methods predict the same gene in 14 out of 16 credible sets. **d**, Enrichment of likely causal genes for 10 blood traits (defined by common coding variants) for various prediction methods. Enrichment reflects the number of correctly predicted genes identified divided by the baseline of choosing random genes in each of the loci with a prediction. **e**, Precision–recall plot for identifying known IBD-associated genes, comparing additional variations on the prediction methods (related to Fig. 1c). For ABC, we compared ABC-Max (assigning each credible set to the gene with the maximum ABC score, red circle), ABC-Max excluding all immune and gut tissue biosamples (orange circle) and ABC-All (assigning each credible set to all genes linked to enhancers, red triangle). For other methods that provided quantitative scores, we similarly compared choosing the gene with the best score per locus (circles) with choosing all genes above the global thresholds previously reported in

each study (triangles). In most cases, the best gene per locus outperformed using a global threshold.

### Extended Data Fig. 7 ABC-Max predictions at *LRRC32* and *RASL11A* loci.

**a, b**, ABC-Max predictions and chromatin state in primary immune cells and fetal colon tissue at two IBD loci: *LRRC32* (**a**) and *RASL11A* (**b**). Red marks variants, enhancer–gene connections and target genes identified by ABC-Max. Grey bars highlight the variants overlapping ABC enhancers. Vertical dotted lines represent TSSs. ‘DCs + LPS’, dendritic cells stimulated with bacterial LPS for 4 h.

### Extended Data Fig. 8 Cell-type specificity of ABC predictions.

**a**, A comparison of the number of biosample groups (cell type lineages) in which the gene promoter is active versus the number of categories in which a variant is predicted to regulate the gene by ABC-Max. **b**, Heat map of ABC scores for predicted IBD-associated genes in resting and stimulated mononuclear phagocytes (from epigenomic data in monocytes<sup>68</sup> and dendritic cells<sup>69</sup>). *IRF4* and *PDGFB* (bold) are two examples for which ABC predictions are specific to a particular stimulated state (+LPS) and are not observed in unstimulated states. **c**, Enrichment for top gene sets identified when performing enrichment analysis among the 23 IBD-associated genes predicted by ABC-Max in mononuclear phagocytes (dark grey), versus when performing the same analysis among the 43 IBD-associated genes predicted in any biosample (light grey). The enrichment for a given gene is calculated as the ratio of the frequency at which ABC-predicted genes belong to the gene set, compared to the frequency at which all genes within 1 Mb of these loci belong to the gene set (Methods). **d**, A variant in an intron of *ANKRD55* is predicted by the ABC model to regulate *IL6ST* in thymus. The grey bar highlights the variant overlapping the predicted ABC enhancer. Vertical dotted lines represent TSSs. The red arc at the top denotes the ABC-Max prediction. The red arc at the bottom denotes that CRISPRi of the highlighted enhancer significantly affects the expression of *IL6ST* only in Jurkat cells.

## Extended Data Fig. 9 Genes linked by ABC to different traits by different variants.

**a**, ABC links *IKZF1* to 2 traits by variants in 18 credible sets. Red boxes mark enhancers predicted to regulate *IKZF1*. The thick black line marks the *IKZF1* TSS. Black dots mark fine-mapped noncoding variants ( $\text{PIP} \geq 10\%$ ) associated with one or more traits linked to *IKZF1* by ABC-Max. **b**, Genes linked to different traits via different variants have more complex enhancer landscapes. Cumulative distribution plots show the number of ABC enhancer–gene connections in all 131 biosamples (left) and the distance between the TSSs of the two closest neighbouring genes on either side of a gene, for each gene linked by ABC-Max to zero traits, one trait, or two or more traits through different variants (right). **c**, The complexity of the enhancer landscape of a gene is correlated with the odds of the gene being linked to multiple GWAS traits. The *x* axis shows the Wald odds ratio that a gene is connected to multiple GWAS traits, comparing genes in the top decile versus all other deciles of the corresponding enhancer complexity metric. The three enhancer complexity metrics are defined for each gene: the total number of enhancers linked to the gene by ABC in any biosample, the number of enhancers linked to a gene per biosample in which the promoter of the gene is active, and the genomic distance to the closest neighbouring TSS on either side of the gene. Dot, mean of the top decile genes ( $n = 1,838$ ) versus all others ( $n = 16,550$ ). Whiskers, 95% confidence intervals.

## Extended Data Fig. 10 Enhancers and variants connected to *PPIF*.

**a**, ABC predictions for variants near *PPIF*. Black dots represent either fine-mapped variants ( $\text{PIP} \geq 10\%$ ) for IBD and UK Biobank traits, or lead variants for any phenotype from the GWAS Catalog<sup>16</sup> (the latter to show the approximate locations of signals for traits for which fine-mapping is not yet available). The ‘IBD’ label points to rs1250566. The ‘MS’ (multiple sclerosis) label points to rs1250568 (fine-mapped in ref. <sup>2</sup>). Red boxes mark enhancers predicted to regulate *PPIF*. Thick back lines mark TSSs. Thin black lines mark selected variants. **b**, CRISPRi-FlowFISH data for *PPIF* in

seven immune cell lines and stimulated states. Red boxes mark distal enhancers (CRISPR gRNAs lead to a significant decrease in the expression of *PPIF*). Dark grey box marks the gene body of *PPIF*, for which CRISPRi cannot accurately assess the effects of putative regulatory elements<sup>4</sup>. **c**, Chromatin accessibility in 5-kb regions around the *PPIF* enhancer (e-PPIF). Signal tracks show ATAC-seq (for THP1 and BJAB) or DNase-seq (for GM12878 and Jurkat) data in reads per million. Arrows show the locations of variants associated with multiple sclerosis and lymphocyte count (Lym, rs1250568) and with IBD (rs1250566), which overlap with enhancers that regulate *PPIF* in distinct sets of cell types. **d**, Effect of each tested gRNA on *PPIF* expression, as measured by CRISPRi-FlowFISH (Methods). Dots, gRNAs for which the effect estimate is >0% (black) or <0% (red). Red bars show regions for which gRNAs have a significant effect on gene expression (FDR < 0.05), compared by a two-sided *t*-test to negative control gRNAs. **e**, Effects of eight individual gRNAs on *PPIF* expression in THP1 cells, as measured by CRISPRi and qPCR (Methods). *PPIF* expression is normalized to expression of *GAPDH* and to cells expressing negative control, non-targeting gRNAs (Ctrl). Error bars, 95% confidence intervals of the mean ( $n = 6$  replicates per gRNA). **f**, Schema of pooled CRISPRi screen to examine the effects of *PPIF* and e-PPIF on mitochondrial membrane potential ( $\Delta\psi_m$ ). Cells expressing a pool of gRNAs were stained with MitoTracker Red and MitoTracker Green and sorted into three bins of increasing red:green ratios. gRNAs from cells in each bin were PCR-amplified, sequenced and counted. **g**, Effects of CRISPRi gRNAs (targeting e-PPIF, *PPIF* promoter or negative controls) on  $\Delta\psi_m$ , quantified as the frequency of THP1 cells carrying those gRNAs with low or medium versus high MitoTracker Red signal (corresponding to bins 1, 2 and 3, respectively; superset of data in Fig. 4d). We tested THP1 cells in unstimulated conditions, stimulated with LPS, and differentiated with PMA and stimulated with LPS (Methods). Error bars, 95% confidence intervals for the mean of 40, 9, and 5 gRNAs for control, *PPIF* and e-PPIF, respectively. Two-sided Wilcoxon rank-sum test versus control; \* $P = 0.0163$ , \*\* $P = 0.00426$ , \*\*\* $P = 0.000356$ . **h**, Ratios of MitoTracker Red (mitochondrial membrane potential) to MitoTracker Green (mitochondrial mass) signal in THP1 cells at baseline, stimulated with LPS and differentiated into macrophages with PMA and stimulated with LPS in biological duplicate (from left to right,  $n = 8,044, 99,683, 99,982, 99,968$ ,

99,886 and 99,878; replicates were cultured, stimulated, stained and flow-sorted independently). Box represents median and interquartile range; whiskers show minimum and maximum. Stimulation with either LPS alone or both PMA and LPS leads to a reduction in red:green signal, indicating a reduction in mitochondrial membrane potential normalized to mitochondrial mass.

## Supplementary information

### Supplementary Information

This file contains Supplementary Notes 1-5, Supplementary Figures 1-2, full legends for Supplementary Tables 1-14 and Supplementary References.

### Reporting Summary

### Supplementary Table 1

Epigenomic data collected in immune cell lines.

### Supplementary Table 2

Metrics for ABC predictions in 131 biosamples.

### Supplementary Table 3

This zipped file contains CRISPRi-FlowFISH data: data per guide.

### Supplementary Table 4

CRISPRi-FlowFISH data: summary per candidate element.

### Supplementary Table 5

Comparison of CRISPR data to enhancer-gene predictions.

## **Supplementary Table 6**

Enrichment of GWAS variants in ABC enhancers across biosamples.

## **Supplementary Table 7**

Summary of diseases and traits.

## **Supplementary Table 8**

ABC predictions for IBD GWAS loci.

## **Supplementary Table 9**

Causal gene predictions in IBD GWAS loci with known genes.

## **Supplementary Table 10**

ABC-Max predictions for 72 diseases and complex traits.

## **Supplementary Table 11**

References linking predicted IBD genes to effects on experimental colitis.

## **Supplementary Table 12**

ABC and ABC-Max metrics for all genes.

## **Supplementary Table 13**

FlowFISH probesets.

## **Supplementary Table 14**

PPIF and mitochondrial membrane potential: CRISPRi data per guide.

# Rights and permissions

[Reprints and Permissions](#)

## About this article



## Cite this article

Nasser, J., Bergman, D.T., Fulco, C.P. *et al.* Genome-wide enhancer maps link risk variants to disease genes. *Nature* **593**, 238–243 (2021).  
<https://doi.org/10.1038/s41586-021-03446-x>

[Download citation](#)

- Received: 20 August 2020
- Accepted: 11 March 2021
- Published: 07 April 2021
- Issue Date: 13 May 2021
- DOI: <https://doi.org/10.1038/s41586-021-03446-x>

## Comments

By submitting a comment you agree to abide by our [Terms](#) and [Community Guidelines](#). If you find something abusive or that does not comply with our terms or guidelines please flag it as inappropriate.

[Access through your institution](#)

[Change institution](#)

## Buy or subscribe

---

This article was downloaded by **calibre** from <https://www.nature.com/articles/s41586-021-03446-x>

| [Section menu](#) | [Main menu](#) |

- Article
- [Published: 28 April 2021](#)

# Coupling of activity, metabolism and behaviour across the *Drosophila* brain

- [Kevin Mann<sup>1</sup>](#) na1,
- [Stephane Deny<sup>2</sup>](#) na1,
- [Surya Ganguli](#) 1,2 &
- [Thomas R. Clandinin](#) ORCID: orcid.org/0000-0001-6277-6849<sup>1</sup>

[Nature](#) volume **593**, pages 244–248 (2021) [Cite this article](#)

- 6590 Accesses
- 153 Altmetric
- [Metrics details](#)

## Subjects

- [Ca2+ imaging](#)
- [Cellular neuroscience](#)
- [Neural circuits](#)

## Abstract

Coordinated activity across networks of neurons is a hallmark of both resting and active behavioural states in many species<sup>1,2,3,4,5</sup>. These global patterns alter energy metabolism over seconds to hours, which underpins

the widespread use of oxygen consumption and glucose uptake as proxies of neural activity<sup>6,7</sup>. However, whether changes in neural activity are causally related to metabolic flux in intact circuits on the timescales associated with behaviour is unclear. Here we combine two-photon microscopy of the fly brain with sensors that enable the simultaneous measurement of neural activity and metabolic flux, across both resting and active behavioural states. We demonstrate that neural activity drives changes in metabolic flux, creating a tight coupling between these signals that can be measured across brain networks. Using local optogenetic perturbation, we demonstrate that even transient increases in neural activity result in rapid and persistent increases in cytosolic ATP, which suggests that neuronal metabolism predictively allocates resources to anticipate the energy demands of future activity. Finally, our studies reveal that the initiation of even minimal behavioural movements causes large-scale changes in the pattern of neural activity and energy metabolism, which reveals a widespread engagement of the brain. As the relationship between neural activity and energy metabolism is probably evolutionarily ancient and highly conserved, our studies provide a critical foundation for using metabolic proxies to capture changes in neural activity.

[Access through your institution](#)

[Change institution](#)

[Buy or subscribe](#)

## Access options

Subscribe to Journal

Get full journal access for 1 year

\$199.00

only \$3.90 per issue

[Subscribe](#)

All prices are NET prices.  
VAT will be added later in the checkout.  
Tax calculation will be finalised during checkout.

Rent or Buy article

Get time limited or full article access on ReadCube.

from \$8.99

[Rent or Buy](#)

All prices are NET prices.

### **Additional access options:**

- [Log in](#)
- [Access through your institution](#)
- [Learn about institutional subscriptions](#)

**Fig. 1: Metabolic and neural networks are highly correlated across the brain.**

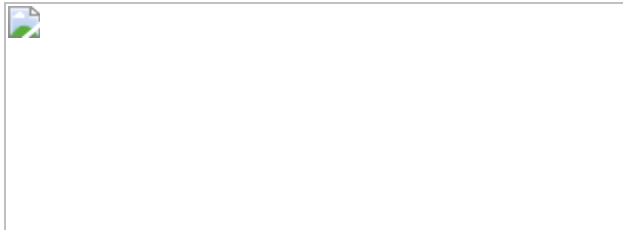


**Fig. 2: Simultaneous measurements of neural activity and metabolic flux reveal correlations that are dominated by low frequencies.**

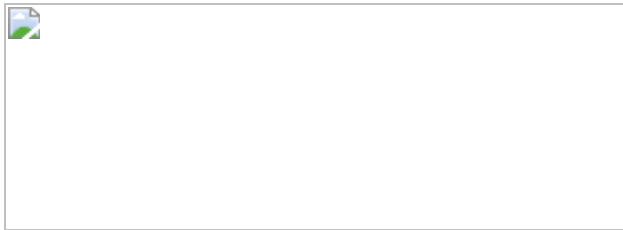


**Fig. 3: Neural activity drives metabolic flux in the brain.**

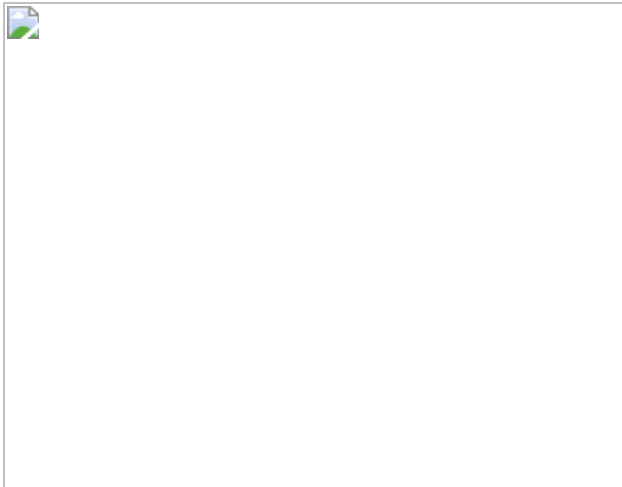
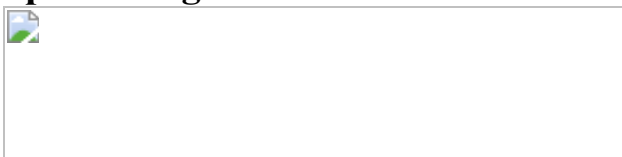


**Fig. 4: Neural activity and metabolic flux are correlated with behaviour in specific regions.**



## Data availability

Raw imaging data are available upon request to the corresponding authors.

## Code availability

Analysis scripts are available upon request from the corresponding authors.

## References

1. 1.

Liska, A., Galbusera, A., Schwarz, A. J. & Gozzi, A. Functional connectivity hubs of the mouse brain. *Neuroimage* **115**, 281–291 (2015).

[Article](#) [Google Scholar](#)

2. 2.

Ahrens, M. B., Orger, M. B., Robson, D. N., Li, J. M. & Keller, P. J. Whole-brain functional imaging at cellular resolution using light-sheet microscopy. *Nat. Methods* **10**, 413–420 (2013).

[CAS](#) [Article](#) [Google Scholar](#)

3. 3.

Mann, K., Gallen, C. L. & Clandinin, T. R. Whole-brain calcium imaging reveals an intrinsic functional network in *Drosophila*. *Curr. Biol.* **27**, 2389–2396.e4 (2017).

[CAS](#) [Article](#) [Google Scholar](#)

4. 4.

Prevedel, R. et al. Simultaneous whole-animal 3D imaging of neuronal activity using light-field microscopy. *Nat. Methods* **11**, 727–730 (2014).

[CAS](#) [Article](#) [Google Scholar](#)

5. 5.

Power, J. D., Schlaggar, B. L. & Petersen, S. E. Studying brain organization via spontaneous fMRI signal. *Neuron* **84**, 681–696 (2014).

[CAS](#) [Article](#) [Google Scholar](#)

6. 6.

Logothetis, N. K. What we can do and what we cannot do with fMRI. *Nature* **453**, 869–878 (2008).

[ADS](#) [CAS](#) [Article](#) [Google Scholar](#)

7. 7.

Magistretti, P. J. & Allaman, I. A cellular perspective on brain energy metabolism and functional imaging. *Neuron* **86**, 883–901 (2015).

[CAS](#) [Article](#) [Google Scholar](#)

8. 8.

Horwitz, B., Soncrant, T. T. & Haxby, J. V. in *Advances in Metabolic Mapping Techniques for Brain Imaging of Behavioral and Learning Functions* (eds Gonzalez-Lima, F. et al.) 189–217 (1992).

9. 9.

Sokoloff, L., Kennedy, C. & Smith, C. B. in *Carbohydrates and Energy Metabolism* (eds Boulton, A. A. et al.) 155–193 (1989).

10. 10.

Passow, S. et al. Default-mode network functional connectivity is closely related to metabolic activity. *Hum. Brain Mapp.* **36**, 2027–2038 (2015).

[Article](#) [Google Scholar](#)

11. 11.

Schölvinc, M. L., Maier, A., Ye, F. Q., Duyn, J. H. & Leopold, D. A. Neural basis of global resting-state fMRI activity. *Proc. Natl Acad. Sci. USA* **107**, 10238–10243 (2010).

[ADS](#) [Article](#) [Google Scholar](#)

12. 12.

Migault, G. et al. Whole-brain calcium imaging during physiological vestibular stimulation in larval zebrafish. *Curr. Biol.* **28**, 3723–3735.e6 (2018).

[CAS](#) [Article](#) [Google Scholar](#)

13. 13.

Harris, D. T., Kallman, B. R., Mullaney, B. C. & Scott, K. Representations of taste modality in the *Drosophila* brain. *Neuron* **86**, 1449–1460 (2015).

[CAS](#) [Article](#) [Google Scholar](#)

14. 14.

Lemon, W. C. et al. Whole-central nervous system functional imaging in larval *Drosophila*. *Nat. Commun.* **6**, 7924 (2015).

[ADS](#) [CAS](#) [Article](#) [Google Scholar](#)

15. 15.

Aimon, S. et al. Fast near-whole-brain imaging in adult *Drosophila* during responses to stimuli and behavior. *PLoS Biol.* **17**, e2006732 (2019).

[Article](#) [Google Scholar](#)

16. 16.

Palva, J. M. & Palva, S. Infra-slow fluctuations in electrophysiological recordings, blood-oxygenation-level-dependent signals, and psychophysical time series. *Neuroimage* **62**, 2201–2211 (2012).

[Article](#) [Google Scholar](#)

17. 17.

Mitra, A. et al. Spontaneous infra-slow brain activity has unique spatiotemporal dynamics and laminar structure. *Neuron* **98**, 297–305.e6 (2018).

[CAS](#) [Article](#) [Google Scholar](#)

18. 18.

Biswal, B., Yetkin, F. Z., Haughton, V. M. & Hyde, J. S. Functional connectivity in the motor cortex of resting human brain using echo-planar MRI. *Magn. Reson. Med.* **34**, 537–541 (1995).

[CAS](#) [Article](#) [Google Scholar](#)

19. 19.

San Martín, A. et al. Imaging mitochondrial flux in single cells with a FRET sensor for pyruvate. *PLoS ONE* **9**, e85780 (2014).

[ADS](#) [Article](#) [Google Scholar](#)

20. 20.

Plaçais, P.-Y. et al. Upregulated energy metabolism in the *Drosophila* mushroom body is the trigger for long-term memory. *Nat. Commun.* **8**, 15510 (2017).

[ADS](#) [Article](#) [Google Scholar](#)

21. 21.

Gonzalez-Gutierrez, A., Ibáñez, A., Esparza, A., Felipe Barros, L. & Sierralta, J. Monocarboxylate transport in *Drosophila* larval brain during low and high neuronal activity. Preprint at <https://doi.org/10.1101/610196> (2019).

22. 22.

Lobas, M. A. et al. A genetically encoded single-wavelength sensor for imaging cytosolic and cell surface ATP. *Nat. Commun.* **10**, 711 (2019).

[ADS](#) [CAS](#) [Article](#) [Google Scholar](#)

23. 23.

Chen, T.-W. et al. Ultrasensitive fluorescent proteins for imaging neuronal activity. *Nature* **499**, 295–300 (2013).

[ADS](#) [CAS](#) [Article](#) [Google Scholar](#)

24. 24.

Jenett, A. et al. A GAL4-driver line resource for *Drosophila* neurobiology. *Cell Rep.* **2**, 991–1001 (2012).

[CAS](#) [Article](#) [Google Scholar](#)

25. 25.

Ito, K. et al. A systematic nomenclature for the insect brain. *Neuron* **81**, 755–765 (2014).

[CAS](#) [Article](#) [Google Scholar](#)

26. 26.

Dana, H. et al. Sensitive red protein calcium indicators for imaging neural activity. *eLife* **5**, e12727 (2016).

[Article](#) [Google Scholar](#)

27. 27.

Saitoe, M., Schwarz, T. L., Umbach, J. A., Gundersen, C. B. & Kidokoro, Y. Absence of junctional glutamate receptor clusters in *Drosophila* mutants lacking spontaneous transmitter release. *Science* **293**, 514–517 (2001).

[CAS](#) [Article](#) [Google Scholar](#)

28. 28.

Klapoetke, N. C. et al. Independent optical excitation of distinct neural populations. *Nat. Methods* **11**, 338–346 (2014).

[CAS](#) [Article](#) [Google Scholar](#)

29. 29.

Stocker, R. F., Heimbeck, G., Gendre, N. & de Belle, J. S. Neuroblast ablation in *Drosophila* P[GAL4] lines reveals origins of olfactory interneurons. *J. Neurobiol.* **32**, 443–456 (1997).

[CAS](#) [Article](#) [Google Scholar](#)

30. 30.

Wagenmakers, E.-J., Farrell, S. & Ratcliff, R. Estimation and interpretation of  $1/f^\alpha$  noise in human cognition. *Psychon. Bull. Rev.* **11**, 579–615 (2004).

[Article](#) [Google Scholar](#)

31. 31.

Weissman, M. B.  $1/f$  noise and other slow, nonexponential kinetics in condensed matter. *Rev. Mod. Phys.* **60**, 537–571 (1988).

[ADS](#) [CAS](#) [Article](#) [Google Scholar](#)

32. 32.

Namiki, S., Dickinson, M. H., Wong, A. M., Korff, W. & Card, G. M. The functional organization of descending sensory-motor pathways in *Drosophila*. *eLife* **7**, e34272 (2018).

[Article](#) [Google Scholar](#)

33. 33.

Bidaye, S. S., Machacek, C., Wu, Y. & Dickson, B. J. Neuronal control of *Drosophila* walking direction. *Science* **344**, 97–101 (2014).

[ADS](#) [CAS](#) [Article](#) [Google Scholar](#)

34. 34.

Hugdahl, K., Raichle, M. E., Mitra, A. & Specht, K. On the existence of a generalized non-specific task-dependent network. *Front. Hum. Neurosci.* **9**, 430 (2015).

[Article](#) [Google Scholar](#)

35. 35.

Cong, L. et al. Rapid whole brain imaging of neural activity in freely behaving larval zebrafish (*Danio rerio*). *eLife* **6**, e28158 (2017).

[Article](#) [Google Scholar](#)

36. 36.

Nguyen, J. P. et al. Whole-brain calcium imaging with cellular resolution in freely behaving *Caenorhabditis elegans*. *Proc. Natl Acad. Sci. USA* **113**, E1074–E1081 (2016).

[CAS](#) [Article](#) [Google Scholar](#)

37. 37.

Steinmetz, N. A., Zatka-Haas, P., Carandini, M. & Harris, K. D. Distributed coding of choice, action and engagement across the mouse brain. *Nature* **576**, 266–273 (2019).

[CAS](#) [Article](#) [Google Scholar](#)

38. 38.

Selemon, L. D. & Goldman-Rakic, P. S. Common cortical and subcortical targets of the dorsolateral prefrontal and posterior parietal cortices in the rhesus monkey: evidence for a distributed neural network subserving spatially guided behavior. *J. Neurosci.* **8**, 4049–4068 (1988).

[CAS](#) [Article](#) [Google Scholar](#)

39. 39.

Oliphant, T. E. Python for scientific computing. *Comput. Sci. Eng.* **9**, 10–20 (2007).

[CAS](#) [Article](#) [Google Scholar](#)

40. 40.

Millman, K. J., Jarrod Millman, K. & Aivazis, M. Python for scientists and engineers. *Comput. Sci. Eng.* **13**, 9–12 (2011).

[Article](#) [Google Scholar](#)

41. 41.

Friard, O. & Gamba, M. BORIS: a free, versatile open-source event-logging software for video/audio coding and live observations. *Methods Ecol. Evol.* **7**, 1325–1330 (2016).

[Article](#) [Google Scholar](#)

[Download references](#)

## Acknowledgements

We thank C. Gallen for providing discussion and support. This work was supported by the Simons foundation (T.R.C. and S.G.), an NSF Career Award 1845166 (S.G.) and the Stanford Wu Tsai neuroscience institute (K.M.)

## Author information

Author notes

1. These authors contributed equally: Kevin Mann, Stephane Deny

## Affiliations

1. Department of Neurobiology, Stanford University, Stanford, CA, USA

Kevin Mann, Surya Ganguli & Thomas R. Clandinin

2. Department of Applied Physics, Stanford University, Stanford, CA, USA

Stephane Deny & Surya Ganguli

## Authors

1. Kevin Mann

[View author publications](#)

You can also search for this author in [PubMed](#) [Google Scholar](#)

2. Stephane Deny

[View author publications](#)

You can also search for this author in [PubMed](#) [Google Scholar](#)

3. Surya Ganguli

[View author publications](#)

You can also search for this author in [PubMed](#) [Google Scholar](#)

4. Thomas R. Clandinin

[View author publications](#)

You can also search for this author in [PubMed](#) [Google Scholar](#)

## Contributions

K.M., S.D., S.G. and T.R.C. conceived the project. K.M. collected the data. K.M. and S.D. analysed the data and generated figures. K.M., S.D., S.G. and T.R.C. wrote the paper.

## Corresponding authors

Correspondence to [Surya Ganguli](#) or [Thomas R. Clandinin](#).

## Ethics declarations

## Competing interests

The authors declare no competing interests.

## Additional information

**Peer review information** *Nature* thanks Marcus Raichle and the other, anonymous, reviewer(s) for their contribution to the peer review of this work. Peer reviewer reports are available.

**Publisher's note** Springer Nature remains neutral with regard to jurisdictional claims in published maps and institutional affiliations.

## Extended data figures and tables

### [Extended Data Fig. 1 Normalized iATPSnFR responses in whole brains to ATP.](#)

Normalized  $\Delta F/F$  values for different concentrations of ATP measured in whole brains expressing iATPSnFR pan-neuronally.  $n = 10$  flies, mean  $\pm$  s.e.m.

### [Extended Data Fig. 2 Example traces and correlations of Pyronic, jRGECO1a and iATPSnFR.](#)

**a**, Pyronic traces over an imaging session in different regions. **b**, A pair of traces that exhibit high correlation over time. **c**, Scatter plot of these two regions demonstrating correlation. **d**, A pair of traces that exhibit lower correlation over time. **e**, Scatter plot of these two regions demonstrating correlation. **f–j**, As in **a–e**, but with jRGECO1a. **k–o**, As in **a–e**, but with iATPSnFR.

**Extended Data Fig. 3 Correlation matrices of GCaMP6s, Pyronic and iATPSnFR.**

**a–c**, Correlation matrices for GCaMP6s, Pyronic and iATPSnFR, reproduced and enlarged from Fig. 1, and labelling each individual region.

**Extended Data Fig. 4 Correspondence of functional networks derived from simultaneous jRGECO1a, Pyronic and iATPSnFR measurements.**

**a**, Left, traces displaying iATPSnFR (green) and corresponding jRGECO1a signal (blue). Right, Pyronic signals (orange) and corresponding jRGECO1a signals (blue) across six different brain regions **b**, Correlation matrix derived from jRGECO1a in the simultaneous imaging experiments from **a** and Fig. 2. **c**, Correlation matrix derived from Pyronic in the simultaneous imaging experiments from **a** and Fig. 2. **d**, Scatter plot of the pairwise correlations between jRGECO1a and Pyronic. **e–g**, As in **b–d**, but with jRGECO1a and iATPSnFR.  $n = 23$  flies for Pyronic and  $n = 9$  flies for iATPSnFR. **h–m**, Comparison of jRGECO1a and Pyronic signals within a single brain region (saddle (SAD)). **h**, Traces of Pyronic and jRGECO1a signals including all frequency components. **i**, Pairwise comparison of Pyronic and jRGECO1a signals including all frequency components and the correlation between these signals. **j**, **k**, As in **h**, **i**, but filtered to include only low-frequency ( $<0.1$  Hz) components. **l**, **m**, As in **h**, **i**, but filtered to include only high-frequency ( $>0.1$  Hz) components.

**Extended Data Fig. 5 Neural activity drives metabolic flux in the brain.**

**a**, jRGECO1a (blue), Pyronic (orange) and iATPSnFR (green) traces in three different brain regions before (left) and after (right) application of TTX. **b**, Region-by-region correlations between jRGECO1a and Pyronic signals (orange) and between jRGECO1a and iATPSnFR signals (green), across all flies, before TTX application (top row) and after TTX application (bottom row). Mean  $\pm$  s.e.m. **c**, GCaMP6s response to 100-ms activation pulse in flies that lack CsChrimson.  $n = 45$  ROIs, mean  $\pm$  s.e.m. **d**, As in **c**, but with iATPSnFR.  $n = 45$  ROIs, mean  $\pm$  s.e.m.

### Extended Data Fig. 6 Example model predictions of behaviour and CsChrimson controls.

**a**, Schematic of the data processing and analysis pipeline used: (i) traces of Pyronic, iATPSnFR, jRGECO1a and behaviour (movement of the legs); (ii) half of the dataset was used to train a logistic regression model relating neural activity and metabolic flux to behaviour; (iii) predicted behavioural outputs were generated using the withheld data and were compared to the actual behaviour during those time periods; and (iv) model prediction was evaluated by correlating predicted behaviour to observed behaviour. **b**, Left, four example flies showing the prediction based on the model for jRGECO1a (blue) with the corresponding behaviour trace (black). Correlation between signals shown above each trace. Right, weights for each ROI generated by the model shown on right (oriented as in Fig. 4c). **c**, As in **b**, but with Pyronic (orange). **d**, **e**, As in **b**, **c**, but with a different set of four flies, with jRGECO1a (blue), iATPSnFR (green) and behaviour trace (black). **f**, Correlation between model weights derived from iATPSnFR and jRGECO1a. **g**, Correlation between model weights derived from Pyronic and jRGECO1a.

### Extended Data Fig. 7 Frequency spectra of jRGECO1a, Pyronic, iATPSnFR and behaviour.

Normalized spectra from data presented in Fig. 4.

### Extended Data Fig. 8 Correlation of model weights for GCaMP6s and descending-neuron innervation.

**a**, Model weights for each brain region generated using GCaMP6s. **b**, The number of descending-neuron processes in each brain region (abbreviations defined as in ref. [32](#)). **c**, Graphical representation of model weights, similar to Fig. [4c](#). **d**, Correlation between model weights and descending-neuron innervation by each region. **e**, Correlation between model weights derived from GCaMP6s and jRGECO1a.

### [Extended Data Fig. 9 Changes in correlations across regions during behaviour for both jRGECO1a and Pyronic.](#)

**a**, Functional connectivity map of jRGECO1a during bouts of rest. **b**, Functional connectivity map of jRGECO1a during bouts of activity. **c**, Correlation of functional connectivity maps during resting and behaving bouts. Correlations increase across the vast majority of regions ( $P = 0.004$ ,  $n = 12$  flies, one-tailed  $t$ -test). **d–f**, As in **a–c**, but for Pyronic ( $P = 0.13$ ,  $n = 7$  flies, one-tailed  $t$ -test). **g–i**, As in **a–c**, but for iATPSnFR ( $P = 0.38$ ,  $n = 13$  flies, one-tailed  $t$ -test).

## Supplementary information

### [Reporting Summary](#)

### [Peer Review File](#)

## Rights and permissions

### [Reprints and Permissions](#)

## About this article



Check for  
updates

## Cite this article

Mann, K., Deny, S., Ganguli, S. *et al.* Coupling of activity, metabolism and behaviour across the *Drosophila* brain. *Nature* **593**, 244–248 (2021).  
<https://doi.org/10.1038/s41586-021-03497-0>

[Download citation](#)

- Received: 11 March 2020
- Accepted: 26 March 2021
- Published: 28 April 2021
- Issue Date: 13 May 2021
- DOI: <https://doi.org/10.1038/s41586-021-03497-0>

## Comments

By submitting a comment you agree to abide by our [Terms](#) and [Community Guidelines](#). If you find something abusive or that does not comply with our terms or guidelines please flag it as inappropriate.

[Access through your institution](#)

[Change institution](#)

[Buy or subscribe](#)

---

This article was downloaded by **calibre** from <https://www.nature.com/articles/s41586-021-03497-0>

- Article
- [Published: 12 May 2021](#)

# High-performance brain-to-text communication via handwriting

- [Francis R. Willett](#) [ORCID: orcid.org/0000-0002-2652-8511](#)<sup>1,2,3</sup>,
- [Donald T. Avansino](#)<sup>1</sup>,
- [Leigh R. Hochberg](#) [ORCID: orcid.org/0000-0003-0261-2273](#)<sup>4,5,6,7</sup>,
- [Jaime M. Henderson](#) [ORCID: orcid.org/0000-0002-3276-2267](#)<sup>2,8,9</sup> na1 &
- [Krishna V. Shenoy](#) [ORCID: orcid.org/0000-0003-1534-9240](#)<sup>1,3,8,9,10,11</sup> na1

[Nature](#) volume 593, pages 249–254 (2021) [Cite this article](#)

- 8986 Accesses
- 3400 Altmetric
- [Metrics details](#)

## Subjects

- [Brain-machine interface](#)
- [Motor cortex](#)

## Abstract

Brain–computer interfaces (BCIs) can restore communication to people who have lost the ability to move or speak. So far, a major focus of BCI research has been on restoring gross motor skills, such as reaching and

grasping<sup>1,2,3,4,5</sup> or point-and-click typing with a computer cursor<sup>6,7</sup>. However, rapid sequences of highly dexterous behaviours, such as handwriting or touch typing, might enable faster rates of communication. Here we developed an intracortical BCI that decodes attempted handwriting movements from neural activity in the motor cortex and translates it to text in real time, using a recurrent neural network decoding approach. With this BCI, our study participant, whose hand was paralysed from spinal cord injury, achieved typing speeds of 90 characters per minute with 94.1% raw accuracy online, and greater than 99% accuracy offline with a general-purpose autocorrect. To our knowledge, these typing speeds exceed those reported for any other BCI, and are comparable to typical smartphone typing speeds of individuals in the age group of our participant (115 characters per minute)<sup>8</sup>. Finally, theoretical considerations explain why temporally complex movements, such as handwriting, may be fundamentally easier to decode than point-to-point movements. Our results open a new approach for BCIs and demonstrate the feasibility of accurately decoding rapid, dexterous movements years after paralysis.

[Access through your institution](#)

[Change institution](#)

[Buy or subscribe](#)

## Access options

Subscribe to Journal

Get full journal access for 1 year

\$199.00

only \$3.90 per issue

[Subscribe](#)

All prices are NET prices.

VAT will be added later in the checkout.

Tax calculation will be finalised during checkout.

Rent or Buy article

Get time limited or full article access on ReadCube.

from \$8.99

[Rent or Buy](#)

All prices are NET prices.

### **Additional access options:**

- [Log in](#)
- [Access through your institution](#)
- [Learn about institutional subscriptions](#)

**Fig. 1: Neural representation of attempted handwriting.**

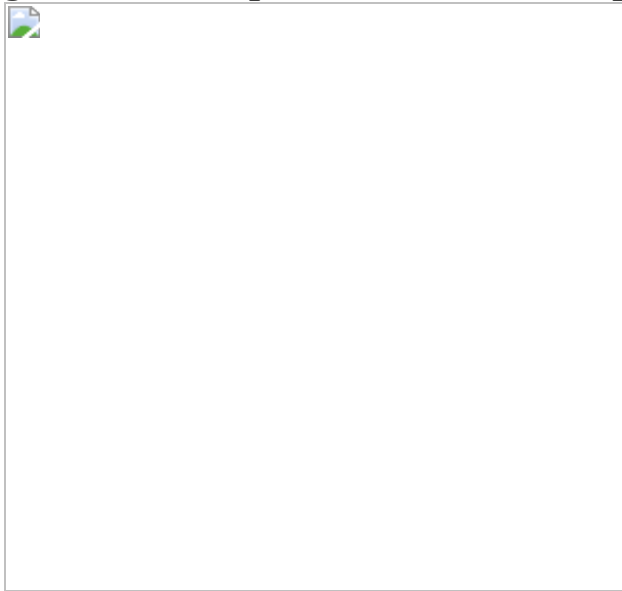


**Fig. 2: Neural decoding of attempted handwriting in real time.**

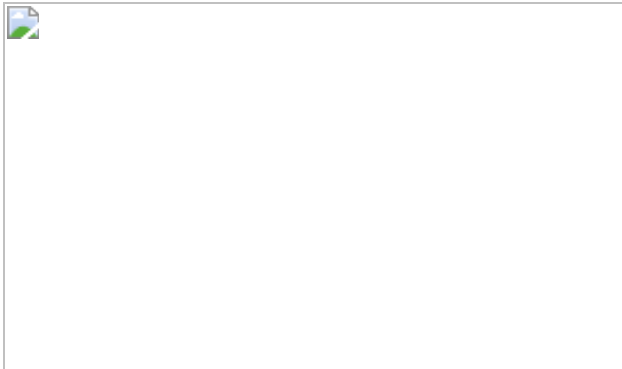
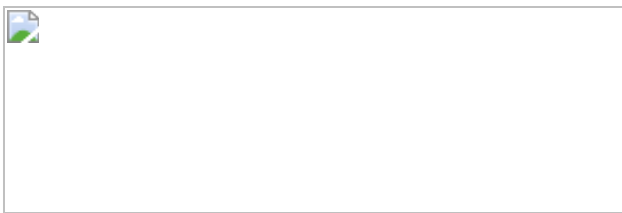


**Fig. 3: Performance remains high when daily decoder retraining is shortened (or unsupervised).**



**Fig. 4: Increased temporal variety can make movements easier to decode.**



## Data availability

All neural data needed to reproduce the findings in this study are publicly available at the Dryad repository (<https://doi.org/10.5061/dryad.wh70rxwmv>). The dataset contains neural activity recorded during the attempted handwriting of 1,000 sentences (43,501 characters) over 10.7 hours.

## Code availability

Code that implements an offline reproduction of the central findings in this study (high-performance neural decoding with an RNN) is publicly

available on GitHub at <https://github.com/fwillett/handwritingBCI>.

## References

1. 1.

Hochberg, L. R. et al. Reach and grasp by people with tetraplegia using a neurally controlled robotic arm. *Nature* **485**, 372–375 (2012).

[ADS](#) [CAS](#) [Article](#) [Google Scholar](#)

2. 2.

Collinger, J. L. et al. High-performance neuroprosthetic control by an individual with tetraplegia. *Lancet* **381**, 557–564 (2013).

[Article](#) [Google Scholar](#)

3. 3.

Aflalo, T. et al. Neurophysiology. Decoding motor imagery from the posterior parietal cortex of a tetraplegic human. *Science* **348**, 906–910 (2015).

[ADS](#) [CAS](#) [Article](#) [Google Scholar](#)

4. 4.

Bouton, C. E. et al. Restoring cortical control of functional movement in a human with quadriplegia. *Nature* **533**, 247–250 (2016).

[ADS](#) [CAS](#) [Article](#) [Google Scholar](#)

5. 5.

Ajiboye, A. B. et al. Restoration of reaching and grasping movements through brain-controlled muscle stimulation in a person with

tetraplegia: a proof-of-concept demonstration. *Lancet* **389**, 1821–1830 (2017).

[Article](#) [Google Scholar](#)

6. 6.

Jarosiewicz, B. et al. Virtual typing by people with tetraplegia using a self-calibrating intracortical brain–computer interface. *Sci. Transl. Med.* **7**, 313ra179 (2015).

[Article](#) [Google Scholar](#)

7. 7.

Pandarinath, C. et al. High performance communication by people with paralysis using an intracortical brain–computer interface. *eLife* **6**, e18554 (2017).

[Article](#) [Google Scholar](#)

8. 8.

Palin, K., Feit, A. M., Kim, S., Kristensson, P. O. & Oulasvirta, A. How do people type on mobile devices? Observations from a study with 37,000 volunteers. In *Proc. 21st International Conference on Human–Computer Interaction with Mobile Devices and Services* 1–12 (Association for Computing Machinery, 2019).

9. 9.

Youssry, T. A. et al. Localization of the motor hand area to a knob on the precentral gyrus. A new landmark. *Brain* **120**, 141–157 (1997).

[Article](#) [Google Scholar](#)

10. 10.

Willett, F. R. et al. Hand knob area of premotor cortex represents the whole body in a compositional way. *Cell* **181**, 396–409 (2020).

[CAS](#) [Article](#) [Google Scholar](#)

11. 11.

Williams, A. H. et al. Discovering precise temporal patterns in large-scale neural recordings through robust and interpretable time warping. *Neuron* **105**, 246–259 (2020).

[CAS](#) [Article](#) [Google Scholar](#)

12. 12.

Hinton, G. et al. Deep neural networks for acoustic modeling in speech recognition: the shared views of four research groups. *IEEE Signal Process. Mag.* **29**, 82–97 (2012).

[ADS](#) [Article](#) [Google Scholar](#)

13. 13.

Graves, A., Mohamed, A. & Hinton, G. Speech recognition with deep recurrent neural networks. In *2013 IEEE International Conference on Acoustics, Speech and Signal Processing* 6645–6649 (2013).

14. 14.

Xiong, W. et al. The Microsoft 2017 Conversational Speech Recognition System. Preprint at <https://arxiv.org/abs/1708.06073> (2017).

15. 15.

He, Y. et al. Streaming end-to-end speech recognition for mobile devices. In *2019 IEEE International Conference on Acoustics, Speech and Signal Processing* 6381–6385 (2019).

16. 16.

Anumanchipalli, G. K., Chartier, J. & Chang, E. F. Speech synthesis from neural decoding of spoken sentences. *Nature* **568**, 493–498 (2019).

[ADS](#) [CAS](#) [Article](#) [Google Scholar](#)

17. 17.

Makin, J. G., Moses, D. A. & Chang, E. F. Machine translation of cortical activity to text with an encoder-decoder framework. *Nat. Neurosci.* **23**, 575–582 (2020).

[CAS](#) [Article](#) [Google Scholar](#)

18. 18.

Chen, X. et al. High-speed spelling with a noninvasive brain–computer interface. *Proc. Natl Acad. Sci. USA* **112**, E6058–E6067 (2015).

[CAS](#) [Article](#) [Google Scholar](#)

19. 19.

Dickey, A. S., Suminski, A., Amit, Y. & Hatsopoulos, N. G. Single-unit stability using chronically implanted multielectrode arrays. *J. Neurophysiol.* **102**, 1331–1339 (2009).

[Article](#) [Google Scholar](#)

20. 20.

Eleryan, A. et al. Tracking single units in chronic, large scale, neural recordings for brain machine interface applications. *Front. Neuroeng.* **7**, 23 (2014).

[Article](#) [Google Scholar](#)

21. 21.

Downey, J. E., Schwed, N., Chase, S. M., Schwartz, A. B. & Collinger, J. L. Intracortical recording stability in human brain–computer interface users. *J. Neural Eng.* **15**, 046016 (2018).

[ADS](#) [Article](#) [Google Scholar](#)

22. 22.

Willett, F. R. et al. Signal-independent noise in intracortical brain–computer interfaces causes movement time properties inconsistent with Fitts’ law. *J. Neural Eng.* **14**, 026010 (2017).

[ADS](#) [Article](#) [Google Scholar](#)

23. 23.

Gao, P. et al. A theory of multineuronal dimensionality, dynamics and measurement. Preprint at <https://doi.org/10.1101/214262> (2017).

24. 24.

Musallam, S., Corneil, B. D., Greger, B., Scherberger, H. & Andersen, R. A. Cognitive control signals for neural prosthetics. *Science* **305**, 258–262 (2004).

[ADS](#) [CAS](#) [Article](#) [Google Scholar](#)

25. 25.

Santhanam, G., Ryu, S. I., Yu, B. M., Afshar, A. & Shenoy, K. V. A high-performance brain–computer interface. *Nature* **442**, 195–198 (2006).

[ADS](#) [CAS](#) [Article](#) [Google Scholar](#)

26. 26.

Cunningham, J. P., Yu, B. M., Gilja, V., Ryu, S. I. & Shenoy, K. V. Toward optimal target placement for neural prosthetic devices. *J. Neurophysiol.* **100**, 3445–3457 (2008).

[Article](#) [Google Scholar](#)

27. 27.

Pels, E. G. M., Aarnoutse, E. J., Ramsey, N. F. & Vansteensel, M. J. Estimated prevalence of the target population for brain–computer interface neurotechnology in the Netherlands. *Neurorehabil. Neural Repair* **31**, 677–685 (2017).

[Article](#) [Google Scholar](#)

28. 28.

Vansteensel, M. J. et al. Fully implanted brain–computer interface in a locked-in patient with ALS. *N. Engl. J. Med.* **375**, 2060–2066 (2016).

[Article](#) [Google Scholar](#)

29. 29.

Nijboer, F. et al. A P300-based brain–computer interface for people with amyotrophic lateral sclerosis. *Clin. Neurophysiol.* **119**, 1909–1916 (2008).

[CAS](#) [Article](#) [Google Scholar](#)

30. 30.

Townsend, G. et al. A novel P300-based brain–computer interface stimulus presentation paradigm: moving beyond rows and columns. *Clin. Neurophysiol.* **121**, 1109–1120 (2010).

[CAS](#) [Article](#) [Google Scholar](#)

31. 31.

McCane, L. M. et al. P300-based brain–computer interface (BCI) event-related potentials (ERPs): people with amyotrophic lateral sclerosis (ALS) vs. age-matched controls. *Clin. Neurophysiol.* **126**, 2124–2131 (2015).

[Article](#) [Google Scholar](#)

32. 32.

Wolpaw, J. R. et al. Independent home use of a brain–computer interface by people with amyotrophic lateral sclerosis. *Neurology* **91**, e258–e267 (2018).

[Article](#) [Google Scholar](#)

33. 33.

Bacher, D. et al. Neural point-and-click communication by a person with incomplete locked-in syndrome. *Neurorehabil. Neural Repair* **29**, 462–471 (2015).

[Article](#) [Google Scholar](#)

34. 34.

Mugler, E. M. et al. Direct classification of all American English phonemes using signals from functional speech motor cortex. *J. Neural Eng.* **11**, 035015 (2014).

[ADS](#) [Article](#) [Google Scholar](#)

35. 35.

Nurmikko, A. Challenges for large-scale cortical interfaces. *Neuron* **108**, 259–269 (2020).

[CAS](#) [Article](#) [Google Scholar](#)

36. 36.

Vázquez-Guardado, A., Yang, Y., Bandodkar, A. J. & Rogers, J. A. Recent advances in neurotechnologies with broad potential for neuroscience research. *Nat. Neurosci.* **23**, 1522–1536 (2020).

[Article](#) [Google Scholar](#)

37. 37.

Simeral, J. D., Kim, S.-P., Black, M. J., Donoghue, J. P. & Hochberg, L. R. Neural control of cursor trajectory and click by a human with tetraplegia 1000 days after implant of an intracortical microelectrode array. *J. Neural Eng.* **8**, 025027 (2011).

[ADS](#) [CAS](#) [Article](#) [Google Scholar](#)

38. 38.

Bullard, A. J., Hutchison, B. C., Lee, J., Chestek, C. A. & Patil, P. G. Estimating risk for future intracranial, fully implanted, modular neuromodulatory systems: a systematic review of hardware complications in clinical deep brain stimulation and experimental human intracortical arrays. *Neuromodulation* **23**, 411–426 (2020).

[Article](#) [Google Scholar](#)

39. 39.

Nuyujukian, P. et al. Cortical control of a tablet computer by people with paralysis. *PLoS One* **13**, e0204566 (2018).

[Article](#) [Google Scholar](#)

40. 40.

Musk, E. An integrated brain-machine interface platform with thousands of channels. *J. Med. Internet Res.* **21**, e16194 (2019).

[Article](#) [Google Scholar](#)

41. 41.

Sahasrabuddhe, K. et al. The Argo: a high channel count recording system for neural recording in vivo. *J. Neural Eng.* **18**, 015002 (2021).

[ADS](#) [PubMed](#) [Google Scholar](#)

42. 42.

Sussillo, D., Stavisky, S. D., Kao, J. C., Ryu, S. I. & Shenoy, K. V. Making brain–machine interfaces robust to future neural variability. *Nat. Commun.* **7**, 13749 (2016).

[ADS](#) [CAS](#) [Article](#) [Google Scholar](#)

43. 43.

Dyer, E. L. et al. A cryptography-based approach for movement decoding. *Nat. Biomed. Eng.* **1**, 967–976 (2017).

[Article](#) [Google Scholar](#)

44. 44.

Degenhart, A. D. et al. Stabilization of a brain–computer interface via the alignment of low-dimensional spaces of neural activity. *Nat. Biomed. Eng.* **4**, 672–685 (2020).

[Article](#) [Google Scholar](#)

[Download references](#)

## Acknowledgements

We thank participant T5 and his caregivers for their dedicated contributions to this research, N. Lam, E. Siauciunas and B. Davis for administrative support and E. Woodrum for the drawings in Figs. [1a](#), [2a](#). F.R.W. and D.T.A. acknowledge the support of the Howard Hughes Medical Institute.

L.R.H. acknowledges the support of the Office of Research and Development, Rehabilitation R&D Service, US Department of Veterans Affairs (A2295R, N2864C); the National Institute of Neurological Disorders and Stroke and BRAIN Initiative (UH2NS095548); and the National Institute on Deafness and Other Communication Disorders (R01-DC009899, U01-DC017844). K.V.S. and J.M.H. acknowledge the support of the National Institute on Deafness and Other Communication Disorders (R01-DC014034, U01-DC017844); the National Institute of Neurological Disorders and Stroke (UH2-NS095548, U01-NS098968); L. and P. Garlick; S. and B. Reeves; and the Wu Tsai Neurosciences Institute at Stanford. K.V.S. acknowledges the support of the Simons Foundation Collaboration on the Global Brain 543045 and the Howard Hughes Medical Institute (K.V.S. is a Howard Hughes Medical Institute Investigator). The funders had no role in study design, data collection and interpretation, or the decision to submit the work for publication.

## Author information

### Author notes

1. These authors jointly supervised this work: Jaimie M. Henderson, Krishna V. Shenoy

## Affiliations

1. Howard Hughes Medical Institute at Stanford University, Stanford, CA, USA

Francis R. Willett, Donald T. Avansino & Krishna V. Shenoy

2. Department of Neurosurgery, Stanford University School of Medicine, Stanford, CA, USA

Francis R. Willett & Jaimie M. Henderson

3. Department of Electrical Engineering, Stanford University, Stanford, CA, USA

Francis R. Willett & Krishna V. Shenoy

4. VA RR&D Center for Neurorestoration and Neurotechnology, Rehabilitation R&D Service, Providence VA Medical Center, Providence, RI, USA

Leigh R. Hochberg

5. School of Engineering, Brown University, Providence, RI, USA

Leigh R. Hochberg

6. Carney Institute for Brain Science, Brown University, Providence, RI, USA

Leigh R. Hochberg

7. Center for Neurotechnology and Neurorecovery, Department of Neurology, Massachusetts General Hospital, Harvard Medical School, Boston, MA, USA

Leigh R. Hochberg

8. Wu Tsai Neurosciences Institute, Stanford University, Stanford, CA, USA

Jaimie M. Henderson & Krishna V. Shenoy

9. Bio-X Institute, Stanford University, Stanford, CA, USA

Jaimie M. Henderson & Krishna V. Shenoy

10. Department of Bioengineering, Stanford University, Stanford, CA, USA

Krishna V. Shenoy

11. Department of Neurobiology, Stanford University, Stanford, CA, USA

Krishna V. Shenoy

## Authors

1. Francis R. Willett

[View author publications](#)

You can also search for this author in [PubMed](#) [Google Scholar](#)

2. Donald T. Avansino

[View author publications](#)

You can also search for this author in [PubMed](#) [Google Scholar](#)

3. Leigh R. Hochberg

[View author publications](#)

You can also search for this author in [PubMed](#) [Google Scholar](#)

4. Jaimie M. Henderson

[View author publications](#)

You can also search for this author in [PubMed](#) [Google Scholar](#)

5. Krishna V. Shenoy

[View author publications](#)

You can also search for this author in [PubMed](#) [Google Scholar](#)

## Contributions

F.R.W. conceived the study, built the real-time decoder, analysed the data and wrote the manuscript. F.R.W. and D.T.A. collected the data. L.R.H. is the sponsor-investigator of the multi-site clinical trial. J.M.H. planned and performed T5's array placement surgery and was responsible for all clinical-trial-related activities at Stanford. J.M.H. and K.V.S. supervised and guided the study. All authors reviewed and edited the manuscript.

## Corresponding author

Correspondence to [Francis R. Willett](#).

## Ethics declarations

### Competing interests

The MGH Translational Research Center has a clinical research support agreement with Neuralink, Paradromics and Synchron, for which L.R.H. provides consultative input. J.M.H. is a consultant for Neuralink, and serves on the Medical Advisory Board of Enspire DBS. K.V.S. consults for Neuralink and CTRL-Labs (part of Facebook Reality Labs) and is on the scientific advisory boards of MIND-X, Inscopix and Heal. F.R.W., J.M.H. and K.V.S. are inventors on patent application US 2021/0064135 A1 (the applicant is Stanford University), which covers the neural decoding approach taken in this work. All other authors have no competing interests.

## Additional information

**Peer review information** *Nature* thanks Karim Oweiss and the other, anonymous, reviewer(s) for their contribution to the peer review of this work. Peer reviewer reports are available.

**Publisher's note** Springer Nature remains neutral with regard to jurisdictional claims in published maps and institutional affiliations.

## Extended data figures and tables

### [Extended Data Fig. 1 Diagram of the RNN architecture.](#)

We used a two-layer gated recurrent unit (GRU) recurrent neural network architecture to convert sequences of neural firing rate vectors  $\mathbf{x}_t$  (which were temporally smoothed and binned at 20 ms) into sequences of character probability vectors  $\mathbf{y}_t$  and ‘new character’ probability scalars  $z_t$ . The  $\mathbf{y}_t$

vectors describe the probability of each character being written at that moment in time, and the  $z_t$  scalars go high whenever the RNN detects that T5 is beginning to write any new character. Note that the top RNN layer runs at a slower frequency than the bottom layer, which we found improved the speed of training by making it easier to hold information in memory for long time periods. Thus, the RNN outputs are updated only once every 100 ms. Also, note that we used a day-specific affine transform to account for day-to-day changes in the neural activity (bottom row)—this helps the RNN to account for changes in neural tuning caused by electrode array micromotion or brain plasticity when training data are combined across multiple days.

## **Extended Data Fig. 2 Overview of RNN training methods.**

**a**, Diagram of the session flow for copy-typing and free-typing sessions (each rectangle corresponds to one block of data). First, single-letter and sentences training data are collected (blue and red blocks). Next, the RNN is trained using the newly collected data plus all of the previous days' data (purple block). Finally, the RNN is held fixed and evaluated (green blocks). **b**, Diagram of the data processing and RNN training process (purple block in **a**). First, the single-letter data are time-warped and averaged to create spatiotemporal templates of neural activity for each character. These templates are used to initialize the hidden Markov models (HMMs) for sentence labelling. After labelling, the observed data are cut apart and rearranged into new sequences of characters to make synthetic sentences. Finally, the synthetic sentences are combined with the real sentences to train the RNN. **c**, Diagram of a forced-alignment HMM used to label the sentence ‘few black taxis drive up major roads on quiet hazy nights’. The HMM states correspond to the sequence of characters in the sentence. **d**, The label quality can be verified with cross-correlation heat maps made by correlating the single character neural templates with the real data. The HMM-identified character start times form clear hotspots on the heat maps. Note that these heat maps are depicted only to qualitatively show label quality and aren't used for training (only the character start times are needed to generate the targets for RNN training). **e**, To generate new synthetic sentences, the neural data corresponding to each labelled character in the real data are cut out of the data stream and put into a snippet library.

These snippets are then pulled from the library at random, stretched or compressed in time by up to 30% (to add more artificial timing variability) and combined into new sentences.

### **Extended Data Fig. 3 The effect of key RNN parameters on performance.**

**a**, Training with synthetic data (left) and artificial white noise added to the inputs (right) were both essential for high performance. Data are shown from a grid search over both parameters, and lines show performance at the best value for the other parameter. Results indicate that both parameters are needed for high performance, even when the other is at the best value. Using synthetic data is more important when the size of the dataset is highly limited, as is the case when training on only a single day of data (blue line). Note that the inputs given to the RNN were  $z$ -scored, so the input white noise is in units of standard deviations of the input features. **b**, Artificial noise added to the feature means (random offsets and slow changes in the baseline firing rate) greatly improves the ability of the RNN to generalize to new blocks of data that occur later in the session, but does not help the RNN to generalize to new trials within blocks of data on which it was already trained. This is because feature means change slowly over time. For each parameter setting, three separate RNNs were trained (circles); results show low variability across RNN training runs. **c**, Training an RNN with all of the datasets combined improves performance relative to training on each day separately. Each circle shows the performance on one of seven days. **d**, Using separate input layers for each day is better than using a single layer across all days. **e**, Improvements in character error rates are summarized for each parameter. 95% CIs were computed with bootstrap resampling of single trials ( $n = 10,000$ ). As shown in the table, all parameters show a statistically significant improvement for at least one condition (CIs do not intersect zero).

### **Extended Data Fig. 4 Changes in neural recordings across days.**

**a**, To visualize how much the neural recordings changed across time, decoded pen-tip trajectories were plotted for two example letters (m and z) for all 10 days of data (columns), using decoders trained on all other days (rows). Each session is labelled according to the number of days passed relative to 9 December 2019 (day 4). Results show that although patterns of neural activity clearly change over time, their essential structure is largely conserved (as decoders trained on past days transfer readily to future days).

**b**, The correlation (Pearson's  $r$ ) between the neural activity patterns of each session was computed for each pair of sessions and plotted as a function of the number of days separating each pair. Blue circles show the correlation computed in the full neural space (all 192 electrodes), whereas red circles show the correlation in the 'anchor' space (top 10 principal components of the earlier session). High values indicate a high similarity in how characters are neurally encoded across days. The fact that correlations are higher in the anchor space suggests that the structure of the neural patterns stays largely the same as it slowly rotates into a new space, causing shrinkage in the original space but little change in structure.

**c**, A visualization of how each character's neural representation changes over time, as viewed through the top two PCs of the original 'anchor' space. Each circle represents the neural activity pattern for a single character, and each x symbol shows that same character on a later day (lines connect matching characters). Left, a pair of sessions with only two days between them (day -2 to 0); right, a pair of sessions with 11 days between them (day -2 to 9). The relative positioning of the neural patterns remains similar across days, but most conditions shrink noticeably towards the origin. This is consistent with the neural representations slowly rotating out of the original space into a new space, and suggests that scaling-up the input features may help a decoder to transfer more accurately to a future session (by counteracting this shrinkage effect).

**d**, Similar to Fig. 3b, copy-typing data from eight sessions were used to assess offline whether scaling-up the decoder inputs improves performance when evaluating the decoder on a future session (when no decoder retraining is used). All session pairs (X, Y) were considered. Decoders were first initialized using all data from session X and earlier, then evaluated on session Y under different input-scaling factors (for example, an input scale of 1.5 means that input features were scaled up by 50%). Lines indicate the mean raw character error rate and shaded regions show 95% CIs. Results show that when long periods of time pass between

sessions, input scaling improves performance. We therefore used an input-scaling factor of 1.5 when assessing decoder performance in the ‘no retraining’ conditions of Fig. 3.

### **Extended Data Fig. 5 Effect of correlated noise on the toy model of temporal dimensionality.**

**a**, Example noise vectors and covariance matrix for temporally correlated noise. On the left, example noise vectors are plotted (each line depicts a single example). Noise vectors are shown for all 100 time steps of neuron 1. On the right, the covariance matrix used to generate temporally correlated noise is plotted (dimensions =  $200 \times 200$ ). The first 100 time steps describe the noise of neuron 1 and the last 100 time steps describe the noise of neuron 2. The diagonal band creates noise that is temporally correlated within each simulated neuron (but the two neurons are uncorrelated with each other). **b**, Classification accuracy when using a maximum likelihood classifier to classify between all four possible trajectories in the presence of temporally correlated noise. Even in the presence of temporally correlated noise, the time-varying trajectories are still much easier to classify. **c**, Example noise vectors and noise covariance matrix for noise that is correlated with the signal (that is, noise that is concentrated only in spatiotemporal dimensions that span the class means). Unlike the temporally correlated noise, this covariance matrix generates spatiotemporal noise that has correlations between time steps and neurons. **d**, Classification accuracy in the presence of signal-correlated noise. Again, time-varying trajectories are easier to classify than constant trajectories. See Supplementary Note 1 for a detailed interpretation of this figure.

### **Extended Data Fig. 6 An artificial alphabet optimized to maximize neural decodability.**

**a**, Using the principle of maximizing the nearest-neighbour distance, we optimized for a set of pen trajectories that are theoretically easier to classify than the Latin alphabet (using standard assumptions of linear neural tuning to pen-tip velocity). **b**, For comparison, we also optimized a set of 26 straight lines that maximize the nearest-neighbour distance. **c**, Pairwise

Euclidean distances between pen-tip trajectories were computed for each set, revealing a larger nearest-neighbour distance (but not mean distance) for the optimized alphabet compared to the Latin alphabet. Each circle represents a single movement and bar heights show the mean. **d**, Simulated classification accuracy as a function of the amount of artificial noise added. Results confirm that the optimized alphabet is indeed easier to classify than the Latin alphabet, and that the Latin alphabet is much easier to classify than straight lines, even when the lines have been optimized. **e**, Distance matrices for the Latin alphabet and optimized alphabets show the pairwise Euclidean distances between the pen trajectories. The distance matrices were sorted into seven clusters using single-linkage hierarchical clustering. The distance matrix for the optimized alphabet has no apparent structure; by contrast, the Latin alphabet has two large clusters of similar letters (letters that begin with a counter-clockwise curl, and letters that begin with a downstroke).

### **Extended Data Fig. 7 Example spiking activity recorded from each microelectrode array.**

**a**, Magnetic resonance imaging (MRI)-derived brain anatomy of participant T5. Microelectrode array locations (blue squares) were determined by co-registration of postoperative CT images with preoperative MRI images. **b**, Example spike waveforms detected during a 10-s time window are plotted for each electrode (data were recorded on post-implant day 1,218). Each rectangular panel corresponds to a single electrode and each blue trace is a single spike waveform (2.1-ms duration). Spiking events were detected using a  $-4.5$  root mean square (RMS) threshold, thereby excluding almost all background activity. Electrodes with a mean threshold crossing rate of at least 2 Hz were considered to have ‘spiking activity’ and are outlined in red (note that this is a conservative estimate that is meant to include only spiking activity that could be from single neurons, as opposed to multiunit ‘hash’). The results show that many electrodes still record large spiking waveforms that are well above the noise floor (the  $y$  axis of each panel spans  $330 \mu\text{V}$ , whereas the background activity has an average RMS value of only  $6.4 \mu\text{V}$ ). On this day, 92 electrodes out of 192 had a threshold crossing rate of at least 2 Hz.

**Extended Data Table 1 Example decoded sentences for one block of copy typing**

[Full size table](#)

**Extended Data Table 2 Example decoded sentences for one block of free typing**

[Full size table](#)

## Supplementary information

### Supplementary Information

This file contains the Supplementary Methods and Supplementary Note 1.

### Reporting Summary

#### Video 1

: Copying sentences in real-time with the handwriting brain-computer interface. In this video, participant T5 copies sentences displayed on a computer monitor with the handwriting-brain computer interface. When the red square on the monitor turns green, this cues T5 to begin copying the sentence.

#### Video 2

: Hand micromotion while using the handwriting brain-computer interface. Participant T5 is paralyzed from the neck down (C4 ASIA C spinal cord injury) and only generates small micromotions of the hand when attempting to handwrite. T5 retains no useful hand function.

#### Video 3

: Freely answering questions in real-time with the handwriting brain-computer interface. In this video, participant T5 answers questions that appear on a computer monitor using the handwriting brain-computer

interface. T5 was instructed to take as much time as he wanted to formulate an answer, and then to write it as quickly as possible.

## Video 4

: Side-by-side comparison between the handwriting brain-computer interface and the prior state of the art for intracortical brain-computer interfaces. In a prior study (Pandarinath et al., 2017) participant T5 achieved the highest typing speed ever reported with an intracortical brain-computer interface (39 correct characters per minute using a point-and-click typing system). Here, we show an example sentence typed by T5 using the point-and-click system (shown on the bottom) and the new handwriting brain-computer interface (shown on the top), which is more than twice as fast.

## Peer Review File

## Rights and permissions

### Reprints and Permissions

## About this article



Check for  
updates

## Cite this article

Willett, F.R., Avansino, D.T., Hochberg, L.R. *et al.* High-performance brain-to-text communication via handwriting. *Nature* **593**, 249–254 (2021). <https://doi.org/10.1038/s41586-021-03506-2>

### Download citation

- Received: 02 July 2020
- Accepted: 26 March 2021
- Published: 12 May 2021
- Issue Date: 13 May 2021
- DOI: <https://doi.org/10.1038/s41586-021-03506-2>

## Comments

By submitting a comment you agree to abide by our [Terms](#) and [Community Guidelines](#). If you find something abusive or that does not comply with our terms or guidelines please flag it as inappropriate.

[Access through your institution](#)

[Change institution](#)

[Buy or subscribe](#)

---

This article was downloaded by **calibre** from <https://www.nature.com/articles/s41586-021-03506-2>

- Article
- [Published: 28 April 2021](#)

# Meningeal lymphatics affect microglia responses and anti-A $\beta$ immunotherapy

- [Sandro Da Mesquita](#) ORCID: [orcid.org/0000-0002-0786-5010<sup>1,2</sup>](https://orcid.org/0000-0002-0786-5010),
- [Zachary Papadopoulos<sup>3,4,5 na1</sup>](#),
- [Taitea Dykstra](#) ORCID: [orcid.org/0000-0001-7756-809X<sup>3,4 na1</sup>](https://orcid.org/0000-0001-7756-809X),
- [Logan Brase](#) ORCID: [orcid.org/0000-0002-7175-3208<sup>6 na1</sup>](https://orcid.org/0000-0002-7175-3208),
- [Fabiana Geraldo Farias](#) ORCID: [orcid.org/0000-0002-5215-7304<sup>6</sup>](https://orcid.org/0000-0002-5215-7304),
- [Morgan Wall<sup>1</sup>](#),
- [Hong Jiang<sup>7</sup>](#),
- [Chinnappa Dilip Kodira<sup>8</sup>](#),
- [Kalil Alves de Lima](#) ORCID: [orcid.org/0000-0002-9149-168X<sup>3,4</sup>](https://orcid.org/0000-0002-9149-168X),
- [Jasmin Herz](#) ORCID: [orcid.org/0000-0001-6325-863X<sup>3,4</sup>](https://orcid.org/0000-0001-6325-863X),
- [Antoine Louveau<sup>1,9</sup>](#),
- [Dylan H. Goldman<sup>1,3,4,10</sup>](#),
- [Andrea Francesca Salvador](#) ORCID: [orcid.org/0000-0002-9197-7575<sup>1,3,4,10</sup>](https://orcid.org/0000-0002-9197-7575),
- [Suna Onengut-Gumuscu<sup>11</sup>](#),
- [Emily Farber<sup>11</sup>](#),
- [Nisha Dabhi<sup>1</sup>](#),
- [Tatiana Kennedy<sup>1</sup>](#),
- [Mary Grace Milam<sup>1</sup>](#),
- [Wendy Baker<sup>1</sup>](#),
- [Igor Smirnov<sup>1,3,4</sup>](#),
- [Stephen S. Rich](#) ORCID: [orcid.org/0000-0003-3872-7793<sup>11</sup>](https://orcid.org/0000-0003-3872-7793),
- [Dominantly Inherited Alzheimer Network](#),

- [Bruno A. Benitez](#) [ORCID: orcid.org/0000-0002-2699-3878<sup>6,12</sup>](#),
- [Celeste M. Karch](#) [ORCID: orcid.org/0000-0002-6854-5547<sup>6,7</sup>](#),
- [Richard J. Perrin](#) [ORCID: orcid.org/0000-0002-3443-7716<sup>4,7</sup>](#),
- [Martin Farlow<sup>13</sup>](#),
- [Jasmeer P. Chhatwal<sup>14</sup>](#),
- [David M. Holtzman<sup>7</sup>](#),
- [Carlos Cruchaga<sup>6,7,12 na2</sup>](#),
- [Oscar Harari](#) [ORCID: orcid.org/0000-0002-2635-6975<sup>6 na2</sup>](#) &
- [Jonathan Kipnis](#) [ORCID: orcid.org/0000-0002-3714-517X<sup>1,3,4,5,10 na2</sup>](#)

[Nature](#) volume **593**, pages 255–260 (2021) [Cite this article](#)

- 12k Accesses
- 460 Altmetric
- [Metrics details](#)

## Subjects

- [Ageing](#)
- [Neuroimmunology](#)

## Abstract

Alzheimer's disease (AD) is the most prevalent cause of dementia<sup>1</sup>. Although there is no effective treatment for AD, passive immunotherapy with monoclonal antibodies against amyloid beta (Aβ) is a promising therapeutic strategy<sup>2,3</sup>. Meningeal lymphatic drainage has an important role in the accumulation of Aβ in the brain<sup>4</sup>, but it is not known whether modulation of meningeal lymphatic function can influence the outcome of immunotherapy in AD. Here we show that ablation of meningeal lymphatic vessels in 5xFAD mice (a mouse model of amyloid deposition that expresses five mutations found in familial AD) worsened the outcome of mice treated with anti-Aβ passive immunotherapy by exacerbating the

deposition of A $\beta$ , microgliosis, neurovascular dysfunction, and behavioural deficits. By contrast, therapeutic delivery of vascular endothelial growth factor C improved clearance of A $\beta$  by monoclonal antibodies. Notably, there was a substantial overlap between the gene signature of microglia from 5xFAD mice with impaired meningeal lymphatic function and the transcriptional profile of activated microglia from the brains of individuals with AD. Overall, our data demonstrate that impaired meningeal lymphatic drainage exacerbates the microglial inflammatory response in AD and that enhancement of meningeal lymphatic function combined with immunotherapies could lead to better clinical outcomes.

[Access through your institution](#)

[Change institution](#)

[Buy or subscribe](#)

## Access options

Subscribe to Journal

Get full journal access for 1 year

\$199.00

only \$3.90 per issue

[Subscribe](#)

All prices are NET prices.

VAT will be added later in the checkout.

Tax calculation will be finalised during checkout.

Rent or Buy article

Get time limited or full article access on ReadCube.

from \$8.99

[Rent or Buy](#)

All prices are NET prices.

### **Additional access options:**

- [Log in](#)
- [Access through your institution](#)
- [Learn about institutional subscriptions](#)

**Fig. 1: Compromised meningeal lymphatic function in 5xFAD mice limits brain A $\beta$  clearance by chimeric mAducanumab and modulates the microglial and neurovascular responses.**

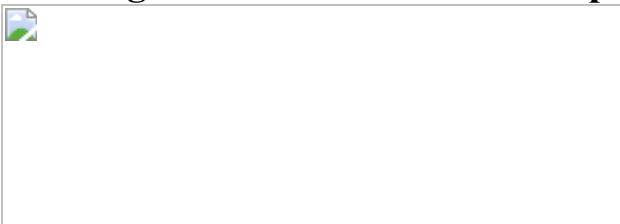


**Fig. 2: Combining mVEGF-C with immunotherapy reprograms the hippocampal transcriptional profile and shapes the microglial and neurovascular responses in aged APPswe mice.**

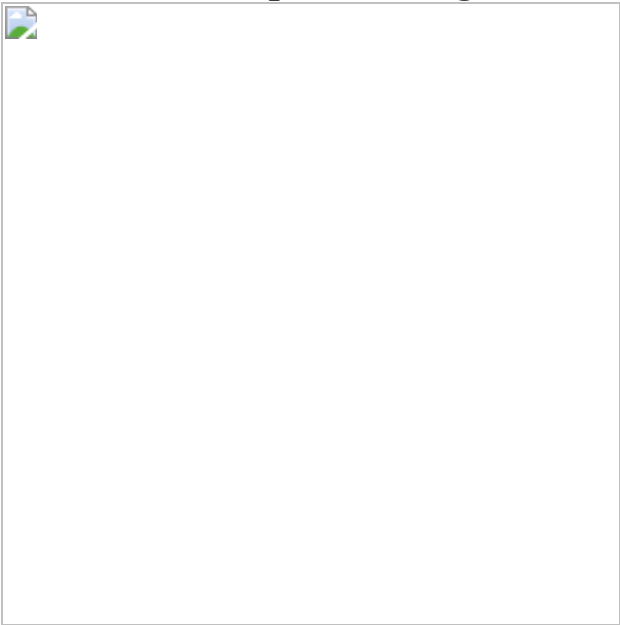


**Fig. 3: Gene-set analysis uncovers a link between impaired meningeal lymphatics and microglial activation in AD.**



## Data availability

Source data files depicting the quantification values mentioned in the text or plotted in graphs shown in Figs. 1, 3 and Extended Data Figs. 1–5, 7–9, and the gene lists used for gene-set analysis in Supplementary Tables 3, 6 are available in the online version of this paper. New RNA-seq datasets have been deposited online in the Gene Expression Omnibus (GEO database) under the accession number [GSE141917](#). Previously published RNA-seq datasets can be found under the accession numbers GSE99743 and GSE104181. [Source data](#) are provided with this paper.

## Code availability

Custom code used to analyse the RNA-seq data and datasets generated and/or analysed in the current study are available from the corresponding authors upon request.

## References

1. 1.

Jack, C. R. Jr et al. NIA-AA Research Framework: toward a biological definition of Alzheimer’s disease. *Alzheimers Dement.* **14**, 535–562 (2018).

[PubMed](#) [PubMed Central](#) [Google Scholar](#)

2. 2.

Logovinsky, V. et al. Safety and tolerability of BAN2401—a clinical study in Alzheimer’s disease with a protofibril selective A $\beta$  antibody.

*Alzheimers Res. Ther.* **8**, 14 (2016).

[PubMed](#) [PubMed Central](#) [Google Scholar](#)

3. 3.

Sevigny, J. et al. The antibody aducanumab reduces A $\beta$  plaques in Alzheimer's disease. *Nature* **537**, 50–56 (2016).

[ADS](#) [CAS](#) [PubMed](#) [Google Scholar](#)

4. 4.

Da Mesquita, S. et al. Functional aspects of meningeal lymphatics in ageing and Alzheimer's disease. *Nature* **560**, 185–191 (2018).

[ADS](#) [PubMed](#) [PubMed Central](#) [Google Scholar](#)

5. 5.

Mawuenyega, K. G. et al. Decreased clearance of CNS beta-amyloid in Alzheimer's disease. *Science* **330**, 1774 (2010).

[ADS](#) [CAS](#) [PubMed](#) [PubMed Central](#) [Google Scholar](#)

6. 6.

Tarasoff-Conway, J. M. et al. Clearance systems in the brain—implications for Alzheimer disease. *Nat. Rev. Neurol.* **12**, 248 (2016).

[PubMed](#) [Google Scholar](#)

7. 7.

Sweeney, M. D., Sagare, A. P. & Zlokovic, B. V. Blood-brain barrier breakdown in Alzheimer disease and other neurodegenerative disorders. *Nat. Rev. Neurol.* **14**, 133–150 (2018).

[CAS](#) [PubMed](#) [PubMed Central](#) [Google Scholar](#)

8. 8.

Da Mesquita, S., Fu, Z. & Kipnis, J. The meningeal lymphatic system: a new player in neurophysiology. *Neuron* **100**, 375–388 (2018).

[PubMed](#) [PubMed Central](#) [Google Scholar](#)

9. 9.

Tucker, S. et al. The murine version of BAN2401 (mAb158) selectively reduces amyloid- $\beta$  protofibrils in brain and cerebrospinal fluid of tg-ArcSwe mice. *J. Alzheimers Dis.* **43**, 575–588 (2015).

[CAS](#) [PubMed](#) [Google Scholar](#)

10. 10.

Kastanenka, K. V. et al. Immunotherapy with Aducanumab restores calcium homeostasis in Tg2576 mice. *J. Neurosci.* **36**, 12549–12558 (2016).

[CAS](#) [PubMed](#) [PubMed Central](#) [Google Scholar](#)

11. 11.

Howard, R. & Liu, K. Y. Questions EMERGE as Biogen claims aducanumab turnaround. *Nat. Rev. Neurol.* **16**, 63–64 (2020).

[PubMed](#) [Google Scholar](#)

12. 12.

Louveau, A. et al. CNS lymphatic drainage and neuroinflammation are regulated by meningeal lymphatic vasculature. *Nat. Neurosci.* **21**, 1380–1391 (2018).

[CAS](#) [PubMed](#) [PubMed Central](#) [Google Scholar](#)

13. 13.

Rustenhoven, J. et al. Functional characterization of the dural sinuses as a neuroimmune interface. *Cell* **184**, 1000–1016.e27 (2021).

[CAS](#) [PubMed](#) [Google Scholar](#)

14. 14.

Cruchaga, C. et al. Rare coding variants in the phospholipase D3 gene confer risk for Alzheimer's disease. *Nature* **505**, 550–554 (2014).

[CAS](#) [PubMed](#) [Google Scholar](#)

15. 15.

Yamazaki, Y., Zhao, N., Caulfield, T. R., Liu, C. C. & Bu, G. Apolipoprotein E and Alzheimer disease: pathobiology and targeting strategies. *Nat. Rev. Neurol.* **15**, 501–518 (2019).

[CAS](#) [PubMed](#) [PubMed Central](#) [Google Scholar](#)

16. 16.

Xiong, M. et al. APOE immunotherapy reduces cerebral amyloid angiopathy and amyloid plaques while improving cerebrovascular function. *Sci. Transl. Med.* **13**, eabd7522 (2021).

[CAS](#) [PubMed](#) [Google Scholar](#)

17. 17.

Abbasi, J. Promising results in 18-month analysis of Alzheimer drug candidate. *J. Am. Med. Assoc.* **320**, 965 (2018).

[Google Scholar](#)

18. 18.

Louveau, A. et al. Structural and functional features of central nervous system lymphatic vessels. *Nature* **523**, 337–341 (2015).

[ADS](#) [CAS](#) [PubMed](#) [PubMed Central](#) [Google Scholar](#)

19. 19.

Ryu, J. K. et al. Fibrin-targeting immunotherapy protects against neuroinflammation and neurodegeneration. *Nat. Immunol.* **19**, 1212–1223 (2018).

[CAS](#) [PubMed](#) [PubMed Central](#) [Google Scholar](#)

20. 20.

Wang, L. et al. Deep cervical lymph node ligation aggravates AD-like pathology of APP/PS1 mice. *Brain Pathol.* **29**, 176–192 (2019).

[CAS](#) [PubMed](#) [Google Scholar](#)

21. 21.

Keren-Shaul, H. et al. A unique microglia type associated with restricting development of Alzheimer’s disease. *Cell* **169**, 1276–1290.e17 (2017).

[CAS](#) [Google Scholar](#)

22. 22.

Krasemann, S. et al. The TREM2-APOE pathway drives the transcriptional phenotype of dysfunctional microglia in neurodegenerative diseases. *Immunity* **47**, 566–581.e9 (2017).

[CAS](#) [PubMed](#) [PubMed Central](#) [Google Scholar](#)

23. 23.

Hong, S. et al. Complement and microglia mediate early synapse loss in Alzheimer mouse models. *Science* **352**, 712–716 (2016).

[ADS](#) [CAS](#) [PubMed](#) [PubMed Central](#) [Google Scholar](#)

24. 24.

Montagne, A. et al. APOE4 leads to blood-brain barrier dysfunction predicting cognitive decline. *Nature* **581**, 71–76 (2020).

[ADS](#) [CAS](#) [PubMed](#) [PubMed Central](#) [Google Scholar](#)

25. 25.

Vanlandewijck, M. et al. A molecular atlas of cell types and zonation in the brain vasculature. *Nature* **554**, 475–480 (2018).

[ADS](#) [CAS](#) [PubMed](#) [Google Scholar](#)

26. 26.

Zhou, Y. et al. Human and mouse single-nucleus transcriptomics reveal TREM2-dependent and TREM2-independent cellular responses in Alzheimer's disease. *Nat. Med.* **26**, 131–142 (2020).

[CAS](#) [PubMed](#) [PubMed Central](#) [Google Scholar](#)

27. 27.

Zhao, Z., Nelson, A. R., Betsholtz, C. & Zlokovic, B. V. Establishment and dysfunction of the blood-brain barrier. *Cell* **163**, 1064–1078 (2015).

[CAS](#) [PubMed](#) [PubMed Central](#) [Google Scholar](#)

28. 28.

Uhlmann, R. E. et al. Acute targeting of pre-amyloid seeds in transgenic mice reduces Alzheimer-like pathology later in life. *Nat. Neurosci.* **23**, 1580–1588 (2020).

[PubMed](#) [Google Scholar](#)

29. 29.

Naj, A. C. et al. Common variants at MS4A4/MS4A6E, CD2AP, CD33 and EPHA1 are associated with late-onset Alzheimer's disease. *Nat. Genet.* **43**, 436–441 (2011).

[CAS](#) [PubMed](#) [PubMed Central](#) [Google Scholar](#)

30. 30.

Bunielo, A. et al. The NHGRI-EBI GWAS catalog of published genome-wide association studies, targeted arrays and summary statistics 2019. *Nucleic Acids Res.* **47**, D1005–D1012 (2019).

[CAS](#) [PubMed](#) [Google Scholar](#)

31. 31.

Corder, E. H. et al. Gene dose of apolipoprotein E type 4 allele and the risk of Alzheimer's disease in late onset families. *Science* **261**, 921–923 (1993).

[ADS](#) [CAS](#) [PubMed](#) [Google Scholar](#)

32. 32.

Yan, Q. et al. Genome-wide association study of brain amyloid deposition as measured by Pittsburgh Compound-B (PiB)-PET imaging. *Mol. Psychiatry* **26**, 309–321 (2021).

[PubMed](#) [Google Scholar](#)

33. 33.

Deming, Y. et al. The *MS4A* gene cluster is a key modulator of soluble TREM2 and Alzheimer's disease risk. *Sci. Transl. Med.* **11**, eaau2291 (2019).

[PubMed](#) [PubMed Central](#) [Google Scholar](#)

34. 34.

Deming, Y. et al. Genome-wide association study identifies four novel loci associated with Alzheimer's endophenotypes and disease modifiers. *Acta Neuropathol.* **133**, 839–856 (2017).

[CAS](#) [PubMed](#) [PubMed Central](#) [Google Scholar](#)

35. 35.

Huang, K. L. et al. A common haplotype lowers PU.1 expression in myeloid cells and delays onset of Alzheimer's disease. *Nat. Neurosci.* **20**, 1052–1061 (2017).

[CAS](#) [PubMed](#) [PubMed Central](#) [Google Scholar](#)

36. 36.

Kunkle, B. W. et al. Genetic meta-analysis of diagnosed Alzheimer's disease identifies new risk loci and implicates A $\beta$ , tau, immunity and lipid processing. *Nat. Genet.* **51**, 414–430 (2019).

[CAS](#) [PubMed](#) [PubMed Central](#) [Google Scholar](#)

37. 37.

Del-Aguila, J. L. et al. Assessment of the genetic architecture of Alzheimer's disease risk in rate of memory decline. *J. Alzheimers Dis.* **62**, 745–756 (2018).

[CAS](#) [PubMed](#) [PubMed Central](#) [Google Scholar](#)

38. 38.

Merlini, M. et al. Fibrinogen induces microglia-mediated spine elimination and cognitive impairment in an Alzheimer's disease model. *Neuron* **101**, 1099–1108.e6 (2019).

[CAS](#) [PubMed](#) [PubMed Central](#) [Google Scholar](#)

39. 39.

Spangenberg, E. E. et al. Eliminating microglia in Alzheimer's mice prevents neuronal loss without modulating amyloid- $\beta$  pathology. *Brain* **139**, 1265–1281 (2016).

[PubMed](#) [PubMed Central](#) [Google Scholar](#)

40. 40.

Shi, Y. et al. Microglia drive APOE-dependent neurodegeneration in a tauopathy mouse model. *J. Exp. Med.* **216**, 2546–2561 (2019).

[CAS](#) [PubMed](#) [PubMed Central](#) [Google Scholar](#)

41. 41.

Tinevez, J. Y. et al. TrackMate: An open and extensible platform for single-particle tracking. *Methods* **115**, 80–90 (2017).

[CAS](#) [PubMed](#) [Google Scholar](#)

42. 42.

Finck, R. et al. Normalization of mass cytometry data with bead standards. *Cytometry A* **83**, 483–494 (2013).

[PubMed](#) [PubMed Central](#) [Google Scholar](#)

43. 43.

Levine, J. H. et al. Data-driven phenotypic dissection of AML reveals progenitor-like cells that correlate with prognosis. *Cell* **162**, 184–197 (2015).

[CAS](#) [PubMed](#) [PubMed Central](#) [Google Scholar](#)

44. 44.

Patro, R., Duggal, G., Love, M. I., Irizarry, R. A. & Kingsford, C. Salmon provides fast and bias-aware quantification of transcript

expression. *Nat. Methods* **14**, 417–419 (2017).

[CAS](#) [PubMed](#) [PubMed Central](#) [Google Scholar](#)

45. 45.

Harrow, J. et al. GENCODE: the reference human genome annotation for The ENCODE Project. *Genome Res.* **22**, 1760–1774 (2012).

[CAS](#) [PubMed](#) [PubMed Central](#) [Google Scholar](#)

46. 46.

Soneson, C., Love, M. I. & Robinson, M. D. Differential analyses for RNA-seq: transcript-level estimates improve gene-level inferences. *F1000Res.* **4**, 1521 (2015).

[PubMed](#) [Google Scholar](#)

47. 47.

Love, M. I., Huber, W. & Anders, S. Moderated estimation of fold change and dispersion for RNA-seq data with DESeq2. *Genome Biol.* **15**, 550 (2014).

[PubMed](#) [PubMed Central](#) [Google Scholar](#)

48. 48.

Yu, G., Wang, L. G., Han, Y. & He, Q. Y. clusterProfiler: an R package for comparing biological themes among gene clusters. *OMICS* **16**, 284–287 (2012).

[CAS](#) [PubMed](#) [PubMed Central](#) [Google Scholar](#)

49. 49.

Yu, G., Wang, L. G., Yan, G. R. & He, Q. Y. DOSE: an R/Bioconductor package for disease ontology semantic and enrichment

analysis. *Bioinformatics* **31**, 608–609 (2015).

[CAS](#) [PubMed](#) [PubMed Central](#) [Google Scholar](#)

50. 50.

Dobin, A. et al. STAR: ultrafast universal RNA-seq aligner. *Bioinformatics* **29**, 15–21 (2013).

[CAS](#) [Google Scholar](#)

51. 51.

Robinson, M. D., McCarthy, D. J. & Smyth, G. K. edgeR: a Bioconductor package for differential expression analysis of digital gene expression data. *Bioinformatics* **26**, 139–140 (2010).

[CAS](#) [Google Scholar](#)

52. 52.

Hong, G., Zhang, W., Li, H., Shen, X. & Guo, Z. Separate enrichment analysis of pathways for up- and downregulated genes. *J. R. Soc. Interface* **11**, 20130950 (2013).

[PubMed](#) [Google Scholar](#)

53. 53.

McCarthy, D. J., Campbell, K. R., Lun, A. T. & Wills, Q. F. Scater: pre-processing, quality control, normalization and visualization of single-cell RNA-seq data in R. *Bioinformatics* **33**, 1179–1186 (2017).

[CAS](#) [PubMed](#) [PubMed Central](#) [Google Scholar](#)

54. 54.

Lun, A. T., Bach, K. & Marioni, J. C. Pooling across cells to normalize single-cell RNA sequencing data with many zero counts. *Genome Biol.*

17, 75 (2016).

[PubMed](#) [Google Scholar](#)

55. 55.

Stuart, T. et al. Comprehensive integration of single-cell data. *Cell* **177**, 1888–1902.e21 (2019).

[CAS](#) [PubMed](#) [PubMed Central](#) [Google Scholar](#)

56. 56.

Van den Berge, K. et al. Observation weights unlock bulk RNA-seq tools for zero inflation and single-cell applications. *Genome Biol.* **19**, 24 (2018).

[PubMed](#) [PubMed Central](#) [Google Scholar](#)

57. 57.

Butler, A., Hoffman, P., Smibert, P., Papalexi, E. & Satija, R. Integrating single-cell transcriptomic data across different conditions, technologies, and species. *Nat. Biotechnol.* **36**, 411–420 (2018).

[CAS](#) [PubMed](#) [PubMed Central](#) [Google Scholar](#)

58. 58.

Durinck, S. et al. BioMart and Bioconductor: a powerful link between biological databases and microarray data analysis. *Bioinformatics* **21**, 3439–3440 (2005).

[CAS](#) [PubMed](#) [Google Scholar](#)

59. 59.

Durinck, S., Spellman, P. T., Birney, E. & Huber, W. Mapping identifiers for the integration of genomic datasets with the

R/Bioconductor package biomaRt. *Nat. Protocols* **4**, 1184–1191 (2009).

[CAS](#) [PubMed](#) [Google Scholar](#)

60. 60.

de Leeuw, C., Sey, N. Y. A., Posthuma, D. & Won, H. A response to Yurko et al: H-MAGMA, inheriting a shaky statistical foundation, yields excess false positives. Preprint at <https://doi.org/10.1101/2020.09.25.310722> (2020).

61. 61.

Mathys, H. et al. Single-cell transcriptomic analysis of Alzheimer’s disease. *Nature* **570**, 332–337 (2019).

[ADS](#) [CAS](#) [PubMed](#) [PubMed Central](#) [Google Scholar](#)

62. 62.

McGinnis, C. S., Murrow, L. M. & Gartner, Z. J. DoubletFinder: doublet detection in single-cell RNA sequencing data using artificial nearest neighbors. *Cell Syst.* **8**, 329–337.e4 (2019).

[CAS](#) [PubMed](#) [PubMed Central](#) [Google Scholar](#)

63. 63.

Hafemeister, C. & Satija, R. Normalization and variance stabilization of single-cell RNA-seq data using regularized negative binomial regression. *Genome Biol.* **20**, 296 (2019).

[CAS](#) [PubMed](#) [PubMed Central](#) [Google Scholar](#)

64. 64.

Del-Aguila, J. L. et al. A single-nuclei RNA sequencing study of Mendelian and sporadic AD in the human brain. *Alzheimers Res. Ther.*

11, 71 (2019).

[PubMed](#) [PubMed Central](#) [Google Scholar](#)

65. 65.

Pliner, H. A., Shendure, J. & Trapnell, C. Supervised classification enables rapid annotation of cell atlases. *Nat. Methods* **16**, 983–986 (2019).

[CAS](#) [PubMed](#) [PubMed Central](#) [Google Scholar](#)

66. 66.

Sul, J. H. et al. Accurate and fast multiple-testing correction in eQTL studies. *Am. J. Hum. Genet.* **96**, 857–868 (2015).

[CAS](#) [PubMed](#) [PubMed Central](#) [Google Scholar](#)

67. 67.

Duong, D. et al. Using genomic annotations increases statistical power to detect eGenes. *Bioinformatics* **32**, i156–i163 (2016).

[CAS](#) [PubMed](#) [PubMed Central](#) [Google Scholar](#)

68. 68.

Darnell, G., Duong, D., Han, B. & Eskin, E. Incorporating prior information into association studies. *Bioinformatics* **28**, i147–i153 (2012).

[PubMed](#) [PubMed Central](#) [Google Scholar](#)

69. 69.

Eskin, E. Increasing power in association studies by using linkage disequilibrium structure and molecular function as prior information. *Genome Res.* **18**, 653–660 (2008).

[CAS](#) [PubMed](#) [PubMed Central](#) [Google Scholar](#)

70. 70.

Nettleton, D. & Doerge, R. W. Accounting for variability in the use of permutation testing to detect quantitative trait loci. *Biometrics* **56**, 52–58 (2000).

[CAS](#) [PubMed](#) [MATH](#) [Google Scholar](#)

[Download references](#)

## Acknowledgements

We thank S. Smith for editing the manuscript and S. Blackburn and N. Al-Hamadani for animal colony maintenance. This work was supported by grants from the National Institutes of Health/National Institute on Aging (AG034113 and AG057496), PureTech Health, the Cure Alzheimer's Fund and the Ed Owens Family Foundation to J.K.; RF1AG053303 and RF1AG058501 to C.C.; AG057777 and AG067764 to O.H.; and AG062734 to C.M.K. O.H. is an Archer Foundation Research Scientist. We thank all members of the Kipnis laboratory for their comments during discussions of this work. We acknowledge the staff of the Neuropathology Cores and other personnel of the Charles F. and Joanne Knight Alzheimer Disease Research Center (P30 AG066444, P01AG026276, P01AG03991). Data collection and sharing for this project were supported by The Dominantly Inherited Alzheimer's Network (DIAN, UF1AG032438) funded by the National Institute on Aging (NIA), the German Center for Neurodegenerative Diseases (DZNE), Raul Carrea Institute for Neurological Research (FLENI), with partial support by the Research and Development Grants for Dementia from Japan Agency for Medical Research and Development, AMED, and the Korea Health Technology R&D Project through the Korea Health Industry Development Institute (KHIDI). This manuscript has been reviewed by DIAN Study investigators for scientific content and consistency of data interpretation with previous DIAN Study publications. We acknowledge the altruism of the participants and their families and contributions of the Knight ADRC and DIAN (see full list of DIAN

consortium members in Supplementary Notes) research and support staff at each of the participating sites for their contributions to this study.

## Author information

### Author notes

1. These authors contributed equally: Zachary Papadopoulos, Taitea Dykstra, Logan Brase
2. These authors jointly supervised this work: Carlos Cruchaga, Oscar Harari, Jonathan Kipnis

### Affiliations

1. Department of Neuroscience, University of Virginia, Charlottesville, VA, USA

Sandro Da Mesquita, Morgan Wall, Antoine Louveau, Dylan H. Goldman, Andrea Francesca Salvador, Nisha Dabhi, Tatiana Kennedy, Mary Grace Milam, Wendy Baker, Igor Smirnov & Jonathan Kipnis

2. Department of Neuroscience, Mayo Clinic, Jacksonville, FL, USA

Sandro Da Mesquita

3. Center for Brain Immunology and Glia (BIG), Washington University in St. Louis, St. Louis, MO, USA

Zachary Papadopoulos, Taitea Dykstra, Kalil Alves de Lima, Jasmin Herz, Dylan H. Goldman, Andrea Francesca Salvador, Igor Smirnov & Jonathan Kipnis

4. Department of Pathology and Immunology, Washington University in St. Louis, St. Louis, MO, USA

Zachary Papadopoulos, Taitea Dykstra, Kalil Alves de Lima, Jasmin Herz, Dylan H. Goldman, Andrea Francesca Salvador, Igor Smirnov, Richard J. Perrin & Jonathan Kipnis

5. Neuroscience Graduate Program, Washington University in St. Louis, St. Louis, MO, USA

Zachary Papadopoulos & Jonathan Kipnis

6. Department of Psychiatry, Washington University in St. Louis, St. Louis, MO, USA

Logan Brase, Fabiana Geraldo Farias, Bruno A. Benitez, Celeste M. Karch, Carlos Cruchaga & Oscar Harari

7. Department of Neurology, Hope Center for Neurological Disorders, Knight Alzheimer's Disease Research Center, School of Medicine, Washington University in St. Louis, St. Louis, MO, USA

Hong Jiang, Celeste M. Karch, Richard J. Perrin, David M. Holtzman & Carlos Cruchaga

8. PureTech Health, Boston, MA, USA

Chinnappa Dilip Kodira

9. Department of Neurosciences, Lerner Research Institute, Cleveland Clinic, Cleveland, OH, USA

Antoine Louveau

10. Neuroscience Graduate Program, University of Virginia, Charlottesville, VA, USA

Dylan H. Goldman, Andrea Francesca Salvador & Jonathan Kipnis

11. Center for Public Health Genomics, University of Virginia, Charlottesville, VA, USA

Suna Onengut-Gumuscu, Emily Farber & Stephen S. Rich

12. NeuroGenomics and Informatics Center, School of Medicine,  
Washington University in St. Louis, St. Louis, MO, USA

Bruno A. Benitez & Carlos Cruchaga

13. Indiana School of Medicine, Indianapolis, IN, USA

Martin Farlow

14. Massachusetts General Hospital, Harvard Medical School, Department  
of Neurology, Boston, MA, USA

Jasmeer P. Chhatwal

## Authors

1. Sandro Da Mesquita

[View author publications](#)

You can also search for this author in [PubMed](#) [Google Scholar](#)

2. Zachary Papadopoulos

[View author publications](#)

You can also search for this author in [PubMed](#) [Google Scholar](#)

3. Taitea Dykstra

[View author publications](#)

You can also search for this author in [PubMed](#) [Google Scholar](#)

4. Logan Brase

[View author publications](#)

You can also search for this author in [PubMed](#) [Google Scholar](#)

5. Fabiana Geraldo Farias

[View author publications](#)

You can also search for this author in [PubMed](#) [Google Scholar](#)

6. Morgan Wall

[View author publications](#)

You can also search for this author in [PubMed](#) [Google Scholar](#)

7. Hong Jiang

[View author publications](#)

You can also search for this author in [PubMed](#) [Google Scholar](#)

8. Chinnappa Dilip Kodira

[View author publications](#)

You can also search for this author in [PubMed](#) [Google Scholar](#)

9. Kalil Alves de Lima

[View author publications](#)

You can also search for this author in [PubMed](#) [Google Scholar](#)

10. Jasmin Herz

[View author publications](#)

You can also search for this author in [PubMed](#) [Google Scholar](#)

11. Antoine Louveau

[View author publications](#)

You can also search for this author in [PubMed](#) [Google Scholar](#)

12. Dylan H. Goldman

[View author publications](#)

You can also search for this author in [PubMed](#) [Google Scholar](#)

13. Andrea Francesca Salvador

[View author publications](#)

You can also search for this author in [PubMed](#) [Google Scholar](#)

14. Suna Onengut-Gumuscu

[View author publications](#)

You can also search for this author in [PubMed](#) [Google Scholar](#)

15. Emily Farber

[View author publications](#)

You can also search for this author in [PubMed](#) [Google Scholar](#)

16. Nisha Dabhi

[View author publications](#)

You can also search for this author in [PubMed](#) [Google Scholar](#)

17. Tatiana Kennedy

[View author publications](#)

You can also search for this author in [PubMed](#) [Google Scholar](#)

18. Mary Grace Milam

[View author publications](#)

You can also search for this author in [PubMed](#) [Google Scholar](#)

19. Wendy Baker

[View author publications](#)

You can also search for this author in [PubMed](#) [Google Scholar](#)

20. Igor Smirnov

[View author publications](#)

You can also search for this author in [PubMed](#) [Google Scholar](#)

21. Stephen S. Rich

[View author publications](#)

You can also search for this author in [PubMed](#) [Google Scholar](#)

22. Bruno A. Benitez

[View author publications](#)

You can also search for this author in [PubMed](#) [Google Scholar](#)

23. Celeste M. Karch

[View author publications](#)

You can also search for this author in [PubMed](#) [Google Scholar](#)

24. Richard J. Perrin

[View author publications](#)

You can also search for this author in [PubMed](#) [Google Scholar](#)

25. Martin Farlow

[View author publications](#)

You can also search for this author in [PubMed](#) [Google Scholar](#)

26. Jasmeer P. Chhatwal

[View author publications](#)

You can also search for this author in [PubMed](#) [Google Scholar](#)

27. David M. Holtzman

[View author publications](#)

You can also search for this author in [PubMed](#) [Google Scholar](#)

28. Carlos Cruchaga

[View author publications](#)

You can also search for this author in [PubMed](#) [Google Scholar](#)

29. Oscar Harari

[View author publications](#)

You can also search for this author in [PubMed](#) [Google Scholar](#)

30. Jonathan Kipnis

[View author publications](#)

You can also search for this author in [PubMed](#) [Google Scholar](#)

## Consortia

### Dominantly Inherited Alzheimer Network

#### Contributions

S.D.M. designed and performed the experiments, analysed and interpreted the data, created the figures and wrote the manuscript; Z.P. optimized experimental techniques, performed experiments, analysed data and participated in manuscript writing; T.D. performed the mouse scRNA-seq data analyses, integrated analysis of mouse and human RNA-seq data and participated in methods writing; L.B. performed the human brain single-nucleus RNA-seq data analysis, integrated analysis of mouse and human RNA-seq data and participated in methods writing; F.G.F. performed the integrative gene-set, genetic variant and AD phenotype and risk analyses; M.W. was involved in the bulk RNA-seq and mass cytometry data analyses and participated in methods writing; H.J. synthesized the mouse chimeric Aducanumab and control antibodies; C.D.K. contributed to bulk RNA-seq data analysis; K.A.d.L., J.H., A.L., D.H.G. and A.F.S. assisted in experiments and data analysis; S.O.-G. and E.F. assisted in bulk RNA-seq experiments; N.D., T.K., M.G.M. and W.B. and I.S. assisted with animal genotyping, experiments and blinded data analyses and quantification; S.S.R. supervised the bulk RNA-seq experiments and participated in manuscript writing; B.A.B., C.M.K., R.J.P., M.F. and J.P.C. were involved in the collection and analysis of human brain single-nucleus RNA-seq data and critical review of the manuscript; D.M.H. provided resources and was involved in experimental design, data interpretation and manuscript writing;

C.C. supervised and interpreted the integrative gene-set, genetic variant and AD phenotype and risk analyses and participated in manuscript writing; O.H. supervised and interpreted the human brain single-nucleus RNA-seq data analysis and participated in manuscript writing; J.K. designed the experiments, provided intellectual contributions, oversaw data analysis and interpretation and wrote the manuscript.

## Corresponding authors

Correspondence to [Sandro Da Mesquita](#) or [Jonathan Kipnis](#).

## Ethics declarations

## Competing interests

J.K. is a member of a scientific advisory group for PureTech. J.K., S.D.M. and A.L. hold patents and patent applications related to the findings described herein. D.M.H. is an inventor on a patent for anti-A $\beta$  antibodies licensed to Eli Lilly by Washington University. D.M.H. and H.J. are inventors on a patent for anti-apoE antibodies licensed to NextCure. D.M.H. and H.J. are listed as inventors on a patent licensed by Washington University to C2N Diagnostics on the therapeutic use of anti-tau antibodies. D.M.H. co-founded and is on the scientific advisory board of C2N Diagnostics. C2N Diagnostics has licensed certain anti-tau antibodies to AbbVie for therapeutic development. D.M.H. is on the scientific advisory board of Denali and consults for Genentech, Merck, and Cajal Neuroscience. C.C. receives research support from Biogen, Eisai, Alector and Parabon. The funders of the study had no role in the collection, analysis, or interpretation of data, in the writing of the manuscript, or in the decision to submit the paper for publication. C.C. is a member of the advisory board of Vivid Genetics, Halia Therapeutics and ADx Healthcare. J.P.C. has served on a medical advisory board for Otsuka Pharmaceuticals. The authors declare no other competing interests.

## Additional information

**Peer review information** *Nature* thanks Trygve Bakken and the other, anonymous, reviewer(s) for their contribution to the peer review of this work.

**Publisher's note** Springer Nature remains neutral with regard to jurisdictional claims in published maps and institutional affiliations.

## Extended data figures and tables

### Extended Data Fig. 1 Morphological assessment and functional enrichment analysis of differentially expressed genes show accelerated meningeal lymphatic dysfunction in 5xFAD mice.

**a**, Representative images of meningeal whole mounts from 5xFAD mice at 5–6 and 13–14 months of age, stained for CD31 (blue), LYVE-1 (green) and A $\beta$  (red, stained with the D54D2 antibody; scale bar, 2 mm; inset scale bar, 500  $\mu$ m). **b**, Scheme depicting the compartmentalization of the meningeal whole mount for quantification of LYVE-1 and A $\beta$  coverage. **c–e**, Graphs showing the coverage by LYVE-1 $^{+}$  vessels and A $\beta$  as a percentage of the region of interest (% of ROI) at the superior sagittal sinus (**c**; SSS), transverse sinus and confluence of sinuses (**d**; TS/COS), and petrosquamosal and sigmoid sinuses (**e**; PSS/SS). Results in **c–e** are presented as mean  $\pm$  s.e.m.;  $n = 8$  per group; two-way ANOVA with Holm–Sidak's multiple comparisons test (for LYVE-1 $^{+}$  vessels) and two-tailed unpaired Student's *t*-test (for A $\beta$  coverage); data are from two independent experiments. **f**, Lymphatic endothelial cells (LECs) were isolated from the brain meninges of male 5xFAD mice and wild-type littermate controls at 6 months of age, and total RNA was extracted and sequenced. **g**, PCA plot showing segregation between wild-type (blue) and 5xFAD (purple) meningeal LEC transcriptomes. **h**, Heat map of top 50 differentially expressed genes in 5xFAD meningeal LECs at 6 months of age. **i**, Gene-sets obtained by functional enrichment of differentially expressed genes in meningeal LECs from 5xFAD mice. **j, k**, Exocytosis (GO: 0006887) and phospholipase D signalling pathway (KEGG: mmu04072) gene-sets obtained by functional enrichment analysis, with corresponding differentially expressed genes. **g–k**,  $n = 3$  per group; individual RNA

samples result from LECs pooled from 10 meninges over 3 independent experiments; the Benjamini–Hochberg correction was used to adjust the associated  $P$  values in **i** ( $P_{\text{adj}} < 0.05$ ); functional enrichment of differential expressed genes in **i** was determined with Fisher’s exact test; colour scale bars in **h** and **k** represent expression values for each sample as standard deviations from the mean across each gene. [Source data](#)

### **Extended Data Fig. 2 Meningeal immune cell profiling by mass cytometry in 5xFAD mice at 5–6 and 11–12 months.**

**a**, Meningeal single-cell suspensions were obtained from male 5xFAD mice at 5–6 months and 11–12 months and processed for mass cytometry. Representative mass cytometry dot plots depicting gating strategy used to select CD45<sup>+</sup> live cells used in further high-dimensional analysis. **b**, Heat maps of the median marker expression values for each immune cell cluster identified using Rphenograph. Median marker expression values are indicated by colour intensity depicted in the scale bar. **c**, *t*-Distributed stochastic neighbour embedding-based visualization (viSNE) plots showing unsupervised clustering of CD45<sup>+</sup> live immune cells. **d**, Number of CD45<sup>+</sup> live meningeal leucocytes at 5–6 (orange) and 11–12 (purple) months in 5xFAD mice. **e**, Numbers of different meningeal immune cells showing a statistically significant increase in B cells, CD4<sup>+</sup> T cells 1, CD8<sup>+</sup> T cells, type 3 innate lymphoid cells (ILC3s) and undefined cells in the meninges of 5xFAD mice at 11–12 months of age. Data are representative of a single experiment; results in **d** and **e** are presented as mean ± s.e.m.;  $n = 7$  per group; two-tailed unpaired Student’s *t*-test. [Source data](#)

### **Extended Data Fig. 3 Compromising meningeal lymphatic function in 5xFAD mice limits brain A $\beta$ clearance by mAb158 and modulates neuritic dystrophy, microglial activation and fibrinogen levels.**

**a–e**, Adult 2-month-old male wild-type mice were injected with 5  $\mu$ l visudyne (i.c.m.) followed by a transcranial photoconversion step (vis/photo) to ablate meningeal lymphatic vessels at the dorsal meninges. Control mice were injected with visudyne without photoconversion (vis).

One week later, each mouse was injected with 5  $\mu$ l of a suspension of fluorescent microspheres (1  $\mu$ m in diameter) into the CSF and 15 min later the lymphatic vessel afferent to the deep cervical lymph node (dCLN) was imaged by live *in vivo* fluorescence stereomicroscopy. **a**, Representative images of skull caps with attached meningeal layers showing microspheres (blue) and lymphatic vessels stained for LYVE-1 (green) around the confluence of sinuses (COS) and transverse sinus (TS) at the dorsal meninges or around the sigmoid (SS) and petrosquamosal (PSS) sinuses at the basal meninges (scale bars, 500  $\mu$ m). **b, c**, Graphs showing total length of LYVE-1 $^{+}$  vessels (in mm) and number of branching points in lymphatics at the dorsal (**b**) and basal (**c**) meninges. Results in **b, c** are presented as mean  $\pm$  s.e.m.;  $n = 10$  per group; two-tailed unpaired Student's *t*-test; data are representative of two independent experiments. **d**, Representative frames showing microspheres flowing through the lymphatic vessel afferent to the dCLN, or cumulative sphere tracking (for 20 s), in mice with intact or ablated meningeal lymphatic vessels. **e**, Quantification of microsphere flow (number of microspheres per minute) in mice from each group. Results in **e** are presented as mean  $\pm$  s.e.m.;  $n = 11$  in vis group and  $n = 14$  in vis/photo group; two-tailed unpaired Student's *t*-test; data are from two independent experiments. **f**, Adult 3- to 3.5-month-old male 5xFAD mice were injected with visudyne with or without photoconversion as in **a**. Upon recovery, mice received intraperitoneal (i.p.) injections of mAb158 (a mouse antibody against A $\beta$  protofibrils) or the control mouse IgG (mIgG) antibodies, each at a dose of 40 mg kg $^{-1}$ . Antibodies were injected weekly for four weeks. Additional steps of meningeal lymphatic vessel ablation or control interventions were followed by four weekly injections with antibodies. Mice were tested in the open field and Morris water maze (Extended Data Fig. 4). **g**, Representative images of brain sections from 5xFAD mice stained for A $\beta$  (red, stained with the D54D2 antibody) and LAMP1 (green; scale bars, 1 mm). **h–l**, Graphs showing number of A $\beta$  plaques per mm $^2$  of brain section (**h**), average size of A $\beta$  plaques ( $\mu$ m $^2$ ) in mAb158 cohort (**i**), average size of A $\beta$  plaques ( $\mu$ m $^2$ ) in mAducanumab cohort (**j**; related to Fig. 1a-e), coverage by A $\beta$  plaques (**k**) and coverage by LAMP1 $^{+}$  dystrophic neurites (**l**; as percentage of brain section) in each group. **m**, Representative images of the brain cortex stained for A $\beta$  (blue, stained with Amylo-Glo), fibrinogen (grey), IBA1 (green) and CD68 (red; scale bar,

100 µm). **n–q**, Graphs showing coverage by IBA1<sup>+</sup> cells (**n**; percentage of field), number of peri-Aβ plaque IBA1<sup>+</sup> cells (**o**), percentage of IBA1 occupied by CD68 (**p**) and fibrinogen coverage (**q**; percentage of field) in each group. Data in **f–q** are representative of a single experiment; results in **h–l** and **n–q** are presented as mean ± s.e.m.;  $n = 9$  in each group; in **h, i, j, l** and **n–q**, two-way ANOVA with Holm–Sidak’s multiple comparisons test; in **k**, two-tailed unpaired Student’s *t*-test. [Source data](#)

### Extended Data Fig. 4 Meningeal lymphatic dysfunction leads to anxiety-like behaviour and worsened spatial learning and memory in 5xFAD mice.

**a**, Adult 5xFAD mice with intact or ablated meningeal lymphatics and treated with mAducanumab (mAdu) or control mIgG antibodies (see Fig. 1 for experimental scheme and more results) were tested in the open field arena and in the Morris water maze. **b–d**, Performance in open field arena: total distance travelled (**b**; in centimetres), velocity (**c**; in centimetres per second) and percentage of time in the centre of the open field arena (**d**; percentage of total time). **e–g**, Performance in Morris water maze: latency to platform in acquisition (**e**; in seconds), percentage of time in the platform quadrant in the probe trial (**f**) and latency to platform in reversal (**g**; in seconds). Data in **a–g** are from a single experiment; results in **b–g** are presented as mean ± s.e.m.;  $n = 10$  (vis) and  $n = 9$  (vis/photo); two-way ANOVA with Holm–Sidak’s multiple comparisons test in **b–d** and **f**; repeated measures two-way ANOVA with Tukey’s multiple comparisons test in **e** and **g**; statistically significant differences between groups in days 3 and 4 of the Morris water maze test are indicated as D3 and D4, respectively. **h**, Adult 5xFAD mice with intact or ablated meningeal lymphatics and treated with mAb158 or control mIgG antibodies (see Extended Data Fig. 3f–q for experimental scheme and more results) were tested in the open field arena and in the Morris water maze. **i–k**, Performance in open field arena: total distance (**i**; in centimetres), velocity (**j**; in centimetres per second) and percentage of time in the centre of the open field arena (**k**; percentage of total time). **l–n**, Performance in Morris water maze: latency to platform in acquisition (**l**, in seconds), percentage of time in the platform quadrant in the probe trial (**m**) and latency to platform

in reversal (**n**; in seconds). Data in **h–n** are from a single experiment; results in **i–n** are presented as mean  $\pm$  s.e.m.;  $n = 9$  in each group; two-way ANOVA with Holm–Sidak’s multiple comparisons test in **i–k** and **m**; repeated measures two-way ANOVA with Tukey’s multiple comparisons test in **I** and **n**; statistically significant differences between groups in days 3, 4 and 7 of the Morris water maze test are indicated as D3, D4 and D7, respectively. [Source data](#)

### Extended Data Fig. 5 Meningeal lymphatic vessel ablation precludes brain A $\beta$ plaque clearance by mAb158 administered into the CSF.

**a**, Adult 4- to 4.5-month-old male 5xFAD mice were injected (i.c.m.) with visudyne (5  $\mu$ l) plus photoconversion (vis/photo) or visudyne without photoconversion (Vis). One week later, 5  $\mu$ l mAb158 antibodies or the same volume of the control mouse IgG (mIgG) antibodies were directly injected into the CSF (i.c.m.), both at 1  $\mu$ g  $\mu$ l $^{-1}$ . Injections with antibodies were repeated two weeks later. Additional steps of meningeal lymphatic vessel ablation or control interventions were followed by two more i.c.m. injections with antibodies, as shown. **b**, Representative images of meningeal whole mounts stained for CD31 (blue), LYVE-1 (green) and A $\beta$  (red, stained with the D54D2 antibody; scale bar, 2 mm). **c**, Coverage by A $\beta$  as a percentage of the meningeal whole mount. **d**, Representative images of brain sections from 5xFAD mice stained for A $\beta$  (red, stained with the D54D2 antibody) and with DAPI (blue; scale bar, 2 mm). **e–g**, Graphs showing number of A $\beta$  plaques per mm $^2$  of brain section (**e**), average size of A $\beta$  plaques (**f**;  $\mu$ m $^2$ ) and total coverage of A $\beta$  plaques (**g**; percentage of brain section) in each group. **h**, Representative inset showing an example of a Prussian blue focus in a brain tissue section of a 5xFAD mouse (scale bar, 100  $\mu$ m). **i**, Quantification of Prussian blue foci per brain section in each group. Data in **a–i** are representative of two independent experiments; results in **c, e–g** and **i** are presented as mean  $\pm$  s.e.m.;  $n = 8$  in vis + mIgG, vis + mAb158 and vis/photo + mIgG,  $n = 7$  in vis/photo + mAb158; two-way ANOVA with Holm–Sidak’s multiple comparisons test. **j**, 5xFAD mice (5 months old) with intact or ablated meningeal lymphatic vasculature were injected (i.c.m.) with 5  $\mu$ l mAb158 (at 1  $\mu$ g  $\mu$ l $^{-1}$ ). One hour later, mice were

transcardially perfused and the brains were collected for assessment of mAb158 linked to A $\beta$  in blood vasculature or A $\beta$  plaques. Images of ten different regions of the brains of 5xFAD mice from each group showing blood vessels stained for CD31 (blue), A $\beta$  plaques (green, stained with Amylo-Glo) and mAb158 (red; scale bar, 200  $\mu$ m). **k**, Colocalization between mAb158 and CD31 (percentage of total CD31 coverage) in each brain region (1 to 10) or presented as the average of all regions. **l**, Colocalization between mAb158 and Amylo-Glo (percentage of total Amylo-Glo-stained A $\beta$  plaques) in each brain region (1 to 10) or presented as the average of all regions. Data in **j–l** are from a single experiment; results in **k** and **l** are presented as mean  $\pm$  s.e.m.;  $n = 5$  per group; two-way ANOVA with Holm–Sidak’s multiple comparisons test (for comparisons between groups in each brain region) and two-tailed unpaired Student’s *t*-test (for comparisons between the two groups). [Source data](#)

### **Extended Data Fig. 6 Effects of meningeal lymphatic vessel ablation and mAducanumab immunotherapy on the microglial and blood endothelial cell transcriptomes in 5xFAD mice.**

**a**, Representative flow cytometry dot plots showing gating strategy used to sort (and enrich for) live (DAPI $^-$ ) singlets that were CD45 $^+$ CD11b $^+$ Ly6G $^-$  (macrophages/microglia), CD45 $^-$ CD11b $^-$ CD31 $^+$  (blood endothelial cells) and CD45 $^-$ CD11b $^-$ CD13 $^+$ CD31 $^-$  (mural cells). **b, c**, Representations of tSNE plots highlighting the brain cells identified by scRNA-seq discriminated by group (**b**) or type (**c**). **d**, Dot plot depicting the average scaled expression levels of specific genes (*x*-axis) used to identify the brain cell populations, as well as the percentage of cells that expressed those genes within each population; choroid plexus blood endothelial cells (cpBECs), border-associated macrophages (BAMs), arterial BECs (aBECs), capillary BECs (cBECs) and venous BECs (vBECs). **e**, Heat map showing expression levels of genes involved in the transition from homeostatic to *Trem2*-independent and *Trem2*-dependent disease-associated microglia phenotypes in the different groups. **f**, Violin plots showing the expression levels of the homeostatic *P2ry12*, *Tmem119*, *Cx3cr1*, *Selplg* and *Hexb* genes, and disease-associated microglial *Apoe*, *Lyz2*, *Fth1*, *B2m*, *Timp2*, *H2-d1*, *Axl*, *Cst7*, *Spp1* and *Lpl* genes in each group. **g**, Top ten Gene

Ontology terms obtained after analysing genes that were significantly downregulated in microglia from the vis/photo + mIgG group compared to the vis + mIgG group. **h**, Volcano plot with significantly downregulated (in blue) and upregulated (in orange) genes after comparing the transcriptomes of cBECs from the vis/photo + mIgG and vis + mIgG groups. **i, j**, Top ten Gene Ontology terms obtained after analysing significantly upregulated (**i**) or downregulated (**j**) genes in cBECs from the vis/photo + mIgG group, when compared to the vis + mIgG group. **k–n**, Volcano plots, with significantly downregulated (blue) and upregulated (orange) genes, and top ten Gene Ontology terms (using upregulated genes) obtained after comparing the transcriptomes of aBECs (**k, l**) and vBECs (**m, n**) from the vis/photo + mIgG and vis + mIgG groups. **o, p**, Violin plots showing the expression levels of *Abcg2*, *Lrp1*, *Picalm*, *Rab5a*, *Rab7* and *Rab11a* in cBECs (**o**) and vBECs (**p**) from each group. Data in **a–p** are from a single experiment in which the transcriptomes of 7,286 cells (isolated from brain hemispheres of 3 mice per group) were analysed, including 2,625 microglia, 1,958 cBECs, 545 aBECs and 1,412 vBECs; scale bar in **e** represents scaled expression at the single-cell level; differentially expressed genes plotted in **h, k** and **m** were determined using an *F*-test with adjusted degrees of freedom based on weights calculated per gene with a zero-inflation model and Benjamini–Hochberg adjusted *P* values; Gene Ontology analyses used over-representation test and scale bars in **g, i, j, l** and **n** represent Benjamini–Hochberg adjusted *P* values for each pathway; gene expression comparison in **f, o** and **p** was done using Wilcoxon rank-sum test with Bonferroni’s adjusted *P* values reported.

### **Extended Data Fig. 7 Improved brain A $\beta$ plaque clearance by delivery of mVEGF-C and mAb158 into the CSF is correlated with lymphatic vessel expansion at the dorsal meninges and transcriptional reprogramming of meningeal LECs.**

**a**, Adult 4- to 5-month-old male 5xFAD mice were injected with 5  $\mu$ l (i.c.m.) of AAV1 expressing eGFP or mouse VEGF-C (mVEGF-C), under the cytomegalovirus (CMV) promoter (each at  $10^{12}$  GC  $\mu$ l $^{-1}$ ), in combination with either mAb158 antibodies or the respective mIgG control antibodies (each at 1  $\mu$ g  $\mu$ l $^{-1}$ ). Antibody injections (5  $\mu$ l at 1  $\mu$ g  $\mu$ l $^{-1}$ , i.c.m.)

were repeated two weeks later. The same regimen of the aforementioned i.c.m. injections was repeated as indicated in the scheme and tissue was collected two weeks after the last injection. **b**, Representative images of brain sections stained for A $\beta$  (red, stained with the D54D2 antibody) and with DAPI (blue; scale bar, 2 mm). **c**, Coverage of A $\beta$  as percentage of brain section in each group. **d**, Representative images from the brain cortex stained for A $\beta$  (blue, stained with the Amylo-Glo), CD68 (green) and IBA1 (red; scale bar, 50  $\mu$ m). **e–g**, Coverage by IBA1 $^{+}$  cells (**e**; percentage of field), number of peri-A $\beta$  plaque IBA1 $^{+}$  cells (**f**) and percentage of IBA1 occupied by CD68 in each group (**g**). Results in **c** and **e–g** are presented as mean  $\pm$  s.e.m.;  $n = 12$  in mVEGF-C + mIgG and  $n = 13$  in eGFP + mIgG, eGFP + mAb158 and mVEGF-C + mAb158; two-way ANOVA with Holm–Sidak's multiple comparisons test; data in **a–g** are from two independent experiments. **h**, Representative fluorescence stereomicroscopy images of skull caps (skull bone signal in blue) and attached meningeal lymphatic vessels stained for LYVE-1 (green) around the transverse sinus (TS) at the dorsal meninges or around the sigmoid (SS) and petrosquamosal (PSS) sinuses at the basal meninges (scale bars, 500  $\mu$ m). **i, j**, Total length of LYVE-1 $^{+}$  vessels (mm) and number of branching points in lymphatics at the dorsal (**i**) and basal (**j**) meninges. Results in **h–j** are presented as mean  $\pm$  s.e.m.;  $n = 6$  in mIgG groups and  $n = 7$  in mAb158 groups; two-way ANOVA with Holm–Sidak's multiple comparisons test; data in **h–j** are representative of two independent experiments. **k**, Representative images of meningeal whole mounts stained for CD31 (green) and LYVE-1 (red; scale bar, 1 mm; inset scale bar, 300  $\mu$ m). **l, m**, Coverage by CD31 $^{+}$ LYVE-1 $^{-}$  vessels (**l**; % of meningeal whole mount) and the number of branching points and coverage by LYVE-1 $^{+}$  vessels (**m**; % of meningeal whole mount). Results in **l** and **m** are presented as mean  $\pm$  s.e.m.;  $n = 7$  in eGFP + mIgG and  $n = 6$  in eGFP + mAb158, mVEGF-C + mIgG and mVEGF-C + mAb158; two-way ANOVA with Holm–Sidak's multiple comparisons test; data in **k–m** are representative of two independent experiments. **n**, Aged wild-type mice (20–24 months of age) were injected with 2  $\mu$ l (i.c.m.) of AAV1 expressing eGFP or mVEGF-C, under the CMV promoter (each at  $10^{13}$  GC  $\mu$ l $^{-1}$ ). One month later, mice were transcardially perfused, skull caps were collected, meninges harvested and LECs were sorted by FACS for bulk RNA-seq. **o**, PCA plot showing segregation between eGFP (orange) and mVEGF-C (blue) meningeal LEC

transcriptomes. **p**, Volcano plot showing genes that were significantly downregulated (blue) or upregulated (orange) between meningeal LECs from the mVEGF-C and eGFP groups. **q**, Ten Gene Ontology terms (selected from the 30 most altered) obtained after analysis of genes that were differentially expressed between meningeal LECs from the mVEGF-C and eGFP groups. **n–q**,  $n = 2$  per group; individual RNA samples result from LECs pooled from ten meninges over two independent experiments; differentially expressed genes ( $P < 0.05$ ) plotted in **c** were determined using an *F*-test with adjusted degrees of freedom based on weights calculated per gene with a zero-inflation model; Gene Ontology analysis in **q** used over-representation test and the scale bar represents the *P* value for each pathway. **r**, Aged APPswe mice (22–26 months of age) were treated with viral vectors expressing eGFP or mVEGF-C (via i.c.m. injections) and with mIgG or mAdu. antibodies (via i.p. injections, according to the regimen in the scheme; related to Fig. 2). **s**, Representative images of brain sections stained for A $\beta$  (red, stained with the D54D2 antibody) and with DAPI (blue; scale bar, 1 mm). **t**, Graph showing coverage of A $\beta$  (as percentage of the brain sections) in each group. Results in **t** are presented as mean  $\pm$  s.e.m.;  $n = 6$  per group; two-way ANOVA with Holm–Sidak’s multiple comparisons test; data in **r–t** are from a single experiment. [Source data](#)

### **Extended Data Fig. 8 Therapeutic effects of mVEGF-C on the clearance of A $\beta$ by antibodies in old APPswe mice and the gene expression profile of brain cells.**

**a**, Aged APPswe mice (26–30 months old) were injected with 5  $\mu$ l (i.c.m.) of AAV1 expressing eGFP or mVEGF-C (each at  $10^{12}$  GC  $\mu$ l $^{-1}$ ) in combination with mAb158 (at 1  $\mu$ g  $\mu$ l $^{-1}$ ) as indicated in the scheme. **b**, Representative images of brain sections from APPswe mice stained for A $\beta$  (red, stained with the D54D2 antibody) and with DAPI (blue; scale bar, 1 mm). **c–e**, Coverage of A $\beta$  (percentage of brain region) in the hippocampus (**c**), cortex/striatum/amygdala (**d**) and combined regions (**e**). Results in **c–e** are presented as mean  $\pm$  s.e.m.;  $n = 11$  per group; two-tailed unpaired Student’s *t*-test; data in **a–e** are from a single experiment. **f**, Aged J20 mice (14–16 months old) were injected with 5  $\mu$ l (i.c.m.) of AAV1

expressing eGFP or mVEGF-C (each at  $10^{12}$  GC  $\mu\text{l}^{-1}$ ) in combination with mAb158 (at 1  $\mu\text{g}$   $\mu\text{l}^{-1}$ ) as indicated in the scheme. **g**, Representative images of brain sections from J20 mice stained for A $\beta$  (red, stained with the D54D2 antibody) and with DAPI (blue; scale bar, 1 mm). **h–j**, Coverage of A $\beta$  (%) of brain region) in the hippocampus (**h**), cortex/striatum/amygdala (**i**) and combined regions (**j**). Results in **h–j** are presented as mean  $\pm$  s.e.m.;  $n = 8$  in eGFP + mAb158 and  $n = 10$  in mVEGF-C + mAb158; two-tailed unpaired Student's *t*-test; data in **f–j** are from a single experiment. **k**, Top ten Gene Ontology terms obtained after analysing genes that were significantly upregulated in hippocampi ( $n = 3$  per group) from the eGFP + mAdu group when compared to the eGFP + mIgG group (related to Fig. [2a–c](#)). **l**, **m**, Heat maps depicting the expression profile of genes in the learning and memory (**l**; GO: 0007611) and synapse organization (**m**; GO: 0050808) Gene Ontology pathways (related to Fig. [2d, e](#)). Data in **k–m** are from a single experiment; Gene Ontology analyses used over-representation test and scale bar in **k** represents Benjamini–Hochberg adjusted *P* values; heat maps in **l** and **m** depict counts-per-million normalized expression minus per-gene mean expression. **n**, Representation of the tSNE plot highlighting sequenced brain cells by group. **o**, Dot plot depicting the average scaled expression levels of specific genes (*x*-axis) used to identify the brain cell populations, as well as the percentage of gene-expressing cells within each population; smooth muscle cells (SMCs) choroid plexus blood endothelial cells (cpBECs), border-associated macrophages (BAMs), venous BECs (vBECs), arterial BECs (aBECs) and capillary BECs (cBECs). **p–s**, Volcano plots, with significantly downregulated (in blue) and upregulated (in orange) genes, and Gene Ontology terms (obtained using upregulated genes; selected from top 20 terms) obtained after comparing the transcriptomes of vBECs (**p**, **q**) and aBECs (**r**, **s**) from the mVEGF-C + mIgG group and the eGFP + mIgG group. **t**, Violin plots showing the expression levels of the *Flt4* gene in microglia, capillary, venous and arterial BECs in each group. Data in **n–t** are related to Fig. [2f–k](#) and resulted from a single experiment in which the transcriptomes of 7,739 cells (isolated from brain hemispheres of 3 mice per group) were analysed, including 2,345 microglia, 2,934 cBECs, 602 vBECs and 766 aBECs; differentially expressed genes plotted in **p** and **r** were determined using an *F*-test with adjusted degrees of freedom based on weights calculated per gene with a zero-inflation model and Benjamini–Hochberg adjusted *P*

values; Gene Ontology analyses used over-representation test and scale bars in **q** and **s** represent Benjamini–Hochberg adjusted *P* values for each pathway; gene expression comparison in **t** was done using Wilcoxon rank-sum test with Bonferroni’s *P* value adjustment. [Source data](#)

**Extended Data Fig. 9 Expression profile of genes associated with Parkinson’s disease, multiple sclerosis and AD in meningeal LECs, brain blood endothelial cells and microglia from different mouse models.**

**a**, Pie chart showing the proportion of Parkinson’s disease-associated genes for which the average expression across all RNA-seq datasets of lymphatic endothelial cells (LECs) was in the top 2nd, 5th, 10th, or 25th percentile out of all genes. **b**, Heat map showing the log<sub>2</sub>-normalized expression values (depicted in the colour scale bar) for Parkinson’s disease-associated genes whose average expression values fall within the top second percentile of all genes expressed across all LEC RNA-seq datasets. **c**, Gene-sets obtained by functional enrichment of 25th percentile Parkinson’s disease-associated genes expressed across all LEC RNA-seq datasets. **d**, Pie chart showing the proportion of multiple sclerosis-associated genes for which the average expression across all LEC RNA-seq datasets was in the top 2nd, 5th, 10th, or 25th percentile out of all genes. **e**, Heat map showing the log<sub>2</sub>-normalized expression values (depicted in the colour scale bar) for multiple sclerosis-associated genes whose average expression values fall within the top second percentile of all genes expressed across all LEC RNA-seq datasets. **f**, Gene-sets obtained by functional enrichment of 25th percentile multiple sclerosis-associated genes expressed across all LEC RNA-seq datasets. **g**, Pie chart showing the proportion of AD-associated genes for which the average expression across all LEC RNA-seq datasets was in the top 2nd, 5th, 10th, or 25th percentile out of all genes. **h**, Heat map showing the log<sub>2</sub>-normalized expression values (depicted in the colour scale bar) for AD-associated genes whose average expression values fall within the top second percentile of all genes expressed across all LEC RNA-seq datasets. **i**, Gene-sets obtained by functional enrichment of 25th percentile AD-associated genes expressed across the different LEC RNA-seq datasets. **a–i**, *n* = 2 or 3 per group; individual RNA samples result from LECs pooled

from 10 mice; genes used in **a–i** are from RNA-seq datasets obtained from LECs isolated from diaphragm, ear skin and meninges at 2–3 months (m.), from meninges at 2–3 or 20–24 months, from meninges at 20–24 months after injections with AAV1-CMV-eGFP (eGFP) or AAV1-CMV-mVEGF-C-WPRE (mVEGF-C, one month after i.c.m. injection; see [Methods](#) for details) and from meninges of 6-month-old wild-type or 5xFAD mice (see Extended Data Fig. [1f-k](#) for related data); in **c, f** and **i** the Benjamini–Hochberg correction was used to adjust the associated *P* values ( $P_{\text{adj}} < 0.05$ ) and the functional enrichment of differential expressed genes was determined with Fisher’s exact test. **j**, Pie charts showing the proportion of AD-associated genes for which the average expression was in the top 2nd, 5th, 10th, or 25th percentile out of all genes in each cluster of brain blood endothelial cells (BECs): capillary BECs 1, capillary BECs 2, arterial BECs and venous BECs. **k**, Heat map showing the expression values for AD-associated genes whose average expression values fall within the top second percentile of all genes expressed in each cluster of BECs. **l**, The transcriptome of myeloid cells (live CD45<sup>+</sup>Ly6G<sup>−</sup>CD11b<sup>+</sup> cells) sorted from the brain cortex of 5.5-month-old 5xFAD mice was analysed by scRNA-seq ([Methods](#)). The graph shows the unsupervised clustering and tSNE representation of four distinct clusters of microglia (Mg). **m**, Pie charts showing the proportion of AD-associated genes for which the average expression was in the top 2nd, 5th, 10th, or 25th percentile out of all genes in each Mg cluster. **n**, Heat map showing the expression values for AD-associated genes whose average expression values fall within the top second percentile of all genes expressed in each Mg cluster. **o**, Venn diagram showing the overlap between AD-associated genes in the top tenth percentile for meningeal LECs (mLECs), brain BECs (bBECs) and microglia. Data in **j** and **k** resulted from the analysis of a published scRNA-seq dataset<sup>[25](#)</sup>; data in **l–n** resulted from the scRNA-seq analysis of 651 microglia; in **k** and **n**, scale bars represent log<sub>2</sub>-normalized expression values. [Source data](#)

## Extended Data Fig. 10 Integrative analyses of gene expression profiles of microglia from the brains of 5xFAD mice with intact or ablated meningeal lymphatics and from the human brain.

**a**, Representation of the tSNE plots showing the segregation of microglia from human donors or 5xFAD mice by groups (dashed lines represent the approximate boundaries between microglial clusters) upon cross-species RNA-seq data integration and analysis (Fig. 3b). **b, c**, Violin plots showing expression levels of the pan-microglial genes *ELMO1*, *MALAT1* and *MEF2A* and the homeostatic genes *P2RY12*, *P2RY13* and *TMEM119* (**b**) and the activation genes *CD83*, *CST3*, *JUN*, *LGMD*, *LPL* and *TNFAIP3* (**c**) in the different human microglial clusters. **d**, Dot plot depicting the average scaled expression levels of specific genes (*x*-axis), as well as the percentage of gene-expressing 5xFAD microglia within each cluster. Data in **a–d** are related to Fig. 3b-g and were obtained from the integrated analysis of a total of 5,462 non-AD, 618 presymptomatic AD, 4,548 familial AD and 6,461 sporadic AD microglia (single-nucleus RNA-seq data) from human brain parietal lobes, and from a total of 781 and 770 microglia (scRNA-seq data) from the brains of 5xFAD mice of the vis + mIgG and vis/photo + mIgG groups, respectively.

## Supplementary information

### Supplementary Information

Full names and credentials of the Dominantly Inherited Alzheimer Network (DIAN) Consortium members.

### Reporting Summary

### Supplementary Table 1

List of DEGs in brain cell types of the Vis./photo. plus mIgG group compared to the Vis. plus mIgG group. Depicts the number of differentially

expressed genes, alongside the respective  $\text{Log}_2(\text{fold change})$  and adjusted  $P$ -values, in microglia, capillary blood endothelial cells, venous blood endothelial cells and arterial blood endothelial cells from the Visudyne/photoconversion plus mIgG group, compared to the control Visudyne plus mIgG group.

### **Supplementary Table 2**

Comparisons between the expression levels of homeostatic and DAM genes in mouse microglia from different groups. This table depicts the  $\text{Log}_2(\text{fold change})$  and adjusted  $P$ -values for the differential expression levels of homeostatic, *Trem2* independent and *Trem2* dependent microglial genes (associated with the acquisition of the disease-associated microglia signature) in Visudyne plus mAducanumab *vs* Visudyne plus mIgG, in Visudyne/photoconversion plus mIgG *vs* Visudyne plus mIgG, in Visudyne/photoconversion plus mAducanumab *vs* Visudyne/photoconversion plus mIgG and in Visudyne/photoconversion plus mAducanumab *vs* Visudyne plus mAducanumab.

### **Supplementary Table 3**

Gene-set based analyses for highly expressed AD-related gene SNPs in meningeal lymphatic endothelial cells, brain blood endothelial cells or microglia. This table depicting the gene-set analyses was performed using the Generalized Gene-Set Analysis of GWAS Data (MAGMA) analyses, which maps every SNP to the nearest gene, takes into account LD structure and uses multiple regression analyses to provide a  $P$ -value for the association of each gene with the tested phenotype, namely amyloid imaging, sTREM2, A $\beta$ <sub>42</sub>, pTau, Tau, age at onset, disease risk and disease progression.

### **Supplementary Table 4**

Demographic characteristics of donor brain samples used in single-nucleus RNA-seq experiments. This table depicts the number of samples, brain regions, sex, age of death, proportions of APOE  $\epsilon$ 4 carriers and *post-*

*mortem* interval for the non-AD, presymptomatic AD, familial AD and sporadic AD patient groups.

### **Supplementary Table 5**

Microglial gene signature of meningeal lymphatic dysfunction in 5xFAD. Table depicting the 54 genes, and corresponding Log<sub>2</sub>(fold change) and *q*-values, that compose the signature of microglial activation in 5xFAD mice with ablated meningeal lymphatics (Visudyne/photoconversion plus mIgG group) compared to 5xFAD mice with intact meningeal lymphatics (Visudyne plus mIgG group).

### **Supplementary Table 6**

Gene-set based analyses for genes overexpressed in microglia upon meningeal lymphatic ablation in 5xFAD or treatment with mVEGF-C in APPswe. Table depicting the gene-set analyses performed using the Generalized Gene-Set Analysis of GWAS Data (MAGMA) analyses, which maps every SNP to the nearest gene, takes into account LD structure and uses multiple regression analyses to provide a *P*-value for the association of each gene with the tested phenotype, namely amyloid imaging, sTREM2, A $\beta$ <sub>42</sub>, pTau, Tau, age at onset and disease risk.

### **Source Data**

This file contains Source Data for Supplementary Table 3.

### **Source Data**

This file contains Source Data for Supplementary Table 6.

### **Video 1**

Drainage of fluorescent microspheres injected into the CSF of mice with intact meningeal lymphatics. Yellow-green fluorescent (505/515 nm) microspheres (0.5  $\mu$ m in diameter) were injected into the CSF of adult mice

with intact meningeal lymphatic vasculature. The video shows microspheres flowing through lymphatic vessels afferent to the deep cervical lymph node for a total of 20 seconds. Tracking of microspheres was highlighted using TrackMate.

## **Video 2**

Drainage of fluorescent microspheres injected into the CSF of mice with ablated meningeal lymphatics. Yellow-green fluorescent (505/515 nm) microspheres (0.5  $\mu\text{m}$  in diameter) were injected into the CSF of adult mice that undergone meningeal lymphatic vessel ablation. The video shows microspheres flowing through lymphatic vessels afferent to the deep cervical lymph node for a total of 20 seconds. Tracking of microspheres was highlighted using TrackMate.

## **Source data**

[\*\*Source Data Fig. 1\*\*](#)

[\*\*Source Data Fig. 3\*\*](#)

[\*\*Source Data Extended Data Fig. 1\*\*](#)

[\*\*Source Data Extended Data Fig. 2\*\*](#)

[\*\*Source Data Extended Data Fig. 3\*\*](#)

[\*\*Source Data Extended Data Fig. 4\*\*](#)

[\*\*Source Data Extended Data Fig. 5\*\*](#)

[\*\*Source Data Extended Data Fig. 7\*\*](#)

[\*\*Source Data Extended Data Fig. 8\*\*](#)

## [Source Data Extended Data Fig. 9](#)

## Rights and permissions

### [Reprints and Permissions](#)

## About this article



Check for  
updates

## Cite this article

Da Mesquita, S., Papadopoulos, Z., Dykstra, T. *et al.* Meningeal lymphatics affect microglia responses and anti-A $\beta$  immunotherapy. *Nature* **593**, 255–260 (2021). <https://doi.org/10.1038/s41586-021-03489-0>

### [Download citation](#)

- Received: 27 January 2020
- Accepted: 25 March 2021
- Published: 28 April 2021
- Issue Date: 13 May 2021
- DOI: <https://doi.org/10.1038/s41586-021-03489-0>

## Comments

By submitting a comment you agree to abide by our [Terms](#) and [Community Guidelines](#). If you find something abusive or that does not comply with our terms or guidelines please flag it as inappropriate.

[Access through your institution](#)

[Change institution](#)

[Buy or subscribe](#)

---

This article was downloaded by **calibre** from <https://www.nature.com/articles/s41586-021-03489-0>

| [Section menu](#) | [Main menu](#) |

- Article
- [Published: 28 April 2021](#)

# *C. difficile* exploits a host metabolite produced during toxin-mediated disease

- [Kali M. Pruss ORCID: orcid.org/0000-0002-8619-5886<sup>1</sup>](#) &
- [Justin L. Sonnenburg ORCID: orcid.org/0000-0003-2299-6817<sup>1</sup>](#)

[Nature](#) volume 593, pages 261–265 (2021)[Cite this article](#)

- 3811 Accesses
- 96 Altmetric
- [Metrics details](#)

## Subjects

- [Bacterial host response](#)
- [Microbial genetics](#)
- [Pathogens](#)

## Abstract

Several enteric pathogens can gain specific metabolic advantages over other members of the microbiota by inducing host pathology and inflammation. The pathogen *Clostridium difficile* is responsible for a toxin-mediated colitis that causes 450,000 infections and 15,000 deaths in the United States each year<sup>1</sup>; however, the molecular mechanisms by which *C. difficile*

benefits from this pathology remain unclear. To understand how the metabolism of *C. difficile* adapts to the inflammatory conditions that its toxins induce, here we use RNA sequencing to define, in a mouse model, the metabolic states of wild-type *C. difficile* and of an isogenic mutant that lacks toxins. By combining bacterial and mouse genetics, we demonstrate that *C. difficile* uses sorbitol derived from both diet and host. Host-derived sorbitol is produced by the enzyme aldose reductase, which is expressed by diverse immune cells and is upregulated during inflammation—including during toxin-mediated disease induced by *C. difficile*. This work highlights a mechanism by which *C. difficile* can use a host-derived nutrient that is generated during toxin-induced disease by an enzyme that has not previously been associated with infection.

[Access through your institution](#)

[Change institution](#)

[Buy or subscribe](#)

## Access options

Subscribe to Journal

Get full journal access for 1 year

\$199.00

only \$3.90 per issue

[Subscribe](#)

All prices are NET prices.

VAT will be added later in the checkout.

Tax calculation will be finalised during checkout.

Rent or Buy article

Get time limited or full article access on ReadCube.

from \$8.99

[Rent or Buy](#)

All prices are NET prices.

### **Additional access options:**

- [Log in](#)
- [Access through your institution](#)
- [Learn about institutional subscriptions](#)

**Fig. 1: Toxin-induced inflammation leads to extensive differential gene expression in *C. difficile* in vivo.**



**Fig. 2: A putative sorbitol utilization locus is responsible for metabolism of sorbitol by *C. difficile* in vitro and in vivo.**



**Fig. 3: Host aldose reductase responds to *C. difficile* infection.**

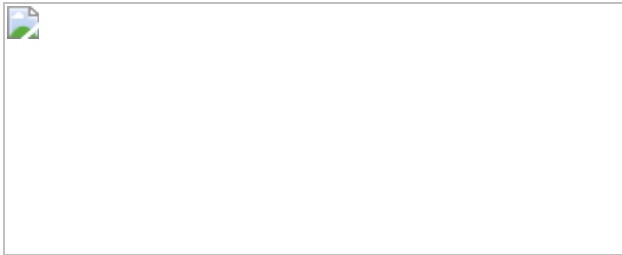
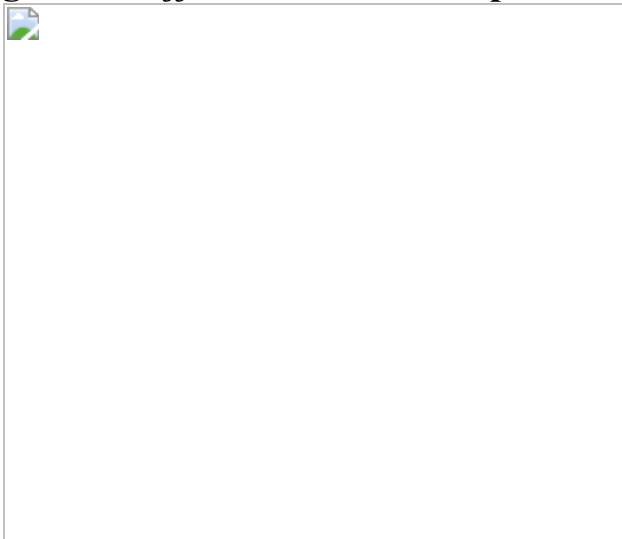


**Fig. 4: *C. difficile* uses sorbitol produced by host aldose reductase.**



## Data availability

Raw RNA-seq source data are available through the NCBI Sequence Read Archive. In vivo RNA-seq (Figs. 1b, 2a, Extended Data Fig. 1c, d, Supplementary Table 2) is available under accession number [PRJNA666929](#), and in vitro RNA-seq (Extended Data Fig. 6, Supplementary Table 3) under accession number [PRJNA667108](#). Publicly available single-cell RNA-seq data (Extended Data Fig. 7b–e) can be obtained from the Single Cell Portal (Broad Institute) under accession numbers [SCP259](#) and [SCP241](#). Microarray data (Fig. 3g) can be found in the Gene Expression Omnibus under accession number [GSE44091](#). [Source data](#) are provided with this paper.

## Code availability

The code used during this study is available at <https://github.com/kpruss/Cdiff-AR>.

# References

1. 1.

Lessa, F. C. et al. Burden of *Clostridium difficile* infection in the United States. *N. Engl. J. Med.* **372**, 825–834 (2015).

[CAS](#) [PubMed](#) [Google Scholar](#)

2. 2.

Rivera-Chávez, F. & Bäumler, A. J. The pyromaniac inside you: *Salmonella* metabolism in the host gut. *Annu. Rev. Microbiol.* **69**, 31–48 (2015).

[PubMed](#) [Google Scholar](#)

3. 3.

Faber, F. et al. Host-mediated sugar oxidation promotes post-antibiotic pathogen expansion. *Nature* **534**, 697–699 (2016).

[ADS](#) [CAS](#) [PubMed](#) [PubMed Central](#) [Google Scholar](#)

4. 4.

Lopez, C. A. et al. Virulence factors enhance *Citrobacter rodentium* expansion through aerobic respiration. *Science* **353**, 1249–1253 (2016).

[ADS](#) [CAS](#) [PubMed](#) [PubMed Central](#) [Google Scholar](#)

5. 5.

Bäumler, A. J. & Sperandio, V. Interactions between the microbiota and pathogenic bacteria in the gut. *Nature* **535**, 85–93 (2016).

[ADS](#) [PubMed](#) [PubMed Central](#) [Google Scholar](#)

6. 6.

Rivera-Chávez, F. & Mekalanos, J. J. Cholera toxin promotes pathogen acquisition of host-derived nutrients. *Nature* **572**, 244–248 (2019).

[PubMed](#) [PubMed Central](#) [Google Scholar](#)

7. 7.

El Feghaly, R. E. et al. Markers of intestinal inflammation, not bacterial burden, correlate with clinical outcomes in *Clostridium difficile* infection. *Clin. Infect. Dis.* **56**, 1713–1721 (2013).

[CAS](#) [PubMed](#) [PubMed Central](#) [Google Scholar](#)

8. 8.

Hryckowian, A. J., Pruss, K. M. & Sonnenburg, J. L. The emerging metabolic view of *Clostridium difficile* pathogenesis. *Curr. Opin. Microbiol.* **35**, 42–47 (2017).

[CAS](#) [PubMed](#) [Google Scholar](#)

9. 9.

Yamada, M. & Saier, M. H., Jr. Glucitol-specific enzymes of the phosphotransferase system in *Escherichia coli*. Nucleotide sequence of the gut operon. *J. Biol. Chem.* **262**, 5455–5463 (1987).

[CAS](#) [PubMed](#) [Google Scholar](#)

10. 10.

Svensäter, G., Edwardsson, S. & Kalfas, S. Purification and properties of sorbitol-6-phosphate dehydrogenase from oral streptococci. *Oral Microbiol. Immunol.* **7**, 148–154 (1992).

[PubMed](#) [Google Scholar](#)

11. 11.

Theriot, C. M. et al. Antibiotic-induced shifts in the mouse gut microbiome and metabolome increase susceptibility to *Clostridium difficile* infection. *Nat. Commun.* **5**, 3114 (2014).

[ADS](#) [PubMed](#) [PubMed Central](#) [Google Scholar](#)

12. 12.

Moing, A. Sugar alcohols as carbohydrate reserves in some higher plants. *Dev. Crop Sci.* **26**, 337–358 (2000).

[Google Scholar](#)

13. 13.

Hryckowian, A. J. et al. Microbiota-accessible carbohydrates suppress *Clostridium difficile* infection in a murine model. *Nat. Microbiol.* **3**, 662–669 (2018).

[CAS](#) [PubMed](#) [PubMed Central](#) [Google Scholar](#)

14. 14.

Collins, J. et al. Dietary trehalose enhances virulence of epidemic *Clostridium difficile*. *Nature* **553**, 291–294 (2018).

[ADS](#) [CAS](#) [PubMed](#) [PubMed Central](#) [Google Scholar](#)

15. 15.

Kumar, N. et al. Adaptation of host transmission cycle during *Clostridium difficile* speciation. *Nat. Genet.* **51**, 1315–1320 (2019).

[CAS](#) [PubMed](#) [Google Scholar](#)

16. 16.

Di Rienzi, S. C. & Britton, R. A. Adaptation of the gut microbiota to modern dietary sugars and sweeteners. *Adv. Nutr.* **11**, 616–629 (2020).

[PubMed](#) [Google Scholar](#)

17. 17.

Tang, W. H., Martin, K. A. & Hwa, J. Aldose reductase, oxidative stress, and diabetic mellitus. *Front. Pharmacol.* **3**, 87 (2012).

[CAS](#) [PubMed](#) [PubMed Central](#) [Google Scholar](#)

18. 18.

Pal, P. B., Sonowal, H., Shukla, K., Srivastava, S. K. & Ramana, K. V. Aldose reductase mediates NLRP3 inflammasome-initiated innate immune response in hyperglycemia-induced Thp1 monocytes and male mice. *Endocrinology* **158**, 3661–3675 (2017).

[CAS](#) [PubMed](#) [PubMed Central](#) [Google Scholar](#)

19. 19.

Kashima, K., Sato, N., Sato, K., Shimizu, H. & Mori, M. Effect of epalrestat, an aldose reductase inhibitor, on the generation of oxygen-derived free radicals in neutrophils from streptozotocin-induced diabetic rats. *Endocrinology* **139**, 3404–3408 (1998).

[CAS](#) [PubMed](#) [Google Scholar](#)

20. 20.

Antunes, A. et al. Global transcriptional control by glucose and carbon regulator CcpA in *Clostridium difficile*. *Nucleic Acids Res.* **40**, 10701–10718 (2012).

[CAS](#) [PubMed](#) [PubMed Central](#) [Google Scholar](#)

21. 21.

Shakov, R., Salazar, R. S., Kagunye, S. K., Baddoura, W. J. & DeBari, V. A. Diabetes mellitus as a risk factor for recurrence of *Clostridium difficile* infection in the acute care hospital setting. *Am. J. Infect. Control* **39**, 194–198 (2011).

[PubMed](#) [Google Scholar](#)

22. 22.

Hassan, S. A., Rahman, R. A., Huda, N., Wan Bebakar, W. M. & Lee, Y. Y. Hospital-acquired *Clostridium difficile* infection among patients with type 2 diabetes mellitus in acute medical wards. *J. R. Coll. Physicians Edinb.* **43**, 103–107 (2013).

[CAS](#) [PubMed](#) [Google Scholar](#)

23. 23.

Ramana, K. V. Aldose reductase: new insights for an old enzyme. *Biomol. Concepts* **2**, 103–114 (2011).

[CAS](#) [PubMed](#) [PubMed Central](#) [Google Scholar](#)

24. 24.

The Tabula Muris Consortium. Single-cell transcriptomics of 20 mouse organs creates a *Tabula Muris*. *Nature* **562**, 367–372 (2018).

[ADS](#) [CAS](#) [Google Scholar](#)

25. 25.

Biton, M. et al. T helper cell cytokines modulate intestinal stem cell renewal and differentiation. *Cell* **175**, 1307–1320.e22 (2018).

[CAS](#) [PubMed](#) [PubMed Central](#) [Google Scholar](#)

26. 26.

Smillie, C. S. et al. Intra- and inter-cellular rewiring of the human colon during ulcerative colitis. *Cell* **178**, 714–730.e22 (2019).

[CAS](#) [PubMed](#) [PubMed Central](#) [Google Scholar](#)

27. 27.

D'Auria, K. M. et al. In vivo physiological and transcriptional profiling reveals host responses to *Clostridium difficile* toxin A and toxin B. *Infect. Immun.* **81**, 3814–3824 (2013).

[PubMed](#) [PubMed Central](#) [Google Scholar](#)

28. 28.

Whitaker, W. R., Shepherd, E. S. & Sonnenburg, J. L. Tunable expression tools enable single-cell strain distinction in the gut microbiome. *Cell* **169**, 538–546.e12 (2017).

[CAS](#) [PubMed](#) [PubMed Central](#) [Google Scholar](#)

29. 29.

Tang, J., Du, Y., Pettrash, J. M., Sheibani, N. & Kern, T. S. Deletion of aldose reductase from mice inhibits diabetes-induced retinal capillary degeneration and superoxide generation. *PLoS ONE* **8**, e62081 (2013).

[ADS](#) [CAS](#) [PubMed](#) [PubMed Central](#) [Google Scholar](#)

30. 30.

Ho, H. T. et al. Aldose reductase-deficient mice develop nephrogenic diabetes insipidus. *Mol. Cell. Biol.* **20**, 5840–5846 (2000).

[CAS](#) [PubMed](#) [PubMed Central](#) [Google Scholar](#)

31. 31.

Kuehne, S. A. et al. The role of toxin A and toxin B in *Clostridium difficile* infection. *Nature* **467**, 711–713 (2010).

[ADS](#) [CAS](#) [PubMed](#) [Google Scholar](#)

32. 32.

Kuehne, S. A. et al. Importance of toxin A, toxin B, and CDT in virulence of an epidemic *Clostridium difficile* strain. *J. Infect. Dis.* **209**, 83–86 (2014).

[CAS](#) [PubMed](#) [Google Scholar](#)

33. 33.

Karasawa, T., Ikoma, S., Yamakawa, K. & Nakamura, S. A defined growth medium for *Clostridium difficile*. *Microbiology* **141**, 371–375 (1995).

[CAS](#) [PubMed](#) [Google Scholar](#)

34. 34.

Ng, K. M. et al. Microbiota-liberated host sugars facilitate post-antibiotic expansion of enteric pathogens. *Nature* **502**, 96–99 (2013).

[ADS](#) [CAS](#) [PubMed](#) [PubMed Central](#) [Google Scholar](#)

35. 35.

Ng, Y. K. et al. Expanding the repertoire of gene tools for precise manipulation of the *Clostridium difficile* genome: allelic exchange using *pyrE* alleles. *PLoS ONE* **8**, e56051 (2013).

[ADS](#) [CAS](#) [PubMed](#) [PubMed Central](#) [Google Scholar](#)

36. 36.

Minton, N. P. et al. A roadmap for gene system development in *Clostridium*. *Anaerobe* **41**, 104–112 (2016).

[CAS](#) [PubMed](#) [PubMed Central](#) [Google Scholar](#)

37. 37.

Thompson, L. R. et al. A communal catalogue reveals Earth's multiscale microbial diversity. *Nature* **551**, 457–463 (2017).

[ADS](#) [CAS](#) [PubMed](#) [PubMed Central](#) [Google Scholar](#)

38. 38.

Caporaso, J. G. et al. Ultra-high-throughput microbial community analysis on the Illumina HiSeq and MiSeq platforms. *ISME J.* **6**, 1621–1624 (2012).

[CAS](#) [PubMed](#) [PubMed Central](#) [Google Scholar](#)

39. 39.

Caporaso, J. G. et al. QIIME allows analysis of high-throughput community sequencing data. *Nat. Methods* **7**, 335–336 (2010).

[CAS](#) [PubMed](#) [PubMed Central](#) [Google Scholar](#)

40. 40.

Love, M. I., Huber, W. & Anders, S. Moderated estimation of fold change and dispersion for RNA-seq data with DESeq2. *Genome Biol.* **15**, 550 (2014).

[PubMed](#) [PubMed Central](#) [Google Scholar](#)

41. 41.

Ge, S. X., Jung, D. & Yao, R. ShinyGO: a graphical gene-set enrichment tool for animals and plants. *Bioinformatics* **36**, 2628–2629

(2020).

[CAS](#) [PubMed](#) [Google Scholar](#)

42. 42.

McKenzie, A. T., Katsyy, I., Song, W. M., Wang, M. & Zhang, B. DGCA: A comprehensive R package for differential gene correlation analysis. *BMC Syst. Biol.* **10**, 106 (2016).

[PubMed](#) [PubMed Central](#) [Google Scholar](#)

43. 43.

Mi, H. et al. Protocol update for large-scale genome and gene function analysis with the PANTHER classification system (v.14.0). *Nat. Protoc.* **14**, 703–721 (2019).

[CAS](#) [PubMed](#) [PubMed Central](#) [Google Scholar](#)

44. 44.

R Core Team. R: a language and environment for statistical computing. <https://www.r-project.org/> (R Foundation for Statistical Computing, 2020).

45. 45.

Wickham, H. *ggplot2: Elegant Graphics for Data Analysis* 2nd edn (Springer, 2016).

[Download references](#)

## Acknowledgements

We thank S. Higginbottom for assistance with all mouse experiments. A. Chien assisted with the development of the GC–MS protocol; S. Kuehne and N. Minton provided the toxin-mutant *C. difficile* strains; A. Shen

provided reagents for the generation of new *C. difficile* mutants; A. Bhatnagar and D. Mosely provided the aldose reductase knockout mice; and D. Davis shared protocols and advice regarding the development of the streptozotocin model of hyperglycaemia. This study was supported by R01-DK08502510 (with thanks to B. Karp for service and support at NIDDK) and the Chan Zuckerberg Biohub, and a Ford Foundation Pre-Doctoral Fellowship and NSF Graduate Research Fellowship to K.M.P. We thank all members of the Sonnenburg laboratory, who provided feedback throughout the development of the project.

## Author information

### Affiliations

1. Department of Microbiology and Immunology, Stanford University School of Medicine, Stanford, CA, USA

Kali M. Pruss & Justin L. Sonnenburg

### Authors

1. Kali M. Pruss

[View author publications](#)

You can also search for this author in [PubMed](#) [Google Scholar](#)

2. Justin L. Sonnenburg

[View author publications](#)

You can also search for this author in [PubMed](#) [Google Scholar](#)

### Contributions

K.M.P. and J.L.S. conceived the project idea, designed the experiments and wrote the manuscript. K.M.P. executed the experiments and performed data analysis.

## Corresponding author

Correspondence to [Justin L. Sonnenburg](#).

## Ethics declarations

### Competing interests

The authors declare no competing interests.

## Additional information

**Peer review information** *Nature* thanks Lora Hooper and the other, anonymous, reviewer(s) for their contribution to the peer review of this work.

**Publisher's note** Springer Nature remains neutral with regard to jurisdictional claims in published maps and institutional affiliations.

## Extended data figures and tables

### [Extended Data Fig. 1 \*C. difficile\* toxin production confers an advantage and alters metabolic pathways in vivo.](#)

**a**, Toxin production (WT) confers an advantage in *C. difficile* relative abundance in the presence of a defined community ( $n = 5$  mice per group, mean  $\pm$  s.e.m., multiple unpaired *t*-tests with Welch's correction, two-stage step-up procedure of Benjamini, Krieger and Yekutieli.). **b**, Transcriptional profiling experimental design: germ-free mice on standard diet were mono-colonized with either wild-type *C. difficile* 630Δerm (WT) or 630ΔermTcdA<sup>-</sup>TcdB<sup>-</sup> (Tox<sup>-</sup>). Three days post-infection, total RNA was isolated from caecal contents for RNA-seq. Created with BioRender.com. **c**, **d**, Significantly enriched Ecocyc (c) and KEGG (d) pathways based on genes differentially expressed during wild-type (positive, red bars,  $n = 4$

mice) or Tox<sup>-</sup> *C. difficile* (negative, purple,  $n = 3$  mice) infection (hypergeometric distribution followed with FDR correction). [Source data](#)

**Extended Data Fig. 2 Sorbitol impacts *C. difficile* growth, gene expression, and increases in the mouse gut after antibiotic treatment.**

**a**, Schematic overview of the sorbitol utilization locus in *C. difficile*. The operon contains three PTS transporter subunits, a 6-phosphate dehydrogenase, an activator and an anti-terminator. **b**, Wild-type (red) and toxin-deficient (Tox<sup>-</sup>, purple) *C. difficile* grow comparably in minimal medium supplemented with various concentrations of sorbitol (mean  $\pm$  s.e.m.,  $n = 5$  replicates per condition). **c**, The  $\Delta srlD$  mutant is unable to achieve increased growth yield with 0.25% or 0.125% w/v sorbitol supplemented to minimal medium (mean  $\pm$  s.e.m.,  $n = 5$  replicates per condition). **d**, Addition of sorbitol to minimal medium leads to upregulation of genes in the operon (*srlD*, annotated as sorbitol dehydrogenase; *srlA*, PTS transporter subunit; *srlR*, transcription anti-terminator) compared to base medium (mean  $\pm$  s.e.m.,  $n = 3$  replicates per condition. Expression levels normalized to wild-type *C. difficile* in unsupplemented base medium, dotted line indicates baseline expression of 1; *srlD*: unpaired two-tailed *t*-test, *srlA* and *srlR*: one-way ANOVA with Tukey's post hoc comparisons; *srlA*:  $F_{(3,8)} = 31.85$ , *srlR*:  $F_{(3,8)} = 27.25$ ). **e**, Sorbitol administered to mice mono-colonized with wild-type *C. difficile* leads to induction of *srlD* in vivo (mean  $\pm$  s.e.m.,  $n = 4$  per group, unpaired two-tailed *t*-test). **f**, Clindamycin (1 mg) treatment ( $n = 5$ ) leads to increased sorbitol and mannitol in stool from conventional mice on standard diet ( $n = 3$ , mean  $\pm$  s.e.m., two-tailed Mann–Whitney *U*-test. Sorbitol levels were below the limit of detection for two of three pre-antibiotic treatment samples and are denoted by squares at a value of 1. Samples are combined from 3 independent experiments). **g**, The  $\Delta srlD$  *C. difficile* mutant is attenuated in colonization of conventional mice fed a standard diet compared to wild-type *C. difficile* ( $n = 5$  mice per group, mean  $\pm$  s.e.m., unpaired two-tailed *t*-test with Welch's correction). **h**, Toxin B detected by ELISA in faecal pellets of conventional mice 24 h post-infection with wild-type or  $\Delta srlD$  *C. difficile*; values were normalized to the absolute

abundance of *C. difficile* from the same stool sample ( $n = 5$  mice per group, mean  $\pm$  s.e.m., unpaired two-tailed *t*-test with Welch's correction). [Source data](#)

### **Extended Data Fig. 3 Dietary sorbitol or mannitol availability increases *C. difficile* density in vivo.**

**a**, Sorbitol (1%) (green,  $n = 4$  mice) or mannitol (1%) (purple,  $n = 5$  mice) were provided in drinking water to gnotobiotic mice harbouring a defined consortium of bacteria for 6 days (days 0–6). Absolute abundance of wild-type *C. difficile* decreases when sorbitol and mannitol are removed from drinking water (days 7–10). Replacing 1% sorbitol and mannitol in drinking water (days 11–14) restores the increase in absolute abundance (mean  $\pm$  s.e.m., shaded boxes denote sorbitol or mannitol supplementation). **b**, Sorbitol (1%) was provided in drinking water (days 0–6, green box) to mice colonized with a defined community and subsequently infected with  $\Delta$ srlD *C. difficile*. Supplementation of 1% mannitol in drinking water leads to an increase in abundance of the  $\Delta$ srlD mutant (days 11–14, purple box) relative to sorbitol supplementation (mean  $\pm$  s.e.m.,  $n = 5$  mice). **c**,  $\Delta$ srlD *C. difficile* ( $n = 5$  mice) incites a lower histopathological score than wild-type *C. difficile* ( $n = 4$  mice) when 1% sorbitol is supplemented in drinking water (12 days post-infection, mean  $\pm$  s.e.m., unpaired two-tailed Student's *t*-test). **d**, No significant differences in blinded histopathological scoring in the caecal blind tip of mice infected with wild-type *C. difficile* when sorbitol ( $n = 4$ ) or mannitol ( $n = 5$ ) is supplemented (as in **a**) or when mannitol is supplemented to  $\Delta$ srlD *C. difficile* (as in **b**,  $n = 5$ , 14 days post-infection, mean  $\pm$  s.e.m.). [Source data](#)

### **Extended Data Fig. 4 Excess sorbitol represses toxin production in vitro and in vivo.**

**a**, Minimal medium supplemented with 1% or 0.5% sorbitol leads to significantly lower expression of *tcdC* and *tcdA* after 8 h growth compared to un-supplemented base medium (mean  $\pm$  s.e.m.,  $n = 4$  replicates per condition. Two-way ANOVA across genes:  $F_{(3,36)} = 3.429$ ,  $P = 0.0271$ ; across sorbitol supplementations:  $F_{(2,36)} = 11.17$ ,  $P = 0.0002$  with Dunnett's

multiple comparisons test using base medium as the control for sorbitol supplementation comparisons within each gene). **b**, Presence of sorbitol ( $n = 4$  mice) or mannitol ( $n = 5$  mice) in drinking water leads to relatively lower toxin production in vivo (days 4 and 12, sugar alcohol supplementation denoted by shaded boxes) compared to when sorbitol or mannitol are absent (day 7; mean  $\pm$  s.e.m., mixed effects analysis with Sidak's multiple comparisons: day is significant  $F_{(0.8915,7.132)} = 18.37$ ,  $P = 0.004$ , mannitol versus sorbitol is not). **c**, Addition of exogenous mannitol (day 12) leads to lower production of toxin in vivo in the  $\Delta srlD$  mutant compared to sorbitol supplementation (days 1, 4) or regular water (day 7;  $n = 5$  mice, mean  $\pm$  s.e.m., one-way ANOVA  $F_{(2,8)} = 45.18$  with Tukey's post hoc multiple comparisons. Day 4 was excluded from the ANOVA, as only 2 data points are present). [Source data](#)

### **Extended Data Fig. 5 Streptozotocin treatment increases fasting blood glucose levels in conventional and mono-colonized mice.**

**a**, Development of streptozotocin (STZ)-induced hyperglycaemia model in Swiss-Webster Excluded Flora mice. Mice were fasted for 4–6 h before measurement of blood glucose levels via tail vein snip. An initial injection (day 0, indicated by dashed arrow) of 4.5 mg STZ was insufficient to increase blood glucose levels. A larger dose of 9.1 mg STZ administered on day 4 (solid arrow) was sufficient to increase blood glucose (mean  $\pm$  s.e.m.,  $n = 6$  mice) and was used for subsequent experiments with *C. difficile* infection. **b**, Unfasted blood glucose in germ-free mice mono-colonized with wild-type or  $\Delta srlD$  at 3 days post-infection (mean  $\pm$  s.e.m., one-way ANOVA  $F_{(3,20)} = 36.73$  with Tukey's post hoc comparisons); STZ-treated groups ( $n = 7$  mice per group) were treated with STZ via intraperitoneal injection 4 days before *C. difficile* infection and had significantly increased blood glucose compared to untreated controls ( $n = 5$  per group). **c**, *C. difficile* gene expression of the sorbitol utilization locus in conventional (wild-type) or streptozotocin-treated (STZ) mice. An outlier (Fig. 3c, tested for with robust nonlinear regression,  $Q = 0.2\%$ ) from one RNA sample isolated from one mouse is indicated by the filled circle ( $n = 5$  mice per group, bars denote median). **d**, Streptozotocin treatment does not alter toxin

production in vivo. *C. difficile* toxin B quantified in the faeces of conventional mice infected with wild-type *C. difficile* 24 h post-infection ( $n = 5$  mice per group, mean  $\pm$  s.e.m.). [Source data](#)

### **Extended Data Fig. 6 Sorbitol and mannitol lead to distinct metabolic programs in vitro.**

**a**, Chemical structures of isomers sorbitol and mannitol. **b**, Sorbitol and mannitol added to minimal medium engender distinct growth kinetics (mean  $\pm$  s.e.m.,  $n = 5$  replicates per condition). **c**, Principal component analysis of variance stabilizing-transformed RNA-seq counts from *C. difficile* grown for 11 h in minimal medium (control, grey), or minimal medium supplemented with 0.25% sorbitol (green), mannitol (purple) or glucose (yellow). **d**, Significantly differentially expressed genes between sorbitol supplementation and base medium or mannitol supplementation ( $n = 3$  replicates per condition; colours represent row-normalized variance stabilizing-transformed counts.  $P < 0.01$ , Wald test with Bonferroni-adjusted  $P$  value.) **e**, Mannitol supplementation to 0.3% soft agar plates leads to significantly increased motility compared to base medium (days 3–6) and sorbitol supplementation (day 5). Sorbitol supplementation does not lead to a significant increase in motility compared to unsupplemented motility plates ( $n = 4$  replicates per condition, mean  $\pm$  s.e.m., two-way ANOVA significant by day  $F_{(4,44)} = 53.50$  and growth condition  $F_{(2,44)} = 25.55$ , Tukey's post hoc comparisons). [Source data](#)

### **Extended Data Fig. 7 Aldose reductase is an immune cell-associated gene.**

**a**, Top 10 cell types with highest *Akr1b3* expression across 20 mouse organs demonstrates high prevalence of aldose reductase in immune-associated cell types<sup>24</sup>. **b**, Percentage of cells in mouse colonic tissue expressing isoforms of aldose reductase and sorbitol dehydrogenase. **c**, Percentage of different cell types in human colonic explants expressing the three isoforms of aldose reductase and sorbitol dehydrogenase. **d**, *Akr1b1* expression ( $\log_2$ -TP10K+1) in cell types exhibiting significantly increased aldose reductase expression in inflammatory colonic explants from patients with ulcerative

colitis (inflamed) compared to within-subject non-inflamed tissue (uninflamed) versus healthy controls that do not have ulcerative colitis (healthy; pairwise Wilcoxon-rank sum test across all immune cell types using non-zero expression levels. Means for each cell type are shown). **e**, Dendritic cells (DC) and plasma cells in mouse large intestine exhibited a significant increase in *Akr1b3* expression ( $\log_2$ -TPM+1) during infection with *H. polygyrus* (Wilcoxon-rank sum test across all immune cell types using non-zero expression levels. Means for each cell type shown). **f**, Expression of *Akr1b3* in the proximal colon of conventional mice infected with wild-type *C. difficile*. An outlier (Fig. 3e, detection method: robust nonlinear regression,  $Q = 0.2\%$ ) is denoted by the filled point, bars denote median. [Source data](#)

### **Extended Data Fig. 8 Epalrestat inhibits *C. difficile* growth in vitro and in vivo.**

**a**, Germ-free mice were mono-colonized with wild-type *C. difficile* and gavaged with the aldose reductase inhibitor epalrestat or vehicle control once per day. Epalrestat treatment significantly reduces *C. difficile* abundance ( $n = 5$  mice per group, mean  $\pm$  s.e.m., unpaired two-tailed *t*-tests). **b**, In the presence of epalrestat, wild-type *C. difficile* produces relatively more toxin in vivo ( $n = 5$  mice per group, mean  $\pm$  s.e.m., unpaired two-tailed *t*-test). **c**, The  $\Delta srlD$  mutant colonizes germ-free mice fed standard diet equally well as does wild-type *C. difficile* ( $n = 5$  mice per group, mean  $\pm$  s.e.m.). **d**, Epalrestat inhibits growth of wild-type *C. difficile* 630 $\Delta erm$  in rich medium in a dose-dependent manner ( $n = 5$  replicates per condition, mean  $\pm$  s.e.m.). **e**, Absolute abundance of wild-type *C. difficile* after 6 h or 12 h of growth in rich medium is inhibited due to incubation with epalrestat (mean  $\pm$  s.e.m.,  $n = 3$  replicates per condition). **f**, Chemical structures of aldose reductase inhibitor epalrestat and an antibiotic with activity against *cis*-prenyl transferase undecaprenyl diphosphate synthase (UPPS). [Source data](#)

### **Extended Data Fig. 9 A model of sorbitol utilization by *C. difficile*.**

*C. difficile* can utilize diet-derived sorbitol, which spikes after disturbance to the microbiota (left). Toxin-induced tissue damage (right) leads to upregulation of host aldose reductase in the epithelium as well as recruitment of immune cells that express aldose reductase. *C. difficile* is able to utilize host-derived sorbitol. Created with BioRender.com.

## Supplementary information

### Supplementary Information

This file contains additional discussion of results for Extended Data Figs. 6 and 8.

### Reporting Summary

### Supplementary Table 1

Detailed results of blinded histopathological scoring for mice mono-colonized with WT or Tox- *Cd*.

### Supplementary Table 2

DESeq2 *in vivo* differential gene expression analysis from mice mono-associated with WT or Tox- *Cd*.

### Supplementary Table 3

*In vitro* differential gene expression analysis comparing different carbohydrate supplements to minimal medium.

### Supplementary Table 4

A list of primers used in the study.

## Source data

[\*\*Source Data Fig. 1\*\*](#)

[\*\*Source Data Fig. 2\*\*](#)

[\*\*Source Data Fig. 3\*\*](#)

[\*\*Source Data Fig. 4\*\*](#)

[\*\*Source Data Extended Data Fig. 1\*\*](#)

[\*\*Source Data Extended Data Fig. 2\*\*](#)

[\*\*Source Data Extended Data Fig. 3\*\*](#)

[\*\*Source Data Extended Data Fig. 4\*\*](#)

[\*\*Source Data Extended Data Fig. 5\*\*](#)

[\*\*Source Data Extended Data Fig. 6\*\*](#)

[\*\*Source Data Extended Data Fig. 7\*\*](#)

[\*\*Source Data Extended Data Fig. 8\*\*](#)

## Rights and permissions

[Reprints and Permissions](#)

## About this article



Check for  
updates

## Cite this article

Pruss, K.M., Sonnenburg, J.L. *C. difficile* exploits a host metabolite produced during toxin-mediated disease. *Nature* **593**, 261–265 (2021). <https://doi.org/10.1038/s41586-021-03502-6>

[Download citation](#)

- Received: 17 March 2020
- Accepted: 26 March 2021
- Published: 28 April 2021
- Issue Date: 13 May 2021
- DOI: <https://doi.org/10.1038/s41586-021-03502-6>

## Comments

By submitting a comment you agree to abide by our [Terms](#) and [Community Guidelines](#). If you find something abusive or that does not comply with our terms or guidelines please flag it as inappropriate.

[Access through your institution](#)

[Change institution](#)

[Buy or subscribe](#)

---

This article was downloaded by **calibre** from <https://www.nature.com/articles/s41586-021-03502-6>

Assessing transmissibility of SARS-CoV-2 lineage B.1.1.7 in England

[Download PDF](#)

- Article
- [Published: 25 March 2021](#)

# Assessing transmissibility of SARS-CoV-2 lineage B.1.1.7 in England

- [Erik Volz](#) [ORCID: orcid.org/0000-0001-6268-8937](#)<sup>1 na1</sup>,
- [Swapnil Mishra](#) [ORCID: orcid.org/0000-0002-8759-5902](#)<sup>1 na1</sup>,
- [Meera Chand](#)<sup>2 na1</sup>,
- [Jeffrey C. Barrett](#)<sup>3 na1</sup>,
- [Robert Johnson](#)<sup>1 na1</sup>,
- [Lily Geidelberg](#) [ORCID: orcid.org/0000-0002-8057-1844](#)<sup>1</sup>,
- [Wes R. Hinsley](#)<sup>1</sup>,
- [Daniel J. Laydon](#) [ORCID: orcid.org/0000-0003-4270-3321](#)<sup>1</sup>,
- [Gavin Dabrera](#)<sup>2</sup>,
- [Áine O'Toole](#)<sup>4</sup>,
- [Robert Amato](#)<sup>3</sup>,
- [Manon Ragonnet-Cronin](#)<sup>1</sup>,
- [Ian Harrison](#)<sup>2</sup>,
- [Ben Jackson](#) [ORCID: orcid.org/0000-0002-9981-0649](#)<sup>4</sup>,
- [Cristina V. Ariani](#)<sup>3</sup>,
- [Olivia Boyd](#)<sup>1</sup>,
- [Nicholas J. Loman](#)<sup>2,5</sup>,
- [John T. McCrone](#)<sup>4</sup>,
- [Sónia Gonçalves](#)<sup>3</sup>,
- [David Jorgensen](#)<sup>1</sup>,
- [Richard Myers](#)<sup>2</sup>,
- [Verity Hill](#)<sup>4</sup>,
- [David K. Jackson](#)<sup>3</sup>,
- [Katy Gaythorpe](#) [ORCID: orcid.org/0000-0003-3734-9081](#)<sup>1</sup>,
- [Natalie Groves](#)<sup>2</sup>,
- [John Sillitoe](#)<sup>3</sup>,
- [Dominic P. Kwiatkowski](#) [ORCID: orcid.org/0000-0002-5023-0176](#)<sup>3</sup>,

- [The COVID-19 Genomics UK \(COG-UK\) consortium](#),
- [Seth Flaxman ORCID: orcid.org/0000-0002-2477-4217<sup>6</sup>](#),
- [Oliver Ratmann<sup>6</sup>](#),
- [Samir Bhatt<sup>1,7</sup>](#),
- [Susan Hopkins<sup>2</sup>](#),
- [Axel Gandy ORCID: orcid.org/0000-0002-6777-0451<sup>6 na1</sup>](#),
- [Andrew Rambaut ORCID: orcid.org/0000-0003-4337-3707<sup>4 na1</sup>](#) &
- [Neil M. Ferguson ORCID: orcid.org/0000-0002-1154-8093<sup>1 na1</sup>](#)

[Nature](#) volume 593, pages 266–269 (2021)[Cite this article](#)

- 15k Accesses
- 7 Citations
- 571 Altmetric
- [Metrics details](#)

## Subjects

- [Population genetics](#)
- [SARS-CoV-2](#)
- [Viral infection](#)

## Abstract

The SARS-CoV-2 lineage B.1.1.7, designated variant of concern (VOC) 202012/01 by Public Health England<sup>1</sup>, was first identified in the UK in late summer to early autumn 2020<sup>2</sup>. Whole-genome SARS-CoV-2 sequence data collected from community-based diagnostic testing for COVID-19 show an extremely rapid expansion of the B.1.1.7 lineage during autumn 2020, suggesting that it has a selective advantage. Here we show that changes in VOC frequency inferred from genetic data correspond closely to changes inferred by *S* gene target failures (SGTF) in community-based diagnostic PCR testing. Analysis of trends in SGTF and non-SGTF case numbers in local areas across England shows that B.1.1.7 has higher transmissibility than non-VOC lineages, even if it has a different latent period or generation time. The SGTF data indicate a transient shift in the age composition of reported cases, with cases of B.1.1.7 including a larger share of under 20-year-olds than non-VOC cases. We estimated time-varying reproduction numbers for B.1.1.7 and co-circulating lineages using SGTF and genomic data. The best-supported models did not indicate a substantial difference in

VOC transmissibility among different age groups, but all analyses agreed that B.1.1.7 has a substantial transmission advantage over other lineages, with a 50% to 100% higher reproduction number.

[Download PDF](#)

## Main

The SARS-CoV-2 lineage B.1.1.7 spread rapidly across England between November 2020 and January 2021. This variant possesses a large number of non-synonymous substitutions of immunological importance<sup>2</sup>. The N501Y replacement on the spike protein has been shown to increase ACE2 binding<sup>3,4</sup> and cell infectivity in animal models<sup>5</sup>, and the P618H replacement on the spike protein adjoins the furin-cleavage site<sup>6</sup>. B.1.1.7 also possesses a deletion at positions 69 and 70 of the spike protein ( $\Delta 69-70$ ) that has been associated with failure of diagnostic tests using the ThermoFisher TaqPath probe, which targets the spike protein<sup>7</sup>. Although other variants with  $\Delta 69-70$  are also circulating in the UK, the absence of detection of the *S* gene target in an otherwise positive PCR test appears to be a highly specific biomarker for the B.1.1.7 lineage. Data from national community testing in November 2020 showed a rapid increase in SGTF during PCR testing for SARS-CoV-2, coinciding with a rapid increase in the frequency of B.1.1.7 observed in genomic surveillance. The B.1.1.7 lineage was designated VOC 202012/01 by Public Health England (PHE) in December 2020.

Phylogenetic studies carried out by the UK COVID-19 Genomics Consortium (COG-UK) (<https://www.cogconsortium.uk>)<sup>8</sup> provided the first indication that B.1.1.7 has an unusual accumulation of substitutions and was growing at a higher rate than other circulating lineages. We investigated time trends in the frequency of sampling VOC genomes and the proportion of PCR tests exhibiting SGTF across the UK, which we calibrated as a biomarker of VOC infection. Using multiple approaches and both genetic and SGTF data, we conclude that B.1.1.7 is associated with a higher reproduction number ( $R$ ) than previous non-VOC lineages.

We examined whole-genome SARS-CoV-2 sequences from randomly sampled residual materials obtained from community-based COVID-19 testing in England, collected between 1 October 2020 and 16 January 2021. These data included 31,390 B.1.1.7 sequences for which the time and location of sample collection were known. Over the same period, 52,795 non-VOC genomes were collected. VOC sequences were initially concentrated in London ( $n = 9,134$ ), the South East ( $n = 5,609$ ), and the East of England ( $n = 4,413$ ), but is now widely distributed across England. Overall, we estimate the median posterior additive difference in growth rates between B.1.1.7 and co-circulating variants to be 0.69 per week (95% credible interval (CrI) 0.61–0.76)

(Fig. 1a, Extended Data Fig. 1, Supplementary Methods section 2), and this difference was largest in November. However, in tandem with geographic expansion of the VOC and imposition of lockdown measures in 2021, this difference declined gradually to 0.43 per week (95% CrI 0.33–0.52) for the week ending 16 January.

**Fig. 1: Expansion of lineage B.1.1.7 relative to co-circulating lineages in England.**



**a**, Estimated frequency of sampling the VOC (lines) over time in NHS regions ( $n = 84,185$ ). Shaded regions, 95% credible region based on Bayesian regression; points, empirical proportions of the VOC in each week; error bars, 95% CI based on binomial sampling error. **b**, Effective population size over time for lineage B.1.1.7 and estimates based on a matched sample of the most abundant co-circulating lineage, B.1.177 ( $n = 3,000$ ). Shaded regions, 95% bootstrap CI. **c**, The effective reproduction number inferred from growth of effective population size for both lineages in **b**.

[Full size image](#)

The rate of genetic diversification of the VOC lineage over time allows epidemic growth rates to be estimated using phylodynamic modelling<sup>9,10</sup>. To contrast VOC and non-VOC growth patterns, we randomly sampled 3,000 VOC sequences paired with up to 3,000 non-VOC sequences and matched by week of sample collection and location (Supplementary Methods section 1). Phylodynamic modelling (Supplementary Methods section 3) of the effective population sizes of B.1.1.7 and the previously dominant non-VOC B.1.177 lineage<sup>11</sup> gave an estimated growth rate difference of 0.33 per week (95% confidence interval (CI) 0.09–0.62), and further indicated that the VOC overtook the B.1.177 lineage on 10 December (Fig. 1b), close to the date at which VOC sampling frequency exceeded 50% in England (3 December). Thus, we estimate that B.1.1.7 reached 50% frequency within 2.5 to 3 months after its emergence in England.

We estimated the ratio of VOC to non-VOC reproduction numbers using a renewal equation based approach (Fig. 1c, Extended Data Fig. 2, Supplementary Methods section 4). This estimator depends on the absolute growth rate of the non-VOC, estimated using the phylodynamic model. We estimate the ratio of reproduction numbers between 25 October 2020 and 16 January 2021 to be 1.89 (95% CrI 1.43–2.65), assuming a gamma-distributed generation time with mean 6.4 days and coefficient of variation of 0.66<sup>12</sup>. This ratio is sensitive to the assumption that the generation time distribution is identical between variants. However, even if the VOC generation time is half that of previous variants, the estimated ratio of reproduction numbers was still 1.53 (95% CrI 1.27–1.79). The ratio trended downwards over time, coinciding with the increasing frequency of the VOC. By mid-January, the ratio had fallen from 1.89 to 1.54 (95% CrI 1.34–1.82) (Extended Data Fig. 2).

## Trends in SGTF attributed to the VOC

Infection with the VOC lineage results in a diagnostic failure on the *S* gene target in an otherwise positive PCR test using the ThermoFisher TaqPath assay, which is widely used for SARS-CoV-2 community PCR testing in the UK. Consequently, we gained a more detailed picture of the spatial and demographic spread of B.1.1.7 by using the

much more abundant diagnostic data with SGTF than by using whole-genome sequencing only. Several SARS-CoV-2 variants can result in SGTF, but since mid-November 2020, more than 97% of PCR tests with SGTF were due to the B.1.1.7 lineage<sup>1</sup>. Approximately 35% of positive test results in UK community PCR testing use the TaqPath assay, and so provide *S* gene target results. Before mid-November 2020, SGTF frequency among PCR positives was a poor proxy for VOC frequency. We therefore developed a spatiotemporal model to predict the proportion of SGTF cases attributable to the VOC by area and week (Supplementary Methods section 5), here termed the true positive proportion (TPP). False positives were attributed to the *S*-gene-positive case (*S*+) category. We found that the effective population size for B.1.1.7 effective population size was highly correlated with TPP-adjusted *S* counts (Extended Data Fig. 3).

Figure 2a–c (and Supplementary Data 1, Extended Data Fig. 4) shows the spatiotemporal trends of SGTF cases (*S*–), *S*+ and total PCR-positive cases by National Health Service (NHS) England Sustainability and Transformation Plan (STP) areas (a geographical subdivision of NHS regions). Visually, it is clear that during the second England lockdown, when schools were open, *S*+ case numbers decreased but *S*– case numbers increased. However, during the third lockdown, when schools were closed, the incidence of both *S*– and *S*+ cases declined.

**Fig. 2: Trends of diagnosed cases and SGTF over time and between regions, and reproduction numbers of the VOC inferred from SGTF.**

---

 **figure2**

**a–c**, The number of diagnosed cases over time for three English STP regions that represent a wide spectrum of outcomes in terms of time of VOC introduction into the region. Each line segment is shaded with the frequency of SGTF in each week (scale at top). Vertical shaded regions represent the times of the second and third UK lockdowns. **d**, The estimated (Bayesian posterior) multiplicative transmission advantage of the VOC over time inferred from STP-level SGTF count data. Shaded regions, 95% CrI. **e**, The reproduction number of *S*-gene-negative cases versus the reproduction number of *S*-gene-positive cases over time and among STP regions for epidemiological weeks 45–55 (1 November 2020 to 16 January 2021).

[Full size image](#)

Using TPP-corrected SGTF frequencies applied to overall PHE case numbers, we jointly estimated weekly effective reproduction numbers ( $R_t$ ) values for the VOC and non-VOC in each of the 42 STP areas using a semi-mechanistic epidemiological model<sup>13</sup> (Supplementary Methods section 6). The model parametrizes VOC  $R_t$  as a multiple of non-VOC  $R_t$ . The model was fitted to case numbers obtained by multiplying overall PHE case numbers by TPP-corrected SGTF frequencies. We estimated  $R_t$  for epidemiological weeks 45–55 (1 November 2020 to 16 January 2021) (Fig. 2d), as before November there were insufficient VOC cases to reliably estimate VOC reproduction numbers across England. VOC  $R_t$  was greater than non-VOC  $R_t$  for all STP–week pairs (points above the diagonal in Fig. 2e). The estimated mean ratio of  $R_t$  for the VOC and non-VOC strains was 1.79 (95% CI 1.22–2.49) over weeks 45–55. As in the phylodynamic analysis, the multiplicative advantage in  $R_t$  for the VOC declined over the time window examined, to approximately 1.5 in week 55 (Fig. 2d).

The greater  $R_t$  estimates of the VOC, even where  $R_t$  of non-VOC variants was below 1, indicates that B.1.1.7 has a transmission advantage, and that the observed frequency trends cannot be explained solely by a reduction in the mean generation time. We repeated the joint estimation of VOC and non-VOC  $R_t$  with the assumption of a 25% reduction in the mean generation time of the VOC (Extended Data Fig. 5), and this estimated the mean ratio of  $R_t$  to be 1.60 (95% CI 1.09–2.23) over weeks 45–55. Incorporating a shorter generation time for the VOC into the model reduced, but did not eliminate, the decreasing trend in transmission advantage over time.

To test whether VOC transmissibility differed by age, we first examined the age distributions of S+ and S– cases. Case numbers were age-standardized at STP area level, and then case age distributions were calculated for each STP–week (Supplementary Methods section 7). Figure 3 shows that individuals aged 19–49 years were the only age group that was consistently over-represented among observed cases relative to their share in the population (40%), with little difference between VOC and non-VOC cases. Secondary school-aged children (11–18 years) were also over-represented among observed cases relative to their share in the population (9%), and the difference between VOC and non-VOC cases was statistically significant for three weeks in November (Fig. 3, Extended Data Fig. 6). This period coincides with the second England lockdown (5 November to 2 December 2020) when schools remained open, and the differing age distributions between variants could arise from altered contact patterns when children were at greater risk of infection from all variants compared to adults.

**Fig. 3: Age distribution of S-gene-positive and -negative cases over time in England.**

---

 figure3

Observed cases were age-standardized at the level of the STP area, and age distributions were calculated for each week in STP areas and then aggregated. Shaded regions, CIs computed by bootstrapping over STP areas within NHS regions for each week.

[Full size image](#)

Next, we formulated models that incorporated a difference in VOC transmission between age groups (Supplementary Methods section 7). The models were fitted variously to genome-derived and/or SGTF-derived VOC frequencies, as well as total age-specific cases in each week and region, and compared using Bayesian leave-one-out cross-validation.

Model comparison consistently favoured models that allowed the transmission advantage to vary over time and between regions, using either genomic or SGTF data. However, models that incorporated an age effect were not significantly favoured (Extended Data Table 1). Indeed, the observed fluctuations in the age distribution are equally well captured by models that do not incorporate age-specific transmission advantages (Extended Data Fig. 6). We also used these model comparisons to test the hypothesis that differences in the VOC growth rates are a consequence of a reduced generation time in B.1.1.7. In principle it is possible to statistically identify such a difference, because the data cover a period during which the overall  $R_t$  has been above and below one. Models that incorporate a change in the mean generation time were sometimes favoured (Extended Data Table 1), but the estimated ratio of mean generation times was not well identified—it varied between 0.75 and 0.96, depending on the model and data being fitted to. The mean ratio of  $R_t$  between the VOC and non-VOC ranged between 1.6 and 2.01, depending on model variant. The best fit model to both SGTF and genomic data gave an estimate of 1.74 (95% CrI 1.03–2.75), which is highly consistent with the estimates obtained from the phylodynamic analysis and the direct estimation of  $R_t$  for VOC and non-VOC described above. This model also reproduces the decline in transmission advantage over time seen in our other analyses (Extended Data Fig. 7).

## Discussion

While substitutions in the B.1.1.7 lineage are associated with substantial changes in viral phenotype<sup>3,4,5,14</sup>, the extent to which these substitutions lead to meaningful differences in transmission between humans is unclear, and cannot be evaluated experimentally. When randomized experimental studies are not possible, observational studies provide strong evidence if consistent patterns are seen in multiple locations and at multiple times. Increasing frequency of a new lineage is consistent with a selective advantage, but changes in frequency result from founder effects, especially for genetic variants that are repeatedly introduced from overseas<sup>11,15</sup>. However, in contrast to previous variants that have achieved high prevalence, we see expansion of the VOC from within the UK.

We find some evidence that the multiplicative transmission advantage of B.1.1.7 (that is, ratio of reproduction numbers) declined in late December 2020 to January 2021, coincident with stricter social distancing, school closures, and the subsequent third England lockdown (Fig. 2d, Extended Data Figs. 2, 6). A number of mechanisms could generate this effect. First, a shorter generation time of the VOC would reduce the ratio of VOC to non-VOC growth rates for small values of the non-VOC growth rate. Thus as interventions reduce both reproduction numbers, their ratio would decline, even in the absence of any underlying change in transmission advantage. Some weak support for this hypothesis is provided by our age-specific model fits to SGTF data, where model comparison generally favours models that include a change in mean generation time (Extended Data Table 1). Second, social distancing changes human contact networks, reducing the number of people contacted per day, but increasing the duration and proximity of remaining (mostly household) contacts. In such circumstances, saturation of transmission probabilities can lead to a reduction in the transmission advantage of the VOC (Extended Data Fig. 8, Supplementary Methods section 7). The observation that secondary attack rates in contacts identified through routine national contact tracing were 30–40% higher for the VOC than for non-VOC cases<sup>16</sup> provides some support for this hypothesis, given that the large majority of contacts identified through the UK Test and Trace system are household contacts.

The data included in this study were collected as part of routine surveillance of community testing and are not representative of SARS-CoV-2 infections in England. However, previous comparisons of community case data to random household prevalence surveys have shown very strong agreement in epidemic trends<sup>17,18</sup>. Furthermore, estimates of the growth advantage of B.1.1.7 obtained during earlier iterations of this study<sup>1</sup> have largely been predictive of its subsequent spread in January, both in the UK and internationally. Independent observations of secondary attack rates inferred from UK contact tracing data have confirmed these findings<sup>19</sup>.

The substantial transmission advantage that we and others<sup>20,21</sup> have estimated has increased the challenges in controlling COVID-19. The B.1.1.7 lineage was identified quickly owing to extensive genomic surveillance in the UK, but other lineages with similar concerning features<sup>22,23</sup> have emerged almost concurrently, and lineages with similar features may be circulating undetected. Improving global genomic surveillance will be important for the control of COVID-19 in the presence of multiple emerging lineages with enhanced transmission or potential for immune escape.

## Reporting summary

Further information on research design is available in the [Nature Research Reporting Summary](#) linked to this paper.

## Data availability

All data used in this study, including SGTF and genome counts aggregated by region and week and multiple sequence alignments, have been deposited in Zenodo at <https://doi.org/10.5281/zenodo.4593885>.

## Code availability

The Zenodo repository <https://doi.org/10.5281/zenodo.4593885> includes code to reproduce all figures and results presented here.

## References

1. 1.

Public Health England Investigation of novel SARS-CoV-2 variant 202012/01: technical briefing 1 <https://www.gov.uk/government/publications/investigation-of-novel-sars-cov-2-variant-variant-of-concern-20201201> (2020).

2. 2.

Rambaut, A. et al. Preliminary genomic characterisation of an emergent SARS-CoV-2 lineage in the UK defined by a novel set of spike mutations. <https://virological.org/t/preliminary-genomic-characterisation-of-an-emergent-sars-cov-2-lineage-in-the-uk-defined-by-a-novel-set-of-spike-mutations/563> (2020).

3. 3.

Chan, K. K., Tan, T. J. C., Narayanan, K. K. & Procko, E. An engineered decoy receptor for SARS-CoV-2 broadly binds protein S sequence variants. *Sci. Adv.* **7**, eabf1738 (2021).

4. 4.

Starr, T. N. et al. Deep mutational scanning of SARS-CoV-2 receptor binding domain reveals constraints on folding and ACE2 binding. *Cell* **182**, 1295–1310.e20 (2020).

[CAS](#) [Article](#) [Google Scholar](#)

5. 5.

Gu, H. et al. Adaptation of SARS-CoV-2 in BALB/c mice for testing vaccine efficacy. *Science* **369**, 1603–1607 (2020).

[ADS](#) [CAS](#) [Article](#) [Google Scholar](#)

6. 6.

Peacock, T. P., Goldhill, D. H., Zhou, J., Baillon, L. & Frise, R. The furin cleavage site of SARS-CoV-2 spike protein is a key determinant for transmission due to enhanced replication in airway cells. Preprint at <https://doi.org/10.1101/2020.09.30.318311> (2020).

7. 7.

Bal, A. et al. Screening of the H69 and V70 deletions in the SARS-CoV-2 spike protein with a RT-PCR diagnosis assay reveals low prevalence in Lyon, France. Preprint at <https://doi.org/10.1101/2020.11.10.20228528> (2020).

8. 8.

The COVID-19 Genomics UK (COG-UK) consortium. An integrated national scale SARS-CoV-2 genomic surveillance network. *The Lancet Microbe* **1**, E99–E100 (2020).

[Article](#) [Google Scholar](#)

9. 9.

Pybus, O. G. & Rambaut, A. Evolutionary analysis of the dynamics of viral infectious disease. *Nat. Rev. Genet.* **10**, 540–550 (2009).

[CAS](#) [Article](#) [Google Scholar](#)

10. 10.

Volz, E. M., Koelle, K. & Bedford, T. Viral phylodynamics. *PLoS Comput. Biol.* **9**, e1002947 (2013).

[CAS](#) [Article](#) [Google Scholar](#)

11. 11.

Hodcroft, E. B. et al. Emergence and spread of a SARS-CoV-2 variant through Europe in the summer of 2020. Preprint at

<https://doi.org/10.1101/2020.10.25.20219063> (2020).

12. 12.

Bi, Q. et al. Epidemiology and transmission of COVID-19 in 391 cases and 1286 of their close contacts in Shenzhen, China: a retrospective cohort study. *Lancet Infect. Dis.* **20**, 911–919 (2020).

[CAS Article](#) [Google Scholar](#)

13. 13.

Mishra, S. et al. A COVID-19 model for local authorities of the United Kingdom. Preprint at <https://doi.org/10.1101/2020.11.24.20236661> (2020).

14. 14.

Kemp, S. et al. Recurrent emergence and transmission of a SARS-CoV-2 spike deletion ΔH69/V70. Preprint at <https://doi.org/10.1101/2020.12.14.422555> (2020).

15. 15.

du Plessis, L. et al. Establishment & lineage dynamics of the SARS-CoV-2 epidemic in the UK. *Science* **371**, 708–712 (2021).

[ADS Article](#) [Google Scholar](#)

16. 16.

Public Health England. Investigation of novel SARS-CoV-2 variant: Variant of Concern 202012/01: technical briefing 3.

[https://assets.publishing.service.gov.uk/government/uploads/system/uploads/attachment\\_data/file/959360/Variant\\_of\\_Concern\\_VOC\\_202012\\_01\\_Technical\\_Briefing\\_3.pdf](https://assets.publishing.service.gov.uk/government/uploads/system/uploads/attachment_data/file/959360/Variant_of_Concern_VOC_202012_01_Technical_Briefing_3.pdf) (2021).

17. 17.

REACT Study Investigators et al. Resurgence of SARS-CoV-2 in England: detection by community antigen surveillance. Preprint at <https://doi.org/10.1101/2020.09.11.20192492> (2020).

18. 18.

Riley, S. et al. REACT-1 round 9 interim report: downward trend of SARS-CoV-2 in England in February 2021 but still at high prevalence. Preprint at <https://doi.org/10.1101/2021.02.18.21251973> (2021).

19. 19.

Public Health England. Investigation of novel SARS-CoV-2 variant: Variant of Concern 202012/01: technical briefing 5.

[https://assets.publishing.service.gov.uk/government/uploads/system/uploads/attachment\\_data/file/957504/Variant\\_of\\_Concern\\_VOC\\_202012\\_01\\_Technical\\_Briefing\\_5\\_England.pdf](https://assets.publishing.service.gov.uk/government/uploads/system/uploads/attachment_data/file/957504/Variant_of_Concern_VOC_202012_01_Technical_Briefing_5_England.pdf) (2021).

20. 20.

Leung, K., Shum, M. H., Leung, G. M., Lam, T. T. & Wu, J. T. Early transmissibility assessment of the N501Y mutant strains of SARS-CoV-2 in the United Kingdom, October to November 2020. *Euro Surveill.* **26**, 2002106 (2021).

[Article](#) [Google Scholar](#)

21. 21.

Davies, N. G. et al. Estimated transmissibility and impact of SARS-CoV-2 lineage B.1.1.7 in England. Preprint at <https://doi.org/10.1101/2020.12.24.20248822> (2020).

22. 22.

Tegally, H. et al. Emergence of a SARS-CoV-2 variant of concern with mutations in spike glycoprotein. *Nature* <https://doi.org/10.1038/s41586-021-03402-9> (2021).

23. 23.

Sabino, E. C. et al. Resurgence of COVID-19 in Manaus, Brazil, despite high seroprevalence. *Lancet* **397**, 452–455 (2021).

[CAS Article](#) [Google Scholar](#)

[Download references](#)

## Acknowledgements

We thank all partners and contributors to the COG-UK consortium who are listed at <https://www.cogconsortium.uk/about/>. We thank the Sanger Covid Team (<https://www.sanger.ac.uk/covid-team>) for data preparation and feedback on the manuscript. COG-UK is supported by funding from the Medical Research Council (MRC) part of UK Research & Innovation (UKRI), the National Institute of Health Research (NIHR) and Genome Research Limited, operating as the Wellcome Sanger Institute. N.M.F., E.V., M.R. and S.B. acknowledge support from the MRC Centre for Global Infectious Disease Analysis (MR/R015600/1). R.J. and E.V. acknowledge funding from the European Commission (CoroNAb 101003653). D.J.L. and N.M.F. were supported by the NIHR VEEPED (PR-OD-1017-20002). S.B. received support from the NIHR BRC Imperial College NHS Trust Infection and COVID themes. S.B and N.M.F were supported by the UK Research and Innovation Fund MR/V038109/1. S.B. is supported by the Academy of Medical Sciences Springboard Award SBF004/1080. S.B. is supported by the Novo Nordisk Foundation Young Investigator Award NNF20OC0059309. O.R. and S.B. were supported by the Bill & Melinda Gates Foundation (OPP1175094, OPP1084362). Computational resources were provided by Amazon AWS and Microsoft AI for Health.

## Author information

### Author notes

1. These authors contributed equally: Erik Volz, Swapnil Mishra, Meera Chand, Jeffrey C. Barrett, Robert Johnson, Axel Gandy, Andrew Rambaut, Neil M. Ferguson

### Affiliations

1. MRC Centre for Global Infectious Disease Analysis, Jameel Institute for Disease and Emergency Analytics, Imperial College London, London, UK

Erik Volz, Swapnil Mishra, Robert Johnson, Lily Geidelberg, Wes R. Hinsley, Daniel J. Laydon, Manon Ragonnet-Cronin, Olivia Boyd, David Jorgensen, Katy Gaythorpe, Samir Bhatt & Neil M. Ferguson

2. Public Health England, London, UK

Meera Chand, Gavin Dabrera, Ian Harrison, Nicholas J. Loman, Richard Myers, Natalie Groves, Elias Allara, Clare Pearson, Husam Osman, Andrew Bosworth, Esther Robinson, Peter Muir, Ian B. Vipond, Richard Hopes, Hannah M. Pymont, Stephanie Hutchings, Angie Lackenby, Tamyo Mbisa, Steven Platt, Shahjahan Miah, David Bibby, Carmen Manso, Jonathan Hubb, Mary

Ramsay, Daniel Bradshaw, Alicia Thornton, Ulf Schaefer, Eileen Gallagher, David Lee, David Williams, Nicholas Ellaby, Hassan Hartman, Nikos Manesis, Vineet Patel, Chloe Bishop, Vicki Chalker, Juan Ledesma, Katherine A. Twohig & Susan Hopkins

3. Wellcome Sanger Institute, Cambridge, UK

Jeffrey C. Barrett, Robert Amato, Cristina V. Ariani, Sónia Gonçalves, David K. Jackson, John Sillitoe, Dominic P. Kwiatkowski, Alex Alderton, Roberto Amato, Mathew A. Beale, Charlotte Beaver, Katherine L. Bellis, Emma Betteridge, James Bonfield, John Danesh, Matthew J. Dorman, Eleanor Drury, Ben W. Farr, Luke Foulser, Sonia Goncalves, Scott Goodwin, Marina Gourtovaia, Ewan M. Harrison, Dorota Jamrozy, Ian Johnston, Leanne Kane, Sally Kay, Jon-Paul Keatley, Dominic Kwiatkowski, Cordelia F. Langford, Mara Lawniczak, Laura Letchford, Rich Livett, Stephanie Lo, Inigo Martincorena, Samantha McGuigan, Rachel Nelson, Steve Palmer, Naomi R. Park, Minal Patel, Liam Prestwood, Christoph Puethe, Michael A. Quail, Shavanti Rajatileka, Carol Scott, Lesley Shirley, Michael H. Spencer Chapman, Scott A. J. Thurston, Gerry Tonkin-Hill, Danni Weldon, Diana Rajan, Iraad F. Bronner, Louise Aigrain, Nicholas M. Redshaw, Stefanie V. Lensing, Robert Davies, Andrew Whitwham, Jennifer Liddle, Kevin Lewis, Jaime M. Tovar-Corona, Steven Leonard, Jillian Durham, Andrew R. Bassett, Shane McCarthy, Robin J. Moll, Keith James, Karen Oliver, Alex Makunin & Jeff Barrett

4. Institute of Evolutionary Biology, University of Edinburgh, Edinburgh, UK

Áine O'Toole, Ben Jackson, John T. McCrone, Verity Hill & Andrew Rambaut

5. Institute of Microbiology and Infection, University of Birmingham, Birmingham, UK

Nicholas J. Loman, Nicholas J. Loman, Joshua Quick, Claire McMurray, Joanne Stockton, Sam Nicholls, Will Rowe, Radoslaw Poplawski & Alan McNally

6. Department of Mathematics, Imperial College London, London, UK

Seth Flaxman, Oliver Ratmann & Axel Gandy

7. Section of Epidemiology, Department of Public Health, University of Copenhagen, Copenhagen, Denmark

Samir Bhatt

8. Barking, Havering and Redbridge University Hospitals NHS Trust, Barking, UK

Cherian Koshy & Amy Ash

9. Basingstoke Hospital, Basingstoke, UK

Emma Wise, Nathan Moore, Matilde Mori, Nick Cortes, Jessica Lynch & Stephen Kidd

10. Belfast Health and Social Care Trust, Belfast, UK

Derek J. Fairley, Tanya Curran & James P. McKenna

11. Betsi Cadwaladr University Health Board, Betsi Cadwaladr, UK

Helen Adams

12. Big Data Institute, Nuffield Department of Medicine, University of Oxford, Oxford, UK

Christophe Fraser, Tanya Golubchik & David Bonsall

13. Brighton and Sussex University Hospitals NHS Trust, Brighton, UK

Mohammed O. Hassan-Ibrahim, Cassandra S. Malone & Benjamin J. Cogger

14. Cambridge Stem Cell Institute, University of Cambridge, Cambridge, UK

Michelle Wantoch & Nicola Reynolds

15. Cambridge University Hospitals NHS Foundation Trust, Cambridge, UK

Ben Warne

16. Cardiff and Vale University Health Board, Cardiff, UK

Joshua Maksimovic, Karla Spellman, Kathryn McCluggage, Michaela John, Robert Beer, Safiah Afifi & Sian Morgan

17. Cardiff University, Cardiff, UK

Angela Marchbank, Anna Price, Christine Kitchen, Huw Gulliver, Ian Merrick, Joel Southgate, Martyn Guest, Robert Munn, Trudy Workman, Thomas R. Connor, William Fuller & Catherine Bresner

18. Centre for Clinical Infection and Diagnostics Research, St. Thomas' Hospital and Kings College London, London, UK

Luke B. Snell & Amita Patel

19. Centre for Clinical Infection and Diagnostics Research, Department of Infectious Diseases, Guy's and St Thomas' NHS Foundation Trust, London, UK

Themoula Charalampous, Gaia Nebbia, Rahul Batra & Jonathan Edgeworth

20. Centre for Enzyme Innovation, University of Portsmouth (PORT), Portsmouth, UK

Samuel C. Robson & Angela H. Beckett

21. Centre for Genomic Pathogen Surveillance, University of Oxford, Oxford, UK

David M. Aanensen, Anthony P. Underwood, Corin A. Yeats, Khalil Abudahab, Ben E. W. Taylor & Mirko Menegazzo

22. Clinical Microbiology Department, Queens Medical Centre, Nottingham, UK

Gemma Clark, Wendy Smith, Manjinder Khakh, Vicki M. Fleming, Michelle M. Lister, Hannah C. Howson-Wells, Louise Berry, Tim Boswell, Amelia Joseph, Iona Willingham & Carl Jones

23. Clinical Microbiology, University Hospitals of Leicester NHS Trust, Leicester, UK

Christopher Holmes, Paul Bird, Thomas Helmer, Karlie Fallon & Julian Tang

24. County Durham and Darlington NHS Foundation Trust, Durham, UK

Veena Raviprakash, Sharon Campbell, Nicola Sheriff, Victoria Blakey & Lesley-Anne Williams

25. Deep Seq, School of Life Sciences, Queens Medical Centre, University of Nottingham, Nottingham, UK

Matthew W. Loose, Nadine Holmes, Christopher Moore, Matthew Carlile, Victoria Wright, Fei Sang & Johnny Debebe

26. Department of Infection Biology, Faculty of Infectious and Tropical Diseases, London School of Hygiene and Tropical Medicine, London, UK

Francesc Coll

27. Department of Infectious Diseases, King's College London, London, UK

Adrian W. Signell, Gilberto Betancor & Harry D. Wilson

28. Department of Microbiology, Kettering General Hospital, Kettering, UK

Sahar Eldirdiri, Anita Kenyon & Thomas Davis

29. Department of Zoology, University of Oxford, Oxford, UK

Oliver G. Pybus, Louis du Plessis, Alex E. Zarebski, Jayna Raghwani, Moritz U. G. Kraemer, Sarah Francois, Stephen W. Attwood, Tetyana I. Vasylyeva, Marina Escalera Zamudio & Bernardo Gutierrez

30. Departments of Infectious Diseases and Microbiology, Cambridge University Hospitals NHS Foundation Trust, Cambridge, UK

M. Estee Torok & William L. Hamilton

31. Division of Virology, Department of Pathology, University of Cambridge, Cambridge, UK

Ian G. Goodfellow, Grant Hall, Aminu S. Jahun, Yasmin Chaudhry, Myra Hosmillo, Malte L. Pinckert & Iliana Georgana

32. East Kent Hospitals University NHS Foundation Trust, Canterbury, UK

Samuel Moses & Hannah Lowe

33. East Suffolk and North Essex NHS Foundation Trust, Ipswich, UK

Luke Bedford

34. Gateshead Health NHS Foundation Trust, Gateshead, UK

Jonathan Moore & Susanne Stonehouse

35. Genomics Innovation Unit, Guy's and St. Thomas' NHS Foundation Trust, London, UK

Chloe L. Fisher & Ali R. Awan

36. Gloucestershire Hospitals NHS Foundation Trust, Gloucester, UK

John BoYes

37. Great Ormond Street Hospital for Children NHS Foundation Trust, London, UK

Judith Breuer, Kathryn Ann Harris, Julianne Rose Brown, Divya Shah, Laura Atkinson, Jack C. D. Lee & Nathaniel Storey

38. Guy's and St. Thomas' BRC, London, UK

Flavia Flaviani

39. Guy's and St. Thomas' Hospitals, London, UK

Adela Alcolea-Medina

40. Hampshire Hospitals NHS Foundation Trust, Winchester, UK

Rebecca Williams & Gabrielle Vernet

41. Health Data Research UK Cambridge, Cambridge, UK

Michael R. Chapman

42. Health Services Laboratories, London, UK

Lisa J. Levett, Judith Heaney, Wendy Chatterton & Monika Pusok

43. Heartlands Hospital, Birmingham, UK

Li Xu-McCrae

44. Hub for Biotechnology in the Built Environment, Northumbria University, Newcastle-upon-Tyne, UK

Darren L. Smith, Matthew Bashton & Gregory R. Young

45. Imperial College Hospitals NHS Trust, London, UK

Alison Holmes, Paul Anthony Randell, Alison Cox, Pinglawathee Madona, Frances Bolt, James Price & Siddharth Mookerjee

46. Imperial College London, London, UK

Manon Ragonnet-Cronin, Fabricia F. Nascimento, David Jorgensen, Igor Siveroni, Rob Johnson, Olivia Boyd, Lily Geidelberg, Erik M. Volz, Aileen

Rowan & Graham P. Taylor

47. Institute of Biodiversity, Animal Health and Comparative Medicine, Glasgow, UK

Katherine L. Smollett

48. King's College London, London, UK

Rocio T. Martinez Nunez

49. Liverpool Clinical Laboratories, Liverpool, UK

Jenifer Mason, Trevor I. Robinson, Elaine O'Toole, Joanne Watts, Cassie Breen & Angela Cowell

50. Maidstone and Tunbridge Wells NHS Trust, Maidstone, UK

Graciela Sluga

51. Manchester University NHS Foundation Trust, Manchester, UK

Nicholas W. Machin, Shazaad S. Y. Ahmad & Ryan P. George

52. Microbiology Department, Wye Valley NHS Trust, Hereford, UK

Fenella Halstead, Venkat Sivaprakasam & Wendy Hogsden

53. MRC Biostatistics Unit, University of Cambridge, Cambridge, UK

Chris J. Illingworth & Chris Jackson

54. MRC-University of Glasgow Centre for Virus Research, Glasgow, UK

Emma C. Thomson, James G. Shepherd, Patawee Asamaphan, Marc O. Niebel, Kathy K. Li, Rajiv N. Shah, Natasha G. Jesudason, Lily Tong, Alice Broos, Daniel Mair, Jenna Nichols, Stephen N. Carmichael, Kyriaki Nomikou, Elihu Aranday-Cortes, Natasha Johnson, Igor Starinskij, Ana da Silva Filipe, David L. Robertson, Richard J. Orton, Joseph Hughes, Sreenu Vattipally, Joshua B. Singer & Seema Nickbakhsh

55. National Infection Service, PHE and Leeds Teaching Hospitals Trust, Leeds, UK

Antony D. Hale, Louissa R. Macfarlane-Smith, Katherine L. Harper & Holli Carden

56. Newcastle Hospitals NHS Foundation Trust, Newcastle, UK

Yusri Taha, Brendan A. I. Payne, Shirelle Burton-Fanning, Sheila Waugh, Jennifer Collins & Gary Eltringham

57. Newcastle University, Newcastle, UK

Steven Rushton & Sarah O'Brien

58. NHS Greater Glasgow and Clyde, Glasgow, UK

Amanda Bradley, Alasdair Maclean, Guy Mollett & Rachel Blacow

59. NHS Lothian, Edinburgh, UK

Kate E. Templeton, Martin P. McHugh, Rebecca Dewar & Elizabeth Wastenge

60. Norfolk and Norwich University Hospital, Norwich, UK

Samir Dervisevic, Rachael Stanley, Emma J. Meader & Lindsay Coupland

61. Norfolk County Council, Norwich, UK

Louise Smith

62. North Cumbria Integrated Care NHS Foundation Trust, Carlisle, UK

Clive Graham, Edward Barton, Debra Padgett & Garren Scott

63. North Tees and Hartlepool NHS Foundation Trust, Stockton-on-Tees, UK

Emma Swindells & Jane Greenaway

64. Northumbria University, Newcastle-upon-Tyne, UK

Andrew Nelson, Clare M. McCann & Wen C. Yew

65. Oxford University Hospitals NHS Foundation Trust, Oxford, UK

Monique Andersson, Timothy Peto, Anita Justice, David Eyre & Derrick Crook

66. PathLinks, Northern Lincolnshire & Goole NHS Foundation Trust, Scunthorpe, UK

Tim J. Sloan, Nichola Duckworth & Sarah Walsh

67. Portsmouth Hospitals University NHS Trust, Portsmouth, UK

Anoop J. Chauhan, Sharon Glaysher, Kelly Bicknell, Sarah Wyllie, Scott Elliott, Allyson Lloyd & Robert Impey

68. Princess Alexandra Hospital Microbiology Department, Harlow, UK

Nick Levene & Lynn Monaghan

69. Public Health Agency, Belfast, UK

Declan T. Bradley & Tim Wyatt

70. Public Health England, Clinical Microbiology and Public Health Laboratory, Cambridge, UK

Martin D. Curran & Surendra Parmar

71. Public Health Scotland, Glasgow, UK

Matthew T. G. Holden & Sharif Shaaban

72. Public Health Wales NHS Trust, Cardiff, UK

Alec Birchley, Alexander Adams, Alisha Davies, Amy Gaskin, Amy Plimmer, Bree Gatica-Wilcox, Caoimhe McKerr, Catherine Moore, Chris Williams, David Heyburn, Elen De Lacy, Ember Hilvers, Fatima Downing, Giri Shankar, Hannah Jones, Hibo Asad, Jason Coombes, Joanne Watkins, Johnathan M. Evans, Laia Fina, Laura Gifford, Lauren Gilbert, Lee Graham, Malorie Perry, Mari Morgan, Matthew Bull, Michelle Cronin, Nicole Pacchiarini, Noel Craine, Rachel Jones, Robin Howe, Sally Corden, Sara Rey, Sara Kumziene-Summerhayes, Sarah Taylor, Simon Cottrell, Sophie Jones & Sue Edwards

73. Quadram Institute Bioscience, Norwich, UK

Justin O'Grady, Andrew J. Page, Alison E. Mather, David J. Baker, Steven Rudder, Alp Aydin, Gemma L. Kay, Alexander J. Trotter, Nabil-Fareed Alikhan, Leonardo de Oliveira Martins, Thanh Le-Viet & Lizzie Meadows

74. Queen Elizabeth Hospital, Birmingham, UK

Anna Casey & Liz Ratcliffe

75. Queen's University Belfast, Belfast, UK

David A. Simpson, Zoltan Molnar, Thomas Thompson & Erwan Acheson

76. Royal Devon and Exeter NHS Foundation Trust, Exeter, UK

Jane A. H. Masoli, Bridget A. Knight, Sian Ellard, Cressida Auckland & Christopher R. Jones

77. Royal Free NHS Trust, London, UK

Tabitha W. Mahungu, Dianne Irish-Tavares, Tanzina Haque, Jennifer Hart & Eric Witele

78. Sandwell and West Birmingham NHS Trust, Birmingham, UK

Melisa Louise Fenton, Ashok Dadrah, Amanda Symmonds & Tranprit Saluja

79. School of Biological Sciences, University of Portsmouth (PORT), Portsmouth, UK

Yann Bourgeois & Garry P. Scarlett

80. School of Pharmacy and Biomedical Sciences, University of Portsmouth (PORT), Portsmouth, UK

Katie F. Loveson, Salman Goudarzi, Christopher Fearn, Kate Cook, Hannah Dent & Hannah Paul

81. Sheffield Teaching Hospitals, Sheffield, UK

David G. Partridge, Mohammad Raza, Cariad Evans & Kate Johnson

82. South Tees Hospitals NHS Foundation Trust, Newcastle, UK

Steven Liggett, Paul Baker, Stephen Bonner & Sarah Essex

83. Swansea University, Swansea, UK

Ronan A. Lyons

84. University Hospitals Southampton NHS Foundation Trust, Southampton, UK

Kordo Saeed, Adhyana I. K. Mahanama, Buddhini Samaraweera, Siona Silveira, Emanuela Pelosi, Eleri Wilson-Davies, Jacqui A. Prieto & Sarah Jeremiah

85. University College London, London, UK

Rachel J. Williams, Mark Kristiansen, Sunando Roy, Charlotte A. Williams, Marius Cotic, Nadua Bayzid, Adam P. Westhorpe, John A. Hartley, Riaz Jannoo, Helen L. Lowe, Angeliki Karamani & Leah Ensell

86. University Hospitals Coventry and Warwickshire, Coventry, UK

Dimitris Grammatopoulos, Sarojini Pandey, Lisa Berry & Katie Jones

87. University of Birmingham, Birmingham, UK

Alex Richter & Andrew Beggs

88. University of Birmingham Turnkey Laboratory, Birmingham, UK

Angus Best, Benita Percival, Jeremy Mirza, Oliver Mogram, Megan Mayhew, Liam Crawford, Fiona Ashcroft, Emma Moles-Garcia & Nicola Cumley

89. University of Brighton, Brighton, UK

Colin P. Smith, Giselda Bucca & Andrew R. Hesketh

90. University of Cambridge, Cambridge, UK

Beth Blane, Sophia T. Girgis, Danielle Leek, Sushmita Sridhar, Sally Forrest, Claire Cormie, Harmeet K. Gill, Joana Dias, Ellen E. Higginson, Mailis Maes, Jamie Young, Leanne M. Kermack, Ravi Kumar Gupta, Catherine Ludden, Sharon J. Peacock, Sophie Palmer, Carol M. Churcher, Nazreen F. Hadjirin, Alessandro M. Carabelli, Ellena Brooks, Kim S. Smith, Katerina Galai, Georgina M. McManus & Chris Ruis

91. University of East Anglia, Norwich, UK

Rose K. Davidson

92. University of Edinburgh, Edinburgh, UK

Andrew Rambaut, Thomas Williams, Carlos E. Balcazar, Michael D. Gallagher, Áine O'Toole, Stefan Rooke, Verity Hill, Kathleen A. Williamson & Thomas D. Stanton

93. University of Exeter, Exeter, UK

Stephen L. Michell, Claire M. Bewshea, Ben Temperton, Michelle L. Michelsen, Joanna Warwick-Dugdale, Robin Manley, Audrey Farbos, James W. Harrison, Christine M. Sambles, David J. Studholme & Aaron R. Jeffries

94. University of Liverpool, Liverpool, UK

Alistair C. Darby, Julian A. Hiscox, Steve Paterson, Miren Iturriaga-Gomara, Kathryn A. Jackson, Anita O. Lucaci, Edith E. Vamos, Margaret Hughes, Lucille Rainbow, Richard Eccles, Charlotte Nelson, Mark Whitehead, Lance Turtle, Sam T. Haldenby, Richard Gregory, Matthew Gemmell, Claudia Wierzbicki & Hermione J. Webster

95. University of Sheffield, Sheffield, UK

Thushan I. de Silva, Nikki Smith, Adrienn Angyal, Benjamin B. Lindsey, Danielle C. Groves, Luke R. Green, Dennis Wang, Timothy M. Freeman, Matthew D. Parker, Alexander J. Keeley, Paul J. Parsons, Rachel M. Tucker, Rebecca Brown, Matthew Wyles, Max Whiteley, Peijun Zhang, Marta Gallis & Stavroula F. Louka

96. University of Warwick, Warwick, UK

Chrystala Constantnidou, Meera Unnikrishnan, Sascha Ott, Jeffrey K. J. Cheng, Hannah E. Bridgewater, Lucy R. Frost, Grace Taylor-Joyce, Richard Stark, Laura Baxter, Mohammad T. Alam & Paul E. Brown

97. University of Cambridge, Cambridge, UK

Dinesh Aggarwal

98. Viapath, London, UK

Alberto C. Cerda, Tammy V. Merrill & Rebekah E. Wilson

99. Guy's and St Thomas' NHS Foundation Trust, London, UK

Alberto C. Cerda, Tammy V. Merrill & Rebekah E. Wilson

100. King's College Hospital NHS Foundation Trust, London, UK

Alberto C. Cerda, Tammy V. Merrill & Rebekah E. Wilson

101. Virology, School of Life Sciences, Queens Medical Centre, University of Nottingham, Nottingham, UK

Patrick C. McClure, Joseph G. Chappell, Theocharis Tsoleridis & Jonathan Ball

102. Wellcome Centre for Human Genetics, Nuffield Department of Medicine,  
University of Oxford, Oxford, UK

David Buck, John A. Todd, Angie Green, Amy Trebes, George MacIntyre-  
Cockett & Mariateresa de Cesare

103. West of Scotland Specialist Virology Centre, NHS Greater Glasgow and Clyde,  
Glasgow, UK

Rory N. Gunson

#### Authors

1. Erik Volz

[View author publications](#)

You can also search for this author in [PubMed](#) [Google Scholar](#)

2. Swapnil Mishra

[View author publications](#)

You can also search for this author in [PubMed](#) [Google Scholar](#)

3. Meera Chand

[View author publications](#)

You can also search for this author in [PubMed](#) [Google Scholar](#)

4. Jeffrey C. Barrett

[View author publications](#)

You can also search for this author in [PubMed](#) [Google Scholar](#)

5. Robert Johnson

[View author publications](#)

You can also search for this author in [PubMed](#) [Google Scholar](#)

6. Lily Geidelberg

[View author publications](#)

You can also search for this author in [PubMed](#) [Google Scholar](#)

7. Wes R. Hinsley  
[View author publications](#)

You can also search for this author in [PubMed](#) [Google Scholar](#)

8. Daniel J. Laydon  
[View author publications](#)

You can also search for this author in [PubMed](#) [Google Scholar](#)

9. Gavin Dabrera  
[View author publications](#)

You can also search for this author in [PubMed](#) [Google Scholar](#)

10. Áine O'Toole  
[View author publications](#)

You can also search for this author in [PubMed](#) [Google Scholar](#)

11. Robert Amato  
[View author publications](#)

You can also search for this author in [PubMed](#) [Google Scholar](#)

12. Manon Ragonnet-Cronin  
[View author publications](#)

You can also search for this author in [PubMed](#) [Google Scholar](#)

13. Ian Harrison  
[View author publications](#)

You can also search for this author in [PubMed](#) [Google Scholar](#)

14. Ben Jackson  
[View author publications](#)

You can also search for this author in [PubMed](#) [Google Scholar](#)

15. Cristina V. Ariani  
[View author publications](#)

You can also search for this author in [PubMed](#) [Google Scholar](#)

16. Olivia Boyd

[View author publications](#)

You can also search for this author in [PubMed](#) [Google Scholar](#)

17. Nicholas J. Loman

[View author publications](#)

You can also search for this author in [PubMed](#) [Google Scholar](#)

18. John T. McCrone

[View author publications](#)

You can also search for this author in [PubMed](#) [Google Scholar](#)

19. Sónia Gonçalves

[View author publications](#)

You can also search for this author in [PubMed](#) [Google Scholar](#)

20. David Jorgensen

[View author publications](#)

You can also search for this author in [PubMed](#) [Google Scholar](#)

21. Richard Myers

[View author publications](#)

You can also search for this author in [PubMed](#) [Google Scholar](#)

22. Verity Hill

[View author publications](#)

You can also search for this author in [PubMed](#) [Google Scholar](#)

23. David K. Jackson

[View author publications](#)

You can also search for this author in [PubMed](#) [Google Scholar](#)

24. Katy Gaythorpe

[View author publications](#)

You can also search for this author in [PubMed](#) [Google Scholar](#)

25. Natalie Groves

[View author publications](#)

You can also search for this author in [PubMed](#) [Google Scholar](#)

26. John Sillitoe

[View author publications](#)

You can also search for this author in [PubMed](#) [Google Scholar](#)

27. Dominic P. Kwiatkowski

[View author publications](#)

You can also search for this author in [PubMed](#) [Google Scholar](#)

28. Seth Flaxman

[View author publications](#)

You can also search for this author in [PubMed](#) [Google Scholar](#)

29. Oliver Ratmann

[View author publications](#)

You can also search for this author in [PubMed](#) [Google Scholar](#)

30. Samir Bhatt

[View author publications](#)

You can also search for this author in [PubMed](#) [Google Scholar](#)

31. Susan Hopkins

[View author publications](#)

You can also search for this author in [PubMed](#) [Google Scholar](#)

32. Axel Gandy

[View author publications](#)

You can also search for this author in [PubMed](#) [Google Scholar](#)

33. Andrew Rambaut

[View author publications](#)

You can also search for this author in [PubMed](#) [Google Scholar](#)

34. Neil M. Ferguson  
[View author publications](#)

You can also search for this author in [PubMed](#) [Google Scholar](#)

## Consortia

### The COVID-19 Genomics UK (COG-UK) consortium

- Cherian Koshy
- , Amy Ash
- , Emma Wise
- , Nathan Moore
- , Matilde Mori
- , Nick Cortes
- , Jessica Lynch
- , Stephen Kidd
- , Derek J. Fairley
- , Tanya Curran
- , James P. McKenna
- , Helen Adams
- , Christophe Fraser
- , Tanya Golubchik
- , David Bonsall
- , Mohammed O. Hassan-Ibrahim
- , Cassandra S. Malone
- , Benjamin J. Cogger
- , Michelle Wantoch
- , Nicola Reynolds
- , Ben Warne
- , Joshua Maksimovic
- , Karla Spellman
- , Kathryn McCluggage
- , Michaela John
- , Robert Beer
- , Safiah Afifi
- , Sian Morgan
- , Angela Marchbank
- , Anna Price
- , Christine Kitchen
- , Huw Gulliver
- , Ian Merrick

- , Joel Southgate
- , Martyn Guest
- , Robert Munn
- , Trudy Workman
- , Thomas R. Connor
- , William Fuller
- , Catherine Bresner
- , Luke B. Snell
- , Amita Patel
- , Themoula Charalampous
- , Gaia Nebbia
- , Rahul Batra
- , Jonathan Edgeworth
- , Samuel C. Robson
- , Angela H. Beckett
- , David M. Aanensen
- , Anthony P. Underwood
- , Corin A. Yeats
- , Khalil Abudahab
- , Ben E. W. Taylor
- , Mirko Menegazzo
- , Gemma Clark
- , Wendy Smith
- , Manjinder Khakh
- , Vicki M. Fleming
- , Michelle M. Lister
- , Hannah C. Howson-Wells
- , Louise Berry
- , Tim Boswell
- , Amelia Joseph
- , Iona Willingham
- , Carl Jones
- , Christopher Holmes
- , Paul Bird
- , Thomas Helmer
- , Karlie Fallon
- , Julian Tang
- , Veena Raviprakash
- , Sharon Campbell
- , Nicola Sheriff
- , Victoria Blakey
- , Lesley-Anne Williams

- , Matthew W. Loose
- , Nadine Holmes
- , Christopher Moore
- , Matthew Carlile
- , Victoria Wright
- , Fei Sang
- , Johnny Debebe
- , Francesc Coll
- , Adrian W. Signell
- , Gilberto Betancor
- , Harry D. Wilson
- , Sahar Eldirdiri
- , Anita Kenyon
- , Thomas Davis
- , Oliver G. Pybus
- , Louis du Plessis
- , Alex E. Zarebski
- , Jayna Raghwani
- , Moritz U. G. Kraemer
- , Sarah Francois
- , Stephen W. Attwood
- , Tetyana I. Vasylyeva
- , Marina Escalera Zamudio
- , Bernardo Gutierrez
- , M. Estee Torok
- , William L. Hamilton
- , Ian G. Goodfellow
- , Grant Hall
- , Aminu S. Jahun
- , Yasmin Chaudhry
- , Myra Hosmillo
- , Malte L. Pinckert
- , Iliana Georgana
- , Samuel Moses
- , Hannah Lowe
- , Luke Bedford
- , Jonathan Moore
- , Susanne Stonehouse
- , Chloe L. Fisher
- , Ali R. Awan
- , John BoYes
- , Judith Breuer

- , Kathryn Ann Harris
- , Julianne Rose Brown
- , Divya Shah
- , Laura Atkinson
- , Jack C. D. Lee
- , Nathaniel Storey
- , Flavia Flaviani
- , Adela Alcolea-Medina
- , Rebecca Williams
- , Gabrielle Vernet
- , Michael R. Chapman
- , Lisa J. Levett
- , Judith Heaney
- , Wendy Chatterton
- , Monika Pusok
- , Li Xu-McCrae
- , Darren L. Smith
- , Matthew Bashton
- , Gregory R. Young
- , Alison Holmes
- , Paul Anthony Randell
- , Alison Cox
- , Pinglawathee Madona
- , Frances Bolt
- , James Price
- , Siddharth Mookerjee
- , Manon Ragonnet-Cronin
- , Fabricia F. Nascimento
- , David Jorgensen
- , Igor Siveroni
- , Rob Johnson
- , Olivia Boyd
- , Lily Geidelberg
- , Erik M. Volz
- , Aileen Rowan
- , Graham P. Taylor
- , Katherine L. Smollett
- , Nicholas J. Loman
- , Joshua Quick
- , Claire McMurray
- , Joanne Stockton
- , Sam Nicholls

- , Will Rowe
- , Radoslaw Poplawski
- , Alan McNally
- , Rocio T. Martinez Nunez
- , Jenifer Mason
- , Trevor I. Robinson
- , Elaine O'Toole
- , Joanne Watts
- , Cassie Breen
- , Angela Cowell
- , Graciela Sluga
- , Nicholas W. Machin
- , Shazaad S. Y. Ahmad
- , Ryan P. George
- , Fenella Halstead
- , Venkat Sivaprakasam
- , Wendy Hogsden
- , Chris J. Illingworth
- , Chris Jackson
- , Emma C. Thomson
- , James G. Shepherd
- , Patawee Asamaphan
- , Marc O. Niebel
- , Kathy K. Li
- , Rajiv N. Shah
- , Natasha G. Jesudason
- , Lily Tong
- , Alice Broos
- , Daniel Mair
- , Jenna Nichols
- , Stephen N. Carmichael
- , Kyriaki Nomikou
- , Elihu Aranday-Cortes
- , Natasha Johnson
- , Igor Starinskij
- , Ana da Silva Filipe
- , David L. Robertson
- , Richard J. Orton
- , Joseph Hughes
- , Sreenu Vattipally
- , Joshua B. Singer
- , Seema Nickbakhsh

- , Antony D. Hale
- , Louissa R. Macfarlane-Smith
- , Katherine L. Harper
- , Holli Carden
- , Yusri Taha
- , Brendan A. I. Payne
- , Shirelle Burton-Fanning
- , Sheila Waugh
- , Jennifer Collins
- , Gary Eltringham
- , Steven Rushton
- , Sarah O'Brien
- , Amanda Bradley
- , Alasdair Maclean
- , Guy Mollett
- , Rachel Blacow
- , Kate E. Templeton
- , Martin P. McHugh
- , Rebecca Dewar
- , Elizabeth Wastenge
- , Samir Dervisevic
- , Rachael Stanley
- , Emma J. Meader
- , Lindsay Coupland
- , Louise Smith
- , Clive Graham
- , Edward Barton
- , Debra Padgett
- , Garren Scott
- , Emma Swindells
- , Jane Greenaway
- , Andrew Nelson
- , Clare M. McCann
- , Wen C. Yew
- , Monique Andersson
- , Timothy Peto
- , Anita Justice
- , David Eyre
- , Derrick Crook
- , Tim J. Sloan
- , Nichola Duckworth
- , Sarah Walsh

- , Anoop J. Chauhan
- , Sharon Glaysher
- , Kelly Bicknell
- , Sarah Wyllie
- , Scott Elliott
- , Allyson Lloyd
- , Robert Impey
- , Nick Levene
- , Lynn Monaghan
- , Declan T. Bradley
- , Tim Wyatt
- , Elias Allara
- , Clare Pearson
- , Husam Osman
- , Andrew Bosworth
- , Esther Robinson
- , Peter Muir
- , Ian B. Vipond
- , Richard Hopes
- , Hannah M. Pymont
- , Stephanie Hutchings
- , Martin D. Curran
- , Surendra Parmar
- , Angie Lackenby
- , Tamyo Mbisa
- , Steven Platt
- , Shahjahan Miah
- , David Bibby
- , Carmen Manso
- , Jonathan Hubb
- , Meera Chand
- , Gavin Dabrera
- , Mary Ramsay
- , Daniel Bradshaw
- , Alicia Thornton
- , Richard Myers
- , Ulf Schaefer
- , Natalie Groves
- , Eileen Gallagher
- , David Lee
- , David Williams
- , Nicholas Ellaby

- , Ian Harrison
- , Hassan Hartman
- , Nikos Manesis
- , Vineet Patel
- , Chloe Bishop
- , Vicki Chalker
- , Juan Ledesma
- , Katherine A. Twohig
- , Matthew T. G. Holden
- , Sharif Shaaban
- , Alec Birchley
- , Alexander Adams
- , Alisha Davies
- , Amy Gaskin
- , Amy Plimmer
- , Bree Gatica-Wilcox
- , Caoimhe McKerr
- , Catherine Moore
- , Chris Williams
- , David Heyburn
- , Elen De Lacy
- , Ember Hilvers
- , Fatima Downing
- , Giri Shankar
- , Hannah Jones
- , Hibo Asad
- , Jason Coombes
- , Joanne Watkins
- , Johnathan M. Evans
- , Laia Fina
- , Laura Gifford
- , Lauren Gilbert
- , Lee Graham
- , Malorie Perry
- , Mari Morgan
- , Matthew Bull
- , Michelle Cronin
- , Nicole Pacchiarini
- , Noel Craine
- , Rachel Jones
- , Robin Howe
- , Sally Corden

- , Sara Rey
- , Sara Kumziene-Summerhayes
- , Sarah Taylor
- , Simon Cottrell
- , Sophie Jones
- , Sue Edwards
- , Justin O'Grady
- , Andrew J. Page
- , Alison E. Mather
- , David J. Baker
- , Steven Rudder
- , Alp Aydin
- , Gemma L. Kay
- , Alexander J. Trotter
- , Nabil-Fareed Alikhan
- , Leonardo de Oliveira Martins
- , Thanh Le-Viet
- , Lizzie Meadows
- , Anna Casey
- , Liz Ratcliffe
- , David A. Simpson
- , Zoltan Molnar
- , Thomas Thompson
- , Erwan Acheson
- , Jane A. H. Masoli
- , Bridget A. Knight
- , Sian Ellard
- , Cressida Auckland
- , Christopher R. Jones
- , Tabitha W. Mahungu
- , Dianne Irish-Tavares
- , Tanzina Haque
- , Jennifer Hart
- , Eric Witele
- , Melisa Louise Fenton
- , Ashok Dadrah
- , Amanda Symmonds
- , Tranprit Saluja
- , Yann Bourgeois
- , Garry P. Scarlett
- , Katie F. Loveson
- , Salman Goudarzi

- , Christopher Fearn
- , Kate Cook
- , Hannah Dent
- , Hannah Paul
- , David G. Partridge
- , Mohammad Raza
- , Cariad Evans
- , Kate Johnson
- , Steven Liggett
- , Paul Baker
- , Stephen Bonner
- , Sarah Essex
- , Ronan A. Lyons
- , Kordo Saeed
- , Adhyana I. K. Mahanama
- , Buddhini Samaraweera
- , Siona Silveira
- , Emanuela Pelosi
- , Eleri Wilson-Davies
- , Rachel J. Williams
- , Mark Kristiansen
- , Sunando Roy
- , Charlotte A. Williams
- , Marius Cotic
- , Nadua Bayzid
- , Adam P. Westhorpe
- , John A. Hartley
- , Riaz Jannoo
- , Helen L. Lowe
- , Angeliki Karamani
- , Leah Ensell
- , Jacqui A. Prieto
- , Sarah Jeremiah
- , Dimitris Grammatopoulos
- , Sarojini Pandey
- , Lisa Berry
- , Katie Jones
- , Alex Richter
- , Andrew Beggs
- , Angus Best
- , Benita Percival
- , Jeremy Mirza

- , Oliver Megram
- , Megan Mayhew
- , Liam Crawford
- , Fiona Ashcroft
- , Emma Moles-Garcia
- , Nicola Cumley
- , Colin P. Smith
- , Giselda Bucca
- , Andrew R. Hesketh
- , Beth Blane
- , Sophia T. Girgis
- , Danielle Leek
- , Sushmita Sridhar
- , Sally Forrest
- , Claire Cormie
- , Harmeet K. Gill
- , Joana Dias
- , Ellen E. Higginson
- , Mailis Maes
- , Jamie Young
- , Leanne M. Kermack
- , Ravi Kumar Gupta
- , Catherine Ludden
- , Sharon J. Peacock
- , Sophie Palmer
- , Carol M. Churcher
- , Nazreen F. Hadjirin
- , Alessandro M. Carabelli
- , Ellena Brooks
- , Kim S. Smith
- , Katerina Galai
- , Georgina M. McManus
- , Chris Ruis
- , Rose K. Davidson
- , Andrew Rambaut
- , Thomas Williams
- , Carlos E. Balcazar
- , Michael D. Gallagher
- , Áine O'Toole
- , Stefan Rooke
- , Verity Hill
- , Kathleen A. Williamson

- , Thomas D. Stanton
- , Stephen L. Michell
- , Claire M. Bewshea
- , Ben Temperton
- , Michelle L. Michelsen
- , Joanna Warwick-Dugdale
- , Robin Manley
- , Audrey Farbos
- , James W. Harrison
- , Christine M. Sambles
- , David J. Studholme
- , Aaron R. Jeffries
- , Alistair C. Darby
- , Julian A. Hiscox
- , Steve Paterson
- , Miren Iturriza-Gomara
- , Kathryn A. Jackson
- , Anita O. Lucaci
- , Edith E. Vamos
- , Margaret Hughes
- , Lucille Rainbow
- , Richard Eccles
- , Charlotte Nelson
- , Mark Whitehead
- , Lance Turtle
- , Sam T. Haldenby
- , Richard Gregory
- , Matthew Gemmell
- , Claudia Wierzbicki
- , Hermione J. Webster
- , Thushan I. de Silva
- , Nikki Smith
- , Adrienn Angyal
- , Benjamin B. Lindsey
- , Danielle C. Groves
- , Luke R. Green
- , Dennis Wang
- , Timothy M. Freeman
- , Matthew D. Parker
- , Alexander J. Keeley
- , Paul J. Parsons
- , Rachel M. Tucker

- , Rebecca Brown
- , Matthew Wyles
- , Max Whiteley
- , Peijun Zhang
- , Marta Gallis
- , Stavroula F. Louka
- , Chrystala Constantinidou
- , Meera Unnikrishnan
- , Sascha Ott
- , Jeffrey K. J. Cheng
- , Hannah E. Bridgewater
- , Lucy R. Frost
- , Grace Taylor-Joyce
- , Richard Stark
- , Laura Baxter
- , Mohammad T. Alam
- , Paul E. Brown
- , Dinesh Aggarwal
- , Alberto C. Cerda
- , Tammy V. Merrill
- , Rebekah E. Wilson
- , Patrick C. McClure
- , Joseph G. Chappell
- , Theocharis Tsoleridis
- , Jonathan Ball
- , David Buck
- , John A. Todd
- , Angie Green
- , Amy Trebes
- , George MacIntyre-Cockett
- , Mariateresa de Cesare
- , Alex Alderton
- , Roberto Amato
- , Cristina V. Ariani
- , Mathew A. Beale
- , Charlotte Beaver
- , Katherine L. Bellis
- , Emma Betteridge
- , James Bonfield
- , John Danesh
- , Matthew J. Dorman
- , Eleanor Drury

- , Ben W. Farr
- , Luke Foulser
- , Sonia Goncalves
- , Scott Goodwin
- , Marina Gourtovaia
- , Ewan M. Harrison
- , David K. Jackson
- , Dorota Jamrozy
- , Ian Johnston
- , Leanne Kane
- , Sally Kay
- , Jon-Paul Keatley
- , Dominic Kwiatkowski
- , Cordelia F. Langford
- , Mara Lawniczak
- , Laura Letchford
- , Rich Livett
- , Stephanie Lo
- , Inigo Martincorena
- , Samantha McGuigan
- , Rachel Nelson
- , Steve Palmer
- , Naomi R. Park
- , Minal Patel
- , Liam Prestwood
- , Christoph Puethe
- , Michael A. Quail
- , Shavanti Rajatileka
- , Carol Scott
- , Lesley Shirley
- , John Sillitoe
- , Michael H. Spencer Chapman
- , Scott A. J. Thurston
- , Gerry Tonkin-Hill
- , Danni Weldon
- , Diana Rajan
- , Iraad F. Bronner
- , Louise Aigrain
- , Nicholas M. Redshaw
- , Stefanie V. Lensing
- , Robert Davies
- , Andrew Whitwham

- , Jennifer Liddle
- , Kevin Lewis
- , Jaime M. Tovar-Corona
- , Steven Leonard
- , Jillian Durham
- , Andrew R. Bassett
- , Shane McCarthy
- , Robin J. Moll
- , Keith James
- , Karen Oliver
- , Alex Makunin
- , Jeff Barrett
- & Rory N. Gunson

## Contributions

Conceptualization: E.V., S.B., A.G., S.M., N.M.F., M.C., S.H., J.C.B., D.P.K., A.R.; writing (first draft): E.V., S.F., S.B., A.G., O.R., S.M., R.J., A.R., N.M.F.; writing (review and editing): E.V., S.F., S.B., A.G., O.R., S.M., R.J., N.M.F., M.R.-C., D.J.L., M.C., S.H., J.C.B., K.G., C.V.A., J.T.M., V.H., B.J., Á.O'T.; analysis: E.V., S.F., S.B., A.G., O.R., S.M., R.J., N.M.F., L.G., D.J., M.C., R.M., N.G., J.C.B., J.S., A.R.; methodology: E.V., S.F., S.B., A.G., O.R., S.M., R.J., N.M.F., A.R.; data generation: S.H., S.M., R.J., O.B., M.C., R.M., N.G., I.H., G.D., N.J.L., J.C.B., D.P.K., R.A., C.V.A., S.G., W.R.H., D.K.J., J.S., O.B., K.G., J.T.M., V.H., B.J., Á.O'T., A.R.; software: E.V., S.F., A.G., S.M., R.J., N.M.F., R.A., S.G., K.G.; validation: E.V., S.B., S.M., N.M.F.; visualization: E.V., S.F., S.B., O.R., S.M., M.R.-C.; supervision: E.V., S.B., O.R., N.M.F., A.R.; funding acquisition: E.V., S.F., S.B., A.G., N.M.F., N.J.L., A.R.

## Corresponding authors

Correspondence to [Erik Volz](#) or [Neil M. Ferguson](#).

## Ethics declarations

## Competing interests

The authors declare no competing interests.

## Additional information

**Peer review information** *Nature* thanks Alexei Drummond and the other, anonymous, reviewer(s) for their contribution to the peer review of this work. Peer reviewer reports are available.

**Publisher's note** Springer Nature remains neutral with regard to jurisdictional claims in published maps and institutional affiliations.

## Extended data figures and tables

### [Extended Data Fig. 1 Weekly growth rate of the VOC relative to other variants and relationship of VOC growth rate with VOC frequency.](#)

**a**, The additive difference in growth rate between VOC and other lineages inferred from observed frequency of VOC genomes over time (Supplementary Methods section 2). **b**, The additive difference in growth rates plotted against estimated frequency of the VOC for different NHS regions. The difference in growth rate correlates more strongly with VOC frequency than with time (data not shown). Estimates are presented for weeks 44–56 for each region.

### [Extended Data Fig. 2 The ratio of the reproduction number for the VOC to that for co-circulating lineages inferred from combining estimating frequencies and phylodynamic estimates of VOC and non-VOC growth rates.](#)

Shaded region, 95% CrI. Sensitivity of estimates to differences in the mean generation time is shown in red and green (25% and 50% reduced generation time in VOC, respectively).

### [Extended Data Fig. 3 Weekly numbers of S-gene-positive samples with TPP correction plotted against the effective population size of the VOC.](#)

Point labels indicate week of data collection. Effective sample size is taken on the final day of the corresponding epidemiological week. Error bars, 95% bootstrap CIs.

### [Extended Data Fig. 4 Empirical data analysis of the advantage in weekly growth factors \(cases in week \$t + 1\$ divided by cases in week \$t\$ \) for the VOC and non-VOC lineages \(Supplementary Methods section 5\).](#)

Each point represents either the ratio (left) or difference (right) of weekly growth factors for the VOC versus the non-VOC for an NHS England STP area and week,

using the raw SGTF data shown in Fig. 2 (not adjusting for TPP). Colours and shapes differentiate epidemiological weeks. Numbers above 1 on the left plot and above 0 on the right plot show a transmission advantage. The blue line represents the mean advantage for a particular proportion of VOC among all cases, and the grey shading the 95% asymptotic CrI ( $\pm 2\sigma$ ). Scatter at low frequencies largely reflects statistical noise resulting from low counts.

**Extended Data Fig. 5 Sensitivity of reproduction number estimates at regional level to differences in the mean generation time in the VOC (0–25% reduction in the mean, while holding coefficient of variation constant).**

Top, scatter plots of estimated ratio of  $S^-$  to  $S^+$  reproduction numbers plotted against the reproduction number of  $S$ -gene-positive cases over time and among STP regions. Grey lines, linear regression—if changes in the generation time were able to completely explain temporal variation in the ratio, we would expect the slope to be zero. Bottom, ratio of reproduction number over time for each assumption about the mean generation time of the VOC. Shaded region, 95% CrI.

**Extended Data Fig. 6 Proportion of all cases in individuals over 10 years of age that were in 11–18-year-olds, stratified by SGTF status, NHS regions and week of testing.**

Top, data; middle, predicted trends from a semi-mechanistic model (Supplementary Methods section 7) fitting a time- and region-varying transmission advantage, but no age variation in transmission advantage; bottom, predicted trends from the model fitting a transmission that which varies by week, region and age group. Shaded region, 95% CrI.

**Extended Data Fig. 7 The overall multiplicative transmission advantage of the VOC over time estimated using a semi-mechanistic model with a VOC transmission advantage that varies by week and region, but not with age (Supplementary Methods section 7).**

The model fitted one transmission advantage parameter per week and per NHS region to SGTF (STP-level) counts by NHS STP area (left; finer scale than region) and SGTF counts by STP area and VOC genome counts by NHS region (right). Solid lines, medians; shading, 95% CrI pooled over all regions.

## [Extended Data Fig. 8 Multiplicative increase in reproduction number seen for different intrinsic infectiousness advantages and probability of transmission per contact for the non-VOC.](#)

**a**, Fixed contact duration. **b**, Exponentially distributed contact durations. See Supplementary Methods section [7](#).

**Extended Data Table 1 Tabulation of parameter estimates and model assessment using Pareto-smoothed importance sampling leave-one-out cross validation (PSIS-LOO CV) and widely applicable information criterion (WAIC)**

[Full size table](#)

## **Supplementary information**

### [Supplementary Information](#)

This file contains the Supplementary Methods, Supplementary References and Supplementary Table 1.

### [Reporting Summary](#)

### [Supplementary Data 1](#)

The number of diagnosed cases over time for all English STP regions. Each line segment is shaded with the frequency of SGTF in each week. Vertical shaded regions represent the time of the 2nd and third UK lockdowns.

### [Supplementary Information](#)

This file contains the full list of members of the COG-UK Consortium.

### [Peer Review File](#)

## **Rights and permissions**

### [Reprints and Permissions](#)

## **About this article**



## Cite this article

Volz, E., Mishra, S., Chand, M. *et al.* Assessing transmissibility of SARS-CoV-2 lineage B.1.1.7 in England. *Nature* **593**, 266–269 (2021).  
<https://doi.org/10.1038/s41586-021-03470-x>

### Download citation

- Received: 31 December 2020
- Accepted: 18 March 2021
- Published: 25 March 2021
- Issue Date: 13 May 2021
- DOI: <https://doi.org/10.1038/s41586-021-03470-x>

## Further reading

- **Implications of a highly transmissible variant of SARS-CoV-2 for children**
  - Oliver Ratmann
  - , Samir Bhatt
  - & Seth Flaxman

*Archives of Disease in Childhood* (2021)

- **Will SARS-CoV-2 variants of concern affect the promise of vaccines?**
  - Ravindra K. Gupta

*Nature Reviews Immunology* (2021)

- [Impact of January 2021 curfew measures on SARS-CoV-2 B.1.1.7 circulation in France](#)

- Laura Di Domenico
- , Chiara E Sabbatini
- , Giulia Pullano
- , Daniel Lévy-Bruhl
- & Vittoria Colizza

*Eurosurveillance* (2021)

- [COVID-19 rise in Bangladesh correlates with increasing detection of B.1.351 variant](#)

- Senjuti Saha
- , Arif M Tanmoy
- , Yogesh Hooda
- , Afroza Akter Tanni
- , Sharmistha Goswami
- , Syed Muktadir Al Sium
- , Mohammad Saiful Islam Sajib
- , Roly Malaker
- , Shuborno Islam
- , Hafizur Rahman
- , Ataul Mustufa Anik
- , Nikkon Sarker
- , Mohammad Shahidul Islam
- , Kinkar Ghosh
- , Probir Kumar Sarkar
- , Mohammed Rizwanul Ahsan Bipul
- , Syed Shafi Ahmed
- , Mohammod Shahidullah
- & Samir K Saha

*BMJ Global Health* (2021)

- [Rapid Emergence and Epidemiologic Characteristics of the SARS-CoV-2 B.1.526 Variant — New York City, New York, January 1–April 5, 2021](#)

- Corinne N. Thompson

- , Scott Hughes
- , Stephanie Ngai
- , Jennifer Baumgartner
- , Jade C. Wang
- , Emily McGibbon
- , Katelynn Devinney
- , Elizabeth Luoma
- , Daniel Bertolino
- , Christina Hwang
- , Kelsey Kepler
- , Cybill Del Castillo
- , Melissa Hopkins
- , Henry Lee
- , Andrea K. DeVito
- , Jennifer L. Rakeman
- & Anne D. Fine

*MMWR. Morbidity and Mortality Weekly Report (2021)*

## Comments

By submitting a comment you agree to abide by our [Terms](#) and [Community Guidelines](#). If you find something abusive or that does not comply with our terms or guidelines please flag it as inappropriate.

[Download PDF](#)

---

This article was downloaded by **calibre** from <https://www.nature.com/articles/s41586-021-03470-x>

Increased mortality in community-tested cases of SARS-CoV-2 lineage B.1.1.7

[Download PDF](#)

- Article
- [Published: 15 March 2021](#)

# Increased mortality in community-tested cases of SARS-CoV-2 lineage B.1.1.7

- [Nicholas G. Davies](#) [ORCID: orcid.org/0000-0002-1740-1412<sup>1</sup>](#),
- [Christopher I. Jarvis<sup>1</sup>](#),
- [CMMID COVID-19 Working Group](#),
- [W. John Edmunds<sup>1</sup>](#),
- [Nicholas P. Jewell<sup>2,3</sup>](#),
- [Karla Diaz-Ordaz<sup>2,3 na1</sup>](#) &
- [Ruth H. Keogh<sup>2,3 na1</sup>](#)

*Nature* volume 593, pages 270–274 (2021) [Cite this article](#)

- 147k Accesses
- 17 Citations
- 8989 Altmetric
- [Metrics details](#)

## Subjects

- [Infectious diseases](#)
- [Risk factors](#)
- [SARS-CoV-2](#)

## Abstract

SARS-CoV-2 lineage B.1.1.7, a variant that was first detected in the UK in September 2020<sup>1</sup>, has spread to multiple countries worldwide. Several studies have established that B.1.1.7 is more transmissible than pre-existing variants, but have not

identified whether it leads to any change in disease severity<sup>2</sup>. Here we analyse a dataset that links 2,245,263 positive SARS-CoV-2 community tests and 17,452 deaths associated with COVID-19 in England from 1 November 2020 to 14 February 2021. For 1,146,534 (51%) of these tests, the presence or absence of B.1.1.7 can be identified because mutations in this lineage prevent PCR amplification of the spike (*S*) gene target (known as *S* gene target failure (SGTF)<sup>1</sup>). On the basis of 4,945 deaths with known SGTF status, we estimate that the hazard of death associated with SGTF is 55% (95% confidence interval, 39–72%) higher than in cases without SGTF after adjustment for age, sex, ethnicity, deprivation, residence in a care home, the local authority of residence and test date. This corresponds to the absolute risk of death for a 55–69-year-old man increasing from 0.6% to 0.9% (95% confidence interval, 0.8–1.0%) within 28 days of a positive test in the community. Correcting for misclassification of SGTF and missingness in SGTF status, we estimate that the hazard of death associated with B.1.1.7 is 61% (42–82%) higher than with pre-existing variants. Our analysis suggests that B.1.1.7 is not only more transmissible than pre-existing SARS-CoV-2 variants, but may also cause more severe illness.

[Download PDF](#)

## Main

Most community SARS-CoV-2 PCR tests in England are processed by one of six national ‘Lighthouse’ laboratories. Among the mutations carried by the B.1.1.7 lineage—also known as variant of concern (VOC) 202012/01—is a six-nucleotide deletion that prevents the amplification of the *S* gene target by the commercial PCR assay that is currently used in three of the Lighthouse laboratories<sup>1</sup>. By linking individual records of positive community tests with and without SGTF to a comprehensive line list of deaths associated with COVID-19 in England, we estimate the relative hazard of death associated with infection with the B.1.1.7 variant. We define confirmed SGTF as a compatible PCR result with cycle threshold ( $C_t$ )  $< 30$  for *orflab*,  $C_t < 30$  for the nucleocapsid (*N*) gene and no detectable *S* ( $C_t > 40$ ); confirmed non-SGTF as any compatible PCR result with  $C_t < 30$  for each of the *orflab*, *N* and *S* genes; and an inconclusive (missing) result as any other positive test, including tests processed by a laboratory that is incapable of assessing SGTF.

## Characteristics of the study population

The study sample (Extended Data Table 1) comprises 2,245,263 individuals who had a positive community ('Pillar 2') test between 1 November 2020 and 14 February 2021. Just over half of those tested (1,146,534; 51.1%) had a conclusive SGTF reading and, of these, 58.8% had SGTF. Female individuals comprised 53.6% of the total sample;

44.3% of individuals were aged 1–34 years, 34.4% aged 35–54 years, 15.1% aged 55–69 years, 4.3% aged 70–84 years and 1.9% aged 85 years or older. The majority of individuals (93.7%) lived in residential accommodation (defined as a house, flat, sheltered accommodation or house in multiple occupancy) and 3.1% lived in a care or nursing home. On the basis of self-identified ethnicity, 74.0% were white, 13.6% were Asian, 4.6% were Black and 7.8% were of other, mixed or unknown ethnicity. All seven NHS England regions are represented, with the London region contributing 22.5% of tests and the South West 5.9%. The first three weeks of the study period (1–21 November) contributed 15.5% of the total tests, and the final three weeks (24 January–14 February) 12.8%. The period between 3 and 23 January contributed 31.6% of tests.

For those samples for which SGTF status was measured, SGTF prevalence was similar in male and female individuals, but lower in the older age groups: 59.0% in 1–34-year-old individuals compared with 55.4% in those aged 85 years and older. In keeping with these age patterns, SGTF prevalence was lower in individuals living in a care or nursing home (54.3%) than those in residential accommodation (58.8%). SGTF prevalence by self-identified ethnicity was 58.0% in the white group, 57.6% in the Asian group, 69.6% in the Black group and 64.8% in the other, mixed or unknown ethnicity group. SGTF prevalence was the lowest in the most-deprived quintile of the index of multiple deprivation<sup>3</sup> (IMD) (53.9%). The highest prevalences of SGTF over the study period were observed in the East of England (77.5%), South East (77.3%) and London (75.4%) regions, and the prevalence of SGTF was the lowest in the North East and Yorkshire region (41.2%). The prevalence of SGTF increased steeply over time (Fig. 1a), from 5.8% during 1–21 November 2020 to 94.3% during 24 January–14 February 2021.

**Fig. 1: Descriptive analyses.**



**a**, The number of samples with and without SGTF by day from 1 November 2020 to 14 February 2021, the period covered by our main analysis. **b**, Number of deaths within 28 days of a positive test by specimen date for all data included in the analysis. **c**, Kaplan–Meier plot showing survival (point estimates and 95% confidence intervals) among individuals tested in the community in England with and without SGTF, in the subset for whom SGTF was measured. The inset shows the full *y*-axis range. **d–i**, Crude death rates (point estimates and 95% confidence intervals) among SGTF versus non-SGTF cases (in the subset for whom SGTF was measured;  $n = 1,146,534$ ) for deaths within 28 days of a positive test stratified by broad age groups and sex (**d**), residence type (**e**), ethnicity (**f**), IMD decile (**g**), region of NHS England (**h**) and specimen date (**i**). Horizontal bars show the overall crude death rates (point estimates and 95% confidence intervals) by age group irrespective of SGTF status.

[Source data](#)

[Full size image](#)

Missing SGTF status was strongly associated with age and residence type. The proportion with SGTF status missing was similar in age groups 1–34 (48.3%), 35–54 (47.8%) and 55–69 (48.2%), and then increased to 54.4% in the 70–84 age group and to 77.7% in the 85 and older age group. SGTF status was missing in 87.9% of tests for individuals living in a care or nursing home, compared with 47.4% of tests among individuals in residential accommodation. This is due in part to more extensive use of lateral flow immunoassay tests in care homes, which do not yield an SGTF reading.

Missingness in SGTF status also differed substantially between regions of NHS England, ranging from 21.2% in the North West to 71.1% in the South West, which is largely explained by proximity to a Lighthouse laboratory that is capable of producing an SGTF reading (Extended Data Fig. 1). Missingness also depended on the date of the specimen, with the percentage missing being lower for the earlier specimen dates and highest (54.4%) in the 21-day period that contributed the most tests (3–23 January). There were also minor differences in missingness depending on ethnicity and IMD. Of the 48.9% of tests with missing SGTF status, 5.1% were inconclusive owing to high  $C_t$  values and the remaining 43.8% were not assessed for SGTF.

In total, 19,615 people in the study sample are known to have died (0.87% of 2,245,263). Crude death rates were substantially higher in the elderly and in those living in a care or nursing home (Supplementary Table 1). The standard definition of a death associated with COVID-19 in England is any death that occurred within 28 days of the first positive SARS-CoV-2 test of an individual; 17,452 of the observed deaths (89.0%) met this criterion (Fig. 1b). Among those with known SGTF status, the crude death rate associated with COVID-19 was 1.86 deaths per 10,000 person-days of follow-up in the SGTF group, versus 1.42 deaths per 10,000 person-days in the non-SGTF group (Fig. 1c and Extended Data Table 2). Stratifying by broad age groups and by sex, residence type, ethnicity, IMD, region and specimen date, death rates within 28 days of a positive SARS-CoV-2 test were higher among SGTF than non-SGTF cases in 98 of the 104 strata assessed (94%; Fig. 1d–i and Supplementary Table 2).

## Cox regression analyses

To estimate the association between SGTF and mortality while controlling for observed confounding (Extended Data Fig. 2), we fitted a series of Cox proportional hazards models<sup>4</sup> to the data. We stratified the baseline mortality hazard by lower-tier local authority (LTLA) and specimen date to control for geographical and temporal differences in the hazard—for example, due to changes in hospital pressure during the study period—and used spline terms for age and IMD and fixed effects for sex, ethnicity and residence type in the hazard model. All models were fitted twice, once using complete cases only, that is, by simply excluding individuals with missing SGTF status, and once using inverse probability weighting (IPW), that is, accounting for missingness by upweighting individuals whose characteristics—age, sex, IMD, ethnicity, residence type, NHS England region of residence and sampling week—are underrepresented among complete cases. The analysis of the complete cases assumes that whether an individual dies is independent of whether their SGTF status is observed or missing, given the individual's other characteristics included in the survival model, whereas the IPW analysis assumes that whether an individual has SGTF is independent of whether their SGTF status is observed or missing, given the

individual's other characteristics included in the model used to derive weights for IPW<sup>5</sup>.

For the analysis of the complete cases, the estimated hazard ratio for SGTF was 1.55 (95% confidence interval, 1.39–1.72), indicating that the hazard of death in the 28 days after a positive test is 55% (39–72%) higher for SGTF than for non-SGTF cases.

To assess the model assumption of proportional hazards, we added an interaction term between SGTF and time since a positive test. There was strong evidence of non-proportionality of hazards (likelihood ratio test  $\chi^2=11$ ,  $P=0.009$ ) (Fig. 2a and Extended Data Fig. 3), with the estimated time-varying hazard ratio increasing over time: 1.14 (0.92–1.40) on day 1 after the positive test, 1.58 (1.42–1.75) on day 14 and 2.24 (1.75–2.87) on day 28. Adding higher-order functions of time into the interaction terms did not significantly improve the fit of the model (likelihood ratio test  $\chi^2=3.3$ ,  $P=0.07$ ). We found no evidence that the effect of SGTF varied depending on age group (likelihood ratio test  $\chi^2=5.8$ ,  $P=0.22$ ), sex ( $\chi^2=0.057$ ,  $P=0.81$ ), IMD ( $\chi^2=11$ ,  $P=0.31$ ), ethnicity ( $\chi^2=1.2$ ,  $P=0.75$ ) or residence type ( $\chi^2=0.33$ ,  $P=0.85$ ). We note, however, that the relatively small number of deaths among 1–34-year-old individuals during the study period (44 deaths) does not permit robust assessment of the effect of SGTF in this age group. Other time-covariate interactions suggested that the time from positive test to death was slightly shorter among women, care home residents and elderly individuals; see Supplementary Note 1 for more details on models with interaction terms.

**Fig. 2: Survival analyses.**

---

 **figure2**

**a–d**, Estimated hazard ratio of death (point estimate and 95% confidence intervals) within 28 days of a positive test for the SGTF analysis for complete cases (**a**), SGTF analysis with IPW (**b**),  $p_{VOC}$  analysis for complete cases (**c**) and  $p_{VOC}$  analysis with IPW (**d**) in a model stratified by LTLA and specimen date and adjusted for the other

covariates. e, Estimated hazard ratio of death (point estimates and 95% confidence intervals) across each model investigated. Death types are coded as follows: d $X$ , all deaths within  $X$  days of a positive test; dNA, all deaths with no restriction on follow-up time; c28, death-certificate-confirmed deaths associated with COVID-19 within 28 days; e60, all deaths within 60 days plus all death-certificate-confirmed deaths associated with COVID-19 within any time period. S, spline term (for age or IMD); L, linear term (for age or IMD); NHSE, NHS England region ( $n = 7$ ); UTLA, upper-tier local authority ( $n = 150$ ); LTLA, lower-tier local authority ( $n = 316$ ). LTLA start date signifies a start date chosen separately for each LTLA; Y:tstop signifies an interaction term between covariate  $Y$  and time since positive test (eth: ethnicity, res: residence type);  $p_{VOC2}$  signifies sequence-based misclassification adjustment (see [Methods](#)).

[Source data](#)

[Full size image](#)

For IPW analysis, a model to predict missingness is required. We evaluated a series of such models, including a cauchit model, which is a robust alternative to logistic regression that is suitable for IPW<sup>5</sup>. We selected the cauchit model as it fit well and resulted in less extreme weights than other models (Extended Data Fig. 4). The IPW analysis gave similar results to the analysis of the complete cases, yielding a hazard ratio of 1.58 (1.40–1.78). Similar to the analysis of the complete cases, the IPW analysis recovered an increasing hazard ratio with time since a positive test, but the increase was less marked (Fig. 2b) and did not significantly differ from zero (Wald test  $\chi^2 = 0.23$ ).

## Misclassification analysis

Before the emergence of B.1.1.7, a number of minor circulating SARS-CoV-2 lineages with mutations in the  $S$  gene could also cause SGTF<sup>1</sup>. Our main analyses are restricted to specimens from 1 November 2020 onwards to avoid diluting the measured effect of B.1.1.7 on mortality due to non-B.1.1.7 lineages that cause SGTF. As an alternative approach, we undertook a misclassification analysis<sup>6</sup>, modelling the relative frequency of SGTF over time for each NHS England region as a low, time-invariant frequency of non-B.1.1.7 samples with SGTF plus a logically growing<sup>2</sup> frequency of B.1.1.7 samples. This allowed us to estimate the probability,  $p_{VOC}$ , that a given SGTF sample was B.1.1.7 based on its specimen date and NHS England region (Extended Data Fig. 5). Again restricting the analysis to specimens from 1 November 2020 onward, we find a hazard ratio associated with  $p_{VOC}$  of 1.58 (1.42–1.76) for the analysis of the complete cases and 1.61 (1.42–1.82) for the IPW analysis (Fig. 2c,d).

## Absolute risks

To put these results into context, we estimated absolute mortality risks by applying hazard ratios for SGTF to the baseline risk of death among individuals tested in the community between August and October 2020 (assumed to be illustrative of the case fatality ratio associated with pre-existing variants of SARS-CoV-2) (Table 1). For the analysis of the complete cases, in women aged 70–84 years, the estimated risk of death within 28 days of a positive SARS-CoV-2 test increases from 2.9% without SGTF to 4.4% with SGTF (95% confidence interval, 4.0–4.9%) and for women 85 years or older, the risk increases from 13% to 19% (17–21%). For men aged 70–84 years, the risk of death within 28 days increases from 4.7% to 7.2% (6.4–7.9%) and for men 85 years or older, the risk increases from 17% to 25% (23–27%). Estimates based on the IPW analysis corrected for misclassification were marginally higher. These estimates reflect a substantial increase in absolute risk among older age groups, but the risk of death associated with COVID-19 after a positive test in the community remains below 1% in most individuals who are younger than 70 years old. Note that these estimates capture the fatality ratio among people tested in the community, and are thus likely to be higher than the infection fatality ratio, as many individuals with a SARS-CoV-2 infection are never tested.

**Table 1 Absolute 28-day mortality risk for B.1.1.7**  
[Full size table](#)

## Further investigations

We conducted a number of sensitivity analyses to verify the robustness of our results. Our main results were largely insensitive to: restriction of the analysis to deaths caused by COVID-19 confirmed on the death certificate; any follow-up time of 21 days or longer; coarseness of geographical and temporal stratification; use of linear versus spline terms for age and IMD; analysis start date; follow-up time–covariate interactions; removal of the 10-day death registration cut-off; and restriction of the analysis to individuals with a full 28-day follow-up period (Fig. 2e). Generally, the IPW analysis yielded marginally higher hazard ratios, with greater uncertainty. As a further sensitivity analysis, we adjusted for an indicator in community testing data for whether the individual was tested because of symptoms or owing to asymptomatic screening. Although we caution that symptomatic screening status may lie on the causal pathway between SGTF status and death, we found that this adjustment had no effect on the relative hazard of SGTF (1.54 (1.39–1.71); analysis of complete cases).

## Discussion

We previously found that B.1.1.7 is substantially more transmissible than pre-existing SARS-CoV-2 variants, but could not robustly identify any associated change in disease severity using population-level analysis of early data<sup>2</sup>. This analysis of individual-level data, which controls for factors that could confound the association between B.1.1.7 infection and death, reveals an increase in COVID-19 mortality associated with the B.1.1.7 lineage. We stratify our analyses by test time and geographical location—mimicking matching on these variables—to account for changes in testing rates and changing pressures on hospital services over time and by region. Our findings are consistent with earlier reports by ourselves and other groups<sup>7</sup> and with contemporaneous studies<sup>8,9,10,11</sup> assessing the risk of severe outcomes among individuals with B.1.1.7 infection. Notably, our study is limited to individuals tested in the community. Indicators for infection with the B.1.1.7 variant are not currently available for most people who die from COVID-19 in England, as they are tested in the hospital rather than in the community and hospitals do not routinely collect genotypic data. However, this restricted focus allows us to capture the combined effect of an altered risk of hospitalization given a positive test and an altered risk of death given hospitalization, while only the latter would be measurable in a study of hospitalized patients only. Unfortunately, we were unable to account for vaccination status in this analysis.

We do not identify any mechanism for the increased mortality here. Infections with the B.1.1.7 variant are associated with higher viral concentrations in nasopharyngeal swabs, as measured by  $C_t$  values using PCR testing (Extended Data Fig. 6). Higher viral load could therefore be partly responsible for the observed increase in mortality; this could be assessed using a mediation analysis. Alternatively, changes in test-seeking behaviour could, in principle, explain our results. If B.1.1.7-associated infections were less likely to cause symptoms, but symptomatic cases of B.1.1.7 were more severe, then our study could overestimate changes in the infection fatality rate. However, we find no clear difference in SGTF frequency among community tests relative to a random sample of SARS-CoV-2 infections in the population (Extended Data Fig. 7), which suggests that variant-associated changes in test-seeking propensity do not explain our findings.

## Methods

### Ethical approval

Approved by the Observational/Interventions Research Ethics Committee at the London School of Hygiene and Tropical Medicine (reference number 24020). Participant consent is not required for national infectious disease notification datasets in England.

## Data sources

We linked three datasets provided by Public Health England: a line list of all positive tests in Pillar 2 (community) testing for SARS-CoV-2 for England, containing specimen date and demographic information on the participants; a line list of cycle threshold ( $C_t$ ) values for the *orflab*, *N* (nucleocapsid), and *S* (spike) genes for positive tests that were processed in one of the three national laboratories (Alderley Park, Glasgow or Milton Keynes) using the Thermo Fisher TaqPath COVID-19 assay; and a line list of all deaths associated with COVID-19 in England, which combines and deduplicates deaths reported by hospitals in England, by the Office for National Statistics, through direct reporting from Public Health England Health Protection Teams, and through Demographic Batch Service tracing of laboratory-confirmed cases<sup>12</sup>. We link these datasets using a numeric identifier for Pillar 2 tests ('FINALID') common to all three datasets. We define SGTF as any test with  $C_t < 30$  for *orflab* and *N* targets but no detectable *S* gene, and non-SGTF as any test with  $C_t < 30$  for *orflab*, *N* and *S* targets. A small proportion (10.4%) of SGTF tests are inconclusive. The study population of interest is defined as all individuals who received a positive Pillar 2 test between 1 November 2020 and 14 February 2021. For our main analysis, we included only tests from after 1 November 2020 to avoid including an excess of tests with SGTF not resulting from infection by lineage B.1.1.7. In sensitivity analyses, we also consider extending the population to include tests performed between 1 September and 31 October 2020.

Our analysis does not include individuals who first tested positive in hospital—that is, those patients who presented to the hospital after the onset of symptoms without first being tested in the community. This is because the cycle threshold values used to ascertain SGTF status are not available for individuals who were not tested in the community. Of the 57,750 deaths associated with COVID-19 in England during the study period, 17,642 deaths (30.5%) can be linked to a positive Pillar 2 test; among these, 4,945 have non-missing SGTF status. So, although our study includes 1,098,729 Pillar 2 tests with non-missing SGTF status, which represents 51.1% of the 2,245,263 Pillar 2 tests over this period and 40.2% of the 2,736,806 combined Pillar 1 (hospital) and Pillar 2 (community) SARS-CoV-2 tests over this period, we can only assess SGTF status for 8.6% (4,945/57,750) of the individuals who died from COVID-19 over the study period. This is explained by differing mortality rates among individuals who first test positive in a hospital compared to those who are tested in the community, as the former group are much more likely to have a severe illness, as well as by missingness in the SGTF data.

There was a small amount of missing data for sex ( $n = 14$ , <0.01%), age ( $n = 171$ , <0.01%), and IMD and regional covariates ( $n = 3,817$ , 0.16%). There were no missing specimen dates. Individuals with missing age, sex or geographical location were

excluded. We also excluded individuals from the dataset whose age was recorded as zero, as there were 17,913 age-0 individuals compared to 10,132 age-1 individuals in the dataset, suggesting that many of these age-0 individuals may have been miscoded. There were some missing data on ethnicity ( $n = 47,491$ , 2.1%) and we created a category that combines missing values with ‘other’ and ‘mixed’. Missing values for residence type ( $n = 63,905$ , 2.8%) were also combined with an ‘other’ category. The full dataset used for the main analysis comprises 2,245,263 individuals, with SGTF status missing or inconclusive for 1,098,729 (48.9%). Missing data on the exposure is addressed in the analysis, described below.

We grouped residence types into three categories: residential, which included the ‘residential dwelling (including houses, flats and sheltered accommodation)’ and ‘house in multiple occupancy’ groups; care or nursing home; and other or unknown, which included the ‘medical facilities (including hospitals and hospices, and mental health)’, ‘no fixed abode’, ‘other property classifications’, ‘overseas address’, ‘prisons, detention centres and secure units’, ‘residential institution (including residential education)’ and ‘undetermined’ groups, as well as an unspecified residence type. We grouped ethnicities into four categories according to the broad categories used in the 2011 UK Census: Asian, which included the ‘Bangladeshi (Asian or Asian British)’, ‘Chinese (other ethnic group)’, ‘Indian (Asian or Asian British)’, ‘Pakistani (Asian or Asian British)’ and ‘any other Asian background’ groups; Black, which included the ‘African (Black or Black British)’, ‘Caribbean (Black or Black British)’ and ‘any other Black background’ groups; white, which included the ‘British (white)’, ‘Irish (white)’ and ‘any other white background’ groups; and ‘other, mixed or unknown’, which included the ‘any other ethnic group’, ‘white and Asian (mixed)’, ‘white and Black African (mixed)’, ‘white and Black Caribbean (mixed)’, ‘any other mixed background’ and ‘Unknown’ groups.

## Statistical methods

There are several factors that we expect are associated with both SGTF and with risk of death, thus confounding the association between SGTF and risk of death in those individuals who were tested. Area of residence and specimen date were expected to be potentially strong confounding factors. Area of residence is expected to be strongly associated with SGTF status due to different virus variants circulating in different areas, and specimen date because the prevalence of SGTF is known to have greatly increased over time. Area of residence and specimen date are also expected to be associated with risk of death after a positive test, including due to differences associated with differential pressure on hospital resources by area and time. The following variables were also identified as potential confounding factors: sex, age, residence type (residential, care or nursing home, or other or unknown), ethnicity (white, Asian, Black or other, mixed or unknown) and IMD. The potential

confounding factors are referred to collectively as the covariates. For descriptive analyses, age (in years) was categorized as 1–34, 35–54, 55–69, 70–84, or 85 and older.

Descriptive analyses were performed. We tabulated the distribution of the covariates in the whole study sample, the association between each covariate and SGTF status in the subset for whom SGTF was measured, and the association between each covariate and missing data in SGTF status (Extended Data Table 1). The subset for whom SGTF status was measured are referred to as the complete cases. The unadjusted association between SGTF and mortality in the complete cases was assessed using a Kaplan–Meier plot (Fig. 1c), and Kaplan–Meier plots and crude 28-day mortality rates are also presented separately according to the categories of the covariates (Extended Data Table 2 and Extended Data Fig. 2). Crude overall mortality rates (that is, not restricted to 28 days after a positive test) were obtained for the whole sample, by SGTF status in the complete cases, and in those with missing SGTF status, according to the categories of each covariate (Supplementary Table 1). We also obtained mortality rates by SGTF status (in the complete cases) for the categories of each covariate stratified by age group (Fig. 1d–i). Exact Poisson confidence intervals are used for mortality rates, assuming constant rates.

Approximately 49% of individuals in the study sample are missing data on SGTF status, due to their test not having been processed at one of the three laboratories using the Thermo Fisher TaqPath COVID-19 assay or the test being inconclusive. We performed analysis on the complete cases, restricted to the subset for whom SGTF status was measured and conclusive. This analysis of complete cases assumes that for each analysis, the missing data—in this case missing SGTF status—are independent of the outcome of interest given the variables included in the models. This is a specific type of ‘missing not at random’ assumption, as in particular it is allowed to depend on the underlying value of SGTF. We also performed an analysis of the complete cases using inverse probability weights<sup>5</sup> (IPW) to address the missing data on SGTF, under a ‘missing at random’ assumption. In the analysis, each individual with SGTF status measured is weighted by the inverse of their probability of having SGTF status measured based on their covariates. For the IPW, the missingness model estimated the probability of missingness using logistic regression with age (restricted cubic spline), sex, IMD decile (restricted cubic spline), ethnicity, residence type by asymptomatic screening indicator and NHS region by specimen week as predictors. We also considered a cauchit and a Gosset link for the missingness model, including the same predictors, as this was expected to provide better stability for the weights<sup>5</sup>. The fit of the missingness model was assessed using a *Q*–*Q* plot (Extended Data Fig. 4), and Hosmer–Lemeshow and Hinkley tests were used to choose the most appropriate model.

Cox regression<sup>4</sup> was used to estimate the association between SGTF and the hazard of mortality, conditioning on the potential confounding factors listed above. The analyses described here were applied to the complete cases and using IPW. For IPW analyses, the standard errors accounted for the weights, although the fact that the weights were estimated was not accounted for; this results in conservative standard errors. The baseline hazard in the Cox model was stratified by both specimen date and LTLA, therefore finely controlling for these variables. The stratification gives a large number of strata matched by specimen date and LTLA. Only those strata that contain individuals who died and individuals who survived contribute to the analysis. The analysis is therefore similar to the analysis that would be performed had we created a matched nested case-control sample. The remaining variables were included as covariates in the model (sex, age, residence type, ethnicity and IMD decile). Age was included as a restricted cubic spline with five knots, and IMD decile was included as a restricted cubic spline with three knots. The time origin for the analysis was specimen date and we considered deaths up to 28 days after the specimen date for the main analyses. Individuals who did not die within 28 days were censored at the earlier of 28 days after the specimen date and the administrative censoring date, which we chose as the date of the most recent death linkable to SGTF status minus 10 days (that is, 14 February 2021) to minimize any potential bias due to late reporting of deaths. We began by assuming the proportionality of the hazards for SGTF and the covariates included in the model. The assumption of proportional hazards was assessed by including in the model an interaction between each covariate and time, which was performed separately for SGTF and for each other covariate. Schoenfeld residual plots were also obtained for each covariate (Extended Data Fig. 3). We assessed whether the association between SGTF and the hazard was modified by age, sex, IMD, ethnicity and residence type. Models with and without interactions were compared using likelihood ratio tests for the analyses of the complete cases. For the analysis using IPW, we used Wald tests based on robust standard errors<sup>13</sup>.

The analysis assumes that censoring is uninformative, which is plausible as all censoring is administrative.

## Misclassification analysis

The exposure of SGTF is subject to misclassification, because a number of minor circulating SARS-CoV-2 lineages in addition to B.1.1.7 are also associated with failure to amplify the *S* gene target. Accordingly, a positive test with SGTF is not necessarily indicative of infection with B.1.1.7. A negative test of SGTF is assumed to be indicative of an absence of infection with B.1.1.7. Misclassification of an exposure can result in bias in its estimated association with the outcome. We fitted a logistic model to Pillar 2 SGTF frequencies by NHS region to estimate a ‘background’ rate of SGTF in the absence of B.1.1.7, assuming a beta-binomial prior. This model is then

used to estimate the probability that an individual testing positive for SGTF is infected with B.1.1.7, separately for individuals in each NHS region. These probabilities can then be used in place of the indicator of SGTF exposure in the Cox models. This is the regression calibration approach<sup>6</sup> to correcting for bias due to measurement error in an exposure.

We fitted models accounting for false-positive results (modelled as regionally varying background rates of SGTF associated with non-B.1.1.7 variants) to the SGTF data. Our logistic model for B.1.1.7 growth over time is as follows:

```
 $$\text{logit} \backslash f(t) = \text{slope} \times (t - \text{intercept}) $$
 $$ s(t) = f(t) + (1-f(t)) \times \text{FP} $$
 $\begin{array}{c} c \sim \text{beta}(k_t, n_t) \\ \text{FP} \sim \text{normal}(0, 1, 000) \\ \text{alpha} = s(t) \times ((c \times o) / (n_t \times (c - 2) + 1)) \\ \text{beta} = (1 - s(t)) \times ((c \times o) / (n_t \times (c - 2) + 1)) \end{array} $
 $\text{slope} \sim \text{normal}(0, 1)$
 $\text{intercept} \sim \text{normal}(0, 1, 000)$
 $\text{FP} \sim \text{beta}(1.5, 15)$
 $\text{conc} \sim \text{normal}(0, 500) \geq 2$
```

where  $f(t)$  is the predicted frequency of B.1.1.7 among positive tests at time  $t$  (in days since 1 September 2020) based on the terms slope and intercept;  $s(t)$  is the predicted frequency of SGTF at time  $t$  due to the combination of B.1.1.7 and a background false-positive rate (FP) among non-B.1.1.7 variants, conc is the ‘concentration’ parameter ( $\text{conc} = \alpha + \beta$ ) of a beta distribution with mode  $s(t)$ ;  $k_t$  is the number of SGTFs detected at time  $t$ ;  $n_t$  is the total number of tests at time  $t$ ; and the tilde ( $\sim$ ) signifies ‘distributed as’. All priors above are chosen to be vague, and the truncation of the concentration parameter to values greater than 2 ensures a unimodal distribution for the proportion of tests that are SGTF. The model above is fitted separately for each NHS England region. Then,  $p_{\text{VOC}}$  for a test with SGTF = 1 at time  $t$  is equal to  $f(t)/s(t)$ , and  $p_{\text{VOC}} = 0$  for all tests with SGTF = 0. The model was fitted using Markov chain Monte Carlo with 10,000 iterations of burn-in and 5,000 iterations of sampling.

The model above was fitted using the same data source (that is, SGTF frequencies among Pillar 2 community tests for SARS-CoV-2) as our survival analysis. To verify the robustness of this model, we performed a sensitivity analysis using sequencing data from the COVID-19 UK Genomics Consortium<sup>14</sup> (<https://www.cogconsortium.uk/>) downloaded from the Microreact platform<sup>15</sup> (<https://microreact.org/>) on 11 January 2020 to estimate  $p_{\text{VOC}}$ . In this alternative analysis, we estimated  $p_{\text{VOC}}$  for each NHS England region and date as the number of

samples that were VOC 202012/01 (that is, lineage B.1.1.7 with mutations Δ69/Δ70 and N501Y in spike) divided by the number of samples that were SGTF (that is, any lineage with Δ69/Δ70, the deletion that causes SGTF) for that NHS England region and date, setting  $p_{VOC} = 1$  for all dates later than 31 December 2020 as there were no sequencing data available past this date, and filling any gaps in the data using linear interpolation. This yielded nearly identical results in our survival analysis compared with the analysis that uses the modelled  $p_{VOC}$  described above (Fig. 2e).

## Absolute risks

Estimates from the final Cox models were used to obtain estimates of absolute risk of death within 28 days of a positive test for SGTF and  $p_{VOC}$ . Given the strong influence of age on risk of death, we present absolute risks by sex and age group (in years; 1–34, 35–54, 55–69, 70–84, 85 and older). Absolute risks of death (case fatality rate) within 28 days were estimated by age group and sex using data on individuals tested during August–October 2020; this is referred to as the baseline risk. The absolute risks of death for individuals with SGTF were then estimated as follows. If the baseline absolute risk of death in a given age group is  $1 - A$ , then the estimated absolute risk of death with SGTF is  $1 - A^{HR}$ , where HR denotes the estimated hazard ratio obtained from the Cox model assuming proportional hazards. Standard errors are obtained via the delta method, and confidence intervals were based on normal approximations.

## Sensitivity analyses

Several sensitivity analyses were performed. After establishing the final model using the process outlined above, we investigated the effect of using different variables for the stratification of the baseline hazard measuring region at a coarser level (the upper-tier local authority or NHS England region), as well as coarser test specimen time (week rather than exact date). Adjusting for these variables instead of using stratification was also explored. We also repeated the main analysis restricting data to specimens collected from September onwards, October onwards, November onwards or December onwards.

To assess the effect of imposing an administrative cut-off to follow-up time of 10 days before data extraction, we first reanalysed the data without this cut-off, as well as reanalysing the data restricting the analysis to individuals with a follow-up of at least 28 days.

Finally, we adjusted for symptomatic status associated with the test (asymptomatic versus symptomatic), which relates to whether the test was given for asymptomatic screening purposes or on the basis of a request by a (presumed symptomatic)

individual, as only symptomatic individuals may request a community SARS-CoV-2 test in England.

## Reporting summary

Further information on research design is available in the [Nature Research Reporting Summary](#) linked to this paper.

## Data availability

An anonymized dataset that enables the replication of the analysis is available at <https://zenodo.org/record/4579857>. [Source data](#) are provided with this paper.

## Code availability

Analysis code deposited at time of publication is available at <https://zenodo.org/record/4579857>. The repository is maintained at <https://github.com/nicholasdavies/cfrvoc>.

## References

1. 1.

Chand, M. et al. *Investigation of Novel SARS-COV-2 Variant: Variant of Concern 202012/01*. Technical Briefing 1  
[https://assets.publishing.service.gov.uk/government/uploads/system/uploads/attachment\\_data/file/959438/Technical\\_Briefing\\_VOC\\_SH\\_NJL2\\_SH2.pdf](https://assets.publishing.service.gov.uk/government/uploads/system/uploads/attachment_data/file/959438/Technical_Briefing_VOC_SH_NJL2_SH2.pdf) (Public Health England, 2020).

2. 2.

Davies, N. G. et al. Estimated transmissibility and impact of SARS-CoV-2 lineage B.1.1.7 in England. *Science* <https://doi.org/10.1126/science.abg3055> (2021).

3. 3.

McLennan, D. et al. *English Indices of Deprivation 2019*.  
<https://www.gov.uk/government/publications/english-indices-of-deprivation-2019-technical-report> (Ministry of Housing, Communities & Local Government 2019).

4. 4.

Cox, D. R. Regression models and life-tables. *J. R. Stat. Soc. B* **34**, 187–202 (1972).

[MathSciNet](#) [MATH](#) [Google Scholar](#)

5. 5.

Seaman, S. R. & White, I. R. Review of inverse probability weighting for dealing with missing data. *Stat. Methods Med. Res.* **22**, 278–295 (2013).

[MathSciNet](#) [Article](#) [Google Scholar](#)

6. 6.

Keogh, R. H. et al. STRATOS guidance document on measurement error and misclassification of variables in observational epidemiology: part 1—basic theory and simple methods of adjustment. *Stat. Med.* **39**, 2197–2231 (2020).

7. 7.

Scientific Advisory Group for Emergencies. *NERVTAG: Update Note on B.1.1.7 Severity, 11 February 2021*.

<https://www.gov.uk/government/publications/nervtag-update-note-on-b117-severity-11-february-2021> (2021).

8. 8.

Challen, R. et al. Risk of mortality in patients infected with SARS-CoV-2 variant of concern 202012/1: matched cohort study. *BMJ* **372**, n579 (2021).

[Article](#) [Google Scholar](#)

9. 9.

Grint, D. J. et al. Case fatality risk of the SARS-CoV-2 variant of concern B.1.1.7 in England. *Euro Surveill.* **26**, 21002 (2021).

10. 10.

Patone, M. et al. Analysis of severe outcomes associated with the SARS-CoV-2 variant of concern 202012/01 in England using ICNARC case mix programme

and QResearch databases. Preprint at  
<https://doi.org/10.1101/2021.03.11.21253364> (2021).

11. 11.

Bager, P. et al. Increased risk of hospitalisation associated with infection with SARS-CoV-2 lineage B.1.1.7 in Denmark. Preprint at  
<https://doi.org/10.2139/ssrn.3792894> (2021).

12. 12.

Public Health England COVID-19 Epidemiology Cell. COVID-19 confirmed deaths in England: report. <https://www.gov.uk/government/publications/covid-19-reported-sars-cov-2-deaths-in-england/covid-19-confirmed-deaths-in-england-report> (accessed 20 February 2021).

13. 13.

Lumley, T. & Scott, A. Partial likelihood ratio tests for the Cox model under complex sampling. *Stat. Med.* **32**, 110–123 (2013).

[MathSciNet](#) [Article](#) [Google Scholar](#)

14. 14.

The COVID-19 Genomics UK (COG-UK) Consortium. An integrated national scale SARS-CoV-2 genomic surveillance network. *Lancet Microbe* **1**, E99–E100 (2020).

[Article](#) [Google Scholar](#)

15. 15.

Argimón, S. et al. Microreact: visualizing and sharing data for genomic epidemiology and phylogeography. *Microbial Genomics* **2**, 93 (2016).

[Article](#) [Google Scholar](#)

[Download references](#)

## Acknowledgements

We gratefully acknowledge the assistance of Public Health England in providing the analysis data and authorizing the release of an anonymized dataset. This work was

supported by grants from UK Research and Innovation, the National Institutes of Health Research (NIHR) Health Protection Research Unit in Immunisation (NIHR200929) and the UK Medical Research Council (MC\_PC\_19065) (N.G.D.); Global Challenges Research Fund project ‘RECAP’ managed through Research Councils UK and the Economic and Social Research Council (ES/P010873/1) (C.I.J.); European Commission project ‘EpiPose’ (101003688) and the NIHR (NIHR200908) (W.J.E.); the National Institutes of Health/National Institute of Allergy and Infectious Diseases (R01AI148127) (N.P.J.); a Royal Society-Wellcome Trust Sir Henry Dale Fellowship (218554/Z/19/Z) (K.D.-O.); and a UKRI Future Leaders Fellowship (MR/S017968/1) (R.H.K.). See Supplementary Note 2 for working group acknowledgements.

## Author information

### Author notes

1. These authors contributed equally: Karla Diaz-Ordaz, Ruth H. Keogh

### Affiliations

1. Centre for Mathematical Modelling of Infectious Diseases, London School of Hygiene and Tropical Medicine, London, UK

Nicholas G. Davies, Christopher I. Jarvis, Kevin van Zandvoort, Samuel Clifford, Fiona Yueqian Sun, Sebastian Funk, Graham Medley, Yalda Jafari, Sophie R. Meakin, Rachel Lowe, Matthew Quaife, Naomi R. Waterlow, Rosalind M. Eggo, Jiayao Lei, Mihaly Koltai, Fabienne Krauer, Damien C. Tully, James D. Munday, Alicia Showering, Anna M. Foss, Kiesha Prem, Stefan Flasche, Adam J. Kucharski, Sam Abbott, Billy J. Quilty, Thibaut Jombart, Alicia Rosello, Gwenan M. Knight, Mark Jit, Yang Liu, Jack Williams, Joel Hellewell, Kathleen O'Reilly, Yung-Wai Desmond Chan, Timothy W. Russell, Simon R. Procter, Akira Endo, Emily S. Nightingale, Nikos I. Bosse, C. Julian Villabona-Arenas, Frank G. Sandmann, Amy Gimma, Kaja Abbas, William Waites, Katherine E. Atkins, Rosanna C. Barnard, Petra Klepac, Hamish P. Gibbs, Carl A. B. Pearson, Oliver Brady & W. John Edmunds

2. Department of Medical Statistics, Faculty of Epidemiology and Population Health, London School of Hygiene and Tropical Medicine, London, UK

Nicholas P. Jewell, Karla Diaz-Ordaz & Ruth H. Keogh

3. Centre for Statistical Methodology, London School of Hygiene and Tropical Medicine, London, UK

Nicholas P. Jewell, Karla Diaz-Ordaz & Ruth H. Keogh

4. Centre for Global Health, Usher Institute of Population Health Sciences and Informatics, University of Edinburgh, Edinburgh, UK

Katherine E. Atkins

#### Authors

1. Nicholas G. Davies

[View author publications](#)

You can also search for this author in [PubMed](#) [Google Scholar](#)

2. Christopher I. Jarvis

[View author publications](#)

You can also search for this author in [PubMed](#) [Google Scholar](#)

3. W. John Edmunds

[View author publications](#)

You can also search for this author in [PubMed](#) [Google Scholar](#)

4. Nicholas P. Jewell

[View author publications](#)

You can also search for this author in [PubMed](#) [Google Scholar](#)

5. Karla Diaz-Ordaz

[View author publications](#)

You can also search for this author in [PubMed](#) [Google Scholar](#)

6. Ruth H. Keogh

[View author publications](#)

You can also search for this author in [PubMed](#) [Google Scholar](#)

#### Consortia

## CMMID COVID-19 Working Group

- Kevin van Zandvoort
- , Samuel Clifford
- , Fiona Yueqian Sun
- , Sebastian Funk
- , Graham Medley
- , Yalda Jafari
- , Sophie R. Meakin
- , Rachel Lowe
- , Matthew Quaife
- , Naomi R. Waterlow
- , Rosalind M. Eggo
- , Jiayao Lei
- , Mihaly Koltai
- , Fabienne Krauer
- , Damien C. Tully
- , James D. Munday
- , Alicia Showering
- , Anna M. Foss
- , Kiesha Prem
- , Stefan Flasche
- , Adam J. Kucharski
- , Sam Abbott
- , Billy J. Quilty
- , Thibaut Jombart
- , Alicia Rosello
- , Gwenan M. Knight
- , Mark Jit
- , Yang Liu
- , Jack Williams
- , Joel Hellewell
- , Kathleen O'Reilly
- , Yung-Wai Desmond Chan
- , Timothy W. Russell
- , Simon R. Procter
- , Akira Endo
- , Emily S. Nightingale
- , Nikos I. Bosse
- , C. Julian Villabona-Arenas
- , Frank G. Sandmann
- , Amy Gimma

- , Kaja Abbas
- , William Waites
- , Katherine E. Atkins
- , Rosanna C. Barnard
- , Petra Klepac
- , Hamish P. Gibbs
- , Carl A. B. Pearson
- & Oliver Brady

## Contributions

N.G.D., C.I.J., K.D.-O. and R.H.K. performed analyses; all authors designed the study and wrote the manuscript.

## Corresponding author

Correspondence to [Nicholas G. Davies](#).

## Ethics declarations

## Competing interests

The authors declare no competing interests.

## Additional information

**Peer review information** *Nature* thanks Sheila Bird, Natalie Dean and Sébastien Haneuse for their contribution to the peer review of this work. Peer review reports are available.

**Publisher's note** Springer Nature remains neutral with regard to jurisdictional claims in published maps and institutional affiliations.

## Extended data figures and tables

### [Extended Data Fig. 1 Missingness in SGTF status and proximity to SGTF-capable Lighthouse laboratories.](#)

The geographical location of the six Lighthouse laboratories in the UK; missingness is higher in the lower-tier local authorities (shaded regions) that are closer to a

Lighthouse laboratory that is not capable of producing an SGTF reading. Map source: Office for National Statistics. [Source data](#)

### **Extended Data Fig. 2 Kaplan–Meier plots of survival within 60 days of a positive test for SGTF versus non-SGTF samples.**

Plots are stratified by sex, age group, place of residence, ethnicity, NHS England region, IMD decile (in five groups) and specimen date. Note that the *y*-axis ranges differ among panels. These curves show the crude survival within each group (unadjusted for other covariates), and so do not necessarily signify differences in the effect of SGTF on survival for any specific group due to possible confounding factors. Shaded areas show 95% confidence intervals. [Source data](#)

### **Extended Data Fig. 3 Schoenfeld residuals for survival model by SGTF stratified by LTLA and specimen date.**

The model uses linear terms for age and IMD and a 28-day follow-up using complete cases. **a–i**, Residuals for SGTF (**a**), age (**b**), sex (**c**), IMD (**d**), ethnicity (**e–g**), and residence type (**h, i**). Two-sided Schoenfeld residual tests were performed.  $P = 0.001$  for SGTF (**a**);  $P = 0.039$  for age (**b**);  $P = 0.101$  for sex (**c**);  $P = 0.937$  for IMD decile (**d**);  $P = 0.969$  for ethnicity (**e–g**);  $P = 0.064$  for residence type (**h–i**); and  $P = 0.027$  globally. The trend line shows the mean and 95% confidence intervals of a loess regression. [Source data](#)

### **Extended Data Fig. 4 Comparison of missingness models.**

**a–c**,  $Q-Q$  plot (left; mean and 95% confidence intervals) and distribution of weights (right) under different missingness models assessed for IPW with a cauchit link (**a**), a robit link (Student's *t*-distribution with d.f. = 4) (**b**) and a logit link (**c**). [Source data](#)

### **Extended Data Fig. 5 Misclassification model.**

For each NHS England region, we fit a beta-binomial model (purple, modelled SGTF) to the observed SGTF frequencies among Pillar 2 tests (black, observed SGTF), which estimates a constant proportion of ‘false-positive’ SGTF samples among non-VOC 202012/01 (that is, non-B.1.1.7) specimens (orange, modelled non-VOC SGTF) and a logically growing proportion of VOC 202012/01 (that is, B.1.1.7) specimens over time (blue, modelled VOC). This allows us to model the conditional probability that a specimen with SGTF represents VOC 202012/01 (teal,  $P(\text{VOC}|\text{SGTF})$ ). For our misclassification survival analysis,  $p_{\text{VOC}} = 0$  for non-SGTF specimens and  $p_{\text{VOC}} = P(\text{VOC}|\text{SGTF})$  for SGTF specimens. Lines show medians and shaded areas

show 95% credible intervals. Dashed vertical lines show the date on which  $P(\text{VOC}|\text{SGTF})$  first exceeds 0.5. [Source data](#)

### **Extended Data Fig. 6 $C_t$ values for SGTF versus non-SGTF.**

**a, b,** The distribution of  $C_t$  values for *orf1ab* (**a**) and *N* (**b**) gene targets among specimens collected between 1 January and 14 February 2021. [Source data](#)

### **Extended Data Fig. 7 S-gene dropout in community tests relative to a random sample of SARS-CoV-2 infections in the community.**

Comparison of the proportion of samples with *S*-gene dropout in the Pillar 2 (that is, community testing) sample used in this analysis compared to Office for National Statistics (ONS) random sampling of the community. This comparison suggests that *S*-gene dropout samples are not overrepresented in testing data relative to the prevalence of *S*-gene dropout in the community, suggesting that the increased hazard of death among positive community tests estimated in this study is not the result of a decrease in the average propensity for test-seeking among individuals infected with B.1.1.7. Point and ranges for ONS data show mean and 95% credible intervals. [Source data](#)

### **Extended Data Table 1 Characteristics of study participants, 1 November 2020–14 February 2021**

[Full size table](#)

### **Extended Data Table 2 Rates of death within 28 days of a positive test among study participants**

[Full size table](#)

## **Supplementary information**

### **Supplementary Information**

This file contains Supplementary Tables 1–2 and Supplementary Notes 1–2. Crude death rates without restriction on follow-up time; crude death rates cross-tabulated by broad categories of specimen date, region, age, and index of multiple deprivation; results for models with interaction terms; CMMID COVID-19 Working Group acknowledgements.

### **Reporting Summary**

### **Supplementary Data**

This file contains source data for Extended Data Table 1.

## **Supplementary Data**

This file contains source data for Extended Data Table 2.

## **Peer Review File**

## **Source data**

### **Source Data Fig. 1**

### **Source Data Fig. 2**

### **Source Data Extended Data Fig. 1**

### **Source Data Extended Data Fig. 2**

### **Source Data Extended Data Fig. 3**

### **Source Data Extended Data Fig. 4**

### **Source Data Extended Data Fig. 5**

### **Source Data Extended Data Fig. 6**

### **Source Data Extended Data Fig. 7**

## **Rights and permissions**

### **Reprints and Permissions**

## **About this article**



Check for  
updates

## Cite this article

Davies, N.G., Jarvis, C.I., CMMID COVID-19 Working Group. *et al.* Increased mortality in community-tested cases of SARS-CoV-2 lineage B.1.1.7. *Nature* **593**, 270–274 (2021). <https://doi.org/10.1038/s41586-021-03426-1>

[Download citation](#)

- Received: 26 January 2021
- Accepted: 08 March 2021
- Published: 15 March 2021
- Issue Date: 13 May 2021
- DOI: <https://doi.org/10.1038/s41586-021-03426-1>

## Further reading

- [One year into the pandemic: Short-term evolution of SARS-CoV-2 and emergence of new lineages](#)

- Fernando González-Candelas
- , Marie-Anne Shaw
- , Tung Phan
- , Urmila Kulkarni-Kale
- , Dimitrios Paraskevis
- , Fabio Luciani
- , Hirokazu Kimura
- & Manuela Sironi

*Infection, Genetics and Evolution* (2021)

- [Vaccinating children against SARS-CoV-2](#)

- Jennie S Lavine
- , Ottar Bjornstad
- & Rustom Antia

*BMJ* (2021)

- **Evaluation of an Automated High-Throughput Liquid-Based RNA Extraction Platform on Pooled Nasopharyngeal or Saliva Specimens for SARS-CoV-2 RT-PCR**

- Allen Wing-Ho Chu
- , Cyril Chik-Yan Yip
- , Wan-Mui Chan
- , Anthony Chin-Ki Ng
- , Dream Lok-Sze Chan
- , Ryan Ho-Ping Siu
- , Cheuk Yiu Tenny Chung
- , Jessica Pui-Ling Ng
- , Harsha Kittur
- , Garrett Lee Mosley
- , Rosana Wing-Shan Poon
- , Ricky Yin-To Chiu
- & Kelvin Kai-Wang To

*Viruses* (2021)

- **Genetic Diversity of SARS-CoV-2 over a One-Year Period of the COVID-19 Pandemic: A Global Perspective**

- Miao Miao
- , Erik De Clercq
- & Guangdi Li

*Biomedicines* (2021)

- **Monitoring differences between the SARS-CoV-2 B.1.1.7 variant and other lineages**

- Britta L Jewell

*The Lancet Public Health* (2021)

## Comments

By submitting a comment you agree to abide by our [Terms](#) and [Community Guidelines](#). If you find something abusive or that does not comply with our terms or guidelines please flag it as inappropriate.

## [Download PDF](#)

---

This article was downloaded by **calibre** from <https://www.nature.com/articles/s41586-021-03426-1>

| [Section menu](#) | [Main menu](#) |

- Article
- [Published: 31 March 2021](#)

# A myeloid–stromal niche and gp130 rescue in NOD2-driven Crohn’s disease

- [Shikha Nayar](#) [ORCID: orcid.org/0000-0001-8519-4569<sup>1,2</sup>](#),
- [Joshua K. Morrison](#) [ORCID: orcid.org/0000-0003-4174-6338<sup>3</sup>](#),
- [Mamta Giri<sup>4</sup>](#),
- [Kyle Gettler<sup>1,4</sup>](#),
- [Ling-shiang Chuang](#) [ORCID: orcid.org/0000-0001-5054-1305<sup>1</sup>](#),
- [Laura A. Walker<sup>5</sup>](#),
- [Huaibin M. Ko](#) [ORCID: orcid.org/0000-0003-1062-2383<sup>6,7 nAff9</sup>](#),
- [Ephraim Kenigsberg](#) [ORCID: orcid.org/0000-0002-4107-3295<sup>1</sup>](#),
- [Subra Kugathasan](#) [ORCID: orcid.org/0000-0002-8686-4189<sup>8</sup>](#),
- [Miriam Merad](#) [ORCID: orcid.org/0000-0002-4481-7827<sup>5</sup>](#),
- [Jaime Chu<sup>3</sup>](#) &
- [Judy H. Cho](#) [ORCID: orcid.org/0000-0002-7959-0466<sup>4</sup>](#)

[Nature](#) volume 593, pages 275–281 (2021) [Cite this article](#)

- 11k Accesses
- 1 Citations
- 187 Altmetric
- [Metrics details](#)

## Subjects

- [Disease genetics](#)
- [Immunogenetics](#)

## Abstract

Crohn's disease is a chronic inflammatory intestinal disease that is frequently accompanied by aberrant healing and stricturing complications. Crosstalk between activated myeloid and stromal cells is critical in the pathogenicity of Crohn's disease<sup>1,2</sup>, and increases in intravasating monocytes are correlated with a lack of response to anti-TNF treatment<sup>3</sup>. The risk alleles with the highest effect on Crohn's disease are loss-of-function mutations in *NOD2*<sup>4,5</sup>, which increase the risk of stricturing<sup>6</sup>. However, the mechanisms that underlie pathogenicity driven by *NOD2* mutations and the pathways that might rescue a lack of response to anti-TNF treatment remain largely uncharacterized. Here we use direct ex vivo analyses of patients who carry risk alleles of *NOD2* to show that loss of *NOD2* leads to dysregulated homeostasis of activated fibroblasts and macrophages. CD14<sup>+</sup> peripheral blood mononuclear cells from carriers of *NOD2* risk alleles produce cells that express high levels of collagen, and elevation of conserved signatures is observed in *nod2*-deficient zebrafish models of intestinal injury. The enrichment of STAT3 regulation and gp130 ligands in activated fibroblasts and macrophages suggested that gp130 blockade might rescue the activated program in *NOD2*-deficient cells. We show that post-treatment induction of the STAT3 pathway is correlated with a lack of response to anti-TNF treatment in patients, and demonstrate in vivo in zebrafish the amelioration of the activated myeloid–stromal niche using the specific gp130 inhibitor bazedoxifene. Our results provide insights into *NOD2*-driven fibrosis in Crohn's disease, and suggest that gp130 blockade may benefit some patients with Crohn's disease—potentially as a complement to anti-TNF therapy.

[Access through your institution](#)

[Change institution](#)

[Buy or subscribe](#)

## Access options

[Subscribe to Journal](#)

Get full journal access for 1 year

\$199.00

only \$3.90 per issue

[Subscribe](#)

All prices are NET prices.

VAT will be added later in the checkout.

Tax calculation will be finalised during checkout.

Rent or Buy article

Get time limited or full article access on ReadCube.

from \$8.99

[Rent or Buy](#)

All prices are NET prices.

### **Additional access options:**

- [Log in](#)
- [Access through your institution](#)
- [Learn about institutional subscriptions](#)

**Fig. 1: Inflamed CD14<sup>+</sup>PDGFRA<sup>+</sup> cells and scRNA-seq orthologies suggest key roles for myeloid–stromal clusters.**

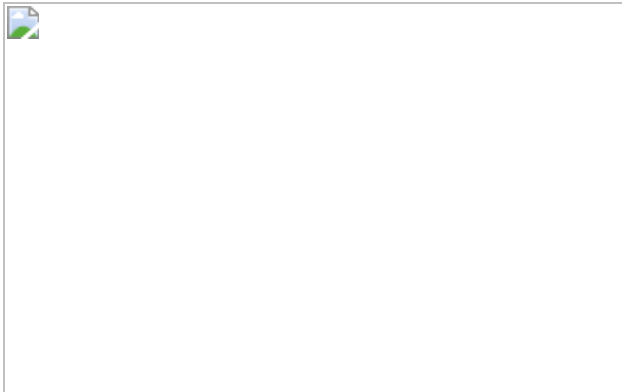


**Fig. 2: *NOD2* deficiency establishes an activated fibroblast signature that implicates IL-11 and WT1.**

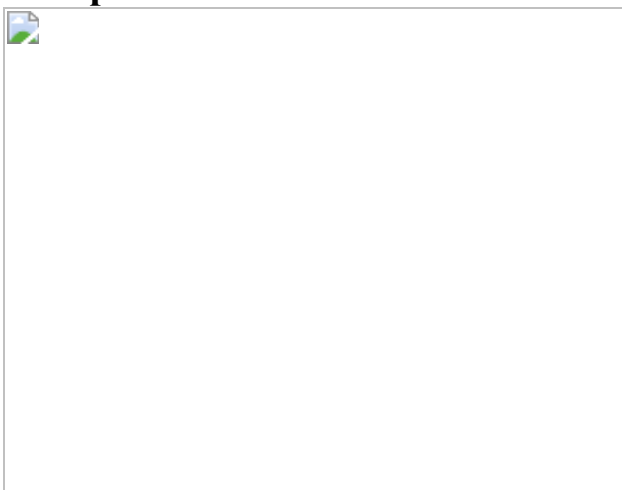


**Fig. 3: Single and recurrent DSS injury defines *nod2*-dependent gene activation, and myeloid and stromal pathway analyses implicate STAT3.**

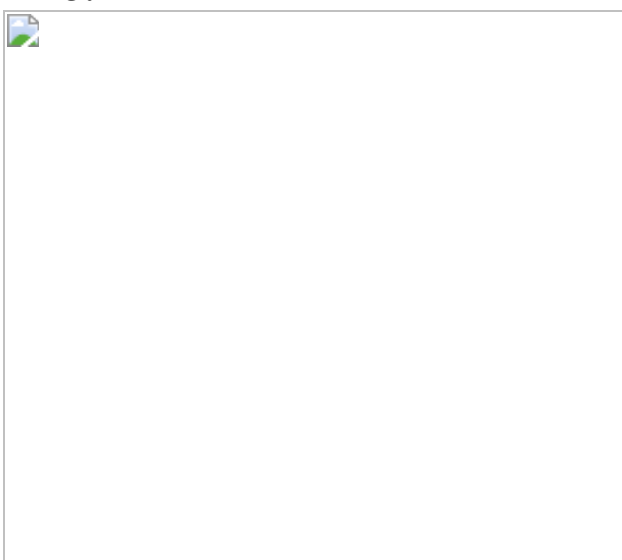
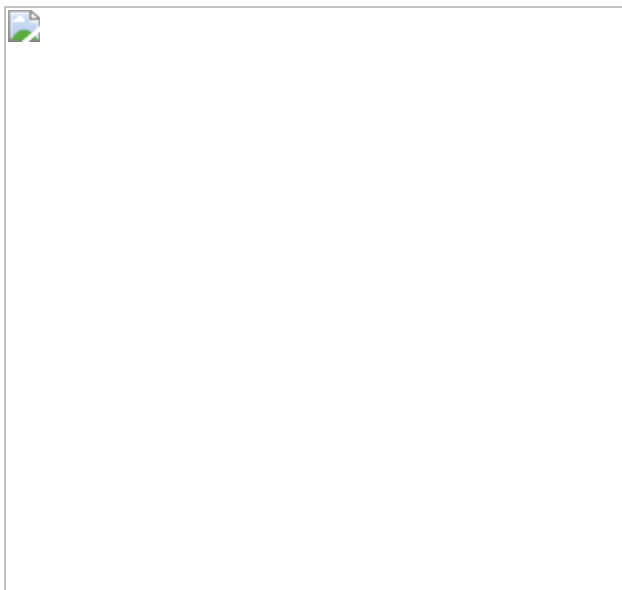


**Fig. 4: gp130 inhibition rescues activation of the myeloid–stromal niche.**



## Data availability

All data and supporting findings of this study are available within the Article and its Supplementary Information. All scRNA-seq data for human ileal samples have been deposited in the Gene Expression Omnibus (GEO) repository with accession code [GSE134809](#). All 10X Chromium zebrafish scRNA-seq data have been deposited in the GEO repository with accession code [GSE150498](#). The previously published<sup>34</sup> dataset can also be found in the GEO repository with accession code GSE16879. The ZFIN genomic databases can be found at <https://zfin.atlassian.net/wiki/spaces/general/pages/1891412257/Genomic+Resources+for+Zebrafish>. [Source data](#) are provided with this paper.

## Code availability

Scripts to reproduce zebrafish scRNA-seq clustering and differential expression analyses, as well as any other scripts used to generate computational figures, are available on GitHub at [https://github.com/Cho-lab-Sinai/Scripts\\_Nayar\\_et\\_al](https://github.com/Cho-lab-Sinai/Scripts_Nayar_et_al).

# References

1. 1.

Kugathasan, S. et al. Prediction of complicated disease course for children newly diagnosed with Crohn's disease: a multicentre inception cohort study. *Lancet* **389**, 1710–1718 (2017).

[PubMed](#) [PubMed Central](#) [Google Scholar](#)

2. 2.

West, N. R. et al. Oncostatin M drives intestinal inflammation and predicts response to tumor necrosis factor-neutralizing therapy in patients with inflammatory bowel disease. *Nat. Med.* **23**, 579–589 (2017).

[CAS](#) [PubMed](#) [PubMed Central](#) [Google Scholar](#)

3. 3.

Martin, J. C. et al. Single-cell analysis of Crohn's disease lesions identifies a pathogenic cellular module associated with resistance to anti-TNF therapy. *Cell* **178**, 1493–1508.e20 (2019).

[CAS](#) [PubMed](#) [PubMed Central](#) [Google Scholar](#)

4. 4.

Ogura, Y. et al. A frameshift mutation in *NOD2* associated with susceptibility to Crohn's disease. *Nature* **411**, 603–606 (2001).

[ADS](#) [CAS](#) [PubMed](#) [PubMed Central](#) [Google Scholar](#)

5. 5.

Hugot, J. P. et al. Association of *NOD2* leucine-rich repeat variants with susceptibility to Crohn's disease. *Nature* **411**, 599–603 (2001).

[ADS](#) [CAS](#) [PubMed](#) [PubMed Central](#) [Google Scholar](#)

6. 6.

Lesage, S. et al. *CARD15/NOD2* mutational analysis and genotype-phenotype correlation in 612 patients with inflammatory bowel disease. *Am. J. Hum. Genet.* **70**, 845–857 (2002).

[CAS](#) [PubMed](#) [PubMed Central](#) [Google Scholar](#)

7. 7.

Zhou, X. et al. Circuit design features of a stable two-cell system. *Cell* **172**, 744–757.e17 (2018).

[CAS](#) [PubMed](#) [PubMed Central](#) [Google Scholar](#)

8. 8.

Verstockt, B. & Cleynen, I. Genetic influences on the development of fibrosis in Crohn's disease. *Front. Med.* **3**, 24 (2016).

[Google Scholar](#)

9. 9.

Vermeire, S. et al. NOD2/CARD15 does not influence response to infliximab in Crohn's disease. *Gastroenterology* **123**, 106–111 (2002).

[CAS](#) [PubMed](#) [PubMed Central](#) [Google Scholar](#)

10. 10.

Mascheretti, S. et al. Pharmacogenetic investigation of the TNF/TNF-receptor system in patients with chronic active Crohn's disease treated with infliximab. *Pharmacogenomics J.* **2**, 127–136 (2002).

[CAS](#) [PubMed](#) [PubMed Central](#) [Google Scholar](#)

11. 11.

Brant, S. R. et al. Defining complex contributions of NOD2/CARD15 gene mutations, age at onset, and tobacco use on Crohn's disease phenotypes. *Inflamm. Bowel Dis.* **9**, 281–289 (2003).

[PubMed](#) [PubMed Central](#) [Google Scholar](#)

12. 12.

Bain, C. C. et al. Constant replenishment from circulating monocytes maintains the macrophage pool in the intestine of adult mice. *Nat. Immunol.* **15**, 929–937 (2014).

[CAS](#) [PubMed](#) [PubMed Central](#) [Google Scholar](#)

13. 13.

Schafer, S. et al. IL-11 is a crucial determinant of cardiovascular fibrosis. *Nature* **552**, 110–115 (2017).

[ADS](#) [CAS](#) [PubMed](#) [PubMed Central](#) [Google Scholar](#)

14. 14.

Lim, W.-W. et al. Transgenic interleukin 11 expression causes cross-tissue fibro-inflammation and an inflammatory bowel phenotype in mice. *PLoS ONE* **15**, e0227505 (2020).

[CAS](#) [PubMed](#) [PubMed Central](#) [Google Scholar](#)

15. 15.

Kim, H.-S. et al. Identification of novel Wilms' tumor suppressor gene target genes implicated in kidney development. *J. Biol. Chem.* **282**, 16278–16287 (2007).

[CAS](#) [PubMed](#) [PubMed Central](#) [Google Scholar](#)

16. 16.

Tamplin, O. J. et al. Hematopoietic stem cell arrival triggers dynamic remodeling of the perivascular niche. *Cell* **160**, 241–252 (2015).

[CAS](#) [PubMed](#) [PubMed Central](#) [Google Scholar](#)

17. 17.

Chuang, L.-S. et al. Zebrafish modeling of intestinal injury, bacterial exposures and medications defines epithelial *in vivo* responses relevant to human inflammatory bowel disease. *Dis. Model. Mech.* **12**, dmm037432 (2019).

[CAS](#) [PubMed](#) [PubMed Central](#) [Google Scholar](#)

18. 18.

Kim, Y.-G. et al. The Nod2 sensor promotes intestinal pathogen eradication via the chemokine CCL2-dependent recruitment of inflammatory monocytes. *Immunity* **34**, 769–780 (2011).

[CAS](#) [PubMed](#) [PubMed Central](#) [Google Scholar](#)

19. 19.

Reilkoff, R. A., Bucala, R. & Herzog, E. L. Fibrocytes: emerging effector cells in chronic inflammation. *Nat. Rev. Immunol.* **11**, 427–435 (2011).

[CAS](#) [PubMed](#) [PubMed Central](#) [Google Scholar](#)

20. 20.

Sun, H. et al. Netrin-1 regulates fibrocyte accumulation in the decellularized fibrotic scleroderma lung microenvironment and in bleomycin induced pulmonary fibrosis. *Arthritis Rheumatol.* **68**, 1251–1261 (2016).

[CAS](#) [PubMed](#) [PubMed Central](#) [Google Scholar](#)

21. 21.

García-de-Alba, C. et al. Expression of matrix metalloproteases by fibrocytes: possible role in migration and homing. *Am. J. Respir. Crit. Care Med.* **182**, 1144–1152 (2010).

[PubMed](#) [PubMed Central](#) [Google Scholar](#)

22. 22.

Girardin, S. E. et al. Nod2 is a general sensor of peptidoglycan through muramyl dipeptide (MDP) detection. *J. Biol. Chem.* **278**, 8869–8872 (2003).

[CAS](#) [PubMed](#) [PubMed Central](#) [Google Scholar](#)

23. 23.

Orekhov, A. N. et al. Monocyte differentiation and macrophage polarization. *Vessel Plus* **3**, 10 (2019).

[CAS](#) [Google Scholar](#)

24. 24.

Ma, G. et al. Nod2–Rip2 signaling contributes to intestinal injury induced by muramyl dipeptide via oligopeptide transporter in rats. *Dig. Dis. Sci.* **60**, 3264–3270 (2015).

[CAS](#) [PubMed](#) [PubMed Central](#) [Google Scholar](#)

25. 25.

Strober, W., Kitani, A., Fuss, I., Asano, N. & Watanabe, T. The molecular basis of NOD2 susceptibility mutations in Crohn’s disease. *Mucosal Immunol.* **1**, S5–S9 (2008).

[CAS](#) [PubMed](#) [PubMed Central](#) [Google Scholar](#)

26. 26.

Liu, Y. et al. Circulating fibrocytes are involved in inflammation and leukocyte trafficking in neonates with necrotizing enterocolitis. *Medicine (Baltimore)* **96**, e7400 (2017).

[Google Scholar](#)

27. 27.

Ishida, M. et al. Muramyl dipeptide enhances lipopolysaccharide-induced osteoclast formation and bone resorption through increased RANKL expression in stromal cells. *J. Immunol. Res.* **2015**, 132765 (2015).

[PubMed](#) [PubMed Central](#) [Google Scholar](#)

28. 28.

Kettleborough, R. N. W. et al. A systematic genome-wide analysis of zebrafish protein-coding gene function. *Nature* **496**, 494–497 (2013).

[ADS](#) [CAS](#) [PubMed](#) [PubMed Central](#) [Google Scholar](#)

29. 29.

Chassaing, B., Aitken, J. D., Malleshappa, M. & Vijay-Kumar, M. Dextran sulfate sodium (DSS)-induced colitis in mice. *Curr. Protoc. Immunol.* **104**, Unit 15.25 (2014).

[Google Scholar](#)

30. 30.

Waldner, M. J. & Neurath, M. F. Master regulator of intestinal disease: IL-6 in chronic inflammation and cancer development. *Semin. Immunol.* **26**, 75–79 (2014).

[CAS](#) [PubMed](#) [PubMed Central](#) [Google Scholar](#)

31. 31.

Thilakasiri, P. et al. Repurposing the selective estrogen receptor modulator *bazedoxifene* to suppress gastrointestinal cancer growth. *EMBO Mol. Med.* **11**, e9539 (2019).

[PubMed](#) [PubMed Central](#) [Google Scholar](#)

32. 32.

Wei, J. et al. Bazedoxifene as a novel GP130 inhibitor for colon cancer therapy. *J. Exp. Clin. Cancer Res. CR* **38**, 63 (2019).

[PubMed](#) [PubMed Central](#) [Google Scholar](#)

33. 33.

Wu, X., Cao, Y., Xiao, H., Li, C. & Lin, J. Bazedoxifene as a novel GP130 inhibitor for pancreatic cancer therapy. *Mol. Cancer Ther.* **15**, 2609–2619 (2016).

[CAS](#) [PubMed](#) [PubMed Central](#) [Google Scholar](#)

34. 34.

Arijs, I. et al. Mucosal gene expression of antimicrobial peptides in inflammatory bowel disease before and after first infliximab treatment. *PLoS ONE* **4**, e7984 (2009).

[ADS](#) [PubMed](#) [PubMed Central](#) [Google Scholar](#)

35. 35.

Yeo, S.-Y. et al. A positive feedback loop bi-stably activates fibroblasts. *Nat. Commun.* **9**, 3016 (2018).

[ADS](#) [PubMed](#) [PubMed Central](#) [Google Scholar](#)

36. 36.

Chen, K. L. A., Zhao, Y. C., Hieronymi, K., Smith, B. P. & Madak-Erdogan, Z. Bazedoxifene and conjugated estrogen combination maintains metabolic homeostasis and benefits liver health. *PLoS ONE* **12**, e0189911 (2017).

[PubMed](#) [PubMed Central](#) [Google Scholar](#)

37. 37.

Sontake, V. et al. Wilms' tumor 1 drives fibroproliferation and myofibroblast transformation in severe fibrotic lung disease. *JCI Insight* **3**, e121252 (2018).

[Google Scholar](#)

38. 38.

Kinchen, J. et al. Structural remodeling of the human colonic mesenchyme in inflammatory bowel disease. *Cell* **175**, 372–386.e17 (2018).

[CAS](#) [PubMed](#) [PubMed Central](#) [Google Scholar](#)

39. 39.

Buechler, M. B. et al. A stromal niche defined by expression of the transcription factor WT1 mediates programming and homeostasis of cavity-resident macrophages. *Immunity* **51**, 119–130.e5 (2019).

[CAS](#) [PubMed](#) [PubMed Central](#) [Google Scholar](#)

40. 40.

Frei, R. et al. Early initiation of anti-TNF is associated with favourable long-term outcome in Crohn's disease: 10-year-follow-up data from the Swiss IBD cohort study. *J. Crohn's Colitis* **13**, 1292–1301 (2019).

[Google Scholar](#)

41. 41.

Danese, S. et al. Randomised trial and open-label extension study of an anti-interleukin-6 antibody in Crohn's disease (ANDANTE I and II). *Gut* **68**, 40–48 (2019).

[CAS](#) [PubMed](#) [PubMed Central](#) [Google Scholar](#)

42. 42.

Sands, B. E. et al. Randomized, controlled trial of recombinant human interleukin-11 in patients with active Crohn's disease. *Aliment. Pharmacol. Ther.* **16**, 399–406 (2002).

[CAS](#) [PubMed](#) [PubMed Central](#) [Google Scholar](#)

43. 43.

Viennois, E., Chen, F., Laroui, H., Baker, M. T. & Merlin, D. Dextran sodium sulfate inhibits the activities of both polymerase and reverse transcriptase: lithium chloride purification, a rapid and efficient technique to purify RNA. *BMC Res. Notes* **6**, 360 (2013).

[PubMed](#) [PubMed Central](#) [Google Scholar](#)

44. 44.

Zhang, X. et al. Luminally polarized mural and vascular remodeling in ileal strictures of Crohn's disease. *Hum. Pathol.* **79**, 42–49 (2018).

[PubMed](#) [PubMed Central](#) [Google Scholar](#)

45. 45.

Dehairs, J., Talebi, A., Cherifi, Y. & Swinnen, J. V. CRISP-ID: decoding CRISPR mediated indels by Sanger sequencing. *Sci. Rep.* **6**, 28973 (2016).

[ADS](#) [CAS](#) [PubMed](#) [PubMed Central](#) [Google Scholar](#)

46. 46.

Haberman, Y. et al. Pediatric Crohn's disease patients exhibit specific ileal transcriptome and microbiome signature. *J. Clin. Invest.* **124**, 3617–3633 (2014).

[CAS](#) [PubMed](#) [PubMed Central](#) [Google Scholar](#)

47. 47.

Gettler, L. et al. Prioritizing Crohn's disease genes by integrating association signals with gene expression implicates monocyte subsets. *Genes Immun.* **20**, 577–588 (2019).

[PubMed](#) [PubMed Central](#) [Google Scholar](#)

48. 48.

Love, M. I. et al. Moderated estimation of fold change and dispersion for RNA-seq data with DESeq2. *Genome Biol.* **15**, 550 (2014).

[PubMed](#) [PubMed Central](#) [Google Scholar](#)

[Download references](#)

## Acknowledgements

We thank S. Grossman of the Dr Sanford J. Grossman Center for Integrative Studies in IBD, which is supported by the generosity of The Sanford J. Grossman Charitable Trust; the ISMMS Department of Pathology for providing human tissue samples; D. Derose, K. Svoboda, C. Chasteau and U. Korie for sample collection and coordination; A. Saha and H. Wen for recall of healthy volunteers with *NOD2* mutations via the ISMMS BioMe Biobank; F. Avila and M. Garcia-Barros from the Biorepository and Pathology core for assistance with staining human ileal strictures; N. Hsu and N. Villaverde (members of the laboratory of J.H.C.) for discussions;

and F. Marlow and B. Rosenberg for discussions relating to zebrafish and single-cell experiments. This work was also supported by National Institutes of Health (NIH) grants R01 DK106593, R01 DK123758-01 and U01 DK062422 to J.H.C.

## Author information

### Author notes

1. Huaibin M. Ko

Present address: Department of Pathology and Cell Biology, Columbia University Medical Center, New York, NY, USA

### Affiliations

1. Department of Genetics and Genomic Sciences, Icahn School of Medicine at Mount Sinai, New York, NY, USA

Shikha Nayar, Kyle Gettler, Ling-shiang Chuang & Ephraim Kenigsberg

2. Graduate School of Biomedical Sciences, Icahn School of Medicine at Mount Sinai, New York, NY, USA

Shikha Nayar

3. Department of Pediatrics, Icahn School of Medicine at Mount Sinai, New York, NY, USA

Joshua K. Morrison & Jaime Chu

4. The Charles Bronfman Institute of Personalized Medicine, Icahn School of Medicine at Mount Sinai, New York, NY, USA

Mamta Giri, Kyle Gettler & Judy H. Cho

5. The Precision Immunology Institute, Icahn School of Medicine at Mount Sinai, New York, NY, USA

Laura A. Walker & Miriam Merad

6. Department of Pathology, The Mount Sinai Hospital, New York, NY, USA

Huaibin M. Ko

7. Department of Medicine, The Mount Sinai Hospital, New York, NY, USA

Huaibin M. Ko

8. Department of Pediatric Gastroenterology, Emory University, Atlanta, GA, USA

Subra Kugathasan

## Authors

1. Shikha Nayar

[View author publications](#)

You can also search for this author in [PubMed](#) [Google Scholar](#)

2. Joshua K. Morrison

[View author publications](#)

You can also search for this author in [PubMed](#) [Google Scholar](#)

3. Mamta Giri

[View author publications](#)

You can also search for this author in [PubMed](#) [Google Scholar](#)

4. Kyle Gettler

[View author publications](#)

You can also search for this author in [PubMed](#) [Google Scholar](#)

5. Ling-shiang Chuang

[View author publications](#)

You can also search for this author in [PubMed](#) [Google Scholar](#)

6. Laura A. Walker

[View author publications](#)

You can also search for this author in [PubMed](#) [Google Scholar](#)

7. Huaibin M. Ko

[View author publications](#)

You can also search for this author in [PubMed](#) [Google Scholar](#)

8. Ephraim Kenigsberg

[View author publications](#)

You can also search for this author in [PubMed](#) [Google Scholar](#)

9. Subra Kugathasan

[View author publications](#)

You can also search for this author in [PubMed](#) [Google Scholar](#)

10. Miriam Merad

[View author publications](#)

You can also search for this author in [PubMed](#) [Google Scholar](#)

11. Jaime Chu

[View author publications](#)

You can also search for this author in [PubMed](#) [Google Scholar](#)

12. Judy H. Cho

[View author publications](#)

You can also search for this author in [PubMed](#) [Google Scholar](#)

## Contributions

J.H.C. and S.N. conceived the project. S.N., J.K.M. and J.H.C. designed the experiments, and S.N. and J.K.M performed them. S.N. and J.H.C. wrote the manuscript, with discussions and edits from E.K., L.-s.C., J.C. and J.K.M. L.-s.C. and M.M. provided intellectual input throughout the study's progression. M.G. and K.G. provided substantial assistance with the generation of computational analyses. S.K. and K.G. assisted in the handling of genetic and clinical data from the RISK dataset. L.A.W. and E.K. provided assistance with scRNA-seq experiments and analysis strategies. H.M.K. provided human ileal stricture slides as well as expertise on histological analyses.

## Corresponding author

Correspondence to [Judy H. Cho](#).

## Ethics declarations

## Competing interests

S.N. and J.H.C., through the Icahn School of Medicine at Mount Sinai, have filed a provisional US patent application (no. 63/130,035) on repurposing BZA for clinical use in a subset of patients with Crohn's disease. All other authors declare no competing interests.

## Additional information

**Peer review information** *Nature* thanks Alison Simmons and the other, anonymous, reviewer(s) for their contribution to the peer review of this work. Peer reviewer reports are available.

**Publisher's note** Springer Nature remains neutral with regard to jurisdictional claims in published maps and institutional affiliations.

## Extended data figures and tables

### Extended Data Fig. 1 scRNA-seq exploration of ileum of patients with Crohn's disease and validation by protein staining.

**a**, Genes (columns) across myeloid and stromal cells (rows) from scRNA-seq of uninflamed ileum of patients with Crohn's disease ( $n = 11$ ). Expression defined as  $\log_2(\text{gene expression}/\text{average})$  across all shown clusters. **b**, Relative expression of *NOD2*, *RIPK2* and *XIAP* (columns) across myeloid and stromal cells (rows) from scRNA-seq of PBMCs and inflamed ileum of patients with Crohn's disease ( $n = 11$ ). **c**, Gene ontology analysis from upregulated genes in activated fibroblasts from inflamed ileum. The number of genes per biological process is shown in parentheses. Processes ranked from top to bottom in decreasing order of  $-\log(P \text{ value})$ . **d**, Percentage of  $\text{COL1A1}^+$ ,  $\text{PDGFRA}^+$ ,  $\text{CD14}^+$  and  $\text{CD14}^+\text{PDGFRA}^+$  double-positive cells of total activated fibroblasts (1,367 cells total) in inflamed ileum. **e**, Number of cells from direct ex vivo sorting of  $\text{CD14}^+\text{PDGFRA}^+$  cells of uninflamed and inflamed ileum of patients with Crohn's disease.  $n = 3$  biological replicates. Data are mean  $\pm$  s.e.m. **f**, Full-thickness sections of inflamed strictures stained with *MPEG1* and *MFAP4*.  $n = 3$  biological replicates per stain. **g**, Full-thickness sections of inflamed strictures showing expression of *WT1*, *PDGFRA* and *CD14*.  $n = 2$  patients per stain (patient 7 and 8 denoted from a previous publication<sup>3</sup>) (left). In inflamed strictures from samples from patients with Crohn's disease, *WT1*, *PDGFRA* and *CD14* expression is seen in muscularis mucosae and lymphoid aggregates; and around blood vessels (right).  $n = 2$  patients per stain; 5 images per patient. Scale bar, approximately 50  $\mu\text{m}$ . **h**, RT-PCR of gene expression at 24 h after 1 $\times$  DSS-treatment of zebrafish *nod2*<sup>+/+</sup> and *nod2*<sup>sa21011/sa21011</sup> larvae, comparing intestinal and carcass expression.  $n = 3$  biological replicates; 3 clutches, 10–15 larvae per genotype per clutch. Data are mean  $\pm$  s.e.m. \* $P < 0.05$ , \*\* $P < 0.01$ ; two-tailed paired Student's *t*-test.

[Source data](#)

## Extended Data Fig. 2 scRNA-seq data from intestines of DSS-treated zebrafish larvae.

**a**, scRNA-seq of intestines of untreated and DSS-treated zebrafish larvae from *nod2*<sup>+/+</sup> and *nod2*<sup>mss13/mss13</sup> backgrounds. UMAP shows joint clustering of 30,069 cells, revealing 32 unique clusters (left). Top 5 markers for each cluster (rows) (right). **b**, UMAP showing human–zebrafish clusters from species integration via scRNA-seq (top); top 3 markers for each cluster (rows) (bottom). Expression is UMI counts per gene per cell. **c**, Homologous expression between zebrafish and human clusters (expression is log-normalized).

## Extended Data Fig. 3 NOD2 deficiency enhances differentiation of spindle cells from CD14<sup>+</sup> monocytes.

**a**, Morphological quantification of PBMC differentiation from *NOD2*<sup>WT/WT</sup> or *NOD2*<sup>MT/MT</sup> cells, with 2.5 µg ml<sup>-1</sup> Pam3Cys, 0.5 µg ml<sup>-1</sup> lipid A and 1 µg ml<sup>-1</sup> MDP. Classification of categories in Methods.  $n = 6$  biological replicates for *NOD2*<sup>WT/WT</sup>,  $n = 3$  biological replicates for *NOD2*<sup>MT/MT</sup> for each treatment condition. Data are mean ± s.e.m. \* $P < 0.05$ , \*\* $P < 0.01$ ; two-sided Wilcoxon signed-rank *t*-test. **b**, Representative morphological images of spindle, intermediate and round cells from *NOD2*<sup>WT/WT</sup>, *NOD2*<sup>WT/MT</sup> and *NOD2*<sup>MT/MT</sup> individuals, unstimulated or treated with 1 µg ml<sup>-1</sup> MDP, 0.5 µg ml<sup>-1</sup> lipid A or 2.5 µg ml<sup>-1</sup> Pam3Cys.  $n = 5$  images per well condition per patient. Scale bar, 100 µm. **c**, Representative images of myeloid (MPEG1) and stromal (MFAP4, COL5A1 and COL1A1) expression by immunofluorescence (left). Quantification of staining (right). Data are mean ± s.e.m. of corrected cellular fluorescence. \*\*\* $P < 0.001$ ; two-way ANOVA test with Sidak correction.  $n = 4$  images per fluorescent marker; individual values, individual cells per image. **d**, Schematic of CD14<sup>+</sup>CD16<sup>-</sup> PBMCs isolated from healthy *NOD2*-mutant carriers and non-carriers, and differentiation assay (left). RT-PCR of gene expression from 1 µg ml<sup>-1</sup> MDP-treated PBMCs after 2 weeks of differentiation from *NOD2*<sup>WT/WT</sup> or *NOD2*<sup>MT/MT</sup> individuals.  $n = 3$  biological replicates (right). Data are mean MDP relative expression (left *y* axis) and individual  $2^{-\Delta C_t}$

expression values (right *y* axis) with error bars representing individual  $\Delta C_t$  values  $\pm$  s.e.m.. **e**, RT–PCR of gene expression of unstimulated CD14 $^+$ CD16 $^+$  PBMCs after two weeks of differentiation from *NOD2*<sup>WT/WT</sup> or *NOD2*<sup>MT/MT</sup> individuals.  $n = 3$  biological replicates. Data are mean untreated relative expression (left *y* axis) and individual  $2^{-\Delta C_t}$  expression values (right *y* axis) with error bars representing individual  $\Delta C_t$  values  $\pm$  s.e.m. **f**, Secreted protein (pg ml $^{-1}$ ) by Luminex from unstimulated PBMCs or PBMCs stimulated with 0.5  $\mu$ g ml $^{-1}$  lipid A, 2.5  $\mu$ g ml $^{-1}$  Pam3Cys or 1  $\mu$ g ml $^{-1}$  MDP.  $n = 2$  *NOD2*<sup>WT/WT</sup>,  $n = 3$  *NOD2*<sup>MT/MT</sup>. Data are mean  $\pm$  s.e.m. \* $P < 0.05$ ; two-way ANOVA. **g**, Schematic of *nod2*<sup>sa21011</sup> mutant from Zebrafish Sanger Mutation Project and *nod2*<sup>mss13/mss13</sup> CRISPR-knockout zebrafish line (left); timeline of 1 $\times$  and 2 $\times$  MDP stimulation of zebrafish larvae (right). [Source data](#)

#### **Extended Data Fig. 4 Staining of key fibrotic protein deposition in zebrafish larvae and human ileal stricture resections.**

**a**, Nod2 expression as assessed by western blotting to show loss of protein levels in *nod2*<sup>sa21011</sup> and *nod2*<sup>mss13/mss13</sup> CRISPR-mutant zebrafish larvae. Larvae were untreated and protein was collected at 6 dpf.  $n = 1$  biological replicate per *nod2* mutation for protein-knockout validation (1 clutch per mutation line with 20 larvae for each genotype). For gel source data, see Supplementary Fig. 1. **b**, UMAP of myeloid and stromal clusters from joint clustering of scRNA-seq data for zebrafish larval cells, grouped by *nod2*<sup>+/+</sup> and *nod2*<sup>mss13/mss13</sup> genotypes. **c**, *NOD2* mutation information of patients in the ileal Crohn’s disease scRNA-seq cohort, used for differential expression analysis between activated and nonactivated fibroblast and macrophage clusters. **d**, Transcription factors from ingenuity pathway analysis upstream of genes enriched in activated fibroblasts and inflammatory macrophages from individuals with *NOD2* risk alleles versus individuals without these alleles.  $P$  values were determined by ingenuity pathway analysis for transcription-factor regulation of genes in differential expression analysis. **e**, Top 5 genes (rows) in each cluster (columns). Expression is in UMI counts. **f**, Feature plots to show localized expression of key transcripts in

*nod2*<sup>WT/WT</sup> larvae from scRNA-seq myeloid and stromal populations (log-normalized expression).

**Extended Data Fig. 5 gp130 blockade by BZA ameliorates fibrotic activation and may provide a supplementary approach to anti-TNF therapy.**

**a**, log<sub>2</sub>-transformed microarray expression from a previous publication<sup>34</sup>, of gp130-associated genes in patients treated with infliximab. Blue bars, patients who responded to infliximab ( $n = 18$ ); red bars, patients who did not respond to infliximab ( $n = 16$ ). Data are mean  $\pm$  s.e.m. \* $P < 0.05$ , \*\* $P < 0.01$ , \*\*\* $P < 0.001$ , \*\*\*\* $P < 0.0001$ ; two-tailed paired Student's *t*-test. **b**, Morphological quantification of *NOD2*<sup>WT/WT</sup> or *NOD2*<sup>MT/MT</sup>-differentiated PBMCs that were unstimulated or stimulated with 0.5  $\mu\text{g ml}^{-1}$  MDP or 0.5  $\mu\text{g ml}^{-1}$  MDP + 1  $\mu\text{M}$  BZA.  $n = 6$  biological replicates for *NOD2*<sup>WT/WT</sup> ( $n = 4$  for MDP + BZA costimulation) and  $n = 3$  biological replicates for *NOD2*<sup>MT/MT</sup> per each treatment condition (top); unstimulated, 0.5  $\mu\text{g ml}^{-1}$  MDP, 0.5  $\mu\text{g ml}^{-1}$  MDP + 1  $\mu\text{M}$  BZA or MDP + 0.05  $\mu\text{g ml}^{-1}$  monoclonal anti-gp130 antibody (bottom).  $n = 2$  biological replicates for each genotype. Data are mean  $\pm$  s.e.m. \* $P < 0.05$ , \*\* $P < 0.01$ ; two-sided Wilcoxon signed-rank test. **c**, Secreted protein (pg  $\text{ml}^{-1}$ ) by Luminex from unstimulated PBMCs or PBMCs stimulated with 0.5  $\mu\text{g ml}^{-1}$  MDP, 0.5  $\mu\text{g ml}^{-1}$  MDP + 1  $\mu\text{M}$  BZA or 0.5  $\mu\text{g ml}^{-1}$  MDP + 0.05  $\mu\text{g ml}^{-1}$  anti-gp130.  $n = 2$  individuals per genotype. data are mean values. **d**, BZA target-gene expression in stromal and myeloid cells of scRNA-seq data from DSS-treated larvae (log-normalized expression). **e**, Percentage of stromal and myeloid populations in total intestinal cells sequenced in DSS-treated versus DSS + BZA-treated larvae. Red boxes, *nod2*<sup>mss13/mss13</sup> differences. **f**, **g**, Violin plots for upregulated genes upon DSS treatment, or for genes downregulated by DSS + BZA cotreatment in *nod2*<sup>+/+</sup> (**f**) and *nod2*<sup>mss13/mss13</sup> (**g**) larvae (log-normalized expression). **h**, Haematoxylin and eosin staining of DSS-treated and DSS + BZA-treated *nod2*<sup>+/+</sup> and *nod2*<sup>mss13/mss13</sup> zebrafish larvae. Intestinal bulb hypertrophy measured as indicated by scale bars, and quantified after 1 $\times$  (left) and 2 $\times$  (right) treatments.  $n = 5$ –10 biological replicates (individual larvae) per condition.

Data are mean  $\pm$  s.e.m. For *nod2*<sup>+/+</sup>, 5 untreated (1 $\times$ ), 3 1 $\times$ DSS, 4 untreated (2 $\times$ ), 10 2 $\times$ DSS; for *nod2*<sup>mss13</sup>,  $n$  = 6 untreated (1 $\times$ , 8 1 $\times$ DSS, 5 untreated (2 $\times$ ), 5 2 $\times$ DSS. \* $P$  < 0.05, \*\* $P$  < 0.01; one way-ANOVA with Tukey's multiple comparison. **i**, Intestine length of 2 $\times$ DSS-treated or 2 $\times$ DSS + BZA-cotreated *nod2*<sup>+/+</sup>, *nod2*<sup>+/-</sup> and *nod2*<sup>-/-</sup> larvae.  $n$  = 3 clutches; 10–15 larvae per group. Data are mean  $\pm$  s.e.m. \* $P$  < 0.05, \*\* $P$  < 0.01; two-way ANOVA test with Tukey's multiple comparison. **j**, RT-PCR of gene expression at 24 h after 1 $\times$  or 2 $\times$ DSS + BZA cotreatment of *nod2*<sup>+/+</sup>, *nod2*<sup>+/-</sup> or *nod2*<sup>-/-</sup> zebrafish larvae.  $n$  = 4 biological replicates for 1 $\times$  treatment; 4 clutches, 10–15 larvae per genotype per clutch.  $n$  = 4 biological replicates for 2 $\times$  treatment; 4 clutches, 10–15 larvae per genotype per clutch. Data are mean  $\pm$  s.e.m. [Source data](#)

## Extended Data Fig. 6 Pathogenesis of Crohn's disease and treatment pathways.

Model to show proposed mechanism of pathophysiology of Crohn's disease under specific genetic and cellular constraints. Individuals who carry a *NOD2* risk allele develop aberrant fibroblast–macrophage homeostasis and differentiation over time. At preclinical stages of disease development, patients with Crohn's disease increase production of antibodies (ASCA and CBir) to contain infection caused by increased bacterial load and elevate inflammatory mediators (cytokines and chemokines such as IL11, CXCL13, IL6, CCL2 and OSM). Patients who carry *NOD2* risk alleles will upregulate a pathogenic activated fibroblast and macrophage signature with disease development. This results in downstream activation of STAT3, among other chronic inflammatory and fibrotic consequences that we have shown in this Article. Some patients administered anti-TNF therapy will not respond, and often develop complications such as stricturing disease. Furthermore, over time, initial primary responders may become secondary nonresponders. Here we show that patients who are treatment-refractory have increased gp130 and activated fibroblast signatures; these would be patients for whom supplementing anti-TNF treatment with the gp130 inhibitor BZA could be beneficial. This model summarizes a two-step candidate selection approach: first by patients with Crohn's disease who carrying *NOD2* risk alleles with elevation of key expression signatures, and then by a lack of response to

anti-TNF) to inform personalized therapeutic decision-making for Crohn's disease.

## Supplementary information

### Supplementary Figure 1

Source gels for Extended Data Figure 4a. Top gel showing protein expression of Nod2 and tubulin control from *nod2<sup>sa21011</sup>* mutant line. Bottom gel showing protein expression of Nod2 and tubulin control from CRISPR-mediated knockout *nod2<sup>ms13</sup>* line. Note that in the bottom gel the homozygote fish lysate is loaded next to the WT lysate, followed by the heterozygote fish lysate. Protein markers are directly overlaid from the BioRad Precision Plus Protein ladder. Red boxes indicate portions of the gels displayed in Extended Data Fig. 4a.

### Reporting Summary

### Supplementary Table 1

UMI counts of all cells and genes in single-cell ileal dataset. Table to illustrate unique molecular identifier counts per gene per cell per sample (as shown by nCount\_RNA). Object indicates sample ID (uninflamed or inflamed ileal tissue from an individual). Supplementary metadata for each tissue sample can be found in Martin et al., 2019. Group indicates tissue inflammation status. Cluster indicates barcode and cell designation to a specific single-cell cluster.

### Supplementary Table 2

UMI counts of CD14+PDGFRA+ cells in single-cell ileal dataset. Table to illustrate unique molecular identifier counts CD14+PDGFRA+ double-expressing cells per sample (as shown by nCount\_RNA). Object indicates sample ID (uninflamed or inflamed ileal tissue from an individual). Group indicates tissue inflammation status. Cluster indicates barcode and cell designation to a specific single-cell cluster; here, cluster 20 is designated as

“activated fibroblasts”, which is the cell type that is predominantly expressing CD14+ and PDGFRA+ in the same cell. UMI distribution does not fall out of the range of all UMIs across all genes and cell types, indicating that these CD14+PDGFRA+ cells are single cells co-expressing both genes, as opposed to doublets.

### **Supplementary Table 3**

Cell-type specific marker expression for all cells in zebrafish single-cell RNA sequencing dataset. Table to illustrate top differentially expressed genes in each cluster for zebrafish single-cell RNA sequencing (joint clustering model; sheet 1) and zebrafish + human scRNAseq integrated model (joint clustering; sheet 2). Analyses were performed using the function “FindAllMarkers()” in Seurat. v3, s. pct.1 shows percent of all cells expressing the gene within that cluster and pct.2 shows percent of all cells expressing the gene in all other clusters being compared in the comparison.

### **Supplementary Table 4**

Differentially expressed genes between activated and residential fibroblast and macrophage populations in inflamed ileal CD scRNA seq data. Table to illustrate top differentially expressed genes between a) activated fibroblasts vs. residential fibroblasts and b) inflammatory macrophages vs. residential macrophages in scRNA sequencing of 11 inflamed CD ileum cells.

“FindAllMarkers()” in Seurat. v3, which uses a two-sided Wilcoxon test to perform differential gene expression analysis. pct.1 shows percent of all cells expressing the gene within activated/inflamed cluster and pct.2 shows percent of all cells expressing the gene in residential clusters being compared in the analysis.

### **Supplementary Table 5**

PCA generation of “activated fibroblasts” and “inflammatory macrophages” correlated with NOD2 risk allele carriers in RISK cohort. Table illustrating top principal components derived from top 200 differentially expressed genes in activated fibroblasts and inflammatory macrophages across each

patient in pediatric inception RISK cohort. Genes are derived from differential expression analysis between activated and non-activated fibroblasts and macrophages from single-cell RNA seq ileal dataset (ref. Supplementary Table 4).

### **Supplementary Table 6**

Regression analyses output for NOD2 allele status and stricture development in RISK cohort. Series of regression tests to test relationships between NOD2 risk alleles and stricture phenotype in RISK cohort. Using all 8 associated SNPs, rs2066847 frameshift NOD2 mutation is significant in predicting stricture status; using total NOD2 minor allele count, the sum of NOD2 risk alleles is significant in predicting stricture status; 0 vs. 1, 0 vs.2 NOD2 alleles to predict stricture status show increasing levels of significance with increasing number of NOD2 risk alleles.

### **Supplementary Table 7**

Cell type-specific marker expression for stromal and myeloid cells only in zebrafish single-cell RNA sequencing dataset. Table to illustrate top differentially expressed genes in each cluster for stromal and myeloid cells only in zebrafish single-cell RNA sequencing (joint clustering model). Analyses were performed using the function “FindAllMarkers()” in Seurat. v3, using a two-sided negative binomial test to perform differential gene expression analysis. pct.1 shows percent of all cells expressing the gene within that cluster and pct.2 shows percent of all cells expressing the gene in all other clusters being compared in the comparison.

### **Supplementary Table 8**

Differential expression analysis between activated fibroblasts and inflammatory macrophages in *NOD2* risk allele carriers from inflamed ileal single-cell RNA seq dataset. Table to show differential expression analysis performed in Seurat v3 between tab 1) activated and non-activated fibroblasts and tab 2) inflammatory and non-inflammatory macrophages between *NOD2* risk allele carriers (N=3) and *NOD2* wildtype carriers (N=4). pct.1 indicates percent of cells of *NOD2* risk allele carriers

expressing specific gene, and pct.2 indicates percent of cells of *NOD2* wildtype patients expressing specific gene. two-sided Wilcoxon test parameter in Seurat 3 used.

### **Supplementary Table 9**

Ingenuity Pathway Analysis output of transcriptional regulators upstream of differentially expressed genes in activated fibroblasts and inflammatory macrophages of *NOD2* risk allele carriers. Supplementary Tables 8 (gene, logFC, adj-p-value) were used as input data for performing Ingenuity Pathway Analysis. Results for upstream transcriptional regulators are shown, along with their target molecules that are a subset of the input differential expression geneset. Transcription factors highlighted are those we here implicate play key roles in orchestrating chronic inflammation and fibrosis in Crohn's disease.

### **Supplementary Table 10**

Patient characteristics for *NOD2* healthy volunteer recall. Clinical and demographic information for each healthy volunteer who participated in blood draw for PBMC isolation. *NOD2* genotype illustrates the mutation status of each patient, and DMSEA indicates all patients were of European Ancestry. An age cutoff of 65 years old was used.

### **Peer Review File**

## **Source data**

### **Source Data Fig. 1**

### **Source Data Fig. 2**

### **Source Data Fig. 3**

### **Source Data Fig. 4**

[\*\*Source Data Extended Data Fig. 1\*\*](#)

[\*\*Source Data Extended Data Fig. 3\*\*](#)

[\*\*Source Data Extended Data Fig. 5\*\*](#)

## Rights and permissions

[Reprints and Permissions](#)

## About this article



Check for  
updates

## Cite this article

Nayar, S., Morrison, J.K., Giri, M. *et al.* A myeloid–stromal niche and gp130 rescue in NOD2-driven Crohn’s disease. *Nature* **593**, 275–281 (2021). <https://doi.org/10.1038/s41586-021-03484-5>

[Download citation](#)

- Received: 08 May 2020
- Accepted: 23 March 2021
- Published: 31 March 2021
- Issue Date: 13 May 2021
- DOI: <https://doi.org/10.1038/s41586-021-03484-5>

## Further reading

- [A molecular connection hints at how a genetic risk factor drives Crohn's disease](#)

- Scott Plevy

*Nature* (2021)

## Comments

By submitting a comment you agree to abide by our [Terms](#) and [Community Guidelines](#). If you find something abusive or that does not comply with our terms or guidelines please flag it as inappropriate.

[Access through your institution](#)

[Change institution](#)

[Buy or subscribe](#)

## Associated Content

### [A molecular connection hints at how a genetic risk factor drives Crohn's disease](#)

- Scott Plevy

Nature News & Views 19 Apr 2021

---

This article was downloaded by **calibre** from <https://www.nature.com/articles/s41586-021-03484-5>

- Article
- [Published: 07 April 2021](#)

# Cell-programmed nutrient partitioning in the tumour microenvironment

- [Bradley I. Reinfeld](#) ORCID: [orcid.org/0000-0003-4161-8301](https://orcid.org/0000-0003-4161-8301)<sup>1,2,3</sup> natl,
- [Matthew Z. Madden](#) ORCID: [orcid.org/0000-0003-4062-4427](https://orcid.org/0000-0003-4062-4427)<sup>1,4</sup> natl,
- [Melissa M. Wolf](#)<sup>2,3</sup>,
- [Anna Chytil](#)<sup>2</sup>,
- [Jackie E. Bader](#)<sup>4</sup>,
- [Andrew R. Patterson](#)<sup>4</sup>,
- [Ayaka Sugiura](#)<sup>1,4</sup>,
- [Allison S. Cohen](#)<sup>5,6</sup>,
- [Ahmed Ali](#)<sup>7,8</sup>,
- [Brian T. Do](#) ORCID: [orcid.org/0000-0003-4992-2623](https://orcid.org/0000-0003-4992-2623)<sup>7,8</sup>,
- [Alexander Muir](#)<sup>9</sup>,
- [Caroline A. Lewis](#) ORCID: [orcid.org/0000-0003-1787-5084](https://orcid.org/0000-0003-1787-5084)<sup>10</sup>,
- [Rachel A. Hongo](#)<sup>2,4</sup>,
- [Kirsten L. Young](#)<sup>2,4</sup>,
- [Rachel E. Brown](#)<sup>1,2,3</sup>,
- [Vera M. Todd](#)<sup>2,3</sup>,
- [Tessa Huffstater](#) ORCID: [orcid.org/0000-0002-7906-807X](https://orcid.org/0000-0002-7906-807X)<sup>11</sup>,
- [Abin Abraham](#)<sup>1,12</sup>,
- [Richard T. O'Neil](#)<sup>2,13</sup>,
- [Matthew H. Wilson](#)<sup>2,13</sup>,
- [Fuxue Xin](#)<sup>5,6</sup>,
- [M. Noor Tantawy](#)<sup>5,6</sup>,
- [W. David Merryman](#) ORCID: [orcid.org/0000-0001-9662-1503](https://orcid.org/0000-0001-9662-1503)<sup>11</sup>,

- [Rachelle W. Johnson<sup>2</sup>](#),
- [Christopher S. Williams<sup>2,13</sup>](#),
- [Emily F. Mason<sup>4</sup>](#),
- [Frank M. Mason](#) ORCID: [orcid.org/0000-0003-1338-494X<sup>2</sup>](https://orcid.org/0000-0003-1338-494X),
- [Katherine E. Beckermann<sup>2</sup>](#),
- [Matthew G. Vander Heiden](#) ORCID: [orcid.org/0000-0002-6702-4192<sup>7,8,14</sup>](https://orcid.org/0000-0002-6702-4192),
- [H. Charles Manning<sup>5,6</sup>](#),
- [Jeffrey C. Rathmell](#) ORCID: [orcid.org/0000-0002-4106-3396<sup>4,15</sup>](https://orcid.org/0000-0002-4106-3396) &
- [W. Kimryn Rathmell](#) ORCID: [orcid.org/0000-0002-4984-0225<sup>2,15</sup>](https://orcid.org/0000-0002-4984-0225)

[Nature](#) volume **593**, pages 282–288 (2021) [Cite this article](#)

- 35k Accesses
- 2 Citations
- 388 Altmetric
- [Metrics details](#)

## Subjects

- [Cancer metabolism](#)
- [Cancer microenvironment](#)
- [Imaging the immune system](#)
- [Tumour immunology](#)

## Abstract

Cancer cells characteristically consume glucose through Warburg metabolism<sup>1</sup>, a process that forms the basis of tumour imaging by positron emission tomography (PET). Tumour-infiltrating immune cells also rely on glucose, and impaired immune cell metabolism in the tumour microenvironment (TME) contributes to immune evasion by tumour cells<sup>2,3,4</sup>. However, whether the metabolism of immune cells is dysregulated

in the TME by cell-intrinsic programs or by competition with cancer cells for limited nutrients remains unclear. Here we used PET tracers to measure the access to and uptake of glucose and glutamine by specific cell subsets in the TME. Notably, myeloid cells had the greatest capacity to take up intratumoral glucose, followed by T cells and cancer cells, across a range of cancer models. By contrast, cancer cells showed the highest uptake of glutamine. This distinct nutrient partitioning was programmed in a cell-intrinsic manner through mTORC1 signalling and the expression of genes related to the metabolism of glucose and glutamine. Inhibiting glutamine uptake enhanced glucose uptake across tumour-resident cell types, showing that glutamine metabolism suppresses glucose uptake without glucose being a limiting factor in the TME. Thus, cell-intrinsic programs drive the preferential acquisition of glucose and glutamine by immune and cancer cells, respectively. Cell-selective partitioning of these nutrients could be exploited to develop therapies and imaging strategies to enhance or monitor the metabolic programs and activities of specific cell populations in the TME.

[Access through your institution](#)

[Change institution](#)

[Buy or subscribe](#)

## Access options

Subscribe to Journal

Get full journal access for 1 year

\$199.00

only \$3.90 per issue

[Subscribe](#)

All prices are NET prices.

VAT will be added later in the checkout.

Tax calculation will be finalised during checkout.

Rent or Buy article

Get time limited or full article access on ReadCube.

from \$8.99

[Rent or Buy](#)

All prices are NET prices.

### **Additional access options:**

- [Log in](#)
- [Access through your institution](#)
- [Learn about institutional subscriptions](#)

**Fig. 1: Glucose is preferentially consumed by immune cells over cancer cells.**

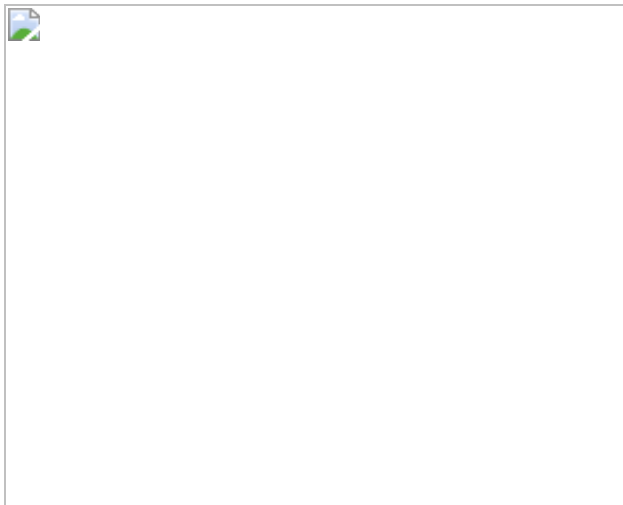


**Fig. 2: TME myeloid cells take up more glucose than cancer cells.**

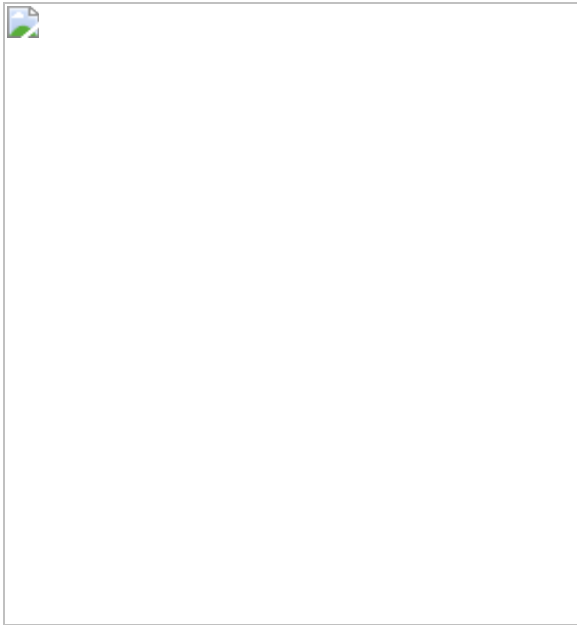
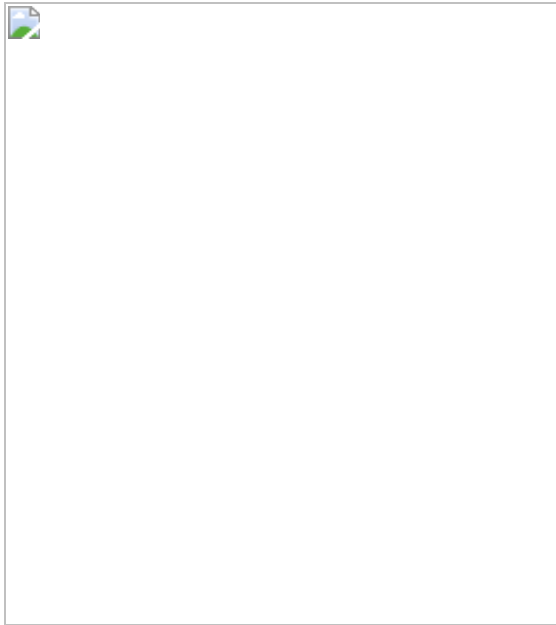


**Fig. 3: mTORC1 supports glucose uptake and metabolism in the TME.**



**Fig. 4: Glutamine partitions into cancer cells in the TME.**



## Data availability

All data will be made available upon reasonable request to J.C.R. or W.K.R. Tumour mRNA transcript data that support the findings of this study have been deposited in the Gene Expression Omnibus (GEO) with accession number [GSE165223](#). These data are also found in Supplementary Table 4. [Source data](#) are provided with this paper.

## Code availability

The code used to support tumour mRNA transcript analysis has been previously published (see Methods references) and will be made available upon request to J.C.R. or W.K.R.

## References

1. 1.

Vander Heiden, M. G. & DeBerardinis, R. J. Understanding the intersections between metabolism and cancer biology. *Cell* **168**, 657–669 (2017).

[Article](#) [Google Scholar](#)

2. 2.

Siska, P. J. et al. Mitochondrial dysregulation and glycolytic insufficiency functionally impair CD8 T cells infiltrating human renal cell carcinoma. *JCI Insight* **2**, e93411 (2017).

[Article](#) [Google Scholar](#)

3. 3.

Ho, P. C. et al. Phosphoenolpyruvate is a metabolic checkpoint of anti-tumor T cell responses. *Cell* **162**, 1217–1228 (2015).

[CAS](#) [Article](#) [Google Scholar](#)

4. 4.

Chang, C. H. et al. Metabolic competition in the tumor microenvironment is a driver of cancer progression. *Cell* **162**, 1229–1241 (2015).

[CAS](#) [Article](#) [Google Scholar](#)

5. 5.

Faubert, B. et al. Lactate metabolism in human lung tumors. *Cell* **171**, 358–371 (2017).

[CAS](#) [Article](#) [Google Scholar](#)

6. 6.

Ma, E. H. et al. Metabolic profiling using stable isotope tracing reveals distinct patterns of glucose utilization by physiologically activated CD8<sup>+</sup> T cells. *Immunity* **51**, 856–870 (2019).

[CAS](#) [Article](#) [Google Scholar](#)

7. 7.

Liu, P. S. et al.  $\alpha$ -Ketoglutarate orchestrates macrophage activation through metabolic and epigenetic reprogramming. *Nat. Immunol.* **18**, 985–994 (2017).

[CAS](#) [Article](#) [Google Scholar](#)

8. 8.

Johnson, M. O. et al. Distinct regulation of Th17 and Th1 cell differentiation by glutaminase-dependent metabolism. *Cell* **175**, 1780–1795 (2018).

[CAS](#) [Article](#) [Google Scholar](#)

9. 9.

Leone, R. D. et al. Glutamine blockade induces divergent metabolic programs to overcome tumor immune evasion. *Science* **366**, 1013–1021 (2019).

[ADS](#) [CAS](#) [Article](#) [Google Scholar](#)

10. 10.

Scharping, N. E. et al. Mitochondrial stress induced by continuous stimulation under hypoxia rapidly drives T cell exhaustion. *Nat. Immunol.* **22**, 205–215 (2021).

[CAS](#) [Article](#) [Google Scholar](#)

11. 11.

Sullivan, M. R. et al. Quantification of microenvironmental metabolites in murine cancers reveals determinants of tumor nutrient availability. *eLife* **8**, e44235 (2019).

[CAS](#) [Article](#) [Google Scholar](#)

12. 12.

Cortese, N. et al. Metabolome of pancreatic juice delineates distinct clinical profiles of pancreatic cancer and reveals a link between glucose metabolism and PD-1<sup>+</sup> cells. *Cancer Immunol. Res.* **8**, 493–505 (2020).

[CAS](#) [Article](#) [Google Scholar](#)

13. 13.

Gemta, L. F. et al. Impaired enolase 1 glycolytic activity restrains effector functions of tumor-infiltrating CD8<sup>+</sup> T cells. *Sci. Immunol.* **4**, eaap9520 (2019).

[CAS](#) [Article](#) [Google Scholar](#)

14. 14.

Sinclair, L. V., Barthelemy, C. & Cantrell, D. A. Single cell glucose uptake assays: a cautionary tale. *Immunometabolism* **2**, e200029 (2020).

[PubMed](#) [PubMed Central](#) [Google Scholar](#)

15. 15.

Nair-Gill, E. et al. PET probes for distinct metabolic pathways have different cell specificities during immune responses in mice. *J. Clin. Invest.* **120**, 2005–2015 (2010).

[CAS](#) [Article](#) [Google Scholar](#)

16. 16.

Hesketh, R. L. et al. Magnetic resonance imaging is more sensitive than PET for detecting treatment-induced cell death-dependent changes in glycolysis. *Cancer Res.* **79**, 3557–3569 (2019).

[CAS](#) [Article](#) [Google Scholar](#)

17. 17.

Spranger, S., Dai, D., Horton, B. & Gajewski, T. F. Tumor-residing Batf3 dendritic cells are required for effector T cell trafficking and adoptive T cell therapy. *Cancer Cell* **31**, 711–723 (2017).

[CAS](#) [Article](#) [Google Scholar](#)

18. 18.

Mabuchi, S. et al. Pretreatment tumor-related leukocytosis misleads positron emission tomography-computed tomography during lymph node staging in gynecological malignancies. *Nat. Commun.* **11**, 1364 (2020).

[ADS](#) [CAS](#) [Article](#) [Google Scholar](#)

19. 19.

Saxton, R. A. & Sabatini, D. M. mTOR signaling in growth, metabolism, and disease. *Cell* **168**, 960–976 (2017).

[CAS](#) [Article](#) [Google Scholar](#)

20. 20.

Yoshida, G. J. Beyond the Warburg effect: N-Myc contributes to metabolic reprogramming in cancer cells. *Front. Oncol.* **10**, 791 (2020).

[Article](#) [Google Scholar](#)

21. 21.

Zhou, R. et al. [<sup>18</sup>F](2S,4R)4-Fluoroglutamine PET detects glutamine pool size changes in triple-negative breast cancer in response to glutaminase inhibition. *Cancer Res.* **77**, 1476–1484 (2017).

[CAS](#) [Article](#) [Google Scholar](#)

22. 22.

Schulte, M. L. et al. Pharmacological blockade of ASCT2-dependent glutamine transport leads to antitumor efficacy in preclinical models. *Nat. Med.* **24**, 194–202 (2018).

[CAS](#) [Article](#) [Google Scholar](#)

23. 23.

Kilgour, M. K. et al. 1-Methylnicotinamide is an immune regulatory metabolite in human ovarian cancer. *Sci. Adv.* **7**, eabe1174 (2021).

[CAS](#) [Article](#) [Google Scholar](#)

24. 24.

Cascone, T. et al. Increased tumor glycolysis characterizes immune resistance to adoptive t cell therapy. *Cell Metab.* **27**, 977–987 (2018).

[CAS](#) [Article](#) [Google Scholar](#)

25. 25.

Li, W. et al. Aerobic glycolysis controls myeloid-derived suppressor cells and tumor immunity via a specific CEBPB isoform in triple-negative breast cancer. *Cell Metab.* **28**, 87–103 (2018).

[CAS](#) [Article](#) [Google Scholar](#)

26. 26.

Chafe, S. C. et al. Targeting hypoxia-induced carbonic anhydrase IX enhances immune-checkpoint blockade locally and systemically. *Cancer Immunol. Res.* **7**, 1064–1078 (2019).

[CAS](#) [Article](#) [Google Scholar](#)

27. 27.

Wenes, M. et al. Macrophage metabolism controls tumor blood vessel morphogenesis and metastasis. *Cell Metab.* **24**, 701–715 (2016).

[CAS](#) [Article](#) [Google Scholar](#)

28. 28.

Jeong, H. et al. Tumor-associated macrophages enhance tumor hypoxia and aerobic glycolysis. *Cancer Res.* **79**, 795–806 (2019).

[CAS](#) [PubMed](#) [Google Scholar](#)

29. 29.

O’Neil, R. T. et al. Transposon-modified antigen-specific T lymphocytes for sustained therapeutic protein delivery in vivo. *Nat. Commun.* **9**, 1325 (2018).

[ADS](#) [Article](#) [Google Scholar](#)

30. 30.

Tracz, A., Mastri, M., Lee, C. R., Pili, R. & Ebos, J. M. L. Modeling spontaneous metastatic renal cell carcinoma (mRCC) in mice following nephrectomy. *J. Vis. Exp.* **86**, 51485 (2014).

[Google Scholar](#)

31. 31.

Parang, B., Barrett, C. W. & Williams, C. S. AOM/DSS model of colitis-associated cancer. *Methods Mol. Biol.* **1422**, 297–307 (2016).

[CAS](#) [Article](#) [Google Scholar](#)

32. 32.

Becker, C. et al. In vivo imaging of colitis and colon cancer development in mice using high resolution chromoendoscopy. *Gut* **54**, 950–954 (2005).

[CAS](#) [Article](#) [Google Scholar](#)

33. 33.

Hassanein, M. et al. Preclinical evaluation of 4-[<sup>18</sup>F]Fluoroglutamine PET to Assess ASCT2 expression in lung cancer. *Mol. Imaging Biol.* **18**, 18–23 (2016).

[CAS](#) [Article](#) [Google Scholar](#)

34. 34.

Canouil, M. et al. NACHO: an R package for quality control of NanoString nCounter data. *Bioinformatics* **36**, 970–971 (2020).

[CAS](#) [PubMed](#) [Google Scholar](#)

35. 35.

Lê, S. Josse, J. Husson, & F. FactoMineR: A package for multivariate analysis. *J. Stat. Softw.* **25**, 1–18 (2008).

[ADS](#) [Article](#) [Google Scholar](#)

36. 36.

Raudvere, U. et al. g:Profiler: a web server for functional enrichment analysis and conversions of gene lists (2019 update). *Nucleic Acids Res.* **47**, W191–W198 (2019).

[CAS](#) [Article](#) [Google Scholar](#)

37. 37.

Robinson, M. D., McCarthy, D. J. & Smyth, G. K. edgeR: a Bioconductor package for differential expression analysis of digital gene expression data. *Bioinformatics* **26**, 139–140 (2010).

[CAS Article](#) [Google Scholar](#)

[Download references](#)

## Acknowledgements

We thank members of the J.C.R. and W.K.R. laboratories for their constructive input; the J. Balko, Y. Kim and P. Hurley laboratories for the use of their tumour dissociators; the Center for Small Animal Imaging at the Vanderbilt University Institute of Imaging Science (VUIIS) for support with PET–CT imaging; and the VUMC Radiochemistry core for synthesis and handling of radioactive material. This work was supported by F30 CA239367 (M.Z.M.), F30 CA247202 (B.I.R.), F30 DK120149 (R.E.B.), R01 CA217987 (J.C.R.), NIH T32 GM007753 (B.T.D.), R01 DK105550 (J.C.R.), AHA 20PRE35080073 (A.A.), VA Merit 1I01BX001426 (C.S.W.), Crohn’s and Colitis Foundation 623541 (C.S.W.), the American Association for Cancer Research (B.I.R. and W.K.R.), T32 GM007347 (M.Z.M., B.I.R., R.E.B., A.A., A.S. and C.S.W.), K12 CA090625 (K.E.B. and W.K.R.), K00 CA234920 (J.E.B.) and the Vanderbilt-Incyte Alliance (J.C.R. and W.K.R.). The Vanderbilt VANTAGE Core, including P. Baker, provided technical assistance for this work. VANTAGE is supported in part by a CTSA Grant (5UL1 RR024975-03), the Vanderbilt Ingram Cancer Center (P30 CA68485), the Vanderbilt Vision Center (P30 EY08126) and the NIH/NCRR (G20 RR030956). For the MC38 THY1.1 cells, we thank the cell and genome engineering core of the Vanderbilt O’Brien Kidney Center (P30 DK114809). Flow-sorting experiments were performed in the VUMC Flow Cytometry Shared Resource by D. K. Flaherty and B. K. Matlock and were supported by the Vanderbilt Ingram Cancer Center (P30 CA68485) and the Vanderbilt Digestive Disease Research Center (P30 DK058404). This work was supported by grant 1S10OD019963-01A1 for the GE TRACERlab FX2 N and Comecer Hotcell, housed in the VUIIS Radiochemistry Core to synthesize <sup>18</sup>F-Gln. The Inveon microPET was funded by NIH 1S10 OD016245. We acknowledge the Translational

Pathology Shared Resource supported by NCI/NIH Cancer Center Support Grant 5P30 CA68485-19 and the Vanderbilt Mouse Metabolic Phenotyping Center Grant 2 U24 DK059637-16, as well as the Shared Instrumentation Grant for the Leica Bond RX MicroArrayer (S10 OD023475-01A1) and the VA shared equipment grant for the LCM (IS1BX003154). Figs. [1d](#), [4k](#), Extended Data Figs. [2d](#), [3f](#) were created with Biorender.com.

## Author information

### Author notes

1. These authors contributed equally: Bradley I. Reinfeld, Matthew Z. Madden

### Affiliations

1. Medical Scientist Training Program, Vanderbilt University, Nashville, TN, USA

Bradley I. Reinfeld, Matthew Z. Madden, Ayaka Sugiura, Rachel E. Brown & Abin Abraham

2. Department of Medicine, Vanderbilt University Medical Center (VUMC), Nashville, TN, USA

Bradley I. Reinfeld, Melissa M. Wolf, Anna Chytil, Rachel A. Hongo, Kirsten L. Young, Rachel E. Brown, Vera M. Todd, Richard T. O’Neil, Matthew H. Wilson, Rachelle W. Johnson, Christopher S. Williams, Frank M. Mason, Katherine E. Beckermann & W. Kimryn Rathmell

3. Graduate Program in Cancer Biology, Vanderbilt University, Nashville, TN, USA

Bradley I. Reinfeld, Melissa M. Wolf, Rachel E. Brown & Vera M. Todd

4. Department of Pathology, Microbiology and Immunology, VUMC, Nashville, TN, USA

Matthew Z. Madden, Jackie E. Bader, Andrew R. Patterson, Ayaka Sugiura, Rachel A. Hongo, Kirsten L. Young, Emily F. Mason & Jeffrey C. Rathmell

5. Department of Radiology and Radiological Sciences, VUMC, Nashville, TN, USA

Allison S. Cohen, Fuxue Xin, M. Noor Tantawy & H. Charles Manning

6. Vanderbilt University Institute of Imaging Science, VUMC, Nashville, TN, USA

Allison S. Cohen, Fuxue Xin, M. Noor Tantawy & H. Charles Manning

7. Koch Institute for Integrative Cancer Research and Department of Biology, Massachusetts Institute of Technology (MIT), Cambridge, MA, USA

Ahmed Ali, Brian T. Do & Matthew G. Vander Heiden

8. Broad Institute of MIT and Harvard University, Cambridge, MA, USA

Ahmed Ali, Brian T. Do & Matthew G. Vander Heiden

9. Ben May Department for Cancer Research, University of Chicago, Chicago, IL, USA

Alexander Muir

10. Whitehead Institute for Biomedical Research, MIT, Cambridge, MA, USA

Caroline A. Lewis

11. Department of Biomedical Engineering, Vanderbilt University, Nashville, TN, USA

Tessa Huffstater & W. David Merryman

12. Vanderbilt Genetics Institute, VUMC, Nashville, TN, USA

Abin Abraham

13. Department of Veterans Affairs, Tennessee Valley Health System, Nashville, TN, USA

Richard T. O'Neil, Matthew H. Wilson & Christopher S. Williams

14. Dana-Farber Cancer Institute, Boston, MA, USA

Matthew G. Vander Heiden

15. Vanderbilt Center for Immunobiology and Vanderbilt-Ingram Cancer Center, VUMC, Nashville, TN, USA

Jeffrey C. Rathmell & W. Kimryn Rathmell

## Authors

1. Bradley I. Reinfeld

[View author publications](#)

You can also search for this author in [PubMed](#) [Google Scholar](#)

2. Matthew Z. Madden

[View author publications](#)

You can also search for this author in [PubMed](#) [Google Scholar](#)

3. Melissa M. Wolf

[View author publications](#)

You can also search for this author in [PubMed](#) [Google Scholar](#)

4. Anna Chytil

[View author publications](#)

You can also search for this author in [PubMed](#) [Google Scholar](#)

5. Jackie E. Bader

[View author publications](#)

You can also search for this author in [PubMed](#) [Google Scholar](#)

6. Andrew R. Patterson

[View author publications](#)

You can also search for this author in [PubMed](#) [Google Scholar](#)

7. Ayaka Sugiura

[View author publications](#)

You can also search for this author in [PubMed](#) [Google Scholar](#)

8. Allison S. Cohen

[View author publications](#)

You can also search for this author in [PubMed](#) [Google Scholar](#)

9. Ahmed Ali

[View author publications](#)

You can also search for this author in [PubMed](#) [Google Scholar](#)

10. Brian T. Do

[View author publications](#)

You can also search for this author in [PubMed](#) [Google Scholar](#)

11. Alexander Muir

[View author publications](#)

You can also search for this author in [PubMed](#) [Google Scholar](#)

12. Caroline A. Lewis

[View author publications](#)

You can also search for this author in [PubMed](#) [Google Scholar](#)

13. Rachel A. Hongo

[View author publications](#)

You can also search for this author in [PubMed](#) [Google Scholar](#)

14. Kirsten L. Young

[View author publications](#)

You can also search for this author in [PubMed](#) [Google Scholar](#)

15. Rachel E. Brown

[View author publications](#)

You can also search for this author in [PubMed](#) [Google Scholar](#)

16. Vera M. Todd

[View author publications](#)

You can also search for this author in [PubMed](#) [Google Scholar](#)

17. Tessa Huffstater

[View author publications](#)

You can also search for this author in [PubMed](#) [Google Scholar](#)

18. Abin Abraham

[View author publications](#)

You can also search for this author in [PubMed](#) [Google Scholar](#)

19. Richard T. O'Neil

[View author publications](#)

You can also search for this author in [PubMed](#) [Google Scholar](#)

20. Matthew H. Wilson

[View author publications](#)

You can also search for this author in [PubMed](#) [Google Scholar](#)

21. Fuxue Xin

[View author publications](#)

You can also search for this author in [PubMed](#) [Google Scholar](#)

22. M. Noor Tantawy

[View author publications](#)

You can also search for this author in [PubMed](#) [Google Scholar](#)

23. W. David Merryman

[View author publications](#)

You can also search for this author in [PubMed](#) [Google Scholar](#)

24. Rachelle W. Johnson

[View author publications](#)

You can also search for this author in [PubMed](#) [Google Scholar](#)

25. Christopher S. Williams

[View author publications](#)

You can also search for this author in [PubMed](#) [Google Scholar](#)

26. Emily F. Mason

[View author publications](#)

You can also search for this author in [PubMed](#) [Google Scholar](#)

27. Frank M. Mason

[View author publications](#)

You can also search for this author in [PubMed](#) [Google Scholar](#)

28. Katherine E. Beckermann

[View author publications](#)

You can also search for this author in [PubMed](#) [Google Scholar](#)

29. Matthew G. Vander Heiden

[View author publications](#)

You can also search for this author in [PubMed](#) [Google Scholar](#)

30. H. Charles Manning

[View author publications](#)

You can also search for this author in [PubMed](#) [Google Scholar](#)

31. Jeffrey C. Rathmell

[View author publications](#)

You can also search for this author in [PubMed](#) [Google Scholar](#)

32. W. Kimryn Rathmell

[View author publications](#)

You can also search for this author in [PubMed](#) [Google Scholar](#)

## Contributions

B.I.R., M.Z.M., J.C.R. and W.K.R. conceived and designed the study and composed the manuscript. B.I.R., R.A.H. and K.L.Y. collected tumour interstitial fluid from patients with ccRCC. K.E.B. provided clinical expertise and samples for interstitial fluid analysis. A. Ali, A.M., B.T.D., C.A.L. and M.G.V.H. performed, analysed and provided expertise for metabolite analysis of tumour interstitial fluid. B.I.R., M.Z.M. and M.M.W. conducted <sup>18</sup>F nutrient uptake and extracellular flux experiments. A.S.C. and H.C.M. provided expertise to develop <sup>18</sup>F nutrient uptake assays. F.X. and M.N.T. injected and handled mice for <sup>18</sup>F nutrient uptake assays, and performed and provided expertise for PET imaging and autoradiography. T.H. and W.D.M. performed and provided expertise for intrarenal Renca

experiments. R.W.J. and V.M.T. generated and provided expertise for PyMT GEMM tumours. R.E.B. and C.S.W. generated and provided expertise for AOM/DSS CRC tumours. B.I.R., R.T.O. and M.H.W. generated the pTZeo-EL-THY1.1 transposon construct and engineered MC38 cells using this transposon system. B.I.R., M.Z.M. and A.S. performed *in vivo* 2-NBDG studies. J.E.B. provided expertise in characterizing TAMs. A.R.P. provided expertise in flow sorting for mRNA transcript analysis. B.I.R. and M.Z.M. performed extracellular flux and mRNA transcript experiments. F.M.M. and E.F.M. performed and provided expertise in cell staining for light microscopy. A.C. provided expertise for and performed animal study monitoring. E.F.M. performed light microscopy and pathological examination of MC38 tumours. A. Abraham conducted transcriptomic analysis. B.I.R. and M.Z.M. analysed all data generated in this study. J.C.R. and W.K.R. obtained funding for this study.

## Corresponding authors

Correspondence to [Jeffrey C. Rathmell](#) or [W. Kimryn Rathmell](#).

## Ethics declarations

## Competing interests

J.C.R. has held stock equity in Sitryx and within the past two years has received unrelated research support, travel and honoraria from Sitryx, Caribou, Nirogy, Kadmon, Calithera, Tempest, Merck, Mitobridge and Pfizer. Within the past two years, W.K.R. has received unrelated clinical research support from Bristol-Meyers Squib, Merck, Pfizer, Peloton, Calithera and Incyte. H.C.M. holds a patent for V9302 (WO 2018/107173 A1). M.G.V.H. is a founder of Auron Therapeutics and is a member of the Scientific Advisory Board for Agios Pharmaceuticals, Aeglea Biotherapeutics and iTeos Therapeutics.

## Additional information

**Peer review information** *Nature* thanks Kevin Brindle and the other, anonymous, reviewer(s) for their contribution to the peer review of this work.

**Publisher's note** Springer Nature remains neutral with regard to jurisdictional claims in published maps and institutional affiliations.

## Extended data figures and tables

### Extended Data Fig. 1 Supporting data for Fig. 1.

**a–f**, Fraction purity, viability and yield for MC38 (**a**;  $n = 5$  mice), CT26 (**b**;  $n = 4$  mice), and Renca (**c**;  $n = 4$  mice) subcutaneous tumours; intrarenal Renca tumours (**d**;  $n = 3$  mice); AOM/DSS CRC tumours (**e**;  $n = 6$  mice for tumours,  $n = 11$  mice for spleens); and spontaneous PyMT GEMM tumours (**f**;  $n = 3$  mice). **g**, Representative flow cytometry analysis of PyMT and AOM/DSS CRC whole tumour, CD45 $^{+}$  immune cell and EPCAM $^{+}$  cancer cell fractions gated on live cells. Each data point represents a biological replicate; data are mean  $\pm$  s.e.m. Data are representative studies performed independently at least twice. [Source data](#)

### Extended Data Fig. 2 Validation of in vivo cellular FDG uptake assay.

**a**, Intravenous (IV) anti-CD45 PE staining of leukocytes from designated tissues gated on live CD45 $^{+}$  cells. **b**, Demonstration of dynamic range of  $^{18}\text{F}$  quantification using serially diluted in vivo FDG-labelled splenocytes. **c**, Correlation plots of CPM per million live cells versus cell viability, cells counted and tumour mass across multiple tumour cell populations. Only the CD45 $^{-}$  and other CD45 $^{+}$  simple linear regressions had slopes significantly different than 0 for tumour mass ( $n = 10$  mice). **d**, FDG-labelled digest supernatant from in vivo labelled MC38 tumours was applied to FDG-naive MC38 tumour single-cell suspensions to determine the contribution of ex vivo background FDG uptake to the final signal. **e**, Cellular FDG avidity in designated ex vivo and in vivo labelled MC38 tumour cell populations ( $n = 4$  mice/group). **f**, Cellular FDG avidity in designated tumour cell

fractions from MC38 THY1.1 tumours ( $n = 2$  mice). **g**, Proportion of CD45 $^{+}$  and THY1.1 $^{+}$  cells, cell viability and live-cell yield from MC38 THY1.1 tumours ( $n = 2$  mice for tumours;  $n = 5$  mice for spleens). **h**, Representative flow cytometry analysis of MC38 THY1.1 tumour fractions. Each data point represents a biological replicate; data are mean  $\pm$  s.e.m. Data in **b**, **d–h** are from a representative study performed independently at least twice. [Source data](#)

### [Extended Data Fig. 3 In vivo 2-NBDG uptake does not mirror FDG uptake.](#)

**a**, Representative histograms of in vivo 2-NBDG uptake in splenic and MC38 tumour cell subsets. **b**, MFI of in vivo 2-NBDG uptake across spleen and MC38 tumour cells ( $n = 3$  mice). **c**, **d**, Representative histograms of 2-NBDG uptake in vivo in splenic CD4 $^{+}$  (**c**) and CD8 $^{+}$  (**d**) T cells. **e**, 2-NBDG staining in splenic CD4 $^{+}$  and CD8 $^{+}$  subsets ( $n = 3$  mice). CM, central memory T cell; EM, effector memory T cell; N, naive T cell; T<sub>conv</sub>, conventional CD4 $^{+}$  T cell; T<sub>reg</sub>, regulatory CD4 $^{+}$  T cell. **f**, Schema for 2-NBDG and FDG co-injection experiment. **g**, Representative histogram of 2-NBDG $^{\text{hi}}$  and 2-NBDG $^{\text{lo}}$  populations collected through flow sorting. **h**, Per-cell FDG avidity of flow-sorted 2-NBDG $^{\text{lo}}$  versus 2-NBDG $^{\text{hi}}$  splenic T cells ( $n = 3$  mice). Each data point represents a biological replicate; data are mean  $\pm$  s.e.m. Data are from representative studies performed independently at least twice.  $P$  values were calculated using the Brown–Forsythe and Welch ANOVA with Dunnett’s T3 for multiple comparison tests (**b**, **e**), two-tailed Welch’s  $t$ -test for CD4 $^{+}$  comparisons (**e**) or a paired  $t$ -test (**h**); \* $P < 0.05$ , \*\* $P < 0.01$ , \*\*\* $P < 0.001$ ; exact  $P$  values are provided in the Source Data. [Source data](#)

### [Extended Data Fig. 4 Spatial organization of immune cells in subcutaneous MC38 tumours.](#)

Representative micrographs of H&E and indicated IHC stains of subcutaneous MC38 tumours. Arrows indicate positive cells on faint CD11B stain. The centre column is a low-power overview (scale bars, 200  $\mu\text{m}$ ). Insets demonstrate high-power images from central (left) and

peripheral (right) tumour locations (scale bars, 20  $\mu$ m). Images are representative of five biological replicates.

## Extended Data Fig. 5 Tumour model characterizations by flow cytometry.

**a–g**, Spleen and tumour CD45 $^{+}$  immune cell populations from MC38 (**a**;  $n = 3$  mice), CT26 (**b**;  $n = 4$  mice) and Renca (**c**;  $n = 4$  mice) subcutaneous tumours; intrarenal Renca tumours (**d**;  $n = 3$  mice); spontaneous PyMT GEMM tumours (**e**;  $n = 3$  mice); AOM/DSS CRC tumours (**f**;  $n = 6$  mice for tumours;  $n = 11$  mice for spleens); and MC38 subcutaneous tumours grown in *Rag1* $^{-/-}$  mice (**g**;  $n = 6$  mice). DC, dendritic cell; NK cell: natural killer cell, PMN-MDSC, polymorphonuclear myeloid-derived suppressor cell. **h**, Gating strategy for immune cell identification using lymphocyte and myeloid-focused antibody panels. Each data point represents a biological replicate; data are mean  $\pm$  s.e.m. Data in **a–f** are representative of independent experiments performed at least twice. [Source data](#)

## Extended Data Fig. 6 Supporting data for Fig. 2.

**a, b**, Fraction composition, viability and live-cell yield from MC38 tumour fractions isolated using CD4 $^{+}$ /CD8 $^{+}$  microbeads ( $n = 3$  mice for tumours;  $n = 4$  mice for spleens) (**a**) and CD11B $^{+}$  microbeads ( $n = 4$  mice) (**b**). **c, d**, Cellular FDG avidity in designated CT26 tumour cell fractions using CD4 $^{+}$ /CD8 $^{+}$  microbeads ( $n = 5$  mice for whole spleens;  $n = 3$  mice for spleen fraction, other CD45 $^{+}$  and whole tumours;  $n = 4$  mice for all others) (**c**) and CD11B $^{+}$  microbeads ( $n = 5$  mice for spleen fraction;  $n = 3$  mice for whole tumours;  $n = 4$  mice for all others) (**d**). **e, f**, Fraction composition, viability and live-cell yield from MC38 tumour fractions isolated using GR1 $^{+}$  microbeads (**e**) and F4/80 $^{+}$  microbeads (**f**) ( $n = 4$  mice). **g**, Cellular FDG avidity in designated MC38 tumour cell fractions from *Rag1* $^{-/-}$  mice ( $n = 6$  mice). **h**, Cellular FDG avidity in MC38 tumour cell fractions using CD11B $^{+}$  and CD11C $^{+}$  microbeads ( $n = 9$  mice for whole spleens;  $n = 5$  mice for spleen fraction;  $n = 10$  mice for all others). **i**, Fraction composition of CD11C $^{+}$  purification ( $n = 9$  mice for whole spleens;  $n = 5$  mice for spleen fraction,  $n = 10$  mice for all others). **j**, Representative flow cytometry

illustrating CD103 and LY6C staining of cDC (CD45<sup>+</sup>CD11B<sup>-</sup>CD11c<sup>+</sup>MHCII<sup>+</sup> cells) from MC38 tumour and spleen. Each data point represents a biological replicate; data are mean ± s.e.m. Data are representative of independent experiments performed at least twice. Data in **h** are from two independent experiments. *P* values were calculated using Welch's two-tailed *t*-test; \**P* < 0.05. \*\**P* < 0.01, \*\*\**P* < 0.001; exact *P* values are provided in the Source Data. [Source data](#)

### **Extended Data Fig. 7 Supporting data for Fig. 3.**

**a**, pS6 levels in CT26 tumour populations (*n* = 5 mice). **b**, MC38 tumour mass at study end-point with rapamycin (*n* = 20 mice for vehicle; *n* = 19 mice for rapamycin). **c**, Metabolite concentrations in tumour interstitial fluid and matched plasma from MC38-tumour-bearing mice treated with rapamycin or vehicle (*n* = 5 mice except for lactate and glutamine plasma and TIF vehicle, *n* = 4 mice). **d**, Immune cell infiltration of MC38 tumours from mice treated with rapamycin or vehicle (*n* = 15 mice for vehicle; *n* = 19 mice for rapamycin). Statistical significance between rapamycin and vehicle treatment for individual populations is indicated. A significant decrease in total CD45<sup>+</sup> cell infiltration is noted. **e**, **f**, Flow cytometry quantification of Ki67 positivity (**e**) and cell size (forward scatter, FSC) (**f**) from MC38 tumour populations in mice treated with rapamycin or vehicle (*n* = 4 mice for vehicle; *n* = 5 mice for rapamycin). **g–k**, MC38 tumour CD3<sup>+</sup>CD8A<sup>+</sup> T cell phenotypes from rapamycin- or vehicle-treated mice for effector memory phenotype (**g**), ex vivo IFN $\gamma$  production (**h**), PD1 and TIM3 expression (**i**), LAG3 expression (**j**) (*n* = 5 mice per group) and ratio of CD8<sup>+</sup> T cells to CD4<sup>+</sup>FOXP3<sup>+</sup> T<sub>reg</sub> (**k**) (*n* = 15 mice for vehicle; *n* = 19 mice for rapamycin). **l**, % M2-like TAMs (CD11C<sup>lo</sup>CD206<sup>hi</sup>) in MC38 tumours from mice treated with rapamycin or vehicle (*n* = 15 mice for vehicle; *n* = 19 mice for rapamycin). **m**, **n**, Myeloid suppression assay representative histogram of CD8A<sup>+</sup> OT-I T cell dilution of CellTrace Violet (CTV), indicative of proliferation (**m**), and quantification of division index (**n**) for MC38 tumour myeloid cells isolated using CD11B<sup>+</sup> microbeads from rapamycin- and vehicle-treated mice (*n* = 5 mice per group). Each data point represents a biological replicate; data are mean ± s.e.m. Data in **a**, **e–j** are representative of independent experiments performed at least twice; **b**,

**d, k–l** display data merged from four independent experiments. *P* values were calculated using the Brown-Forsythe and Welch ANOVA with Dunnett's T3 for multiple comparison tests (**a**) or Welch's two-tailed *t*-test (**b–l, n**); \**P* < 0.05. \*\**P* < 0.01, \*\*\**P* < 0.001; exact *P* values are provided in the Source Data. [Source data](#)

### Extended Data Fig. 8 Metabolic transcriptional signatures of MC38 tumour cell populations.

**a**, Cell sorting scheme of MC38 tumour cell populations used for mRNA transcript analyses. **b**, Clustering analysis heat map of differentially expressed metabolic genes from MC38 tumour cell populations. Selected genes are annotated. **c**, Reactome gene set enrichment analysis for genes most highly expressed in each MC38 tumour population. Significantly enriched gene sets are shown and coloured according to metabolic pathway. OXPHOS, oxidative phosphorylation; TCA, tricarboxylic acid cycle.

[Source data](#)

### Extended Data Fig. 9 Effect of rapamycin on metabolic markers of MC38 tumour cell populations.

**a–e**, Heat maps of significantly altered metabolic genes between rapamycin- and vehicle-treated MC38 tumour cell populations for the indicated metabolic pathways. White spaces indicate non-significant changes with rapamycin treatment for that gene and tumour cell population. Genes were grouped and classified manually. (*n* = 3 per group, except *n* = 2 for rapamycin-treated M-MDSCs and CD4<sup>+</sup> T cells). AA, amino acid; FAO, fatty acid oxidation; NT, nucleotide; PPP, pentose phosphate pathway; PTGS, prostaglandin synthases; reg, regulatory genes; RNR, ribonucleotide reductase; SLCs, solute carrier proteins. **f**, Flow cytometry quantification of GLUT1 expression in MC38 tumour populations from mice treated with rapamycin or vehicle (*n* = 4 mice for vehicle; *n* = 5 mice for rapamycin). Each data point represents a biological replicate; data are mean ± s.e.m; exact *P* values are provided in the Source Data. [Source data](#)

### Extended Data Fig. 10 Supporting data for Fig. 4.

**a, b**, Representative histograms (**a**) and quantification (**b**) for ex vivo staining of C16 BODIPY by indicated MC38 tumour cell populations from tumour single-cell suspensions ( $n = 5$  mice). **c**, Per cent contribution to total tumour C16 BODIPY signal from indicated tumour cell populations ( $n = 5$  mice). **d–f**, Cellular  $^{18}\text{F}$ -Gln avidity in designated tumour cell fractions in CT26 (**d**;  $n = 4$  mice for spleen;  $n = 3$  mice for tumour) and Renca (**e**;  $n = 5$  mice) subcutaneous tumours and AOM/DSS spontaneous tumours (**f**;  $n = 4$  mice). **g**, MC38 tumour mass from mice treated with V9302 or DMSO ( $n = 13$  mice for V9302;  $n = 12$  mice for DMSO). **h**, Immune cell infiltration of MC38 tumours from mice treated with V9302 or DMSO ( $n = 13$  mice for V9302;  $n = 12$  mice for DMSO). Statistical significance between V9302 and DMSO treatment in distinct populations is indicated. There is no significant change in total CD45 $^+$  cell infiltration ( $n = 13$  mice for V9302;  $n = 12$  mice for DMSO). **i, j**, Representative plot (**i**) and abundance (**j**) of MC38 M2-like TAMs from mice treated with V9302 or DMSO ( $n = 13$  mice for V9302;  $n = 12$  mice for DMSO). Each data point represents a biological replicate; data are mean  $\pm$  s.e.m. Data are representative of at least two independent experiments; **g–j** are data combined from two experiments.  $P$  values were calculated using the Brown-Forsythe and Welch ANOVA with Dunnett's T3 for multiple comparison tests (**b, c**) or Welch's two-tailed  $t$ -test (**d–j**); \* $P < 0.05$ , \*\* $P < 0.01$ , \*\*\* $P < 0.001$ ; exact  $P$  values are provided in the Source Data.

[Source data](#)

## Supplementary information

### [Supplementary Figures](#)

Additional Flow Cytometry Gating. Gating schemes for Figure 3, and extended data figures 3/7.

### [Reporting Summary](#)

### [Supplementary Table 1](#)

ccRCC Patient Characteristics.

## **Supplementary Table 2**

mRNA transcript data from flow-sorted MC38 tumour populations.  
TAM=Tumour Associated Macrophages (CD11b+ Ly6C/Glo F4/80+), M-MDSC= Monocytic-Myeloid Derived Suppressor Cell (CD11b+ Ly6C+), Wh tumour=unfractionated whole tumour.

## **Supplementary Table 3**

Genes most highly expressed in distinct MC38 tumour populations.

## **Supplementary Table 4**

Effect of rapamycin on MC38 tumour cell mRNA transcripts. Includes gene selected for metabolic clustering in Figure 3I.

## **Source data**

[\*\*Source Data Fig. 1\*\*](#)

[\*\*Source Data Fig. 2\*\*](#)

[\*\*Source Data Fig. 3\*\*](#)

[\*\*Source Data Fig. 4\*\*](#)

[\*\*Source Data Extended Data Fig. 1\*\*](#)

[\*\*Source Data Extended Data Fig. 2\*\*](#)

[\*\*Source Data Extended Data Fig. 3\*\*](#)

[\*\*Source Data Extended Data Fig. 5\*\*](#)

[\*\*Source Data Extended Data Fig. 6\*\*](#)

[\*\*Source Data Extended Data Fig. 7\*\*](#)

[\*\*Source Data Extended Data Fig. 8\*\*](#)

[\*\*Source Data Extended Data Fig. 9\*\*](#)

[\*\*Source Data Extended Data Fig. 10\*\*](#)

## Rights and permissions

[Reprints and Permissions](#)

## About this article



Check for  
updates

## Cite this article

Reinfeld, B.I., Madden, M.Z., Wolf, M.M. *et al.* Cell-programmed nutrient partitioning in the tumour microenvironment. *Nature* **593**, 282–288 (2021). <https://doi.org/10.1038/s41586-021-03442-1>

[Download citation](#)

- Received: 09 August 2020
- Accepted: 10 March 2021
- Published: 07 April 2021
- Issue Date: 13 May 2021
- DOI: <https://doi.org/10.1038/s41586-021-03442-1>

# Further reading

- [Preferential glutamine uptake in cancer cells](#)

- Monica Wang

*Nature Reviews Nephrology* (2021)

- [A guide to interrogating immunometabolism](#)

- Kelsey Voss
- , Hanna S. Hong
- , Jackie E. Bader
- , Ayaka Sugiura
- , Costas A. Lyssiotis
- & Jeffrey C. Rathmell

*Nature Reviews Immunology* (2021)

## Comments

By submitting a comment you agree to abide by our [Terms](#) and [Community Guidelines](#). If you find something abusive or that does not comply with our terms or guidelines please flag it as inappropriate.

[Access through your institution](#)

[Change institution](#)

[Buy or subscribe](#)

---

This article was downloaded by **calibre** from <https://www.nature.com/articles/s41586-021-03442-1>

---

HP1 drives de novo 3D genome reorganization in early *Drosophila* embryos  
[Download PDF](#)

- Article
- Open Access
- [Published: 14 April 2021](#)

# HP1 drives de novo 3D genome reorganization in early *Drosophila* embryos

- [Fides Zenk](#) ORCID: [orcid.org/0000-0002-0324-0902](https://orcid.org/0000-0002-0324-0902)<sup>1,2 na1</sup>,
- [Yinxiu Zhan](#) ORCID: [orcid.org/0000-0001-7702-6207](https://orcid.org/0000-0001-7702-6207)<sup>3,4 na1</sup>,
- [Pavel Kos](#) ORCID: [orcid.org/0000-0002-3625-0939](https://orcid.org/0000-0002-3625-0939)<sup>3</sup>,
- [Eva Löser](#)<sup>1</sup>,
- [Nazerke Atinbayeva](#)<sup>1,2,5</sup>,
- [Melanie Schächtle](#)<sup>1</sup>,
- [Guido Tiana](#)<sup>6</sup>,
- [Luca Giorgetti](#) ORCID: [orcid.org/0000-0002-9664-9087](https://orcid.org/0000-0002-9664-9087)<sup>7</sup> &
- [Nicola Iovino](#) ORCID: [orcid.org/0000-0002-3335-7618](https://orcid.org/0000-0002-3335-7618)<sup>1</sup>

[Nature](#) volume 593, pages 289–293 (2021) [Cite this article](#)

- 18k Accesses
- 186 Altmetric
- [Metrics details](#)

## Subjects

- [Chromatin](#)
- [Embryogenesis](#)
- [Epigenetic memory](#)
- [Epigenetics](#)
- [Nuclear organization](#)

This article has been [updated](#)

## Abstract

Fundamental features of 3D genome organization are established de novo in the early embryo, including clustering of pericentromeric regions, the folding of chromosome arms and the segregation of chromosomes into active (A-) and inactive (B-) compartments. However, the molecular mechanisms that drive de novo organization remain unknown<sup>1,2</sup>. Here, by combining chromosome conformation capture (Hi-C), chromatin immunoprecipitation with high-throughput sequencing (ChIP-seq), 3D DNA fluorescence in situ hybridization (3D DNA FISH) and polymer simulations, we show that heterochromatin protein 1a (HP1a) is essential for de novo 3D genome organization during *Drosophila* early development. The binding of HP1a at pericentromeric heterochromatin is required to establish clustering of pericentromeric regions. Moreover, HP1a binding within chromosome arms is responsible for overall chromosome folding and has an important role in the formation of B-compartment regions. However, depletion of HP1a does not affect the A-compartment, which suggests that a different molecular mechanism segregates active chromosome regions. Our work identifies HP1a as an epigenetic regulator that is involved in establishing the global structure of the genome in the early embryo.

[Download PDF](#)

## Main

In metazoans, fertilization triggers global de novo chromatin reorganization into heterochromatin and euchromatin. The clustering of pericentromeric heterochromatin and the folding of chromosome arms lead to a highly regular Rabl configuration during zygotic genome activation (ZGA)<sup>3,4</sup>. Concomitantly, active and inactive chromatin regions start to associate to form the A- and B-compartments, respectively<sup>2,5,6,7,8,9</sup>. The molecular determinants of compartmental forces remain unknown.

Constitutive heterochromatin is enriched for histone 3 lysine 9 di- and trimethylation (H3K9me2/3) and is important for chromatin structure<sup>10,11</sup>. Members of the heterochromatin protein family bind to constitutive heterochromatin and perform related functions in all eukaryotes<sup>12</sup>. All family members contain a chromodomain<sup>13</sup>, which binds to H3K9me2/3, and a chromoshadow domain, which supports homodimerization and protein–protein interactions<sup>14</sup>. *Drosophila* expresses five

different heterochromatin protein family members<sup>12</sup> termed HP1a–HP1e. HP1a (hereafter termed as HP1, encoded by *Su(var)2-5*) was discovered in *Drosophila*<sup>15</sup> and is essential for early embryonic development, as is the mammalian protein HP1β<sup>16,17</sup>. HP1 localizes mainly to H3K9me2/3-rich heterochromatin<sup>10,15,18</sup>, but also to euchromatic sites along chromosome arms<sup>19</sup>. HP1 might promote heterochromatin compaction through phase separation<sup>20</sup>, similar to human HP1α<sup>21</sup>. Whether HP1 is required to initiate genome reorganization in early embryos is unclear.

To address this question, we performed immunofluorescence of *Drosophila* embryos before ZGA and the establishment of higher-order chromatin architecture<sup>5,6</sup>, observing diffuse nuclear localization of HP1 (Fig. 1a, Extended Data Fig. 1a). By ZGA, both HP1 and H3K9me3 were strongly enriched at pericentromeric heterochromatin, which was localized apically (reflecting the Rabl configuration) and overlapped with DAPI-dense regions (Fig. 1b, Extended Data Fig. 1b,c). The HP1 signal was around 30 times higher in these regions (Supplementary Methods).

**Fig. 1: Localization of HP1 during early embryonic development.**

---

 **figure1**

**a**, Top, schematic of early embryonic development. Bottom, immunofluorescence staining at different stages of early embryonic development. HP1 localizes to chromatin before ZGA and becomes enriched at the pericentromeric heterochromatin at ZGA. Scale bar, 20  $\mu$ m. **b**, Close-up view of HP1 localization at ZGA. Top,

---

schematic shows the Rabl configuration of the chromosomes at this developmental stage, with the centromeres localizing on top and the chromosome arms reaching to the bottom of the nucleus. Bottom, the centromeric regions display strong HP1 signals. Images in **a** and **b** are representative from four biological replicates. Scale bar, 5  $\mu$ m. **c**, Heat maps of HP1 ChIP-seq signal at three different early embryonic developmental time points. The signal is centred on HP1 peaks within chromosome arms called at ZGA and ranked by signal intensity at cycles 9–13. HP1 binding to chromatin is already observed before cycle 9, and becomes more enriched during development. **d**, Box plots of HP1 peak size distribution within chromosome arms at cycle 9, cycles 9–13 and ZGA. **e**, Box plots of HP1 peak size distribution within pericentromeric regions at cycle 9, cycles 9–13 and ZGA, showing that HP1 peaks get broader at the pericentromeric regions at ZGA. In all box plots, centre line denotes the median; boxes denote lower and upper quartiles (Q1 and Q3, respectively); whiskers denote 1.5 $\times$  the interquartile region (IQR) below Q1 and above Q3; points denote outliers.

[Source data](#)

[Full size image](#)

To characterize HP1 binding at different developmental stages, we performed HP1 ChIP-seq in precisely hand-staged *Drosophila* wild-type (control) embryos (Fig. [1c](#), Extended Data Fig. [1d,e](#)). At ZGA, HP1 localized not only to constitutive heterochromatin, such as pericentromeric and telomeric regions (4,394 peaks, 67%) (Extended Data Fig. [1d](#)), but also within chromosome arms (2,213 peaks, 33%) at repeat sequences (43% of non-pericentromeric peaks, 10% long interspersed nuclear elements (LINEs), 30% long-terminal repeats (LTRs)) and unique sequences (57% of peaks) (Extended Data Fig. [1d–g](#)). Consistent with the immunofluorescence analysis (Fig. [1a](#)), HP1 was bound to chromatin even in totipotent nuclei (Fig. [1c–e](#)), albeit at a lower enrichment (16% of the ZGA enrichments) (Supplementary Methods). Notably, the peak size on chromosome arms did not change markedly (Fig. [1d](#)), whereas HP1 spreading occurred at pericentromeric regions during development (Fig. [1e](#), Extended Data Fig. [1d](#), Supplementary Methods).

Next, we generated Hi-C data for control embryos precisely hand-staged at ZGA (Fig. [2a](#), Extended Data Fig. [2a](#)). Chromosomes were clearly segregated into A- and B-compartments (Fig. [2a,b](#)). HP1 was bound not only within B-compartment but also within A-compartment sequences (Fig. [2c,d](#), Extended Data Fig. [2b–d](#), Supplementary Methods). As expected, HP1 binding in B-compartment regions systematically overlapped with H3K9me3, localized around repeats and occasionally extended over several kilobases (median peak size 730 bp) (Fig. [2c](#)). By contrast, we detected two different modes of HP1 binding in A-compartment regions. We found that 46% of HP1 binding sites in the A-compartment were sharply localized and

enriched for active chromatin marks, and did not overlap with repeats (Fig. 2d, Extended Data Fig. 2d, cluster 2). A second class of HP1 peaks resembled those in the B-compartment (Extended Data Fig. 2d, cluster 1). These might correspond to short stretches of repetitive repressed DNA that cannot be resolved unequivocally by Hi-C. ChIP-seq analysis thus suggests that HP1 binds (1) within active, H3K9ac-rich chromatin in the A-compartment, and (2) within inactive, constitutive heterochromatic domains of the B-compartment.

**Fig. 2: HP1 binds both A- and B-compartment regions at ZGA.**

 figure2

**a**, Hi-C contact map of an 8-Mb region on chromosome 3L (resolution 40 kb). Pooled Hi-C data of seven biological replicates are shown (Extended Data Fig. 2a). **b**, Compartment scores (first eigenvector of the Hi-C map, resolution: 10 kb), same region as in **a** (Supplementary Methods). **c**, Heat maps of HP1, H3K9me3 and H3K9ac ChIP-seq signals as well as repeat positions,  $\pm 10$  kb centred on HP1 peaks occurring in B-compartment regions. HP1 binding overlaps with broad H3K9me3 peaks, repeats and is devoid of H3K9ac. **d**, As in **c** for HP1 peaks in A-compartment regions, showing enrichment in H3K9ac and absence of repeats (Extended Data Fig. 2b-d).

[Full size image](#)

To explore the role of HP1 in establishing 3D chromosome organization, we examined early embryos that were depleted of maternally supplied HP1. Because HP1 is essential in *Drosophila*<sup>15</sup>, we performed conditional knockdown<sup>22</sup> (Extended Data Fig. 3a, Supplementary Methods).

Complete depletion of HP1 blocked development before ZGA, whereas partial knockdown of HP1 still supported development to ZGA (Extended Data Fig. 3b,c, Supplementary Methods). Therefore, we used the partial HP1-knockdown (HP1-KD) embryos in all subsequent experiments. The embryonic lethality of the partial HP1-KD embryos was rescued with a short hairpin RNA (shRNA)-resistant HP1 (HP1-rescue)

(Extended Data Fig. 3d), confirming the specificity. HP1 depletion led to strongly reduced binding of HP1 genome-wide, and to upregulation of the telomeric retroelement Het-A that was rescued in HP1-rescue embryos (Extended Data Figs. 1g, 3e,f).

Hi-C analysis of HP1-KD embryos at ZGA revealed major genome-wide changes in chromosome organization (Fig. 3a, Extended Data Fig. 3g,h); we found perturbed Rabl configuration with decreased contact frequencies within and between pericentromeric regions and reduced inter-arm and inter-chromosomal contacts (Fig. 3a). Unexpectedly, we also observed increased intra-chromosomal contacts and milder decay of contact probabilities within chromosome arms (Fig. 3b-d), which suggests an overall increase in chromosome compaction within arms.

**Fig. 3: Depletion of HP1 causes increased intra-chromosome compaction and reduced compartmentalization.**

 figure3

**a**, Differential Hi-C contact map ( $\log_2$ -transformed), highlighting increased contact frequencies within chromosome arms, decreased inter-arm and inter-chromosome contacts, reduced associations within and between pericentromeric regions, and increased interactions of pericentromeric regions with chromosome arms in HP1-KD embryos. Biological replicates were pooled;  $n = 7$  control and  $n = 5$  HP1-KD embryos. **b**, HP1-KD embryos show a milder decay of contact probabilities above 100 kb. **c**, Hi-C contact maps of 19 Mb on chromosome 2R in control embryos (resolution: 120 kb). **d**, As in c, in HP1-KD embryos. **e**, Differential contact enrichment in HP1-KD versus control embryos, sorted by compartment score (Supplementary Methods), shows decreased B-compartment interactions and increased A/B intermixing. Changes relative to the control. **f**, Scheme of FISH probe design to quantify inter-arm distance and intra-arm compaction. **g**, Representative 3D-DNA FISH staining of control and

HP1-KD embryos at ZGA. Signals from probes on chromosome 2R and chromosome 3L are shown separately and merged with DAPI staining. Scale bar, 5  $\mu$ m. **h**, Quantification of physical distances between FISH signals from chromosome 2R and 3L (mean  $\pm$  s.d., nuclei: control  $n = 55$ , HP1-KD  $n = 35$ ). **i**, Quantification of compaction of FISH signals from chromosome 2R (mean  $\pm$  s.d., nuclei: control  $n = 63$ , HP1-KD  $n = 75$ ). **j**, Differential Hi-C contact map ( $\log_2$ -transformed), highlighting decreased inter-arm and inter-chromosomal contacts, reduced associations within and between pericentromeric regions, and increased interactions of pericentromeric regions with chromosome arms in H3K9M embryos. Biological replicates were pooled;  $n = 7$  control and  $n = 2$  H3K9M embryos. See Supplementary Methods and Extended Data Fig. 5 for further details.  $P$  values were determined by Wilcoxon two-sided test.

[Source data](#)

[Full size image](#)

Notably, HP1-KD embryos also showed reduced segregation of A- and B-compartments, with a 20% decrease in B-compartment strength (Fig. 3e, Extended Data Fig. 3i, j). This effect was consistent across replicates, chromosome arms and for inter-arm and inter-chromosome contacts (Extended Data Fig. 3j, k). We found almost no compartment switching (Extended Data Fig. 3l). We also detected decreased insulation across topologically associating domains (TADs) (Extended Data Fig. 3m, n). By excluding short-range contacts (less than 500 kb or 3 Mb), we confirmed that the reduction of the B-compartment signal is independent of the reduction in TAD insulation (Extended Data Fig. 3o). Crucially, all of these phenotypes were rescued in HP1-rescue embryos (Extended Data Fig. 4a–d).

To validate the structural defects observed in HP1-KD embryos by Hi-C analysis, we performed 3D DNA fluorescence *in situ* hybridization (3D DNA FISH) with oligonucleotide probes spanning several megabases on chromosomes 2R and 3L (Fig. 3f, g). Quantitative image analysis of single cells showed that chromosomes were on average separated by larger distances (around 30% increase) in HP1-KD embryos (Fig. 3h, Supplementary Methods), in line with reduced inter-arm and inter-chromosome interactions observed in Hi-C data (Fig. 3a). In agreement with Hi-C data (Fig. 3b), we also found that the volume of the FISH signals was significantly decreased (around 10% decrease) (Supplementary Methods) in HP1-KD embryos (Fig. 3i), which suggests increased compaction of chromosome arms.

HP1 depletion thus perturbs the overall nuclear structure, with reduced proximity between pericentromeric regions, reduced alignment of chromosome arms and increased intra-chromosomal compaction. These global effects are accompanied by a prominent loss of contacts within B-compartment regions. The structural defects of

HP1-KD embryos are notable, given that depletion of HP1 was only partial to allow embryos to reach ZGA. Our findings reveal that HP1 has a key role in establishing the 3D genome structure during development.

Only a small fraction of genes and repeats was misregulated in HP1-KD embryos at ZGA (Extended Data Fig. 4e). The most highly upregulated retroelements were localized at telomeric regions (Het-A, TAHRE and TART retrotransposons) and cannot account for the structural changes that we observed genome-wide (Extended Data Fig. 4e,f). We confirmed that HP1-KD embryos did not show defects in the onset of transcription at ZGA, and that both the control and the HP1-KD embryos at ZGA were in interphase (Extended Data Fig. 4g,h).

To investigate the role of HP1 in the establishment versus the maintenance of chromatin structures, we performed Hi-C experiments with differentiated, somatic *Drosophila* S2 cells. Notably, HP1 depletion did not considerably affect genome architecture (Extended Data Fig. 4i–o), which suggests that HP1 is not required to maintain chromatin structure.

Because HP1 interacts with chromatin by binding to H3K9me2/3, we generated embryos depleted of H3K9me2/3 by overexpressing the histone 3 lysine 9-to-methionine (H3K9M) mutation<sup>23</sup> (Extended Data Fig. 5a). Quantitative ChIP-seq for HP1 in precisely hand-staged H3K9M embryos at ZGA showed that HP1 binding was greatly reduced on pericentromeric and repeat regions as well as chromosome arms (Extended Data Fig. 5b–d). However, HP1 was 20% more retained on chromosome arms in H3K9M compared to HP1-KD embryos (Extended Data Fig. 5b, right), which could be due to some residual H3K9me2/3 and/or H3K9me2/3-independent binding of HP1 (Extended Data Fig. 5d, right, cluster 2). ChIP-seq analysis of chromodomain-mutant HP1 (HP1-CD)<sup>13</sup> also revealed some residual binding on chromosome arms, further supporting H3K9me2/3-independent binding of HP1 (Extended Data Fig. 5e).

Hi-C maps of H3K9M embryos revealed pericentromeric heterochromatin de-clustering and reduced chromosome arm alignment, but only a mild gain in chromosome arm compaction and mild defects in compartmentalization (Fig. 3j, Extended Data Fig. 5f–j), which could be explained by higher retention of HP1 along chromosome arms in H3K9M embryos (Extended Data Fig. 5b).

Overall, our data indicate that HP1 has a major role in establishing chromatin architecture in early embryos by: (1) mediating the clustering and condensation of constitutive heterochromatin at pericentromeric regions through H3K9me2/3-dependent binding; (2) aiding the overall configuration of chromosome arms; and (3) contributing to the formation of the B-compartment.

Next, we set out to exclude that folding defects observed at chromosome arms in HP1-KD embryos could arise as a mere consequence of the expansion of pericentromeric chromatin. Because it is impossible to completely decouple these effects *in vivo*, we turned to a genome-wide polymer modelling approach in which chromosomes are represented as chains of three types of 10-kb beads (A, B and C corresponding to A- and B-compartment and pericentromeric/telomeric regions, respectively) confined in a cylindrical nucleus (Fig. 4a, Supplementary Methods). We first optimized a set of interaction energies to reproduce contact probability scaling and compartment strength within arms in control embryos (Extended Data Fig. 6a–c). Next, we mimicked centromere de-clustering by decreasing interactions among C-type beads and their interactions with the nuclear surface (mutant) (Fig. 4b,c). The model recapitulated reduced alignment between chromosome arms (Fig. 4c, right) and increased interactions between pericentromeric regions and chromosome arms (Fig. 4c), but not compaction and compartmentalization defects within arms (Extended Data Fig. 6d,e). These results do not depend on the numbers of centromeric and telomeric beads (Extended Data Fig. 6f–l). This suggests that compartment defects and intra-arm compaction are a consequence of decreased HP1 binding on chromosome arms.

**Fig. 4: HP1 establishes de novo chromatin architecture during development via two independent mechanisms.**

 figure4

- a**, Whole-genome polymer model. A- and B-type beads correspond to 10-kb A- and B-compartment regions. C-type beads correspond to pericentromeric and telomeric regions. **b**, Snapshots of wild-type control (left) and mutant (right) simulations. **c**, Genome-wide simulated distance maps of control (left) and mutant (centre). Right, differential distance map highlighting increased distances within and between centromeric and telomeric regions and reduced chromosome arm alignment (arrows). **d**, Polymer model of multi-megabase chromosome arm regions. Interaction energies between 40-kb beads are inferred to reproduce the experimental Hi-C map. **e**, Experimental and simulated contact maps in control (top) and HP1-KD (bottom) embryos (chr3R 17–20.6 Mb). **f**, Inferred interaction energies are overall more attractive in the HP1-KD model. *P* value determined by two-sided Wilcoxon test. Box

plots are as in Fig. 1d. g, Left, interaction energies between B-type beads (B–B) become comparatively less attractive in HP1-KD embryos, but more attractive between A-type beads (A–A) and between A and B types (A–B). Right, average interaction energy changes between HP1-KD and control models. B-compartment attractions decrease in the HP1-KD model. Data are mean  $\pm$  s.e.m., interactions: 990 (A–A), 2,069 (A–B), 1,035 (B–B). h, Chromatin is modelled as a chain of two types (A and B) of interacting 40-kb beads (chr3R 17–20.6 Mb). i, Scaling exponents increase when attractions between all beads are increased by a multiplicative factor, and vice versa. j, Compartment strength (bold line: mean) decreases when attractions between beads are increased, and vice versa. Confidence interval (shaded area) calculated using t-based approximation.

[Source data](#)

[Full size image](#)

To understand the cause of compartment defects in HP1-KD embryos and determine whether they might simply arise from increased intra-arm compaction (Fig. 3a–d), we implemented two smaller-scale polymer models designed to uncover the energies driving the folding of chromosome arms.

In the first approach, interaction energies between 40-kb beads were optimized to reproduce experimental Hi-C maps within multi-megabase regions of chromosome arms<sup>24,25</sup> (Fig. 4d, Supplementary Methods). For control contact maps (Fig. 4e, top), we found that interaction energies were globally attractive, which accounts for the correct contact probability scaling (Extended Data Fig. 7a). The model predicted that A–A and B–B interactions were on average more attractive than A–B interactions (Extended Data Fig. 7b). For HP1-KD contact maps (Fig. 4e, bottom, Extended Data Fig. 7c,d), we found increased attractions overall between all bead types but comparatively less attractive B–B interactions (Fig. 4f,g). Notably, our findings do not depend on the specific region that is simulated (Extended Data Fig. 7e–l). This suggests that decreased compartmentalization is not a mere consequence of increased compaction after HP1 knockdown (Fig. 3a–d) but instead requires the simultaneous loss of B-specific attractive interactions.

To confirm these findings, we used a more general model that is not designed to reproduce the experimental Hi-C maps but instead describes the behaviour of a polymer when interaction energies between its constituent A- and B-type beads are systematically varied (Fig. 4h, Supplementary Methods). Increasing all A–A, A–B and B–B interaction energies correctly predicted milder scaling of contact probabilities (such as HP1-KD), but led to stronger compartments (Fig. 4i,j, Extended Data Fig. 7m). By contrast, decreasing all interaction energies correctly predicted compartment loss but led to the wrong scaling behaviour (steeper decay) (Fig. 4i,j, Extended Data

Fig. 7m). Finally, decreasing only B–B attractions reproduced the observed decrease in compartment strength but resulted in a steeper scaling (Extended Data Fig. 7n). Thus, modifying chromosome compaction alone cannot explain the HP1-KD structural phenotype, which suggests that HP1 depletion perturbs compartmental forces. Notably, these results do not depend on the distribution of A- and B-compartment beads (Extended Data Fig. 7o–r). Analysis of this general polymer model shows that the HP1-KD structural phenotype within arms (increased compaction, lower compartmentalization) arises from two independent mechanisms: decreased specific interactions between B-compartment regions, and increased attraction between all genomic locations.

Our data and modelling approaches suggest that HP1-mediated interactions, which might occur through HP1 oligomerization<sup>14</sup> or phase separation<sup>20,21</sup>, have a major role in establishing 3D genome conformation during embryogenesis. Decreased HP1 binding in pericentromeric heterochromatin led to declustering and decondensation of constitutive heterochromatin and a perturbed Rabl configuration. By contrast, decreased HP1 levels within chromosome arms caused decreased B–B compartment attractions and increased arm compaction, possibly owing to decreased chromatin stiffness. Reduced segregation of B-compartment regions after HP1 knockdown might facilitate interactions between A- and B-type chromatin and allow attractions between active regions to dominate, resulting in globally increased compaction (Extended Data Fig. 7s). This is consistent with quantitative compartment analysis (Fig. 3e, Extended Data Fig. 3i, j) and the overall increase in A–A and A–B interactions in simulations (Fig. 4g). Alternatively, increased attractions could arise from HP1 counteracting condensin II-mediated homologous chromosome pairing or cohesin-mediated loop extrusion.

In the A-compartment, HP1-mediated compartmental forces might be counteracted by surrounding active chromatin modifications such as H3K9ac (Fig. 2d, Extended Data Fig. 7s). Because the A-compartment is not affected after disruption of the B-compartment (Fig. 3e), we suggest that it is controlled by a distinct driving force independent of HP1.

Our study shows that HP1 is required to establish pericentromeric heterochromatin clustering in early embryos but is dispensable in differentiated cells, consistent with a recent report in mammals<sup>26</sup>. In differentiated cells, clustering might be driven by other HP1 paralogues or heterochromatin proteins<sup>2</sup> favoured by the slower cell cycle, or result from other mechanisms involving solid-like states in heterochromatin condensates<sup>27</sup>. We also showed that HP1 prevents the collapse of chromosome arms while they elongate to establish the characteristic Rabl configuration. Finally, HP1 is directly involved in the formation of the B- but not the A-compartment region.

Because pericentromeric clustering and compartmentalization also occur in mammals, HP1 could have similar functions during mammalian embryogenesis.

## Reporting summary

Further information on research design is available in the [Nature Research Reporting Summary](#) linked to this paper.

## Data availability

All Hi-C, ChIP-seq and RNA sequencing raw files generated in this study have been uploaded to the Gene Expression Omnibus (GEO) under accession [GSE140542](#). The following public databases were used: BSgenome.Dmelanogaster.UCSC.dm6, org.Dm.eg.db and TxDb.Dmelanogaster.UCSC.dm6.ensGene. [Source data](#) are provided with this paper.

## Code availability

Custom code generated in this study is available at:  
[https://github.com/zhanyinx/Zenk\\_Zhan\\_et\\_al\\_Nature2021](https://github.com/zhanyinx/Zenk_Zhan_et_al_Nature2021).

## Change history

- [28 April 2020](#)

This Article was amended to correct the Peer review information, which was originally incorrect.

## References

1. 1.

Falk, M. et al. Heterochromatin drives compartmentalization of inverted and conventional nuclei. *Nature* **570**, 395–399 (2019).

[ADS](#) [CAS](#) [Article](#) [Google Scholar](#)

2. 2.

Hildebrand, E. M. & Dekker, J. Mechanisms and functions of chromosome compartmentalization. *Trends Biochem. Sci.* **45**, 385–396 (2020).

[CAS Article](#) [Google Scholar](#)

3. 3.

Marshall, W. F., Dernburg, A. F., Harmon, B., Agard, D. A. & Sedat, J. W. Specific interactions of chromatin with the nuclear envelope: positional determination within the nucleus in *Drosophila melanogaster*. *Mol. Biol. Cell* **7**, 825–842 (1996).

[CAS Article](#) [Google Scholar](#)

4. 4.

Merico, V. et al. Epigenomic differentiation in mouse preimplantation nuclei of biparental, parthenote and cloned embryos. *Chromosome Res.* **15**, 341–360 (2007).

[CAS PubMed](#) [Google Scholar](#)

5. 5.

Hug, C. B., Grimaldi, A. G., Kruse, K. & Vaquerizas, J. M. Chromatin architecture emerges during zygotic genome activation independent of transcription. *Cell* **169**, 216–228 (2017).

[CAS Article](#) [Google Scholar](#)

6. 6.

Ogiyama, Y., Schuettengruber, B., Papadopoulos, G. L., Chang, J. M. & Cavalli, G. Polycomb-dependent chromatin looping contributes to gene silencing during *Drosophila* development. *Mol. Cell* **71**, 73–88 (2018).

[CAS Article](#) [Google Scholar](#)

7. 7.

Du, Z. et al. Allelic reprogramming of 3D chromatin architecture during early mammalian development. *Nature* **547**, 232–235 (2017).

[ADS](#) [CAS Article](#) [Google Scholar](#)

8. 8.

Collombet, S. et al. Parental-to-embryo switch of chromosome organization in early embryogenesis. *Nature* **580**, 142–146 (2020).

[ADS](#) [CAS](#) [Article](#) [Google Scholar](#)

9. 9.

Lieberman-Aiden, E. et al. Comprehensive mapping of long-range interactions reveals folding principles of the human genome. *Science* **326**, 289–293 (2009).

[ADS](#) [CAS](#) [Article](#) [Google Scholar](#)

10. 10.

Fodor, B. D., Shukeir, N., Reuter, G. & Jenuwein, T. Mammalian *Su(var)* genes in chromatin control. *Annu. Rev. Cell Dev. Biol.* **26**, 471–501 (2010).

[CAS](#) [Article](#) [Google Scholar](#)

11. 11.

Allshire, R. C. & Madhani, H. D. Ten principles of heterochromatin formation and function. *Nat. Rev. Mol. Cell Biol.* **19**, 229–244 (2018).

[CAS](#) [Article](#) [Google Scholar](#)

12. 12.

Vermaak, D. & Malik, H. S. Multiple roles for heterochromatin protein 1 genes in *Drosophila*. *Annu. Rev. Genet.* **43**, 467–492 (2009).

[CAS](#) [Article](#) [Google Scholar](#)

13. 13.

Lachner, M., O'Carroll, D., Rea, S., Mechtler, K. & Jenuwein, T. Methylation of histone H3 lysine 9 creates a binding site for HP1 proteins. *Nature* **410**, 116–120 (2001).

[ADS](#) [CAS](#) [Article](#) [Google Scholar](#)

14. 14.

Machida, S. et al. Structural basis of heterochromatin formation by human HP1. *Mol. Cell* **69**, 385–397 (2018).

[CAS](#) [Article](#) [Google Scholar](#)

15. 15.

James, T. C. & Elgin, S. C. Identification of a nonhistone chromosomal protein associated with heterochromatin in *Drosophila melanogaster* and its gene. *Mol. Cell. Biol.* **6**, 3862–3872 (1986).

[CAS](#) [Article](#) [Google Scholar](#)

16. 16.

Aucott, R. et al. HP1-beta is required for development of the cerebral neocortex and neuromuscular junctions. *J. Cell Biol.* **183**, 597–606 (2008).

[CAS](#) [Article](#) [Google Scholar](#)

17. 17.

Santos, F., Peters, A. H., Otte, A. P., Reik, W. & Dean, W. Dynamic chromatin modifications characterise the first cell cycle in mouse embryos. *Dev. Biol.* **280**, 225–236 (2005).

[CAS](#) [Article](#) [Google Scholar](#)

18. 18.

James, T. C. et al. Distribution patterns of HP1, a heterochromatin-associated nonhistone chromosomal protein of *Drosophila*. *Eur. J. Cell Biol.* **50**, 170–180 (1989).

[CAS](#) [PubMed](#) [Google Scholar](#)

19. 19.

Marsano, R. M., Giordano, E., Messina, G. & Dimitri, P. A New Portrait of Constitutive Heterochromatin: Lessons from *Drosophila melanogaster*. *Trends Genet.* **35**, 615–631 (2019).

[CAS](#) [Article](#) [Google Scholar](#)

20. 20.

Strom, A. R. et al. Phase separation drives heterochromatin domain formation. *Nature* **547**, 241–245 (2017).

[ADS](#) [CAS](#) [Article](#) [Google Scholar](#)

21. 21.

Larson, A. G. et al. Liquid droplet formation by HP1 $\alpha$  suggests a role for phase separation in heterochromatin. *Nature* **547**, 236–240 (2017).

[ADS](#) [CAS](#) [Article](#) [Google Scholar](#)

22. 22.

Zenk, F. et al. Germ line-inherited H3K27me3 restricts enhancer function during maternal-to-zygotic transition. *Science* **357**, 212–216 (2017).

[ADS](#) [CAS](#) [Article](#) [Google Scholar](#)

23. 23.

Herz, H. M. et al. Histone H3 lysine-to-methionine mutants as a paradigm to study chromatin signaling. *Science* **345**, 1065–1070 (2014).

[ADS](#) [CAS](#) [Article](#) [Google Scholar](#)

24. 24.

Giorgetti, L. et al. Predictive polymer modeling reveals coupled fluctuations in chromosome conformation and transcription. *Cell* **157**, 950–963 (2014).

[CAS](#) [Article](#) [Google Scholar](#)

25. 25.

Zhan, Y., Giorgetti, L. & Tiana, G. Modelling genome-wide topological associating domains in mouse embryonic stem cells. *Chromosome Res.* **25**, 5–14 (2017).

[CAS](#) [Article](#) [Google Scholar](#)

26. 26.

Erdel, F. et al. Mouse heterochromatin adopts digital compaction states without showing hallmarks of HP1-driven liquid-liquid phase separation. *Mol. Cell* **78**,

236–249 (2020).

[CAS](#) [Article](#) [Google Scholar](#)

27. 27.

Strickfaden, H. et al. Condensed chromatin behaves like a solid on the mesoscale in vitro and in living cells. *Cell* **183**, 1772–1784.e13 (2020).

[CAS](#) [Article](#) [Google Scholar](#)

[Download references](#)

## Acknowledgements

We thank the Iovino laboratory, in particular R. Schiavo, D. Ibarra Morales and E. Ponzo; T. Kulkarni, A. Panhale and M. Samata from the Akhtar department; A. Andersen, A. Akhtar, T. Boehm, R. Paro, R. Sawarkar and M. Wiese for crucial reading of the manuscript and discussion; T. Jenuwein, G. Reuter and P. Dimitri for the lengthy and insightful discussion about heterochromatin; The Bioinformatics and Sequencing facilities at the MPI-IE; T. Manke, L. Arrigoni and in particular D. Ryan, M. Rauer, L. Rabbani and G. Renschler. M. Stadler for discussions on data analysis; The Imaging facility, Proteomics facility and Fly facility at the MPI-IE. We thank The Bloomington *Drosophila* Stock Center (NIH P40OD018537) and the TRIP at Harvard Medical School (NIH/NIGMS R01-GM084947) for providing fly stocks and DSHB (HP1) for antibodies; G. Pyrowolakis for initial help in designing overexpression and deletion fly lines; A. Akhtar (Rpb3), C. Margulis (Rpb3), G. Reuter (HP1) and S. Heidmann (Rad21, SMC1) for providing antibodies. NIBR computing resources, D. Flanders and E. Tagliavini for help with cluster and server supports. F.Z., M.S. and E.L. are supported by the Max Planck Society and IMPRS program. N.A. was supported by the DFG (German Research Foundation) under Germany's Excellence Strategy (EXC-2189) Project ID: 390939984. N.I. is supported from the Max Planck Society; Deutsche Forschungsgemeinschaft - Project ID 192904750 - CRC 992 Medical Epigenetics; Behrens-Weise Stiftung; EMBO YIP; CIBSS EXC-2189. This project has also received funding from the European Research Council (ERC) under the European Union's Horizon 2020 research and innovation programme (grant agreement no. 819941) ERC CoG, EpiRIME. Research in the Giorgetti laboratory is supported by the Novartis Research Foundation and the European Research Council (ERC) under the European Union's Horizon 2020 research and innovation (grant agreement no. 759366, BioMeTre).

## Funding

Open access funding provided by Max Planck Society.

## Author information

### Author notes

1. These authors contributed equally: Fides Zenk, Yinxiu Zhan

### Affiliations

1. Max Planck Institute of Immunobiology and Epigenetics, Freiburg im Breisgau, Germany

Fides Zenk, Eva Löser, Nazerke Atinbayeva, Melanie Schächtle & Nicola Iovino

2. Albert-Ludwigs-Universität Freiburg, Freiburg im Breisgau, Germany

Fides Zenk & Nazerke Atinbayeva

3. Friedrich Miescher Institute for Biomedical Research, Basel, Switzerland

Yinxiu Zhan, Pavel Kos & Luca Giorgi

4. University of Basel, Basel, Switzerland

Yinxiu Zhan

5. CIBSS – Centre for Integrative Biological Signalling Studies, University of Freiburg, Freiburg im Breisgau, Germany

Nazerke Atinbayeva

6. Università degli Studi di Milano and INFN, Milan, Italy

Guido Tiana

### Authors

1. Fides Zenk

[View author publications](#)

You can also search for this author in [PubMed](#) [Google Scholar](#)

2. Yinxiu Zhan

[View author publications](#)

You can also search for this author in [PubMed](#) [Google Scholar](#)

3. Pavel Kos

[View author publications](#)

You can also search for this author in [PubMed](#) [Google Scholar](#)

4. Eva Löser

[View author publications](#)

You can also search for this author in [PubMed](#) [Google Scholar](#)

5. Nazerke Atinbayeva

[View author publications](#)

You can also search for this author in [PubMed](#) [Google Scholar](#)

6. Melanie Schächtle

[View author publications](#)

You can also search for this author in [PubMed](#) [Google Scholar](#)

7. Guido Tiana

[View author publications](#)

You can also search for this author in [PubMed](#) [Google Scholar](#)

8. Luca Giorgetti

[View author publications](#)

You can also search for this author in [PubMed](#) [Google Scholar](#)

9. Nicola Iovino

[View author publications](#)

You can also search for this author in [PubMed](#) [Google Scholar](#)

## Contributions

F.Z. performed all the experimental work and initial computational analysis; Y.Z. performed all the computational analysis. P.K. contributed and optimized the genome wide simulation. G.T. contributed to experimental design and data interpretation

concerning data simulation. E.L. contributed to microscopy data collection and optimized the 3D FISH protocol. N.A. contributed to fly genetics, immunofluorescence staining and sample collection. M.S. helped in sample collection. N.I. and F.Z. conceived the project. N.I. and L.G. designed and supervised the project with inputs from F.Z. and Y.Z. F.Z., Y.Z., L.G. and N.I. wrote the manuscript.

## Corresponding authors

Correspondence to [Luca Giorgetti](#) or [Nicola Iovino](#).

## Ethics declarations

## Competing interests

The authors declare no competing interests.

## Additional information

**Peer review information** *Nature* thanks Leonid Mirny and the other, anonymous, reviewer(s) for their contribution to the peer review of this work.

**Publisher's note** Springer Nature remains neutral with regard to jurisdictional claims in published maps and institutional affiliations.

## Extended data figures and tables

### [Extended Data Fig. 1 Characterization of HP1 binding during early embryonic development.](#)

**a**, Cartoon of early *Drosophila* developmental timing showing the onset of genome organization, chromatin modifications and transcription. **b**, Immunofluorescence staining of an embryo at ZGA. H3K9me3 and HP1 are enriched at the pericentromeric heterochromatin (clustering on top and corresponding to the DAPI dense signal; see cartoon). Representative image from four biological replicates. Scale bar, 5  $\mu$ m. Quantification of the immunofluorescence signal shows that HP1 intensity is 30 times higher in the pericentromeric regions (co-localizing with H3K9me3) than in the rest of the nucleus. Average signal of 300 nuclei from 2 independent experiments. **c**, Cellular fractionation of embryonic extracts at 0–4 h (corresponding to ZGA) of development and from late embryos (corresponding to gastrulation and segmentation). HP1 is already detectable in the chromatin fraction at 0–4 h and becomes further enriched

during differentiation. Representative of two independent experiments. For western blot source data, see Supplementary Fig. 1. **d**, **e**, Representative genomic regions showing HP1 signal as log<sub>2</sub>-transformed fold change over the input before cycle 9, between cycle 9–13 and at ZGA by ChIP-seq. HP1 peaks and repetitive sequences (UCSC RepeatMasker) are represented below. **d**, Strong enrichment of HP1 close to the pericentromeric heterochromatin. **e**, One euchromatic HP1 binding region. **f**, IGV browser snapshots of different genomic regions showing HP1 binding in euchromatin regions. We validated the HP1 ChIP-seq by performing replicate experiments with the same antibody from DSHB (rep1 and rep2). All further tracks in this Article show the merged track (top). To further validate our findings, we mapped the binding of HP1 by performing ChIP-seq against a Flag-haemagglutinin (HA)-tagged transgene and used a second commercial antibody (Covance) and detected the same peaks. We also used disuccinimidyl glutarate (DSG) as crosslinking agent to recover more extended regions of HP1 binding and obtained a similar result of HP1 binding. **g**, Heat maps of HP1, ChIP-seq signals ± 10 kb centred on HP1 peaks occurring along the chromosome arms at ZGA. We validated the binding profiles by performing ChIP-seq against HP1 with different antibodies (DSHB, HA, Covance) and also used the crosslinker DSG (left). To further validate the peaks within chromosome arms, we performed quantitative ChIP-seq in the HP1-KD background, using λ-DNA spike-in as normalizer. The HP1 signal is strongly reduced at HP1 peaks within chromosome arms at ZGA (right). See Supplementary Methods for further details. [Source data](#)

## **Extended Data Fig. 2 Characterization of HP1 binding within A- and B-compartment.**

**a**, Hi-C contact maps with contact frequencies of chromosome 3L (7–15 Mb) at a resolution of 40 kb. Four out of seven biological replicates are shown. **b**, Representative example of HP1 binding in a B-compartment region. **c**, Representative example of HP1 binding in an A-compartment region. **d**, Extended characterization of HP1 binding in A-compartment regions. The heat maps show ChIP-seq signal and repeat coordinates in ±10 kb centred around HP1 peaks. Figure 2d shows only cluster 2 containing HP1 peaks that localize within non-repetitive, active regulatory sequences enriched in H3K9ac, H3K27ac, H3K4me1/3 as well as polymerase II. We validated this cluster in active regions by performing ChIP-seq with different antibodies against HP1 (HA antibody against a Flag-HA-HP1-tagged transgene (second heat map) and HP1 Covance antibody (third heat map)). We further performed ChIP-seq in HP1-KD embryos using λ-DNA spike-in to normalize the signal and found a strong reduction of HP1 binding. This further validates the specificity of the HP1 peaks. See Supplementary Methods for further information. A second cluster of HP1 binding events (cluster 1) occurs in repetitive chromatin regions that are largely devoid of active histone modification marks. [Source data](#)

## Extended Data Fig. 3 Characterization of HP1 knockdown and its effect on 3D genome organization.

**a**, Schematic of the mode of action of the RNA interference (RNAi) knockdown. shRNA against HP1 is expressed only at late stages of oogenesis and does not interfere with the production of fertilized embryos. The resulting early embryo is devoid of maternally loaded mRNA and protein. The bottom part shows the two knockdowns and embryo collection strategy. **b**, Western blot showing reduction of HP1 protein in early embryos after shRNA-mediated knockdown. shRNA#1 was used to perform the Hi-C experiments and generated embryos carrying residual HP1; shRNA#2 completely depleted HP1 proteins. Rbp3, H3 and Ponceau staining were used as loading controls. Representative of two independent experiments. For western blot source data, see Supplementary Fig. 1. **c**, Following the use of shRNA#1, between 5% and 10% of the embryos reach ZGA, therefore allowing the study of 3D chromatin conformation. shRNA#2 blocked embryonic development at the first or second mitotic division, with 0% embryos reaching ZGA, therefore preventing the study of the 3D chromatin conformation establishment. Data are mean ± s.d. Number of biological replicates: 3 for control; 3 for HP1-KD shRNA#1; 3 for HP1-KD shRNA#2. **d**, Both shRNA#1 and shRNA#2 are specific towards HP1 depletion as both can be rescued by a Flag–HA-tagged HP1-rescue construct (Extended Data Fig. 4a). Data are mean ± s.d. Number of biological replicates: 6 for control; 7 for HP1-KD shRNA#1; shRNA#3 for HP1-KD shRNA#2. **e**, Box plot showing reduction of the HP1 ChIP-seq signal in HP1-KD embryos at zygotic genome activation on HP1 peaks at pericentromeric (PC) regions (left) and on HP1-peaks along the chromosome (Chr) arms (right). The signal is overall more reduced within pericentromeric regions compared to peaks along the chromosome arms. For comparison, quantitative ChIP-seq data using spike-in normalization have been used. See Supplementary Methods for definition of the pericentromeric regions. Box plots are as in Fig. 1d. **f**, Quantitative PCR (qPCR) measuring the upregulation of the telomeric repeat element Het-A caused by HP1-KD. The overexpression of Het-A can be rescued by the introduction of a HP1-rescue construct, that cannot be targeted by the hairpin. Data are mean ± s.d. Number of biological replicates:  $n = 4$  for control;  $n = 4$  for HP1-KD; 3 for HP1-rescue. **g**, Genome-wide Hi-C contact maps of control (left, 7 replicates) and HP1-KD (right, 5 replicates) embryos. **h**, Hi-C contact map in control (top) and HP1-KD (bottom) embryos across chromosome 2R 6–25 Mb at a resolution of 120 kb. Five biological replicates are shown. **i**, Hi-C contact enrichment in control (top) and HP1-KD (bottom) embryos, sorted by compartment score showing strong decrease in B-compartment contacts and gain in A/B intermingling upon depletion of HP1. Quantification of the enrichment in compartment interactions is indicated in the respective corner of the plot. See Supplementary Methods for further details. **j**, Differential Hi-C contact enrichment in HP1-KD versus control Hi-C maps, sorted by compartment score for all individual replicates used in the study (top) and the

individual chromosome arms (bottom), confirming the consistency of the phenotype across replicates and chromosome arms. **k**, Hi-C contact maps in control (left) and HP1-KD (right) embryos showing the inter-arm interactions (3L 2640000–14160000 and 3R 15840000–27240000) of chromosome 3 (left) as well as inter-chromosome interactions between chromosome 2L (6000000–17880000) and chromosome 3R (6600000–23760000). In both cases, contacts and compartmentalization are strongly reduced after HP1 knockdown. **l**, Scatter plot of compartment scores (first eigenvector values at 10-kb resolution) in control and HP1-KD embryos (Spearman correlation 0.85), indicating the complete absence of compartment switches between control and HP1-KD embryos. **m**, Hi-C contact map across a 1-Mb region on chr3L, showing decreased insulation across topologically associating domains in HP1-KD embryos. **n**, Insulation scores in  $\pm 100$  kb surrounding TAD boundaries (Supplementary Methods) showing decreased insulation after HP1 depletion. **o**, Differential Hi-C contact enrichment in HP1-KD versus control Hi-C maps, sorted by compartment score for regions further apart than 500 kb (left) and regions further apart than 3 Mb (right). B-compartment contacts are also decreased at distances that exceed typical TAD sizes in *Drosophila*, which confirms that the moderately decreased insulation cannot account for the loss of B-compartment interactions. [Source data](#)

#### [Extended Data Fig. 4 Characterization of HP1 rescue, transcriptomic changes after HP1 knockdown and its effect on 3D genome organization in differentiated S2 cells.](#)

**a**, Western blot showing the expression of the Flag-HA-tagged HP1 transgene in the background of control and HP1-KD embryos. Rpd3, tubulin and Ponceau were used as loading controls. After depletion of endogenous HP1, the expression of the transgene is increased. Blots are representative of two independent experiments. For western blot source data, see Supplementary Fig. 1. **b**, Genome-wide Hi-C contact maps in control (left) and HP1-rescue (right) embryos (40-kb resolution). The HP1-rescue and HP1-KD embryos show an inversion on chromosome 2L. **c**, Genome-wide differential Hi-C contact maps ( $\log_2$ -transformed fold change) in HP1-rescue versus control embryos. The HP1-rescue construct reverses the structural effects of HP1-KD (reduced contact frequency between the pericentromeric regions, as well as inter-chromosome arm interactions and compaction defects). **d**, Same genomic region as in Fig. 3c, d, with control and HP1-KD embryos expressing HP1-rescue. **e**, Left, MA plot illustrating differential expression of genes at zygotic genome activation in HP1-KD versus control embryos. In total, we detected 359 differentially expressed genes using RNA-seq (red dots) (Supplementary Methods) (of the total 277 genes are in A-compartment, 72 genes are in the B-compartment regions and 10 genes are on chrUn\_CP007120v1). Right, MA plot showing the differential expression of types of repeat. We detected 15 differentially expressed repeat types, highlighted in the plot (Supplementary Methods). **f**, Box plot showing the distribution of gene expression changes within A- and B-

compartments. We did not detect any differences in the distribution of gene expression changes in A- and B-compartments either considering all genes (left,  $P = 0.95$ , one-sided Wilcoxon test) or only significant differentially expressed genes (right,  $P = 0.95$ , one-sided Wilcoxon test). Box plots are as in Fig. 1d; outliers not shown. **g**, Expression of a panel of 17 purely zygotically expressed transcription factors in control and HP1-knockdown embryos. In unfertilized eggs all factors are not expressed and become upregulated at zygotic genome activation. The expression of the zygotic transcription factors confirms that HP1-KD embryos undergo zygotic genome activation. Each dot represents the normalized counts for a given transcription factor of a replicate RNA sequencing (RNA-seq) experiment. **h**, Immunofluorescence staining of control and HP1-KD embryos at zygotic genome activation with the mitosis marker H3S10 phosphorylated. Until the cellular blastoderm stage (ZGA), all nuclei undergo mitosis synchronously and then enter G2 phase at ZGA. The ratio of mitotic cells and the timing of mitosis is not altered in HP1-KD embryos. Scale bar, 50  $\mu\text{m}$ . As a control for antibody specificity, an earlier stage of embryogenesis (before ZGA) was stained showing a strong H3S10phospho signal after synchronous entry into mitosis (right). Representative images from three biological replicates. Scale bar, 10  $\mu\text{m}$ . **i**, Western blot showing the reduction of HP1 after treatment with double-stranded RNA (dsRNA) treatment in S2 cells (cell culture cells derived from a primary culture of late-stage (20–24 h old) *Drosophila* embryos, probably from a macrophage-like lineage). Rpd3, tubulin and Ponceau were used as loading controls. To control for unspecific effects of the dsRNA treatment, control cells were treated with a dsRNA against glutathione S-transferases (GST) and two different dsRNAs were used to deplete HP1. Representative of two independent experiments. For western blot source data, see Supplementary Fig. 1. See Supplementary Methods for further details. **j**, qPCR analysis showing the reduction of HP1 mRNA after dsRNA treatment in S2 cells. The signal is relative to *rp49*. To control for unspecific effects of the dsRNA treatment, control cells were treated with a dsRNA against GST and two different dsRNAs were used to deplete HP1. See Supplementary Methods for further details. Data are mean of two independent experiments. **k**, Hi-C contact enrichment in control (left) and HP1-KD (right) in S2 cells, sorted by compartment score, showing no decrease in B-compartment contacts after depletion of HP1 with either dsRNA. This indicates that HP1 is required for the establishment of the B-compartment during early embryonic development but does not affect the maintenance of compartmentalization in late differentiated cells. **l**, Hi-C contact frequencies of a 19-Mb region on chromosome 3L at a resolution of 120 kb. Pooled Hi-C data of two biological replicates are shown. **m**, Genome-wide Hi-C contact map in control S2 cells (120-kb resolution). **n**, Genome wide differential Hi-C contact maps ( $\log_2$ -transformed fold change) in HP1-KD versus control S2 cells. The differential contact maps show the HP1-KD with two independent shRNA on the left and right, respectively. **o**, Contact probabilities over the genomic distance of control and HP1-KD S2 cells. The contact probability of the HP1-KD cells closely resembles the control. Pericentromeric regions

were excluded from the analysis of contact probabilities (Supplementary Methods).

[Source data](#)

## **Extended Data Fig. 5 Characterization of H3K9M.**

**a**, Immunofluorescence staining of embryos at ZGA showing that H3K9me2 is completely lost after expression of the H3K9M mutant. H3K9M depletes H3K9me2/3 from chromatin, and acts as a competitive inhibitor of the histone methyltransferases. Representative image from three biological replicates. Scale bar, 20  $\mu$ m. **b**, Box plot showing the reduction of the HP1 ChIP-seq signal over the control embryos at ZGA at HP1 peaks in HP1-KD (green) and H3K9M (red) embryos. The signal is reduced overall in HP1-KD embryos, with more loss in the pericentromeric region (left) compared to chromosome arms (right). For comparison, quantitative ChIP-seq data using spike-in normalization has been used. Box plots are as in Fig. [1d](#). **c**, Characterization of HP1 binding in B-compartment regions after HP1 knockdown (left) and H3K9M overexpression (right). Heat maps of HP1 ChIP-seq signals are  $\pm 10$  kb centred on HP1 peaks and show that HP1 is retained at a higher level in H3K9M embryos compared to the HP1-KD embryos. Spike-in normalization has been used to quantify the enrichment. **d**, As in **c**, but in A-compartment regions. **e**, Characterization of HP1 binding in ovaries. Left, binding of a control HP1-Flag-HA-tagged transgene. Middle, binding of a Flag-HA-tagged chromodomain mutant of HP1 (HP1-CD) that cannot bind to H3K9me2/3. Right, the enrichment of H3K9me3 in ovaries. The heat maps of HP1 ChIP-seq signals are  $\pm 10$  kb centred on HP1 peaks called in the HP1 chromodomain mutant. **f**, Genome-wide Hi-C contact maps in control (left) and H3K9M (middle) embryos (120-kb resolution, pooled Hi-C data of two biological replicates). Right, differential Hi-C contact map ( $\log_2$ -transformed fold change in HP1-KD versus H3K9M), highlighting milder compaction within arms in H3K9M with respect to HP1-KD. **g**, H3K9M shows decay of contact probability similar to control embryos within arms. This suggests that compaction in the H3K9M mutant is milder than in HP1-KD embryos. **h**, Hi-C contact maps on chr2R (6–25 Mb) in control and H3K9M embryos (120-kb resolution). **i**, Hi-C contact enrichment in H3K9M (left) and differential Hi-C contact enrichment in H3K9M versus control (right) in embryos, sorted by compartment score showing no decrease in B-compartment contacts upon H3K9M expression. **j**, Differential Hi-C contact enrichment in HP1-KD versus H3K9M Hi-C maps, sorted by compartment score. B-compartment interactions are more strongly decreased in HP1-KD embryos than in H3K9M embryos. [Source data](#)

## **Extended Data Fig. 6 Genome-wide simulations show that loss of HP1 at pericentromeric regions does not cause the phenotype within chromosome arms.**

**a**, Snapshots of control (left) and mutant (decreased interactions between C-type beads and between C-type beads and the nuclear envelope, right) simulations, reproducing the experimental scaling and compartment strength. Colour code as in Fig. 4a. **b**, Scaling of contact probabilities in experimental and simulated contact maps. **c**, Simulated and experimental compartment strength.  $P$  values determined by two-sided Wilcoxon test. **d**, Scaling of contact probabilities in experimental HP1-KD and simulated control embryos and mutant contact maps. No differences between simulated control and mutant are detected. **e**, Experimental compartment strength in HP1-KD and simulated compartment strength in control and mutant samples. No differences between simulated control and mutant are detected.  $P$  values determined by two-sided Wilcoxon test. **f**, Snapshots of the control simulations with different amounts of C-type beads (30% and 50%). A single full chromosome is highlighted in each snapshot. **g**, Scaling of contact probabilities in experimental and simulated contact maps with different amounts of C-type beads. **h**, Experimental and simulated compartment strength with different amounts of C-type beads. **i**, Snapshots of the simulations with decreased interactions between C-type beads and their interaction with nuclear surface. A single chromosome is highlighted in each snapshot. Different amounts of C-type beads (30% and 50% of the total number of beads) are shown. **j**, Genome-wide simulated distance maps of control (left) and mutant samples with decreased interaction within and between C-type beads and their interaction with nuclear surface (middle). Differential distance map ( $\log_2$ -transformed fold change in mutant versus control) highlighting increased distance within and between centromeric and telomeric regions (right). Different amounts of C-type beads (30% and 50% of the total number of beads) are shown. **k**, Scaling of contact probabilities in experimental HP1-KD and simulated control and mutant contact maps with different amounts of C-type beads. No differences between simulated control and mutants are detected. **l**, Experimental compartment strength in HP1-KD and simulated compartment strength in mutants with different amounts of C-type beads. No differences between the simulated mutants are detected. Box plots are as in Fig. 1d. [Source data](#)

### **Extended Data Fig. 7 HP1-KD phenotype is driven by two independent mechanisms, both mediated by HP1.**

**a**, Scaling of contact probabilities in experimental and simulated contact maps shown in Fig. 4e. **b**, Inferred interaction energies between pairs of beads are overall attractive, with interactions between B-compartment beads being more attractive than interactions between A–A and A–B beads. Simulated region: chr3R 17–20.6 Mb. **c**, Scaling of contact probabilities in experimental and simulated Hi-C maps, compared to the scaling in the experimental control Hi-C heat map as a reference. Simulated region: chr3R 17–20.6 Mb. **d**, Simulated and experimental compartment strength (chr3R 17–20.6 Mb). **e**, Experimental and simulated contact maps of control embryos. Simulated region: chr3R 25.4–29 Mb. **f**, Scaling of contact probabilities in

experimental and simulated contact maps shown in **e**, **g**, Inferred interaction energies between pairs of beads are overall attractive, with attractions between B-compartment beads being more attractive than interactions between A–A and A–B beads. Simulated region: chr3R 25.4–29 Mb. **h**, Experimental and simulated HP1-KD contact maps in the same region as in **e**. **i**, Scaling of contact probabilities in experimental and simulated Hi-C maps, compared to the scaling in the experimental control. Simulated region: chr3R 25.4–29 Mb. **j**, Simulated and experimental compartment strength in the same chr3R region. Simulated region: chr3R 25.4–29 Mb. **k**, Inferred interaction energies are overall more attractive in the HP1-KD model. *P* value determined by two-sided Wilcoxon test. Simulated region: chr3R 25.4–29 Mb. **l**, Left, interaction energies between B-compartment type beads become comparatively less attractive, whereas interactions between A-type compartment beads and between A- and B-type beads become more attractive. Data are mean and s.e.m. across each interaction energy class (number of interactions: 465 for A–A; 1,858 for A–B; and 1,769 for B–B). Right, average changes in inferred interaction energies between HP1-KD and the control models, classified according to whether they are within or across A- and B-compartment regions. Attractions between B-compartment regions are decreased in the HP1-KD model. Data are mean and s.e.m. across each interaction energy class (number of interactions: 465 for A–A; 1,858 for A–B; and 1,769 for B–B). Average changes in inferred interaction energies between HP1-KD and the control models, irrespective of being within or across A- and B-compartment regions, are set to zero. Interaction energies between B-compartment type beads become less attractive, whereas energies between A-type compartment beads and between A and B become more attractive. **m**, Example of the simulated contact maps for different levels of compartment strength, corresponding to different energy rescaling factors (i, ii and iii, as in Fig. [4j](#)). Arrangement of A and B beads based on: chr3R 17–20.6 Mb. **n**, Same plot as in Fig. [4i](#), [j](#), when only attractions between B-compartment regions are decreased. Mean (bold line) with the confidence interval (shaded area) calculated using t-based approximation is shown. Arrangement of A and B beads based on: chr3R 17–20.6 Mb. **o**, Scaling exponents in simulated contact maps are plotted against increasing or decreasing (by a multiplicative scaling factor) A–A, A–B and B–B attractive interaction. The scaling exponent increases when increasing attractions between all beads and vice versa. Arrangement of A and B beads based on chr3R 25.4–29 Mb. **p**, Compartment strength in simulated contact maps decreases upon increase in attractions between all types of bead, and vice versa. Mean (bold line) with the confidence interval (shaded area) calculated using t-based approximation is shown. Arrangement of A and B beads based on chr3R 25.4–29 Mb. **q**, Example of the simulated contact maps for different levels of compartment strength, corresponding to different energy rescaling factors. Arrangement of A and B beads based on chr3R 25.4–29 Mb. **r**, As in **o** and **p**, when only attractions between B-compartment regions are decreased. Mean (bold line) with the confidence interval (shaded area) calculated using t-based approximation is shown. Arrangement of A and B beads based on chr3R

25.4–29 Mb. **s**, Proposed model in which chromatin-bound HP1 mediates B–B attractions. A–A attractions independent of HP1 promote establishment of the A-compartment. Depletion of HP1 causes pericentromeric region declustering and increased chromosome arm compaction. B–B interactions are reduced, leading to an overall increase in A–A and A–B attractive energies (Supplementary Methods, Extended Data Fig. 6). Box plots are as in Fig. 1d; outliers not shown in k. [Source data](#)

## Supplementary information

### Supplementary Information

This file contains all Materials and Methods as well as Supplementary Fig. 1 with all raw images of the Western Blots performed in the study.

### Reporting Summary

### Supplementary Table 1

Compartments called using HiTC in control embryos at ZGA.

### Supplementary Table 2

Compartments called using HiTC in HP1-KD embryos at ZGA.

### Supplementary Table 3

Drosophila genomic regions annotated as pericentromeric heterochromatin.

### Supplementary Table 4

UCSC annotation of Drosophila repeats.

### Supplementary Table 5

HP1 peaks called with MACS2 using the broad peaks option before cycle 9.

### Supplementary Table 6

HP1 peaks called with MACS2 using the broad peaks option between cycle 9–13.

### Supplementary Table 7

HP1 peaks called with MACS2 using the broad peaks option at ZGA.

## **Supplementary Table 8**

RNA-Seq count table comparing the HP1-KD and control embryos at ZGA.

## **Source data**

**Source Data Fig. 1**

**Source Data Fig. 3**

**Source Data Fig. 4**

**Source Data Extended Data Fig. 1**

**Source Data Extended Data Fig. 2**

**Source Data Extended Data Fig. 3**

**Source Data Extended Data Fig. 4**

**Source Data Extended Data Fig. 5**

**Source Data Extended Data Fig. 6**

**Source Data Extended Data Fig. 7**

## **Rights and permissions**

**Open Access** This article is licensed under a Creative Commons Attribution 4.0 International License, which permits use, sharing, adaptation, distribution and reproduction in any medium or format, as long as you give appropriate credit to the original author(s) and the source, provide a link to the Creative Commons license, and indicate if changes were made. The images or other third party material in this article are included in the article's Creative Commons license, unless indicated otherwise in a credit line to the material. If material is not included in the article's Creative Commons license and your intended use is not permitted by statutory regulation or exceeds the permitted use, you will need to obtain permission directly from the copyright holder. To view a copy of this license, visit <http://creativecommons.org/licenses/by/4.0/>.

## [Reprints and Permissions](#)

## About this article



Check for  
updates

## Cite this article

Zenk, F., Zhan, Y., Kos, P. *et al.* HP1 drives de novo 3D genome reorganization in early *Drosophila* embryos. *Nature* **593**, 289–293 (2021).  
<https://doi.org/10.1038/s41586-021-03460-z>

## [Download citation](#)

- Received: 25 November 2019
- Accepted: 16 March 2021
- Published: 14 April 2021
- Issue Date: 13 May 2021
- DOI: <https://doi.org/10.1038/s41586-021-03460-z>

## Comments

By submitting a comment you agree to abide by our [Terms](#) and [Community Guidelines](#). If you find something abusive or that does not comply with our terms or guidelines please flag it as inappropriate.

## [Download PDF](#)

---

This article was downloaded by **calibre** from <https://www.nature.com/articles/s41586-021-03460-z>.

- Article
- [Published: 14 April 2021](#)

# Structural basis of long-range to short-range synaptic transition in NHEJ

- [Siyu Chen<sup>1,2</sup>](#),
- [Linda Lee](#) [ORCID: orcid.org/0000-0002-4744-7243<sup>3,4</sup>](#),
- [Tasmin Naila<sup>5,6,7</sup>](#),
- [Susan Fishbain<sup>1</sup>](#),
- [Annie Wang<sup>1</sup>](#),
- [Alan E. Tomkinson](#) [ORCID: orcid.org/0000-0002-2671-1711<sup>5,6,7</sup>](#),
- [Susan P. Lees-Miller](#) [ORCID: orcid.org/0000-0001-5809-2516<sup>3,4</sup>](#) &
- [Yuan He](#) [ORCID: orcid.org/0000-0002-1455-3963<sup>1,2,8,9</sup>](#)

[Nature](#) volume 593, pages 294–298 (2021) [Cite this article](#)

- 5850 Accesses
- 221 Altmetric
- [Metrics details](#)

## Subjects

- [Cryoelectron microscopy](#)
- [Double-strand DNA breaks](#)
- [Non-homologous-end joining](#)

## Abstract

DNA double-strand breaks (DSBs) are a highly cytotoxic form of DNA damage and the incorrect repair of DSBs is linked to carcinogenesis<sup>1,2</sup>. The conserved error-prone non-homologous end joining (NHEJ) pathway has a key role in determining the effects of DSB-inducing agents that are used to treat cancer as well as the generation of the diversity in antibodies and T cell receptors<sup>2,3</sup>. Here we applied single-particle cryo-electron microscopy to visualize two key DNA–protein complexes that are formed by human NHEJ factors. The Ku70/80 heterodimer (Ku), the catalytic subunit of the DNA-dependent protein kinase (DNA-PKcs), DNA ligase IV (LigIV), XRCC4 and XLF form a long-range synaptic complex, in which the DNA ends are held approximately 115 Å apart. Two DNA end-bound subcomplexes comprising Ku and DNA-PKcs are linked by interactions between the DNA-PKcs subunits and a scaffold comprising LigIV, XRCC4, XLF, XRCC4 and LigIV. The relative orientation of the DNA-PKcs molecules suggests a mechanism for autophosphorylation in *trans*, which leads to the dissociation of DNA-PKcs and the transition into the short-range synaptic complex. Within this complex, the Ku-bound DNA ends are aligned for processing and ligation by the XLF-anchored scaffold, and a single catalytic domain of LigIV is stably associated with a nick between the two Ku molecules, which suggests that the joining of both strands of a DSB involves both LigIV molecules.

[Access through your institution](#)

[Change institution](#)

[Buy or subscribe](#)

## Access options

Subscribe to Journal

Get full journal access for 1 year

\$199.00

only \$3.90 per issue

[Subscribe](#)

All prices are NET prices.  
VAT will be added later in the checkout.  
Tax calculation will be finalised during checkout.

Rent or Buy article

Get time limited or full article access on ReadCube.

from \$8.99

[Rent or Buy](#)

All prices are NET prices.

### **Additional access options:**

- [Log in](#)
- [Access through your institution](#)
- [Learn about institutional subscriptions](#)

**Fig. 1: Cryo-electron microscopy structure of the LR synaptic complex.**

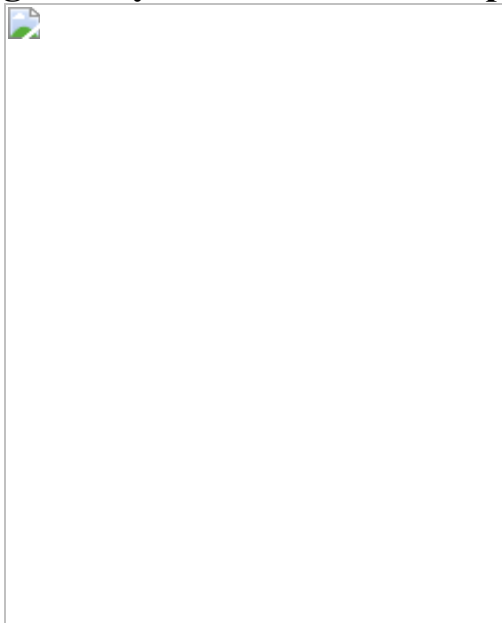


**Fig. 2: Activation mechanism of DNA-PKcs in the LR synaptic complex.**

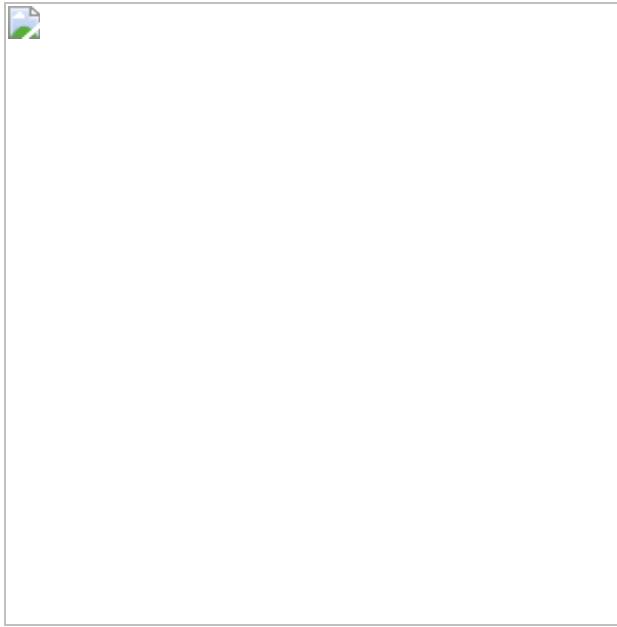
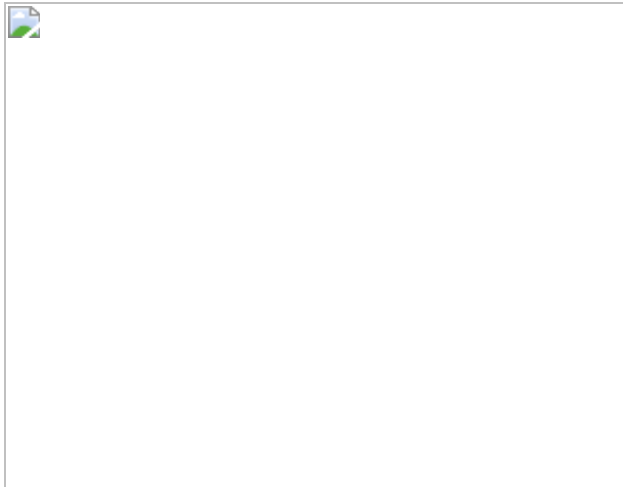


**Fig. 3: Cryo-electron microscopy structure of the SR synaptic complex.**



**Fig. 4: Structural transition from the LR to the SR synaptic complex.**



## Data availability

Cryo-EM density maps have been deposited in the Electron Microscopy Data Bank under accession numbers [EMD-23510](#) (overall LR complex), [EMD-23511](#) (DNA-PK-N-BRCT in the LR complex), [EMD-23512](#) (LigIV–XRCC4–XLF–XRCC4–LigIV in the LR complex), [EMD-23509](#) (overall SR complex), [EMD-23513](#) (distal Ku–LigIV catalytic domain in the SR complex), [EMD-23514](#) (proximal Ku in the SR complex) and [EMD-23515](#) (LigIV–XRCC4–XLF–XRCC4–LigIV in the SR complex). Model coordinates have been deposited in the Protein Data Bank under accession numbers [7LT3](#) (the LR complex) and [7LSY](#) (the SR complex).

## References

1. 1.

Aplan, P. D. Causes of oncogenic chromosomal translocation. *Trends Genet.* **22**, 46–55 (2006).

[CAS](#) [PubMed](#) [Google Scholar](#)

2. 2.

Zhao, B., Rothenberg, E., Ramsden, D. A. & Lieber, M. R. The molecular basis and disease relevance of non-homologous DNA end

joining. *Nat. Rev. Mol. Cell Biol.* **21**, 765–781 (2020).

[CAS](#) [PubMed](#) [Google Scholar](#)

3. 3.

Malu, S., Malshetty, V., Francis, D. & Cortes, P. Role of non-homologous end joining in V(D)J recombination. *Immunol. Res.* **54**, 233–246 (2012).

[PubMed](#) [Google Scholar](#)

4. 4.

Gottlieb, T. M. & Jackson, S. P. The DNA-dependent protein kinase: requirement for DNA ends and association with Ku antigen. *Cell* **72**, 131–142 (1993).

[CAS](#) [PubMed](#) [Google Scholar](#)

5. 5.

Yin, X., Liu, M., Tian, Y., Wang, J. & Xu, Y. Cryo-EM structure of human DNA-PK holoenzyme. *Cell Res.* **27**, 1341–1350 (2017).

[CAS](#) [PubMed](#) [PubMed Central](#) [Google Scholar](#)

6. 6.

Mari, P.-O. et al. Dynamic assembly of end-joining complexes requires interaction between Ku70/80 and XRCC4. *Proc. Natl Acad. Sci. USA* **103**, 18597–18602 (2006).

[ADS](#) [CAS](#) [PubMed](#) [Google Scholar](#)

7. 7.

Yano, K. & Chen, D. J. Live cell imaging of XLF and XRCC4 reveals a novel view of protein assembly in the non-homologous end-joining

pathway. *Cell Cycle* **7**, 1321–1325 (2008).

[CAS](#) [PubMed](#) [Google Scholar](#)

8. 8.

DeFazio, L. G., Stansel, R. M., Griffith, J. D. & Chu, G. Synapsis of DNA ends by DNA-dependent protein kinase. *EMBO J.* **21**, 3192–3200 (2002).

[CAS](#) [PubMed](#) [PubMed Central](#) [Google Scholar](#)

9. 9.

Chen, L., Trujillo, K., Sung, P. & Tomkinson, A. E. Interactions of the DNA ligase IV-XRCC4 complex with DNA ends and the DNA-dependent protein kinase. *J. Biol. Chem.* **275**, 26196–26205 (2000).

[CAS](#) [PubMed](#) [Google Scholar](#)

10. 10.

Ramsden, D. A. & Gellert, M. Ku protein stimulates DNA end joining by mammalian DNA ligases: a direct role for Ku in repair of DNA double-strand breaks. *EMBO J.* **17**, 609–614 (1998).

[CAS](#) [PubMed](#) [PubMed Central](#) [Google Scholar](#)

11. 11.

Riballo, E. et al. XLF-Cernunnos promotes DNA ligase IV-XRCC4 re-adenylation following ligation. *Nucleic Acids Res.* **37**, 482–492 (2009).

[CAS](#) [PubMed](#) [Google Scholar](#)

12. 12.

Andres, S. N. et al. A human XRCC4-XLF complex bridges DNA. *Nucleic Acids Res.* **40**, 1868–1878 (2012).

[CAS](#) [PubMed](#) [PubMed Central](#) [Google Scholar](#)

13. 13.

Lees-Miller, S. P., Chen, Y. R. & Anderson, C. W. Human cells contain a DNA-activated protein kinase that phosphorylates simian virus 40 T antigen, mouse p53, and the human Ku autoantigen. *Mol. Cell. Biol.* **10**, 6472–6481 (1990).

[CAS](#) [PubMed](#) [PubMed Central](#) [Google Scholar](#)

14. 14.

Meek, K., Douglas, P., Cui, X., Ding, Q. & Lees-Miller, S. P. *trans* Autophosphorylation at DNA-dependent protein kinase's two major autophosphorylation site clusters facilitates end processing but not end joining. *Mol. Cell. Biol.* **27**, 3881–3890 (2007).

[CAS](#) [PubMed](#) [PubMed Central](#) [Google Scholar](#)

15. 15.

Uematsu, N. et al. Autophosphorylation of DNA-PK<sub>CS</sub> regulates its dynamics at DNA double-strand breaks. *J. Cell Biol.* **177**, 219–229 (2007).

[CAS](#) [PubMed](#) [PubMed Central](#) [Google Scholar](#)

16. 16.

Mahaney, B. L., Hammel, M., Meek, K., Tainer, J. A. & Lees-Miller, S. P. XRCC4 and XLF form long helical protein filaments suitable for DNA end protection and alignment to facilitate DNA double strand break repair. *Biochem. Cell Biol.* **91**, 31–41 (2013).

[CAS](#) [PubMed](#) [PubMed Central](#) [Google Scholar](#)

17. 17.

Chang, H. H. Y. et al. Different DNA end configurations dictate which NHEJ components are most important for joining efficiency. *J. Biol. Chem.* **291**, 24377–24389 (2016).

[CAS](#) [PubMed](#) [PubMed Central](#) [Google Scholar](#)

18. 18.

Conlin, M. P. et al. DNA ligase IV guides end-processing choice during nonhomologous end joining. *Cell Rep.* **20**, 2810–2819 (2017).

[CAS](#) [PubMed](#) [PubMed Central](#) [Google Scholar](#)

19. 19.

Zhao, B. et al. The essential elements for the noncovalent association of two DNA ends during NHEJ synapsis. *Nat. Commun.* **10**, 3588 (2019).

[ADS](#) [PubMed](#) [PubMed Central](#) [Google Scholar](#)

20. 20.

Sibanda, B. L., Chirgadze, D. Y., Ascher, D. B. & Blundell, T. L. DNA-PKcs structure suggests an allosteric mechanism modulating DNA double-strand break repair. *Science* **355**, 520–524 (2017).

[ADS](#) [CAS](#) [PubMed](#) [Google Scholar](#)

21. 21.

Sharif, H. et al. Cryo-EM structure of the DNA-PK holoenzyme. *Proc. Natl Acad. Sci. USA* **114**, 7367–7372 (2017).

[CAS](#) [PubMed](#) [Google Scholar](#)

22. 22.

Walker, J. R., Corpina, R. A. & Goldberg, J. Structure of the Ku heterodimer bound to DNA and its implications for double-strand break repair. *Nature* **412**, 607–614 (2001).

[ADS](#) [CAS](#) [PubMed](#) [Google Scholar](#)

23. 23.

Andres, S. N., Modesti, M., Tsai, C. J., Chu, G. & Junop, M. S. Crystal structure of human XLF: a twist in nonhomologous DNA end-joining. *Mol. Cell* **28**, 1093–1101 (2007).

[CAS](#) [PubMed](#) [Google Scholar](#)

24. 24.

Wu, P.-Y. et al. Structural and functional interaction between the human DNA repair proteins DNA ligase IV and XRCC4. *Mol. Cell. Biol.* **29**, 3163–3172 (2009).

[CAS](#) [PubMed](#) [PubMed Central](#) [Google Scholar](#)

25. 25.

Kaminski, A. M. et al. Structures of DNA-bound human ligase IV catalytic core reveal insights into substrate binding and catalysis. *Nat. Commun.* **9**, 2642 (2018).

[ADS](#) [PubMed](#) [PubMed Central](#) [Google Scholar](#)

26. 26.

Graham, T. G. W., Walter, J. C. & Loparo, J. J. Two-Stage synapsis of DNA ends during non-homologous end joining. *Mol. Cell* **61**, 850–858 (2016).

[CAS](#) [PubMed](#) [PubMed Central](#) [Google Scholar](#)

27. 27.

Graham, T. G. W., Carney, S. M., Walter, J. C. & Loparo, J. J. A single XLF dimer bridges DNA ends during nonhomologous end joining. *Nat. Struct. Mol. Biol.* **25**, 877–884 (2018).

[CAS](#) [PubMed](#) [PubMed Central](#) [Google Scholar](#)

28. 28.

Carney, S. M. et al. XLF acts as a flexible connector during non-homologous end joining. *eLife* **9**, e61920 (2020).

[CAS](#) [PubMed](#) [PubMed Central](#) [Google Scholar](#)

29. 29.

Nemoz, C. et al. XLF and APLF bind Ku80 at two remote sites to ensure DNA repair by non-homologous end joining. *Nat. Struct. Mol. Biol.* **25**, 971–980 (2018).

[CAS](#) [PubMed](#) [PubMed Central](#) [Google Scholar](#)

30. 30.

Chaplin, A. K. et al. Dimers of DNA-PK create a stage for DNA double-strand break repair. *Nat. Struct. Mol. Biol.* **28**, 13–19 (2021).

[CAS](#) [PubMed](#) [Google Scholar](#)

31. 31.

Andres, S. N. & Junop, M. S. Crystallization and preliminary X-ray diffraction analysis of the human XRCC4-XLF complex. *Acta Crystallogr. F* **67**, 1399–1402 (2011).

[CAS](#) [Google Scholar](#)

32. 32.

Ropars, V. et al. Structural characterization of filaments formed by human XRCC4-Cernunnos/XLF complex involved in nonhomologous DNA end-joining. *Proc. Natl Acad. Sci. USA* **108**, 12663–12668 (2011).

[ADS](#) [CAS](#) [PubMed](#) [Google Scholar](#)

33. 33.

Hammel, M. et al. XRCC4 protein interactions with XRCC4-like factor (XLF) create an extended grooved scaffold for DNA ligation and double strand break repair. *J. Biol. Chem.* **286**, 32638–32650 (2011).

[CAS](#) [PubMed](#) [PubMed Central](#) [Google Scholar](#)

34. 34.

Doré, A. S. et al. Structure of an Xrcc4-DNA ligase IV yeast ortholog complex reveals a novel BRCT interaction mode. *DNA Repair* **5**, 362–368 (2006).

[PubMed](#) [Google Scholar](#)

35. 35.

Costantini, S., Woodbine, L., Andreoli, L., Jeggo, P. A. & Vindigni, A. Interaction of the Ku heterodimer with the DNA ligase IV/Xrcc4 complex and its regulation by DNA-PK. *DNA Repair* **6**, 712–722 (2007).

[CAS](#) [PubMed](#) [Google Scholar](#)

36. 36.

Normanno, D. et al. Mutational phospho-mimicry reveals a regulatory role for the XRCC4 and XLF C-terminal tails in modulating DNA bridging during classical non-homologous end joining. *eLife* **6**, e22900 (2017).

[PubMed](#) [PubMed Central](#) [Google Scholar](#)

37. 37.

Tate, J. G. et al. COSMIC: the Catalogue Of Somatic Mutations In Cancer. *Nucleic Acids Res.* **47**, D941–D947 (2019).

[CAS](#) [PubMed](#) [Google Scholar](#)

38. 38.

Lees-Miller, J. P. et al. Uncovering DNA-PKcs ancient phylogeny, unique sequence motifs and insights for human disease. *Prog. Biophys. Mol. Biol.* <https://doi.org/10.1016/j.pbiomolbio.2020.09.010> (2020).

39. 39.

Chen, X. et al. Structure of an activated DNA-PK and its implications for NHEJ. *Mol. Cell* **81**, 801–810 (2021).

[CAS](#) [PubMed](#) [Google Scholar](#)

40. 40.

Yang, H. et al. mTOR kinase structure, mechanism and regulation. *Nature* **497**, 217–223 (2013).

[ADS](#) [CAS](#) [PubMed](#) [PubMed Central](#) [Google Scholar](#)

41. 41.

Bao, Z. Q., Jacobsen, D. M. & Young, M. A. Briefly bound to activate: transient binding of a second catalytic magnesium activates the structure and dynamics of CDK2 kinase for catalysis. *Structure* **19**, 675–690 (2011).

[CAS](#) [PubMed](#) [PubMed Central](#) [Google Scholar](#)

42. 42.

Baretić, D. et al. Structures of closed and open conformations of dimeric human ATM. *Sci. Adv.* **3**, e1700933 (2017).

[ADS](#) [PubMed](#) [PubMed Central](#) [Google Scholar](#)

43. 43.

Rao, Q. et al. Cryo-EM structure of human ATR-ATRIP complex. *Cell Res.* **28**, 143–156 (2018).

[CAS](#) [PubMed](#) [Google Scholar](#)

44. 44.

Hammel, M. et al. An intrinsically disordered APLF links Ku, DNA-PKcs, and XRCC4-DNA ligase IV in an extended flexible non-homologous end joining complex. *J. Biol. Chem.* **291**, 26987–27006 (2016).

[CAS](#) [PubMed](#) [PubMed Central](#) [Google Scholar](#)

45. 45.

Pryor, J. M. et al. Ribonucleotide incorporation enables repair of chromosome breaks by nonhomologous end joining. *Science* **361**, 1126–1129 (2018).

[ADS](#) [CAS](#) [PubMed](#) [PubMed Central](#) [Google Scholar](#)

46. 46.

Riballo, E. et al. Cellular and biochemical impact of a mutation in DNA ligase IV conferring clinical radiosensitivity. *J. Biol. Chem.* **276**, 31124–31132 (2001).

[CAS](#) [PubMed](#) [Google Scholar](#)

47. 47.

Wang, Y., Lamarche, B. J. & Tsai, M.-D. Human DNA ligase IV and the ligase IV/XRCC4 complex: analysis of nick ligation fidelity. *Biochemistry* **46**, 4962–4976 (2007).

[CAS](#) [PubMed](#) [Google Scholar](#)

48. 48.

Tsai, C. J., Kim, S. A. & Chu, G. Cernunnos/XLF promotes the ligation of mismatched and noncohesive DNA ends. *Proc. Natl Acad. Sci. USA* **104**, 7851–7856 (2007).

[ADS](#) [CAS](#) [PubMed](#) [Google Scholar](#)

49. 49.

Gerodimos, C. A., Chang, H. H. Y., Watanabe, G. & Lieber, M. R. Effects of DNA end configuration on XRCC4-DNA ligase IV and its stimulation of Artemis activity. *J. Biol. Chem.* **292**, 13914–13924 (2017).

[CAS](#) [PubMed](#) [PubMed Central](#) [Google Scholar](#)

50. 50.

Stinson, B. M., Moreno, A. T., Walter, J. C. & Loparo, J. J. A mechanism to minimize errors during non-homologous end joining. *Mol. Cell* **77**, 1080–1091 (2020).

[CAS](#) [PubMed](#) [Google Scholar](#)

51. 51.

Kysela, B. et al. Ku stimulation of DNA ligase IV-dependent ligation requires inward movement along the DNA molecule. *J. Biol. Chem.* **278**, 22466–22474 (2003).

[CAS](#) [PubMed](#) [Google Scholar](#)

52. 52.

Goodarzi, A. A. & Lees-Miller, S. P. Biochemical characterization of the ataxia-telangiectasia mutated (ATM) protein from human cells. *DNA Repair* **3**, 753–767 (2004).

[CAS](#) [PubMed](#) [Google Scholar](#)

53. 53.

Yu, Y. et al. DNA-PK and ATM phosphorylation sites in XLF/Cernunnos are not required for repair of DNA double strand breaks. *DNA Repair* **7**, 1680–1692 (2008).

[CAS](#) [PubMed](#) [PubMed Central](#) [Google Scholar](#)

54. 54.

Han, Y., Reyes, A. A., Malik, S. & He, Y. Cryo-EM structure of SWI/SNF complex bound to a nucleosome. *Nature* **579**, 452–455 (2020).

[ADS](#) [CAS](#) [PubMed](#) [PubMed Central](#) [Google Scholar](#)

55. 55.

Patel, A., Toso, D., Litvak, A. & Nogales, E. Efficient graphene oxide coating improves cryo-EM sample preparation and data collection from tilted grids. Preprint at <https://doi.org/10.1101/2021.03.08.434344> (2021).

56. 56.

Suloway, C. et al. Automated molecular microscopy: the new Leginon system. *J. Struct. Biol.* **151**, 41–60 (2005).

[CAS](#) [Google Scholar](#)

57. 57.

Mastronarde, D. N. Automated electron microscope tomography using robust prediction of specimen movements. *J. Struct. Biol.* **152**, 36–51 (2005).

[PubMed](#) [PubMed Central](#) [Google Scholar](#)

58. 58.

Lander, G. C. et al. Appion: an integrated, database-driven pipeline to facilitate EM image processing. *J. Struct. Biol.* **166**, 95–102 (2009).

[CAS](#) [PubMed](#) [PubMed Central](#) [Google Scholar](#)

59. 59.

Voss, N. R., Yoshioka, C. K., Radermacher, M., Potter, C. S. & Carragher, B. DoG Picker and TiltPicker: software tools to facilitate particle selection in single particle electron microscopy. *J. Struct. Biol.* **166**, 205–213 (2009).

[CAS](#) [PubMed](#) [PubMed Central](#) [Google Scholar](#)

60. 60.

Mindell, J. A. & Grigorieff, N. Accurate determination of local defocus and specimen tilt in electron microscopy. *J. Struct. Biol.* **142**, 334–347 (2003).

[PubMed](#) [Google Scholar](#)

61. 61.

van Heel, M., Harauz, G., Orlova, E. V., Schmidt, R. & Schatz, M. A new generation of the IMAGIC image processing system. *J. Struct. Biol.* **116**, 17–24 (1996).

[PubMed](#) [Google Scholar](#)

62. 62.

Tang, G. et al. EMAN2: an extensible image processing suite for electron microscopy. *J. Struct. Biol.* **157**, 38–46 (2007).

[CAS](#) [PubMed](#) [Google Scholar](#)

63. 63.

Punjani, A., Rubinstein, J. L., Fleet, D. J. & Brubaker, M. A. cryoSPARC: algorithms for rapid unsupervised cryo-EM structure determination. *Nat. Methods* **14**, 290–296 (2017).

[CAS](#) [Google Scholar](#)

64. 64.

Kimanius, D., Forsberg, B. O., Scheres, S. H. W. & Lindahl, E. Accelerated cryo-EM structure determination with parallelisation using GPUs in RELION-2. *eLife* **5**, e18722 (2016).

[PubMed](#) [PubMed Central](#) [Google Scholar](#)

65. 65.

Zhang, K. Gctf: real-time CTF determination and correction. *J. Struct. Biol.* **193**, 1–12 (2016).

[ADS](#) [CAS](#) [PubMed](#) [PubMed Central](#) [Google Scholar](#)

66. 66.

Rohou, A. & Grigorieff, N. CTFFIND4: fast and accurate defocus estimation from electron micrographs. *J. Struct. Biol.* **192**, 216–221 (2015).

[PubMed](#) [PubMed Central](#) [Google Scholar](#)

67. 67.

Scheres, S. H. W. & Chen, S. Prevention of overfitting in cryo-EM structure determination. *Nat. Methods* **9**, 853–854 (2012).

[CAS](#) [PubMed](#) [PubMed Central](#) [Google Scholar](#)

68. 68.

Zivanov, J. et al. New tools for automated high-resolution cryo-EM structure determination in RELION-3. *eLife* **7**, e42166 (2018).

[PubMed](#) [PubMed Central](#) [Google Scholar](#)

69. 69.

Kucukelbir, A., Sigworth, F. J. & Tagare, H. D. Quantifying the local resolution of cryo-EM density maps. *Nat. Methods* **11**, 63–65 (2014).

[CAS](#) [PubMed](#) [Google Scholar](#)

70. 70.

Pettersen, E. F. et al. UCSF Chimera—a visualization system for exploratory research and analysis. *J. Comput. Chem.* **25**, 1605–1612 (2004).

[CAS](#) [PubMed](#) [PubMed Central](#) [Google Scholar](#)

71. 71.

Sánchez-García, R. et al. DeepEMhacer: a deep learning solution for cryo-EM volume post-processing. Preprint at <https://doi.org/10.1101/2020.06.12.148296> (2020).

72. 72.

Emsley, P., Lohkamp, B., Scott, W. G. & Cowtan, K. Features and development of Coot. *Acta Crystallogr. D* **66**, 486–501 (2010).

[CAS](#) [PubMed](#) [Google Scholar](#)

73. 73.

Croll, T. I. ISOLDE: a physically realistic environment for model building into low-resolution electron-density maps. *Acta Crystallogr. D* **74**, 519–530 (2018).

[CAS](#) [Google Scholar](#)

74. 74.

Saltzberg, D. J. et al. SSEThread: integrative threading of the DNA-PKcs sequence based on data from chemical cross-linking and hydrogen deuterium exchange. *Prog. Biophys. Mol. Biol.* **147**, 92–102 (2019).

[CAS](#) [PubMed](#) [PubMed Central](#) [Google Scholar](#)

75. 75.

Hepburn, M. et al. The active DNA-PK holoenzyme occupies a tensed state in a staggered synaptic complex. *Structure* <https://doi.org/10.1016/j.str.2020.12.006> (2021).

76. 76.

Yang, J. et al. Improved protein structure prediction using predicted interresidue orientations. *Proc. Natl Acad. Sci. USA* **117**, 1496–1503 (2020).

[CAS](#) [PubMed](#) [Google Scholar](#)

77. 77.

Afonine, P. V. et al. Real-space refinement in PHENIX for cryo-EM and crystallography. *Acta Crystallogr. D* **74**, 531–544 (2018).

[CAS](#) [Google Scholar](#)

78. 78.

Chang, H. H. Y., Watanabe, G. & Lieber, M. R. Unifying the DNA end-processing roles of the Artemis nuclease: Ku-dependent Artemis resection at blunt DNA ends. *J. Biol. Chem.* **290**, 24036–24050 (2015).

[CAS](#) [PubMed](#) [PubMed Central](#) [Google Scholar](#)

[Download references](#)

## Acknowledgements

We thank J. Pattie for computer support, J. Meyers, R. M. Haynes and H. Scott at the PNCC for data collection support, D. Ramsden for the gift of a rabbit anti-phosphoT2609 reagent, A. Rosenzweig and I. Radhakrishnan for discussion and comments on the manuscript. This work was supported by a Cornew Innovation Award from the Chemistry of Life Processes Institute at Northwestern University (to Y.H.), a Catalyst Award by the Chicago Biomedical Consortium with support from the Searle Funds at The Chicago Community Trust (to Y.H.), an Institutional Research Grant from the American Cancer Society (IRG-15-173-21 to Y.H.), an H Foundation Core Facility Pilot Project Award (to Y.H.), a Pilot Project Award under U54CA193419 (to Y.H.) and NIH grant R01 GM135651 (to Y.H.). S.C. is supported by the Molecular Biophysics Training Program from NIGMS/NIH (5T32 GM008382). A portion of this research was supported by NIH grant U24GM129547 and performed at the PNCC at OHSU and accessed through EMSL (grid.436923.9), a DOE Office of Science User Facility sponsored by the Office of Biological and Environmental Research. This work used the Sapphire imager from the Northwestern University Keck Biophysics Facility funded by NIH grant 1S10OD026963-01, as well as the resources of the Northwestern University Structural Biology Facility, which is generously supported by NCI CCSG P30 CA060553 grant awarded to the Robert H. Lurie Comprehensive Cancer Center. The Gatan K2 direct electron detector was purchased with funds provided by the Chicago Biomedical Consortium with support from the Searle Funds at The Chicago Community Trust. Work in the Lees-Miller laboratory was supported by Canadian Institutes of Health grant 16939 and the Engineered Air Chair in Cancer Research. Work in the Tomkinson laboratory was supported by NIH grant R01GM047251, as well as the University of New

Mexico Comprehensive Cancer Center supported by NCI CCSG P30 CA118100 grant. The collaboration between the He, Lees-Miller and Tomkinson laboratories was supported by NCI P01 CA092584.

## Author information

### Affiliations

1. Department of Molecular Biosciences, Northwestern University, Evanston, IL, USA

Siyu Chen, Susan Fishbain, Annie Wang & Yuan He

2. Interdisciplinary Biological Sciences Program, Northwestern University, Evanston, IL, USA

Siyu Chen & Yuan He

3. Department of Biochemistry and Molecular Biology, University of Calgary, Calgary, Alberta, Canada

Linda Lee & Susan P. Lees-Miller

4. Robson DNA Science Centre, Charbonneau Cancer Institute, University of Calgary, Calgary, Alberta, Canada

Linda Lee & Susan P. Lees-Miller

5. Department of Internal Medicine, University of New Mexico, Albuquerque, NM, USA

Tasmin Naila & Alan E. Tomkinson

6. Department of Molecular Genetics & Microbiology, University of New Mexico, Albuquerque, NM, USA

Tasmin Naila & Alan E. Tomkinson

7. University of New Mexico Comprehensive Cancer Center, University of New Mexico, Albuquerque, NM, USA

Tasmin Naila & Alan E. Tomkinson

8. Chemistry of Life Processes Institute, Northwestern University, Evanston, IL, USA

Yuan He

9. Robert H. Lurie Comprehensive Cancer Center of Northwestern University, Northwestern University, Chicago, IL, USA

Yuan He

## Authors

1. Siyu Chen

[View author publications](#)

You can also search for this author in [PubMed](#) [Google Scholar](#)

2. Linda Lee

[View author publications](#)

You can also search for this author in [PubMed](#) [Google Scholar](#)

3. Tasmin Naila

[View author publications](#)

You can also search for this author in [PubMed](#) [Google Scholar](#)

4. Susan Fishbain

[View author publications](#)

You can also search for this author in [PubMed](#) [Google Scholar](#)

5. Annie Wang

[View author publications](#)

You can also search for this author in [PubMed](#) [Google Scholar](#)

6. Alan E. Tomkinson

[View author publications](#)

You can also search for this author in [PubMed](#) [Google Scholar](#)

7. Susan P. Lees-Miller

[View author publications](#)

You can also search for this author in [PubMed](#) [Google Scholar](#)

8. Yuan He

[View author publications](#)

You can also search for this author in [PubMed](#) [Google Scholar](#)

## Contributions

Y.H., S.P.L.-M. and A.E.T. conceived the project. S.C. performed most of the experiments and collected and analysed cryo-EM data with Y.H. L.L. and T.N. contributed to protein purification. S.C. built the models with help from Y.H. S.C., S.F., A.W. and Y.H. wrote the manuscript with input from all other authors.

## Corresponding author

Correspondence to [Yuan He](#).

## Ethics declarations

## Competing interests

The authors declare no competing interests.

## Additional information

**Peer review information** *Nature* thanks the anonymous reviewers for their contribution to the peer review of this work. Peer reviewer reports are available.

**Publisher's note** Springer Nature remains neutral with regard to jurisdictional claims in published maps and institutional affiliations.

## Extended data figures and tables

### [Extended Data Fig. 1 Optimization of the LR synaptic complex assembly with various DNA substrates.](#)

**a**, Schematic showing the Y35 blunt-end DNA substrate. Complex assembly was attempted (supplying DNA-PKcs, Ku, XLF and LigIV–XRCC4) before purification by RNase H elution. **b**, A representative negative-staining raw micrograph of the complex assembled as described in **a**. The raw micrograph is representative of 24 micrographs. **c**, Representative two-dimensional class averages of the complex assembled as described in **a**, showing the appearance of only the DNA-PK complex despite the addition of XLF and LigIV–XRCC4. **d–f**, Same procedure as **a–c**, showing the complex assembly with the same Y35 substrate, but adding XLF and LigIV–XRCC4 to the purified DNA-PK complex after RNase H elution. The raw micrograph is representative of 27 micrographs. In **f**, the two-dimensional class averages representing the characteristic view of scarce but existing LR complex were obtained. **g–i**, Same procedure as **a–c**, showing the complex assembly using Y30–T40–c8 DNA substrate with 40 nt flexible poly(T) and 8 bp of complementary ends as the 3' overhang. Although the single-stranded poly(T) overhang and the 8-bp complementary region contribute to the stability of the complex, they are not observed in any part of the reconstructed density map, presumably because these single-strand DNA tethers are too flexible to be aligned with the rest of the complex. The raw micrograph is representative of 24 micrographs. The complex was assembled before RNase H elution as described in **a**. In **i**, the majority of the two-dimensional classes correspond to the LR complex. **j**, A representative cryo-EM raw micrograph (out of 17,114 micrographs in total) of the LR complex assembled with the Y30–

T40–c8 DNA substrate shown in **g**. **k**, Representative two-dimensional class averages of particles (329,784 in total) contributing to the final reconstruction of the LR complex. **l**, Silver-stained SDS-PAGE (4–12% gradient, biologically replicated three times) showing the input purified subunits (Ku, DNA-PKcs, LigIV–XRCC4, and XLF) and the RNase H purified LR and SR complex for cryo-EM data collection. All representative micrographs in **b**, **e**, **h**, **j** are from at least three biologically replicated experiments. For gel source data, see Supplementary Fig. [1](#). **m**, Protein–protein interaction network between the components of the LR complex. Major unmodelled regions are shown in grey. Well-documented hetero- or homo-dimers are grouped by red dashed lines. Alternative protein–protein interactions are depicted by black dashed lines. The globular domain within the Ku80 C-terminal region (CTR) is completely flexible in the LR complex, and we do not see evidence of the Ku80 CTR domain swap that was previously observed<sup>[30](#)</sup>. The putative distance between one Ku80 CTR globular domain and the other copy of the Ku80 C-terminal helix is too far to be reached by the 18-amino acid linker within Ku80. BRCTs, tandem BRCT domains; CC, coiled-coil domain; CTD, C-terminal domain; HD, head domain; KD, kinase domain; M-HEAT, middle HEAT domain; N-HEAT, N-terminal HEAT domain; NTD, N-terminal domain; OBD, OB-fold domain.

### **Extended Data Fig. 2 Data-processing scheme of the LR synaptic complex sample.**

**a**, Flow chart of the cryo-EM data processing procedure. The gold-standard Fourier shell correlation (FSC) curves (0.143 cut-off) show the final resolution of the holo-complex and each body. **b**, sample maps and fitted models of DNA-PKcs (olive) and dsDNA substrate (cyan) from the LR complex are shown at 4.1 Å resolution. Maps are shown as transparent surfaces and models are shown as sticks.

### **Extended Data Fig. 3 Comparing the structure of Ku among the LR synaptic complex, the SR synaptic complex and previously published models.**

**a**, Ku structure in the LR complex showing outward rotations of both Ku70 and Ku80 vWA domains. **b**, Crystal structure of the XLF Ku-binding motif (KBM) bound to Ku showing the outward rotation of only the Ku80 vWA domain<sup>29</sup>. **c**, Crystal structure of apo Ku showing no rotation of either Ku70 or Ku80 vWA domains<sup>22</sup>. **d**, Conformation of Ku shown in the cryo-EM structure of the apo DNA-PK complex<sup>30</sup>. The Ku70 vWA domain is rotated outward, triggered by binding of DNA-PKcs. **e**, **f**, Two copies of the XLF Ku-binding motif bound to Ku in the SR complex. The conformation of both copies is the same as the one in the LR complex (**a**), despite the fact that DNA-PKcs is not present. Colour codes for Ku70 and Ku80 are the same as in Fig. 1.

**Extended Data Fig. 4 Comparing the structure of the LigIV–XRCC4–XLF scaffold among the LR synaptic complex, the SR synaptic complex and previously published models.**

**a**, Structure of XRCC4–XLF from the LR complex is shown in comparison to the XRCC4–XLF filamentous repeat crystal structures and the ones from the SR complex (both copies). The XLF dimer is used to align all of the models shown here. Solid lines are aligned with the coiled-coils of XLF (vertical) and XRCC4 (tilted), and the angles in between are shown. Dashed lines are aligned with the C-terminal half of the coiled-coil domain of XRCC4 when full helices are present, and the bending angles are also shown. **b**, XRCC4 in the crystal structure of the human and yeast LigIV–XRCC4 complexes<sup>24,34</sup> are shown after aligning with XRCC4 in the LR complex shown in **a**. The bending of the coiled-coil domain of XRCC4 is more similar to the one in the SR than in the LR complex. **c**, Structure of the LigIV–XRCC4 complex from the LR complex is shown in comparison to human and yeast LigIV–XRCC4 crystal structures and ones from the SR complex (both copies). Colour codes for XLF, XRCC4 and LigIV BRCT domains are the same as in Fig. 1.

**Extended Data Fig. 5 Surface electrostatic potential and conservation of different areas in the LR synaptic complex.**

**a**, Magnified view of the interaction surface between LigIV N-BRCT domain and Ku70 vWA domains coloured by sequence conservation. **b**, Magnified view of the DNA-PKcs–DNA-PKcs interaction surface coloured by sequence conservation. **c**, Surface electrostatic potential view of DNA-PKcs near its FAT domain, showing its negatively charged interface with the XRCC4 C-terminal region (ribbon). The approximate path of the XRCC4 C-terminal peptide containing multiple phosphorylation sites is depicted. The sphere depicts the location of a cancer-associated truncation mutation that occurs at the interface. **d**, Surface electrostatic potential view of DNA-PKcs DEB and DEB-A helix. The DNA-interaction surface is positively charged. When models are not coloured by either surface electrostatic potential or sequence conservation, the colour codes are the same as in Fig. 1. We cannot rule out the unlikely possibility that the stabilization of the DEB helix is due to the presence of a 3' overhang that existed in our DNA substrate design (Extended Data Fig. 1g).

### Extended Data Fig. 6 Comparing the dimerization of DNA-PKcs in the LR synaptic complex with other PIKK family dimers.

**a**, Structure of the two DNA-PKcs in the LR complex. The kinase domain is aligned with the homologous domains in **b** and **c** as an anchor point. **b**, **c**, Dimer of ATR–ATRIP (**b**) and ATM (**c**) showing the aligned kinase domain and corresponding N-HEAT regions in the aligned copy. The symmetric-look front views are shown at the bottom left corner. Each protomer of ATR–ATRIP and ATM is coloured the same as the corresponding DNA-PKcs protomer, in olive (the aligned copy) and dark khaki (the other copy). **d**, Domain organization of DNA-PKcs compared with ATR and ATM. Abbreviations are as in Fig. 1. In our model, both the ABCDE (T2609, S2612, T2620, S2624, T2638 and T2647) and the PQR (S2023, S2029, S2041, S2053 and S2056) phosphorylation sites are located within disordered loops of DNA-PKcs 2606–2720 and 1993–2084, respectively (Fig. 2b,d). The kinase active centre from the opposite side cannot reach most of the ABCDE sites unless the YRPD-interaction (YRPD-I) loop (residues 2586–2604) is peeled off from the YRPD motif (Fig. 2d). In turn, this conformational change potentially disrupts the DNA-PKcs–DNA-PKcs dimerization interface through loop 2569–2585 (Fig. 1d). Similarly, some

PQR sites are located too far from the trans kinase active centre. PQR-autophosphorylation-induced changes could have a direct effect on the Ku80 CTR–DNA-PKcs interface at the bottom of the cradle (Fig. 2d), potentially inducing the domain swap of Ku80 that was previously observed<sup>30</sup>.

## Extended Data Fig. 7 Optimization of the SR synaptic complex assembly with various DNA substrates.

**a**, Schematic showing the Y30–c4 DNA substrate with 4-nt 3' complementary overhang. The complex was assembled before RNase H elution. **b**, A representative negative-staining raw micrograph of the complex assembled as described in **a**. The raw micrograph is representative of 23 micrographs. **c**, Representative two-dimensional class averages of the complex assembled as described in **a**. **d**, Cryo-EM map reconstructed from a small dataset using Y30–c4 DNA substrate shown in **a**. The map is coloured according to the estimation of the local resolution. **e–h**, Same procedure as **a–d**, showing the complex assembly with the Y30 blunt-end substrate. Stably assembled SR complexes on DNA substrates with either complementary or blunt ends indicates that these complexes are stable in the absence of any bridging effect from DNA. The raw micrograph is representative of 24 micrographs. **i–l**, Same procedure as **a–d**, showing the complex assembly with the Y14–T2–c20–n10–10 substrate, with one central single non-ligatable nick. The raw micrograph is representative of 24 micrographs. Strand e is added last after mixing the two halves together with NHEJ factors. **m**, A representative cryo-EM raw micrograph (out of 32,723 total images) of the SR complex assembled with the Y14–T2–c20–n10–10 DNA substrate shown in **i**. **n**, Representative two-dimensional class averages of particles (175,866 in total) contributing to the final reconstruction of the SR complex. All representative micrographs in **b, f, j, m** are from at least three biologically replicated experiments. **o**, Protein–protein interaction network between the components of the SR complex. Major unmodelled regions are shown in grey. Well-documented hetero- or homo-dimers are grouped by red dashed circles. Alternative protein–protein interactions are depicted by black dashed lines.

## Extended Data Fig. 8 Data-processing scheme of the SR synaptic complex sample.

Flow chart of the cryo-EM data processing procedure. The gold-standard Fourier shell correlation curves (0.143 cut-off) show the final resolution of the holo-complex and each body.

## Extended Data Fig. 9 Surface conservation of different areas in the SR synaptic complex.

**a**, Magnified view of the interaction surface between the LigIV DBD and Ku70 vWA domain coloured by sequence conservation. DNA-PKcs clashes with LigIV DBD when Ku is aligned between the LR and SR complex. **b**, Magnified view of the coiled-coil domain of XLF at its C-terminal tip coloured by sequence conservation. When models are not coloured by sequence conservation, the colour codes are the same as in Fig. 3. **c**, Superimposition of two asymmetric SR complexes after a 180° flip shown in front (top) and top (bottom) views. The XLF homodimer is used for aligning the two conformers. LigIV catalytic domains are hidden for clarity purposes. The transition from the apo state to the flipped state indicates potential conformational changes during the tandem ligation. Paths of DNA are also highlighted by dashed lines. **d**, Magnified view showing the relative positions of the two off-centred nicks between the two conformers. The two preferential nick positions are separated by approximately 4 bp. Consistently, dsDNA with 4-nt 3' overhang, a major end-processing product of the NHEJ nuclease Artemis<sup>78</sup>, is reported to be a favoured substrate for NHEJ<sup>50</sup>. Our model suggests that dsDNA with a 4-nt 3' overhang will experience minimum DNA translocation to accommodate the two ligation steps (Supplementary Video 3).

## Extended Data Fig. 10 Both LR and SR synaptic complexes are able to perform double ligation during NHEJ in vitro.

**a**, Substrate design for the ligation assay. An internal Cy5 label is added to only the right half of the substrate to visualize the ligation products. A 4-nt 3' complementary overhang has been introduced on both sides of the

substrate. **b**, Denaturing gel analysis of end joining by the LR complex. The reaction comprised 100 nM of DNA, 200 nM of DNA-PKcs and Ku70/80, 500 nM of XLF and 70 nM of X4L4. The asterisk indicates an alternative secondary structure or impurity of the Cy5-labelled oligomer. The size of the DNA substrates and ligation products are labelled on the left (unit: bp). **c**, Denaturing gel analysis of end joining by the SR complex. The final factor concentrations are the same as in **b**. For gel source data, see Supplementary Fig. 1. Similar conditions for the gels have been replicated as biological replicates twice.

## Supplementary information

### [Supplementary Information](#)

This file contains Supplementary Tables 1-2 and Supplementary Figures 1-7.

### [Reporting Summary](#)

### [Peer Review File](#)

### [Video 1](#)

Density map and model fitting of the Long-range synaptic complex.

### [Video 2](#)

Density map and model fitting of the Short-range synaptic complex.

### [Video 3](#)

Model showing the conformational changes within the Short-range synaptic complex during the tandem ligation of two dsDNA nicks. DNA substrate with 4nt 3' overhang is used as the example.

### [Video 4](#)

Model showing the conformational changes during the transition from the Long-range to the Short-range synaptic state.

## Rights and permissions

[Reprints and Permissions](#)

## About this article



Check for  
updates

## Cite this article

Chen, S., Lee, L., Naila, T. *et al.* Structural basis of long-range to short-range synaptic transition in NHEJ. *Nature* **593**, 294–298 (2021).  
<https://doi.org/10.1038/s41586-021-03458-7>

[Download citation](#)

- Received: 18 December 2020
- Accepted: 15 March 2021
- Published: 14 April 2021
- Issue Date: 13 May 2021
- DOI: <https://doi.org/10.1038/s41586-021-03458-7>

## Comments

By submitting a comment you agree to abide by our [Terms](#) and [Community Guidelines](#). If you find something abusive or that does not comply with our terms or guidelines please flag it as inappropriate.

[Access through your institution](#)

[Change institution](#)

[Buy or subscribe](#)

---

This article was downloaded by **calibre** from <https://www.nature.com/articles/s41586-021-03458-7>

| [Section menu](#) | [Main menu](#) |

# Amendments & Corrections

- **[Author Correction: A 20-year retrospective review of global aquaculture](#)** [ 26 April 2021]  
Author Correction •
- **[Author Correction: Towards real-time photorealistic 3D holography with deep neural networks](#)** [ 26 April 2021]  
Author Correction •

Author Correction: A 20-year retrospective review of global aquaculture  
[Download PDF](#)

- Author Correction
- [Published: 26 April 2021](#)

# Author Correction: A 20-year retrospective review of global aquaculture

- [Rosamond L. Naylor](#) ORCID: [orcid.org/0000-0002-1260-3322<sup>1,2</sup>](https://orcid.org/0000-0002-1260-3322),
- [Ronald W. Hardy<sup>3</sup>](#),
- [Alejandro H. Buschmann](#) ORCID: [orcid.org/0000-0003-3246-681X<sup>4</sup>](https://orcid.org/0000-0003-3246-681X),
- [Simon R. Bush<sup>5</sup>](#),
- [Ling Cao<sup>6</sup>](#),
- [Dane H. Klinger](#) ORCID: [orcid.org/0000-0003-4178-8167<sup>7,8</sup>](https://orcid.org/0000-0003-4178-8167),
- [David C. Little<sup>9</sup>](#),
- [Jane Lubchenco](#) ORCID: [orcid.org/0000-0003-3540-5879<sup>10</sup>](https://orcid.org/0000-0003-3540-5879),
- [Sandra E. Shumway<sup>11</sup>](#) &
- [Max Troell](#) ORCID: [orcid.org/0000-0002-7509-8140<sup>12,13</sup>](https://orcid.org/0000-0002-7509-8140)

[Nature](#) volume 593, page E12 (2021)[Cite this article](#)

- 534 Accesses
- 4 Altmetric
- [Metrics details](#)

## Subjects

- [Environmental impact](#)

- [Environmental sciences](#)

The [Original Article](#) was published on 24 March 2021

A Correction to this paper has been published:  
<https://doi.org/10.1038/s41586-021-03508-0>.

[Download PDF](#)

Correction to: *Nature* <https://www.nature.com/articles/s41586-021-03308-6>  
Published online 24 March 2021

This Article should have included the following competing interests statement: ‘R.L.N. is a member of the Forest Protection Advisory Panel at Cargill, and the Center on Food Security and the Environment (FSE) has received funding from the Cargill Foundation for visiting scholars and staff support (but not for research). There has been no overlap between Cargill and research activities relating to aquaculture at the FSE’. The original Article has been corrected online.

## Author information

### Affiliations

1. Department of Earth System Science, Stanford University, Stanford, CA, USA

Rosamond L. Naylor

2. Center on Food Security and the Environment, Stanford University, Stanford, CA, USA

Rosamond L. Naylor

3. Aquaculture Research Institute, University of Idaho, Moscow, ID, USA

Ronald W. Hardy

4. Centro i-mar & CeBiB, Universidad de Los Lagos, Puerto Montt, Chile

Alejandro H. Buschmann

5. Environmental Policy Group, Wageningen University, Wageningen, The Netherlands

Simon R. Bush

6. School of Oceanography, Shanghai Jiao Tong University, Shanghai, China

Ling Cao

7. Center for Oceans, Conservation International, Arlington, VA, USA

Dane H. Klinger

8. Department of Nutrition, Harvard T. H. Chan School of Public Health, Boston, MA, USA

Dane H. Klinger

9. Institute of Aquaculture, University of Stirling, Stirling, UK

David C. Little

10. Department of Integrative Biology, Oregon State University, Corvallis, OR, USA

Jane Lubchenco

11. Department of Marine Sciences, University of Connecticut, Groton, CT, USA

Sandra E. Shumway

12. Beijer Institute, Royal Swedish Academy of Sciences, Stockholm, Sweden

Max Troell

13. Stockholm Resilience Centre, Stockholm University, Stockholm, Sweden

Max Troell

## Authors

1. Rosamond L. Naylor

[View author publications](#)

You can also search for this author in [PubMed](#) [Google Scholar](#)

2. Ronald W. Hardy

[View author publications](#)

You can also search for this author in [PubMed](#) [Google Scholar](#)

3. Alejandro H. Buschmann

[View author publications](#)

You can also search for this author in [PubMed](#) [Google Scholar](#)

4. Simon R. Bush

[View author publications](#)

You can also search for this author in [PubMed](#) [Google Scholar](#)

5. Ling Cao

[View author publications](#)

You can also search for this author in [PubMed](#) [Google Scholar](#)

6. Dane H. Klinger

[View author publications](#)

You can also search for this author in [PubMed](#) [Google Scholar](#)

7. David C. Little

[View author publications](#)

You can also search for this author in [PubMed](#) [Google Scholar](#)

8. Jane Lubchenco

[View author publications](#)

You can also search for this author in [PubMed](#) [Google Scholar](#)

9. Sandra E. Shumway

[View author publications](#)

You can also search for this author in [PubMed](#) [Google Scholar](#)

10. Max Troell

[View author publications](#)

You can also search for this author in [PubMed](#) [Google Scholar](#)

## Corresponding author

Correspondence to [Rosamond L. Naylor](#).

## Rights and permissions

[Reprints and Permissions](#)

## About this article



Check for  
updates

## Cite this article

Naylor, R.L., Hardy, R.W., Buschmann, A.H. *et al.* Author Correction: A 20-year retrospective review of global aquaculture. *Nature* **593**, E12 (2021). <https://doi.org/10.1038/s41586-021-03508-0>

[Download citation](#)

- Published: 26 April 2021
- Issue Date: 13 May 2021
- DOI: <https://doi.org/10.1038/s41586-021-03508-0>

## Comments

By submitting a comment you agree to abide by our [Terms](#) and [Community Guidelines](#). If you find something abusive or that does not comply with our terms or guidelines please flag it as inappropriate.

[Download PDF](#)

---

This article was downloaded by **calibre** from <https://www.nature.com/articles/s41586-021-03508-0>

Author Correction: Towards real-time photorealistic 3D holography with deep neural networks

[Download PDF](#)

- Author Correction
- [Published: 26 April 2021](#)

# Author Correction: Towards real-time photorealistic 3D holography with deep neural networks

- [Liang Shi](#) [ORCID: orcid.org/0000-0002-4442-4679<sup>1,2</sup>](#),
- [Beichen Li](#) [ORCID: orcid.org/0000-0002-9271-0055<sup>1,2</sup>](#),
- [Changil Kim<sup>1,2</sup>](#),
- [Petr Kellnhofer<sup>1,2</sup>](#) &
- [Wojciech Matusik](#) [ORCID: orcid.org/0000-0003-0212-5643<sup>1,2</sup>](#)

[Nature](#) volume 593, page E13 (2021) [Cite this article](#)

- 473 Accesses
- 12 Altmetric
- [Metrics details](#)

## Subjects

- [Computational science](#)
- [Computer science](#)
- [Displays](#)
- [Optical manipulation and tweezers](#)

The [Original Article](#) was published on 10 March 2021

[Download PDF](#)

Correction to: *Nature* <https://doi.org/10.1038/s41586-020-03152-0> Published online 10 March 2021

In Fig. 3a of this Article, the direction of the beamsplitter (transparent rectangle next to the spatial light modulator) was mistakenly drawn at 90° from its actual orientation. We clarify that the physical setup corresponding to the model in Fig. 3a that is shown in Extended Data Fig. 8 is correct. In addition, after equation (5), “where  $\Delta p$  is the SLM pixel pitch” should read “where  $\Delta p$  is the grating pitch (twice the SLM pixel pitch)”. This means that the minimal number of convolution layers required for the CNN to model our 3D scene should be halved from 30 to 15 (see ‘CNN small’ in Fig. 2d). The original Article has been corrected online.

## Author information

### Affiliations

1. Computer Science and Artificial Intelligence Laboratory,  
Massachusetts Institute of Technology, Cambridge, MA, USA

Liang Shi, Beichen Li, Changil Kim, Petr Kellnhofer & Wojciech Matusik

2. Electrical Engineering and Computer Science Department,  
Massachusetts Institute of Technology, Cambridge, MA, USA

Liang Shi, Beichen Li, Changil Kim, Petr Kellnhofer & Wojciech Matusik

### Authors

1. Liang Shi  
[View author publications](#)

You can also search for this author in [PubMed](#) [Google Scholar](#)

2. Beichen Li

[View author publications](#)

You can also search for this author in [PubMed](#) [Google Scholar](#)

3. Changil Kim

[View author publications](#)

You can also search for this author in [PubMed](#) [Google Scholar](#)

4. Petr Kellnhofer

[View author publications](#)

You can also search for this author in [PubMed](#) [Google Scholar](#)

5. Wojciech Matusik

[View author publications](#)

You can also search for this author in [PubMed](#) [Google Scholar](#)

## Corresponding authors

Correspondence to [Liang Shi](#) or [Wojciech Matusik](#).

## Rights and permissions

[Reprints and Permissions](#)

## About this article



Check for  
updates

## Cite this article

Shi, L., Li, B., Kim, C. *et al.* Author Correction: Towards real-time photorealistic 3D holography with deep neural networks. *Nature* **593**, E13 (2021). <https://doi.org/10.1038/s41586-021-03476-5>

### [Download citation](#)

- Published: 26 April 2021
- Issue Date: 13 May 2021
- DOI: <https://doi.org/10.1038/s41586-021-03476-5>

## Comments

By submitting a comment you agree to abide by our [Terms](#) and [Community Guidelines](#). If you find something abusive or that does not comply with our terms or guidelines please flag it as inappropriate.

### [Download PDF](#)

---

This article was downloaded by **calibre** from <https://www.nature.com/articles/s41586-021-03476-5>